Structure, emplacement and textural evolution of young obsidian lavas in the Aeolian Islands, Italy

Liam Adam Bullock

This thesis is submitted in accordance with the requirements of the University of Keele for the degree of Doctor of Philosophy

June 2015

Keele University

Abstract

Silicic volcanism defines the recent volcanic activity in the Aeolian Islands, Italy. Such activity on the islands of Lipari and Vulcano has generally involved an explosive phase, ending with viscous lava extrusion and a period of quiescence. This late effusive extrusion has resulted in a number of obsidian lava flows and domes.

Obsidian lavas on Lipari and Vulcano are texturally heterogeneous, and many of the young lava flows show signs of flow deformation associated with flow emplacement. Preservation of such textures and structures is important for the reconstruction of the structural and textural evolution of young obsidian lava flows, in the Aeolian Islands lavas and elsewhere. Models of emplacement of obsidian lavas are still relatively limited, and there is still a need for a detailed model for obsidian lava flow emplacement. Questions also remain regarding spherulite formation in obsidian lavas, including when spherulites begin to form, over what timescale, and their relationship to deformation. Obsidian flows on Lipari and Vulcano exhibit a number of textures relating to both magmatic and post-magmatic processes. These textures provide an opportunity to build a model that categorises textural evolution in an active volcanic setting.

This study incorporates a number of petrographic, geochemical and textural methods in order to fully characterise the structure, emplacement and textural evolution of young obsidian lavas in the Aeolian Islands. The findings contribute towards our understanding of silicic volcanism in the Aeolian Islands, our overall understanding of obsidian lava flow emplacement and spherulite formation, and the complex structural and textural relationships within obsidian lavas.

Acknowledgements

I would like to thank my supervisors, Dr Ralf Gertisser and Dr Brian O'Driscoll, for giving me the opportunity to do this PhD, their continued support, advice, knowledge, patience and critique for the duration of my project. I would like to thank them for all their help with field and laboratory work, their constant availability despite their own high workloads, and keeping me on track throughout. Thanks to their support this project has been most fulfilling and highly enjoyable.

I would also like to thank my research institute the Environment, Physical Sciences & Applied Mathematics (EPSAM) for its financial support and open access to facilities. I would like to thank Richard Burgess, David Emley, Ian Wilshaw, Andy Lawrence, Peter Greatbatch and David Wilde for their technical support and their friendly approach. I wish to gratefully acknowledge Andy Tindle (The Open University) for his assistance with electron microprobe analyses; I thank Dr Richard Darton, Prof Alun Vaughan and Nicola Freebody (University of Southampton) for their assistance with laser Raman spectroscopy and offering a different perspective on my project, and David Evans for his assistance with x-ray diffraction analyses. My appreciation also goes to my fellow post-graduates in the School of Physical and Geographical Sciences, with a special thanks to my fellow Keele Petrology Group postgraduate member Adam Jeffery for his time and input. I would also like to thank the Mineralogical Society, the Volcanic and Magmatic Studies Group and the Keele Postgraduate Association for additional financial support.

Special thanks go to my field assistants, Leanne Patrick, James Watling and April Fitzgerald. I wish to thank the many helpful and friendly people I met in Lipari, particularly Marco Mazza for offering me his apartment for weeks at a time during the summer tourist season, and assisting me in sending my many boxes of obsidian back from the Aeolian Islands to Keele. I would also like to thank Holly Ellson for helping me out during the 2012 fieldwork season with my compass clinometer-based emergency.

Finally, I would like to thank my dad Dave, my brother David, my aunt Josie, my close friends Jack Ford, Lianne Joynson and Tom Cooper for their emotional (and financial) support in the last four years, and generally putting up with me.

I thank you all so very much.

In loving memory of my mother,

Kathleen Bullock

Contents

List of Figures

List of Tables

List of Appendices

List of Plates

Abbreviations

α-c – Alpha cristobalite

Ab – Albite

AFC – Assimilation and fractional crystallisation

An – Anorthite

A.u – Arbitrary units

β-c – Beta cristobalite

Ca – Castello lava dome

CSD – Crystal size distribution

Cpx – Clinopyroxene

Cr – Capo Rosso lava dome

CVP – Coarsely vesicular pumice

Di – Diopside

EMP and EMPA – Electron microprobe (analysis)

En – Enstatite

Fa – Fayalite

Fa2 and Fr – Falcone (rhyolite) lava dome

Fa3 and Fd – Falcone (dacite) lava dome

f.a.p. – Fold axial plane

FC – Fractional crystallisation

FMQ – Fayalite-magnetite-quartz buffer assemblage

Fo – Forsterite

***f*O$_2$** – Oxygen fugacity

Frr1 – Rocche Rosse pyroclastic sequence

Fs – Ferrosilite

Fsp – Feldspar

Fv – Forgia Vecchia lava flow

FVP – Finely vesicular pumice

GdP – Grotta dei Palizzi lava flow

HF – High frequency

HKCA – High-K calc-alkaline

I – Intermediate axis

La and L – Long axis

LF – Low frequency

ln – Population density

Mg – Monte Giardina lava dome

Mt – (Titano)magnetite

NNO - Nickel-nickel oxide buffer assemblage

OBS – obsidian

Ol – Olivine

Or – Orthoclase

Pc and Pc2 – Pietre Cotte lava flow

Pc1 – Pietre Cotte pyroclastic sequence

Pd and PdC – Punta di Costa lava dome

PdL – Punta di Levante lava dome

PI – Porphyritic index

Pl – Plagioclase

Po – Pomiciazzo lava flow

ppm – Parts per million

Px – Pyroxene

Qz – Quartz

R. Int – Relative intensity

RHY – Lithoidal rhyolite

Rr – Rocche Rosse lava flow

Sa and S – Short axis

Sa1 – Sciarra dell'Arena pyroclastic sequence

Sa2 – Sciarra dell'Arena lava flow

Sph – spherulite

SPO – Spherulite Preferred Orientation

T(K) – Temperature (Kelvin)

TAS – Total alkali vs. silica

TL – Tindari-Letojanni Malta Fault System

T_g – Glass transition

u.c – Undercooling

Usp – Ulvöspinel

Vg – Vallone del Gabellotto pyroclastic sequence

VSD – vesicle size distribution

Wo – Wollastonite

XRD – X-ray diffraction

XRF – X-ray fluorescence

Chapter 1

Introduction

Chapter outline

This chapter provides a brief outline of the study, including a general background in to obsidian characteristics, flow behaviour, spherulite formation and their occurrence in the Aeolian Islands study area. Further details upon obsidian emplacement, spherulite formation, mafic-silicic magma interaction and the Aeolian Islands geological setting is provided within Introduction sections in Chapters 2-4.

1.1 Background and thesis aims and objectives

Most studies of obsidian lava flows are confined to Holocene North American examples due to their exceptional exposure (Fink 1978, 1980a, b, 1983; Fink & Manley 1987). However, these studies reveal a number of variations in terms of structure (e.g. vesiculation and brecciation) and crystallinity (including spherulite content), relating to primary effervescence, devitrification, lava rheology and migration of water vapour (Manley and Fink, 1987). Controls on effusive emplacement of obsidian, the mechanical aspects of obsidian flow emplacement, obsidian genesis and spherulite formation remain poorly understood. This is mostly due to the fact that rhyolite has been rarely observed to erupt. Emplacement mechanisms and textural evolution provide a necessary element in volcanic hazard studies of active rhyolite volcanoes. Due to these factors, this study aims to determine emplacement conditions and textural formation for a number of obsidian lava flows in the Aeolian Islands, Italy.

This study addresses the structure, emplacement and textural evolution of young obsidian lavas in the Aeolian Islands. This involves a detailed evaluation of obsidian flows and domes, including a structural investigation of the Rocche Rosse lava flow (Lipari), a study of spherulite occurrence in flows and domes on Lipari and Vulcano, and a textural study of the Pietre Cotte lava flow (Vulcano). A brief introduction to obsidian behaviour and textural development is provided below, with further detail provided in Chapters 2-5. The genesis of obsidian lavas, obsidian flow emplacement mechanisms, and the formation of spherulites in obsidian lavas is still poorly understood (see below and chapter

introductions). The purpose of this study is to address these issues, specifically addressing the following research subjects:

1. Determination of the emplacement and structural evolution of the Rocche Rosse obsidian lava flow.
2. Development of a new model of spherulite formation in young obsidian samples from the Aeolian Islands.
3. Construction of the magmatic and post-magmatic history of the Pietre Cotte obsidian lava flow.

In order to address these subjects, a number of qualitative and quantitative techniques have been implemented in order to reconstruct the petrological, textural and structural evolution of obsidian lavas in the Aeolian Islands. This introduction briefly outlines our current understanding and some of the important principles, concepts and models associated with the rheology of rhyolitic melts, obsidian lava flow morphology, and spherulite occurrence in obsidian lava flows. Further details from previous studies are also provided in each chapter. The thesis is a compilation of three individual studies that specifically address the three aforementioned key issues. The overall aim of this study is to investigate the structure, emplacement and textural evolution of obsidian lavas in the Aeolian Islands, from magmatic processes including mafic-felsic magma interaction, through spherulite formation, to obsidian lava flow emplacement and deformation. The evolution of obsidian lava flows is constrained using petrographic, textural and structural investigations, based on case studies from obsidian lavas on the islands of Lipari and Vulcano.

Key outcomes of this study include a new structural model for Rocche Rosse lava flow emplacement and deformation, a new classification scheme for spherulites in obsidian lavas, and a new model for the magmatic and post-magmatic evolution of the Pietre Cotte

lava flow. These findings also contribute to the understanding of the magmatic system under Lipari and Vulcano, how spherulites form in obsidian, how textures can be used to constrain igneous processes and how obsidian lava flows behave upon extrusion.

1.2 Rheology of rhyolitic melts

Obsidian flow deformation is akin to that of ductile rocks in metamorphic settings, and obsidian flows are subject to compression, fracturing, radial expansion and diapirism (resulting in complex surface patterns). Obsidian lavas emplace across the ductile-brittle transition (related to glass transition and strain rate; Figs. 1.1-1.4), resulting in ductile and brittle deformational structures (Gottsmann and Dingwell, 2001a, b).

Despite the general recurrence of certain textural facies within rhyolite flows, individual lithologies in different domes are highly variable in texture and general appearance (Richnow, 1999; Tuffen et al., 2009). Complex internal stratification results from primary vesiculation, devitrification, second boiling, gas exsolution and water migration (Gottsmann and Dingwell, 2001a). Obsidian lava flows can remain mobile for days to months following final extrusion (due to insulation from crust; Manley and Fink, 1987), resulting in a range of ductile and brittle deformational structures (Fink, 1983; Manley and Fink, 1987; Gottsmann and Dingwell, 2001b; Tuffen et al., 2013). Lava rheology is a vital parameter governing the textural and structural evolution in obsidian lavas (discussed further in Chapters 2-6).

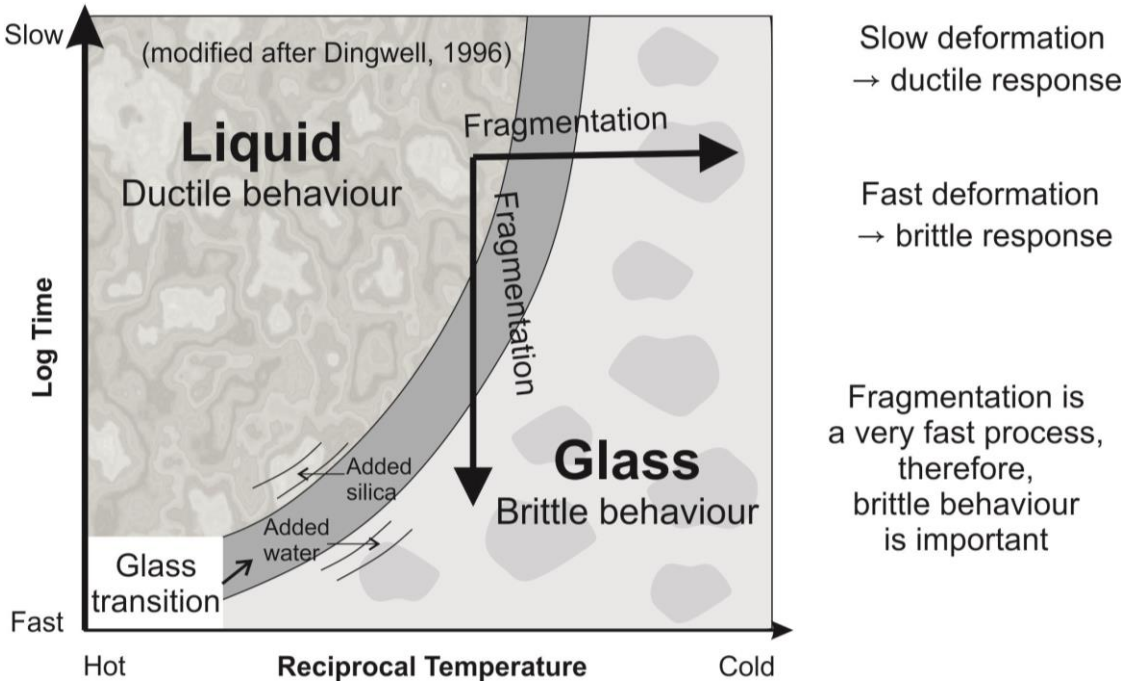

Figure 1.1: Deformation of magma and the relation between deformation time and temperature (Dingwell, 1996).

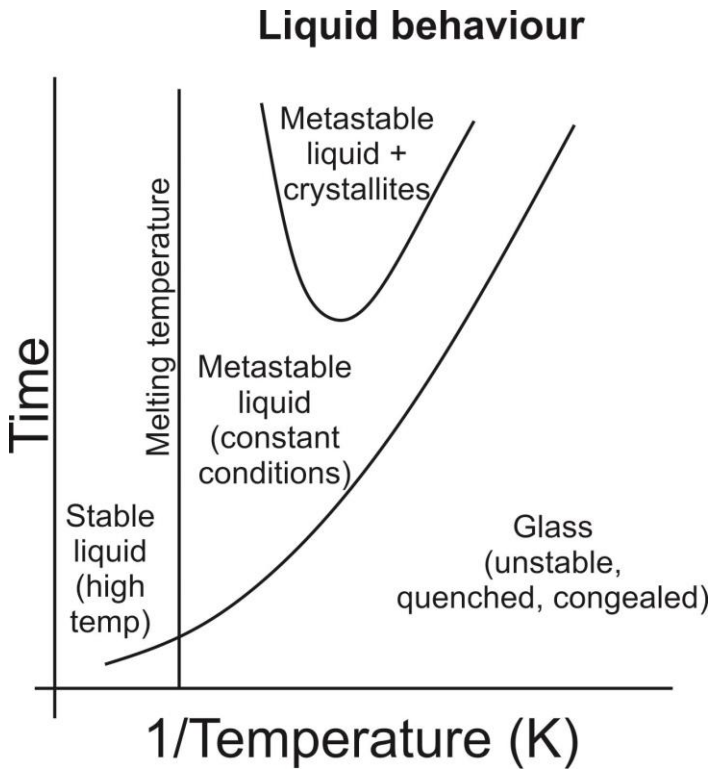

Figure 1.2: Liquid behaviour and state/stability of magma in relation to time and temperature conditions (Dingwell, 1995; 1996).

Rheology, along with crystallinity and vesicularity, is temperature and strain rate-dependent (Figs. 1.1-1.4); for instance, a higher temperature results in a lower viscosity (Friedman et al., 1963; Fink, 1978; Gottsmann and Dingwell, 2001a, b; Giordano et al., 2008). A calculated value from viscosity x strain rate of $<10^7$ pa.s defines Newtonian flow behaviour, while $>10^7$ pa.s sub-liquidus temperatures defines non-Newtonian (Bingham) behaviour (Dingwell, 1996). Rheological estimates of rhyolite magmas are provided by Bottinga and Weill (1972), and a few examples are outlined here. The liquidus (temperature at which crystals first appear in the liquid) of rhyolite is generally considered to be ~1,050°C, with a hydrous solidus (solidification temperature) of 650°C and anhydrous solidus of 750°C (Griffiths, 2000). Water content in rhyolites may range from <0.5 wt% up to 7 wt%, and variations in water content will result in variations in viscosity and solidus temperature (as implied by the general hydrous and anhydrous rhyolite solidus temperatures outlined above). Viscosity of rhyolitic magma ranges from 10^8 to 10^{11} Pa.s at temperatures of 700-750°C, though viscosity decreases with increasing temperature and volatile content (e.g. H_2O, CO_2). Rheology of erupted lava is dependent upon a number of variables, including composition, temperature, crystal content and bubble content, and is therefore a function of cooling, crystallisation and vesiculation (Griffiths, 2000). The viscosity of lava is a function of the temperature, the volume fraction of crystals, volatile content, and, to a lesser extent, the size and shape of the crystals. Rhyolitic magmas have a greater melt viscosity due to a high silica composition and a cooler temperature. Crystallinity may depend on water content, because the crystal fraction is related to the temperature and composition of the lava (Griffiths, 2000). Bubbles variably affect rheology based on their size. Very small bubbles are rigid under surface tension forces and can increase the viscosity, while larger bubbles deform in shear, leading to shear-thinning

(Cashman et al., 1999). A similar response may occur if elongate crystals align with the shear (Griffiths, 2000).

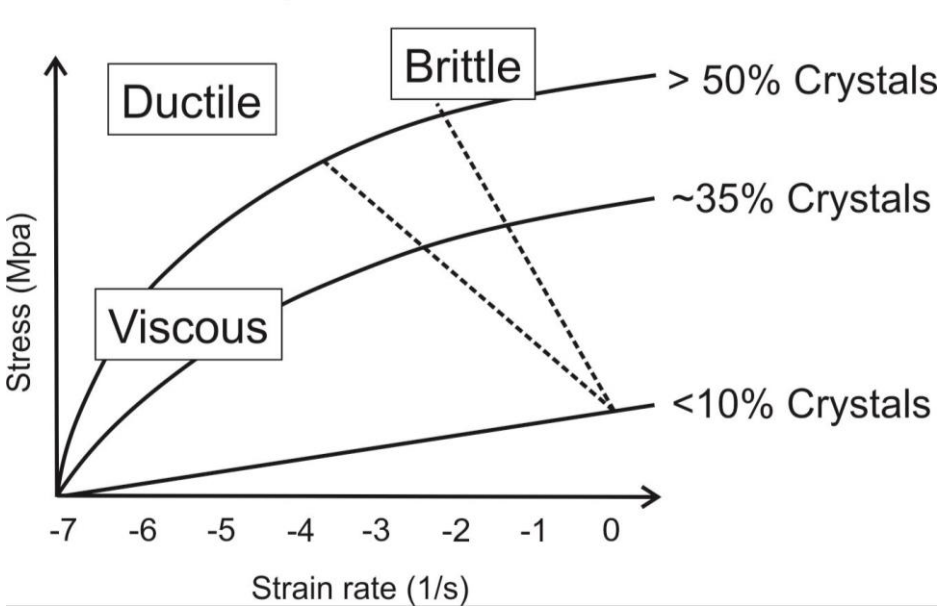

Figure 1.3: Effects of crystallisation on the onset of brittle deformation. Crystals slow the onset of the brittle field by up to 4 orders of strain rate (Dingwell, 1995; 1996).

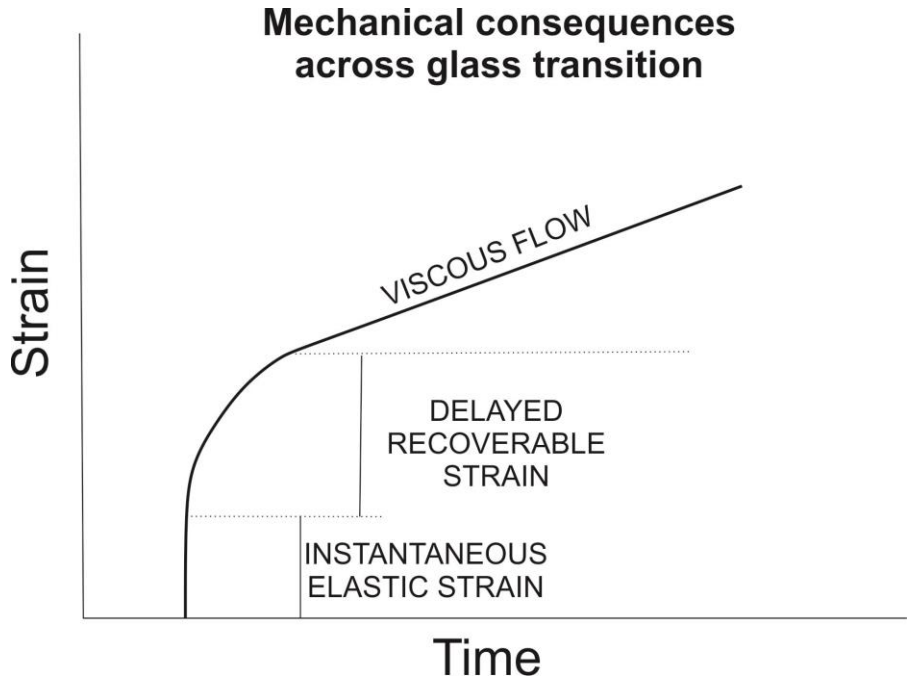

Figure 1.4: Effects of strain and mechanical consequences on magma state and stability across glass transition (Dingwell, 1995; 1996).

1.3 Glass transition

Cooling history directly influences flow morphology, structures and textures. Cooling history is preserved in obsidian glass in the glass transition, i.e. the relaxation temperature range of glass. Glass transition is the phase alteration from viscous behaviour to hard ductile and brittle behaviour (Hess and Dingwell, 1998; Gottsmann and Dingwell, 2001a, b; Figs. 1.1; 1.5), also expressed as the viscous to brittle transition in terms of deformation. This kinetic boundary marks the change in physical properties of a melt, from liquid-like to solid-like behaviour, thus allowing a flow to deform in an initially ductile manner and retain the resultant structures. Glass transition (T_g) depends upon lava composition (including volatile content) and cooling rate. For anhydrous rhyolites, a temperature bracket of 620-750°C may be assumed for the T_g interval, based on values attributed and/or calculated in various studies (Swanson et al., 1989; Manley, 1992; Westrich et al., 1988; Hess and Dingwell, 1996; Dingwell, 1998; Gottsmann et al., 2002; Castro et al., 2009; Tuffen et al., 2012; Clay et al., 2013). Glass transition is typically measured by differential scanning calorimetry, whereby the energy release on heating defines the transition temperature. This is defined by a kink from a constant plot of temperature vs. heat capacity at a specified cooling or heating rate. The kink represents an increase in heat capacity of a material; polymers have a higher heat capacity above glass transition and, therefore, T_g can be identified. This technique has been used in obsidian T_g studies, e.g. Gottsmann and Dingwell (2001b). Glass transition in terms of viscosity is generally attributed to a value of 10^{12} Pa.s, close to the annealing point of many glasses (IUPAC, 1997).

1.4 Characteristics of obsidian

Obsidian lavas are often characterised as vesicle- and crystal-poor, with high silica content, high glass content and low water content. Obsidian glass is metastable, and devitrifies over time, beginning at high temperatures with initial spherulite crystallisation (Fenn, 1977; Swanson, 1977; Smith et al., 2001). Obsidian lavas are dense and highly viscous, and are generally short and low volume, though not always (e.g. exceptionally large obsidian flows in Oregon, USA). Though there is not always a clear distinction between obsidian domes and flows (also referred to as lava couleés), obsidian domes are characterised by a predominantly upward movement, while lava flows involve a greater degree of lateral spreading (Fink, 1983). The shapes of obsidian lava flows are controlled by the underlying slope (see Chapter 5), conduit geometry, total output volume, eruption rate and lava rheology (Fink, 1983; Stevenson et al., 1994a; Manga, 1998; Castro, 1999; Gottsmann and Dingwell, 2001a, b; Tuffen et al., 2013).

Principle processes associated with active obsidian lavas are vesiculation, crystallisation and lava emplacement-related deformation (Fink, 1978, 1983; Gottsmann and Dingwell, 2001a, b; Tuffen et al., 2012, 2013; see also Fig. 1.5). Magmatic chamber processes, conduit mechanisms (during magma acent) and emplacement dynamics (upon extrusion) result in the production of a range of heterogeneous textures in obsidian lavas. Notable textures include flow banding, spherulite and lithophysae formation, bubbles and microlites (Manley and Fink, 1987; Swanson et al., 1989; Manga, 1998; Tuffen and Castro, 2009; Clay et al., 2013). Following extrusion, a number of surface structures form due to syn- and post-emplacement flow deformation. Flow banding preserves a record of flow deformation (Gonnermann and Manga, 2003; Tuffen et al., 2003; Castro et al., 2005).

Bands are defined by differences in crystallinity, vesicularity, chemistry or are created in response to shear stress (which can lead to enhanced crystallisation or vesiculation) against a fixed surface (e.g. along conduit walls or against the underlying topography) (Gonnermann and Manga, 2003; 2005; Tuffen et al., 2003; Castro et al., 2005; Tuffen and Dingwell, 2005). Much is known about the textural development and flow emplacement of basaltic and andesitic lava flows from direct observations (e.g. Self et al., 1997; Blake and Bruno, 2000; Byrnes and Crown, 2001). Obsidian lava flows have rarely been observed in motion (Tuffen et al., 2012, 2013), so emplacement models are largely derived from field and petrographic observations, analogue modelling and geochemical heterogeneities.

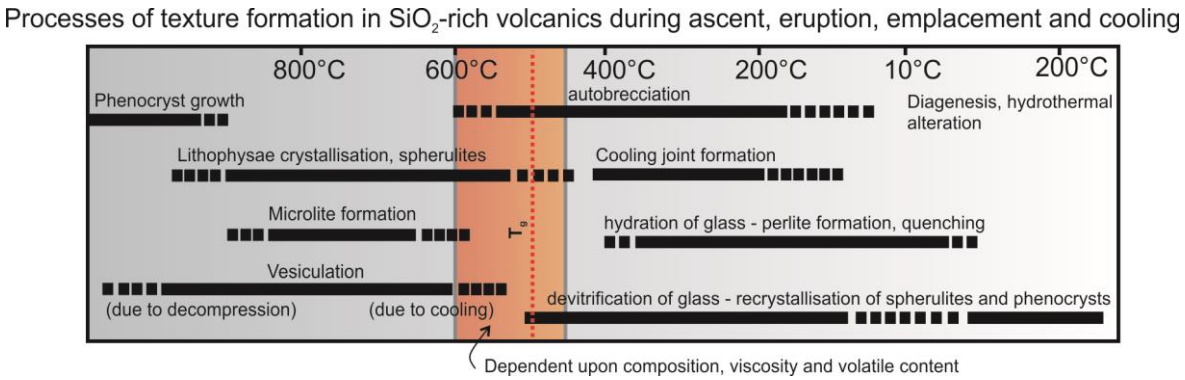

Figure 1.5: Model for processes of texture formation in SiO_2-rich magmas during ascent, eruption, emplacement and cooling. Spherulite crystallisation occurs at high (from ~900°C) to low (~<200°C) temperatures, and microlite formation occurs at ~850°C (from Breitkreuz, 2001 and Wnorowska, 2004).

1.5 Obsidian eruptive behaviour

Obsidian flow morphology is a function of emplacement mechanisms and rheology. A model for emplacement from Fink (1983) details such mechanisms. Models for rhyolitic

magma reaching the surface during dome formation include the model of rhyolite lava reaching the surface as an expanded foam (pumice), emplacing as a collapsing foam during flow (Eichelberger et al. 1986; Westrich et al. 1988), and the traditional model of rhyolite extrusion, whereby a decreased load pressure leads to vesiculation in the upper portion of the dome (Fink, 1987; Fink et al., 1992). The latter is detailed here below, due to discrepancies with the collapsing foam model (field observations of dense obsidian on the surfaces of other domes suggest that obsidian never was emplaced as a foam (Fink et al., 1992), and other silicic lava domes and flows such as Mt St Helens dacite (Swanson et al., 1987; Anderson and Fink, 1990), Tuluman rhyolite (Reynolds et al., 1980) and the Puyehue-Cordón Caulle rhyolite (Tuffen et al., 2013) were also not observed to emplace as collapsing foams). It is also worth noting the results of strain-induced degassing experiments of Carrichi et al. (2011), whereby strain enhances bubble coalescence and degassing, and deformation produced a strongly water-undersaturated melt. Carrichi et al. (2011) conclude that degassing may therefore occur at depth within the conduit, resulting in a super-cooled magma during ascent and potentially contributing to the formation of obsidian.

As a rhyolitic body rises through a conduit towards the surface, volatiles exsolve and rise to the top. Lower confining pressure, as well as contact with groundwater, results in frothing and production of a volatile-rich cap. This vesiculation may result in initial explosive eruptions of tephra. The remaining volatile-rich magma reaches the surface as an inflated pumiceous lava. The transition to a continuous lava flow occurs when gas pressure in vesicles can no longer overcome tensile strength of the magma. The bubble-free obsidian lava extrudes atop the earlier emplaced coarsely vesicular pumice, with further volatile exsolution from the upper surface forming a finely vesicular carapace. Degassing due to repeated fracturing and healing events in conduits could also explain the temporal

shift from an explosive to effusive eruption (Fink, 1983; Eichelberger et al., 1986; Castro and Dingwell, 2009; Cabrera et al., 2011). The final material to extrude has more time to crystallise, resulting in a more crystalline rhyolitic lava extruding over the vent. Cracks in this doming rhyolite allow for further extrusion, and explosive "throat clearing" (Fink, 1983). Textural stratigraphy of obsidian lava flows has been well-documented in North American flows by Manley and Fink (1987) and Fink and Manley (1987). The upper surface is characterised by fractured, finely vesicular pumice, grading downwards into a glassy upper obsidian layer. The upper obsidian layer surrounds coarsely vesicular pumice, with crystalline rhyolite in the centre of the flow. This overlies a basal obsidian layer, and the top and bottom of the flow is encased in a breccia unit. Such textural stratification is the result of volatile distribution within erupted lavas (Fink, 1984), as well as variations in degree of crystallisation.

1.6 Obsidian lava flow emplacement model

Generally, obsidian lava flow movement is characterised by a very highly viscous interior, a rigid crust with crustal folding, enveloped by angular blocks and a frontal talus (Fink, 1978; Manley and Fink, 1987; Tuffen et al., 2013; Fig. 1.6). Blocks of surface crust are overridden, creating the envelope, explicitly an upper and basal breccia. During lava motion, blocks continually fall off the front, forming the talus pile. This pile is overridden, and the flow moves as a "modified tractor tread", with a fluid interior enclosed by angular blocks (Krauskopf, 1949; Fink, 1979; Fig. 1.6). Gravity currents drive flow, with crustal

and basal cooling and solidification occurring during flow. Emplacement occurs over a series of flow regimes, including Newtonian viscous, creeping and non-Newtonian brittle rheologies. Cooling can lead to changes in rheology, and result in a number of structural and textural formations.

Obsidian lava flows show a complex internal sequence of variably vesicular, devitrified and deformed textures, and complex surface deformation patterns (Manley and Fink, 1987; Figs. 1.6 and 1.7). The traditional view of rhyolitic flow interiors includes (from the surface downwards) an upper breccia, a thick vitrophyre, foliated rhyolite, a thinner vitrophyre, and a basal breccia (Fink, 1978; 1983; Manley and Fink, 1987; Tuffen and Castro, 2009; Figs. 1.6 and 1.7). This traditional cross section has been correlated in Obsidian Dome core drills in California and the Banco Bonito flow in New Mexico (Fig. 1.7, see also Chapter 5). Spherulitic (and crystalline) material commonly marks the central part of the flow, but this may vary depending on the length and thickness of the flow (Manley and Fink, 1987). Over time, volcanic glass will devitrify, which may lead to the overprinting of some original textures.

Textural zonation is likely to vary from flow to flow, but may be considered to consist of air-fall tephra deposits, basal breccia, coarsely vesicular pumice, obsidian (if no devitrification has occurred), finely vesicular pumice and surface breccia, with textures corresponding to the aforementioned cross sections previously mentioned (Manley and Fink, 1987). The distribution of textures in a typical obsidian lava flow has been previously described by Fink (1978, 1984), Manley and Fink (1987), Bonnichsen and Kauffman (1987), Fink and Manley (1987), Westrich et al. (1988) and Swanson et al. (1989). These textural facies are further discussed in Chapters 2 and 5.

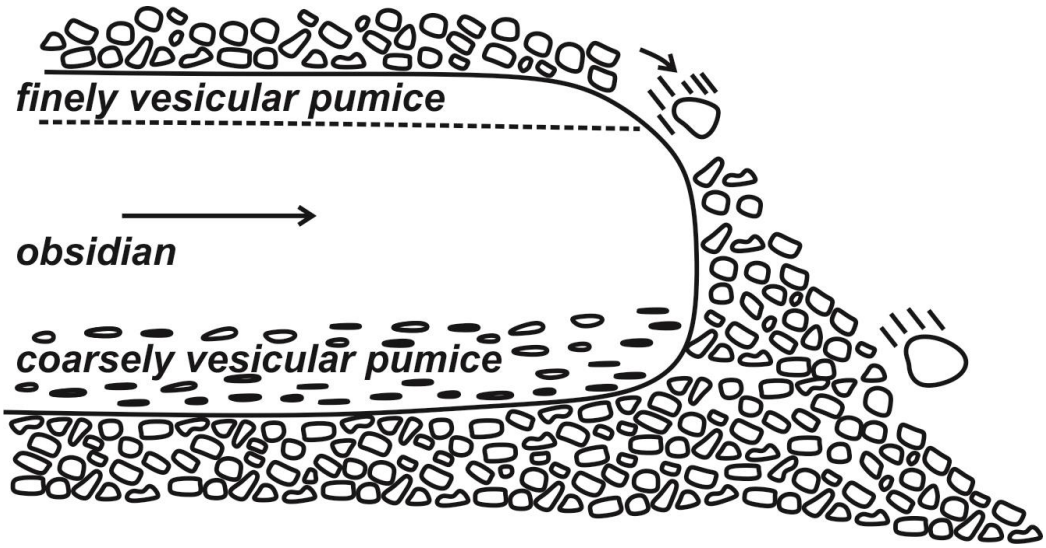

Figure 1.6: Schematic diagram showing the motion and simplistic internal textural make-up of an idealised obsidian lava flow (from Fink, 1978).

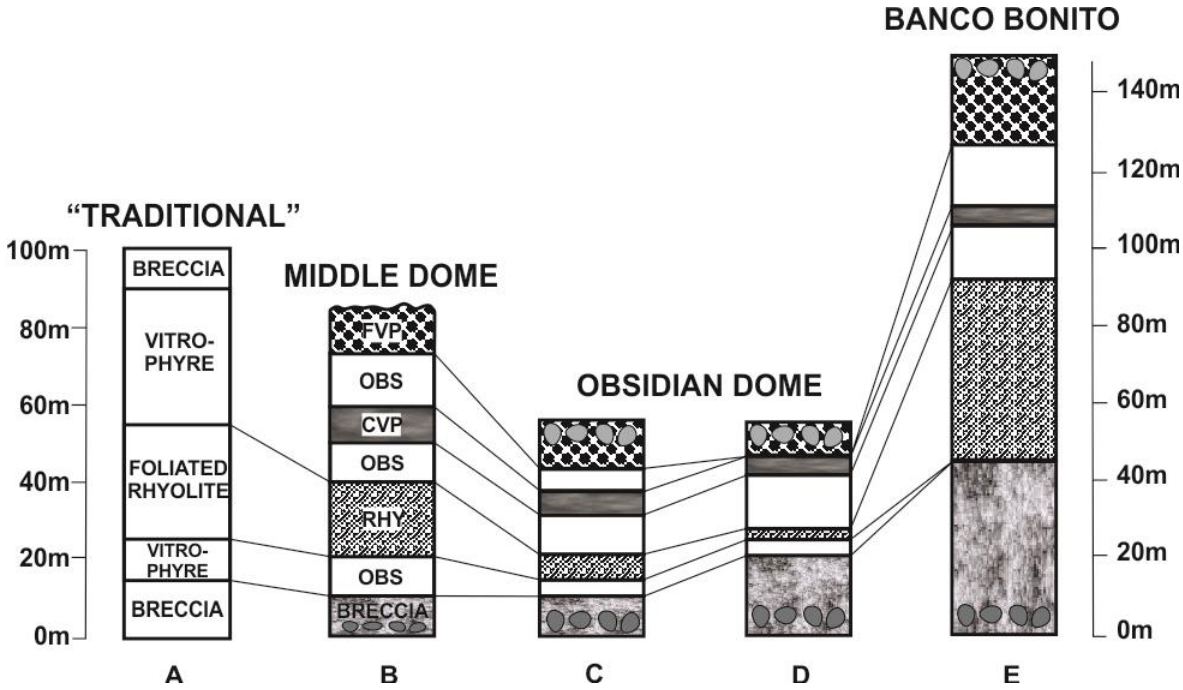

Figure 1.7: Cross sections through four studied rhyolite flows. A: "Traditional" view of rhyolitic flows with approximated thicknesses (from Christiansen and Lipman, 1966; Williams and McBirney, 1979; Ekren et al., 1984). B-E: Textural zonation within studied flows. FVP = finely vesicular pumice; OBS = obsidian; CVP = coarsely vesicular pumice; RHY = lithoidal rhyolite. Diagonal lines indicate correlations of textural zones (from Manley and Fink, 1987).

1.7 Structural development of obsidian lava flows

The structure of obsidian lava flows is generally a reflection of their relative viscosity (Fink, 1978). A flow of low viscosity forms a long, thin flow, while more viscous flows are emplaced as shorter, thicker flows and domes. Viscosity is a function of, among other factors, temperature, volatile content and chemical composition (e.g. silica content). Obsidian flows exhibit a textural zonation, with a massive interior sandwiched between an upper and lower breccia consisting of blocks of various sizes (Fink, 1978). The proportion of breccia is a function of lava viscosity, with more viscous material behaving in a more brittle manner, allowing for more complete brecciation during flow (Fink, 1978). Deformational processes such as rising pumice diapirs, compressive stresses and extension, and fracture propagation due to thermal contraction produce a range of complex surface structural relations (documented from Holocene rhyolitic flow and dome studies by Fink, 1983). Such surface structural features have been previously identified in field studies, and by satellite and remote sensing imagery methods (see Fig. 1.8).

Obsidian lavas travel most of the distance from source as a ductile to brittle flow regime. During emplacement, obsidian lavas inherit a number of flow-related structures, including flow bands, flow folds and elongation lineations, generally forming from shear adjacent to conduit margins (Gonnermann and Manga, 2005). Repeated surges from the vent and "squeeze up" extrusions result in ridges known as ramp structures in obsidian flows (Macdonald, 1972; Fink, 1980a). The deformational process during motion is best described as vertical collapse and horizontal spreading of the viscous fluid in the direction of the surface slope. This means that up-hill flow can also occur. This follows from the much-used relationship between the shear stress along the base of the spreading mass and

the angle of the surface slope (Goguel, 1948; Nye, 1952; Elliott, 1976; Ramberg, 1977; Merle, 1998). Experimentation by Merle (1998) showed that flow over an inclined base resulted in complex stretch and flattening plane trajectories in the vertical profile, changing in time from sigmoidal to concave trajectories. Experiments also showed flow over a horizontal base revealed convex stretch and flattening plane trajectories, and flow within a channel caused stretching parallel to displacement direction. However, wrenching at lateral margins resulted in stretching showing an oblique direction to displacement (Merle, 1998). Flow beyond such channels resulted in radial spreading (lower flow) and concentric stretching (upper flow). These experiments further highlight the role of slope on patterns of flow advance. Flow thickness is a function of yield strength, with a higher yield strength resulting in thicker flows. As a consequence, flows are generally thinner on steep slopes. Flow length may be a factor of eruption conditions that force flow to come to a halt. Eruption conditions of obsidian lava flows may be cooling-limited (i.e. flow ceases due to excessive cooling), or volume-limited (flow ceases due to exhaustion of magma supply in source area) (Wilson and Head, 2008). Cooling-limited flows are maintained until full flow extent is realised, and the limits are defined by cooling and rheology, while volume-limited flows cease once the available volume has been used up, irrespective of rheological parameters (Harris, 2013).

Though the structure and associated processes outlined above demonstrate a clear and accurate overview of obsidian flow emplacement, this simplified model provides only general guidelines for interpretation of rhyolitic structures and emplacement (Manley and Fink, 1987). Variations in vesicularity, spherulite and crystalline content and brecciation have been identified in silicic flows of North America, the result of primary effervescence, devitrification, lava rheology and migration of water vapour (Manley and Fink, 1987).

Flow and refs	Satellite/Aerial imagery	Interpretive diagrams
Obsidian dome (California, USA) Castro et al., 2002 Interpretive diagram shows sample collection points, feeder dyke, ridges and flow edge traces	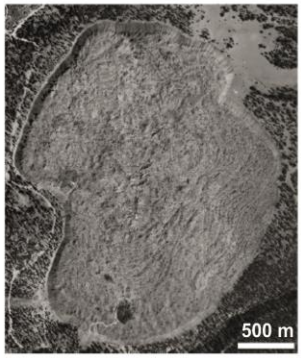	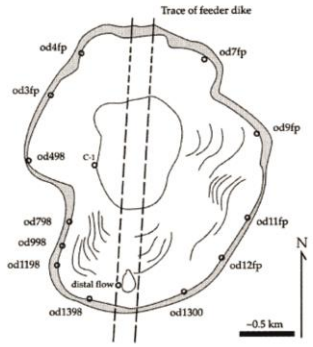
Big Glass Mountain, N lobe (California, USA) Fink, 1980a; b Interpretive diagram shows regularly spaced areas of coarsely vesicular pumice in the centre of the flow		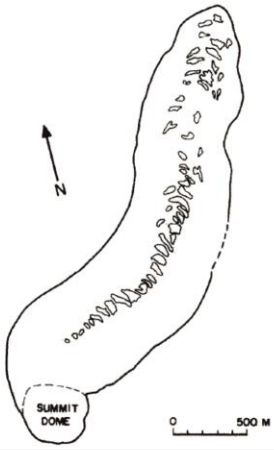
Little Glass Mountain (NE and NW lobes) (California, USA) Fink, 1980b Interpretive diagrams show coarsely vesicular pumice areas outlined		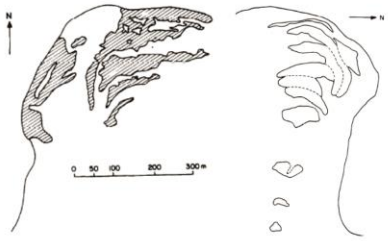
2011–2012 eruption at Cordón Caulle (Chile) Tuffen et al., 2013 Interpretive diagrams show evolving marginal position and breakout lobes (Land Imager image), and marginal flow advance	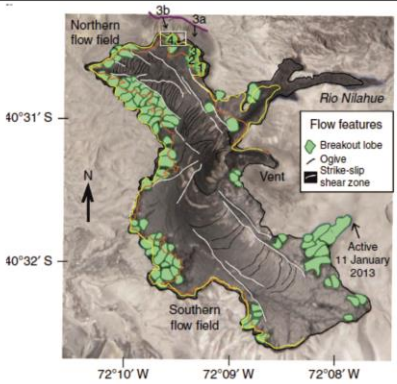	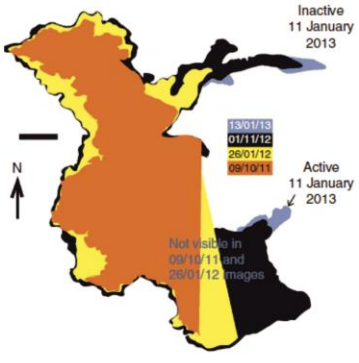

Figure 1.8: Examples of previously studied obsidian lava flows, including aerial/satellite imagery of the flows, and interpretive sketches.

1.8 Laboratory simulations of silicic lava flows

Laboratory simulations using a polyethylene glycol were conducted by Fink and Griffiths (1990), and Griffiths and Fink (1992). Such experimentation concluded that lava surfaces will only fold when the advection velocity within the flow and the rate of heat loss from the surface fall within specific ranges. These rates are a function of the ratio of the time required for the surface to solidify to the time required for lateral flow through a distance on the order of flow thickness. To simplify, the identification of folds on a surface can help to provide flow viscosity, temperature and effusion rate estimations (based on fold wavelengths). Gregg (1995) performed similar laboratory simulations but with a variable underlying slope angle. These simulations commonly resulted in two or more generations of folds, with small scale folding (<0.3 cm) forming within seconds of eruption onset, with a second generation (>2 cm) superposed on the first. Further compression resulted in fracturing. Gregg et al. (1998) further expanded these experiments, identifying that the ratio of first and second generation folding can be correlated with relative importance of cooling and compression during flow emplacement. Simple experiments with a viscous silicone fluid flowing over a rigid base have conducted in order to assess principal stretch directions, types of strain ellipsoids and strain regimes during motion (Merle, 1998). This experimentation indicates that the stretching direction in three-dimensional flow can sometimes be perpendicular to the flow direction, indicating that the direction of maximum susceptibility as well as the long axis of deformed bubbles may not always reflect the displacement direction (Merle, 1998). Gregg and Fink (2000) modelled the effects of slope on flow emplacement dynamics by extruding a polyethylene glycol at a constant rate onto a uniform surface at various inclinations. The lowest extrusion rates, lowest slopes and

highest cooling rates produced flows that crusted over rapidly and advanced through bulbous toes. As extrusion rate and slope angle was increased, and cooling rate decreased, rifted flows were produced, with folded flows, and finally leveed flows, which solidified at the margins only. These experiments emphasise the role of underlying slope on flow advance and subsequent structural evolution of advancing lava flows.

1.9 Spherulites occurrence in obsidian lavas

Cooling of an obsidian lava body leads to partial or complete devitrification of glass. Quench crystals, such as anhydrous cristobalite and feldspar, grow to spherulites using a nucleation surface (e.g. a crystal, bubble or crack) (Breitkreuz, 2001). Spherulites are generally as spherical to ellipsoidal bodies of radiating, intergrown crystals that form by rapid crystallization of lava in response to significant undercooling (Lofgren 1971a, b; Fenn, 1977; Swanson, 1977; Castro et al., 2009; Watkins et al., 2009; Gardner et al., 2012; Clay et al., 2013). Spherulites occur almost exclusively in glass, requiring conditions in which crystal nucleation is suppressed (Swanson 1977; Fenn 1977). Silica and feldspar constituents of spherulites grow in acicular or fibrous crystal morphologies due to large undercooling (Kirkpatrick, 1975; Swanson, 1977; Fenn, 1977). McPhie et al. (1993) characterised spherulites as a characteristic product of high-temperature (700-450°C) devitrification (crystallisation from glassy state) of glass, consisting of radiating arrays of individual crystal fibres.

Spherulite morphology can be a function of their formation temperature. Lofgren (1971b) conducted experiments in order to produce devitrification textures (including spherulites)

under controlled conditions. Spherulite morphologies include an axiolitic structure (radiating from a plane), radial fanning from a central point, bowtie shaped, plumose (branching) spherulites, spherical spherulites, pectinate (growing inwards from walls of a juvenile pyroclast), lithophysae (fibres radiating from a central hollow), and lithophysae with concentric hollows. Though generally less than 2 cm, spherulites can grow to several tens of centimetres or over a metre (Carmichael et al. 1974; Davis and McPhie 1996; MacArthur et al. 1998; Smith et al. 2001; Castro et al. 2008; Watkins et al. 2009; Seaman et al. 2009). As spherulites crystallise, H_2O diffuses away and becomes concentrated in a halo around the spherulite, expelled as the spherulite grows (Kesler and Weiblen, 1968; Friedman and Long, 1984; Manley and Fink, 1987; Castro et al., 2008; Watkins et al., 2009; Gardner et al., 2012; Clay et al., 2013). The relative enrichment of expelled incompatible constituents has been used as a proxy for thermal conditions during spherulite growth (Castro et al., 2008; Watkins et al., 2009; Seaman et al., 2009; Gardner et al., 2012; Clay et al., 2013).

Experiments by Lofgren (1980) produced spherulites by experimental crystallisation from a melt akin to those produced by devitrification, suggesting that spherulites can form from a primary origin (close to, and above, glass transition temperatures), and during devitrification (during local flow cessation in a glassy state). To date, questions still remain regarding the formation of spherulites in terms of when spherulites begin to form, do spherulites grow below glass transition, and is there a link between spherulite formation and flow deformation (Watkins et al., 2009; Clay et al., 2013). One of the aims of this study is to identify and classify individual spherulite populations forming at different stages of obsidian emplacement and cooling. This information is deciphered from spatial distribution of spherulites, textural characterisation, spherulite (crystal) size distribution plots and geochemistry.

Experimental insights into spherulite occurence include the work of Lofgren (1974), and Castro et al. (2008). Lofgren (1974) modelled isothermal crystallisation of plagioclase, and showed that plagioclase shape varies systematically with the degree of undercooling (Fig. 1.9). Lofgren (1974) and Kirkpatrick (1975) showed that with large degrees of undercooling, the growth rate greatly exceeds the diffusion rate (depending on species, see Gardner et al., 2012). With increased undercooling, plagioclase shape alters from tabular to more elongate skeletal, dendritic and finally spherulitic (Lofgren, 1974; Fig. 1.9). Crystallisation from the glassy state (i.e. devitrification) occurs with long time periods at low temperatures (Bouška, 1993; Clay et al., 2013). Devitrification involves the same atomic rearrangement as is found in melt crystallisation (Marshall, 1961). Spherulites crystallising at high temperatures (i.e. above or during the glass transition (T_g) interval) are considered to be of primary origin (Stevenson et al., 1994a, b; Lejeune and Richet, 1995). Low T_g transition temperatures are the lowest temperatures at which spherulites may grow in degassed rhyolites under near surface conditions, prior to spherulite modification and re-crystallisation processes below T_g (Ryan and Sammis, 1981; Richnow, 1999; Clay et al., 2013). Dissolved salts also accelerated low temperature devitrification (Lofgren, 1974).

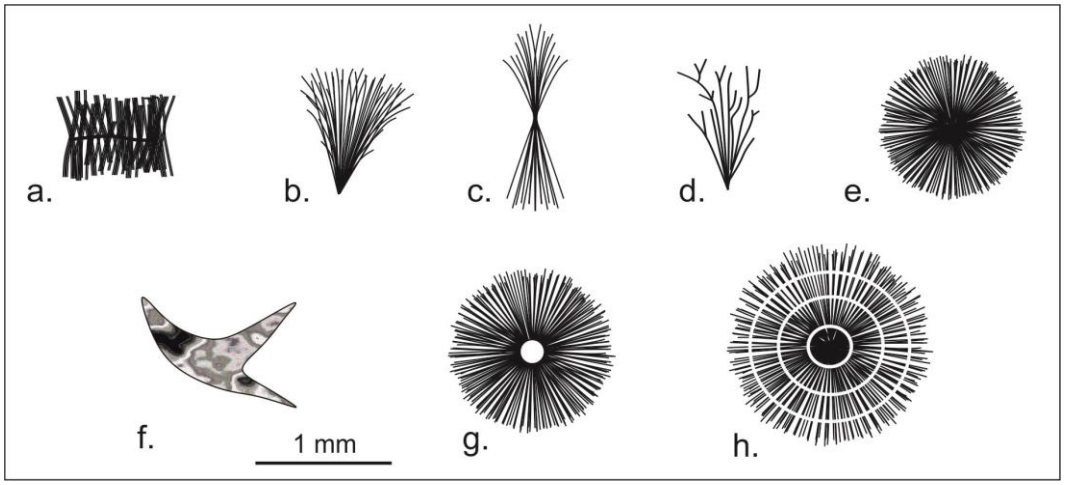

Figure 1.9: Examples of spherulite morphology based on experimentation by Lofgren (1947). (a) Axiolitic structure (spherulitic fibres radiate from a plane), (b) fan spherulite (fibres radiate from a point), (c) bowtie

spherulite (two fan-like arrays joined at their apices), (d) plumose spherulite (branching, but not on crystallographic axis), (e) typical spherical spherulite, (f) pectinate texture (inward growth from walls of a juvenile pyroclast), (g) lithophysae structure (radiating from a central hollow), and (h) lithophysae with concentric hollows arranged parallel to crystallisation front (after Lofgren, 1974; MacArthur et al., 1998; Breitkreuz, 2001; Wnorowska, 2004).

Spherulites occur in rhyolitic obsidian, and have been subject to much interest from petrologists for more than a century (e.g. Judd, 1888). Spherulites are a commonly observed texture in obsidian lava flows (e.g. Swanson et al., 1989; Castro et al., 2008, 2009; Tuffen and Castro, 2009; Gardner et al., 2012; Tuffen et al., 2012; Clay et al., 2013). Spherulites are considered to form at high undercooling (>100°C), often nucleating on the surfaces of existing crystals, bubbles or cracks (Breitkreuz, 2013). Importantly, spherulites may nucleate due to a number of processes, and grow over a range of temperatures, which may yield information on textural relationships and the conditions under which they formed (e.g. above or below T_g). Crystallisation of spherulites can also trigger volatile enrichment in glass/melt, as well as viscosity (bulk lava), which in turn influences flow behaviour (Tuffen et al., 2012; Clay et al., 2013).

1.10 Obsidian lavas in the Aeolian Islands, Italy

The most recent cycle of volcanic activity on the islands of Lipari and Vulcano (Aeolian archipelago, Italy; Fig. 1.10) has produced a number of obsidian lava flows and domes (Pichler, 1980; Cortese et al., 1986; Sheridan et al., 1987; Crisci et al., 1991; Lucchi et al.,

2010, 2013; De Astis et al., 2013b; Forni et al., 2013). Coeval mafic enclaves are commonly found in the majority of obsidian lavas on Lipari and Vulcano. For instance, recent studies have identified mafic enclaves in the Pietre Cotte lava flow (Perugini et al., 2007; Piochi et al., 2009; De Astis et al., 2013b), Monte Guardia and Monte Giardina lava domes (De Rosa et al., 2003) and Rocche Rosse lava flow (Davì et al., 2009, 2010). Mafic-felsic magma interaction has been suggested as the triggering mechanism for this most recent cycle of eruptions (De Astis et al., 1997, 2013b; Davì et al., 2009, 2010; Piochi et al., 2009). Effusive obsidian lava flows and domes commonly follow a period of explosive activity in the Aeolian Islands (Forni et al., 2013).

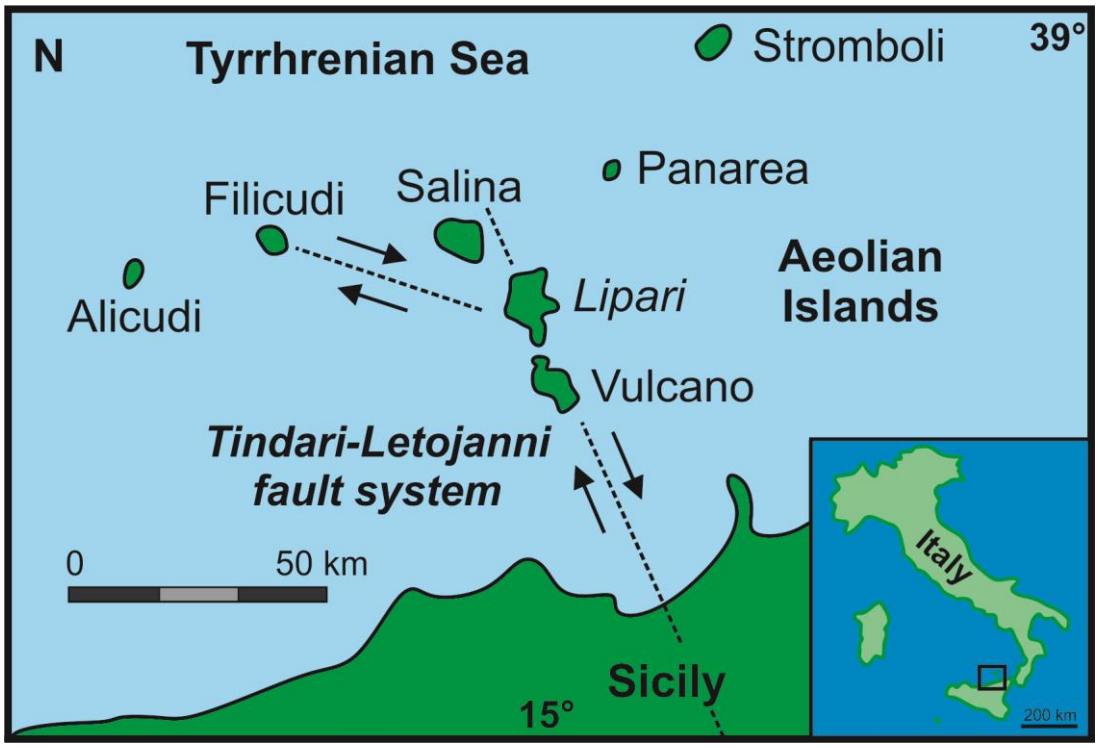

Figure 1.10: The Aeolian archipelago, South Tyrrhenian Sea (Italy), with the islands of Lipari and Vulcano in the centre, straddling the Tindari-Letojanni fault system (after Donato et al., 2006).

Obsidian lavas in the Aeolian Islands are relatively unaltered and well exposed due to their young age (<42 ka). Obsidian lava exposure in the Aeolian Islands is fresh or variably

devitrified, and includes a range in ages (~40 ka to 1739 AD), with textures and structures well exposed, and mafic-felsic interaction often apparent. The Aeolian Islands are therefore an ideal location for petrological, textural and structural investigations into obsidian lava flow processes. Understanding eruptive and emplacement processes is potentially useful for volcanic hazard assessment for obsidian lavas in the Aeolian Islands and future flows, which is important as Lipari and Vulcano are both volcanically active and highly populated, particularly during the tourist season (Piochi et al., 2009). Hazard assessment, for instance, is particularly critical in terms of the association of explosive vent activity and secondary explosions. This study provides a greater understanding of pre- and post-extrusive volcanic processes associated with obsidian lavas in the Aeolian Islands through a detailed petrographic, textural and structural study.

1.11 Thesis outline

The study is focused around three independent studies, the results and conclusions of which combine to provide a greater understanding of textural development within obsidian lavas, spherulite formation, post-extrusive emplacement and deformation of the Rocche Rosse obsidian lava flow (Lipari), and mafic-felsic magma interaction associated with the active Fossa system (Vulcano).

Chapter 2 (The structure and emplacement of the Rocche Rosse obsidian lava flow, Lipari, Aeolian Islands, Italy) combines satellite- and field-based observations of flow structures and Spherulite Preferred Orientation methods with surface mapping and rheological estimates of the Rocche Rosse obsidian lava flow in order to gain insights into flow

mechanics and emplacement history. The findings in this chapter offer insights into the physical nature of the Rocche Rosse lava flow, the role played by differential flow rheology, progressive deformation and channelled flow morphology in structural evolution, and offers an evaluation of obsidian lava flow emplacement compared to other silicic lava flows in the Aeolian Islands and silicic flows reported in previous studies.

Chapter 3 (Spherulites in young obsidian lavas in the Aeolian Islands, Italy) combines geochemical and textural techniques in order to identify physical and chemical heterogeneity of spherulites across obsidian formations, fully classify different types of spherulites and determine their formation conditions. The results of this study provide details upon the timing of spherulite formation, the role of flow deformation, and the processes responsible for spherulite heterogeneity. Such results are important for our understanding of spherulite formation within obsidian lavas.

Chapter 4 (Magmatic and post-magmatic history of the Pietre Cotte obsidian lava flow, Vulcano, Aeolian Islands, Italy) combines petrographic observations, mineral and glass geochemistry, thermobarometry, field observations and structural measurements in order to conceptualise a new sequential process model of the Pietre Cotte lava flow. The observations, results and model presented here provide quantitative and qualitative information on the systematic evolution of the Fossa magmatic system and subsequent heterogeneous Pietre Cotte lava flow. These findings place a greater understanding of conditions of crystallisation associated with multiple magmas, applicable to this and other mafic-felsic interaction systems.

The key findings of these three chapters are disseminated in order to fully interpret obsidian flow emplacement processes in the Aeolian Islands, from pre- to post-extrusion (Chapter 5: Synthesis and Discussion). In Chapter 5, implications for pre-existing concepts and models for obsidian emplacement, spherulite formation, the use of textures to constrain

magmatic and post-magmatic processes, the influence of topography on obsidian flow emplacement and comparisons with rheomorphic ignimbrites are discussed. A summary of new findings is presented, and used to assess the general behaviour of obsidian lava, applicable to other obsidian lava flows. The study is concisely summarised in Chapter 6 (Conclusions), and future studies are specified as a result of the conclusions and new findings of this study.

Chapter 2

The structure and emplacement of the Rocche Rosse obsidian lava flow, Lipari, Aeolian Islands, Italy

Chapter outline

This chapter addresses the structure, emplacement and deformation of the Rocche Rosse obsidian lava flow (Lipari). The study incorporates multi-scale observations, including satellite imagery, flank examination, field observations and structural measurements, and microscopic Spherulite Preferred Orientation methods. The study also provides rheological estimates, based on estimated lava temperature and viscosity, and accounting for compositional variations. The study integrates these findings into a multi-stage flow emplacement evolution model, controlled by a number of processes and differential flow regimes, and resulting in a range of complex, multi-scale structures.

2.1 Introduction

While the structural emplacement of basaltic lava flows is reasonably well constrained (e.g. Pinkerton and Sparks, 1978; Kilburn and Guest, 1993; Pinkerton and Norton, 1995; Anderson et al., 1999; Calvari and Pinkerton, 1999; Cashman et al., 1999; Bondre, 2003; Jerram, 2002, Keszthelyi and Self, 1998; Passey and Bell, 2007; Self et al., 1996), studies of obsidian lava flow emplacement are relatively few (e.g. Fink, 1983; Stevenson et al., 1994a; Castro et al., 2002; Tuffen et al., 2012, 2013). This is in part due to a lack of observations of active flows and solidified lavas having been subjected to considerable chemical alteration and erosion (Fink, 1983). However, the nature of obsidian lava flow transport and deformation can be inferred from textures and structures preserved in the rocks (e.g. Fink, 1983; Manga, 1998; Castro et al., 1999), and through rheological estimates based on fluid deformation models (e.g. temperature, viscosity, water content, Hess et al., 1995, Castro, 1999; Gottsmann and Dingwell, 2001a, b). Close examination of satellite image, field and microscopic structural studies, combined with rheological properties, can serve as important tracers for obsidian lava flow emplacement and deformation. In this study, satellite- and field-based observations of flow structures, Spherulite Preferred Orientation methods, surface mapping and rheological estimates of the Rocche Rosse obsidian lava flow are explored in order to gain insights into flow mechanics and emplacement history.

Studies of obsidian lava flows focus upon the textural and structural arrangement of prominent flow features, used in order to infer processes at work during emplacement. The structural arrangement of flow foliations preserves a record of rheologically-controlled

deformation associated with flow emplacement (Gonnermann and Manga, 2003), a record of brittle-ductile processes (Castro et al., 2008), and the analysis of foliation patterns contributes to the understanding of the structural evolution undergone by rocks within regions of polyphase deformation (e.g. Bastida et al., 1986; Fink, 1980a, b; Forbes et al., 2004; Gregg et al., 1998; Gonnerman and Manga, 2005). The determination of a preferred orientation of crystals and crystallite phases can also provide a petrographic record of strain, lava flow and deformation (Shelley, 1985; Smith et al., 1994; Launeau and Robin, 1996; Ventura et al., 1996; Manga, 1998).

Fink (1983) described the textural relations (i.e. flow stratigraphy) of Little Glass Mountain (California, USA). These textures define the initial configuration of the lava flow, meaning that the final structural arrangement is the product of emplacement and deformational processes. Fink (1983) identified three deformational processes disrupting the foliation of the flow during advance: (1) low density coarsely vesicular pumice diapirs, which rise and result in surface doming and plunging anticlines, (2) flow-parallel compressional stresses near the flow front, resulting in flow folding oriented transverse to flow direction (ogives), and (3) extensional regime, resulting in inward propagating surface fractures. Other studies examined how textures preserved in silicic lavas provide information on emplacement mechanisms (e.g. Manga, 1998; Ventura, 2001; Befus et al., 2014). For instance, Manga (1998) analysed the shape and three dimensional orientation distribution of microlites in obsidian from Little Glass Mountain in order to provide constraints on obsidian emplacement dynamics. Model fits to data suggest microlites were distributed in accordance to a Newtonian fluid undergoing simple shear flow, aligning to flow. Ventura (2001) analysed two dimensional strain based on basaltic enclaves within a dacitic lava flow. Deformation during flow emplacement involved lateral extension near

the vent, with non-coaxial deformation occurring further from the vent, behaving as a simple shear flow.

These previous studies show that, although the emplacement of silicic lava flows is well understood, there is still a need for a detailed model for obsidian lava flow emplacement. Tuffen et al. (2013) present the first observations of an active rhyolitic lava flow, from the 2011-2012 eruption at Cordón Caulle (Chile). Tuffen et al. (2013) documented the emplacement evolution of the advancing flow, highlighting the role of thermal insulation in prolonging flow-horizontal transport, identifying the formation of breakout lobes and flow frontal stalling, and drawing comparisons to basaltic lava flow fields. Tuffen et al. (2013) conclude by stating that their study provides new insights into poorly constrained aspects of obsidian flow emplacement, and places an emphasis on the necessity for further developments in a multi scale model for lava flow emplacement. This study aims to place such constraints on our understanding of obsidian flow emplacement, and provide additional implications for a generalised obsidian lava flow emplacement model. The study focuses on the emplacement of the Rocche Rosse obsidian lava flow (Lipari, Aeolian Islands, Italy, Fig. 2.1). A study of melt facturing and healing as a mechanism for degassing and the formation of obsidian by Cabrera et al. (2011) assessed the Monte Pilato-Rocche Rosse sequence and Lami pyroclastic cone that pre-date the Rocche Rosse lava flow. The study recognises the importance of degassing through autobrecciation and fractures (determined by water concentration profiles) as an important mechanism for obsidian formation and conduit processes. Such mechanisms may be responsible for the temporal shift from explosive to effusive activity in silicic systems such as those in Lipari, with particular emphasis on Rocche Rosse activity (Cabrera et al., 2011).

The Rocche Rosse obsidian lava flow (Fig. 2.1) displays exceptionally well-preserved surface and internal features, structural assemblages and microscopic structures due to its

young age (1230 ± 40 AD determined by archaeomagnetic dating methods; Arrighi et al., 2006). This exposure provides an ideal opportunity to study flow structures in order to conceptualise a model for the conditions of obsidian lava flow transport mechanisms and structural emplacement. The Rocche Rosse lava flow represents the youngest outpourings of the Monte Pilato pumice cone on the north-eastern coast of Lipari (Fig. 2.1). The flow surface is generally characterised by orange-weathered loose obsidian blocks and a brecciated flow top and flow ridges, with widespread folding dominating the surface. The Rocche Rosse lava flow is variably spherulitic across the flow extent, with spherulites carrying the flow foliation and stretching lineations. A link between flow deformation and spherulite formation in the Rocche Rosse lava flow has been suggested by Clay et al. (2013), and has been highlighted as an aspect that would require further study (see also: Chapters 3 and 5).

Satellite imagery provides an opportunity to study large scale geological structures that may be unidentifiable on the ground. The use of satellite imagery for the study of the physical properties of lava flows, both terrestrial and extra-terrestrial, can give insights into flow development (Hulme, 1974; Fink, 1980a, b; Abrams et al., 1991; Legelay-Padovanie et al., 1997; Honda, et al., 2002; Lu et al., 2004; Vicari et al., 2009; Harris et al., 2011; Branca et al., 2013). In this study, high resolution satellite imagery observations are directly compared to field observations and structural mapping. The Rocche Rosse lava flow is also compared to other lava flows in order to identify common structural trends and relationships. Calculated rheological parameters, including temperature and viscosity, as well as the contribution of spherulite nucleation resulting in a secondary heating, provide a primary control over obsidian advance, flow longevity and subsequent structural development. Spherulite occurrence observations and Spherulite Preferred Orientation (SPO) methods highlight the link between lava emplacement and spherulite nucleation and

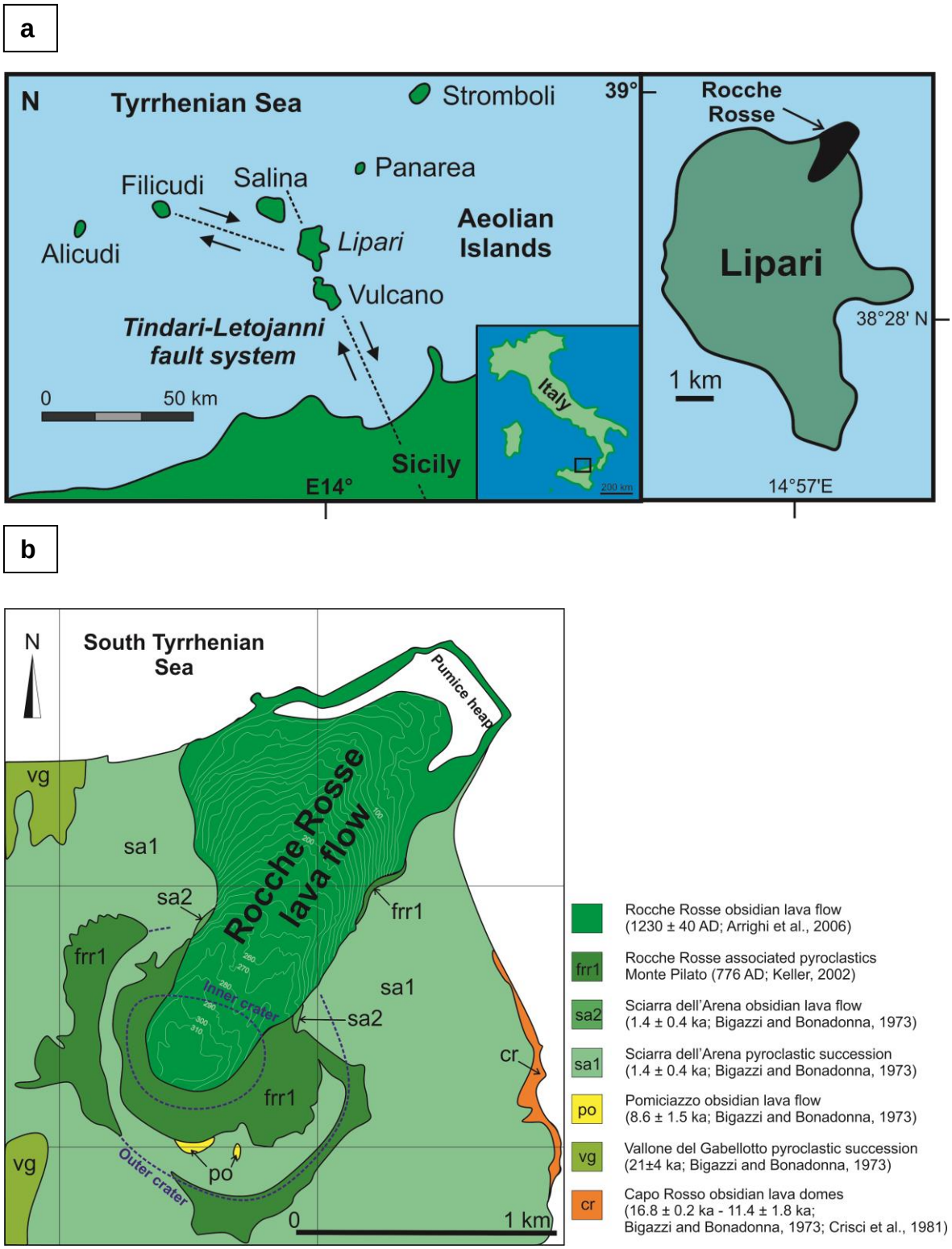

Figure 2.1: (a) The island of Lipari, part of the Aeolian Islands, South Tyrrhenian Sea (Italy), showing the location of the Tindari-Letojanni fault system (from Donato et al., 2006), and (b) the Rocche Rosse lava flow in NE Lipari (below - schematic map and generalised stratigraphic units based on the geological map of Lucchi et al., 2010, 2013).

growth, and emphasise the localisation of deformation in the lava flow.

The high coverage and assessment of structural features documented in this study show that while structures associated with obsidian lava flows are remarkably complex, they are inherently related and form sequentially during continuous effusion, preserve evidence for progressive deformation and a channelled flow morphology, and can be used to decipher mechanisms of obsidian flow emplacement. This study examines large scale features across-flow, surface/internal features and flank characteristics (including height calculations, textural stratigraphy, planar and linear measurements and fold characterisation), and localised (small scale) deformational structures using Spherulite Preferred Orientation (SPO) methods. These findings offer insights into the physical nature of the Rocche Rosse lava flow, the important role played by rheologically-controlled progressive deformation and channelled flow morphology in structural evolution, and offer an evaluation of obsidian lava flow emplacement compared to other silicic lava flows. The study concludes with a new sequential model for the emplacement for the Rocche Rosse lava flow.

2.2 Geological Setting

The Aeolian Archipelago (South Tyrrhenian Sea) consists of seven main islands (Alicudi, Filicudi, Salina, Lipari, Vulcano, Panarea and Stromboli), and is the result of the complex collision between the African and Eurasian plates (Caputo et al., 1972; Gasparini et al., 1982, 1985; Keller, 1982; Anderson and Jackson, 1987; De Astis et al., 2003; Ventura, 2013). The historically active island of Lipari is located in the central sector of the Aeolian

Islands, and is the largest island in the arc (Fig. 2.1). A NNW-SSE striking fault system defines the alignment of volcanoes, along the Tindari-Letojanni structural fault system (Barberi et al., 1994, Fig. 2.1), with re-activation of the fault during the middle- to late-Pleistocene responsible for recent volcanism in the central arc (Ghisetti, 1979; Barberi et al., 1994; Gvirtzman and Nur, 2001; Ventura, 2013). Lipari rises ~600 m above sea level, and lies on 20 km thick continental crust (Finetti and Morelli, 1973; Schütte, 1978; De Astis et al., 2003).

The most recent activity comprised explosive pyroclastic deposits and obsidian lava flows, culminating in the extrusion of the Rocche Rosse and Forgia Vecchia obsidian lava flows (Pichler, 1980; Lucchi et al., 2010, 2013). The pattern of this recent activity has generally involved a hydromagmatic phase, explosive extrusion of a vesicular magma, accompanying fall and surge deposits, degassed viscous lava extrusion and a period of quiescence (Cortese et al., 1986; Dellino and La Volpe, 1995; Tranne et al., 2002; Lucchi et al., 2010, 2013; Clay et al., 2013; Forni et al., 2013). Prior to the extrusion of the Rocche Rosse lava flow, a period of volcanic quiescence lasting 440 years (from AD 776 to AD 1230±40; Forni et al., 2013) has been identified by a surface of subaerial erosion, marked by the angular discordance between the Monte Pilato (AD 776) and Fossa delle Rocche Rosse products (AD 1230±40) (Keller, 2002; Arrighi et al., 2006; Lucchi et al., 2010, 2013; Forni et al., 2013). After recent dating studies, the Rocche Rosse lava flow has been deemed to represent a renewal of activity, following the initial Monte Pilato-Rocche Rosse explosive phase (frr1 pyroclastic sequence – see Fig. 2.1). This early explosive phase has been dated at 776 AD using short-lived plant remains, and constrained using historical records (Keller, 2002). The age of the Rocche Rosse lava flow was determined by archaeomagnetic methods, dated at 1,220 ±30 AD (Tanguy et al., 2003), and later revised to 1,230 ±40 AD (Arrighi et al., 2006). The extrusion of the 2 km long Rocche Rosse

obsidian lava flow at the north-eastern coast of Lipari marks the end of the sequence of explosive activity (repetitive alternation of fall and pyroclastic density current beds; Davì et al., 2011) at the Monte Pilato pumice cone (Keller, 1970; Cortese et al., 1986; Sheridan et al., 1987; Dellino and La Volpe, 1995; Lucchi et al., 2010, 2013; Clay et al., 2013; Forni et al., 2013). The Rocche Rosse eruption started with low-energy hydromagmatic to magmatic activity, culminating in the effusion of the viscous obsidian lava flow (Dellino and La Volpe, 1995; Tranne et al., 2002). The Monte Pilato cone was partly destroyed by the Rocche Rosse effusive phase (Dellino and La Volpe, 1995).

The flow is typically considered to be up to 60 m in thickness (Lucchi et al., 2010, 2013; Clay et al., 2013; Forni et al., 2013), with a brecciated surface and obsidian ridges. The texturally heterogeneous Rocche Rosse obsidian is characterised by a black groundmass, with sparse to widespread spherulites, flow banding, devitrified zones, microlites and rare euhedral to subhedral alkali feldspar, plagioclase and quartz phenocrysts (typically 0.5-2 mm in length). The obsidian varies from completely glassy to completely devitrified, and is also variably vesicular. Some spherulites, pumiceous zones and vesicles are stretched or sheared. The Rocche Rosse obsidian also contains latitic and trachytic enclaves (detailed by Davì et al., 2009, 2010).

2.3 Rheological properties of obsidian

The rheological properties of obsidian play an important role in the deformation of the lava flow. Rheological properties of rhyolite (both from the Rocche Rosse obsidian lava flow and other sources), are comprehensively discussed in various studies (e.g. Shaw, 1972;

Murase and McBirney, 1973; Spera et al., 1988; Manga et al., 1998; Castro and Cashman, 1999; Gottsmann and Dingwell, 2001a, b), and some of the key studies and parameters are summarised here. The rheological properties of lava flows are affected by a number of parameters, including effusion rate, flow thickness, viscosity, slope angle and cooling processes (Pinkerton and Sparks, 1978; Dragoni and Tallarico, 1994; Fink and Bridges, 1995; Griffiths, 2000). Studies have focused in detail on surface morphologies (Anderson and Fink, 1990, 1992; Griffiths and Fink, 1992), flow structures (Sampson, 1987), kinetic and physico-chemical properties such as extrusion rate (Fink, 1983; Anderson and Fink, 1989), degassing history (Barclay et al., 1996), viscosity (Fink, 1980a) and cooling rates (Gottsmann and Dingwell, 2001a). In advancing lava flows, properties such as composition, temperature, viscosity and water content are all intrinsically related (Griffiths, 2000). Higher temperatures result in a more fluid substance (i.e. lower viscosity), and higher quantities of silica result in a higher degree of polymerisation, and therefore a greater viscosity (Friedman et al., 1963; Fink, 1978; Gottsmann and Dingwell, 2001a, b; Giordano et al., 2008). Higher crystal content and vesiculation will also influence (increase) viscosity. Disparities in rheology can be manifested in lava flow petrological and structural variations (Chevrel et al., 2013). The intrinsic relationships between primary rheological properties are displayed in figure 2.2.

Obsidian undergoes complex phase alteration and rheological change from liquid to solid during flow. Cooling history is a key control on obsidian flow rheology, and subsequently plays a major role in flow emplacement and the subsequent formation of surface structures (Gottsmann and Dingwell, 2001a, b). Importantly, flow emplacement occurs across the kinetic boundary (glass transition). Obsidian material changes from liquid- or viscous-like behaviour to a more plastic state, before eventually cooling to a brittle-state deformation. This structural relaxation interval is known as the rheological glass transition (T_g)

(Dingwell, 1995; Wilding et al., 1995; Gottsmann and Dingwell, 2001a, b). The temperature region of T_g has been estimated or calculated for rhyolites in various studies, and lies within an approximate range of 600-750°C (Swanson et al., 1989; Manley, 1992; Westrich et al., 1988; Hess and Dingwell, 1996; Gottsmann and Dingwell, 2001a, b; Castro et al., 2009; Tuffen et al., 2012). Across (and above) this temperature gradient, lava has the ability to behave in a ductile manner. This stage is preserved in the final solidified lava flow in ductile deformational features, such as multi-scale folding. Rhyolitic magma can behave in a brittle or ductile manner over a wide range in temperature with variations in strain rate. For instance, high strain can result in brittle behaviour of obsidian at high temperatures. The presence of crystals and bubbles, in terms of volume fraction, size distribution, number density, shape and anisotropy, can significantly influence magma viscosity and magma/flow rheology. For instance, the presence of bubbles can result in a marked increase or decrease in relative viscosity of a system with increasing vesicularity (see experimental strain tests of Carrichi et al., 2007; see also Bagdassarov and Dingwell, 1992; Stein and Spera, 1992; Manga et al., 1998; Llewellin and Manga, 2005). The presence of crystals produces an increase of viscosity with increasing crystal content, promoting non-Newtonian behaviour (Caricchi et al., 2007).

It has been previously reported that the Rocche Rosse lava flow behaved as a non-Newtonian (Binghamian) fluid during emplacement, behaving in a viscoplastic manner (Clay et al., 2013). Due to the high viscosity of flowing rhyolitic lavas, the kinematics of the flow emplacement mechanisms are partly preserved in the structures that are evident in the final solidified flow (Clay et al., 2013). It has also been suggested that just above, within, or below T_g can mark the onset of high temperature spherulite growth (Ryan and Sammis, 1981; Manley, 1992; Davis and McPhie, 1996; Castro et al., 2008; Watkins et al., 2009; Gardner et al., 2012; Clay et al., 2013). It has been determined by applying

relaxation geospeedometry using differential scanning calorimetry that the Rocche Rosse lava flow viscously deformed following extrusion before the entire flow came to rest (Gottsmann and Dingwell, 2001b). Cooling rates of tens of Kelvins per day across T_g controlled such late stage deformation, sustaining flow in such a highly viscous rhyolitic lava, resulting in active deformation and advance of the flow front for days to weeks after effusion had ceased (Gottsmann and Dingwell, 2001b).

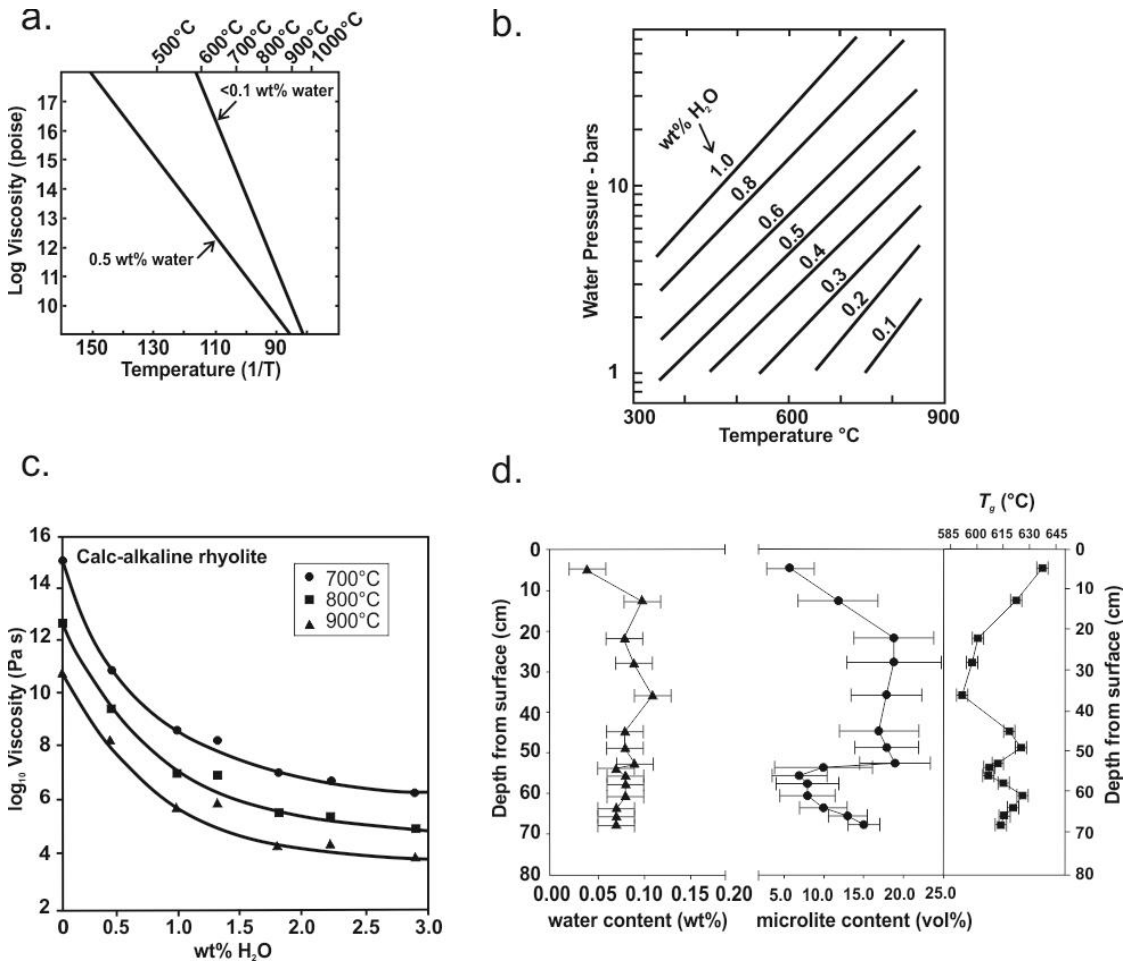

Figure 2.2: Relationships between rheological properties of obsidian lava flows. (a) Log viscosity vs. 1/T for obsidian at two water contents (from Friedman et al., 1963). (b) Temperature vs. water vapour pressure for obsidian with superimposed water weight percent values in obsidian (from Friedman et al., 1963). (c) Viscosity of obsidian as a function of weight percent water in obsidian (from Friedman et al., 1963; Fink, 1978; Giordano et al., 2008). (d) Water and microlite content as a function of depth, with glass transition temperatures also shown (from Gottsmann and Dingwell, 2001a).

Obsidian shows viscoelastic behaviour at T_g transition temperatures (Tuffen and Castro, 2008). Elasticity is relatively insensitive to rising temperatures, up to ~700°C, at which point the young's modulus drops rapidly and the lava will deform as a viscous fluid (Sakuma, 1951; Fink, 1978). Viscosity (typically 10^{12} Pa.s during T_g; Giordano et al., 2008) decreases with increasing temperature and water content (Fink, 1978; Giordano et al., 2008), emphasising the importance of these rheological parameters in lava flow emplacement. Crystalline structures (such as microlites and spherulites) increase the bulk viscosity of lava, and the presence of spherulites can increase rigidity, provide yield strength and tensile strength (stiffness) at yield point. Bands of spherulites, for instance, are more resistant to the surrounding fluidal- or glassy obsidian, promoting simple shear. To summarise, cooling history is a key control on obsidian flow rheology, and subsequently plays a major role in flow emplacement and the subsequent formation of surface structures and textures (Gottsmann and Dingwell, 2001a, b).

2.4 Methodologies

2.4.1 Satellite Imagery

Large scale surface structures of the Rocche Rosse lava flow were observed, highlighted and measured in detail from high resolution Infoterra GeoEye-1 satellite imagery obtained from Airbus Defence and Space at 0.5 m pan data resolution, cubic convolution and 4 Band Pan sharpened specifications. The GeoEye-1 scene was obtained on 07 July 2011 (0% cloud cover) and made available as a shape file on GeoTIFF format. Full dynamic

range was achieved through 11-bit image selection, with Dynamic Range Adjustment off (in order to maintain absolute radiometric accuracy and full dynamic range for scientific applications), providing more discernable and subtle differences among objects, and to extract information from shadows (each pixel is represented by 2048 shades of grey). The satellite image map was radiometrically corrected, and the image oriented to north at the top. Satellite image co-ordinates are:

Top Left 38° 31' 27.71"N, 14° 56' 44.11"E

Top Right 38° 31' 27.40"N, 14° 57' 48.64"E

Bottom Right 38° 30' 26.64"N, 14° 57' 43.69"E

Bottom Left 38° 30' 29.78"N, 14° 56' 45.60"E

The camera model mapped the respective ground co-ordinates to image product co-ordinates. The satellite image covers an area of 5010 km^2, at a scale of 1:10,000. The Geo product, coupled with a digital elevation model (acquired through interferometric synthetic aperture radar) and control data, permits image query, editing and manipulation using *ArcMap 10* geospatial processing program.

Large scale geological structures and flow structural contrasts were identified and traced over with line shape files, and measured using *ArcMap 10* geo-referenced measurement tools. More prominent structures were traced using a thicker line. Known measurements, such as flow length and width or large scale folds, were cross checked with GPS data collected in the field. Divisions of flow (e.g. identification of flow lobes) were determined using satellite imagery. Satellite image interpretations were substantiated or refuted based on field observations.

2.4.2 Flow stratigraphy and height calculations

Fink (1983) identified several distinct textural units in cross section of the Little Glass Mountain obsidian dome (eastern California). These stratigraphic units (from the bottom upwards) include fragmental air-fall tephra (pumice) deposits, basal breccia, coarsely vesicular pumice, non-vesicular glassy obsidian, finely vesicular pumice and surface breccia. In a similar manner, distinct textural units were identified in the Rocche Rosse lava flow. Textural units were distinguished on the bases of colour, size, shape and abundance of vesicles. In this study, identified units include a basal breccia (denoted by fragmented clasts of variable lithologies), a pumiceous zone (white to dark grey zone of predominantly welded pumice), devitrified obsidian and glassy obsidian. Units are often gradual and do not show sharp boundaries. The flow stratigraphy and thickness of the Rocche Rosse lava flow is observable at various points along the eastern and western flank exposures. Sketches, photographs, observations and samples were collected in order to create a flow stratigraphy for the Rocche Rosse lava flow. Flow thickness was calculated at various points (in order to limit error) at the flanks using a comparable scaling technique (comparing the face of the flank with an object of known height – either a 1.8 m person or a 1 m scale bar).

2.4.3 Mapping surface structures

Field measurements and mapping of surface structures were carried out over the summers of 2010 and 2011 on the Rocche Rosse lava flow (see Map 1). This involved field mapping of the main flow structures as well as detailed sampling and observations. Localities were

marked by GPS co-ordinates (maximum error of 5 m). Specific structures exposed at the flow surface were explicitly identified and targeted prior to field mapping using satellite imagery. As well as flow structures, areas of vegetation cover and urbanised areas were also mapped and highlighted. The topographic baseline map and anticipated lava flow coverage were based on the geological map produced by Lucchi et al. (2010, 2013).

Flow foliation was identified as flow bands defined by spherulites, microlites and vesicularity (bubbles). Foliation attitude was recorded and mapped as strike, dip and dip direction. The primary flow foliation allowed for the identification of flow folding. Folds were measured and described based on their fold axial plane (strike, dip and dip direction of theoretical three dimensional planes), and fold hinge (inclination of hinge-line down from the horizontal measured as a lineation - dip angle and dip azimuth). Wavelength and amplitude were also measured in order to classify scale of folds. Folds were qualitatively characterised based on their closing and facing directions and the vergence of the fold axial plane. Folds were also classified based on the straightness of the hinge line, tightness, roundness and attitude of fold, fold symmetry, vergence and harmony. Parasitic folds were noted where observed. Sheath folds were also described, and their trend orientation recorded. Stretching lineations were measured in terms of dip angle and azimuth where lineations were readily accessible and could be observed in three dimensions.

Stereographic representation, density (contour) mapping and rose diagrams were constructed in order to better project structural orientation data, summarise results, identify localised trends and trends relating to scale of structure (e.g. small scale folds). Stereonets and diagrams were created using *Stereo32* software (Röller and Trepmann, 2008). The data was projected in equal area, lower hemisphere. An A2 overview map is provided in Plate 1 at the back of the thesis.

2.4.4 Spherulite Preferred Orientation

The Spherulite Preferred Orientation technique is a modified method which can be used for the quantification of a spherulitic (or other spherical objects) fabric anisotropy on a two dimensional image. The method is based on the counting of a number of intercepted segments of a set of objects on the image by a set of parallel scan lines along a number of orientations (Launeau et al., 1990; Launeau and Robin, 1996). Polar plots, or rose diagrams, of the number of intercepts in each direction, serve to quantify the fabric, its symmetry, direction(s) and intensity. Intercepts roses can yield a strain direction. The resulting Fourier series presents a rose of intercept counts and directions (characteristic shape). A linear filter minimises the effects of grid anisotropy on the counting of intercepts. The method can be applied to isolated crystals and aggregates, meaning digitised spherulites identified in an image are suitable for this procedure (avoiding overlapping or coalesced spherulites). Typically, sections with at least 200-250 spherulites were selected in order to provide a reliable representative section (consistent with crystal shape and CSD methods implemented by Morgan and Jerram, 2006). Assuming the population of spherulites started with an originally spherical or near-spherical habit, the rose intercepts and orientations provides an indicator of sectional strain (Launeau and Robin, 1996; Launeau et al., 1990, 2010).

Spherulite Preferred Orientations were identified using the freeware *Intercepts 2003* (Launeau and Robin, 1996). *Intercepts 2003* analyses the interconnection of grains in rocks vs. inertia tensor of individualised grains. The intercept counting method developed by Launeau and Robin (1996) has been applied to thin-sections from 14 localities on the Rocche Rosse lava flow in order to highlight any preferential strain axes orientation relating to deformation. Orientated samples were collected from the field for

microstructural analysis, with samples showing well defined foliation planes (and, if possible, lineations) selected and marked in-situ. Marked in-situ samples from each locality were cut as standard petrographic thin sections normal to the foliation plane, perpendicular to the plane, within the plane and, where apparent based on field evidence, parallel to stretching lineations. Thin sections were scanned and manually digitised, and strain fabric ellipsoids were determined using *Intercepts 2003* software. A comprehensive and critical review of the method of *Intercepts* is provided by Launeau and Robin (1996).

2.4.5 Rheological calculations

Eruptive temperature (°C) was calculated for six localities on the Rocche Rosse lava flow. These properties were determined based on obsidian glass chemical composition (oxides wt%), from polished thin sections. Mineral major element and volatile (S, Cl and F) analyses of the sampled obsidian glasses were undertaken at The Open University (UK) using a CAMECA SX 100 electron microprobe. The peak count per element for glass analyses was 15-30 s using a 10-20 µm defocused beam diameter, with an acceleration voltage of 20 kV and beam current of 10 nA for glass and crystals. Natural silicate minerals (garnet and olivine) were used as primary standards to calibrate the instrument, with silicate mineral and volcanic glass standards (VG-568 and KN-18) routinely analysed as secondary standards. Unknown glass results regularly checked and systematically controlled against standards, with glass standards and certified values are also reported (see Appendix IV).

Rheological estimates were calculated based on the derived glass compositions using *Pele 8.00* software (Boudreau, 1999). A pressure of 1 bar was selected (~atmospheric pressure)

for calculations. The program requires input of weight percent major oxide composition of the glass, as well as a pressure value (1 bar at surface). Compositional data was normalised, and eruptive temperature (and oxygen fugacity relative to FMQ) was determined. This provides a first order model for many of the properties of a crystallising silicate liquid (Boudreau, 1999). Chemical compositions were also applied to calculate non-Arrhenian temperature dependence of rhyolitic magma viscosity for naturally-occurring silicate melts at atmospheric pressure (viscosity in Pa s), using the model for viscosity of volatile-bearing melts developed by Giordano et al. (2008).

2.5 Results

Field observations and structural measurements (Plate 1) are important for identifying localised trends and deformational structures. Satellite imagery provides an opportunity to identify and assess large scale structural features. However, field-based observations are also essential in order to ground-truth and constrain the observed satellite observations. Generally, large scale linear and curvilinear features can be identified in satellite imagery, and may represent a number of structural features. Satellite image features are interpreted as ogives (surface ridges formed by the extrusion of individual lava units), large scale surface folding and late-stage overlapping lava extrusions. Ogives are a common ridge expression in silicic lavas (e.g. the Bracks Rhyolite (Texas, USA) - Henry et al., 1990; the Chao dacite (Chile) - de Silva et al., 1994; Cordón Caulle (Chile) - Tuffen et al., 2013). Similar features have been identified as crease structures in Mount St Helens dacite lava dome and Medicine Lake dacite flow (Anderson and Fink, 1992).

2.5.1 Petrography

A detailed overview of Rocche Rosse petrography and geochemistry, including a comprehensive description and interpretation of spherulite occurrence, is provided in chapter 3. Here, geochemistry and petrographic features which are important to structural understanding are discussed. For instance, composition plays a pivotal role in rheological properties of rhyolitic magma, as a higher SiO_2 concentration results in a higher degree of polymerisation and therefore a greater viscosity. Microlite and spherulite abundance can also greatly influence temperature and viscosity, with higher crystallinity resulting in higher bulk density and bulk viscosity (Gottsmann and Dingwell, 2001b), and spherulite crystallisation may provide an important latent heat source (Tuffen et al., 2012).

The Rocche Rosse obsidian varies from completely glassy to microcrystalline, and is variably vesicular. The Rocche Rosse obsidian has a variable SiO_2 content of ~69-76 wt% (variability possibly due to mingling activity or evolution of system), Al_2O_3 content of ~3-5 wt%, Na_2O content of ~3-5 wt%, K_2O content of ~3-5 wt%, FeO content of ~0.6-1.6 wt% and trace amounts of other major oxides (see Chapter 3 and Appendix I). Though the obsidian is dominantly crystal-free, there are scarce crystal phases, including alkali feldspar, plagioclase and quartz. Microphenocrysts (<50 μm) of augitic pyroxene, olivine, biotite and zircon have also been identified and previously reported (Davì et al., 2009). Microlites are variable across flow (minute crystals (<10 μm) of orthoclase, Fe-edenite and biotite; Davì et al., 2009; 2010), often showing a prevalent orientation (parallel to foliation), and also preserve evidence of micrometre scale folding. The lava flow shows evidence of interactions with mafic magmas, with widespread ellipsoidal and spherical mafic enclaves identified sporadically across the flow (possibly explaining compositional range). This latitic-trachytic magma mingling is discussed comprehensively by Davì et al.

(2009, 2010). Mafic enclaves contain a crystal assemblage of plagioclase, clinopyroxene, olivine and titanomagnetite. There is more than one type of enclave present within the Rocche Rosse obsidian, with evidence for mixed porphyritic enclaves, cumulus-textured enclaves and pumiceous enclaves. Trachytic enclaves contain clinopyroxene, plagioclase, alkali feldspar, olivine and biotite, set in a cryptocrystalline groundmass (Davì et al., 2009).

Spherulites occur throughout the flow, ranging in size from less than 0.1 mm up to 5 mm (Clay et al., 2013), and occupying ~3-5% of the obsidian groundmass (calculated in selected thin section samples using *ImageJ* software (Schneider et al., 2012); see Chapter 3). Spherulites are radial crystal aggregates, with fibres radiating from the centre, and dark and light colour interior zonation. Spherulites show a sporadic distribution across flow, varying from completely spherulite-free obsidian to completely spherulitic obsidian. The spherulites are predominantly comprised of cristobalite and alkali feldspar fibres (Clay et al., 2013; see also Chapter 3). The majority of spherulites are either perfectly spherical or mildly elongate. Spherulites generally display a spherical shape, though some interjoined spherulites show a bowtie shape. Some spherulites are flattened and contain small quartz, plagioclase and alkali feldspar inclusions. There are also examples of spherulites that show a greater degree of elongation.

2.5.2 Satellite imagery

The lava flow and surrounding features are shown in Figure 2.3. The satellite image covers an area of 5,010 km^2, at a scale of 1:10,000 (calculated using *ArcMap 10* software). The maximum length of the flow is 2,060 m, and the maximum width of the flow is 1,130 m.

The majority of the flow shows clear exposure, with exceptions in flow frontal regions (exposure is restricted by buildings and a man-made pumice heap). The Monte Pilato pumice cone source region is located in the south west of the image, identifiable by a semi-circular crater rim (Fig. 2.3). The flow widens from the source, with two distinguishable flow lobes to the north and north-east.

Tracing surface features reveals a number of linear and curvilinear features across the flow extent (Fig. 2.4). The more prominent features (highlighted in bold) widen over tens to hundreds of metres. There are two key features evident – lineaments aligned roughly SW-NE (sub-parallel to flow direction from source), and curvilinear features roughly parallel to the flow front (i.e. the eastern, more prominent branching frontal region). "Lineament" is a term that has been previously applied in satellite imagery analyses as a descriptive term for a linear or curvilinear feature, often associated with faults, fractures, geomorphological features, fold axes and lithological contacts (e.g. El Hadani, 1997; Kassou et al., 2012). Large curvilinear features are more prominent in flow frontal regions, whereas lineaments extend from near-vent to mid-flow regions.

In western mid-flow regions, where the flow width increases, the orientation of both the curvilinear and linear features differs. Lineaments align in a more N-S orientation, and curvilinear features trend in a more E-W and NE-SW alignment (parallel to the flow margins). Less prominent, but still traceable features show smaller scale structures confined to larger scale structures (thin red lines within bolder red lines – Fig. 2.4). These smaller scale features are more sporadic in occurrence and orientation, but are often parallel or perpendicular to larger scale structures (bold red lines – Fig. 2.4). At ground level, lineaments represent channelled flow morphology, crescent-shaped ogives and large scale folds (see later).

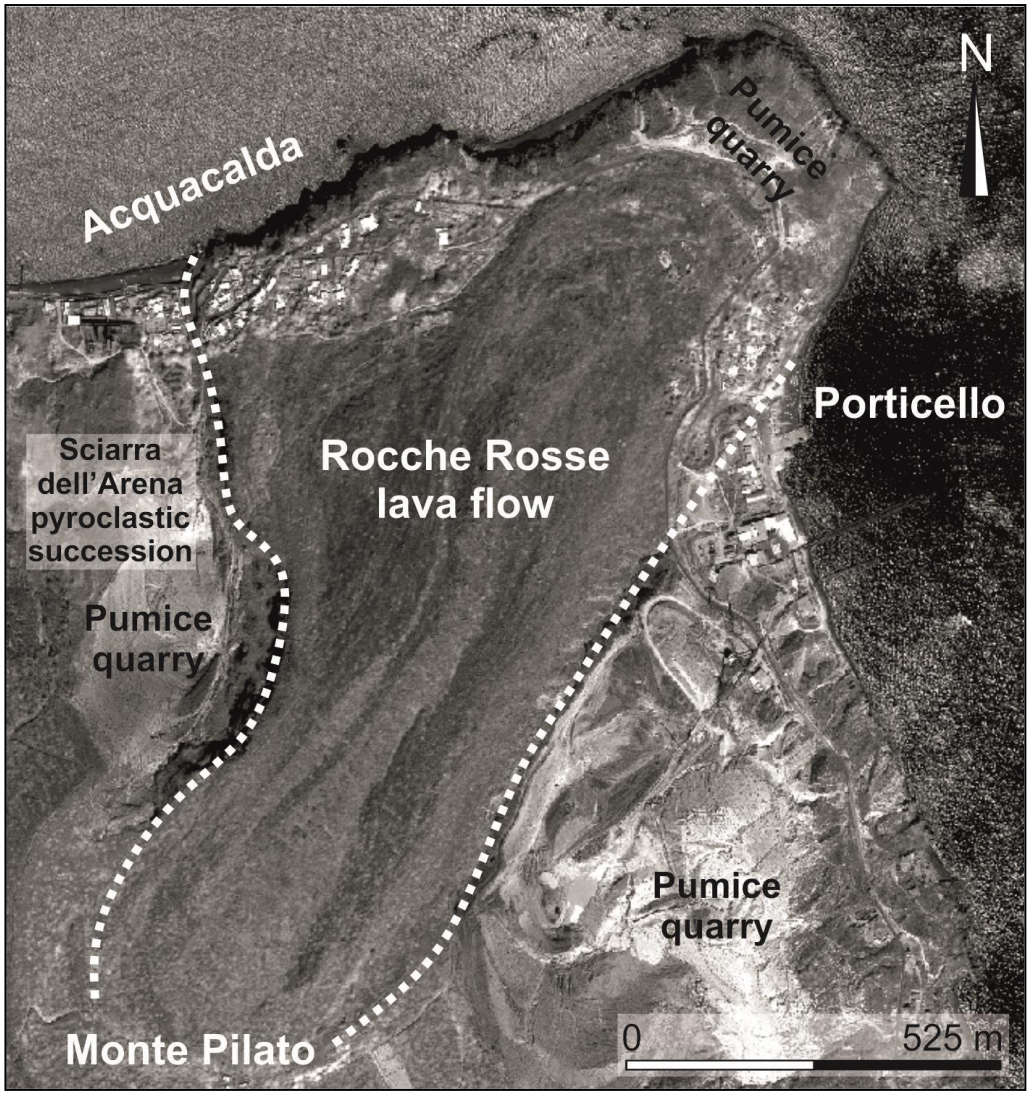

Figure 2.3: Satellite image of the Rocche Rosse lava flow, with Monte Pilato source area to the south west, and the surrounding Sciarra dell'Arena pyroclastic succession (Lucchi et al., 2010, 2013) surrounding the flow. The towns of Acquacalda and Porticello are also highlighted.

From source to the more distal flow regions, flow complexity increases (Figs. 2.4-2.5). The flow margins show a relatively simple flow regime from the source, with the east and west flow margins running parallel at a SW-NE orientation, before laterally spreading at 810 m from the source (Figs. 2.4-2.5). The western flow margin then runs in a N-S orientation, while the eastern flow margin continues in the SW-NE orientation. This lateral spreading coincides with a change in the closure direction of crescent-shaped ogives in the western

flow region (perpendicular to the flow margin, parallel to the western flow front). Ogives are a common feature of obsidian lava flows (Fink, 1980a, b; 1983; Castro and Cashman, 1999; Castro et al., 2002; Tuffen et al., 2013), and have been previously reported in the Rocche Rosse lava flow (Gottsmann and Dingwell, 2001b; Lucchi et al., 2010; 2013). Using the central closure point of the ogives, flow direction has been inferred (Fig. 2.4). Satellite imagery and ogive closure direction suggests flow moved in two distinct directions, forming two prominent flow lobes (Fig. 2.4). The flow direction to the north resulted in a more westerly flow lobe (indicated by the blue shaded zone in Fig. 2.5), responsible for the N-S aligned flow margin, and flow to the north east resulted in an eastern flow lobe, and the SW-NE flow margin (red zone in Fig. 2.5).

The flow contains a number of smaller breakout lobes (Welhan et al., 2002; Guilbaud et al., 2005; Applegarth et al., 2010; Tuffen et al., 2013), whereby areas of the flow extend beyond the straight margin of the flow, particularly at the flow front (Figs. 2.4-2.5). Such small breakout lobes are commonly identified in basaltic lava flows (e.g. Self et al., 1997; Blake and Bruno, 2000; Byrnes and Crown, 2001), and have been identified in other obsidian lava flows. For instance, Tuffen et al., (2013) identify over 80 breakout lobes on the 2011-2012 obsidian lava flow from Cordón Caulle (Chile). Tuffen et al., (2013) mapped breakout lobes on an advanced Land Imager image. This methodology has been applied here to the satellite imagery of the Rocche Rosse lava flow. In the western flow lobe, at least 7 breakout lobes have been identified (Figs. 2.4-2.6). One prominent breakout lobe has been identified in the eastern flow lobe. Breakout lobe length varies from ~26 m to ~48 m, width varies from ~20 m to ~56 m, and the area varies from 369 m^2 to 1,824 m^2 (see Fig. 2.6 and Table 2.1). Though there are instances of loose rocks within the sea at the edge of the flow, significant evidence of erosion from the sea is lacking.

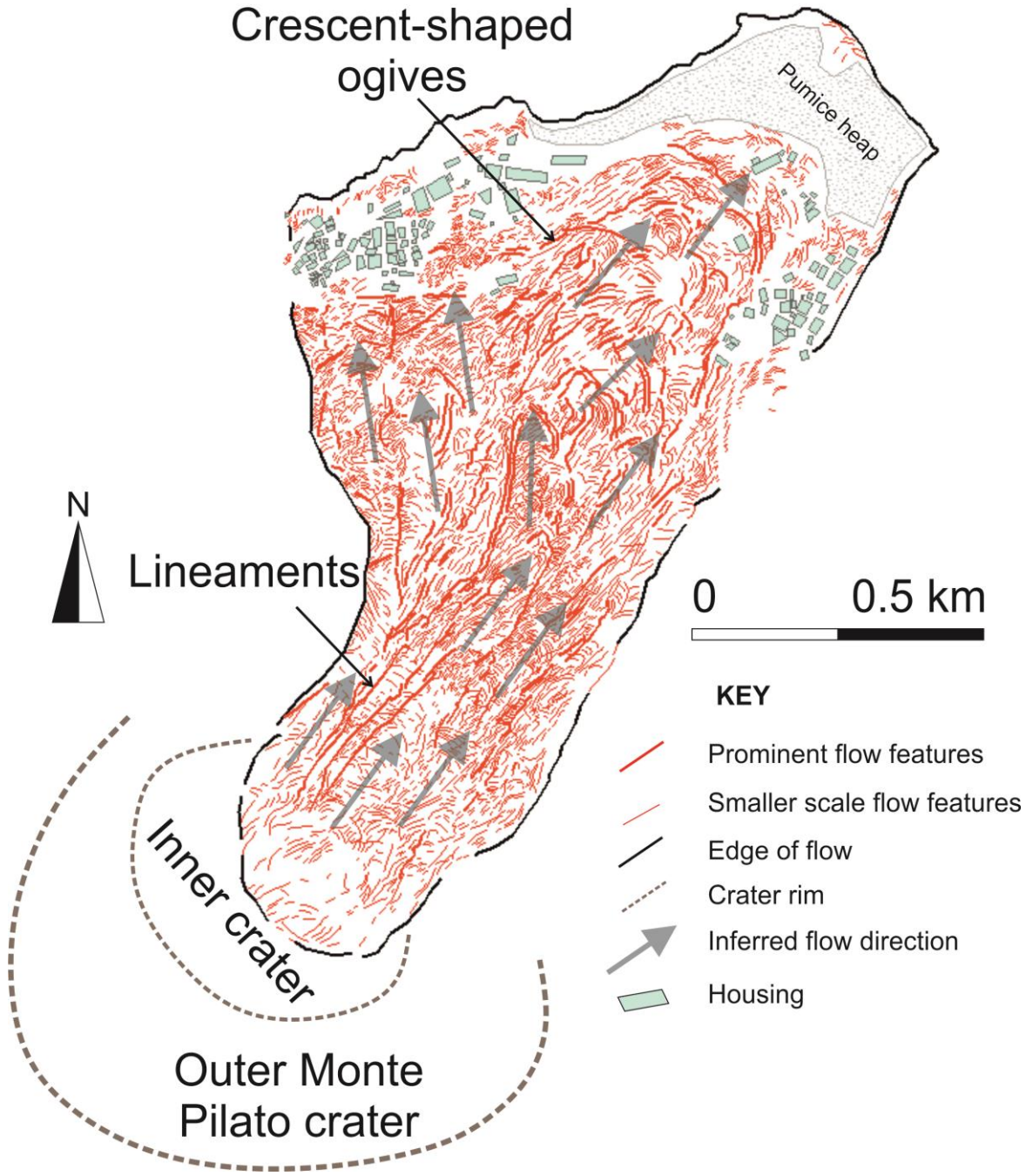

Figure 2.4: Annotations of the Rocche Rosse lava flow satellite image, displaying the Monte Pilato crater source and inner crater (brown dashed lines), flow margin outline (black lines), pervasive lineaments (bold red lines), curvilinear features (thin red lines) and anticipated flow lobe directions (grey arrows).

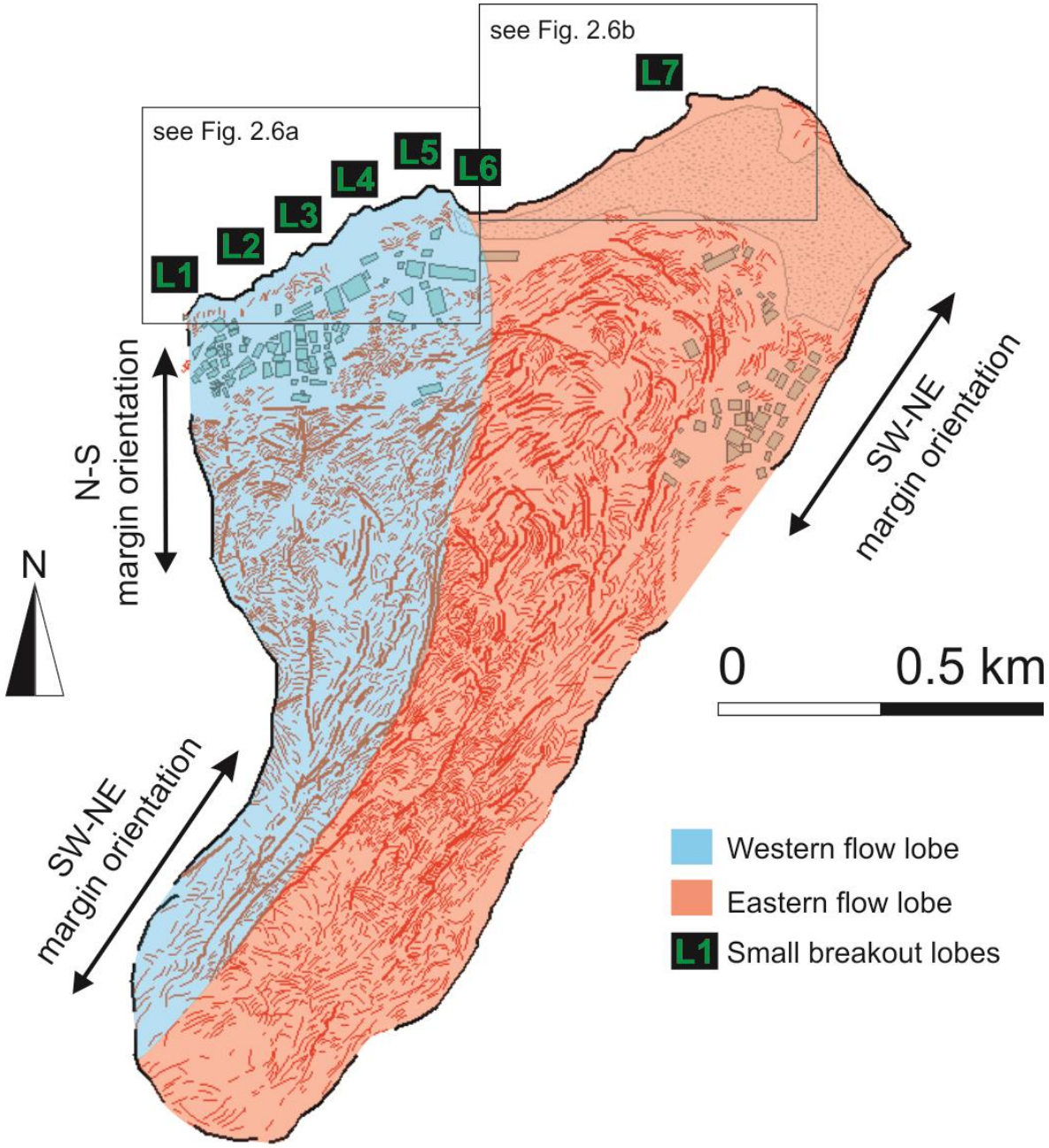

Figure 2.5: Annotation of satellite image highlighting two prominent flow lobes to the west and east, and smaller breakout lobes at the flow front. Orientation of margin orientation is also shown.

Table 2.1: Breakout lobe (see also Figs. 2.4-2.6) dimensional parameters (max. error ±5 m).

Breakout lobe	Lobe length	Lobe width	Lobe area
L1	~48 m	~56 m	1,824 m^2
L2	~40 m	~21 m	748 m^2
L3	~26 m	~33 m	552 m^2
L4	~26 m	~55 m	1,634 m^2
L5	~33 m	~30 m	749 m^2
L6	~30 m	~20 m	369 m^2
L7	~40 m	~60 m	1,704 m^2

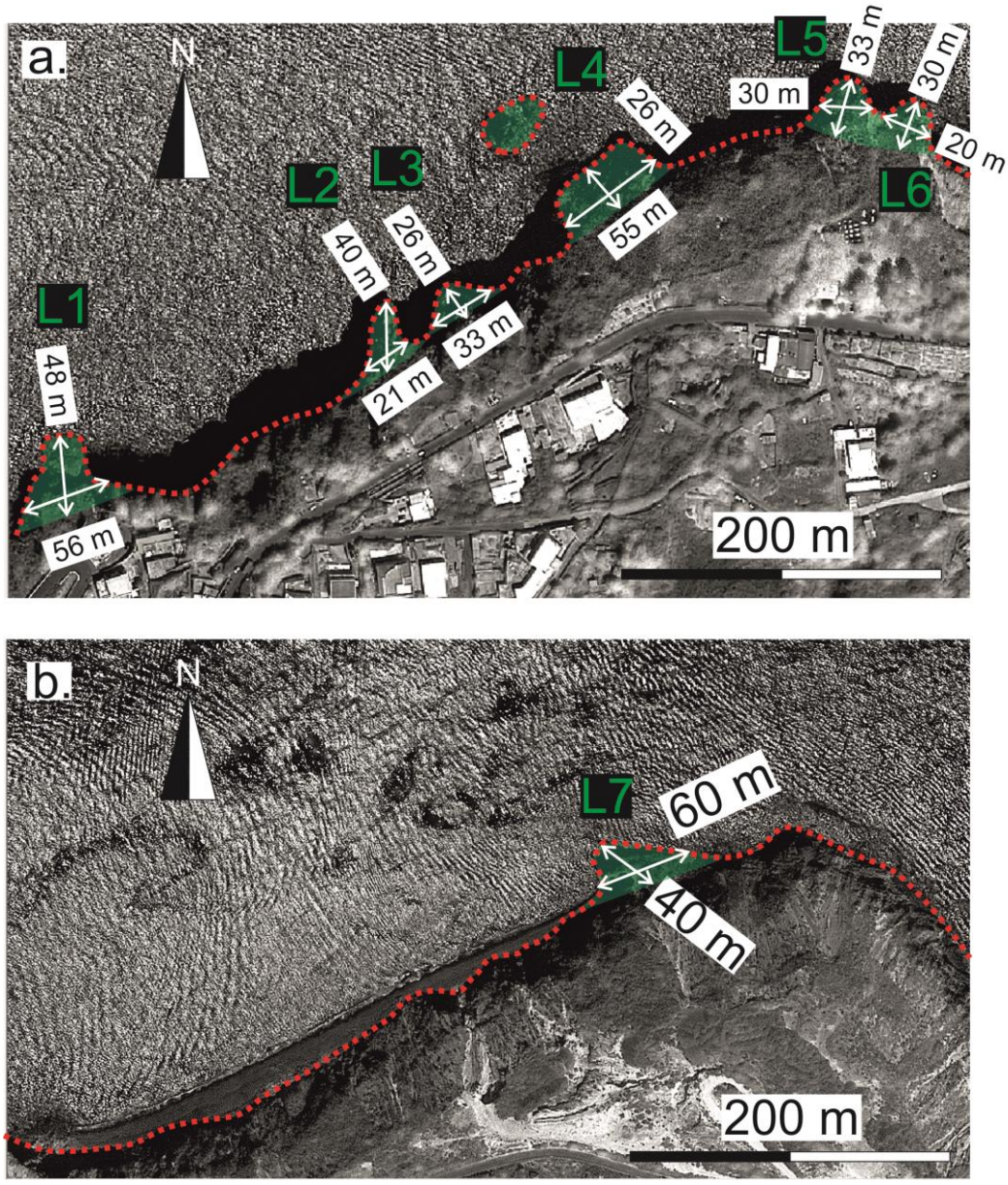

Figure 2.6: Small lava breakout lobes inferred from satellite imagery at the flow front. (a) Breakout lobes at the flow front of the western flow lobe. (b) Breakout lobe at the front of the eastern flow lobe.

2.5.3 Field observations and structural measurements

Flow Thickness and Stratigraphy

The flow extends from a 310 m elevation down to sea level (Fig. 2.7). Generally, the flow

thickens from the vent area (where the exposure is limited due to heavy vegetation) to mid-flow areas (approximately 1 km from the vent), before thinning gradually down to the flow front (determined from basal breccia unit). Along the western flank, the flow thickens from the vent to at least 40 m, before the flow diverts from a SW-NE orientation to a N-S orientation, thinning to 15 m at the flow front. The eastern lobe flank shows a more continuous orientation (~SW-NE, as previously identified in satellite imagery), and the flow thickens to 51 m, before gradually decreasing to 9 m at the flow front. Flow thickness is not always easily distinguishable due to variable vegetation, weathering, and man-made structures such as road cuttings, buildings and quarries. For instance, a man-made pumice heap in the distal region of the flow makes it difficult to identify the true height at the front.

Flow stratigraphy exposure varies along the flanks (Figs. 2.8-2.9). Key textural units, such as glassy and devitrified obsidian, brecciated zones and pumiceous units, can be identified at middle- and upper-flow regions (Figs. 2.8-2.10, summarised in Fig. 2.11). The Rocche Rosse lava flow sits atop older tephra deposits (Lucchi et al., 2010, 2013; Forni et al., 2013). There is evidence of sharp contacts between the underlying tephra deposits and the basal breccia of the lava flow (Figs. 2.8-2.9). The basal breccia is made up of angular obsidian blocks, from a few centimetres up to 0.5 m in size. Clasts are variably devitrified, and are commonly weathered orange. Basal breccia varies in thickness from 3 m to 10 m. The boundary between the basal breccia and obsidian is often difficult to distinguish, with pumiceous zones doming upwards in areas (Figs. 2.8d, f; 2.9), reaching the flow surface in upper flow regions (Fig. 2.8i). The pumiceous unit is a grey-white deposit, containing elongate vesicles. The pumiceous unit is a much more consistently thicker unit, ranging from ~7 m to ~25 m. The boundary between the pumiceous unit and the glassy obsidian is

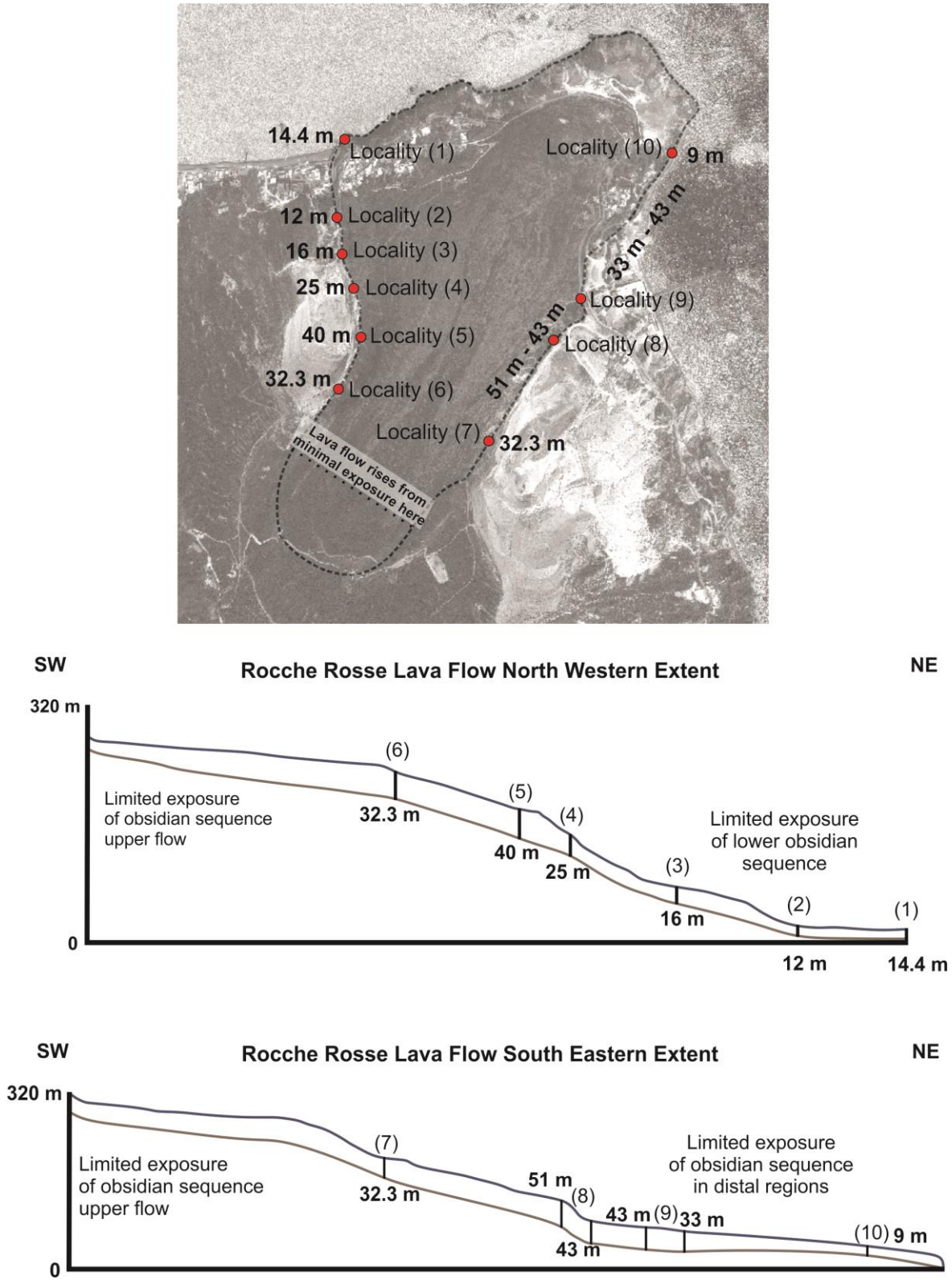

Figure 2.7: Flank height calculations (calculated at specific localities along each margin) of the flanks of the Rocche Rosse lava flow, showing an initial increase in flow thickness, followed by a thickness decrease towards the flow front.

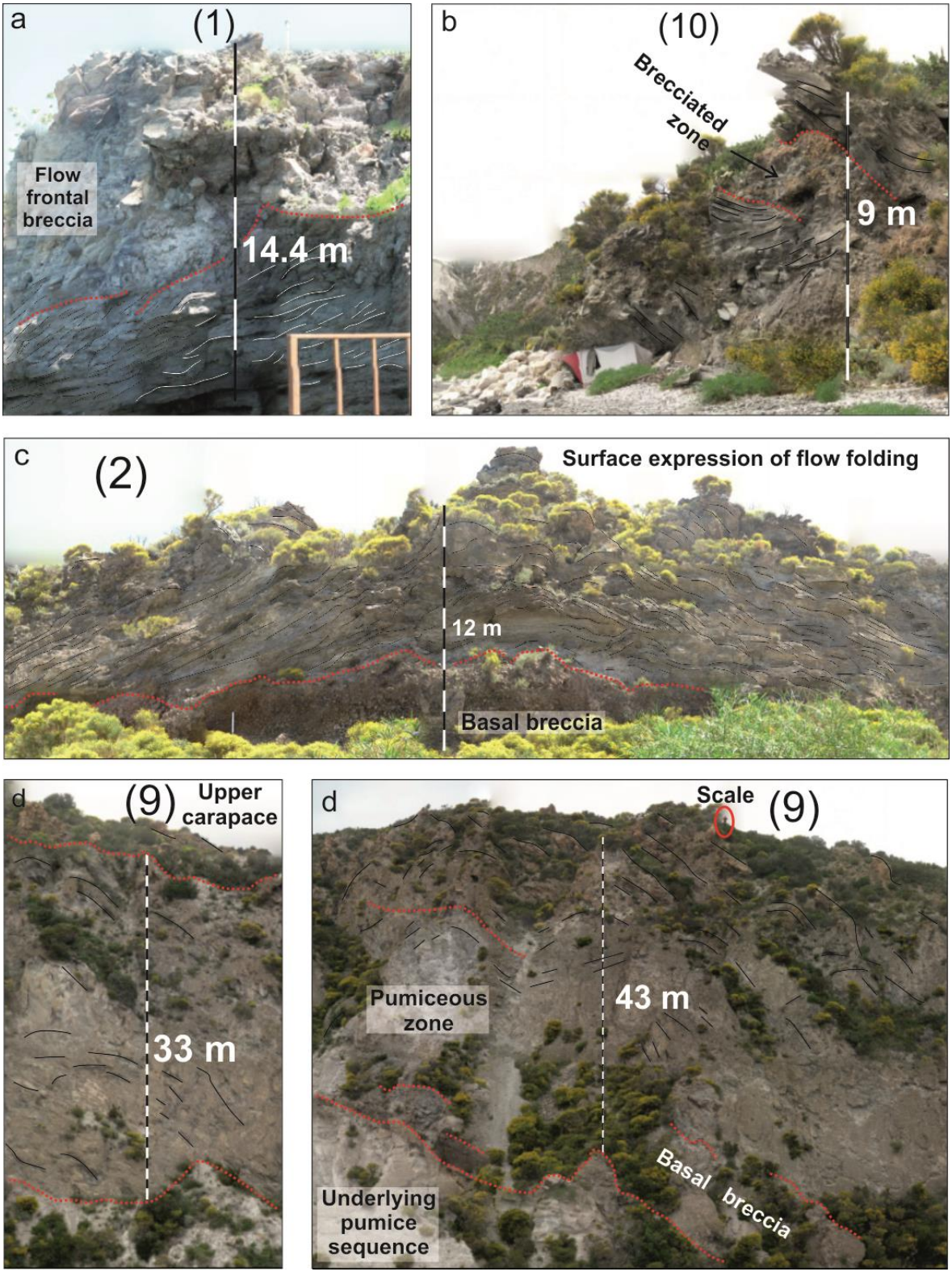

(Image continued on next page)

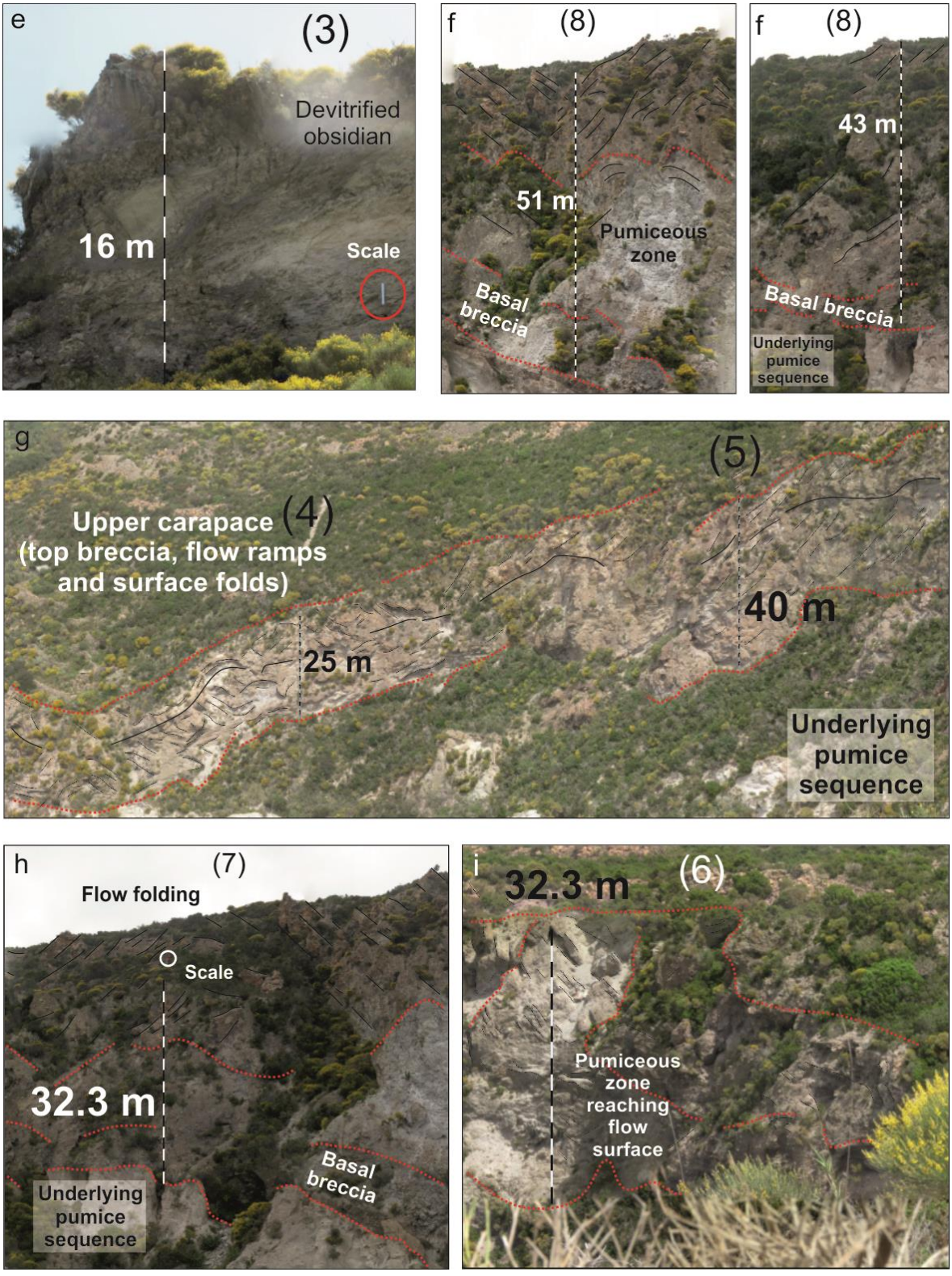

Figure 2.8: Flank photographs (with locality numbers from Fig. 2.7 also indicated), with distinguishable textural units, including obsidian, pumiceous and brecciated zones. (a) North-western flow front. (b) North-eastern flow front. (c) Western flank. (d) Eastern flank. (e) Mid-flow western flank. (f) Mid-flow eastern flank. (g) Mid- to upper-flow western flank. (h) Upper eastern-flow flank. (i) Upper western-flow flank.

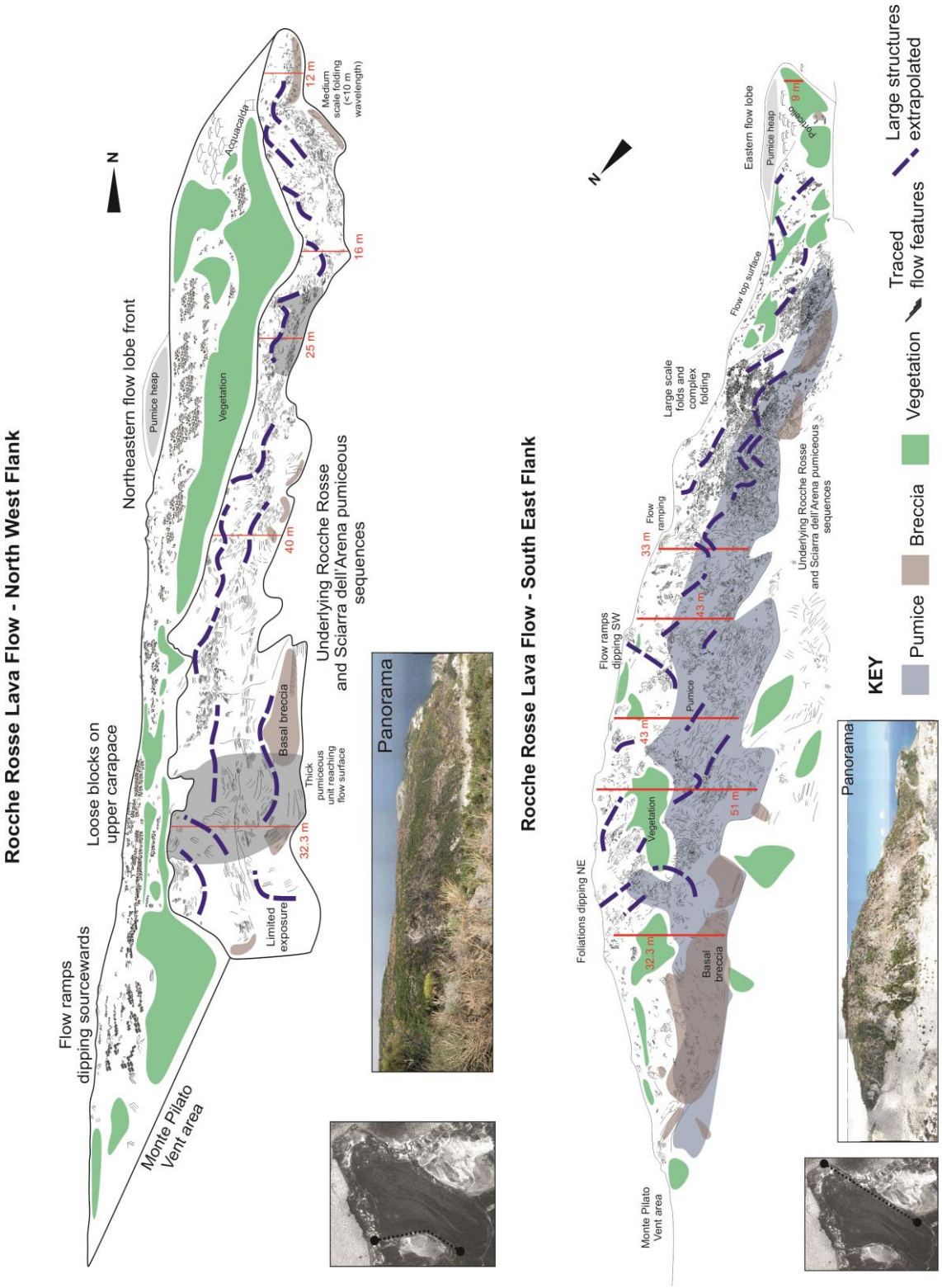

Figure 2.9: Digitisation of flow flanks (with panoramic photos shown) showing thickness variations, textural stratigraphy, foliation attitude and folds. General attitude of foliations indicated by dashed purple lines.

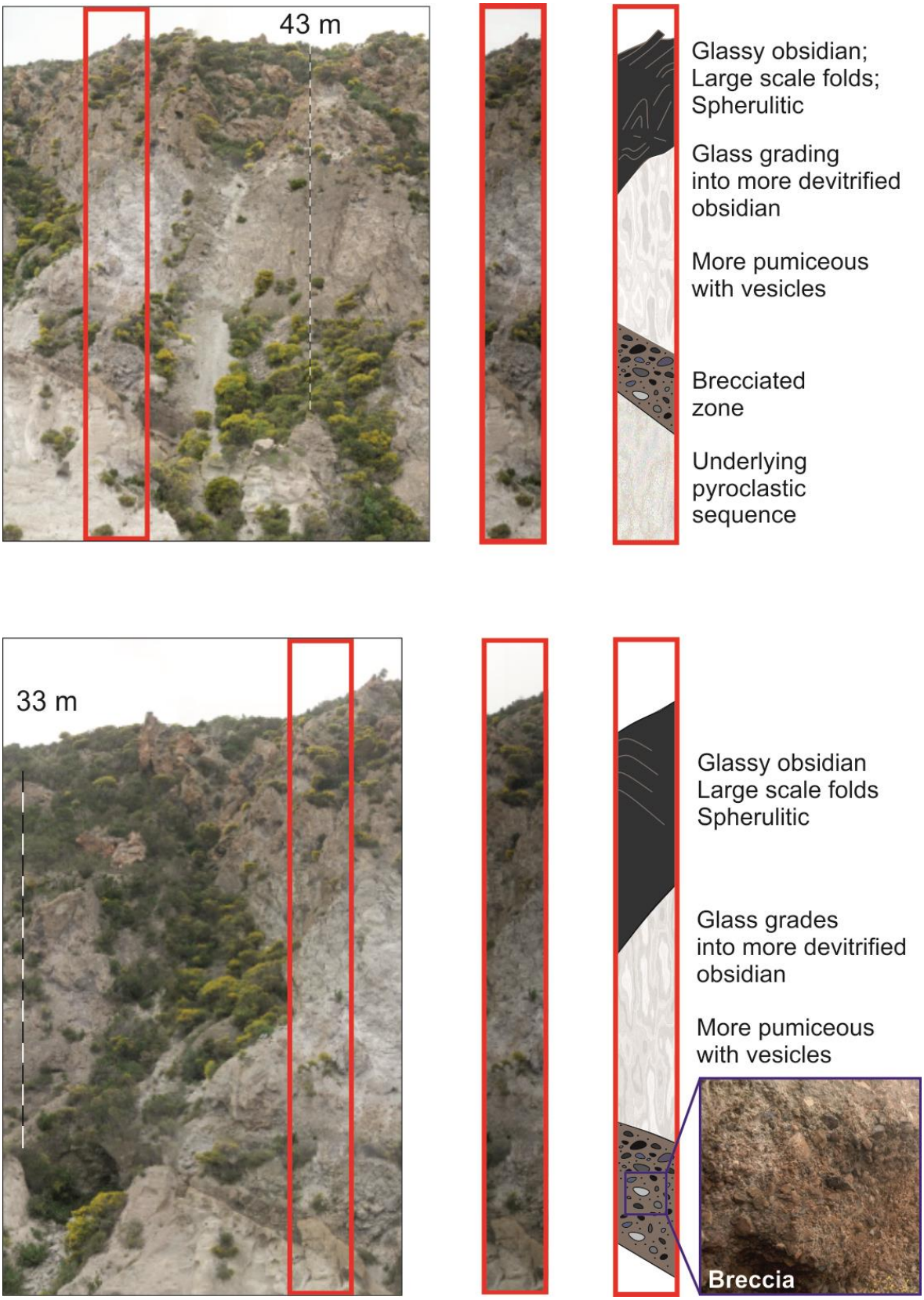

Figure 2.10: Extrapolated Rocche Rosse flow height and stratigraphy based on flank observations, showing an upper obsidian unit, pumiceous unit, basal breccia and underlying pyroclastic material.

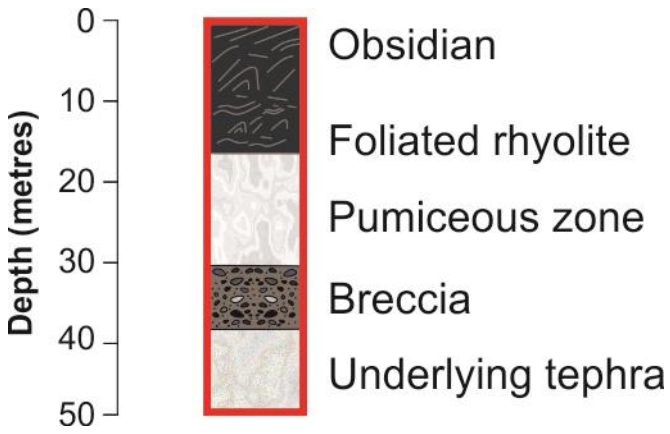

Figure 2.11: Simplified Rocche Rosse flow stratigraphic sequence based on flank observations and measurements, showing an upper obsidian unit, pumiceous unit, basal breccia and underlying pyroclastic material.

sometimes indistinguishable. The obsidian is weathered orange, often ramping away from the vent, and preserves widespread evidence of flow folding.

The thickness of the obsidian unit is in excess of 35 m in areas, and is sometimes the only exposed stratigraphic unit in lower, more distal flow regions, including at the flow front. The obsidian unit is more vesicular and microcrystalline in near-vent regions. There is evidence for an upper breccia and widespread loose blocks, often concentrating at the base of large folds and linear ridges. There is a lack of textural fabrics within the brecciated unit, generally displaying a poorly sorted and massive appearance. The pumiceous zone is generally welded, containing pumice, vesicular obsidian and ash, coloured white to dark grey. The boundary between the basal breccia and the pumiceous zone is often gradational over ~0.5 m. The pumiceous zone hosts multi-scale folding, (from <1 m up to >10 m) and thrust faulting (low to high-angle). The boundary between the pumiceous zone and the obsidian is again gradational, often indistinguishable. The unit grades into coherent, devitrified obsidian, before grading to glassy obsidian.

Flow foliation attitude

The Rocche Rosse obsidian contains foliation bands ranging in thickness from less than a millimetre up to several centimetres. Pumiceous zones also show foliations defined by differences in vesicularity. The arrangement of spherulites, microlites and vesicles often defines the foliation in obsidian, making it possible to recognise and measure planar structures in the field. Flow foliation measurements are shown in figure 2.12. Flow foliations are generally parallel to each other and are continuous across several metres, although they may be truncated or disrupted by small faults, with a few centimetres of displacement (Clay et al., 2013). Foliation attitude varies across flow from near vertical to horizontal dip (Figs. 2.12-2.15), and there are several areas where dip abruptly changes from shallow to steep. Generally, foliation strike can be traced across the flow in an ENE-WSW orientation at the flow front (perpendicular to the inferred flow movement), and in a N-S orientation in the more near-vent regions (parallel to flow movement). Foliation dip directional trends vary across the flow, but there are large localised areas where the foliations dips show a similar strike orientation. For instance, there are widespread regions mid-flow where the foliation dips away from the vent region, and regions at the front of the flow where foliation dips back towards the vent region.

Near the front of the flow and at the flanks, there are regions where the foliation dips towards, or away from, the centre of the flow. The orientation of strike and degree of dip vary significantly in flow frontal areas, as shallow as 12-14° in localised areas, but more commonly steeper than 60°. Strike often shows a NW-SE orientation, and is less commonly orientated SW-NE. In mid-flow and near-vent regions, foliation typically dips at 30-50° and, locally, dipping as shallow as 2-4° in near-vent regions. In more flow frontal regions, there is evidence of stacks of flow ramps, previously identified in Rocche Rosse

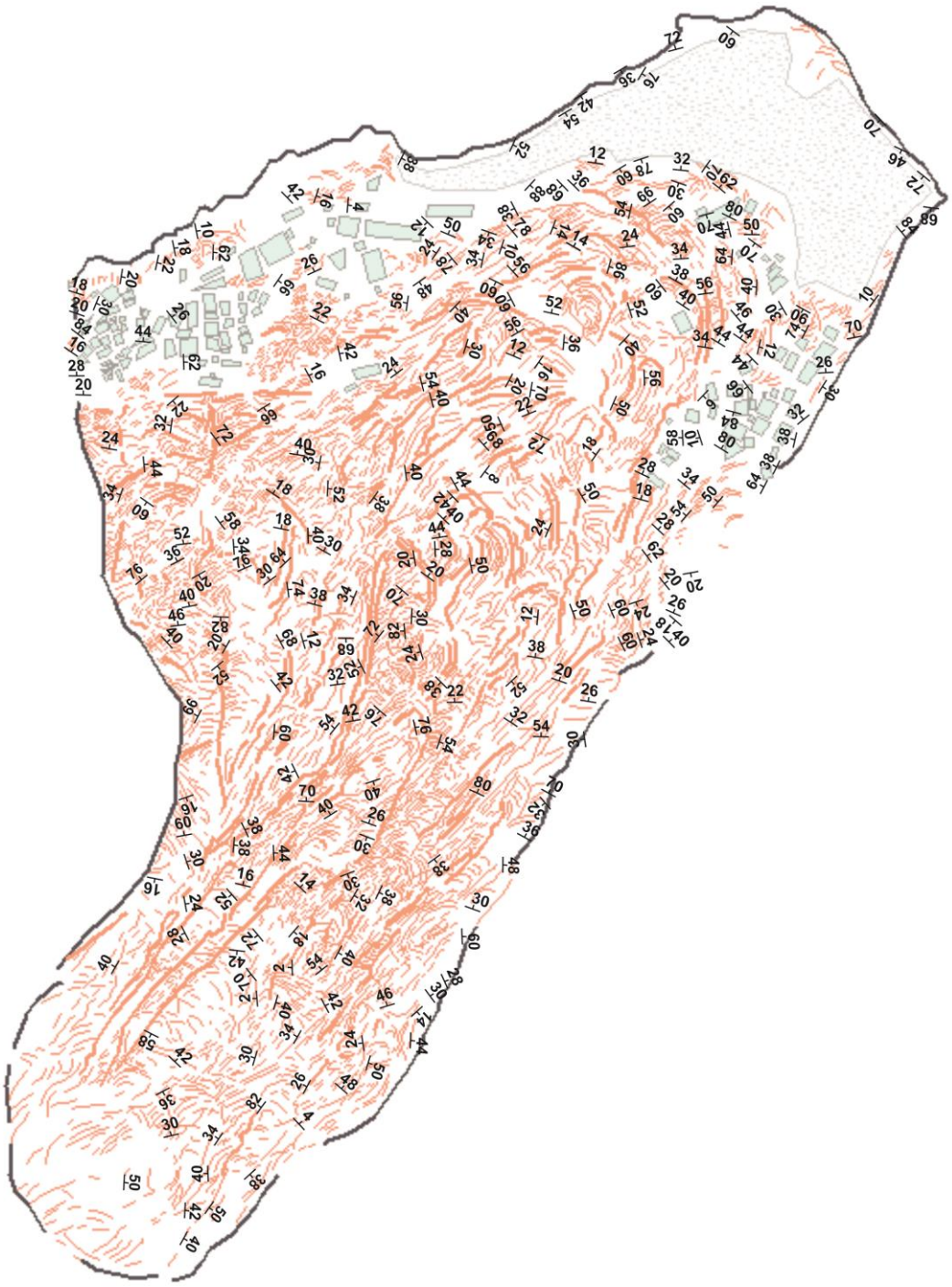

Figure 2.12: Mapped strike and dip measurements of flow foliations (overlain on satellite imagery traces).

studies (Cas and Wright, 1987; Gottsmann and Dingwell, 2001b; Lucchi et al., 2010; 2013). These individual ramps dip steeply back towards the source, and show a concave shape. At the north-easterly flow front, ramping foliation typically dips 60-70° back

towards the vent (south-westerly). At the north-western flow front, ramping is apparent with foliations dipping from near-horizontal (16°SW) up to near-vertical (84°SW) over a few metres. These steep ramping features form ridges parallel to flow margins, identified in satellite imagery.

A summary of orientation distribution data for foliations is represented on equal area stereographic plots shown in figures 2.13-2.15. Flow has been subdivided into quadrants based on flow morphology and topographic constraints (see Fig. 2.13), which has an effect on overall structural trends (e.g. planar foliation dip direction). For instance, two flow frontal lobes (identified in satellite imagery) have been categorised, with the eastern lobe extended continuously from source, and the western lobe extending in a northerly direction. Topographic contours indicate that the western lobe is a product of a change in topography, with a valley subdividing the lobes and contours dipping north-north westerly on the western side of the valley. Mid-flow has been subdivided based on the advance over a continuously steep topography before a break in slope and change in underlying topography in flow frontal areas (i.e. the eastern and western frontal lobes), and the upper flow is characterised by a relatively shallow topography in the source area prior to the steep incline.

Figure 2.13a displays all structural data across the Rocche Rosse flow extent, the stereoplot in figure 2.13b represents data from the front north-western flow lobe, figure 2.13c shows front north-eastern flow lobe data, figure 2.13d shows mid-flow region data and figure 2.13e shows upper (near-vent) flow region data. Overall, the structural data shows a relatively random distribution (high variability of strike and dip measurements). The distribution is a product of the steep to shallow ranging dips and a wide range of strike orientations. Figure 2.13a shows the main cluster of data trending roughly NNW-SSE, though it is generally sporadic. Flow divisions show slight variation (frontal lobes show a

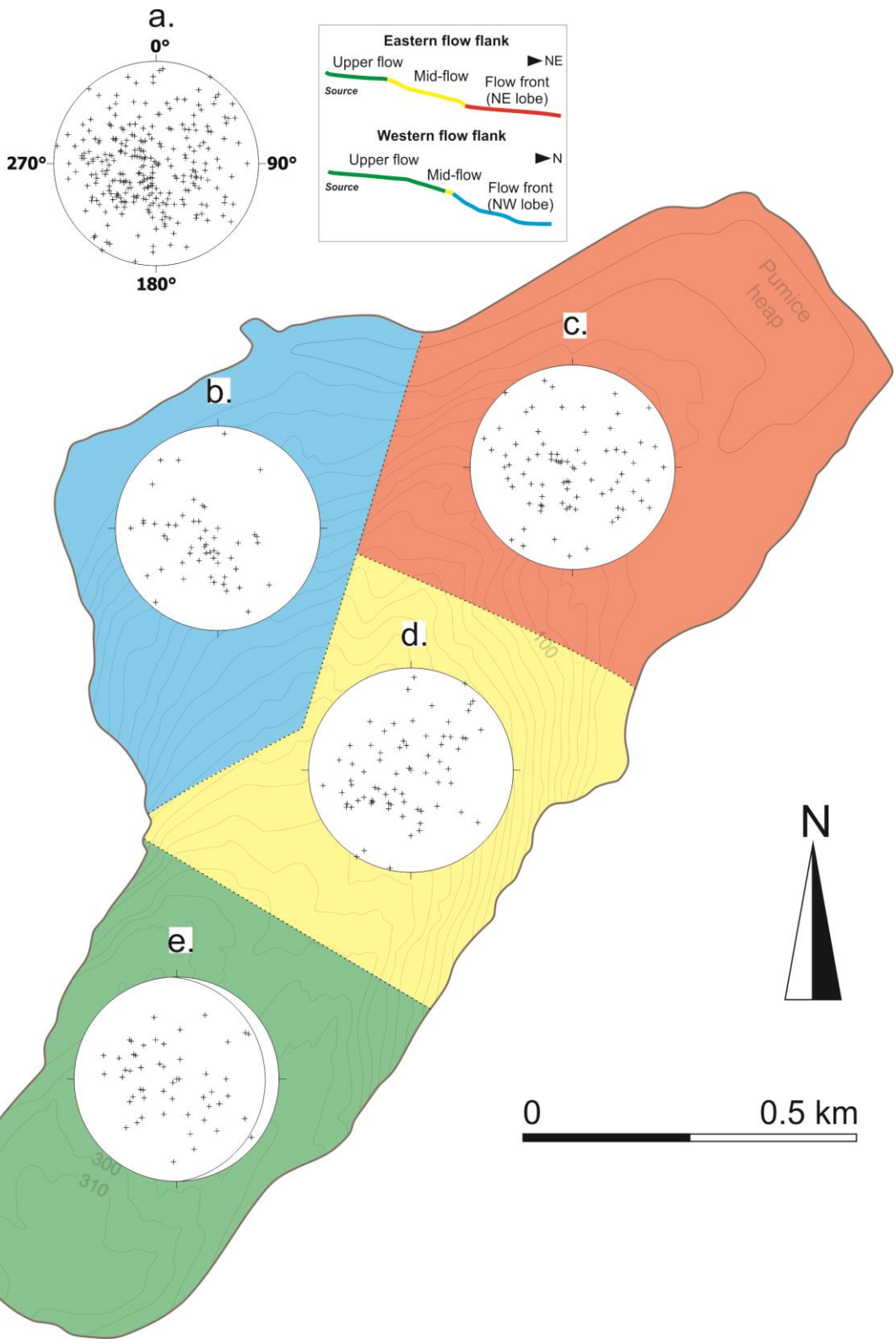

Figure 2.13: Stereographic plots of poles to foliations for structural measurements on the Rocche Rosse lava flow (equal area projection, lower hemisphere). (a) All structural data from across flow. (b) Front north-western flow lobe. (c) Front north-eastern flow lobe. (d) Mid-flow region. (e) Upper (near-vent) flow region. Key for flow segregation also shown (based on underlying topography).

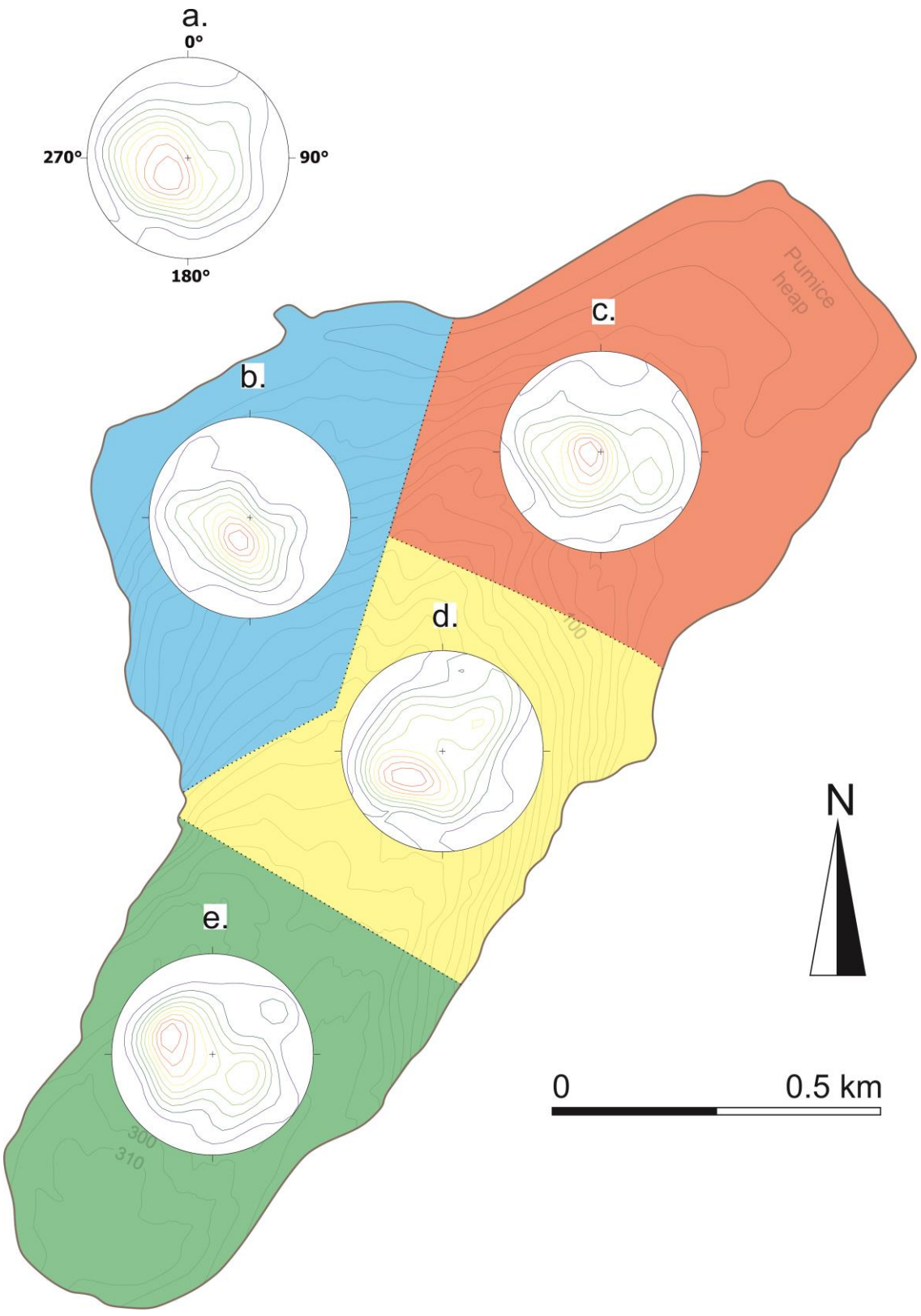

Figure 2.14: Contour density plots (showing density concentrations of data) of poles to foliations for structural measurements on the Rocche Rosse lava flow (equal area projection, lower hemisphere). (a) All structural data from across flow. (b) Front north-western flow lobe. (c) Front north-eastern flow lobe. (d) Mid-flow region. (e) Upper (near-vent) flow region.

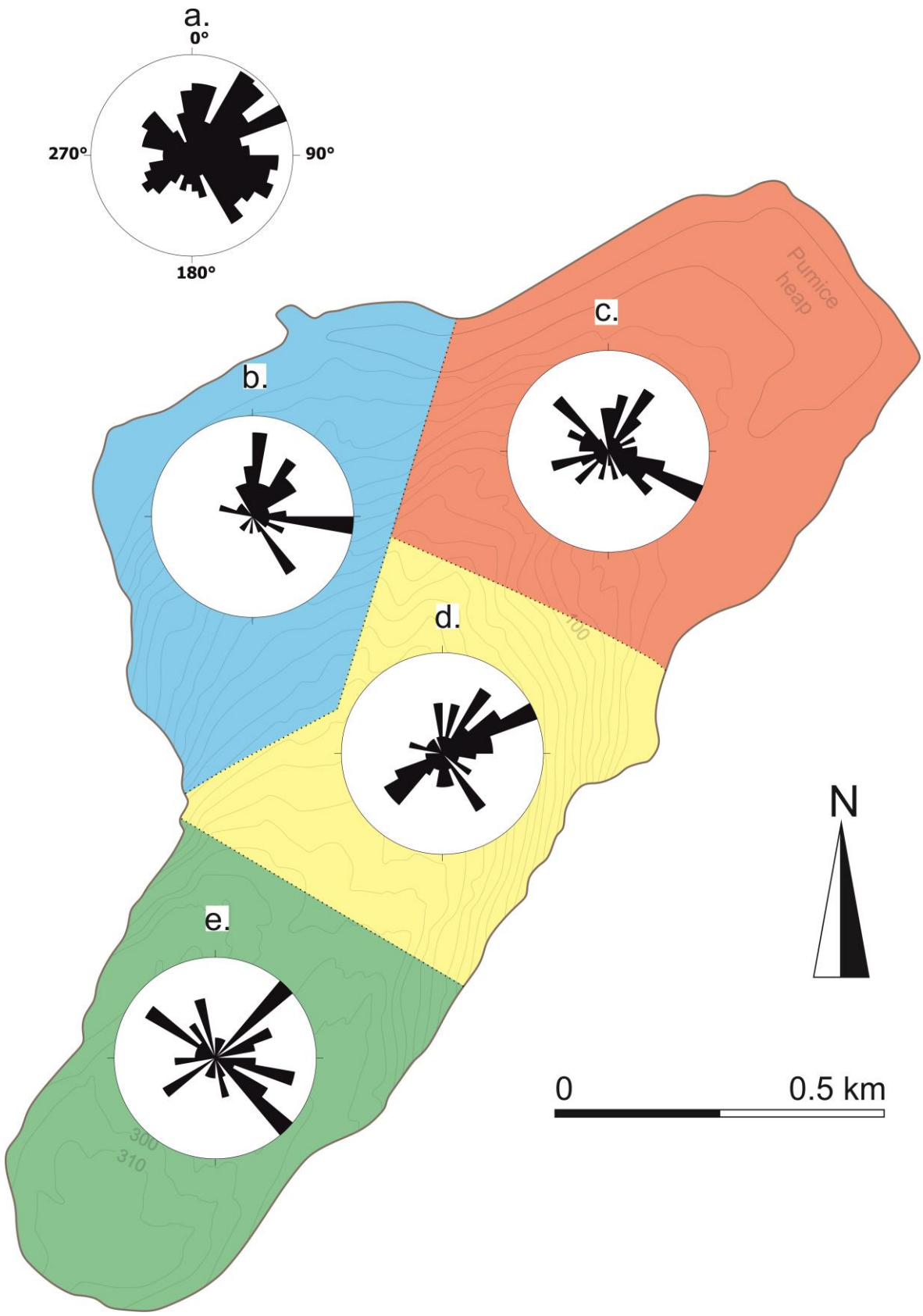

Figure 2.15: Rose diagrams of poles to foliations on the Rocche Rosse lava flow (equal area projection, lower hemisphere). (a) All structural data from across flow. (b) Front north-western flow lobe. (c) Front north-eastern flow lobe. (d) Mid-flow region. (e) Upper (near-vent) flow region.

rough NW-SE trend, mid-flow shows NNE-SSE trend and upper flow shows a N-S trend). The front north-western lobe shows a more relative degree of alignment distribution compared to the other sub-divisions. This is evident in the kinematic pole plot in figure 2.14b (red indicating a high plot correlation, with blue representing more scattered plots). Figure 2.14e indicates that the upper flow region has a relatively good correlation compared to the mid-flow and front north-eastern regions. Though there is a high dispersion, there is evidence for dip generally favouring a north easterly or south westerly direction (i.e. towards or away from source region in anticipated flow direction, see rose diagrams in Fig. 2.15). The front north-eastern lobe and upper flow region shows a more overall NW-SE dip direction, as indicated by rose plots (Figs. 2.15c, e). In the mid-flow region the foliation dips in a south-westerly and north-easterly direction (see Fig. 2.15d).

Folds

The primary flow foliation allows for the identification of flow folding, with folded bands showing differences in vesicularity and crystallinity (microlites and spherulites). Folds have been qualitatively characterised based on their closing and facing directions, and the vergence of the fold axial plane. Folds have also been described qualitatively based on the straightness of the hinge line, tightness, roundness and attitude of fold, fold symmetry, vergence and harmony. Parasitic folds (minor folds sitting upon the major fold) were also noted where observed. Complex folds are widespread across the entire lava flow, on a scale of decimetres to tens of metres, exhibiting differing structural characteristics (Fig. 2.16). Small scale flow folding (Fig. 2.16a) on a decimetre scale is extensive, as is larger scale folding (Fig. 2.16g, h), and parasitic folding is common (Fig. 2.16a, b, g). Fold axial

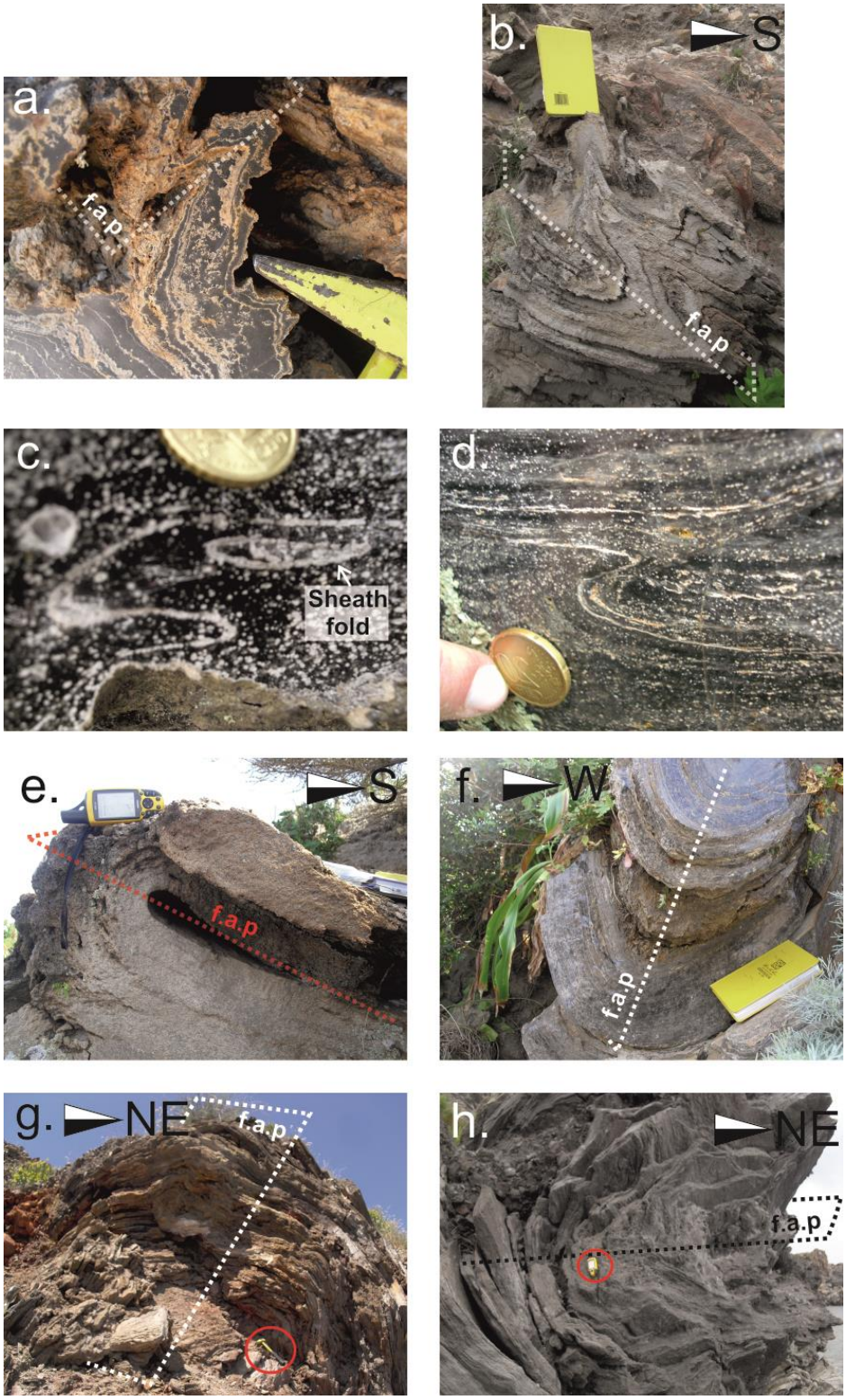

Figure 2.16: Rocche Rosse flow folding. (a) Small scale (less than 20 cm in wavelength and amplitude, see text for size set) folding. (b) Small scale folds superimposed on to medium scale (up to 2 m in wavelength and amplitude) folding (parasitic folds). (c) S-type folding. (d) Z-type folding. (e) Tight, recumbent fold. (f) Slightly inclined fold. (g) Large scale (several metres in wavelength and amplitude), inclined folding, with medium- and small scale parasitic folds (hammer for scale). (h) Large scale, recumbent fold (GPS for scale).

planes commonly dip steeply (typically 60-80°), orientated predominantly parallel to the eastern flow flank (SW-NE), or, to a lesser extent, parallel to the north-eastern flow lobe front (NW-SE; Fig. 2.17).

Generally, more folds (in terms of number of folds) are observed in areas from the flow more distal of the vent region, and measured larger scale folding is identifiable as surface ridges on the satellite image, and in flank exposures. Larger scale folding (2 m up to 15 m in amplitude and/or wavelength) is prevalent mid-flow, and more distally from the vent region, and often shows an inclined or recumbent attitude (Fig. 2.16e), open or close tightness, with parasitic folding. This small scale folding (<20 cm) is widespread across the flow, either as parasitic folding, or independent of any larger scale folding, upright and uniform. Parasitic folds verge towards the fold axial plane, showing typical asymmetric S and Z type sense of symmetry. In some complex areas of multiple folds, axial planes are disharmonic and hinge lines are curvilinear (at any scale). Sheath folds are also observed in select areas (Fig. 2.16c), more distal and northeast of the vent region. These are identifiable by their characteristic eye structures, normal to the transport direction. A common feature, particularly in larger scale folds, is the presence of highly crystalline (spherulitic) material at the centre of fold hinge zones, an observation also noted in the Rocche Rosse lava flow by Clay et al. (2013).

Fold axial plane data is displayed in Figure 2.17. Stereoplots of fold axial planes highlight a relatively random distribution of fold axial plane orientations and plane dips (Fig. 2.18). Density plots (Fig. 2.19) suggest that fold axial planes are generally steeply dipping, particularly in the front north-western flow lobe and mid-flow regions (Figs. 2.19b, d). Rose diagrams (Fig. 2.20) suggest some ordered fold axial plane dip directions in mid-flow and upper-flow regions, with mid-flow fold axial planes generally dipping north-easterly, and upper-flow regions showing a N-S dip orientation. The stereoplots emphasise a high

degree of folding has occurred in flow frontal regions, particularly the front north-eastern flow lobe (~48% of 125 total folds measured are located in this flow sub-division), with less folding evident in mid- to upper-flow regions (~14% and 12% respectively). Plots of fold axial planes have also been produced at differing fold magnitude (Figs. 2.21-2.23). Small scale folds (Fig. 2.21a), medium scale folds (Fig. 2.21b) and large scale folds (Fig. 2.20c) are classified on the basis of fold height and width. Small scale folds have been categorised as folds with height and width less than 20 cm, medium scale folds have a height and width between 0.2 m and 2 m, and large scale folds have a height and width over 2 m.

Stereoplots (Fig. 2.21) indicate there is generally no strong correlation within these sub-categories in terms of fold axial plane orientation or dip, with the exception of large scale folds. There is a minor uniform dip trend in larger scale folding of SW-NE, normal to flow direction (Fig. 2.22c). In total, 47% of folds are classified as medium scale, 37% are small scale, and only 17% of measured folds are classified as large scale folds (though identifying and measuring large scale folds may prove more difficult than medium and small scale folds).

Fold hinges and stretching lineations

Folds are often cylindrical, with straight fold hinges, and some examples of curvilinear folds (curved hinge lines). Fold hinges are typically orientated parallel to the north-eastern flow lobe front (NW-SE) (Fig. 2.24), with a slight orientation rotation to the SW-NE in the north-western flow lobe. Fold hinges generally dip shallowly (<30°) in flow frontal regions, becoming steeper in mid-flow (up to 30-60°) and near-vent regions (up to 70-80°).

Figure 2.17: Strike and dip measurements of fold axial planes on the Rocche Rosse lava flow (overlain on satellite imagery traces). Corresponding fold hinges (measured as dip and dip direction (azimuth) are shown and discussed below).

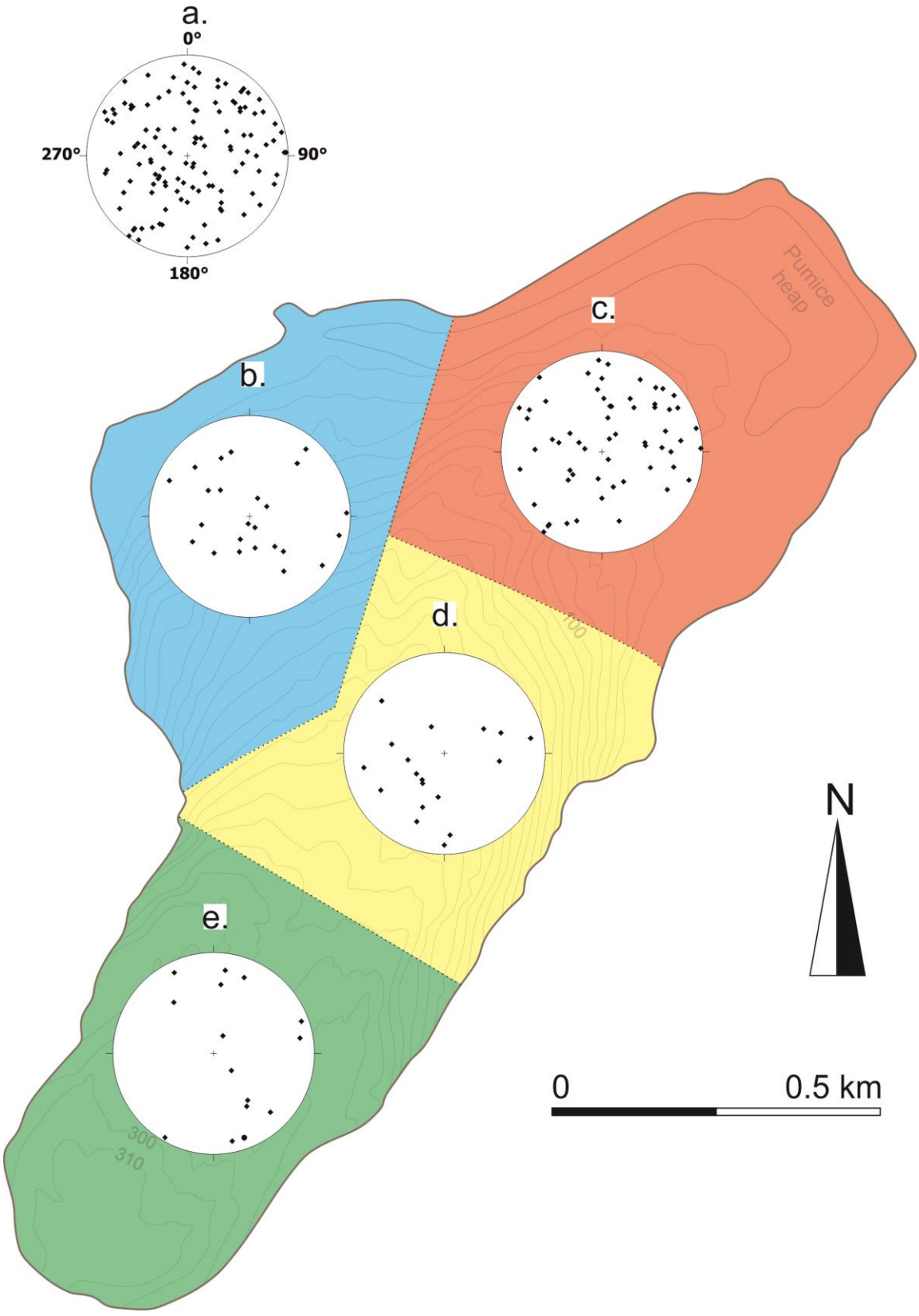

Figure 2.18: Stereographic plots of fold axial planes on the Rocche Rosse lava flow (equal area projection, lower hemisphere). (a) All structural data from across flow. (b) Front north-western flow lobe. (c) Front north-eastern flow lobe. (d) Mid-flow region. (e) Upper (near-vent) flow region.

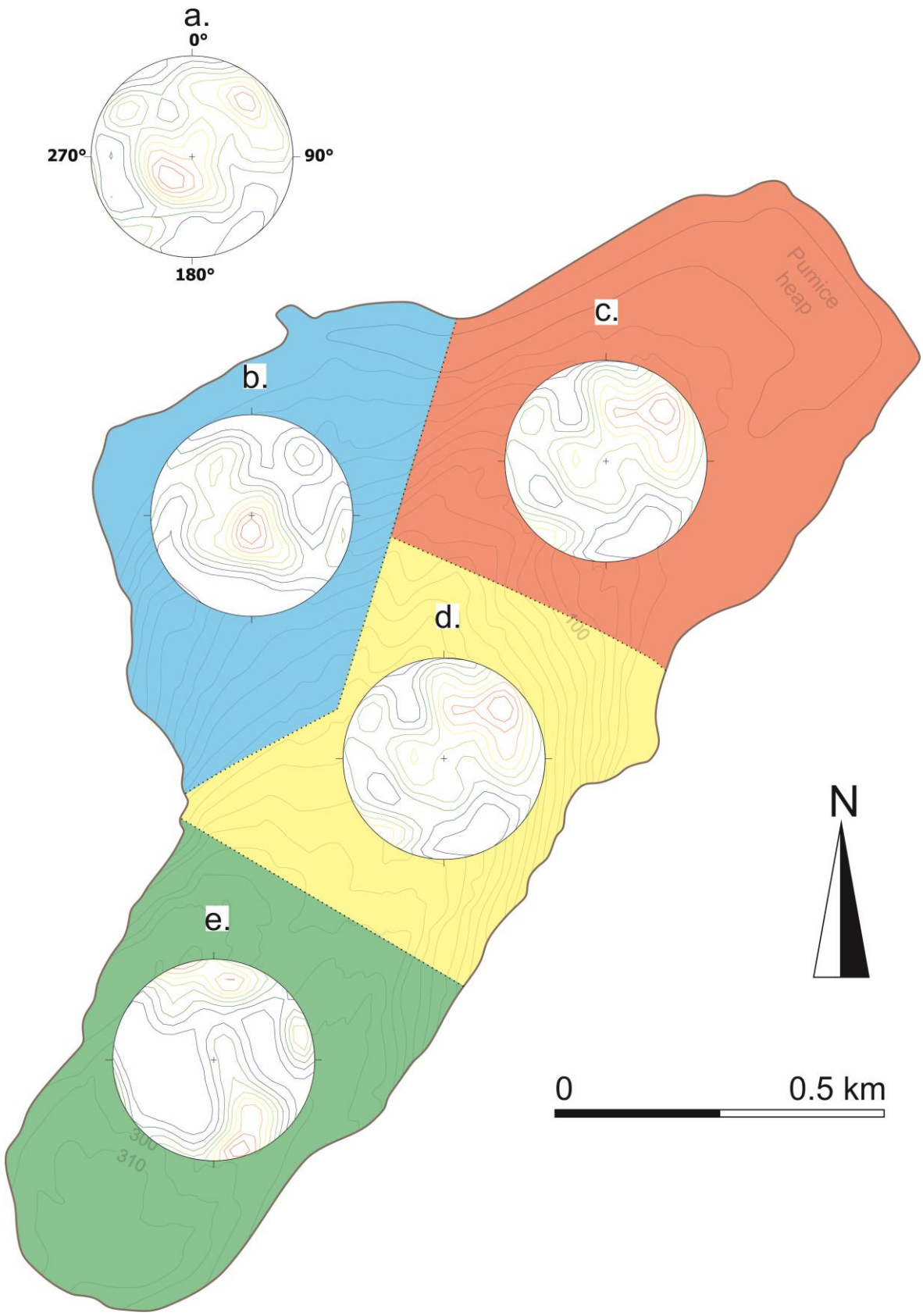

Figure 2.19: Contour density plots of fold axial planes on the Rocche Rosse lava flow (equal area projection, lower hemisphere). (a) All structural data from across flow. (b) Front north-western flow lobe. (c) Front north-eastern flow lobe. (d) Mid-flow region. (e) Upper (near-vent) flow region.

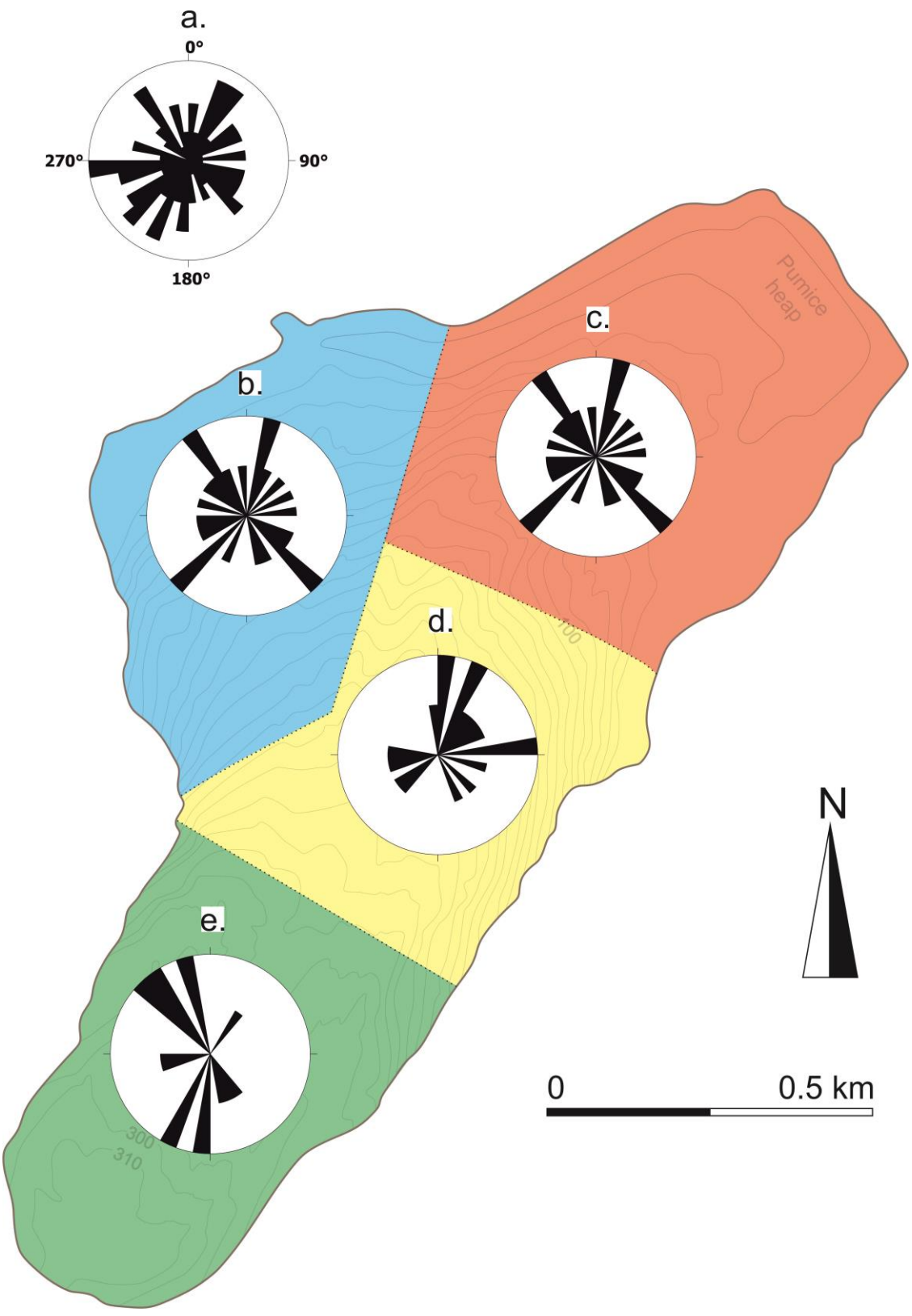

Figure 2.20: Rose diagrams of fold axial planes on the Rocche Rosse lava flow (equal area projection, lower hemisphere). (a) All structural data from across flow. (b) Front north-western flow lobe. (c) Front north-eastern flow lobe. (d) Mid-flow region. (e) Upper (near-vent) flow region. Division of flow as previously described.

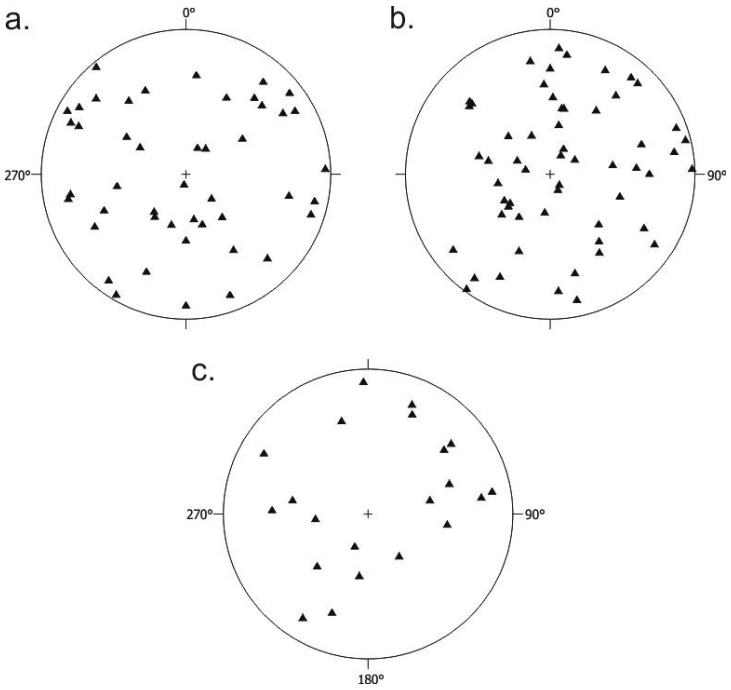

Figure 2.21: Stereographic plots of fold axial planes on the Rocche Rosse lava flow (equal area projection, lower hemisphere). (a) Small scale folds. (b) Medium scale folds. (c) Large scale folds. See text for fold classification specifications.

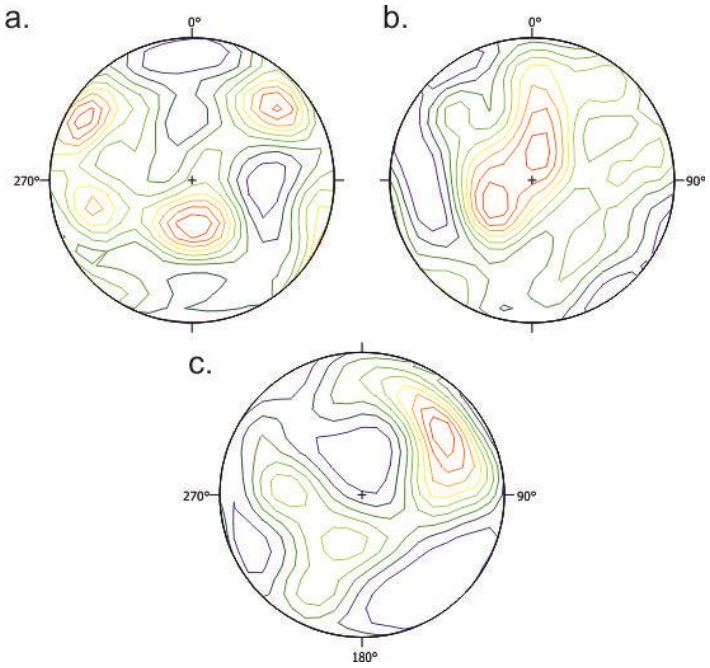

Figure 2.22: Contour (density) plots of fold axial planes on the Rocche Rosse lava flow (equal area projection, lower hemisphere). (a) Small scale folds. (b) Medium scale folds. (c) Large scale folds. See text for fold classification specifications.

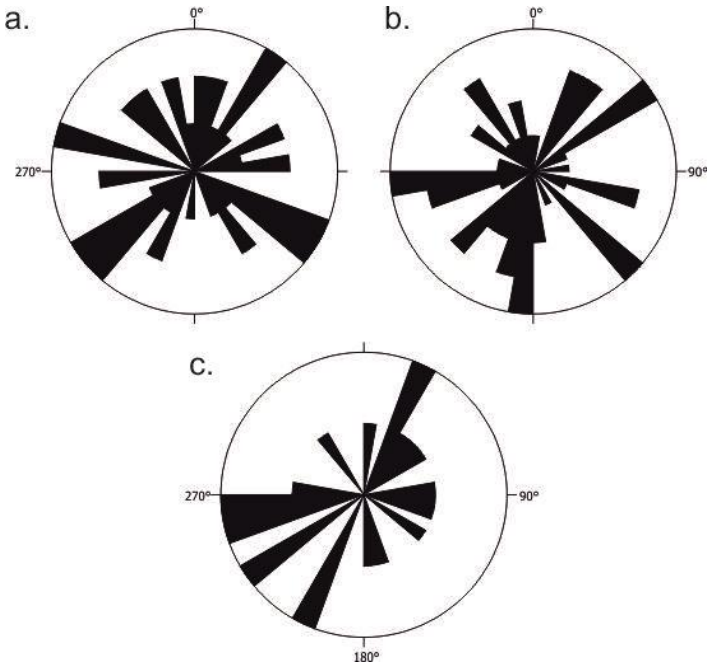

Figure 2.23: Rose diagrams of fold axial planes on the Rocche Rosse lava flow (equal area projection, lower hemisphere). (a) Small scale folds. (b) Medium scale folds. (c) Large scale folds. See text for fold classification specifications.

Stereoplots of fold hinges highlight a relatively scattered distribution (with fold hinges dipping in a variety of directions, see Fig. 2.25), dipping relatively steeply overall. This is further emphasised by the density plots (Fig. 2.26), showing a higher concentration of higher dips (above 60°). This is particularly evident in flow frontal regions (Figs. 2.25b, c; 2.26b, c; 2.27b, c) compared to mid-flow and upper-flow regions (Figs. 2.25d; 2.26d; 2.27d). Fold hinges show an overall E-W trending attitude (shown by the rose diagrams in figure 2.27), trending more north-easterly in the frontal north-eastern flow lobe, and south-easterly in upper-flow regions. Smaller scale folds show a more scattered attitude distribution compared to medium- and large scale folds (Figs. 2.28-2.30).

Stretching lineations (penetrative elongate linear features) are prevalent across the flow extent (Fig. 2.31). In the Rocche Rosse lava flow, stretching lineations form a parallel alignment of flattened spherulites, with their long axes stretched during deformation.

Stretching lineations are assumed to form parallel to the long axis of the finite strain ellipsoid, i.e. in direction of shear (Tikoff and Green, 1997). Stretching lineations are penetrative, and can either be continuous (Figs. 2.31a, b), over tens of centimetres, or manifested as prolate- or cigar-shaped spherulites, in the plane of the foliation (often observed on the underside of the plane – Fig. 2.31b). Stretching lineations are more common in mid-flow areas, particularly over prominent ridges identified in satellite imagery, and are generally absent at the flanks in middle- to upper-flow regions. Measured stretching lineations coincide with prevalent lineaments identified in satellite imagery (Fig. 2.32). Stretching lineations are widespread at the frontal regions of the flow, with more dispersed orientations.

The most common direction of stretching lineations is a dip towards NNE, coinciding with the overall flow direction (Figs. 2.33-2.35). As previously mentioned, this is most evident in middle- and upper flow regions, centrally, occurring predominantly within ridge depressions. In some instances in these regions, the stretching lineations dip back sourcewards (likely due to surface folding), but are still orientated in agreement with a NNE flow direction. In flow- frontal regions, the majority of stretching lineations still show a NNE dip (or SSW dip with a comparable dip azimuth), but there is also notable evidence for stretching lineations plunging westwards and, more commonly, eastwards. Stretching lineations are much more widespread in frontal regions, and in the western-frontal region, orientations and dip favour a more north-north westerly direction. The dip of the stretching lineations varies from near- horizontal (2°) up to 90°. These dips are more variable on a localised scale in flow frontal regions, but typically dip ~30-40°. Mid-flow, the stretching lineations dip more shallowly, commonly less than 30°. In some localities, individual measurements vary as much as 40° within a few metres of each other.

Figure 2.24: Dip and dip direction measurements of fold hinges on the Rocche Rosse lava flow (corresponding to fold axial planes mapped and described above).

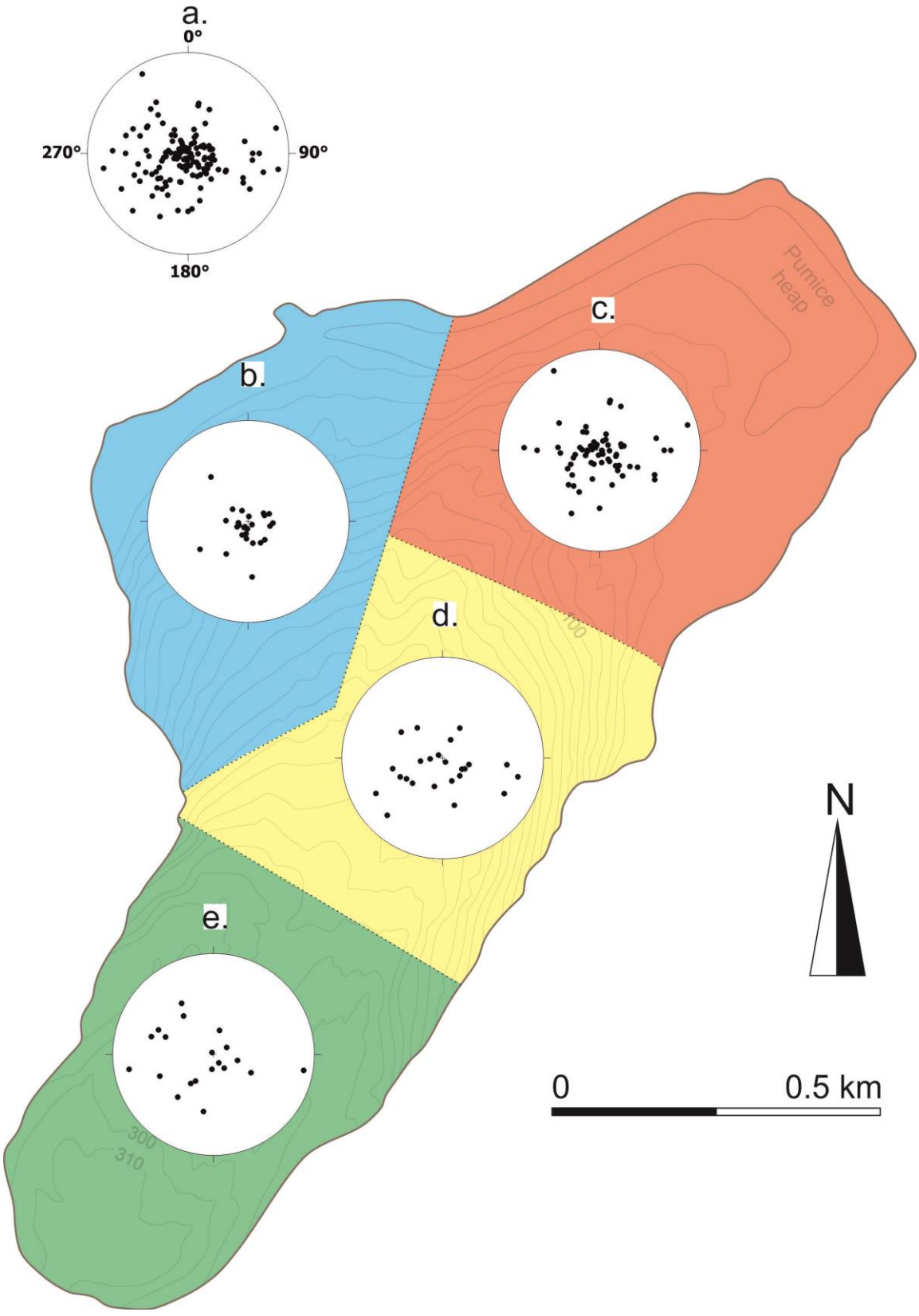

Figure 2.25: Stereographic plots of fold hinges on the Rocche Rosse lava flow (equal area projection, lower hemisphere). (a) All structural data from across flow. (b) Front north-western flow lobe. (c) Front north-eastern flow lobe. (d) Mid-flow region. (e) Upper (near-vent) flow region.

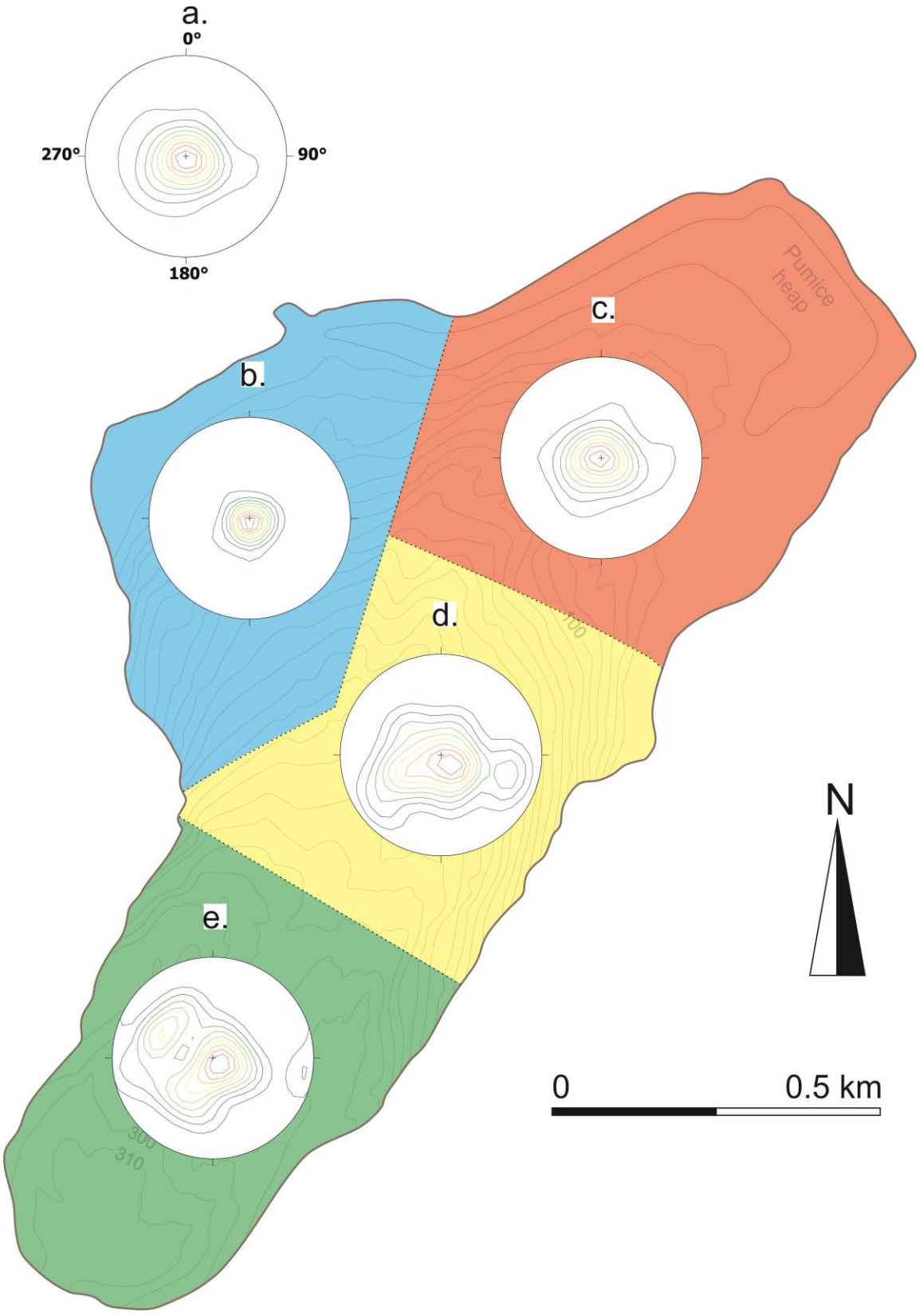

Figure 2.26: Contour density plots of fold hinges on the Rocche Rosse lava flow (equal area projection, lower hemisphere). (a) All structural data from across flow. (b) Front north-western flow lobe. (c) Front north-eastern flow lobe. (d) Mid-flow region. (e) Upper (near-vent) flow region.

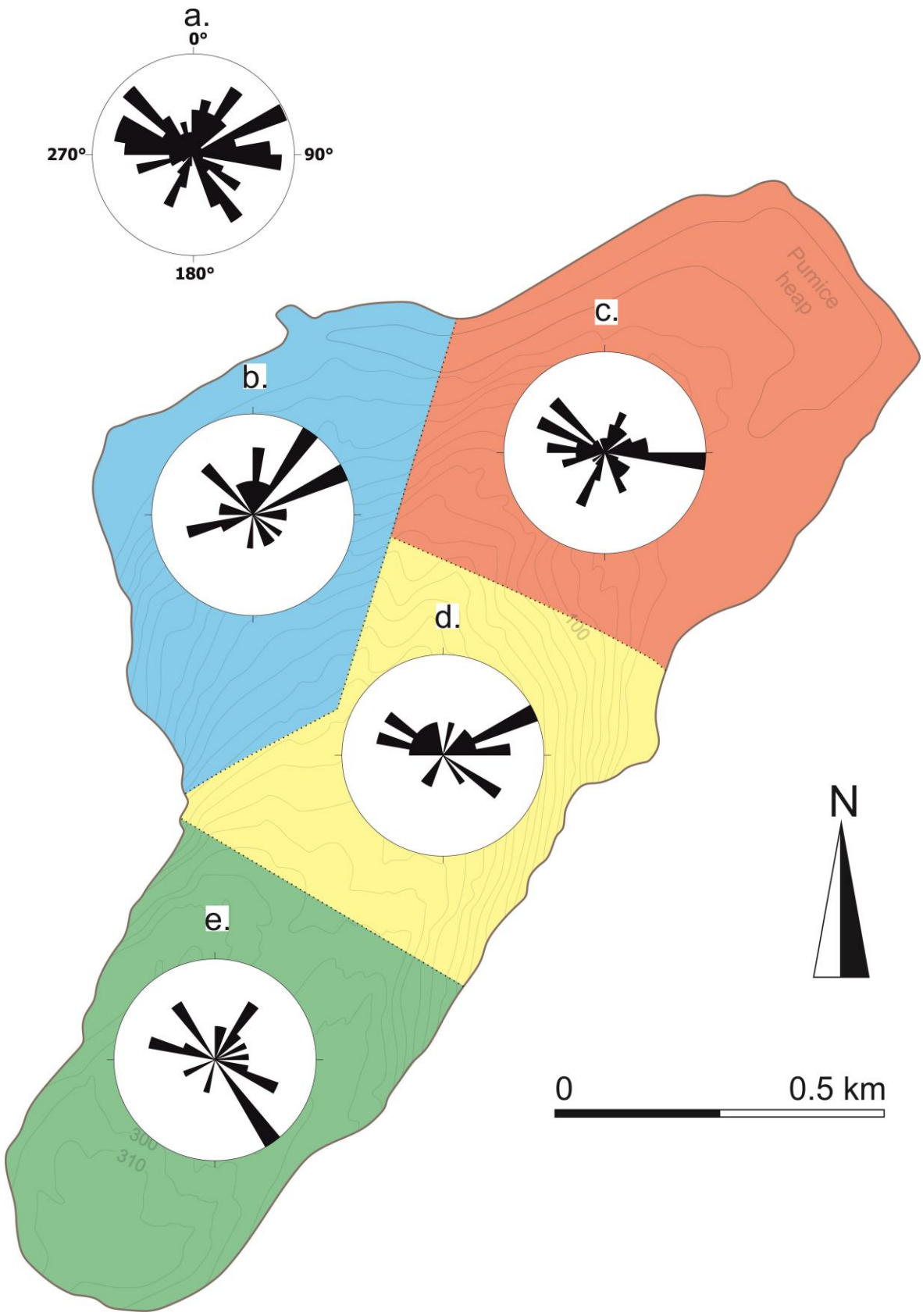

Figure 2.27: Rose diagrams of fold hinges on the Rocche Rosse lava flow (equal area projection, lower hemisphere). (a) All structural data from across flow. (b) Front north-western flow lobe. (c) Front north-eastern flow lobe. (d) Mid-flow region. (e) Upper (near-vent) flow region.

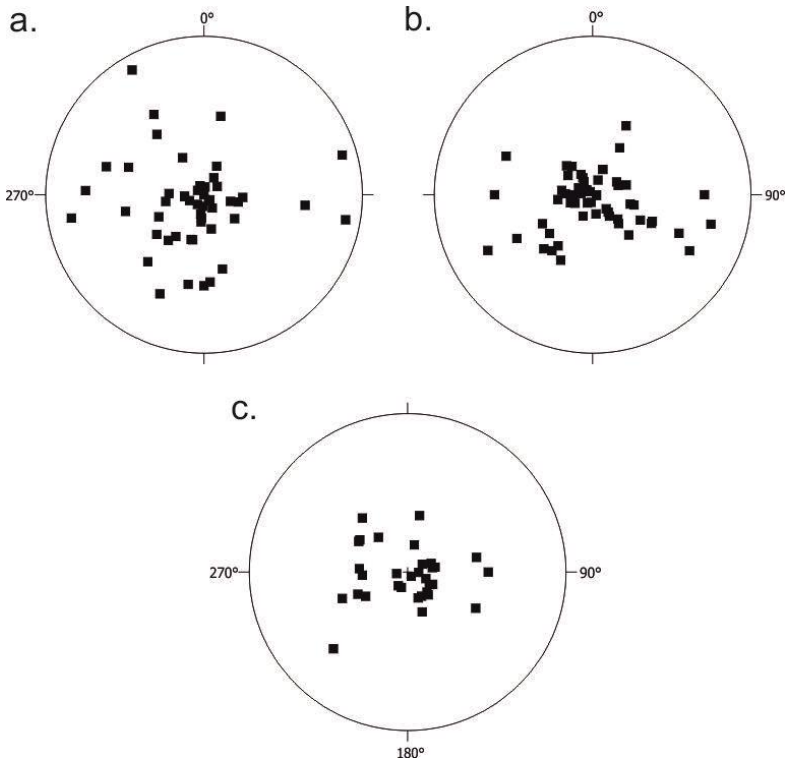

Figure 2.28: Stereographic plots of fold hinges of Rocche Rosse lava flow (equal area projection, lower hemisphere). (a) Small scale folds. (b) Medium scale folds. (c) Large scale folds.

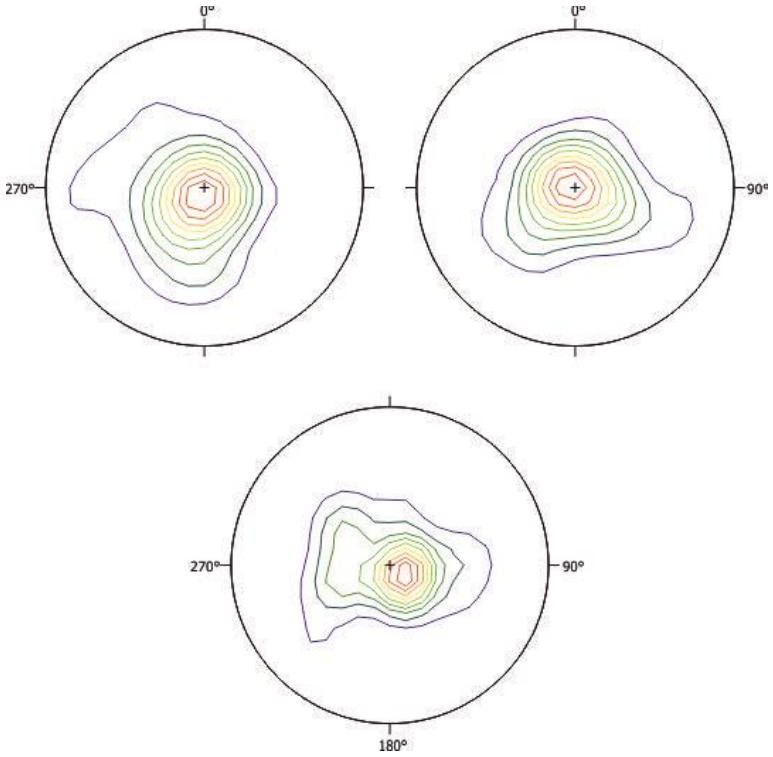

Figure 2.29: Contour density plots of fold hinges of Rocche Rosse lava flow (equal area projection, lower hemisphere). (a) Small scale folds. (b) Medium scale folds. (c) Large scale folds.

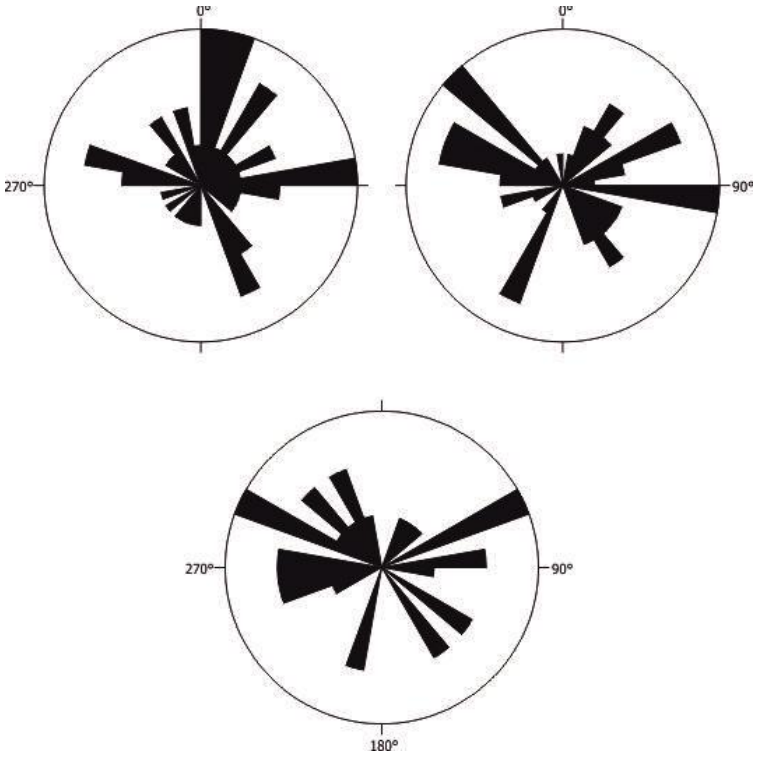

Figure 2.30: Rose diagrams of fold hinges of Rocche Rosse lava flow (equal area projection, lower hemisphere). (a) Small scale folds. (b) Medium scale folds. (c) Large scale folds.

Stretching lineation data shows variable dips and azimuths, with a general SW-NE trend (i.e. trending with flow direction; Figs. 2.32-2.35). The rose diagrams (Fig. 2.35) show that, although there is a strong SW-NE trend, there is a wide spread of dip directions, and the north-western frontal lobe differs from the other flow sub-divisions, with stretching lineations predominantly dipping in a SE-NW orientation (parallel to the north-east flow lobe margin). The majority of stretching lineations plunge steeply (above 60°, see density plots in Fig. 2.34), with sporadic examples of shallow (near horizontal) dips in the north-eastern flow frontal region and mid-flow (Figs. 2.33c, d; 2.34c, d). The north-western frontal lobe exclusively hosts steeply dipping stretching lineations.

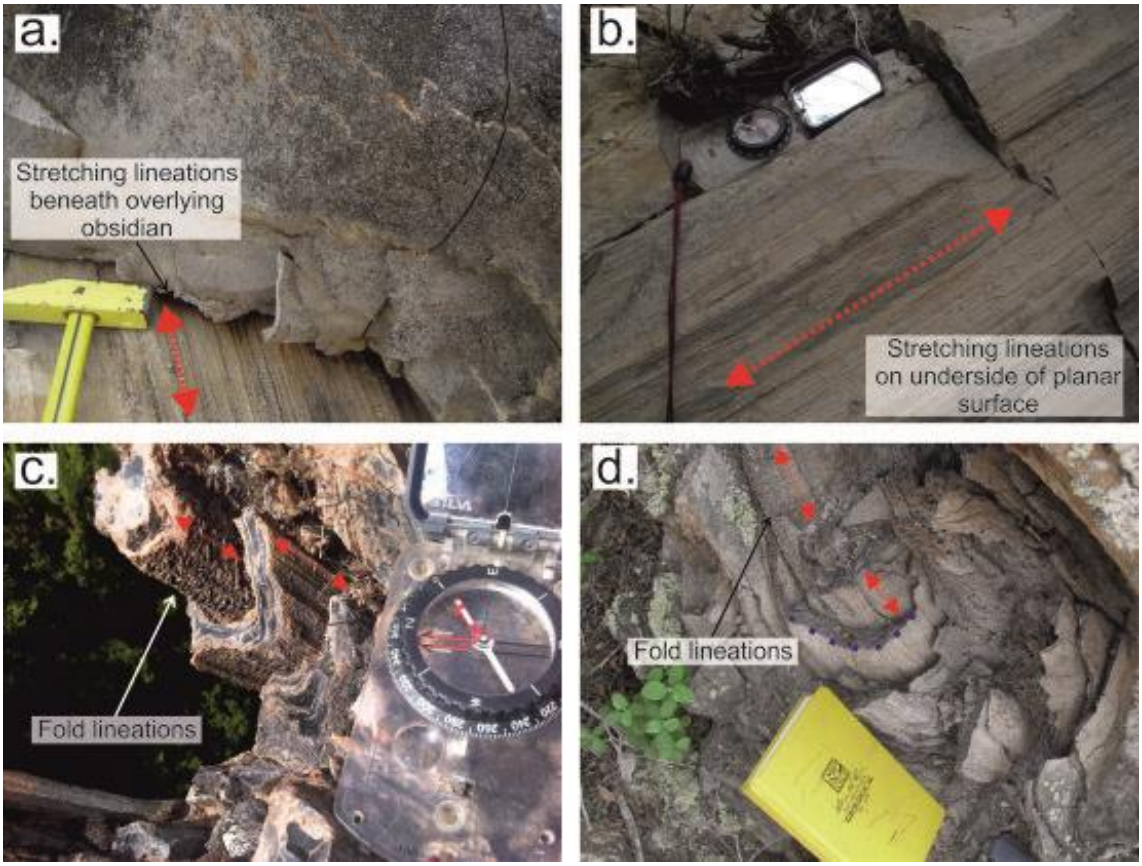

Figure 2.31: Lineations on the Rocche Rosse lava flow. (a) Continuous stretching lineations mid-flow. (b) Stretching lineations on the underside of a planar surface. (c) Lineations associated with folding episodes, resulting in parasitic folds. (d) Lineations associated with folding episodes, showing the fold hinge (red arrow).

Brittle Deformation

Brittle deformation manifests in specific areas of the flow as an internal or upper and lower brecciated carapace (Figs. 2.36a, b). The brecciated zones are clast-supported, made up of sheared and angular fragments of variably devitrified and pumiceous obsidian, with finer material (ash-sized) infilling the gaps. Brecciated surfaces appear as jigsaw-fit and sporadically distributed clasts, often tightly packed and in some cases completely welded.

Clasts vary in size from <1 cm up to 30 cm. Brecciated zones vary from <50 cm up to 10's of metres in thickness.

Figure 2.32: Dip and dip direction measurements of stretching lineations, predominantly occurring in flow-frontal and mid-flow regions.

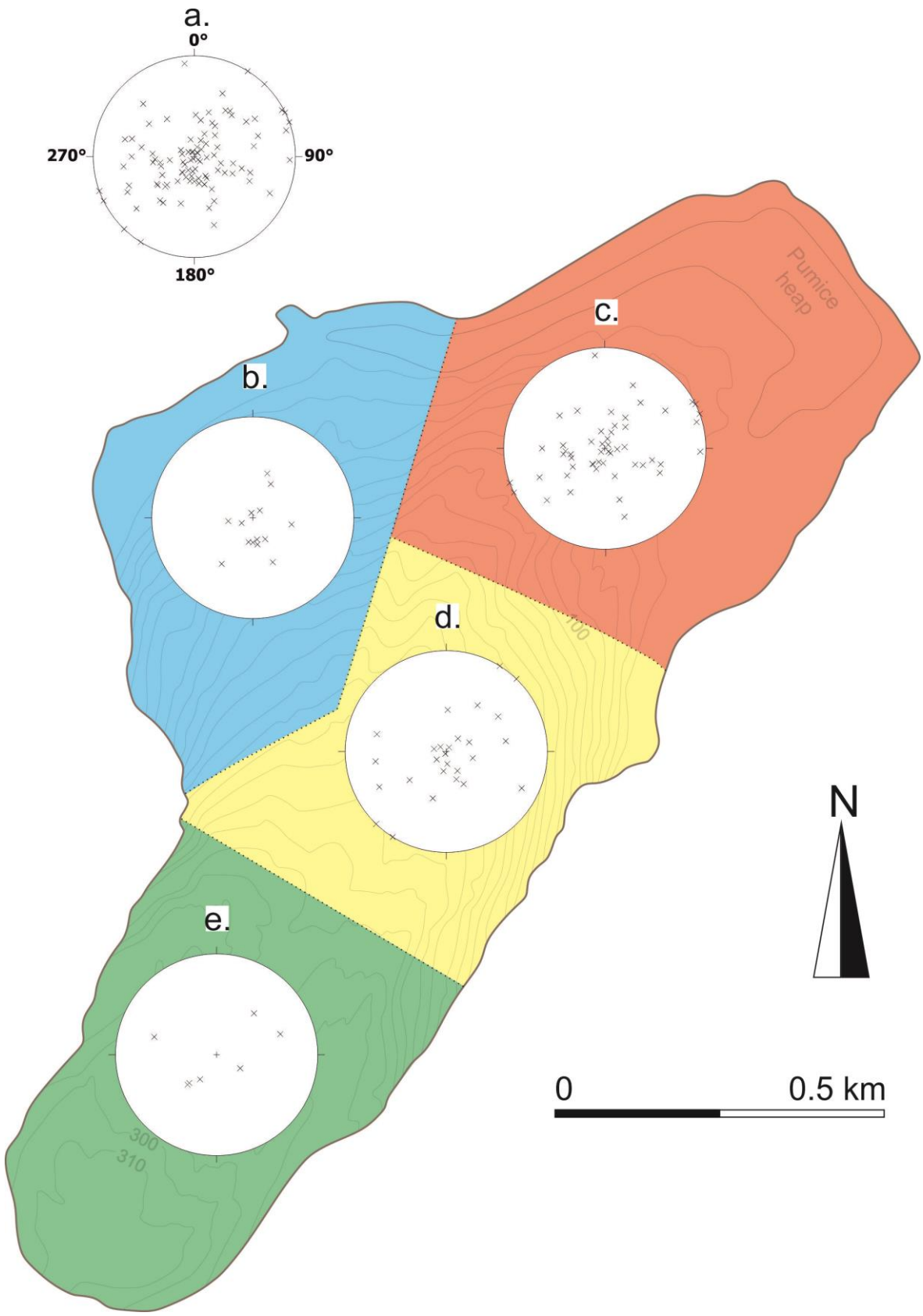

Figure 2.33: Stereographic plots of stretching lineations on the Rocche Rosse lava flow (equal area projection, lower hemisphere). (a) All structural data from across flow. (b) Front north-western flow lobe. (c) Front north-eastern flow lobe. (d) Mid-flow region. (e) Upper (near-vent) flow region.

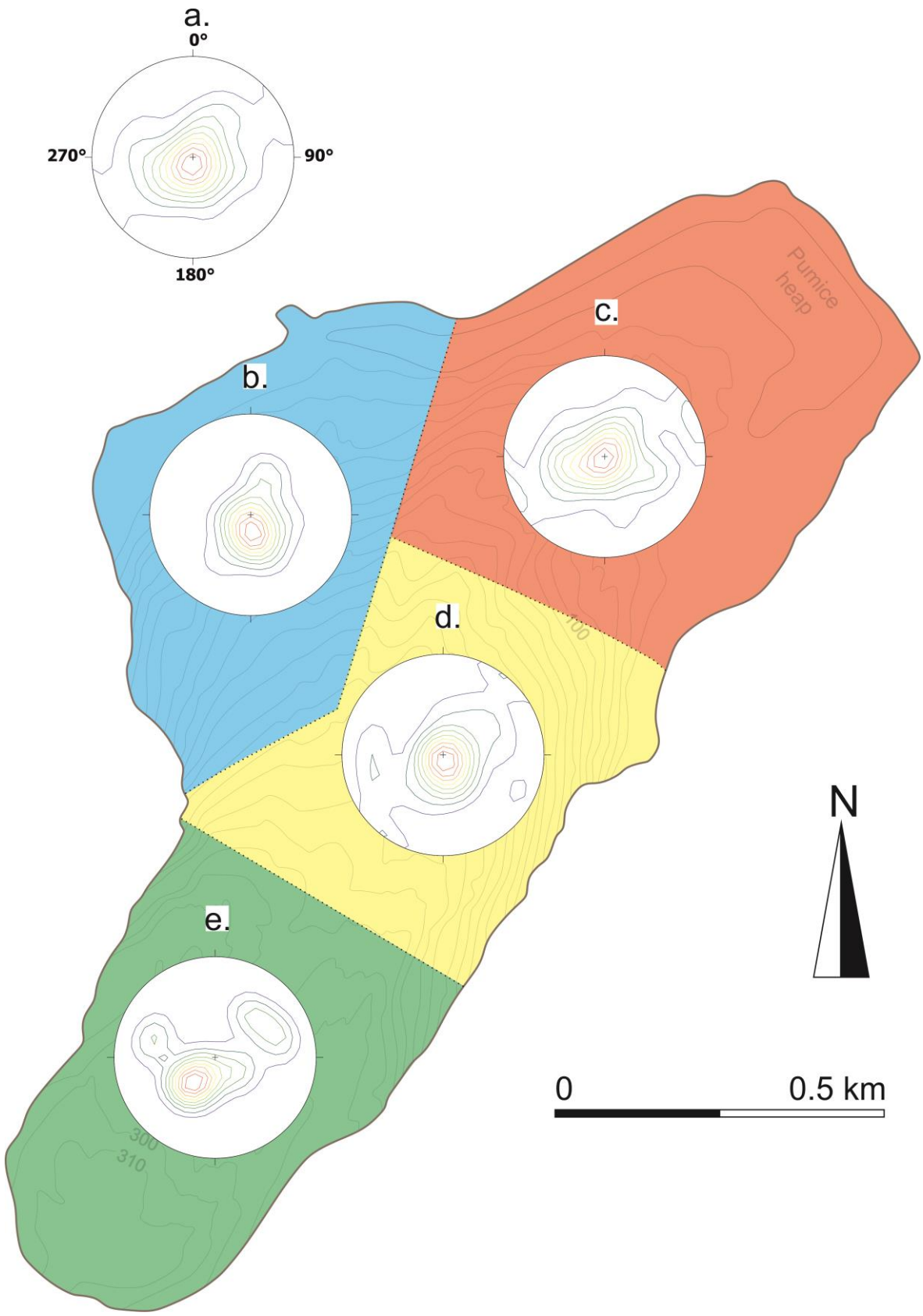

Figure 2.34: Contour density plots of stretching lineations on the Rocche Rosse lava flow (equal area projection, lower hemisphere). (a) All structural data from across flow. (b) Front north-western flow lobe. (c) Front north-eastern flow lobe. (d) Mid-flow region. (e) Upper (near-vent) flow region.

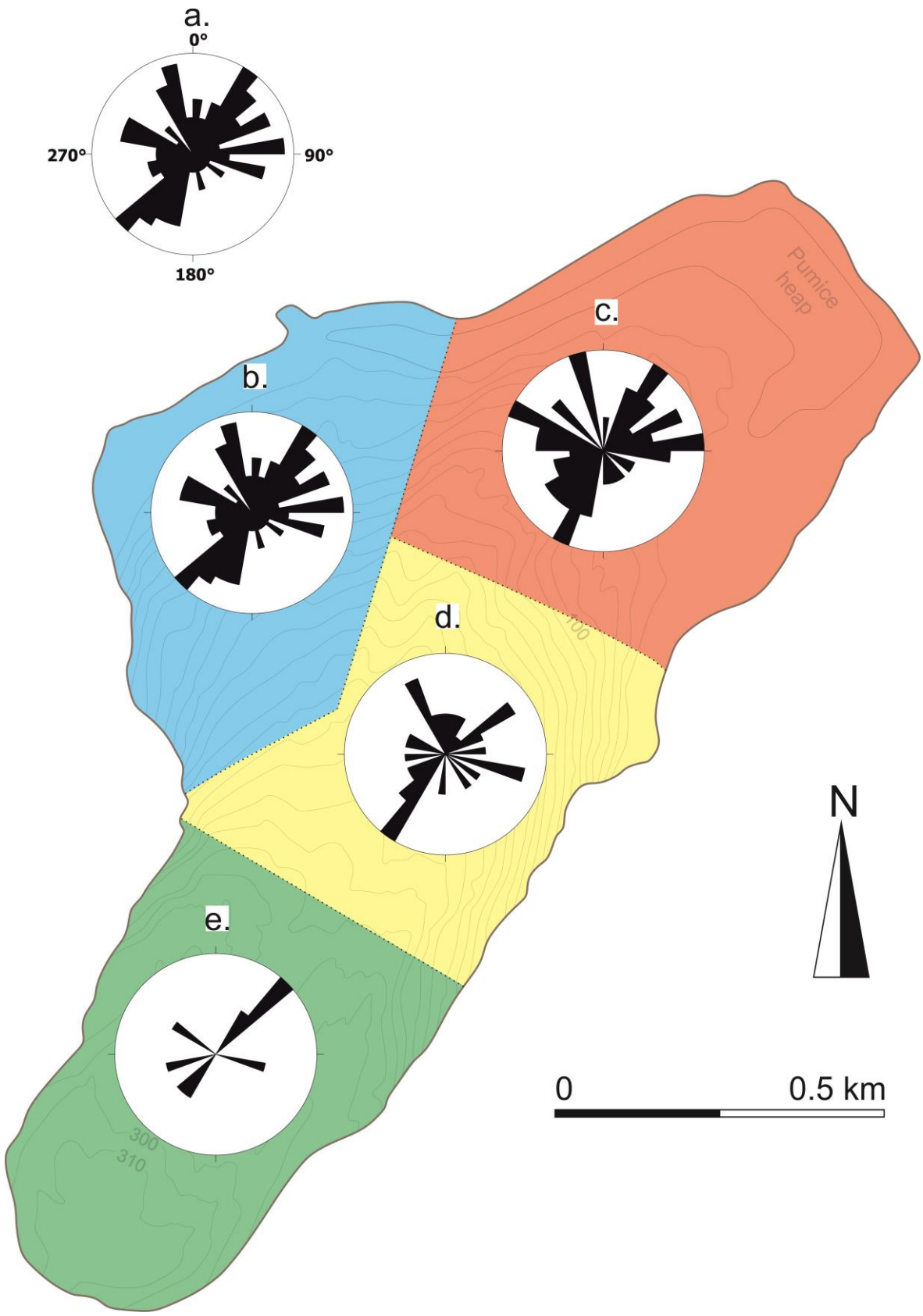

Figure 2.35: Rose diagrams of stretch lineations on the Rocche Rosse lava flow (equal area projection, lower hemisphere). (a) All structural data from across flow. (b) Front north-western flow lobe. (c) Front north-eastern flow lobe. (d) Mid-flow region. (e) Upper (near-vent) flow region.

Brecciated zones do not show any obvious structure or bedding. Brecciated zones occur at the upper surface of the flow, the base of the flow and also as in-situ or internal brecciation. The vast majority of identified brecciated zones are in the eastern, larger flow lobe. These brecciated zones concentrate considerably at the south- eastern flow flank, extending along the margin for approximately 800 m, and in the centre of the flow for approximately 300 m. There is also evidence for brecciated material at the northern and north eastern extent of the flow. The extensive area of brecciated material at the south eastern flank is exposed at the base of the flow, and therefore represents the basal breccia. Mid-flow, there are examples of brecciated material on the top surface of outcrops, and also in between coherent lava flow units. Loose blocks on the flow surface are widespread, and tend to accumulate in linear ridges on the upper surface (Fig. 2.37), particularly mid-flow and in near-vent regions. Such seams were previously identified using satellite imagery and traced as lineaments down flow (sub-parallel to flow margins). These lineaments are humped in cross section, and extend for tens of metres, often in a NE-SW orientation. These humped linear ridges contain large blocks, up to ~1 m in length, and occasionally contain folded in-situ obsidian lava exposures. As well as linear ridges running sub-parallel to the flow margin, smaller, more elliptical ridges were identified by satellite imagery and at ground level (Fig. 2.38). These curvilinear ridges are typically 10-20 m in length, and show a steep-sided talus of loose material, dipping away from the source region (dipping NW, N, NE). Curvilinear ridges also show a bowl-like depression in the sourceward direction, concentrating loose large blocks.

Jointing (cooling/unloading) or brittle breakage of individual flow units (Fig. 2.39) is marked by an abrupt change in foliation dip and dip direction. This abrupt change occurs on a scale of a few centimetres, with no observed evidence of a fold closure between the two planes dipping in opposite directions. In mid-flow, there are cases of foliations dipping

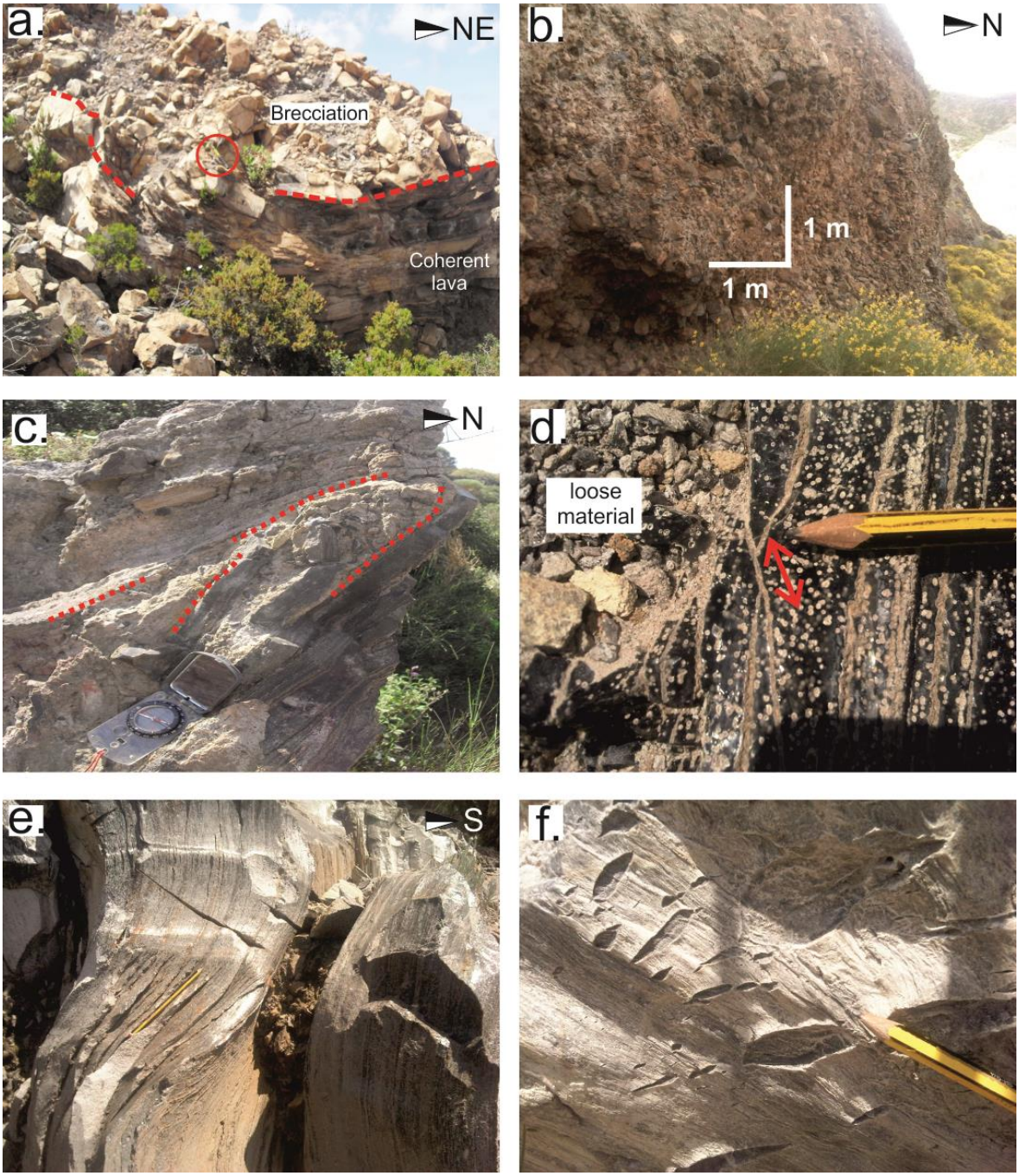

Figure 2.36: Brittle features of the Rocche Rosse lava flow. (a) Upper breccia and sharp contact with coherent lava (hammer for scale). (b) Basal breccia (estimated thickness of ~7 m). (c) Internal brecciation sandwiched between obsidian lava, and platy fractures parallel to flow banding. (d) Small scale faulting, red arrow indicates 1 cm offset of foliation bands. (e) Fractured obsidian lava, showing a twisted appearance. (f) En echelon fractures on underside of foliation plane.

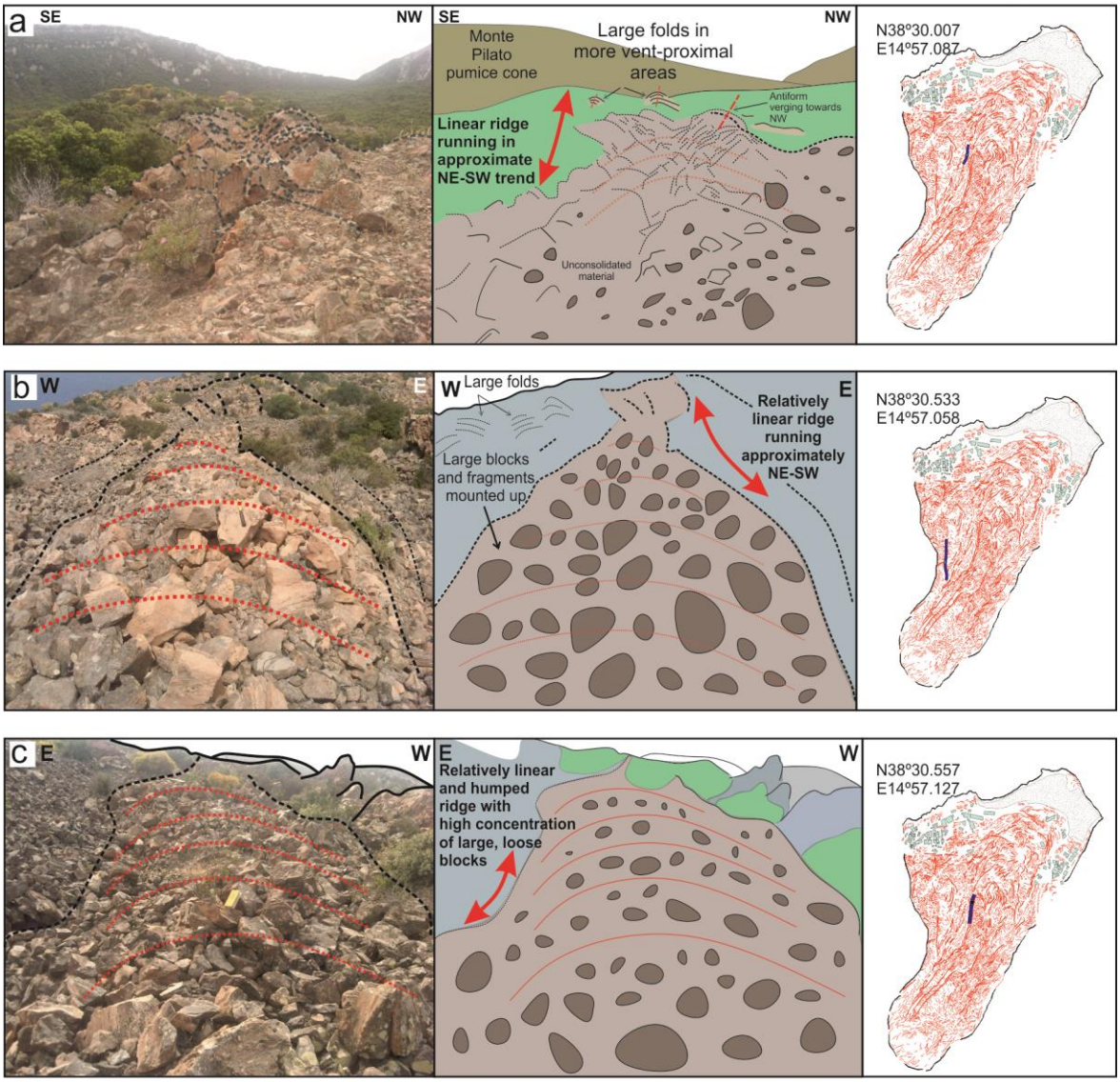

Figure 2.37: Linear ridges, showing a humped appearance and concentration of loose blocks. Position on flow and satellite imagery trace indicated.

~42° in a south westerly direction, and less than 1 m to the north, foliations dip 44° to the north east, with no tight folding, and near the south eastern flank, foliations alter from 88° SW to 44° north east in <1 m distance. Brittle deformation is also evident, particularly in flow- frontal regions, by smaller scale fractures (cracks; Figs. 2.36e, f) and faults (displacement; Fig. 2.36d) on planar surfaces. Closely spaced, unfilled and parallel en echelon and sigmoidal fractures (tension gashes) are observed in flow frontal regions in the

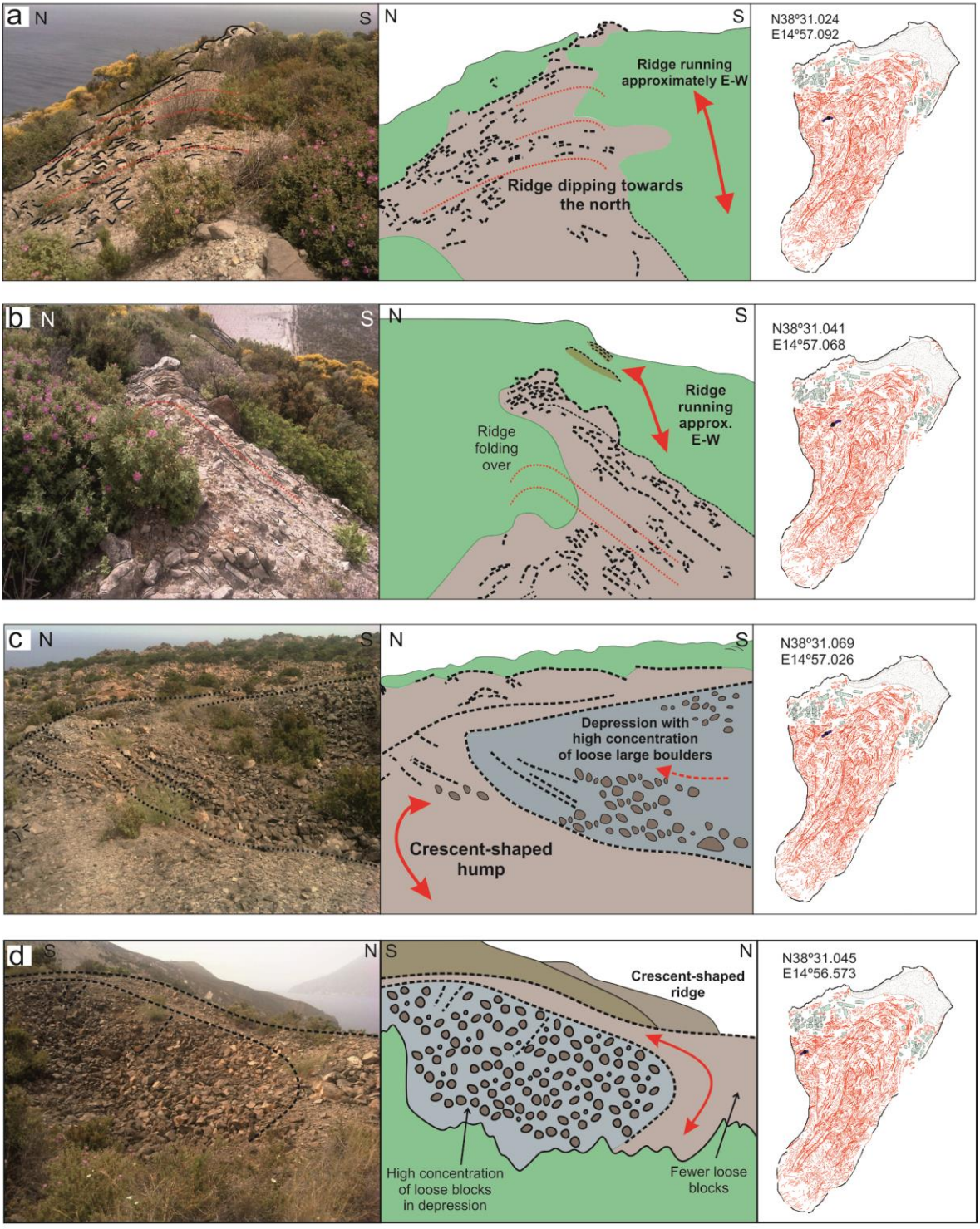

Figure 2.38: Curvilinear ridges, showing an ellipsoidal depression with a high concentration of loose blocks, and steep sided talus in (a) and (b). Position on flow and satellite imagery trace indicated.

north eastern flow lobe, on a scale of ~2 cm up to ~15 cm in length. Small scale conjugate

fractures are widely observed, showing dihedral angle intersections of fractures. Small scale planar faulting displaces flow banding by a few centimetres.

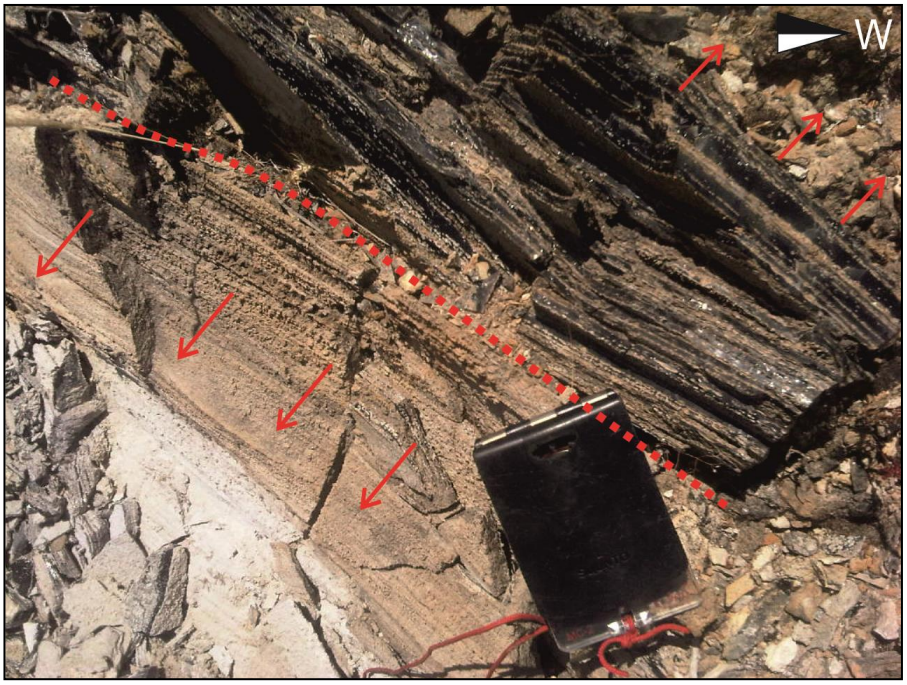

Figure 2.39: Brittle jointing (along dotted line), with planar surfaces in close proximity dipping in opposite directions (indicated by red arrows).

2.5.4 Spherulite Preferred Orientation

As well as large scale structural evidence for flow direction and deformation associated with obsidian lava emplacement, microscopic scale textures also reflect such events. The arrangement of spherulites often defines the planar foliation, and spherulites have been observed as variable in occurrence, i.e. individual spherulites, clustered, laminated, rounded and flattened (Fig. 2.40). Spherulite shape in two- or three-dimensions can be used as an indicator for deformation behaviour as they may alter from an originally spheroid shape with no preferred orientation, to a flatter and preferentially orientated arrangement.

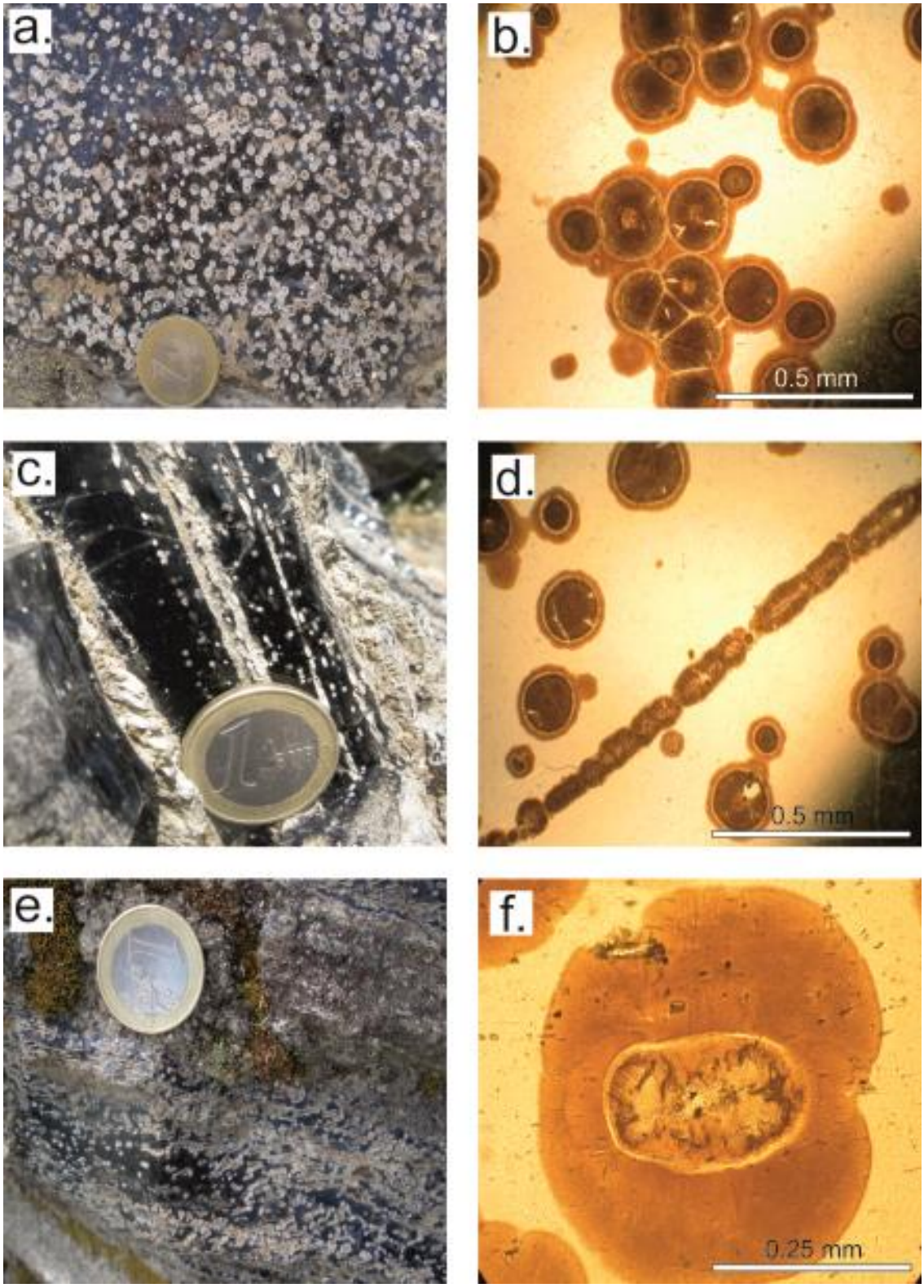

Figure 2.40: Spherulite occurrence in the Rocche Rosse lava flow. (a) Individual and clustered spherulites. (b) Microscopic image of clustered spherulites. (c) Spherulites in linear bands. (d) Microscopic image of spherulites concentrated within planar band. (e) Elongate spherulites (elongation ~45° to foliation). (f) Microscopic image of an elongate spherulite.

Assuming the population of spherulites started with an originally spherical habit, the rose intercepts and orientations provides an indicator of sectional strain. This assumption is only made on spherulites that do not show a typical bowtie shape or elongate nucleus (i.e. spherulites that have preferentially grown in an elongate shape). The intensity of the spherulite shape fabric has been determined by the r value, i.e. the eccentricity of the shape fabric ellipse. The calculated r value is a shape parameter which analyses the object shape (i.e. the roundness of the spherulite). Calculated r values of 2 represent more elliptical shapes (strong elongation), whereas an r value of 1 indicates a perfect circle due to a weak elongation intensity (values above 1 indicate a degree of elongation); spherulite shape values above 1 therefore show some degree of elliptical properties. The Spherulite Preferred Orientation method presented here shows these shape properties, both qualitatively and quantitatively. Spherulite Preferred Orientation (SPO) results are summarised in Figures 2.42-2.45 and Table 2.2 (sample localities shown in Fig. 2.41).

Generally, the sections cut normal to the foliation plane show slight deviation from a spherical shape and linear orientation (Fig. 2.42). Sample localities 15 to 19 form part of a heavily deformed flow region, exhibiting a large recumbent fold, parasitic folding, sheath folding and jointing. Sample localities 20-22 are also part of a deformed area, with multi-scale folding near the flow-front. Sample locality 24 is at the flow front, hosting large scale folding, and sample localities 49, 53 and 405 are mid-flow. In these areas, stretching lineations occur, but overall, the areas are largely undeformed. Generally, sample localities hosting spherulites of weak elongation are 15, 20, 21, 22, 49, 53, 405 and 413. Sample locality 49 shows a very weak elongation. Sample localities 17 to 19 (in area of complex deformation) show a slightly stronger degree of spherulite elongation, (19 shows a stronger elongation degree parallel to strike of planar foliation). Sample locality 317 (at the edge of

Table 2.2: Spherulite Preferred Orientation quantitative parameters and shape ratios for select localities (*Intercepts 2003*; Launeau and Robin, 1996). Long axis angle represents angle of longest dimension from 0°.

Sample and locality	Mean length (long) a	Mean length (short) b	Shape ratio r	Long axis angle	Figure	Description
15A	0.029 cm	0.027 cm	1.06	152.9°	2.41	Oblate (sub-spherical), with variable long axis rotation in all planes
15B	0.029 cm	0.027 cm	1.11	12.5°	2.42	
15C	0.033 cm	0.031 cm	1.08	28.7°	2.43	
16A	0.071 cm	0.067 cm	1.41	159°	2.41	High degree of shape alteration normal to fol. plane. Oblate (pure shear)
16B	0.086 cm	0.077 cm	1.11	125.7°	2.42	
16C	0.070 cm	0.065 cm	1.08	80.6°	2.43	
17A	0.028 cm	0.023 cm	1.24	12.53°	2.41	More prolate shape (pure stretching) in lin. Plane, flattened profile
17B	0.027 cm	0.022 cm	1.22	169.8°	2.42	
17C	0.033 cm	0.030 cm	1.10	166.1°	2.43	
17D	0.025 cm	0.021 cm	1.22	80.9°	2.44	
18A	0.025 cm	0.020 cm	1.28	5.7°	2.41	Significant degree of prolate pure stretching
18B	0.042 cm	0.035 cm	1.18	9.1°	2.42	
18C	0.030 cm	0.030 cm	1.05	52.8°	2.43	
19A	0.026 cm	0.021 cm	1.23	2.6°	2.41	Characteristic spherical shape (minor oblate profile in lin plane)
19B	0.025 cm	0.024 cm	1.07	10.7°	2.42	
19C	0.033 cm	0.031 cm	1.07	67.2°	2.43	
19D	0.025 cm	0.021 cm	1.18	178.9°	2.44	
20A	0.012 cm	0.012 cm	1.02	6.3°	2.41	Predominantly spherical (minor oblate profile), flattened profile
20B	0.014 cm	0.012 cm	1.18	83.4°	2.42	
20C	0.013 cm	0.012 cm	1.09	123.6°	2.43	
20D	0.014 cm	0.012 cm	1.18	94.4°	2.44	
21A	0.011 cm	0.011 cm	1.05	3.6°	2.41	Similar results to locality 20
21B	0.012 cm	0.010 cm	1.14	83.5°	2.42	
21C	0.022 cm	0.020 cm	1.17	132.8°	2.43	
21D	0.020 cm	0.017 cm	1.06	14.7°	2.44	
22A	0.030 cm	0.030 cm	1.03	34.2°	2.41	Similar results to locality 20
22B	0.030 cm	0.030 cm	1.07	92.5°	2.42	

Sample and locality	Mean length (long) a	Mean length (short) b	Shape ratio r	Long axis angle	Figure	
22C	0.030 cm	0.028 cm	1.05	45.4°	2.43	
22D	0.030 cm	0.028 cm	1.02	156.8°	2.44	
24A	0.020 cm	0.014 cm	1.43	13.9°	2.41	Prolate and highly
24B	0.020 cm	0.015 cm	1.34	85.0°	2.42	elliptical normal to
24C	0.020 cm	0.018 cm	1.04	90.4°	2.43	foliation plane and
						perp. to foliation plane
49A	0.016 cm	0.016 cm	0.99	105.2°	2.41	
49B	0.021 cm	0.021 cm	0.97	104.9°	2.42	Almost perfectly
49C	0.011 cm	0.010 cm	1.09	9.6°	2.43	spherical
49D	0.020 cm	0.011 cm	1.06	134°	2.44	more rigid shape
53A	0.030 cm	0.027 cm	1.07	3.3°	2.41	Almost perfectly
53B	0.027 cm	0.026 cm	1.02	171.3°	2.42	spherical
53C	0.016 cm	0.014 cm	1.14	84.1°	2.43	
317A	0.040 cm	0.021 cm	1.86	179.3°	2.41	Almost elliptical
317B	0.030 cm	0.024 cm	1.18	66.1°	2.42	normal to fol. Plane, a
317C	0.050 cm	0.025 cm	1.96	173.1°	2.43	clear prevailing
						flattened orientation
405A	0.024 cm	0.024 cm	1.02	71.5°	2.41	
405B	0.030 cm	0.030 cm	1.04	25.6°	2.42	Weak elongation,
405C	0.030 cm	0.030 cm	1.13	105.0°	2.43	spherical shape
413A	0.031 cm	0.030 cm	1.04	67.3°	2.41	Weak elongation,
413B	0.052 cm	0.048 cm	1.07	25.9°	2.42	spherical shape
413C	0.034 cm	0.033 cm	1.05	82.6°	2.43	

the flow) shows a very strong elongation degree, particularly parallel to strike of foliation and in the dip plane. The large majority of sample locations show some degree of shape alteration (no spherulites are 100% circular) and variable rotation of the long axis. Sample locality 317 spherulites differs drastically, with almost elliptical spherulites in the sample normal to the foliation plane (high r value of 1.86) and within the foliation plane (r value of

1.96), characteristically highly prolate, indicating pure stretching. Stretching lineation sample cuts do not show a high degree of elongation, with the exception of sample localities 17 and 19, with a calculated r value of 1.22 and 1.18 respectively, and a flattened characteristic shape apparent in both samples. There is evidence for flattening in a number of samples in the 0° to 180° orientation, with a rotation from vertical (0° or 180° orientation) of 2-30°.

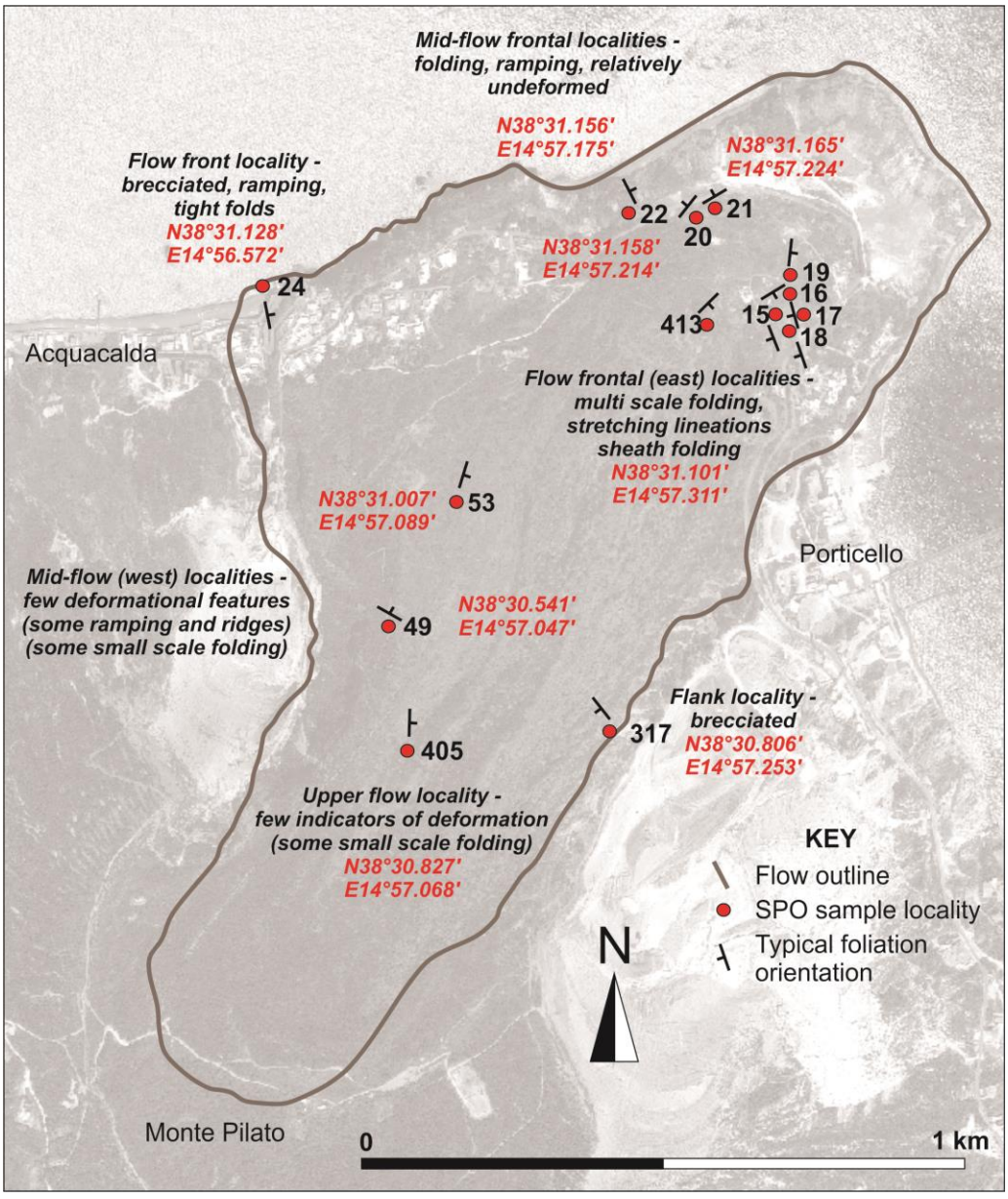

Figure 2.41: Spherulite sample localities and representative structural information for Spherulite Preferred Orientation (SPO) analysis.

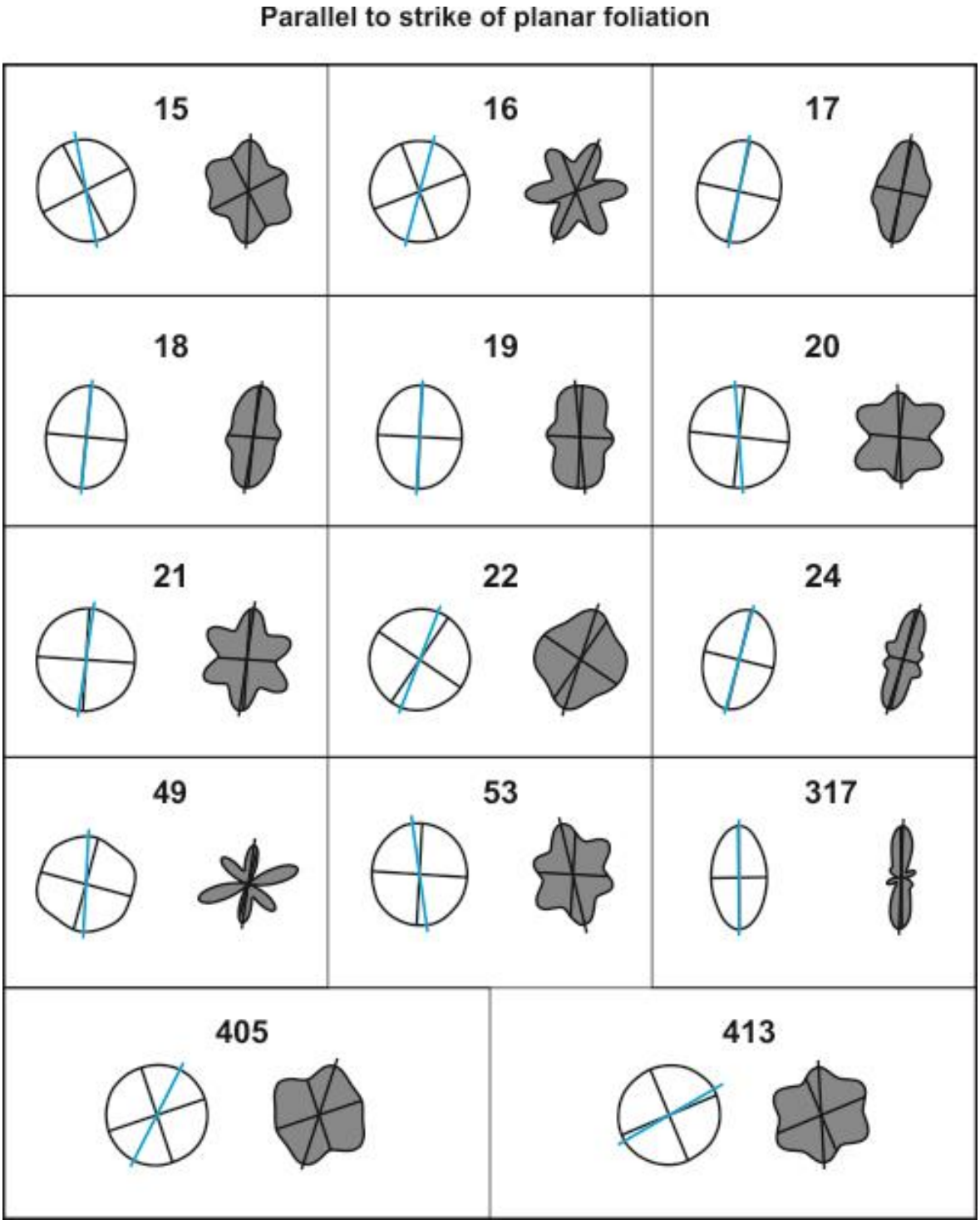

Figure 2.42: Spherulite Preferred Orientation results for samples cut parallel to strike of the planar foliation surface. Samples from selected localities on the Rocche Rosse lava flow (see Fig. 2.41). Left image represents characteristic shape, right image represents rose of boundary directions.

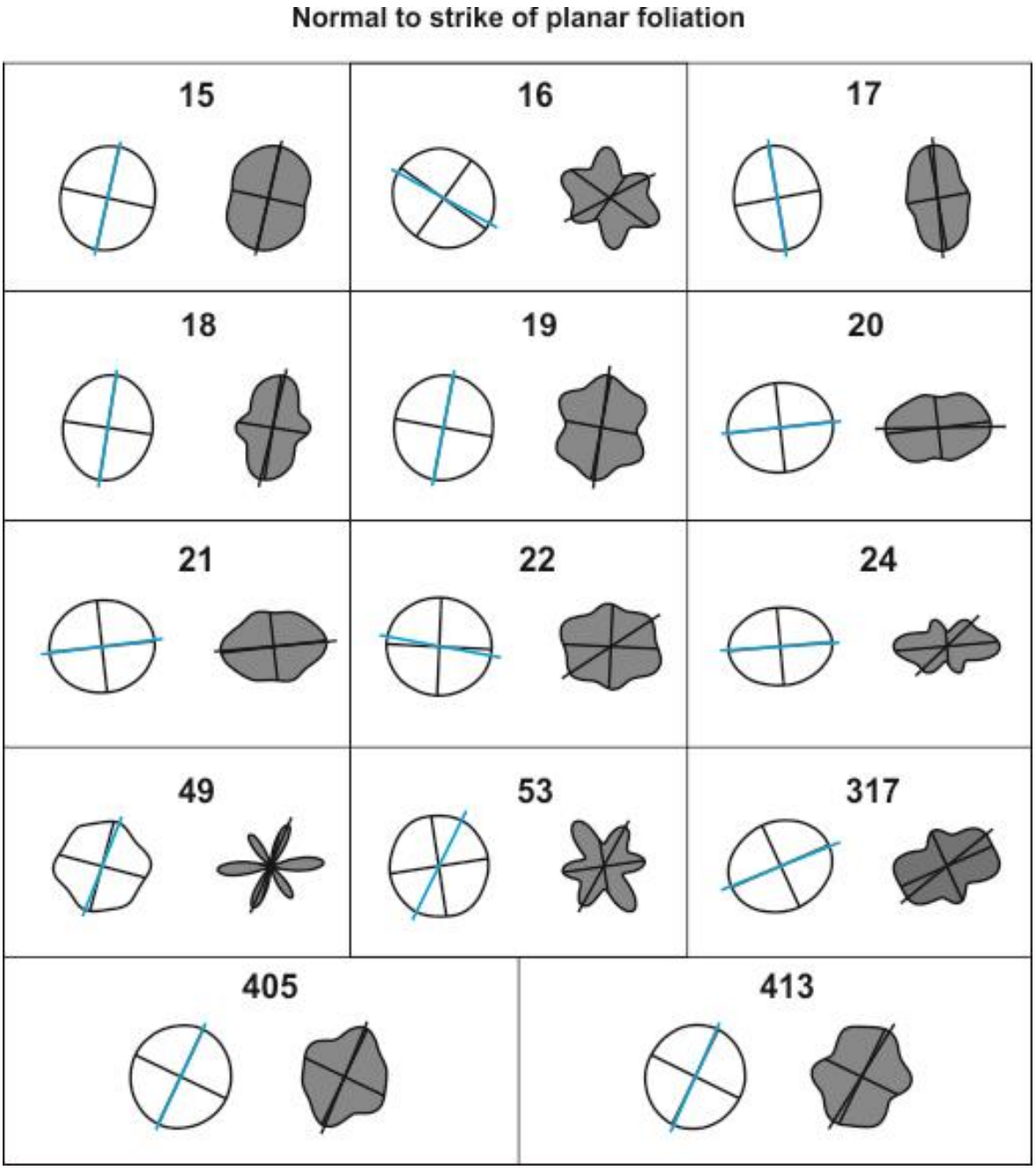

Figure 2.43: Spherulite Preferred Orientation results for samples cut normal to the strike of the planar foliation surface (sample localities as above).

The thin sections cut perpendicular to the foliation plane often show a pure flattened characteristic shape profile, identifiable by a flattening of the axes in the 90°-270° orientation. Some samples appear to show a more sporadic preferred shape and orientation, i.e. no obvious trend in spherulite shape.

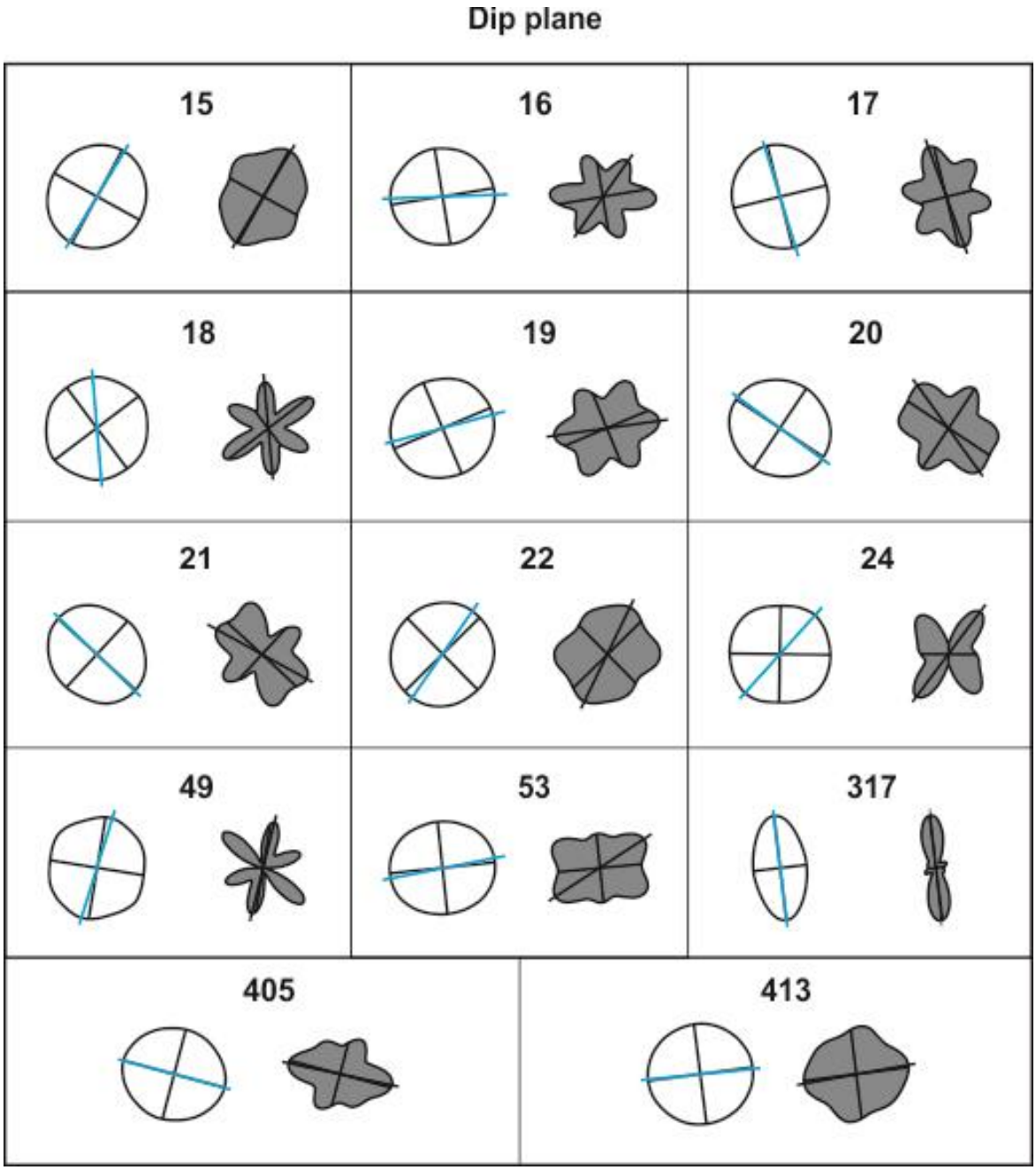

Figure 2.44: Spherulite Preferred Orientation results for samples cut within (parallel) the dip plane.

Samples cut within the foliation plane generally show no preferred axial orientation, with the exception of samples 15, 20, 53, 317, 405 and 413 (Fig. 2.44). Sample 317 is the only sample to show a clear prevailing flattened orientation (in the 0°-180° orientation, with a vertical offset of ~7°).

Sample localities 17, 19, 20, 21, 22 and 49 showed clear field evidence for stretching lineations (Fig. 2.45), allowing for samples to be cut parallel to the observed lineations (Fig. 2.44). Sample localities 17 and 20 show a flattened shape (preferential horizontal profile) with a horizontal offset of ~4-10°, while sample 19 shows a more flattened shape in a vertical orientation (offset of ~1°). Sample localities 21, 22 and 49 show a more rounded characteristic shape and no preferred orientation.

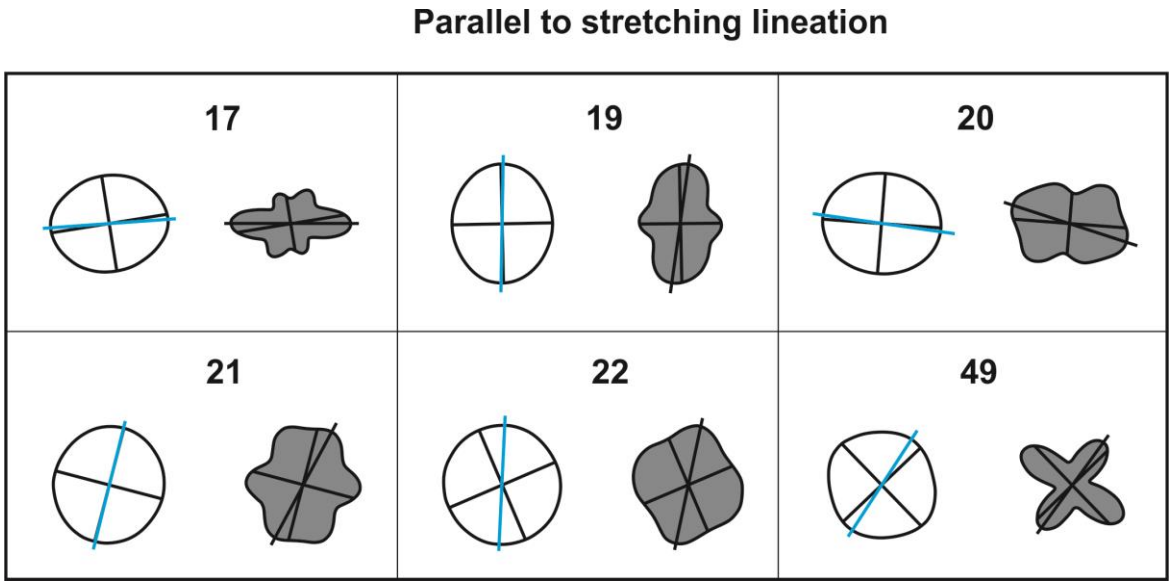

Figure 2.45: Spherulite Preferred Orientation results for samples cut parallel to stretching lineations.

It is important to note that emphasis from the presented SPO results is placed on spherulites that show a deviation from a near-spherical shape, and the processes which may result in such deviation. In particular, spherulites show shape alteration in the plane of the foliation and parallel to stretching lineations. This may indicate that some spherulites modify or change in shape as a response to (and concomitantly with) foliation- and lineation-forming processes, and/or nuclei has been preferentially elongated and aligned as a response (see: Discussion).

2.6 Discussion

2.6.1 The physical nature of the Rocche Rosse lava flow

Emplacement overview

When determining the mechanisms of lava flow emplacement, it is important to consider lava flow parameters such as the dimensions and the physical characteristics of lava flows (Hulme, 1974; Gregg and Fink, 2000). Such characteristics, such as thickness, stratigraphy and structural attitude, are discussed here. The thickness of the Rocche Rosse lava flow becomes thinner over the steeper underlying topographic slope angle, and towards the flow front, which indicates that advancing flow thickened and/or thinned in response to forces at work during flow mobility. Advancing flow was hindered during advance (evident by widespread, multi scale folding), slowing the flow and resulting in flow compression, flow ramping and a localised thicker flow in mid-flow regions (see Figs. 2.9; 2.46).

Flow dynamics, behaviour and resultant structure depends on the properties of the erupted magma, extrusion rate, ground topography and rate of heat loss (Griffiths, 2000). Liquid polyethylene glycol experiments by Fink and Griffiths (1990) showed a radial current advancing away from the inlet, with a solidified surface (with cooling), and folding and fracturing occurring. For warmer experiments, solidification did not occur, and the radius of the current increased. Spreading rate decreased with more rapid cooling. Progressive cooling experiments resulted in surface morphologies akin to those observed in lava flows, with the development of levees channelling the current (Fink and Griffiths, 1990).

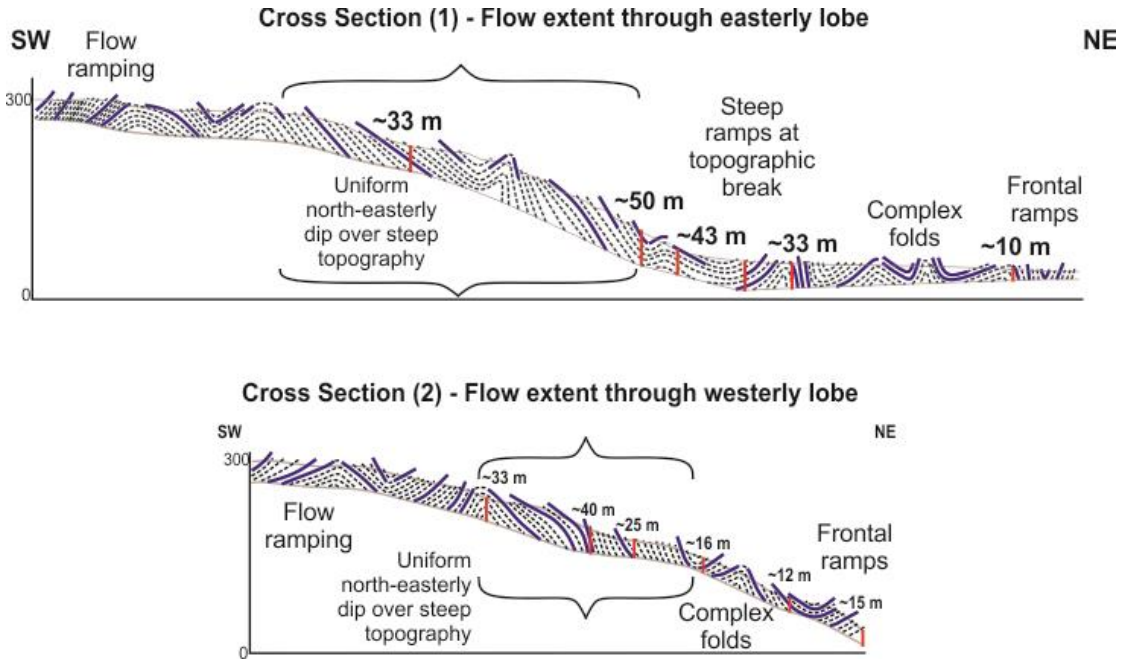

Figure 2.46: Cross sectional representation (to scale) of foliation measurements for the eastern and western flow lobes. Bold purple lines represent direct measurements of foliations in the field; dashed black lines indicate the interpretation of foliation attitude based on observations and direct measurements.

The experiments also showed that decreasing extrusion rate also resulted in the transition to surface deformation, effectively showing that flow structures can be generated by varying flow rate or temperature (with variable effects on viscosity and crustal strength, generally increasing with cooling) (Fink and Griffiths, 1990). In the case of the Rocche Rosse, as the flow segregated into two prevailing directions, the flow became thinner over a shorter distance along the western flank. The flow thickness decreases from ~40 m to ~25 m over a 200 m distance, compared to a decrease from 43 m to 33 m on the opposite eastern flank (Fig. 2.9). This indicates that the flow advanced over a steeper topography on the western side, resulting in the flow diverting to a more northerly direction, and thinning considerably more than the eastern side. This is supported by flow foliation dip orientation data, which shows a shift from a NE-SW trend in mid- and upper-flow regions, to a more northerly dip in the western flow frontal lobe, and a complete alteration of orientation to

NW-SE in the eastern flow frontal region (see Figs. 2.12-2.15). The eastern flank is longer and more continuous than the western flank, mirrored by the main channelled flow direction (to the NE), resulting in a more gradational flow thickness decrease from the thickest mid-flow region to the flow front. Cross sectional representation of the planar field measurements reveals a relatively simple extensional and compressional flow regime (Fig. 2.46), with typical flow ramps previously described in the Rocche Rosse and comparable rhyolitic flows (MacDonald, 1972; Cas and Wright, 1987; Gottsmann and Dingwell, 2001b; Forni et al., 2013). These flow ramps consist of ridges of fold structures extending downward into the flow by up to tens of metres. In mid-flow regions, over a steeper topography and where the flow is thickest, the lava flow shows a more uniform linear arrangement, where extensional forces prevail. At the flow front, over shallower topographic gradients and where the flow becomes thinner, the flow is more readily deformable, ramping up and folding in response to friction and flow hindrance at the flow front. This flow resistance is also manifested at the near-vent regions, where the flow ramps up again.

Relationship with underlying pyroclastics and topography

The underlying tephra deposits (Figs. 2.7-2.11; 2.47) are associated with the initial explosive stage of the Rocche Rosse volcanic activity, and the older Sciarra dell'Arena pyroclastic succession (Lucchi et al., 2010, 2013; Forni et al., 2013). The hydromagmatic pumice cone consists of coarse-grained pumice alternating with ash layers (Dellino and La Volpe, 1995; see Fig.). The Rocche Rosse explosive products outcrop in upper Monte Pilato vent regions, forming a poorly-bedded pyroclastic breccia, consisting of obsidian clasts and pumices (fallout deposits), and interbedded lapilli tuff layers (surge deposits),

reaching a maximum thickness of 15 m (Lucchi et al., 2010, 2013; Fig. 2.47). The Sciarra dell'Arena pumiceous succession has a maximum thickness of 150 m, consisting of coherent, poorly-bedded lapilli tuffs (fallout deposits) and intercalated lapilli tuff layers (surge deposits) (Lucchi et al., 2010, 2013).

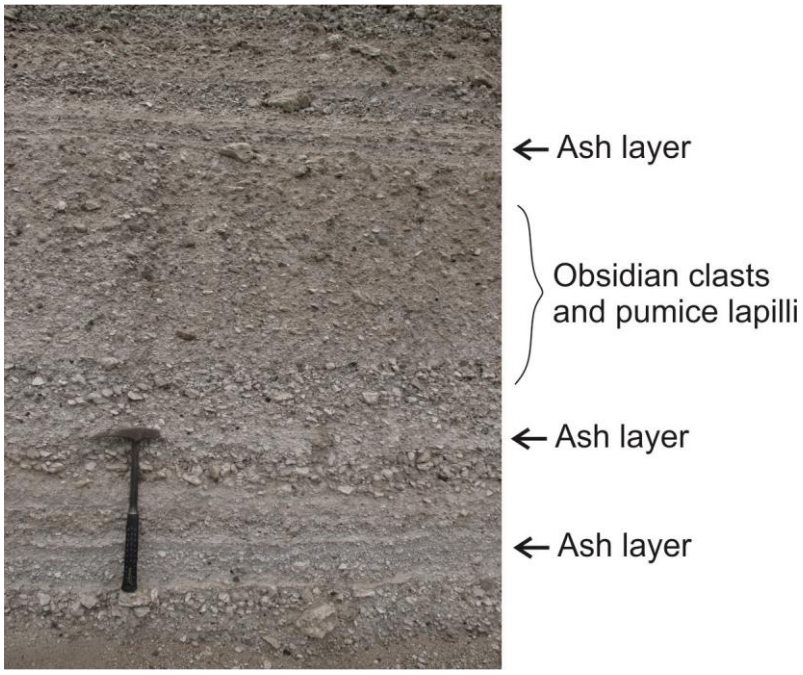

Figure 2.47: Example of underlying Rocche Rosse tephra deposits from Monte Pilato pumice cone.

Fink (1983) interpreted the spatial arrangement of similar textural units at Little Glass Mountain (California) as a reflection of the distribution of volatiles in the magma source region. Fink (1983) described how volatile exsolution and rising of a frothy volatile-rich cap result in the initial explosive phase and underlying tephra deposits. This transition may have been driven by diffusive transfer of volatiles in to an area of low chemical potential, and adjective transport of exsolved volatiles to surroundings during transport from storage to surface, while shear-induced magma fragmentation also plays a critical role by fostering volatile loss from fragmentary magma (Castro et al., 2012). The remaining volatile-rich magma rose as pumiceous magma, followed by bubble-free Little Glass Mountain obsidian

lava. During transport, some volatiles continued to exsolve from the cooling upper flow surface, resulting in a finely vesicular carapace. By comparison, this finely vesicular carapace is seldom observed on the Rocche Rosse lava flow (possibly due to erosion), though is evident in upper (near source) flow regions. As the lava flow surface cooled, fracturing occurred and developed an upper breccia (which is overridden to form a basal breccia, see Figs. 2.36a, b). Brecciation also occurred due to high strain rates. Repetition of any of these stages caused variations in the stratigraphy. Fink (1983) identified rising coarse pumice diapirs from the base of Little Glass Mountain, which disrupted flow configuration. Gravitational instability and density contrast resulted in the coarsely vesicular pumice buoyantly rising through the overlying obsidian, reaching the flow surface. It is speculated here that this occurred in the Rocche Rosse lava flow, in upper flow regions, with a grey-white pumiceous unit doming upwards and outcropping at the flow surface (Figs. 2.9; 2.48). This resulted in the obsidian lava ramping upwards towards the pumiceous unit.

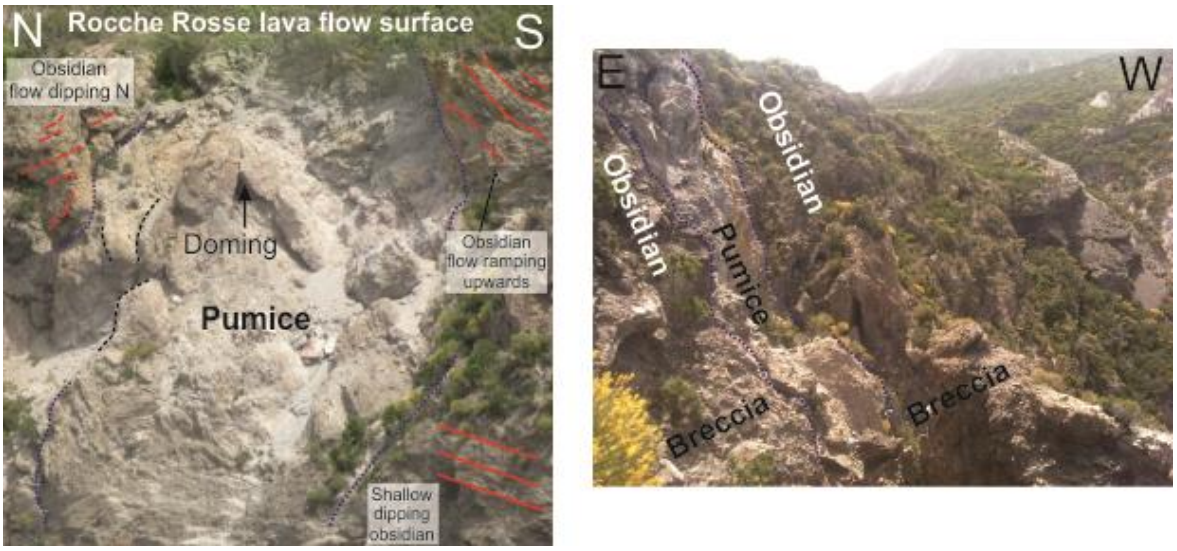

Figure 2.48: Flank exposure of a grey-white pumiceous unit reaching the Rocche Rosse lava flow surface, resulting in steep dipping overlying obsidian planes.

Structural observations and measurements

Field measurements of foliations at the flow surface allow for the construction of cross sections in order to represent the variation in planar attitude of the flow, and extrapolate information on large scale internal flow structures (Fig. 2.46). Cross sections are also useful where field and flank exposure is limited. In general, cross sections reveal flow ramping in near-source and distal flow regions, uniform north-easterly dipping foliations in the mid-flow regions, and complex folding in frontal regions.

Cross sections based on field measurements reveal large scale folding, often manifested as ramp structures (Fig. 2.46). These large folds and steep ramps are evident in flank imagery from the town of Acquacalda (Fig. 2.9), and were identified in previous Rocche Rosse lava flow studies (Cas and Wright, 1987; Gottsmann and Dingwell, 2001b; Lucchi et al., 2010, 2013; Forni et al., 2013). In both cross sections, these steep ramp structures are found in near-source regions, dipping back towards the source, and also occur at the flow front. In mid-flow regions, where the flow is thickest (see Fig. 2.7), cross sections of both flow lobes show the planar foliations dipping in a more continuous (undisturbed) pattern. Foliations appear more sporadic and disturbed in flow-frontal regions at shallower topographies and thinner flow thickness. Foliations ramp up steeply at the break in slope (particularly evident in eastern flow lobe), and contains complex internal folding. Such internal complex folds are evident in flank imagery traces (Fig. 2.9), and in field observations (Figs. 2.16b, c).

Steep flow ramps in the near-source and most-distal regions are the result of active flow advance stagnation, with a cooling crustal control (and increased yield strength) at the flow front (caused by flow cooling and topographic constrictions) resulting in hindrance of flow advance, promoting compressional forces and ramping up at the flow front. This also

resulted in folding at the flow front. Complexity of folding arose due to progressive deformation (see later). These compressional forces at the flow front also promoted ramping of newly-extruded lava (exacerbated by a relatively shallow underlying topography in near-source regions). Uniformly dipping foliations in mid-flow regions (where flow is thicker and is therefore likely to require more energy to deform; Fig. 2.7-2.8) were formed by slope-aided advance (less crustal control), where cooling did not greatly hinder flow advance, and promoted extensional forces (evident by uniform stretching lineations in mid-flow regions, forming perpendicular to the principle plane of shortening; Fig. 2.32).

Ground-based structural observations and measurements often coincide with the traced features identified in the satellite image of the Rocche Rosse lava flow. The strikes of foliations often run parallel to traced surface ridges, dipping steeply back towards source, representing ogives and flow ramps. Combined satellite image observations and measurements of foliations on the Rocche Rosse lava flow reveal large scale folding over a region that was not identified in the field and only evident through structural measurements. However, other prominent surface features traced in satellite imagery have been identified and measured as large scale folding in the field, with fold hinges commonly orientated parallel to linear ridges (see Fig. 2.24). The most striking relationship between the satellite image observations and the ground-based structural measurements is a prevailing stretching lineation pattern following the large scale lineament features identified in mid- to upper-flow regions (Fig. 2.49). Similar linear features have been previously identified in obsidian lava flows and analogue experiments. Tuffen et al. (2013) observed the formation of these features in the Cordón Caulle 2011-2012 eruption in the field and by satellite imagery, identifying them as channelised flow margins. Tuffen et al. (2013) described these channelled flows as strike-slip shear zones, representing the main

channel flow, with corresponding breakout zones perpendicular to this channel zone. They were observed forming by channel margins stalling despite lava advance, forming curvilinear ridges. Such marginal shear zones have also been identified in glaciers. Comparisons between structures in glaciers and silicic lava flows have been previously identified (e.g. Christiansen and Lipman, 1966; Cas and Wright, 1987; Henry et al., 1990; Lawson et al., 2000). Glacier margins host zones that are subject to simple shearing, with pure shearing of longitudinal compression in mid-glacier (Lawson et al., 2000).

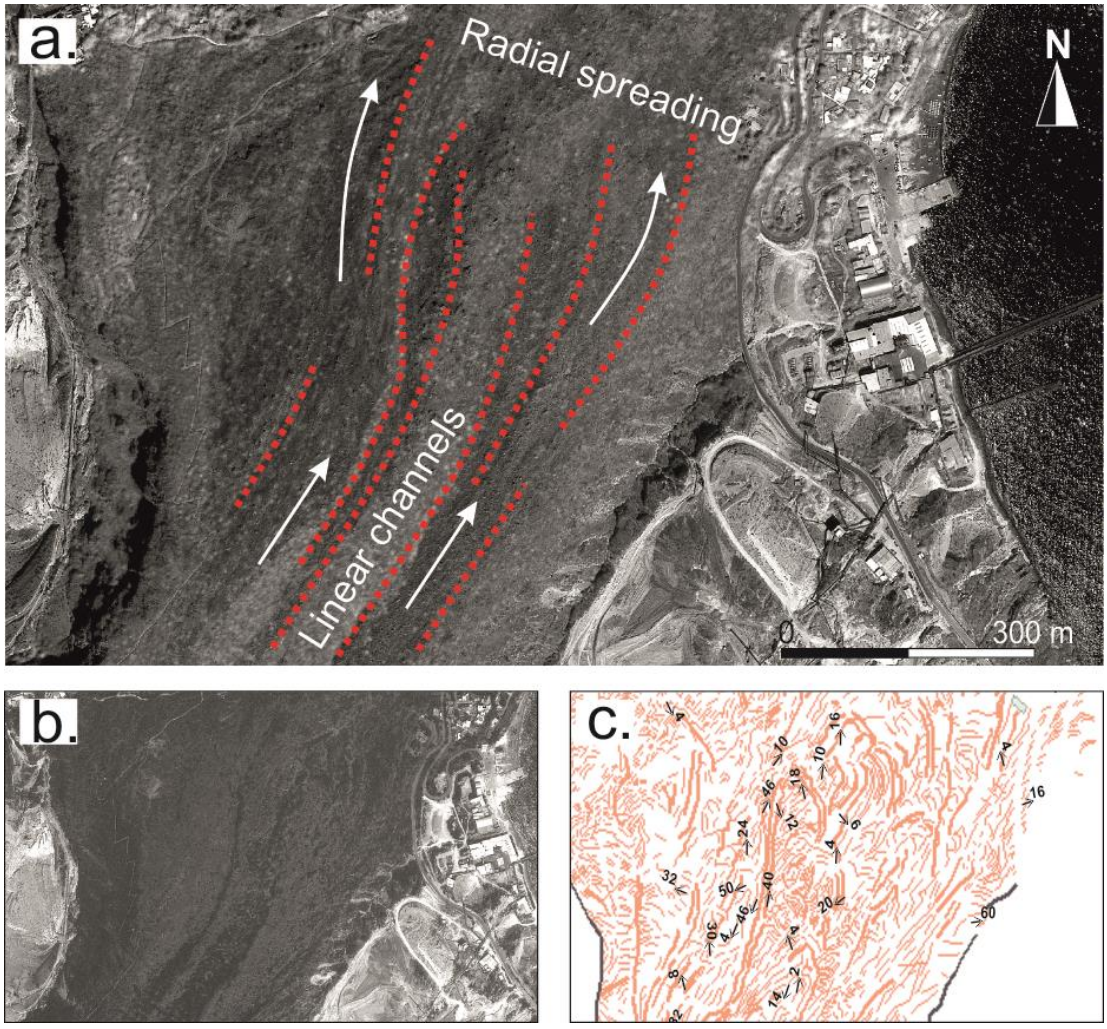

Figure 2.49: Linear flow channel ridges mid-flow on the Rocche Rosse lava flow. (a) Interpretation of satellite image with traced flow channels and radial spreading beyond channel. (b) Original satellite image. (c) Structural measurements of stretching lineations in mid-flow region, the majority of measurements trending approximately NE-SW (flow direction).

There are a number of parallels in terms of material properties and structural processes at work between obsidian flows and ice glaciers. Shear zones are concentrated near shear boundaries at the glacier margin and bed (Lawson et al., 2000). For instance, shear zones in the West Antarctic Ice Sheet mark the boundary between fast-moving ice streams and slow-moving ice in the inter-stream area (Raymond et al., 2001). Hudleston (1983) also identified the development of thin shear zones in the margins of glaciers.

Stretching lineations identified and measured along such linear ridges indicate that stretching lineations may have formed due to strike-slip shear. Big Glass Mountain (USA) also hosts such linear ridges (Fink, 1980b). These features were identified in Big Glass Mountain by aerial photographs and traced outlines, and have been suggested to have developed as marginal levées channelling the lava flow and suppressing radial expansion (Fink, 1980b). Levées and distinct channelised flow lobes have also been shown to form in experimental studies, via analogue modelling of silicic lava extrusions, using a polyethylene glycol wax and Kaolin slurries (Fink and Griffiths, 1998; Gregg and Fink, 2000; Griffiths, 2000), and viscous silicone fluid over a rigid base (Merle, 1998). Experimental studies by Merle (1998) showed channels forming in a straight passage along a basal slope, producing stretch trajectories related to shearing components, further supporting the development of stretching lineations along such ridges on the Rocche Rosse lava flow. Merle (1998) also showed that lava spreads radially beyond a straight channelled flow, with stretching changing from parallel to the flow mid-channel to concentric in the diverging flow zone. There is evidence to suggest that this occurred at the Rocche Rosse lava flow, with satellite imagery indicating channelled flow geometry in mid-flow regions, with stretching lineations running parallel to flow direction, followed by lateral spreading at the flow front (possibly due to changes in effusion rate and generation of lava pulses and/or influenced by changes in topography), and more sporadic stretching

lineation attitudes (Fig. 2.49). Lateral friction along margins can also generate a wrenching component which, together with a viscosity contrast, can induce folding at the vicinity of the lateral sides (Merle, 1998). Further shearing strain caused stretch direction rotation and fold axis rotation (Merle, 1998; see below: Progressive deformation). Channels promoted compressional forces and folding, and developed as a function of changes in channel morphology (Fink, 1980a). This feature is more typical in basaltic flows, where pahoehoe ropes develop due to channel slope decrease or flow constriction (Fink and Fletcher, 1978; Griffiths, 2000). Compressional stress concentration is also promoted by deceleration of the flow front, lateral friction or due to a topographic boundary (Fink and Fletcher, 1978), as well as a crustal cooling (Dragoni et al., 1992).

Satellite imagery allowed for the identification of two prominent lava flow lobes, as well as at least seven smaller breakout lobes (Welhan et al., 2002; Guilbaud et al., 2005; Tuffen et al., 2013; Figs. 2.5 and 2.6), whereby areas of the flow extend beyond the channelled margin of the flow, particularly at the flow front. Tuffen et al., (2013) observed a longer, more prominent lobe, forming due to overtopping a topographic barrier and flowing down a steepening slope. This may reflect the processes responsible for the development of the prominent north-westerly lava flow lobe in the Rocche Rosse lava flow (Fig. 2.5). Rock falls were also observed at the front of advancing breakouts of the 2011-2012 Cordón Caulle obsidian lava flow, outside marginal shear zones, following the initial main channel flow (Tuffen et al., 2013). Such breakout lobes may create complex internal structures related to strain localisation and lateral flow (Tuffen et al., 2013), an observation in the 2011-2012 Cordón Caulle obsidian lava flow that is consistent with field observations of complex internal zonation in obsidian lava bodies fed by a rhyolitic dyke at Krafla volcano, Iceland (Tuffen and Castro, 2009), and complex structures observed here in flow-frontal regions of the Rocche Rosse lava flow.

The large scale features identified in satellite imagery (constrained at ground-level) are the result of flow mechanisms controlling flow transport and deformation. These include compressional forces, resulting in large scale folding (identified as a third generation of folds at ground-level by the presence of smaller scale parasitic folds, recumbent folding and sheath folding) and flow ramping (resulting in foliations steeply dipping back towards the vent region), as well as mid-flow stretching lineations (due to gravity on a relatively steep slope) and limited folding. Extensive lineaments represent channelled flow geometry, producing prominent linear levees identifiable in satellite imagery (controlled by effusion rate and influenced by underlying slope), and controlling flow compression, extension and the outlined flow shape. The final effusive episodes produced stretching lineations due to extensional forces and stretch trajectories related to shearing components, before the flow motion terminated.

The development and complex occurrence of small, medium and large scale structures show a relationship in terms of formation mechanisms and spatial arrangement. Large scale structures, including folds (height and width >2 m), ogives (ramp structures) and flow channels (levees) that were predominantly identified in satellite imagery (and ground truthed) provide localised controls on deformation and therefore medium and small scale structures. Overall, the flow can be described as a compound lava flow (Walker, 1971), i.e. made up of two or more lobes. Slope variability created localised flow zones including flow lobes and channel boundaries. The flow is characterised by two dominant flow lobes and a number of breakout lobes (identified in satellite imagery).

Channel formation was predominantly controlled by slope morphology, with the initial configuration of flow influenced by distribution of volatiles, underlying slope, extrusion volume and cooling. Channels were created over a steeper (mid-flow) slope, before shallowing out and resulting in spreading. Within channels, folding, ramping and

fracturing is hosted (and often restricted). Such larger scale deformational structures superimpose smaller, pre-existing structures such as small-scale folding, spherulite and microlite alignment (defining the primary foliation) and lineation formation. These smaller scale structures formed due to primary cooling processes and a conventional compressional/extensional regime, and structures were re-aligned or modified due to progressive deformation (see later), controlled by variables such as slope and flow localisation. Satellite imagery shows how structures are orientated preferentially within individual flow lobes (e.g. western flow lobe, curvilinear structures orientated NE-SW; within channels, curvilinear structures are perpendicular to channels; structures more complex towards flow front at break in slope). Small scale folding formed upon extrusion, and medium scale folding formed later from continual extrusion, the influence of underlying slope, and cooling. This results in smaller scale folds superimposed upon medium scale folds (parasitic folding). Larger scale folds (regional, identified in satellite imagery) formed by further extrusion, cooling, progressive deformation and flow localisation (restricted by lobes and channels). Such progressive generations of folding has been identified in laboratory simulations. For instance, simulations using a polyethylene glycol over a variable slope by Gregg (1995) and Gregg et al., (1998) resulted in two or more generations of folds, with small scale folding forming within seconds of eruption onset, a second generation superposed on the first, and further compression resulting in a third generation of folding and finally fracturing. To summarise, smaller scale structures and structural formed by primary cooling processes and emplacement mechanisms, and were later modified and hosted by medium-scale textures which, in turn, were controlled by larger scale structures (which are again controlled by primary cooling and emplacement processes).

Configuration of flow stratigraphy in the case of the Rocche Rosse lava flow (and Monte Pilato deposits) is akin to the models of Fink (1987) and Fink et al. (1992), further detailed in North American flows by Manley and Fink (1987) and Fink and Manley (1987). The model indicates that a decreased load pressure leads to vesiculation in the upper portion of the extrusion (leading to explosive tephra deposits), followed by extrusion of a (predominantly) bubble-free obsidian lava (see Introduction). This is evident in the Monte Pilato by the presence of the underlying Rocche Rosse pyroclastic material. The Rocche Rosse lava flow hosts an upper and basal breccia (containing angular blocks), akin to models outlined in the thesis Introduction, suggesting similar well-constrained mechanisms of emplacement of a gravity-driven motion, a "modified tractor tread", with a viscous interior enclosed by angular blocks (Krauskopf, 1949; Fink, 1978), with Newtonian viscous, creeping and non-Newtonian brittle rheologies during emplacement.

The unique nature of the Rocche Rosse, and indeed all obsidian lava flows, arises from the structural development of the flow relating to the influence of variable factors such as the underlying slope, simple and compound flow evolution and cooling- or volume-limited flow regimes. Flank imagery and cross sectional interpretations indicate that the Rocche Rosse flowed over a variable slope (shallow at the vent, steeper over mid-flow region and shallow again at the flow front). Thickness variations may also indicate variations in extrusion volume during eruption, coupled with the influence of cooling and slope. For instance, in upper and frontal flow regions where flow thickens, this may be a response to repeated surges from the vent, responsible for the ramp structures that are also evident in these regions, and comparable to observations made at other obsidian lava flows (e.g. Macdonald, 1972; Fink, 1980a). Thicker flow configuration in near-vent regions may be the product of cooling-limited flow, resulting in flow stagnation (due to cooling) and flow build-up (due to continual extrusion). In mid-flow regions, stretching lineations are

commonly observed. Such structures were produced by experimentation of Merle (1998), with complex stretch and flattening plane trajectories produced in the vertical profile, changing in time from sigmoidal to concave trajectories over an inclined trajectory. This was followed by radial spreading at flatter trajectories, and this is what is suggested in the Rocche Rosse lava flow by satellite structural observations, particularly in the eastern flow lobe.

Experimentation and laboratory simulations by Gregg and Fink (2000) on the effects of slope on flow emplacement over a variable slope indicated that the lowest extrusion rates, lowest slopes and highest cooling rates produced flows that crusted over rapidly and advanced through bulbous toes. This may have occurred at the front of the Rocche Rosse lava flow, where the flow advanced over a flat underlying slope, the flow has had more time to cool and breakout lobes ("bulbous toes" as described by Gregg and Fink, 2000) are identified. The simulations of Gregg and Fink (2000) also show that as extrusion rate and slope angle was increased, and cooling rate decreased, rifted flows were produced, and folds and leveed flows were promoted. This again is evident in mid-flow regions of the Rocche Rosse lava flow, with a distinct channel morphology identified by satellite imagery and ground observations.

2.6.2 Rheological properties of the Rocche Rosse lava flow

Lava rheology is a primary control on lava flow transport and subsequent morphology, specifically viscosity, chemical composition, water content and temperature (Hess and Dingwell, 1996; Giordano and Dingwell, 2002; Gottsmann et al., 2002). Rheological estimates suggest there is some degree of variation across the flow in terms of H_2O content

(assumed at 1 atmospheric pressure), temperature, viscosity and redox state (Table 2.3 and Fig. 2.50). *Pele 8.00* (Boudreau, 1999) was used to calculate the Rocche Rosse obsidian lava (eruptive) temperature and oxygen fugacity conditions.

As previously stated (Thesis introduction and section 2.3), temperature and viscosity and H_2O content are all intrinsically linked, and this is reflected by the similar rheology results at different sample localities across flow. H_2O content is important as, for instance, water breaks chains of silica polymers in melts, resulting in a lower viscosity (Carrasco-Núñez, 1997). Previous Rocche Rosse studies calculated a water content ranging 0.15-0.21 wt% (Davì et al., 2001; Gottsmann and Dingwell, 2001b). Slight variations in H_2O content may be the result of secondary hydration and glass alteration (Friedman et al., 1966; Giachetti et al., 2014), affecting other rheological parameters and structural relaxation. Eruptive temperatures range from 730°C to 763°C, with no apparent trend relating to position of sample (Fig. 2.48). This temperature agrees with a temperature calculation for the Rocche Rosse obsidian of 750°C (Davì et al., 2001; Holtz et al. 2001; Gottsmann and Dingwell, 2001b - estimated slightly higher than the upper temperature limit of T_g). The non-Arrhenian temperature dependence of viscosity has been calculated by the VFT equation of Giordano et al. (2008). The equation is:

$$Log(\eta) = A + \frac{B}{T(K) - C}$$

where (η) is viscosity, T(K) is temperature (Kelvin), A is a constant independent of composition and B and C are adjustable parameters ascribed to compositional dependence (i.e. calculated using 10 major and minor oxide components and volatile components). The model is capable of modelling both strong (near-Arrhenian T-dependence) and fragile (non-Arrhenian T-dependence) behaviour of silicate melts. The viscosity model of Giordano et al. (2008) calculates Log(η) at a range of input temperatures, and has been applied here (Table 2.3 and Fig. 2.50). In this case, calculated temperatures for each of the

six sample localities were selected. As anticipated based on the low variation in temperature calculations, log η does not show significant variation across localities, ranging from $10^{10.53}$ Pa s to $10^{11.12}$ Pa s (Table 2.3 and Fig. 2.50).

Temperature (and as a result, viscosity) may show slight fluctuations across flow relating to syn- and post-emplacement spherulite crystallisation releasing heat, which may also enhance flow mobility. Temperature estimations suggest emplacement took place across the T_g kinetic boundary, affecting the mechanical response of the advancing lava (with the associated applied stress). The applied stress will therefore be accommodated by an elastic response, before terminating at brittle failure of the lava (Gottsmann et al., 2002). A uniform cooling pattern of 20-60 K per day (40-120 cm depths, calculated for the Rocche Rosse lava flow by Gottsmann and Dingwell, 2001b) indicates that the lava flow may actively deform across T_g for 1-3 days. Across the select sample localities, SiO_2 content varies from ~69 wt% to ~76 wt%, possibly due to magma mingling (Davì et al., 2010). As mentioned in section 2.3, higher SiO_2 content results in higher degrees of polymerisation and, therefore, greater viscosity. SiO_2 variation across the Rocche Rosse lava flow may play a role in structural variations.

Table 2.3: Summary of rheological parameters of the Rocche Rosse lava flow at specific localities.

Sample locality	**Eruptive temperature (°C) (*Pele 8.00*)**	***f*O2 (at eruptive temperature)**	**Viscosity (Pa s) (Giordano et al., 2008)**
105	748	-16.03	11.1
99	740	-16.15	10.5
332	763	-15.66	10.9
398	743	-16.15	10.5
64	746	-16.07	11.0
58	731	-16.45	10.9

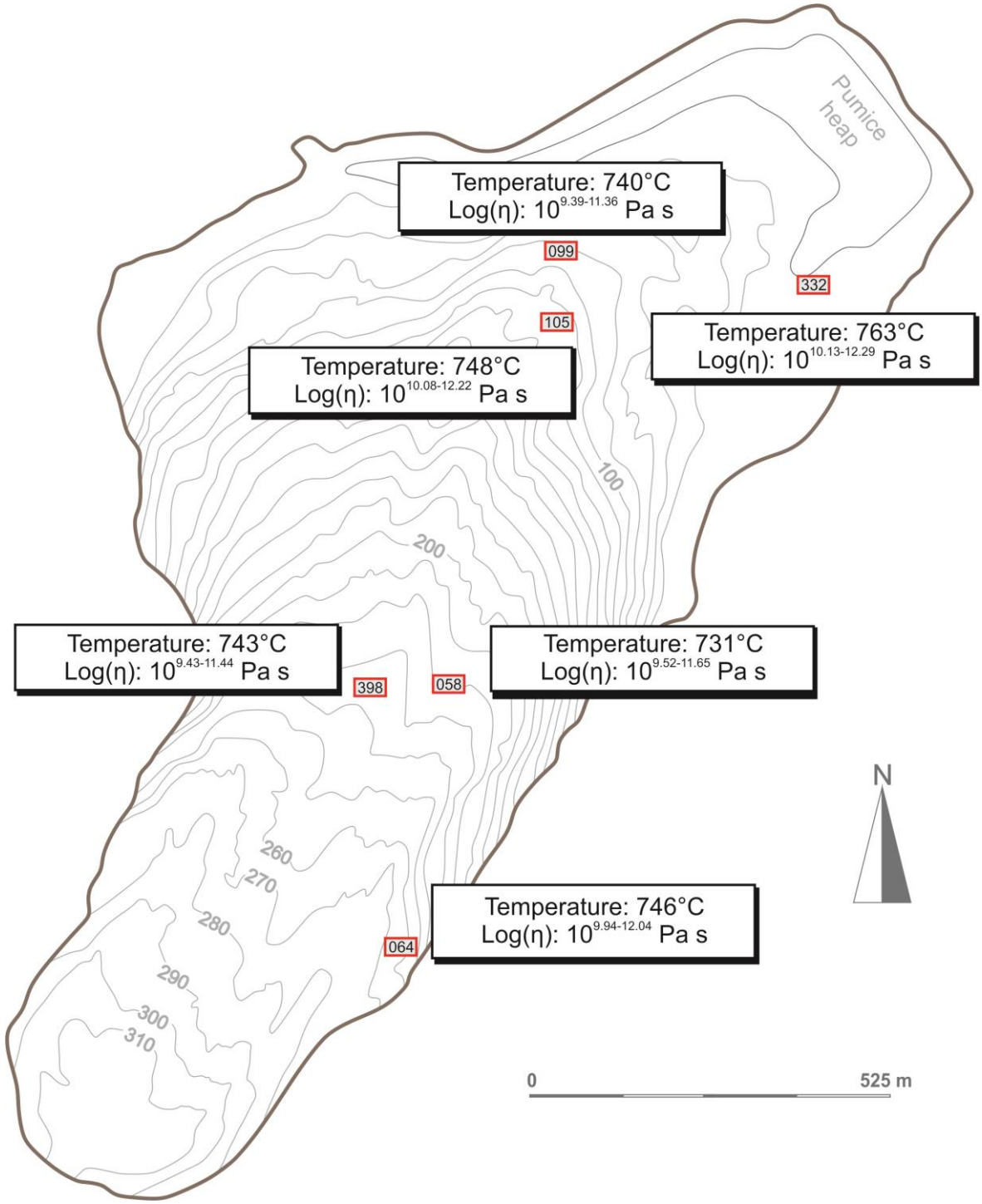

Figure 2.50: Map of sampled localities and calculated eruptive temperatures and viscosities.

Despite a calculated temperature of 731°C to 763°C (and previous estimates of 750°C; Davì et al., 2001; Holtz et al. 2001; Gottsmann and Dingwell, 2001b), Davì et al. (2010) suggest that eruptive temperature must be higher (~900°C; Zhang et al. 2003) in order for viscosity to allow flow to travel over a long distance. This is previously mentioned in

section 2.3, whereby higher temperatures result in a more fluid substance (i.e. lower viscosity). Davì et al. (2010) state that mingling of a hotter shoshonitic-latitic magma can invoke such high temperatures. Davì et al. (2010) note that the absence of microlites in the large majority of Rocche Rosse rhyolites sampled in their study indicates that microlite crystallisation must have been inhibited by the high viscosity of the melt (and low diffusivity) and/or by the absence of nucleation sites. However, field and petrographic observations in this study would argue that microlite content is variable across the flow, and spherulite content (and size) is highly variable (despite low average spherulite content, variation from spherulite-free to completely-spherulitic). The effects of viscous heating and heat generation by viscous friction may also play an important role in locally increasing temperature (Costa and Macedonio, 2003). It may also be argued that spherulite growth can significantly heat parts of the lava (latent heat release due to crystallisation; Tuffen et al., 2012), which may keep the lava mobile and extend the flow distance from vent. Spherulites are also likely to act in a more rigid manner (spherulites are at least partially crystalline structures, and will increase viscosity) than the less polymerised fluidal rhyolite or obsidian glass (above and below T_g respectively), and are therefore more resistant to deformation. This rigidity contrast can produce deformational structures, such as folds and bands (e.g. bands of spherulites are likely to be more resistant to deformation than the surrounding glass, which is more flexible, resulting in simple shearing). This may result in the highly deformed areas of flow that also show heavy spherulite content (see Chapter 3). Spherulites also result in increased water content in to surrounding melt, locally affecting viscosity. An increase in spherulite crystallisation may lead to an increase in temperature due to latent heat release (depending upon growth rate, density and background cooling rate) and, following growth and heat release, an increase in stiffness or rigidity, and yield strength. To summarise, rheological parameters estimated here

(temperature, viscosity, water content and spherulite crystallisation) provide primary controls over lava motion, morphology and subsequent structures, including flow length and the production of folds and bands, and variable rheological properties promoted flow localisation.

2.6.3 The role of progressive deformation

Structural observations and orientation measurements indicate no clear planar or linear trend across the Rocche Rosse lava flow, and highlight localised trends and sporadic linear and planar attitudes, particularly in flow-frontal regions. This structural complexity suggests that the Rocche Rosse lava flow underwent a deformational history that was a sustained, stepped process. This process is defined as progressive deformation (Flinn, 1962; Ramsay, 1967). The final solidified flow is the result of a series of earlier deformation stages. This is evident by the superimposition of smaller scale structures on to larger scale structures, brittle structures cross-cutting ductile structures, and the scattered distribution of foliation, lineation, fold axial plane and fold hinge orientation measurements. During- and following flow motion, the development of randomly orientated planar and linear structures is, in part, the result of rotation towards shear direction (Ramsay, 1979). The role of progressive deformation is significant in the structural evolution of the Rocche Rosse lava flow.

Multiple fold generations have been identified across the flow surface and flank exposure, with smaller scale folds superimposed on to larger scale folds (see Figs. 2.16a-d), providing evidence for relative timing of different fold scales. Curvilinear, isoclinal, recumbent and sheath folds have also been identified, and stereographic representation of

fold axial plane and fold hinge orientations indicate that earlier-formed folds may have been re-orientated. Curvilinear, isoclinal and recumbent folds, as well as sheath folds, have previously been identified in silicic lavas, rheomorphic ignimbrites, soft-sediment slumping and glacier emplacement as the result of progressive deformation (e.g. Tobisch, 1984; Azuma and Higashi, 1985; Alley, 1992; Martinsen, 1994; Castro and Cashman, 1999; Branney et al., 2004; Andrews, 2006; Andrews and Branney, 2011). Progressive shear modifies, refolds and transposes early-formed folds and produces sheath folds (Farrell, 1984; Smith, 2000; Branney et al., 2004; Andrews, 2006; Andrews and Branney, 2011). Asymmetry of folds has also been previously identified as a result of increasing strain (Smythe, 1971; Ramsay, 1980; Brun and Merle, 1988; Iezzi and Ventura, 2000). These flow studies show that asymmetry of folds increases away from the vent. These observations are again consistent with structures identified in the Rocche Rosse lava flow, with a higher quantity of folds (multiple generations at variable scales, tightness and attitudes) in the frontal north-eastern and north-western flow lobes, compared to mid- and upper-flow (near-vent) regions (see Figs. 2.17-2.18; 2.28-2.30). The dip angle of fold hinges and fold axial planes shallows from the flow frontal lobes to the upper-flow region, where later folds formed during progressive deformation. This suggests that the dip angle of folds decreased during progressive deformation, an observation which has been observed in experimental studies (Dell'ertole and Schellart, 2013).

Deformational structures are more apparent in terms of quantity and complexity (i.e. the scatter of planar and linear orientation) at the flow frontal lobes, in particular the north-westerly flow front (see Figs. 2.9; 2.21-2.23; 2.33-2.35). This suggests that progressive deformation had a more pronounced effect at the flow front in the anticipated NW flow direction. This is the result of downslope gravity-driven flow (over a down dipping topography, Fig. 2.7), radial flow spreading (Fig. 2.49) and flow localisation. Progressive

stagnation at the flow front, topographic constraints and cooling-driven crustal thickening (forming flow folds) have been previously observed in active obsidian lava flows (e.g. Tuffen et al., 2013), and are suggested as processes responsible for more deformational structures at the flow front. The superimposition of smaller folds on to larger folds in the Rocche Rosse lava flow indicates that flow folds were increasing in size with time. Fold size is controlled by the thickness of the layer being folded (Ramsay, 1967); therefore the thickness of the actively deforming layer increased with time. This observation in the Rocche Rosse lava flow is consistent with similar observations made in lava-like rhyolitic ignimbrites (Andrews and Branney, 2011). The time period in which the Rocche Rosse lava flow progressively deformed was likely to be weeks following effusion (Gottsmann and Dingwell, 2001b), and it has been generally suggested that deformation in rhyolitic lava flows can span a year or more (Lu et al., 2005; Tuffen et al., 2013). Stretching lineations, extensional and thrust faults have also been suggested as the products of rapid and progressive deformation (Gill, 1979; Tobisch, 1984; Elliot and Williams, 1988; Martinsen and Bakken, 1990; Paterson and Tobisch, 1993; Smith, 2000). Stretching lineations show slight uniform orientation arrangement (SE-NW orientation, parallel to the north-east flow lobe margin, see Figs. 2.31-2.35; 2.49). However, orientation distribution for stretching lineations is largely scattered, indicating that progressive deformation re-orientated stretching lineations as a secondary deformational stage, (stretching lineations being earlier formed in an extensional strain regime).

Progressive deformation concomitantly produced different types of structures at different parts of the flow, depending upon flow regime. This again is governed by flow rheology, and differences in rheological properties in different areas of the flow, both during and following flow advance. Previous studies illustrate that rheology and cooling rate varies with depth from surface (in terms of water content, microlite content, temperature,

chemical composition and viscosity; Gottsmann and Dingwell, 2001b). For instance, in one scenario, some areas of the flow may have a higher temperature than others due to spherulite crystallisation resulting in secondary heating and secondary boiling (Manley and Fink, 1987; Swanson et al., 1989; Tuffen et al., 2012), water content may be higher in some areas of flow, and SiO_2 is also lower in some areas. This results in flow acting in a more fluidal (less viscous) manner compared to areas which show lower temperatures, lower water content and higher SiO_2 content (higher temperature results in lower viscosity; higher water content and lower SiO_2 content result in depolymerisation). This hotter, more fluidal flow regime enhances flow mobility and therefore attempts to actively deform the cooler, more viscous flow which is more resistant to deformation (e.g. the outer crust which is in contact with the air and underlying topography, or flow frontal regions which have travelled furthest), resulting in structures such as sheath folds, and re-orientating earlier formed foliations and lineations. Areas of flow with higher viscosity are more resistant to flow deformation, and again may be producing complex structures as a less viscous flow regime preferentially deforms with respect to the more viscous regime, which results in simple shearing and/or lineation development overprinting or re-orientating earlier formed structures. This may be evident where spherulite shapes have altered due to foliation- and lineation-forming processes. Field evidence makes it clear that compressional and extensional strain regimes have resulted in a wide range of structural features across the Rocche Rosse lava flow. However, the heterogeneity of observed structures, as well as the scatter of planar and linear and orientations on the Rocche Rosse lava flow, is wide ranging, consistent with previous studies of gravity-driven emplacement, in particular that of rheomorphic ignimbrites (e.g. Branney et al., 2004; Andrews and Branney, 2011). Therefore, the role of progressive deformation across the Rocche Rosse

lava flow is highly emphasised, and plays an important role in the development and distribution of structures across the flow, both during and following flow extrusion.

2.6.4 Spherulites as indicators of flow deformation

The use of satellite imagery, field- and flank observations, and surface measurements provide information on lava flow emplacement. However, such methods may preferentially highlight overall or regional scale emplacement and deformation trends. The use of smaller scale fabrics provides an opportunity to assess flow emplacement and deformation on a localised scale. The occurrence and habit of spherulites in obsidian provides such an opportunity. Spherulites occur across flow exposure, and trails of spherulites often define the foliation (also observed by Clay et al., 2013). The presence of spherulites in flow bands of the Rocche Rosse lava flow has been previously identified as an indicator that spherulites were capable of nucleating and growing while the flow was still mobile (Clay et al., 2013), or that nuclei preferentially formed within specific flow bands. Spherulites preferentially form in radial shapes (Lofgren, 1971b; Castro et al., 2008, 2009; Gardner et al., 2012), appearing circular in 2D sections. Stretched or flattened spherulites indicates that deformation has occurred and altered the spherulite shape. Flattened spherulites have been reported in the Rocche Rosse lava flow by Clay et al., (2013), and highly flattened spherulite trains have been identified in Obsidian Dome, California, USA (Kingsbury, 2012). Flattened spherulites have also been historically reported in the black pitchstones of Planitz, Germany (Cole, 1886), the aporhyolite rocks of the Monterey District, Pennsylvania, USA (Walcott, 1896) and the intrusive rocks of the Kudaru Hills, Nigeria (Bain, 1932). Such flattened spherulites, forming an elongate ellipsoidal profile, differ in

profile from that of bow tie spherulites, which usually show two conical bundles of fibres joined at their apices, and are thought to form between 400°C and 600°C (Lofgren, 1971b; 1974; Breitkreuz, 2001).

Uniform deformation in one orientation (e.g. compression or constriction) can alter a spherical shape to an ellipse (Park, 1989). Progressive deformation in 2D during homogeneous coaxial and non-coaxial strains results in shortening of one axis and lengthening of another. An oblate shape is the result of oblate strain, i.e. pure flattening. Prolate shape and strain are the result of pure stretching. Heterogeneous strain also causes straight and parallel shape axes to become curved and non-parallel (Park, 1989). Undeformed, spherical spherulites can become dilated, distorted (i.e. change shape), and/or rotated, resulting in a final total strain ellipse (Park, 1989). Spherulite Preferred Orientation (SPO) results of spherulites from sampled localities provide an opportunity to assess deformational style in select areas of flow. Calculated r values and characteristic shapes present spherulites with spherical, oblate and prolate shapes. Oblate strain is the result of pure flattening and prolate strain indicates pure stretching (Park, 1989).

Rather than one single or large scale deformational event resulting in a preferred orientation, the sporadic but often definitive preferred orientations suggest more localised deformational events resulting in individual shape profiles. For instance, sample localities 15 to 19 are in close proximity to each other, and form part of a heavily folded area (small to large scale folding at various attitudes, sheath folding), resulting in pronounced SPO trends. Sample localities 20 and 21 are also part of a considerably deformed flow region, where multi scale folding and stretching lineations, both of variable attitudes, are common. Sample locality 24 shows ramping up at the front of the flow, with some tight folding, and shows a clear SPO trend. Sample locality 317 is located at the edge of the flow, where strike-slip shearing is likely to occur (Tuffen et al., 2013; also evident in glaciers -

Huddleston, 1983, 1989; Hambrey and Lawson, 2000; Raymond et al., 2001), and samples show a preferred orientation, flattened in relation to strike and within the foliation plane, and elongated in relation to dip. Samples 20, 22, 49, 53, 405 and 413 show minimal evidence for a pronounced SPO trend, which can be attributed to their respective sample localities, which are relatively undeformed (i.e. areas of low strain). The majority of sample localities showing spherical shapes are located on the western side of the front of the north-western flow lobe, while samples from localities on the eastern side of the front of the north-western lobe, as well as at the front of the north-eastern lobe, show a prolate and oblate profile. The lowest degree of spherulite deformation (based on characteristic shape and r values) was identified from localities in mid-flow (sample localities 19, 20, 21, 22, 405, 413). The highest degree of spherulite deformation observed in SPO results are those located at the eastern margin of the flow (locality 317). This indicates that pure and simple shear deformation is at least partly the function of the position of flow, with pure shearing occurring at the flow margins (and an extension direction parallel or normal to flow direction), and simple shear increasing towards the middle of the flow. Pure shear at the margins is likely to occur as the result of strike-slip movement and friction between the advancing flow and the surrounding topographic borders (stalling the advancing flow at the flow margins). Such marginal shear zones have also been identified in the 2011-2012 obsidian lava flow at Cordón Caulle Volcano, Chile (Tuffen et al., 2013). It could be argued that spherulites may be the result of extensional- and shear-induced spherulite crystallisation (see Chapter 3). Strike-slip shearing and spherulite crystallisation may also buffer cooling, prolonging lava advance (Tuffen et al., 2013).

Emphasis has been placed on spherulites that show deviation from a spherical shape. This deviation and degree of lineation may be caused by strain, linked to extnesional forces and flow extension, ultimately relating to flow rheology. The initial nucleation of spherulites in

areas of flow extension and lineation-forming extension may be the product of shear-enhanced nucleation (Kneller, 2002; Graham and Olmsted, 2009). Flow may enhance nucleation and trigger the formation of elongate crystals (Graham and Olmsted, 2009). Nucleation depends on the change of the free energy difference between the crystal and the melt phases; the degree of order in the melt phase increases under shear conditions, and the free energy difference increases. The entropic penalty for crystallisation is lowered and, therefore, the nucleation rate increases, with elongate chains of nucleation sites promoting elongate spherulites from strain (Keller and Kolnaar, 1997; Coccorullo et al., 2008). Spherulite crystallisation may then promote a rigidity contrast between spherulites and the obsidian glass, with spherulites more resistant to deformation than the surrounding obsidian, and the obsidian behaving in an elastic manner. This resulted in the elongation of spherulites (alteration in shape to elongate), and, in some instances, the production of stretching lineations. Spherulite crystallisation may also result in increased bulk viscosity, or spherulite growth may release latent heat and water, locally raising the temperature and lowering viscosity of rhyolitic magma (Tuffen et al., 2012) and enhancing flow mobility which, in turn, may promote progressive deformation, modifying earlier-formed structures (e.g. the formation of sheath folds). Results also show that some spherulites have an elongate shape in the plane of foliation. Planar foliation is considered to form as a result of simple shearing, forming parallel to a rigid surface such as conduit walls or an underlying topography (Fink, 1983). Spherulites forming prior to- and during foliation-forming processes may therefore elongate or flatten as a response to this process (by simple and/or pure shearing). Late-stage syn- and post-foliation spherulites nucleation may preferentially concentrate within foliation bands as a response to deformation. Spherulites forming and deforming (shape alteration) in response to both extensional forces and due to foliation forming processes may be an indicator of progressive deformation, i.e. multiple stepped

deformational events resulting in spherulite shape alteration, or complete shearing of spherulites. Results show that events are localised, contributing to the overall complexity of structures and structural distribution across the lava flow.

2.6.5 Silicic lava flows in the Aeolian Islands and other localities

Comparing the Rocche Rosse lava flow to other silicic lavas allows for the identification of common flow structures and an assessment of structure-forming mechanisms that occur during and following flow emplacement. Structurally comparable lava flows and domes have been emplaced across the Aeolian Islands. Silicic volcanism has defined recent activity on Lipari (since ~43 ka; Lucchi et al., 2010; 2013; Forni et al., 2013). A number of obsidian lava flows and domes, including the Forgia Vecchia lava flow (~1.6 ka, Lucchi et al., 2010; 2013; Forni et al., 2013), Pomiciazzo lava flow (~8.6 ka; Bigazzi and Bonadonna, 1973; Lucchi et al., 2010, 2013; Forni et al., 2013) and Monte Giardina lava dome (~24 ka; Crisci et al., 1981; Lucchi et al., 2010, 2013; Forni et al., 2013) contain stretching lineations, ramp structures and folds, exposed sporadically due to erosion, vegetation, urban cover and coverage by younger deposits. For a detailed field description of these obsidian lavas on Lipari, see chapter 3. A lava flow from Porri on the neighbouring island of Salina has been investigated by Iezzi and Ventura (2000) and Ventura (2001). The Porri lava flow hosts folds formed by deformation of enclaves and banded structures. Near the vent, the lava is identified as a non-ideal (coaxial and non-coaxial) shear flow; away from the vent, the lava is an ideal (coaxial) shear flow. Gravity-driven mechanisms control the contribution of pure and simple shear to the bulk deformation (from 2D strain and kinematic analysis). Folds are asymmetric, antiform-

synform sequences, with sub horizontal fold hinges. The presence of sub-circular to elliptical enclaves upper-flow, stretched enclaves mid-flow, and folds in the flow frontal region indicates that shear strain is heterogeneous (Iezzi and Ventura, 2000). Two dimensional strain and kinematic analysis of the enclaves show that most deformation occurs due to gravity-driven emplacement, and the mechanism of flow emplacement is consistent with a mixed `viscous gliding spreading' transport model at the back and with a `viscous gliding' model at the front (Ventura, 2001).

The island of Vulcano, which neighbours Lipari to the south, hosts another historic, well-preserved obsidian lava flow – the Pietre Cotte lava flow (see Chapter 4 for a detailed evaluation of the Pietre Cotte lava flow). The Pietre Cotte obsidian lava flow marks the latest effusive outpourings of the 1739 AD activity of the active Fossa cone on Vulcano (Frazzetta et al., 1984b). While the Rocche Rosse lava flow is ~2 km in length, the Pietre Cotte is comparatively short, less than 1 km. Another key difference between the two flows is that the Rocche Rosse advances over a variable topography (see Figs. 2.7; 2.9), whereas the Pietre Cotte advances over a uniform, steep topography (the Fossa cone NE flank). Spherulites in the Pietre Cotte are often mildly deformed, and small microlites and flow banding wrap around mafic enclaves. Stretching lineations also are common across flow. Small vesicles and xenocrysts are also present, each showing the effects of shear-related deformation. Structural mapping of foliations, lineations and folding revealed a more consistent and uniform arrangement of orientations compared to the Rocche Rosse lava flow (Fig. 2.51). Foliations show a prominent SW-NE strike, dipping towards and away from the vent. Foliations typically dip 30-50°, dipping steeper in higher up the flow (60-80°). Foliations align in a curvilinear pattern across the flow, sub-parallel to the flow front. At the western and eastern flow flanks, foliation strike and dip vary much more significantly, often dipping westwards, as shallow as 10-12°.

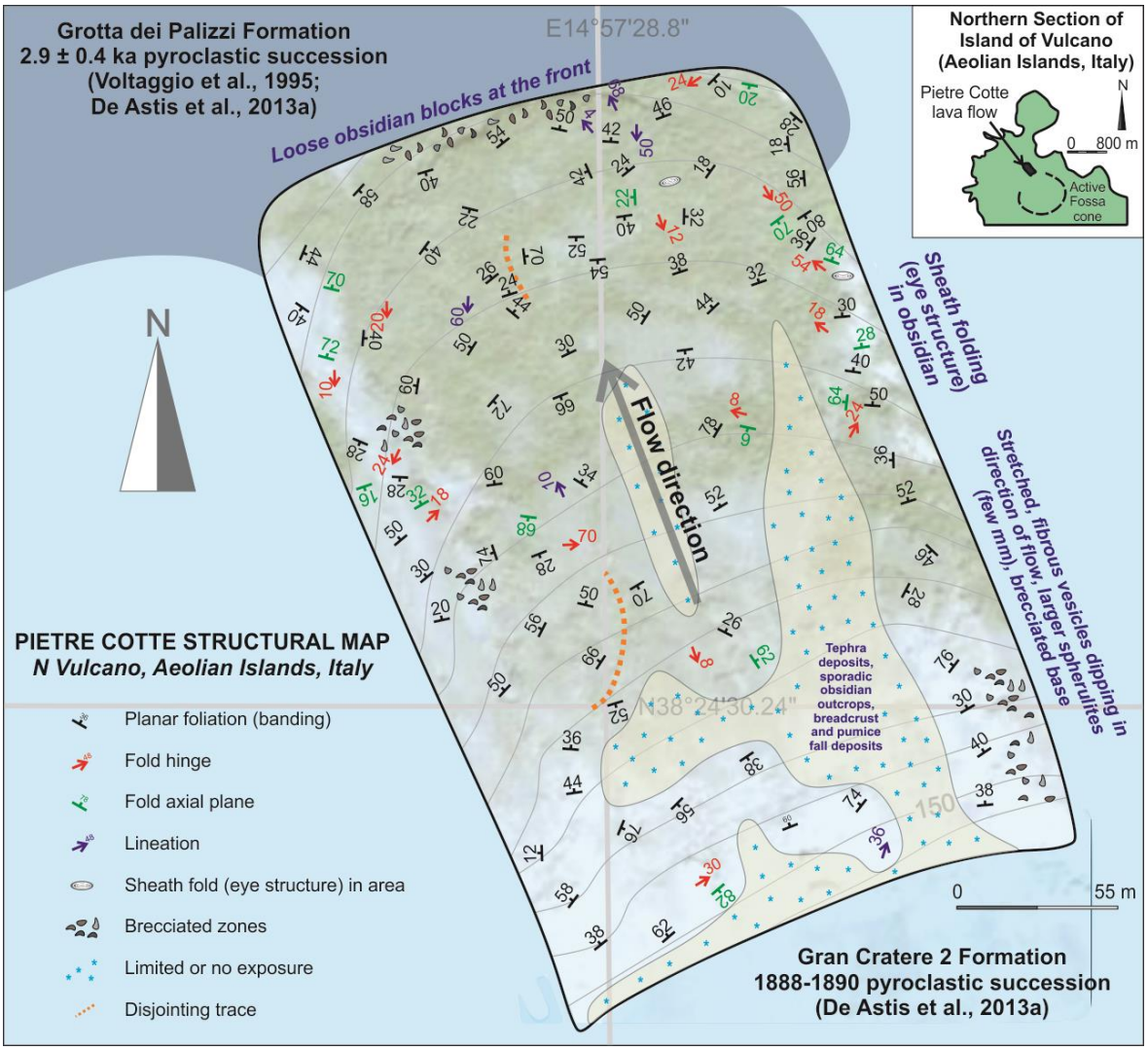

Figure 2.51: New structural data map of the Pietre Cotte lava flow, Vulcano, Aeolian Islands, Italy (flow position and topography from geological map of Keller, 1970 and De Astis et al., 2013a).

Folds are also more prominent at the flow margins, with fold axial planes and fold hinges often orientated N-S and NE-SW. Sheath folding is evident in the north eastern flow frontal region, an indicator of progressive deformation. There are also some cases of visible brittle separation of flow units, manifested as foliations dipping in opposite directions significantly within close proximity. Stretching lineations show a relatively uniform alignment compared to stretching lineations measured in the Rocche Rosse lava flow, occurring predominantly in mid-flow regions (comparable to the Rocche Rosse).

These are identifiable as sheared or stretched spherulites, and fibrous vesicles. Stretching lineations align in a N-S orientation, dipping from shallow (10°) to steep (68°). This suggests a single flow direction towards the north (as opposed to at least two identifiable flow directions in the Rocche Rosse). Autobrecciation is apparent at the flow margins, with a top breccia at the front and basal breccia in near-vent regions, and there are widespread tephra outcrops in middle and upper flow regions. Other than sporadic breadcrust bombs (from 1888-1890 activity; Mercalli and Silvestri, 1891), there is a general absence of large loose blocks compared to the Rocche Rosse flow surface.

The Pietre Cotte lava flow shows many of the same structures as the Rocche Rosse lava flow, associated with similar pre-extrusive, post-extrusive and structural processes. Both flows show evidence of elongate spherulites, planar foliations defined by the arrangement of spherulites, stretching lineations, polyphase folding, sheath folds, autobrecciation and jointing. The Pietre Cotte shows a more uniform pattern of foliation and lineation orientations, and no obvious evidence of multiple flow directions. There are also fewer large loose blocks on the upper surface. The relative uniform structural orientations can be attributed to a more uniform and steep underlying topography, resulting in less substantial compressional forces. The flow terminated at shallower topographies, meaning that although compression has occurred, resulting in ogives and folding at flow margins, it has not resulted in the typical large scale folding and complex re-folding apparent across the Rocche Rosse lava flow. The Pietre Cotte lava flow underwent an extensional and compressional strain regime. This produced stretching lineations and folding, with continual extrusion and progressive deformation resulting in sheath folding. The flow deformation culminated with brittle deformation. This suggests that lava flow volume and the underlying topography played a key role in the nature and complexity of deformation. The Rocche Rosse lava flow advanced over a variable topography, resulting in a series of

complex folds and re-folded folds, channelled flow regime, sporadic foliation and lineation orientations and discreet and multidirectional lava flow breakout lobes. The smaller Pietre Cotte lava flow advanced over a more uniform topography, resulting in more consistent foliation and lineation orientations mid-flow, some complex folding and orientations at the flow margins, a single flow direction and single, tongue-like lava flow lobe (no flow channels or breakout lobes, smaller lava volume and one pulse).

A number of comparisons have already been drawn to the 2011-2012 Cordón Caulle eruption (Chile), as well as Little Glass Mountain and Big Glass Mountain (USA). There are also comparable lava flows in the Aeolian Islands, including the Porri lava flow from Salina, and the Pietre Cotte lava flow from Vulcano. The Cordón Caulle 2011-2012 obsidian flow (Tuffen et al., 2013) shares many striking similarities to the Rocche Rosse lava flow in terms of structural features, including prominent lava lobes, breakout lobes, ogives, tension fractures, strike slip shear zones, a channelled flow geometry and radial spreading (Tuffen et al., 2013). This study is particularly useful as this lava flow was observed during emplacement, meaning that the origin of such similar features can be deduced from observations. Observations highlight the thermal efficiency of rhyolitic flows, which significantly increases their flow mobility and lengthens their timescale of advance (this is also highlighted in the Rocche Rosse study of Gottsmann and Dingwell, 2001b). Endogenic flow inflation, flow frontal advance by breakouts, and transitions from juvenile slabby to mature rubbly flow textures are all observed syn-eruptively for the first time in a rhyolitic lava flow (Tuffen et al., 2013). These are common processes identified in basaltic flows, and thus point towards universal models of compound flow development (Tuffen et al., 2013). The comparable features in both flows suggests that thermal efficiency in the Rocche Rosse lava flow may have increased flow mobility, and breakouts formed at the flow margin are akin to those that form in basaltic lava flows.

Little Glass Mountain and the Rocche Rosse lava flow also share similar characteristics in terms of size, rhyolitic composition, relative stratigraphic arrangement, chemical homogeneity, lack of phenocrysts and multiple folding episodes (Fink, 1980a, b). Fink (1980a) attributes multi scale and multi-generational folding to compressional stresses, concluding that this is a common process across lava compositions. A simple shear regime in Little Glass Mountain is indicated by measured and calculated microlitic alignment (Manga, 1998). Flow configuration is disrupted in Little Glass Mountain by rising pumice diapirs, inward propagation of fractures in areas of extension, and surface folding in sites of flow-parallel compression (Fink, 1980a. b). Rising of such pumice diapirs is also suggested as a process of surface folding in Big Glass Mountain (Fink, 1980b), with regularly spaced areas of coarsely vesicular pumice diapirs that rose from the base of the flow in response to a density inversion inherent in flow stratigraphy. Though this process has been tentatively suggested in the Rocche Rosse lava flow (see Fig. 2.48), limited access and exposure make this difficult to confirm. Obsidian Dome (USA) shows similar features to the Rocche Rosse lava flow, including microlitic alignment, and well developed lineations in the plane of flow banding (Castro et al., 2002). These lineations are orientated parallel to the flow margin and flow direction (similar to the Rocche Rosse lava flow, see Fig. 2.49 and text), with later influence from compression against a thickening flow crust, marginal talus piles and topography. Radial spreading and flattening are identified as dominant processes in flow emplacement (Castro et al., 2002), similar to the radial spreading process inferred here (see Fig. 2.49 and text).

Cioni and Funedda (2005) investigated the structural geology of crystal-rich, silicic lava flows on San Pedro Island (Sardinia, Italy). Though these lava flows are crystal-rich, they share similar features to that of crystal-poor obsidian lava flows such as the Rocche Rosse lava flow. Flow banding, curvilinear ridges and parallel-flattened spherulites are all

highlighted. Three types of foliation are identified, relating to flow, mechanical rotation, shearing and compression, and two types of fold were identified, relating to flow-parallel compression and fold re-folding (i.e. progressive deformation as inferred in the Rocche Rosse lava flow). Thrusts (which correspond to ramp structures evident in the Rocche Rosse lava flow), joints and crevasses are also identified, related to continuous lava effusion, thermal contraction and the final stages of cooling. Ductile deformation is highlighted as particularly important during emplacement, with brittle structures noted as having only limited importance. The whole thickness of the lava was involved in folding, explained by compression related to thermally-induced, downflow rheological changes in the lava body, with a progressive increase of total deformation toward the frontal sectors (also inferred here for the Rocche Rosse lava flow). Such structural evolution is compared to that of metamorphic basements and that of surge-type glaciers.

As well as compositionally similar lava flows, flows of differing composition also show similar structural features to that of the Rocche Rosse lava flow. For instance, the Chao dacite flow in Chile contains individual flow lobes, ridges and ogive structures (Guest and Sanchez, 1969; Fink, 1980b; de Silva et al., 1994). Mount St Helens dacite lava dome and Medicine Lake dacite flow contain crease structures, which form by lateral spreading (Anderson and Fink, 1992). Morphologically, these structures show inward dipping towards the centre, with multiple striations and a central valley (Anderson and Fink, 1992). These structures may be evident in the Rocche Rosse lava flow, based on linear traces in satellite imagery and in the field. Valleys are also evident at ground level, which are heavily vegetated, making it difficult to identify morphological indicators highlighted by Anderson and Fink (1992). For that reason, crease structures in the Rocche Rosse lava flow are not inferred here, but are also not ruled out.

2.6.6 Structural evolution of the Rocche Rosse lava flow

The identification and measurement of multi scale structures across the Rocche Rosse lava flow allows for a reconstruction of the flow's structural evolution (i.e. emplacement and deformation mechanisms; Fig. 2.52). The Rocche Rosse obsidian lava flow contains a number of structures, forming across different stages of pre- and post-extrusive evolution and lava flow emplacement, often concomitantly. These structures formed from magmatic processes at depth within the crust, during magma ascent and extrusion, during flow emplacement, cooling, and in the solid state when the lava flow has ceased. Deformation of the flow also occurred sequentially and in some cases repeatedly, from a ductile phase (above and within T_g) to brittle deformation, depending upon flow regime and rheology. The earliest pre-extrusive (magmatic) processes involved the generation of a shoshonitic-latitic magma body in a deep reservoir, evolving at different depths within the crust before being injected into a shallower rhyolitic magma, mobilising the rhyolite and triggering an eruption (Davì et al., 2009). The injection of the more mafic magma led to magma mingling and the formation of mafic enclaves in the rhyolitic host. The next stage of Rocche Rosse obsidian evolution is the eruptive phase. Following the initial explosive phase, the denser, vesicle-free rhyolitic magma ascended, possibly a product of explosive degassing during lava extrusion. The lava extruded and advanced downslope towards the northeast.

The emplacement of the Rocche Rosse lava flow is summarised in Figure 2.52. The flow emplaced in five sequential stages: (1) Initial extrusion, (2) Extensional strain onset, (3) compressional forces at topographic break, (4) progressive deformation, and (5) a brittle dominance due to prolonged cooling.

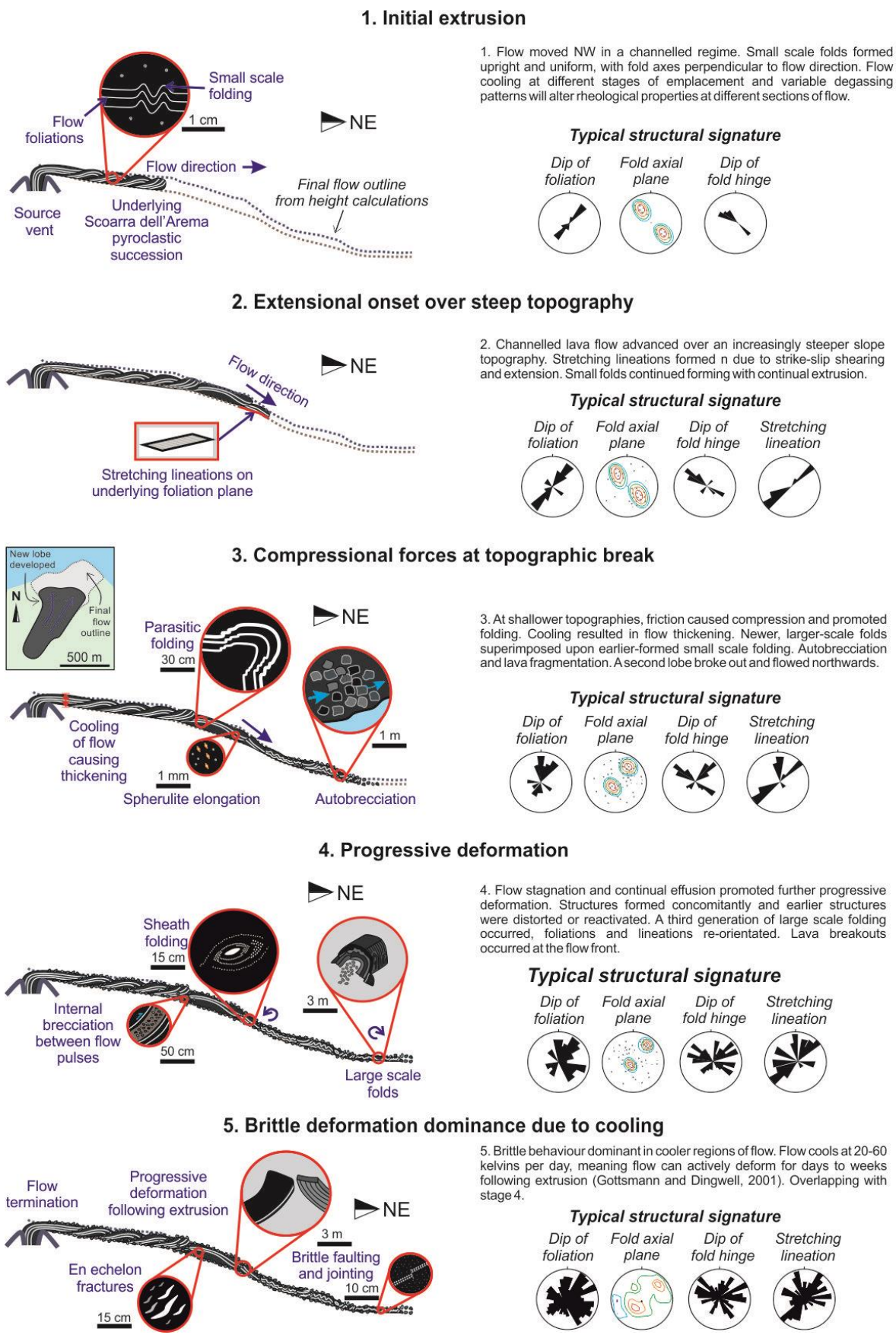

Figure 2.52: Model for the emplacement of the Rocche Rosse lava flow. The flow emplaced sequentially over five stages: (1) Initial extrusion of the lava flow; (2) Extensional strain regime onset resulting in

stretching lineations; (3) Compressional strain regime onset resulting in multi scale folding; (4) Progressive deformation, altering structural orientations; (5) Brittle deformational dominance and deformation following flow termination.

Satellite imagery reveals two prominent lobes (forming due to topographic constraints), linear channels with radial spreading towards the flow front, curvilinear ogives formed by advancing flow, and smaller breakout lobes extending beyond the main flow margins. Humped seams of accumulated loose blocks run sub-parallel to flow margins, representing the surface expression of these identified channels. Satellite imagery and field observations suggest that the flow was channelled, before radially spreading beyond channels (see Fig. 2.49). Extrusion and non-Newtonian flow emplacement occurred, with lava breaking out from channels (forming breakout lobes, Fig. 2.6) and thrusting upon earlier lava units (forming ramp structures). At temperatures around T_g, obsidian lava deformed in a ductile manner. During a compressional strain regime, the first phase of folding produced small scale folds (<20 cm in wavelength and amplitude), evident by their occurrence as parasitic folds on larger scale folds. This folding initially formed upright and uniform, with fold axes perpendicular to flow direction. As the lava continued to advance downslope, individual flow units advanced and overlapped, forming flow ramps, identified in satellite imagery and field observations, as well as previous studies (Cas and Wright, 1987; Gottsmann and Dingwell, 2001b). As the ductile lava flow advanced over variable topography (Figs. 2.7; 2.9), spherulites sheared and extended during an extensional strain regime. This formed stretching lineations, often evident on underlying planar surfaces. Progressive deformation resulted in the sub parallel re-orientation and re-alignment of earlier-formed foliations and folds. As the flow cooled through T_g, increasing viscosity and crustal thickening promoted compressional forces and a second generation of surface folding. Medium- to large scale ductile folds were superimposed upon the older, smaller

scale folding (forming parasitic folds, Fig. 2.16a-d, g). The cooling of the upper surface promoted the onset of autobrecciation and lava fragmentation, which the advancing flow overrode to form the top and basal breccia evident in flank and surface exposures. As the flow was hindered by autobrecciation, friction, cooling and compression at the flow front, the extensional strain regime mid-flow weakened, a second prominent lava flow lobe broke out from the main advancing lava flow channel to the NE and advanced in a north westerly direction. This is evident in satellite imagery, with the identification of a second prominent lobe, channels and ogives indicating a north-westerly moving flow.

As the lava flow cooled during emplacement, the flow is likely to have advanced at a more restricted rate (due to crustal cooling effects, talus/breccia development and compressional forces; Griffiths and Fink, 1993), but with continual extrusion and variable rheology, progressive deformation resulted in the onset of a third generation of largest scale surface folding. This stage of deformation can also occur following flow emplacement. Gottsmann and Dingwell (2001b) modelled the cooling history of the Rocche Rosse lava flow, and showed that the flow cooled, remained mobile and actively deformed slowly, lasting for weeks following emplacement, and cooling at a rate of tens of degrees K per day at a depth of 40-120 cm. Large scale folds were difficult to identify on the ground, but were evident in flow flanks (Fig. 2.9) and with the aid of foliation measurements. This progressive deformation sheared and distorted earlier formed stretching lineations, small and medium scale folding and foliations, resulting in differentially orientated structures. For instance, earlier formed folds became inclined or recumbent (evident by stereoplots in Figs. 2.18; 2.21; 2.25), and sheath folds were formed. Sheath folds in the flow likely formed due to extension and amplification of pre-existing curvilinear folds and structures (Ez, 2000; Mandal et al., 2009; Reber et al., 2013). Though the flow had undergone significant stages of flow deformation, the earlier-stage orientation distribution of micro-textures associated

with flow advance were not significantly overprinted. With continual but restricted extrusion, flow thrusting formed flow ramp structures which steeply dip towards the vent (ramps associated with large scale folding). Fragmented lava became sandwiched between individual flow units, forming internal brecciation between flow ramps. Brecciation may also have formed due to high strain rate acting upon material at the vent. Once flow had cooled sufficiently (below T_g), a brittle deformational phase dominated. Below T_g, the obsidian is considered a glass, and is no longer capable of viscous flow (Sakka and MacKenzie, 1971). Flow cooling resulted in small scale faulting, fracturing and jointing, whereby the flow no longer folded in a ductile manner and broke in a brittle style.

2.7 Conclusions

Combined satellite imagery, structural measurements and observations, rheological estimates and Spherulite Preferred Orientation methods were applied in order to constrain emplacement and deformation conditions of the Rocche Rosse obsidian lava flow. Satellite imagery revealed two prominent lava lobes, at least seven breakout lobes, a channelled flow regime and radial spreading. Field measurements and observations revealed a number of ductile and brittle structures (e.g. flow foliations, multi-scale folding, stretching lineations, fractures), and approximate flow-perpendicular foliation attitude (flow foliations defined by the arrangement of spherulites) and flow-parallel stretching lineation trends. Overall, the flow shows a broad range of complex structures and structural trends (more obvious in flow frontal regions).

Complexity may relate to underlying topography (change in slope promoting friction and a shift from extension to compression during flow advance), and was greatly influenced by changes in flow regime and variations in rheological properties. Structures formed due to the original flow extrusion, channelled flow advance, topography (also controlling flow advance and resulting in lobe formation), compression and extension. Micro-scale structures show an inherent relationship to meso- and macro-scale structures, forming initially due to cooling and emplacement mechanisms, with their arrangement and distribution being controlled by larger scale structures such as flow lobes and a channelled flow morphology. This results in small scale structures (such as folds) superimposed upon larger (medium scale) scale folds, with these medium scale structures contained and orientated within even larger (regional scale) structures. Changes in the underlying slope resulted in morphological changes in flow, including the production of channelled flow over a steeper slope inclination, and spreading at shallower slope. Further structural formation, structure modification and complexity arose from changes in rheology and progressive deformation. H_2O content varies (up to 0.21 wt% as revealed by studies; Gottsmann and Dingwell, 2001b; Davì et al., 2009), eruptive temperature varies from 730°C to 763°C, viscosity ranges $10^{10.5}$-$10^{11.2}$ Pa s, and SiO_2 varies from 69 wt% to 76 wt%. Spherulite and microlite content also varies dramatically across flow. Rheological properties are intrinsically linked. Variations in viscosity relate to temperature, composition and water variations. Such variations alter the flow regime, and may also combine with continual effusion and flow stagnation to promote progressive deformation (and therefore structural complexity). Brittle and ductile features formed concomitantly depending on flow regime, and earlier structures may be altered, re-activated or re-orientated due to progressive deformation.

Rheology varies across flow (and within the interior) due to differences in cooling rate, and also due to spherulite and microlite crystallisation. Spherulite crystallisation may be of particular importance to rheological differences, due to the significant occurrence of spherulites across flow, and variations in spherulite size, shape and population density. Spherulite growth releases water (Castro et al., 2008; Watkins et al., 2008; Clay et al., 2013) and results in secondary heating (Tuffen et al., 2012). The presence of spherulites also increases bulk density and bulk viscosity of the lava, and a rigidity contrast between spherulites and surrounding melt/glass, leading to spherulite shape alteration of lineation development. The presence of mafic enclaves may also locally affect temperature, viscosity, crystallinity and composition.

Rocche Rosse flow emplacement can be summarised into five temporally controlled stages, with significant overlap in space and time due to variations in rheology. These include (1) Initial extrusion of the lava flow, (2) the onset of extensional deformation over steep topography, (3) significant compressional forces at shallower topographies, (4) progressive deformation relating to rheological differences and continual effusion vs. stagnation, and (5) the brittle dominance in cooler areas of flow. Importantly, all five stages may be occurring at any time across flow (due to differences in flow regime), and flow actively deformed for days to weeks following extrusion (Gottsmann and Dingwell, 2001b).

This study presents new structural data and maps, rheological estimates, Spherulite Preferred Orientation data and detailed emplacement model for the Rocche Rosse lava flow. The study emphasises the role of flow rheology and progressive deformation in promoting structural complexity, particularly in flow frontal regions, and how channelled flow geometry may influence flow configuration and deformation. The role of rheology, progressive deformation, channelled flow geometry, flow localisation and spherulite

crystallisation are important parameters which may be applicable to emplacement of other obsidian lava flows.

Chapter 3

Spherulites in young obsidian lavas in the Aeolian Islands, Italy

Chapter outline

This study addresses spherulite heterogeneity in young obsidian lavas on the islands of Lipari and Vulcano. Spherulite heterogeneity relates to their formation (i.e. nucleation trigger), physical characteristics, composition, spatial distribution and modification. The study incorporates petrographic observations, electron microprobe compositional data, laser Raman spectroscopy, x-ray diffraction and crystal size distribution methods in order to fully classify spherulite types in Aeolian island obsidian lavas. Individual spherulite populations ("Types"), spherulite heterogeneity and textural complexity relate to different nucleation stimuli, obsidian emplacement characteristics and obsidian lava rheology.

3.1 Introduction

Recent activity in the active Aeolian volcanic province has centred on silicic volcanism, with rhyolitic activity involving both effusive and explosive phases. On the islands of Lipari and Vulcano (Aeolian Islands, Italy), rhyolitic eruptions (often accompanied by mingled mafic enclaves) have occurred from ~43 ka (Tranne et al., 2002; Gioncada et al., 2003; Lucchi et al., 2010, 2013; Forni et al., 2013), with the youngest eruptions occurring in historical time (Lipari - AD 776-1220, Forni et al., 2013; Vulcano – AD 1888-1890, Mercalli and Silvestri, 1891; De Astis et al., 2013b). As a result of this most recent activity, a number of obsidian lava flows and domes are well exposed on the islands of Lipari and Vulcano. The majority of these flows and domes contain abundant spherulites, making Lipari and Vulcano an ideal area to study spherulite formation in obsidian lavas. The study of spherulites is of keen interest to petrologists as, to this day, questions remain regarding the conditions and processes of their formation. For instance, Watkins et al. (2008) highlight the following open questions: on what timescale do spherulites form? When do spherulites begin to form? Do spherulites grow below the glass transition temperature bracket? Also, Clay et al. (2013) highlight the need for a detailed evaluation of the link between spherulite formation and rheologically-controlled deformation of obsidian lava flows. These questions point to a necessity for more detailed constraints on spherulite occurrence in obsidian lavas. Through combined petrological, textural and geochemical techniques, this study aims to decipher the formation conditions of spherulites in obsidian lavas on Lipari and Vulcano, including the identification of spherulite heterogeneity, origin of different spherulite types, the role of obsidian rheology and flow deformation.

Spherulites preserved in obsidian lavas can be used to identify the role of key magmatic and post-magmatic processes such as crystallisation history, glass transition and deformation (Lofgren et al., 1971a, b; Swanson et al., 1989; Smith et al., 2001; Castro et al., 2008; Watkins et al., 2008; Clay et al., 2013). Combined textural, petrological and geochemical approaches can offer insights into such igneous processes. Macro- to micro-scale obsidian lava flow structures and textures have been rigorously studied (e.g. Fink, 1983; Manley and Fink, 1987; Swanson et al., 1989; Manga, 1998; Castro and Cashman, 1999; Castro et al., 2002; Tuffen and Castro, 2009; Clay et al., 2013) due to the preservation of a range of textures in young silicic lava flows. Spherulitic textures are commonly observed in obsidian lava flows. Spherulites are radial fibrous crystallites, usually comprised of silica polymorphs and feldspar (Lofgren, 1971a; Swanson, 1977; MacArthur et al., 1998; Gardner et al., 2012; Breitkreuz, 2013). Spherulites are considered to progressively nucleate as a down temperature continuum during syn- and post-emplacement cooling (Clay et al., 2013), originally nucleating in response to an enhanced rate of undercooling brought on by degassing (Kirkpatrick, 1975; Swanson, 1977; Castro et al., 2009; Clay et al., 2013). Enhanced undercooling is the process of rapid cooling of a liquid system (below the liquidus), affecting crystal nucleation, growth and diffusion. As well as undercooling, plastic deformation following extrusion has also been tentatively suggested as a trigger for the formation of spherulites (Clay et al., 2013), and is particularly emphasised as a trigger in organic and inorganic compounds and polymers (Shtukenberg et al., 2012). It is also suggested that spherulites form as a hydration and devitrification texture at lower temperatures (Lofgren 1971b; Swanson et al., 1989), with post-eruption hydration of glass from adsorption of atmospheric H_2O, contemporaneous with diffusion of alkalis, Ca and Mg out of glass resulting in spherulite growth (Anovitz et al., 2006; Clay et al., 2013).

Volcanic glass undergoes a phase alteration with cooling, whereby the material changes from liquid-like to solid via the viscoelastic glass transition (Gottsmann et al., 2002; Tuffen et al., 2003). This structural relaxation interval is known as the rheological glass transition (Dingwell, 1995; Wilding et al., 1995; Gottsmann and Dingwell, 2001a, b; Gottsmann et al., 2002). Glass transition (T_g) has been reported in rhyolites in various studies, and shows an approximate range of 750-600°C (Swanson et al., 1989; Manley, 1992; Westrich et al., 1988; Hess and Dingwell, 1996; Dingwell, 1998; Gottsmann et al., 2002; Castro et al., 2009; Tuffen et al., 2012; Clay et al., 2013). Obsidian brittle-ductile behaviour and rheological parameters are intrinsically related (see Introduction and Chapter 2, section 2.3), in particular the relationship of temperature and strain rate. For instance, uniaxial and triaxial deformation experiments on glassy and crystalline samples at variable temperature (up to 900°C) and under variable strain rates by Tuffen and Castro (2008) indicate that brittle rupture can occur at high (eruptive) temperatures. The intrinsic relationship between primary rheological properties is displayed in Chapter 2 (Figure 2.2). For instance, elastic behaviour occurs at temperatures below T_g. Cooling history is a key control on obsidian flow rheology, and subsequently plays a major role in the formation of textures (Gottsmann and Dingwell, 2001a). Obsidian undergoes complex phase alteration and rheological change from liquid to solid during flow, and can actively deform following final effusion (Gottsmann and Dingwell, 2001b). For instance, with the Rocche Rosse lava flow (NE Lipari), cooling rates of tens of Kelvins per day across T_g control late stage deformation, thus sustaining flow in such a highly viscous rhyolitic lava, resulting in active deformation and advance of the flow front for days or weeks after effusion had ceased (Gottsmann and Dingwell, 2001b). It has been suggested that spherulite growth can occur above, within, and below T_g (Ryan and Sammis, 1981; Manley, 1992; Davis and McPhie, 1996; Watkins et al., 2008; Gardner et al., 2012; Clay et al., 2013), meaning that the

cooling history, emplacement mechanisms and deformation of obsidian lavas may play a key role in spherulite formation.

Petrographic observations, mineral and glass geochemistry, laser Raman spectroscopy, x-ray diffraction and crystal size distribution methods are used in order to constrain spherulites formation in obsidian lavas in the Aeolian Islands suite. Spherulites are classified in terms of their physical characteristics, chemical composition and formation origin. Petrographic observations suggest that there are spherulites with distinctive optical properties – spherulites with radial and non-radial interiors, surrounding brown rims and no rims, spherical and elongate spherulites, and internal zonation. Spherulites predominantly occur individually (often in zones of low shear), or concentrate within shear bands, folds, faults and fractures. Spherulites have a variable effect on microlite alignment, with microlites overprinted or deflected around spherulites. Spherulites contain cristobalite and orthoclase feldspar, with interstitial glass, minor clinopyroxene, titanomagnetite and quartz. In the majority of sampled flows and domes, there is a population of smaller spherulites (evident in spherulite CSD plots), with a significant degree of associated complexity, and one or more populations of larger spherulites. Based on physical characteristics, spatial distribution, composition and interpretation of nucleation stimuli, spherulites can be classified as five spherulite types (forming and modifying pre-, syn- and post-emplacement at temperatures above, during and below T_g).

These spherulite types result from different magmatic and post-magmatic processes (enhanced undercooling, flow-induced deformation and devitrification). The results demonstrate how different spherulite types in Aeolian Islands obsidian lavas show variable physical characteristics and spatial distribution as a result of their origin, including the important role played by rheological controls on deformation and resultant flow-induced spherulite crystallisation.

3.2 Geological framework and field observations

Obsidian lavas exhibiting spherulites are common across the islands of Lipari and Vulcano (Aeolian Islands, Italy; see Fig. 3.1). Silicic volcanism defines recent volcanic activity on these islands. Lava dome growth began in southern Lipari at 42.0 ± 0.3 ka (Crisci et al., 1991; Lucchi et al., 2010; Forni et al., 2013), resulting in the formation of the Punta di Levante, Falcone, Monte Giardina and Punta di Costa lava domes (Crisci et al., 1981; Lucchi et al., 2010; Forni et al., 2013). This was later followed by further lava dome growth in north-eastern Lipari, with the formation of the Castello and Capo Rosso lava domes (Lucchi et al., 2010; Forni et al., 2013). At 8.6 ± 1.5 ka ago, activity shifted further north on Lipari, with the Pomiciazzo obsidian lava flow extruded from the Vallone del Gabellotto eruptive vent (Bigazzi and Bonadonna, 1973; Lucchi et al., 2010; Forni et al., 2013). The extrusion of the Forgia Vecchia and Rocche Rosse obsidian lava flows mark the end of this most recent period of activity on Lipari, with the Rocche Rosse obsidian flow dated at 1230 ± 40 AD by archaeomagnetic dating methods (Arrighi et al., 2006). Rhyolitic lava flows and domes have also formed on the island of Vulcano (De Astis et al., 1997, 2013b; Piochi et al., 2009). The Grotta dei Palizzi obsidian lava flow on the southern flank of the active Fossa cone (Vulcano) has been dated at 2.1 ± 0.3 ka (Voltaggio et al., 1995; De Astis et al., 2013b), and, on the northern flank, the Pietre Cotte obsidian lava flow marks the latest outpourings of the 1739 AD activity of the Fossa cone (Frazzetta et al., 1984b).

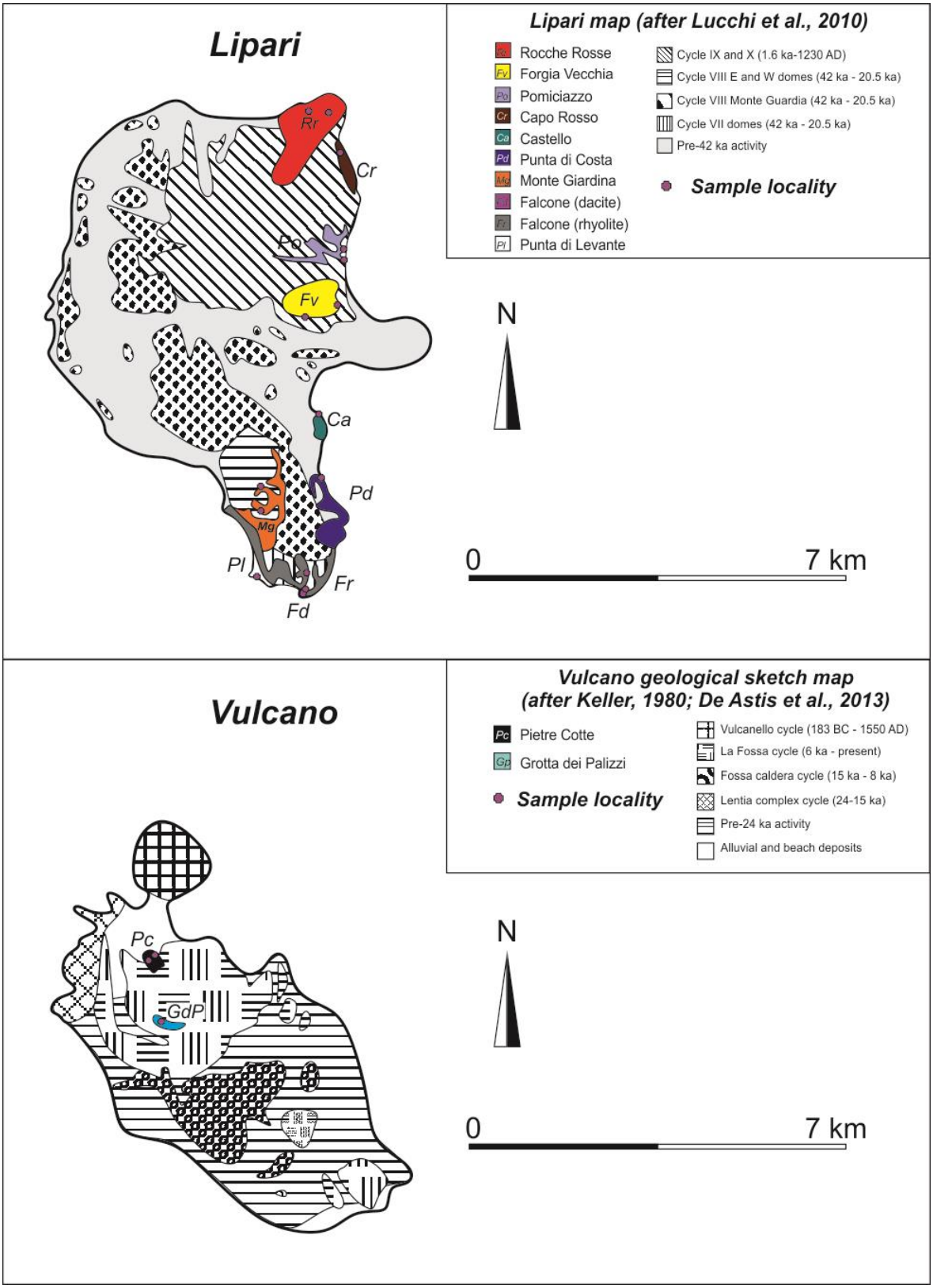

Figure 3.1: Sampled obsidian flows and domes and locations on Lipari and Vulcano, with older deposits also indicated (geological maps after Keller, 1970; Pichler, 1976; Lucchi et al., 2010; De Astis et al., 2013a; Forni et al., 2013).

Table 3.1: Sampled flows and domes and localities, as dated and described in previous studies.

Flow or dome	Locality	Age	Unit Description	GPS Co-ordinates
Pietre Cotte	North western Fossa cone, N Vulcano	1739 (Frazzetta et al., 1984b)	Tongue-like obsidian lava flow, 20 m thick, flow foliation, folding, blocky surface, abundant xenoliths (De Astis et al., 2013b)	N38°24'37.77" E14°57'26.01" N38°24'36.60" E14°57'24.56"
Rocche Rosse	North eastern Monte Pilato cone, NE Lipari	1230 ± 40 AD (Arrighi et al., 2006)	Lobate obsidian flow, well-developed flow foliation, basal carapace, ramp structures, ogives (Lucchi et al., 2010; Forni et al., 2013)	N38°31'11.20" E14°57'20.27" N38°31'09.38" E14°57'26.72"
Forgia Vecchia	South of Vallone del Gabellotto, E Lipari	1.6 ± 0.4 ka (Bigazzi and Bonadonna, 1973)	Bilobate obsidian lava flow, up to 30 m thick, well-developed carapace and foliation (Lucchi et al., 2010)	N38°29'08.54" E14°57'17.77" N38°29'19.94" E14°57'38.62"
Grotta dei Palizzi	Southern Fossa cone, N Vulcano	2.1 ± 0.3 ka (Voltaggio et al., 1995; De Astis et al., 2013b)	Garland-shaped obsidian lava flow, up to 20 m thick, flow foliation, folding, blocky surface, fumarolised, porphyritic lava xenoliths (La Volpe and De Astis, 2013)	N38°23'58.72" E14°57'25.03"
Pomiciazzo	Eastern Vallone del Gabellotto vent, NE Lipari	8.6 ± 1.5 ka; 11.4 ± 1.8 ka (Bigazzi and Bonadonna, 1973)	Lobate obsidian lava flow, up to 45 m thick, 3 well visible lobes, flow foliation (Lucchi et al., 2010)	N38°29'44.80" E14°57'41.78" N38°29'58.01" E14°57'41.51"
Capo Rosso	East of Monte Pilato NE Lipari	~8.7-24.5 ka (Crisci et al., 1983; Zanchetta et al., 2011; Forni et al., 2013)	Strongly hydrothermally altered endogenous rhyolitic lava domes, well-developed flow foliation (Lucchi et al., 2010)	N38°30'45.41" E14°57'42.69"
Castello	Lipari town (intensely urbanised), E Lipari	~8.7-24.5 ka (Crisci et al., 1983; Zanchetta et al., 2011; Forni et al., 2013)	Small endogenous rhyolitic lava domes, well-developed flow foliation (Lucchi et al., 2010)	N38°28'10.72" E14°57'23.77"
Punta di Costa	Punta San Giuseppe, SE Lipari	16.8-23.5 la (Crisci et al., 1981;1983; Lucchi et al., 2010)	Xenocryst-rich endogenous rhyolitic lava domes, flow foliation, pit crater (Lucchi et al., 2010)	N38°27'34.03" E14°57'24.15"

Table continued

Flow or dome	Locality	Age	Unit Description	GPS Co-ordinates
Monte Giardina	North of Monte Guardia, Central Lipari	19.9-24 ka (Crisci et al., 1981; Lucchi et al., 2013; Forni et al., 2013)	Endogenous lava domes, well-developed flow foliation of interbanded obsidian and lithic rhyolite, rampart structures (Lucchi et al., 2010)	N38°28'02.98" E14°56'30.67" N38°27'12.86" E14°56'44.44"
Falcone fa2 (Lucchi et al., 2010)	Capparo, S Lipari	40-43 ka (Gillot, 1987; Leocat et al., 2010; Forni et al., 2013)	Endogenous rhyolitic lava domes, 70-80m thick, well-developed flow foliation (Lucchi et al., 2010)	N38°26'21.87" E14°57'11.72"
Falcone fa3 (Lucchi et al., 2010)	Punta della Crapazza, Capparo, S Lipari	40-43 ka (Gillot, 1987; Crisci et al., 1991; Leocat et al., 2010; Forni et al., 2013)	Small, black HKCA dacitic lava-dome, very rich in xenocrysts (Lucchi et al., 2010)	N38°26'27.97" E14°57'14.27"
Punta di Levante	South west of Monte Guardia, SW Lipari	40.0-56 ka (Gillot, 1987; Crisci et al., 1991; Kraml et al., 1997; Forni et al., 2013)	Endogenous rhyolitic lava domes, 70 m maximum thickness, thick pumiceous upper carapace, poorly developed columnar jointing and onion-skin flow foliation (Lucchi et al., 2010)	N38°26'42.33" N14°56'40.18"

Twelve obsidian lava bodies were sampled from the islands of Lipari and Vulcano (Fig. 3.1 and Table 3.1). Of the twelve sampled flows and domes, ten are classified as informal stratigraphic units from the two most recent eruptive periods on Lipari ("Formations" as defined by Lucchi et al., 2010; Forni et al., 2013), and two are classified as informal stratigraphic units from the two most recent eruptive periods on Vulcano (defined by De Astis et al., 2013b). Sampled flows and domes and their localities are listed in Table 3.1, in order of age (youngest to oldest). Important characteristics to highlight include variable deformational structures, glassy state, spherulite occurrence and physical characteristics, and the presence of mafic enclaves and/or phenocrysts. These characteristics are

highlighted as important as they may trigger or affect spherulite nucleation, growth and modification.

3.2.1 Obsidian lava exposure

Generally, the youngest obsidian lavas show the best outcrop exposure, and the exposure of older lava bodies is variable due to a number of factors, including vegetation cover, construction and weathering. The Pietre Cotte lava flow (Figs. 3.1; 3.2a) is a short, tongue-like obsidian lava flow on the northern slope of the Fossa cone (Vulcano), formed over a relatively steep slope inclination (~30-35°; Frazzetta et al., 1984b). The flow is ~500 m in length, ~250 m in width, and reaches a maximum thickness of ~15-20 m at the flow front, coinciding with a break in slope (see Chapter 4 for more details). The Rocche Rosse lava flow (Figs, 3.2b, d), due in part to its young age and considerable size (2 km long, up to 51 m in thickness, see Chapter 2 for more details), displays exceptional exposure of glassy, spherulitic obsidian across the entire flow extent. The Rocche Rosse lava flow outcrops in NE Lipari from the partially-destroyed Monte Pilato eruptive vent. The flow extends over a variable topography, with two distinguishable flow lobes. The Forgia Vecchia lava flow shows good exposure in the source region and at the flow front (west of the town of Canneto). The flow extends from a vent region near the Pirrera area, displaying a tongue-like shape which manifests as 2 flow lobes. The Grotta dei Palizzi lava flow outcrops as a prominent overhang feature on the south side of the Fossa cone on Vulcano.

Figure 3.2: (a) Pietre Cotte lava flow front, with devitrified obsidian and frontal talus. (b) Larger spherulites in the Rocche Rosse lava flow. (c) Variably glassy and devitrified obsidian in the Forgia Vecchia lava flow. (d) Spherulites occurring individually and concentrated in bands (Rocche Rosse lava flow). Spherulites are also elongate in areas and sheared out.

The flow exposure is ~20 m thick, and is characterised by a blocky surface and planar foliations (carried by spherulites). The flow is heavily altered in areas more proximal to the Fossa vent. The Pomiciazzo lava flow is exposed sporadically in north eastern Lipari from the Vallone del Gabellotto tuff cone crater, reaching the eastern coast in several distinct lobes. Exposure is limited due to weathering, extensive urbanisation and younger pyroclastic succession coverage. However, there are sporadic exposures along the eastern coast and within the Vallone del Gabellotto. The Capo Rosso lava dome exposures are also sporadic due to later pyroclastic coverage, as well as extensive pumice quarrying on the

eastern coast of Lipari. The Castello lava dome shows limited exposure as it has been built upon (the town of Lipari). However, there are limited exposures on the coastal cliff underneath the cathedral, at the portside and in-situ within housing walls, with very limited spherulitic outcrop exposed. The Monte Giardina lava dome is ~0.5 km^3 in volume, alternating with explosive pyroclastic material (De Rosa et al., 2003). The Falcone lava domes outcrop at the most southerly point of the Lipari southern dome field. The Falcone lava domes are heavily weathered and eroded. A small, black dome near Punta della Crapazza has been sub-classified as a dacitic Falcone member (Lucchi et al., 2010). The Punta di Levante lava dome (also referred to as Punta del Perciato; Lucchi et al., 2010; Forni et al., 2013) represents remnants of two endogenous lava domes the coastal cliff of Scogliera sotto il Monte. The dome is ~70 m thick (Lucchi et al., 2010), and is heavily weathered. The dome is predominantly grey in colour.

3.2.2 Flow characteristics

Typical flow/dome characteristics, including deformational features, spherulite occurrence, mafic enclaves and mineral assemblages, are summarised in Table 3.2, including individual characteristics relating to each flow and dome. A number of well exposed lava flows and domes show brittle and ductile deformational fabrics (Figs. 3.3-3.4), with multi-scale folding (Fig. 3.3a-f, 3.4) and stretching lineations (Fig. 3.3g) and sheared spherulites (Fig. 3.4h) evident across obsidian lava bodies. Such deformational structures often coincide with areas of high spherulite density (Figs. 3.3 and 3.4), and elongate spherulites. Generally, the younger flows exhibit the best exposure of glassy and spherulitic outcrops.

Table 3.2: Typical features and characteristics of obsidian domes and flows on Lipari and Vulcano, including deformational fabrics, spherulite occurrence, mafic enclave occurrence and mineral assemblages.

Flow/dome	Typical flow characteristics	Nature of spherulites	Mafic enclaves and mineral assemblage
Pietre Cotte	Heavily altered in upper flow regions, extensive folding, stretching lineations, jointing and fracturing, deformational fabrics more prominent in flow-frontal regions	Predominantly less than 1 mm in diameter, and often define the planar foliation. Microlites often deflect around small, radial spherulites	Common throughout flow - trachytic in composition, (see Chapter 4 and Piochi et al., 2009). Quartzite xenoliths observed in upper flow (Piochi et al., 2009)
Rocche Rosse	Multi-scale folding of variable attitude and tightness, as well as stretching lineations, jointing and autobrecciation, widespread deformational fabrics	Highly variable degrees of spherulite occurrence, from completely glassy to completely devitrified on a <1 m scale. Individual, interjoined and in folds and fractures. Some spherulites show an elongate shape (often occurring within close proximity of folds or bands). Spherical spherulites predominantly occur in between flow bands in areas of low shear-indicators. Vary in size considerably	Red to purple mafic enclaves are found sporadically across the Rocche Rosse lava flow (latitic to trachytic in composition, see Davì et al., 2009, 2010 for more details on Rocche Rosse mafic enclaves)
Forgia Vecchia	Flow ramping and folding (folded foliations), extensive exposure of flow ramps along the southern flank from il Vallonaccio, flow foliations, variable-attitude small scale folding (<20 cm in fold wavelength and amplitude) and stretching lineations	Complete radial spherulitic intergrowth and microcrystalline glass alteration at flanks. Not entirely prevalent throughout the flow, but occur at the flow front and in flank exposures, and are generally small (<1 mm diameter), occurring in concentrated clusters. Elongate spherulites can be observed within or in close proximity of bands or folded outcrop	No enclaves identified, rare alkali feldspar, quartz and plagioclase observed

Flow/dome	Typical flow characteristics	Nature of spherulites	Mafic enclaves and mineral assemblage
Grotta dei Palizzi	Flow banding (foliations), variable-attitude small scale folding (<20 cm in fold wavelength and amplitude) and stretching lineations	Predominantly less than 1 mm in diameter, and often define the planar foliation	Trachytic enclaves are common throughout flow
Pomiciazzo	Extensive flow banding, brecciation (particularly at flow front), flow ramping	Much larger than those in younger flows at 2-3 mm diameter, particularly in exposures on the beach at Canneto. Pomiciazzo, predominantly spherical in shape, and occur individually or in clusters	No enclaves identified, rare alkali feldspar, plagioclase and quartz phenocrysts apparent
Capo Rosso	Limited exposure due to pyroclastic coverage, exposure at flow front – flow banding, fracturing	Individual and clustered spherulites (typically 0.5-1.5 mm diameter) are common, and are often spherical in shape	Clinopyroxene-rich latitic enclaves have been identified (Gioncada et al., 2003; Forni et al., 2013)
Castello	Limited exposure due to urban coverage, sporadic exposure shows flow banding, vesiculation	Typically spherical and 0.5-1.5 mm diameter, occur individually or in clusters	Clinopyroxene-rich latitic enclaves have been identified (Gioncada et al., 2003; Forni et al., 2013)
Punta di Costa	Predominantly devitrified, some fresh glass, steep flow bands, flow ramps	Typically spherical and 0.5-1.5 mm diameter, occur individually or in clusters	Mafic (shoshonitic-latitic) enclaves and crustal xenoliths (De Rosa et al., 2003; Gioncada et al., 2005; Forni et al., 2013)
Monte Giardina	Flow ramping, with foliations dipping sourcewards, highly vesicular in areas	Visible with the naked eye in the Monte Giardina lava dome, particularly in roadside exposures of the Valle Muria, are typically 2-3 mm in diameter, and generally occur individually and clustered	Latitic enclaves containing abundant plagioclase and clinopyroxene (De Rosa and Sheridan, 1983; Crisci et al., 1991; De Rosa et al., 2003)

Flow/dome	Typical flow characteristics	Nature of spherulites	Mafic enclaves and mineral assemblage
Falcone (rhyolite)	Predominantly devitrified, some fresh glass, steep flow bands, flow ramps, folding, stretching lineations	Typically 2-3 mm in diameter, and generally occur individually and clustered, spherical shape	Abundant mafic (shoshonitic-latitic) enclaves and crustal xenoliths (De Rosa et al., 2003; Gioncada et al., 2005; Forni et al., 2013)
Falcone (dacite)	Predominantly devitrified, some fresh glass, steep flow bands, flow ramps	Typically 2-3 mm in diameter, and generally occur individually and clustered, spherical shape	Rich in crustal xenoliths, with latitic enclaves common (Gioncada et al., 2003, 2005; Forni et al., 2013), and rare quartz phenocrysts are evident
Punta di Levante	Predominantly devitrified, few textures and structures preserved	Highly devitrified, and spherulites are rarely evident to the naked eye	Porphyritic, containing alkali feldspar and quartz within a devitrified groundmass

Elongate spherulites can be observed in the Pietre Cotte, Rocche Rosse and Forgia Vecchia lava flows. Importantly, these elongate spherulites tend to occur within or in close proximity of bands or folded outcrop (Fig. 3.4). Generally, across all flows and domes, large (1-3 mm), spherical spherulites occur individually in zones of low shear (Figs. 3.2d; 3.3a) or in zones of no banding or shear indicators. Monte Giardina and Falcone lava domes spherulites are typically 2-3 mm in diameter, and generally occur individually and clustered. Falcone domes are predominantly glass-free or devitrified, with minor glassy and spherulitic areas, while Punta di Levante lava dome is highly devitrified, and spherulites are rarely evident to the naked eye.

A number of obsidian lavas show evidence for rhyolite interaction with a more mafic magma, and rare crystals are apparent. Mafic enclaves are common throughout the Pietre

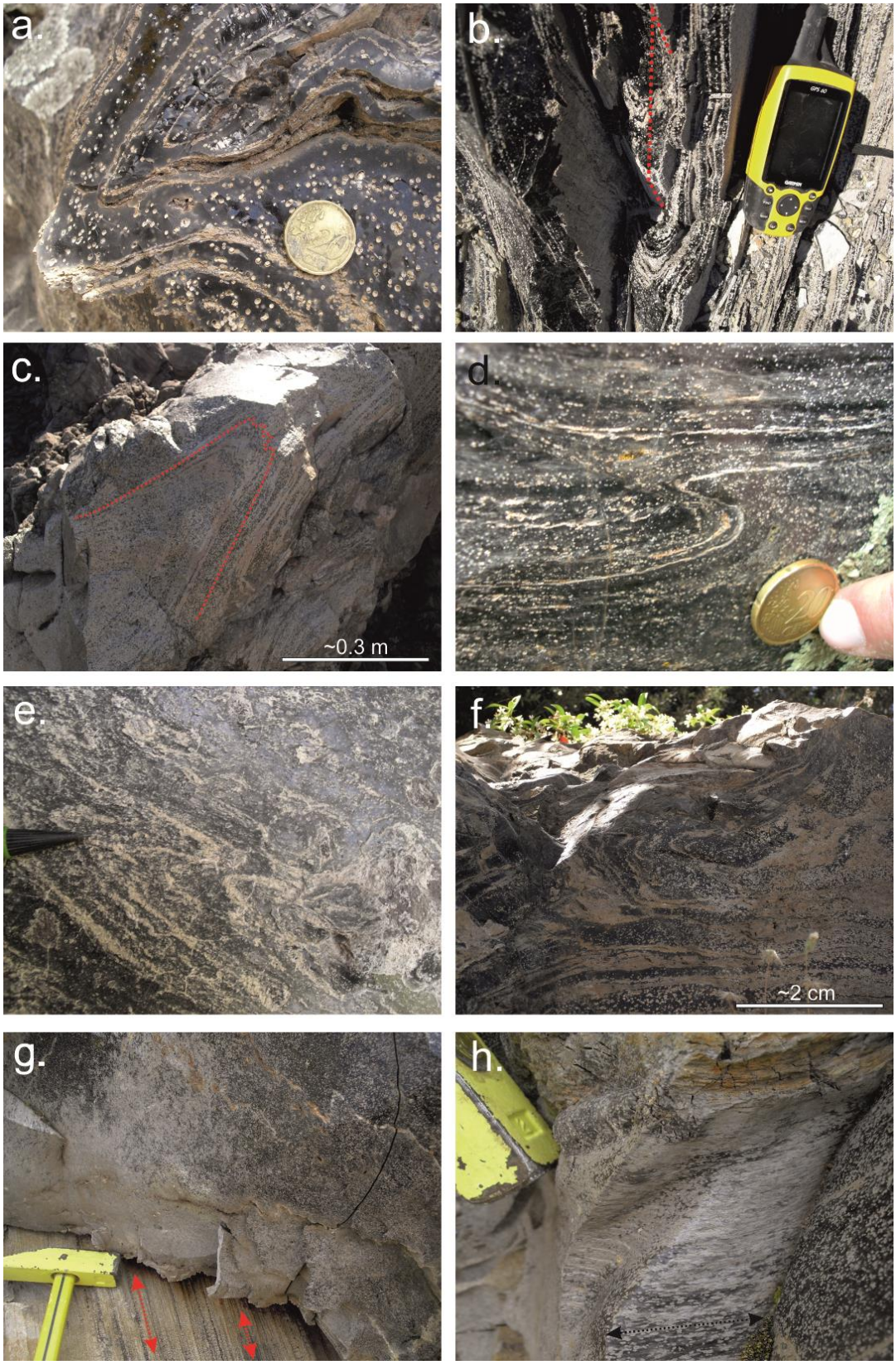

Figure 3.3: Evidence for spherulitic obsidian coinciding with areas of flow deformation, including (a)-(f) compressive folding (red line in b. highlighting the fold axial plane, and in c. representing fold outline) and (g)-(h) structures resulting from extensional forces (arrows indicate stretching lineations).

a

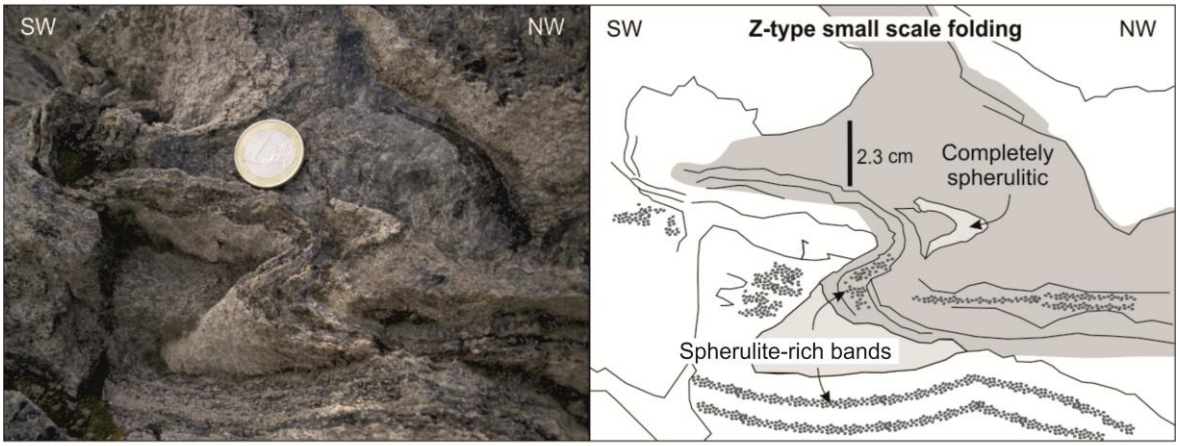

b

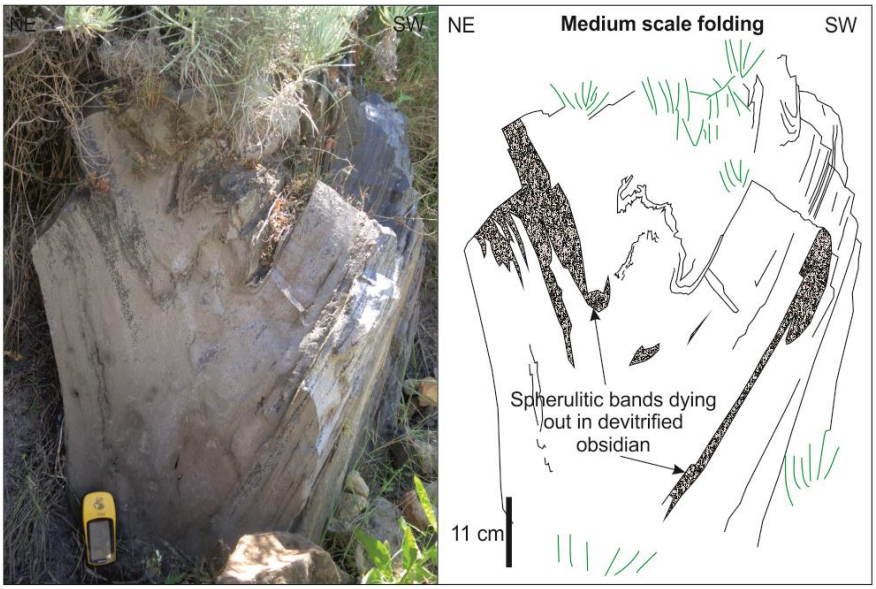

c

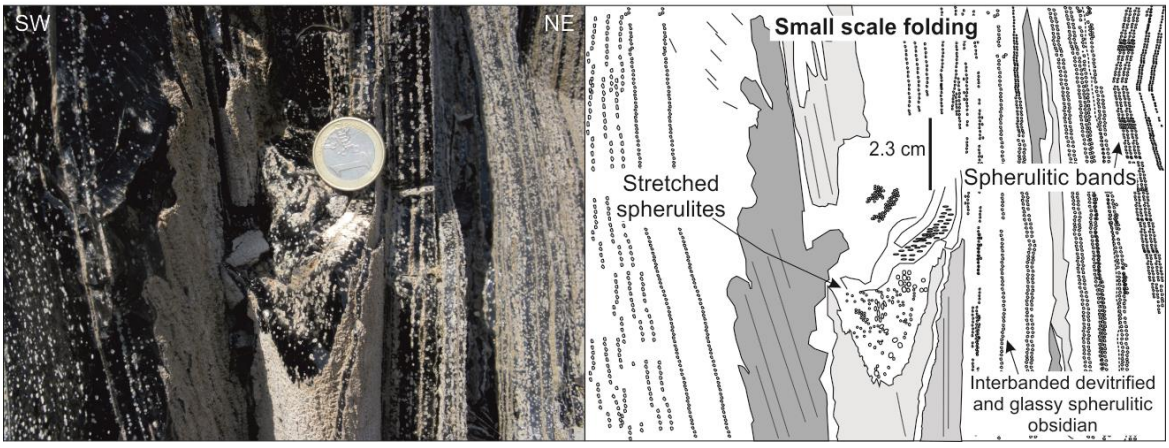

(Image continued on next page)

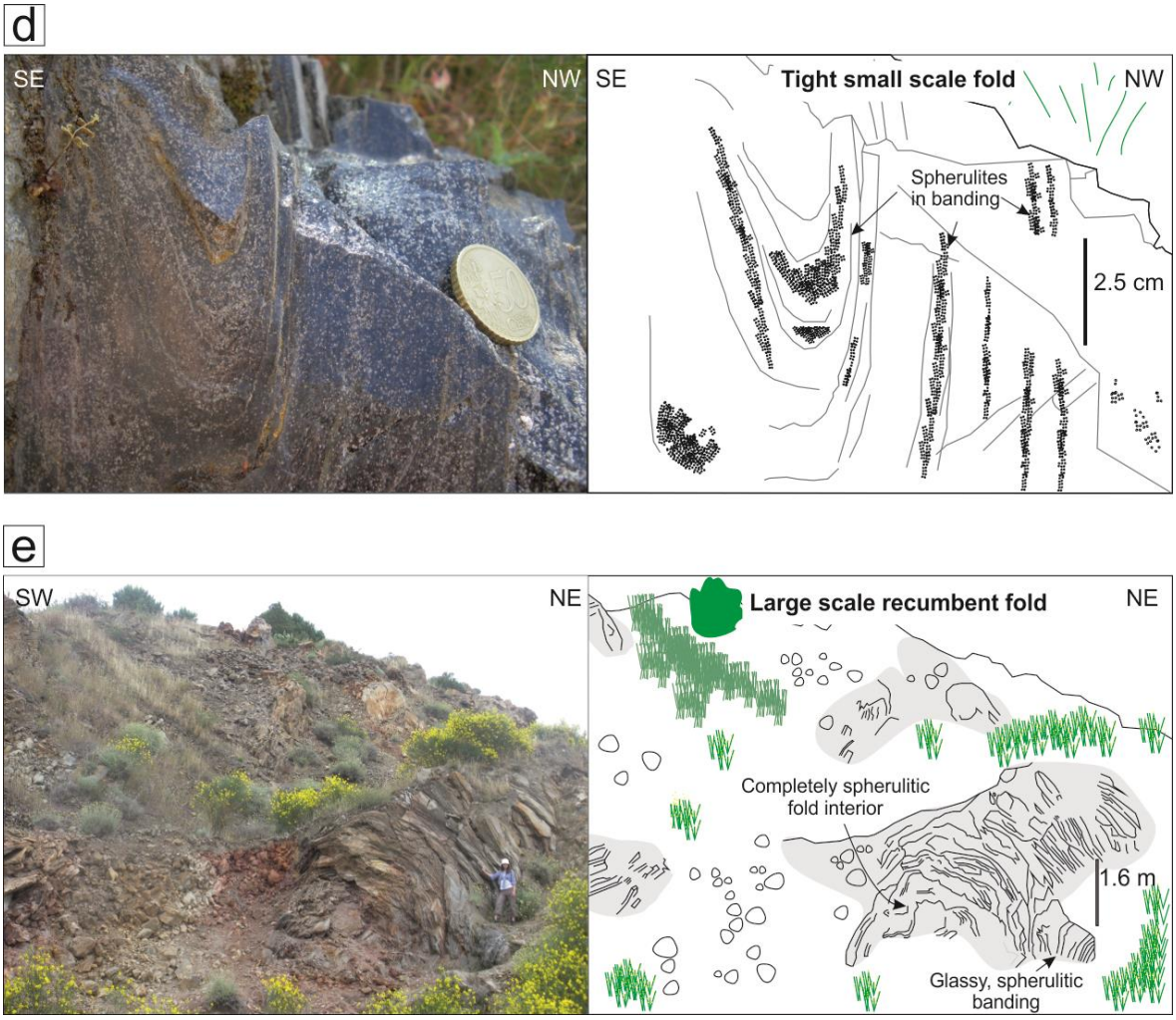

Figure 3.4: Photographs and annotated sketches of multi-scale structures (folds) and associated spherulitic occurrence in the Rocche Rosse lava flow. (a) Small scale (<20 cm in wavelength and amplitude) z-type (parasitic) folding with concentrated spherulites within fold limbs and in surrounding glass. (b) Medium scale (up to 2 m in wavelength and amplitude) folding with spherulitic bands dying out towards the centre of the fold, and completely devitrified obsidian in the centre. (c) Small scale folding with heavily spherulitic, completely spherulitic and stretched and sheared spherulites within, and in close proximity to, the fold. (d) Highly spherulitic small scale folding. (e) Large scale (>2 m in wavelength and amplitude) folding, with spherulitic obsidian on outer edges of fold, becoming progressively more spherulitic and completely devitrified towards the centre of the fold.

Cotte and Grotta dei Palizzi lava flows (lati-trachytic in composition, Piochi et al., 2009), and cristobalite occurs within vesicles. Red to purple mafic enclaves are found sporadically across the Rocche Rosse lava flow (latitic to trachytic in composition, see Davì et al.,

2009, 2010 for more details on Rocche Rosse mafic enclaves. The lava domes of southern Lipari contain abundant mafic (shoshonitic-latitic) enclaves and crustal xenoliths (De Rosa et al., 2003; Gioncada et al., 2005; Forni et al., 2013), and are more porphyritic than younger flows (containing alkali feldspar, clinopyroxene, amphibole and zircon; Forni et al., 2013).

3.3 Analytical Methods

The combination of qualitative and quantitative techniques in this study provides a comprehensive characterisation of the complexity of spherulites in obsidian. Methods include textural and petrological observations, detailed glass and spherulite geochemistry, laser Raman spectroscopy, x-ray diffraction and crystal size distribution methods. These techniques have been implemented to best identify the geochemical composition of glass and spherulites, the fabric and spatial distribution of spherulites, shape morphology and indicators of deformation behaviour.

Rock samples from twelve spherulitic obsidian flows and domes across Lipari and Vulcano were analysed in the course of this study. The majority of samples were collected from the lava flows and domes of north-eastern Lipari, lava domes in southern Lipari and lava flows surrounding the Fossa cone in northern Vulcano. The studied suite comprises obsidian lava flows and domes, and excludes explosive products. After close examination with a petrographic microscope, individual spherulite phases, mineral and glass composition were determined in polished, uncovered thin sections. Mineral major element and volatile (S, Cl

and F) analyses of the sampled obsidian glasses, spherulites and enclave-derived crystal assemblages were undertaken at The Open University (UK) using a CAMECA SX 100 electron microprobe. The peak count per element for glass analyses was 15-30 s using a 10-20 µm defocused beam diameter (1 µm for enclave-derived crystals), with an acceleration voltage of 20 kV and beam current of 10 nA for glass and crystals. Natural silicate minerals were used as primary standards to calibrate the instrument, with silicate mineral and volcanic glass standards (VG-568 and KN-18) were routinely analysed as secondary standards. Unknown glass results were regularly checked and systematically controlled against standards, with glass standards and certified values are also reported (Appendix IV). Element maps (Si, Al, K, Ca, Fe) were produced for spherulites, as individual phases that make up spherulites were often too small to detect with standard point measurement. Maps of x-ray intensity were produced using an imaging area of 512 x 512 pixels. The maps were collected with an acceleration voltage of 20 kV and beam current of 10 nA, using a 1 µm step size and 20 milliseconds DS time at each point.

Laser Raman spectroscopy analyses of glass and spherulites for crystal content and glass structural variations was performed with a Leica microscope coupled to a Renishaw Raman RM1000 system at the University of Southampton (UK), using a Renishaw NIR 780TF semiconductor diode laser (wavelength 780 nm) of power 25 mW. The spectrometer was set up in line with Renishaw recommendations for confocal operation of the spectrometer, calibrated using single crystal silicon with a known peak of 520 cm^{-1}. Spectra were obtained using an extended scan between 3700 cm^{-1} and 100 cm^{-1}, built up of 9 accumulative scans of 10 s, with a spot size of 1-2 µm, and processed using *SigmaPlot 10* (Freebody et al., 2010). A beam of monochromatic light from the laser was applied to the samples, scattering the incident beam (Freebody et al., 2010). The energy of the scattered light was analysed by the spectrometer (McMillan, 1989), identified using

published data openly accessible via the RRUFF Project Database (Downs, 2006). The spectral range selected for the analysis of obsidian glass was 200-2000 cm^{-1}, as Raman bands from silicate structures often occur within this frequency region (Rossano and Mysen, 2012).

The samples in the Raman study were first selected based on petrographic identification of textural heterogeneities, such as spherulites with or without radial interiors, surrounding colourless haloes and brown rims (see Fig. 3.5). Literature examples of Raman spectral response to glass and minerals are also provided in Appendix VI. Samples were prepared by being cut to wafer-thin sections, ~20 µm in thickness, and polished on both sides. Optical observations suggest distinct textural features within the selected obsidian samples (see section 3.4: Sample petrography), including spherulites, glassy groundmass containing microlites, a brown rim surrounding most spherulites, a mesh-texture found within some spherulites and a thin clear halo surrounding some spherulites. Specific positions in the glassy groundmass, spherulites and brown rims were targeted using a high magnification petrological microscope. Spots of glassy groundmass free of microlites and alteration were targeted. The main spherulitic phase interior, mesh-textured spherulite interior, surrounding colourless halo and brown material were analysed where evident (see Fig. 3.5).

X-ray diffraction provides a technique for identification of crystalline and amorphous components in a wide range of multi-component materials (e.g. Ruland, 1964). For instance, x-rays variably scatter in several directions as a response to amorphous material, leading to a broad "humped" distributed in a wide range (2 Theta), whilst the response to crystalline material leads to high intensity narrower peaks. For x-ray diffraction, samples from each flow or dome were crushed and sieved, spherulites were hand-picked using a binocular microscope, and coarsely powdered (~100-125 µm) in order to distinguish

compositional phases. The coarsely-powdered samples were placed on a flat disk sample holder, gently compressed, and scanned on a Bruker D8 Advance x-ray diffractometer at Keele University (UK), using CuKα radiation, a scan range from 5 to 90° (2 Theta), a 0.03° step size and a data collection time of 30 s per step. Examples of published x-ray diffraction responses are provided in Appendix IX.

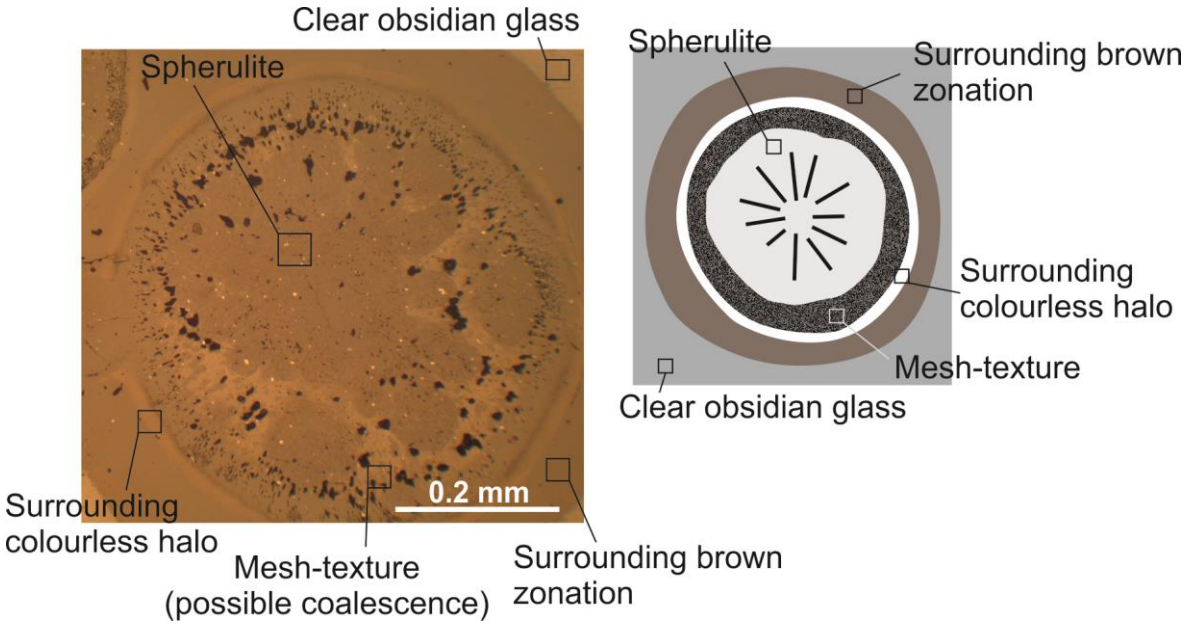

Figure 3.5: Reflective light image and schematic sketch of a typical spherulite showing targeted areas for Raman spectroscopy beam position.

Clay et al. (2013) show that crystal size distribution (CSD) quantitative textural analysis can be successfully applied to spherulitic samples, as the rate of isothermal spherulitic crystallisation was proven to be log linear in a given growth stage, despite being a non-equilibrium crystallisation process. The use of CSD methods is therefore an effective tool for the interpretation of spherulitic textures (Clay et al., 2013). Samples were cut for thin section, and scanned for spherulite CSD analyses. Spherulite outlines were checked and corrected using a polarising microscope. To keep the influence of the drawing outline edging effect to a minimum, a thickness of one device pixel in width was used. The image

processing program *ImageJ* (Schneider et al., 2012) was used to set an accurate scale and analyse all particles in the image, including total spherulite count and spherulite phase abundance. *CSDCorrections 1.37* (Higgins, 2000; 2002; 2006), was used in order to calculate 3D crystal size distributions from 2D data.

Before running the CSD plot calculation, the roundness, volumetric phase abundance, phase percentage, shape and area were input in order to represent the sample and fabric estimation. An aspect ratio of 1:1:1 was selected for an idealised (spherical) spherulite shape profile. This is a representative short (S), intermediate (I) and long (L) axis aspect ratio (S:I:L) for the entire population of a sample. Short axis (Sa) and long axis (La) dimensions were acquired using *CSDCorrections*. These values were used in *CSDCorrections* to calculate a CSD plot, and the values were also applied to a Zingg Diagram for shape classification (Zingg, 1935).

The adapted Zingg diagram can be used to plot the relative dimensions of the S, I and L axes of spherulites, allowing for spherulite shape to be classified as bladed, rod, spherical or disc-shaped. Shape parameters were also characterised by a sphericity value. This is a method developed in sedimentology (Higgins, 2006) whereby the S, I and L values can be reduced to a single sphericity parameter using the equation:

$$Sphericity = \sqrt[3]{(I \times (S \div L)^2)}$$

A perfect spheroid will give an answer of 1, with values decreasing towards zero indicating more elongation (Higgins, 2006). Length and width plots provide an idea of spherulite aspect ratio. Aspect ratios <1.0 indicate that spherulites are not perfectly spherical. Dimension results were provided by *ImageTool*, *ImageJ*, and *CSDCorrections* packages.

3.4 Sample petrography

All sampled lava flows and domes share similar mineral and textural characteristics, with minor differences across lava bodies in terms of spherulite size, shape, abundance and spatial distribution. Important features include those that may relate to spherulite nucleation, growth, modification and their relationship to time- and temperature-constrained features (e.g. microlites, brittle faults). As well as spherulite appearance and occurrence, the characteristic groundmass, microlite occurrence, mafic enclaves, phenocrysts and deformational microstructures have also been identified as key features.

3.4.1 Spherulites

Spherulites differ across and within lava bodies in terms of shape, size, distribution and physical characteristics (Figs. 3.6a-l). For instance, spherulites occur individually, clustered (Fig. 3.6l), in trails or bands (Fig. 3.6j), and some concentrate at the edge of phenocrysts and xenocrysts (Fig. 3.6m). Some spherulites show crystals in the centre (Fig. 3.6n), or concentrate within or around deformational features (Figs. 3.6-v). Spherulites are predominantly radial or microcrystalline (Figs. 3.6e-i), and occasionally show a clear halo at the edge (Figs. 3.6b-h). A brown non-isotropic rim is common (Figs. 3.6b-i, k-n). Spherulites within a number of flows and domes show an internal concentric dark and light colour zonation (growth rings, Ewart, 1971; Figs. 3.6h-i). Spherulites concentrate within folded bands (Fig. 3.6t), regular or conjugate micro-fractures in the obsidian (Figs. 3.6u-v), particularly in the Rocche Rosse and Forgia Vecchia lava flows. Older domes show larger,

more spherical-shaped spherulites (Figs. 3.6g-i), predominantly occurring individually or in clusters.

A number of commonly occurring features in spherulites allow for a preliminary and broad classification of spherulite "types". Type 1 spherulites are typically small (<0.5 mm), radial and sub-spherical; Type 2 spherulites, typically slightly larger and more elongate with a radial interior; Type 3 spherulites are larger (0.5-1.5 mm) and spherical, with a predominantly radial interior, a clear halo and thick brown rim; Type 4 spherulites concentrate within deformational fabrics; Type 5 spherulites show a complete or near-complete mesh-like microcrystalline interior (lack of radial interior). This classification has been applied to spherulites in individual lava flows and domes (Tables 3.3 and 3.4). Table also outlines typical spherulite features in the individual flows and domes.

Table 3.3: Spherulite "type" classification scheme based on physical characteristics and optical properties (see text).

Spherulite "type" classification	Physical description
Type 1	Typically small (<0.5 mm), radial and sub-spherical, occasional clear halo and brown rim
Type 2	0.5-1.5 mm, elongate, radial interior, surrounding clear halo and brown rim common
Type 3	0.5-1.5 mm, spherical, radial interior, occasional mesh-like interior, surrounding clear halo and brown rim common
Type 4	Concentrate within folds, faults and fractures
Type 5	Complete or near-complete mesh-like (microcrystalline) interior, lack of radial texture, occasional clear halo and brown rim

Table 3.4: Description and classification of spherulites based on petrographic observations. Broad type classification based on commonly observed features (see Table 3.3).

Flow/dome	Size	Comments	Typical type classification (in relative order of occurrence)
Pietre Cotte	Typically <0.5 mm in diameter, occupying ~1% volume of the groundmass	Slightly ellipsoidal, radial interior, often surrounded by a thin clear halo and brown rim, occur individually, clustered or at the edges of crystals and enclaves	Type 1, Type 2
Rocche Rosse	Less than 0.1 mm to 5 mm, occupying ~3-5% of the obsidian groundmass	Spherulites occur individually, interjoined, clustered or in bands, and concentrate within bands, folds and fractures. contain Radial and microcrystalline interiors, spherical, ellipsoidal or bowtie shape, Brown rims range from <0.1 mm up to 1 mm thick	Type 3, Type 5 Type 2, Type 1, Type 4
Forgia Vecchia	Typically 0.5-1.5 mm	Spherulites concentrate within bands, folds and fractures, ellipsoidal and bowtie shaped spherulites are common, showing a uniform alignment of the long axes	Type 3, Type 2 Type 4
Grotta dei Palizzi	Typically <0.5 mm in diameter, ~2% volume groundmass	Radial interior, often surrounded by a thin clear halo and brown rim, occur individually, clustered or at the edges of crystals and enclaves	Type 1, Type 2
Pomiciazzo	From less than 0.5 mm up to several millimetres, tend to be either small (<0.5 mm) or exceptionally large (>2 mm)	Smaller spherulites in the Pomiciazzo show a typical spherical shape, radial interior, minor dark/light colour zonation and a brown rim. Larger Pomiciazzo spherulites are more sub-rounded, and appear to lack an obvious radial interior (Fig. 3.6g), The interior of these larger spherulites have a non-radial, microcrystalline interior, with minor colour zonation and brown rim	Type 3, Type 5, Type 1, Type 2

Flow/dome	Size	Comments	Type classification (see Table 3.3)
Capo Rosso	Typically 0.5-1.5 mm	Bands of interlocking quartz and alkali feldspar. Some devitrified bands are relatively thick, up to 1 cm in thickness, spherulites typically spherical with clear halo and brown rim	Type 3, Type 5, Type 1
Castello	Typically 0.5-1.5 mm	Radial interior, spherical, individually occurring (or clusters), clear halo and thick brown rim	Type 3, Type 5
Punta di Costa	Typically 0.5-3 mm	Radial interior, spherical, individually occurring (or clusters), clear halo and thick brown rim, mesh-interiors (microcrystalline, non-radial centre) also common	Type 3, Type 5
Monte Giardina	Typically 1-4 mm	Radial interior, spherical, individually occurring (or clusters), clear halo and thick brown rim, mesh-interiors also common	Type 3, Type 5
Falcone (rhyolite)	Typically 1-4 mm, up to several mm for largest spherulites	Radial interior, spherical, individually occurring (or clusters), clear halo and thick brown rim, mesh-interiors (microcrystalline, non-radial centre) also common	Type 3, Type 5
Falcone (dacite)	Typically 1-4 mm	Radial interior, spherical, individually occurring (or clusters), clear halo and thick brown rim, mesh-interiors also common	Type 3, Type 5
Punta di Levante	Typically 0.5-1.5 mm in diameter, occupying ~5% of the total groundmass volume	Spherulites often difficult to distinguish from the devitrification-texture groundmass (Fig. 3.6r-s). Both radial and non-radial spherulites occur within the microcrystalline groundmass	Type 1, Type 5

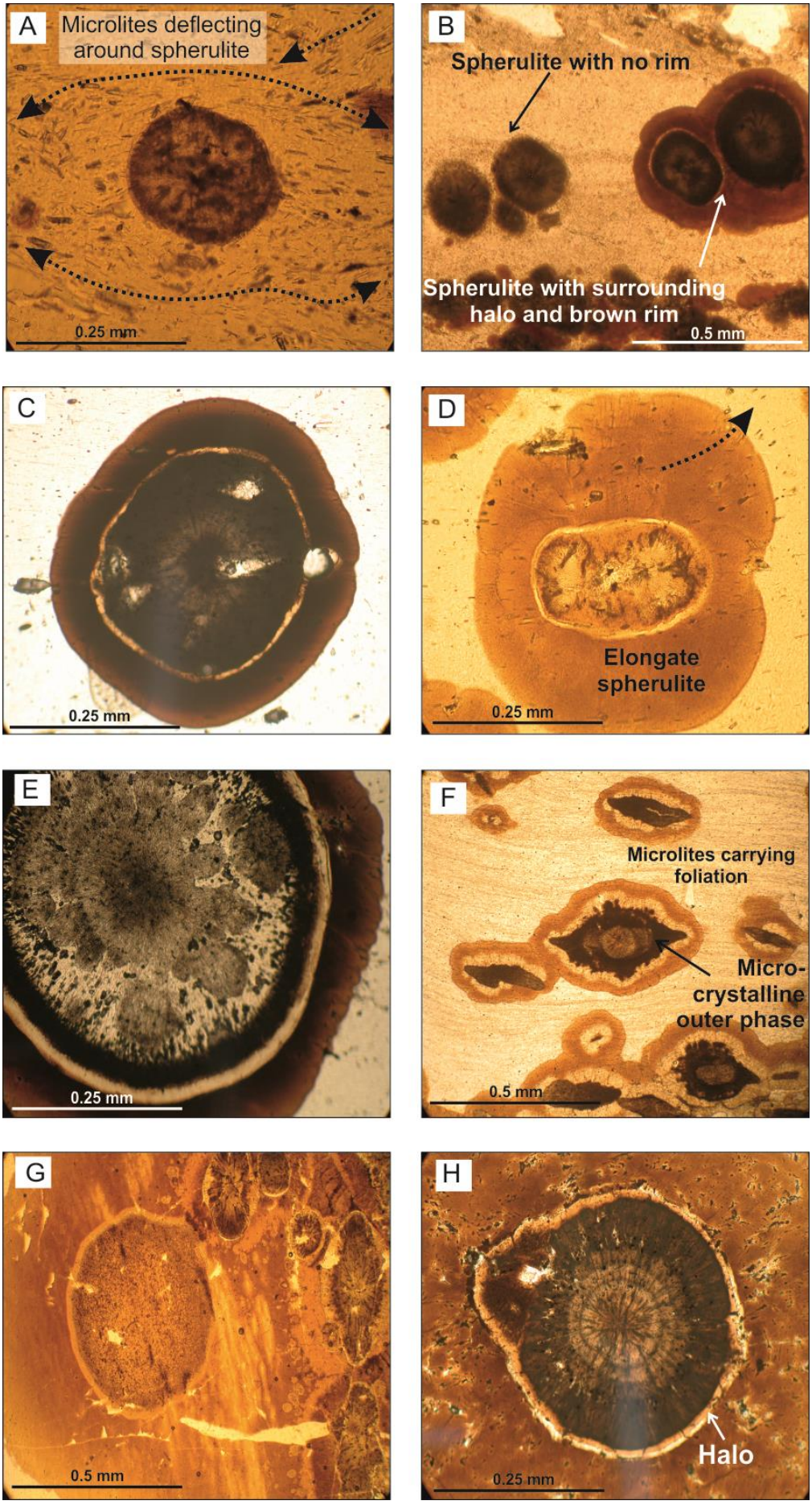
A
Microlites deflecting around spherulite
0.25 mm
B
Spherulite with no rim
Spherulite with surrounding halo and brown rim
0.5 mm
C
0.25 mm
D
Elongate spherulite
0.25 mm
E
0.25 mm
F
Microlites carrying foliation
Micro-crystalline outer phase
0.5 mm
G
0.5 mm
H
Halo
0.25 mm

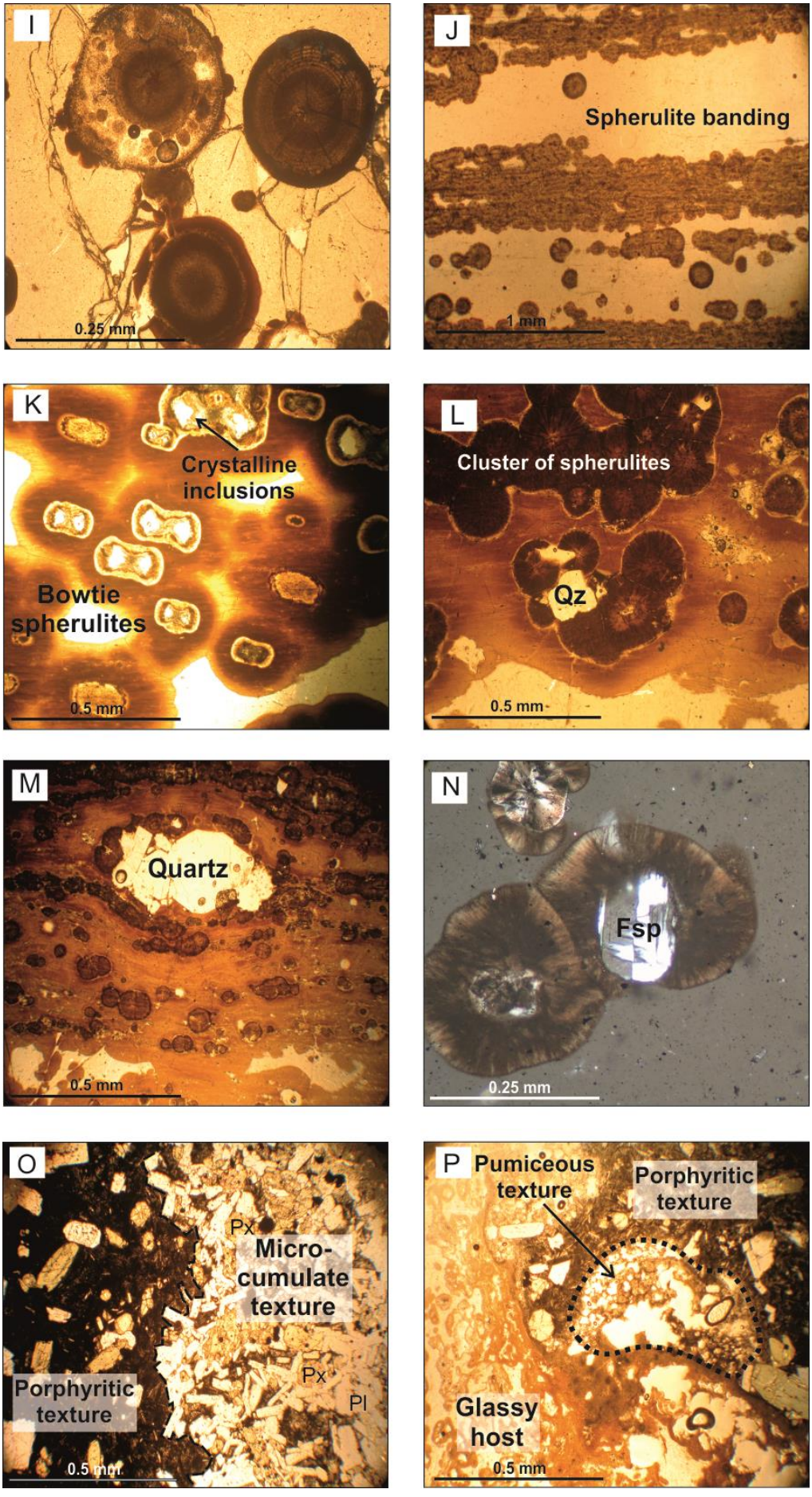
I
0.25 mm
J
Spherulite banding
1 mm
K
Crystalline inclusions
Bowtie spherulites
0.5 mm
L
Cluster of spherulites
Qz
0.5 mm
M
Quartz
0.5 mm
N
Fsp
0.25 mm
O
Px
Micro-cumulate texture
Px
Pl
Porphyritic texture
0.5 mm
P
Pumiceous texture
Porphyritic texture
Glassy host
0.5 mm

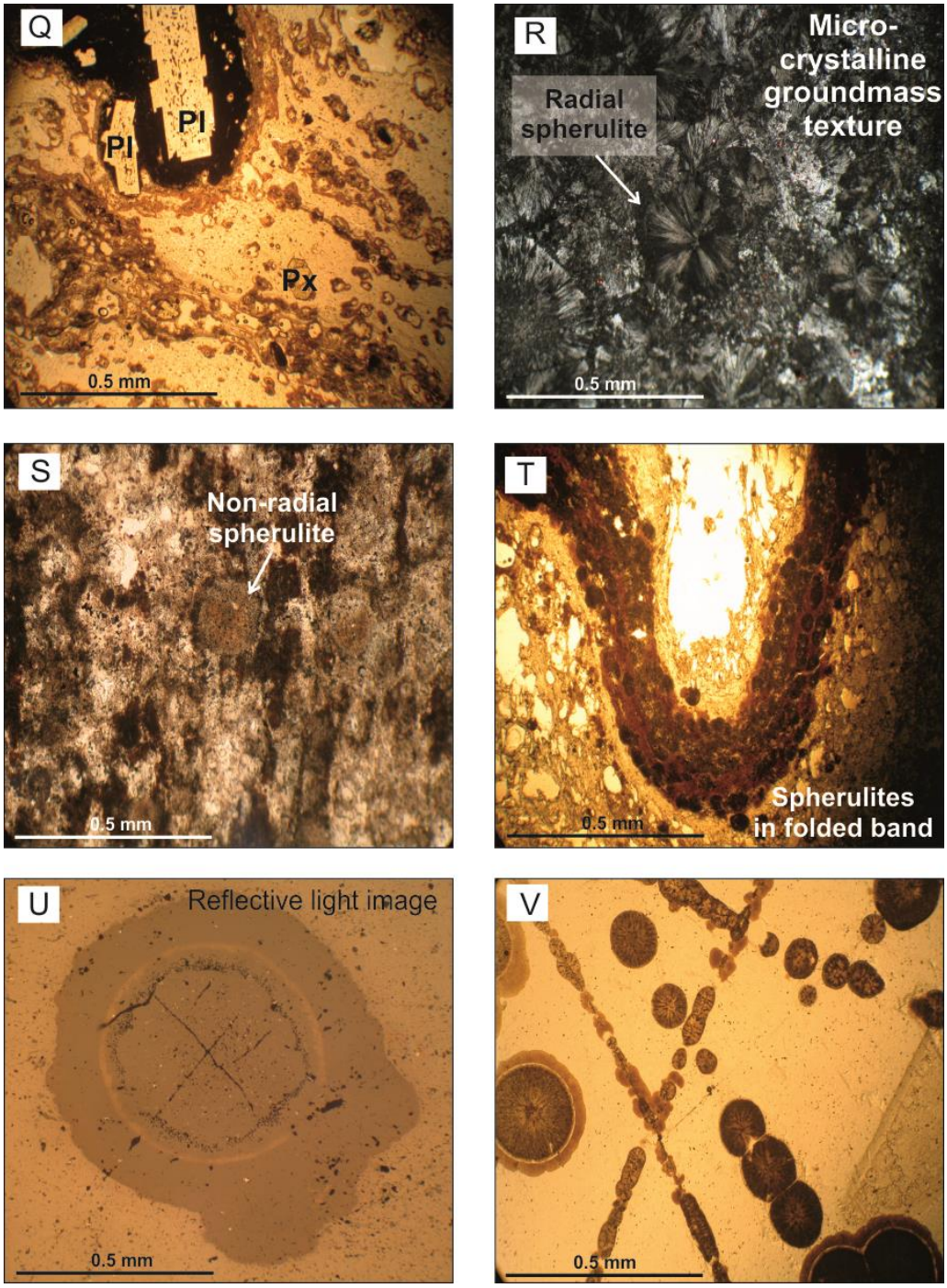

Figure 3.6: Petrographic observations of sampled flows and domes across Lipari and Vulcano, including spherulite physical characteristics and occurrence (A-L), occurrence and relationship to crystals, enclaves and groundmass (M-S), and relationship of spherulites to deformational features (T-V). (A) – Spherulite (Pietre Cotte) with no rim, microlites deflected. (B) – Spherulites with and without surrounding brown rims (Rocche Rosse). (C) – Spherulite with surrounding clear halo and brown rim (Rocche Rosse). (D) – Ellipsoidal spherulite, with microlites deflected (Forgia Vecchia). (E) – Spherulite with radial centre and mesh-texture near spherulite edge (Falcone rhyolite). (F) – Central spherulite with surrounding micro-crystalline texture,

clear halo and brown rim (Rocche Rosse). (G) – Microcrystalline spherulite (non-radial) and ellipsoidal spherulites (Pomiciazzo). (H) – Spherulite with concentric colour zonation rings (growth rings) (Castello). (I) – Spherulites containing colour zonation and pockets of crystalline material near outer spherulite (Punta di Costa). (J) – Spherulites carrying foliation (Rocche Rosse). (K) – Ellipsoidal and bowtie shaped spherulites, with crystalline inclusions (Forgia Vecchia). (L) – Spherulites concentrated in clusters (Capo Rosso). (M) – Spherulites wrapping and nucleating at the edges of quartz phenocrysts (Monte Giardina). (N) – Feldspar crystal at centre of spherulite (Falcone) (XPL). (O) – Mafic enclave (Rocche Rosse) containing both porphyritic and micro-cumulate textured groundmass. (P) – Mafic enclave-rhyolite contact (Rocche Rosse), with pumiceous texture within enclave. (Q) Spherulite-rich rhyolite (Grotta dei Palizzi) and enclave-derived plagioclase. (R) – Devitrified groundmass and radial spherulite (Punta di Levante) (XPL). (S) – Devitrified groundmass and non-radial spherulite (Punta di Levante). (T) – Micro-folding, with folded spherulitic band (Rocche Rosse). (U) – Spherulite centred on conjugate fracture (Rocche Rosse) (Reflected light image). (V) – Spherulites concentrated within conjugate fracture (Rocche Rosse).

3.4.2 Microlites

Microlites occur in the majority of sampled lava bodies. In relation to spherulites, they are generally unaffected (i.e. spherulites overprint microlites) or are deflected around spherulites (Figs. 3.6a, d). Bands of microlite enrichment are common across samples, including bands that are enriched in both microlites and spherulites. Microlites are typically less than 50 μm in length, but are in some cases up to 100 μm (in older dome samples – Giardina and Falcone samples). Spherulites and microlites often define the foliation (also preserving folding). Microlites show a slender appearance, and often show a preferred orientation (Fig. 3.6f). In Pietre Cotte and Rocche Rosse lava flow samples, microlites are both overprinted by spherulites and deflected around spherulites (typically deflecting around smaller, radial spherulites lacking a brown rim). Pietre Cotte microlites

are sanidine and plagioclase in composition (Piochi et al., 2009), and Rocche Rosse microlites are orthoclase, Fe-edenite and biotite in composition (Davì et al., 2009; 2010). In Castello and Capo Rosso lava dome samples, microlites are variable in quantity, in some areas showing a high concentration (fully microlitic). Microlites are scarcer in Monte Giardina lava dome samples but, where present, show an alignment with foliation (anorthic in composition; Gioncada et al., 2005).

3.4.3 Groundmass

Groundmass is often glassy or spherulitic, or variable within individual samples and across sampled lavas. Groundmass sometimes shows radial and microcrystalline interlocking alkali feldspar and quartz (Figs. 3.6r, s), particularly in older samples (e.g. the Punta di Levante lava dome groundmass is completely devitrified). Lava bodies are variably vesicular, for instance, the Pietre Cotte lava flow samples are vesicle poor (typically 1000 μm in size, Piochi et al., 2009), and are infilled with cristobalite. Rocche Rosse lava flow samples vary from completely glassy to completely devitrified. The Punta di Costa glassy groundmass is heavily fractured (Fig. 3.6i), and shows a speckled, fibrous texture (perlitic texture).

3.4.4 Enclaves, phenocrysts and xenocrysts

Phenocrysts are rare in all lava bodies, but are slightly more abundant in older domes, and bodies containing mafic enclaves. The Pietre Cotte and Grotta dei Palizzi lava flows show

abundant enclaves, containing a mineral assemblage of olivine, clinopyroxene, plagioclase, titanomagnetite and apatite. Some of these minerals separate in to the rhyolitic hosts (Fig. 3.6q), with microlitic-diktytaxitic enclave groundmass surrounding minerals (for more details on the Pietre Cotte lava flow enclaves, see Chapter 4). The Rocche Rosse lava flow also shows enclaves, though they are not as common as those in the Pietre Cotte or Grotta dei Palizzi lava flows. Rocche Rosse enclaves (Figs. 3.6o-p) contain a mineral assemblage of plagioclase, clinopyroxene, olivine, biotite and titanomagnetite. Mafic enclaves show different textures, including cryptocrystalline, micro-cumulate and pumiceous textures, (latitic and trachytic enclaves, detailed by Davì et al. 2009) and the rhyolitic host contains rare alkali feldspar, plagioclase and quartz phenocrysts (Fig. 3.6m). Older flows and domes (e.g. Pomiciazzo, Falcone and Punta di Levante lava bodies) more commonly show alkali feldspar and quartz phenocrysts, and the Monte Giardina lava dome shows minor amounts of clinopyroxene, hornblende, titanomagnetite, apatite, ilmenite, fayalite and zircon (Gioncada et al., 2005).

3.5 Glass and Mineral Chemistry

3.5.1 Glass

All glass compositional data is summarised in Figure 3.7 and Table 3.5, and the data set is available in Appendices I-IV. A total of 144 analyses were obtained for glass from all lava bodies. The glass compositions range from rare dacitic/trachytic to rhyolitic (Fig. 3.7). The

vast majority of the suite is rhyolitic in composition. The minimum SiO_2 content is ~68 wt% (the Falcone lava dome and Punta di Levante lava dome) and the maximum SiO_2 content is ~79 wt% (also from the Falcone lava dome, suggesting considerable compositional variation within this lava dome). High-K dacites and trachydacites have been previously reported for in the Lipari volcanic suites (eruptive epochs 7 and 8, the Valle Muria synthem; Lucchi et al., 2010; Forni et al., 2013). The average SiO_2 content for the obsidian glasses is ~75 wt% (consistent with the silica content reported by Davì et al., 2009 for Rocche Rosse obsidian). Al_2O_3 content varies from ~11 wt% to ~19 wt% (averaging ~13 wt%), and Na_2O content ranges from ~2 wt% to ~7 wt%. Despite this large range, the typical Na_2O content is ~3-5 wt% (averaging ~4 wt%), with slightly higher Na_2O content in the Grotta dei Palizzi lava flow (~5-6 wt%).

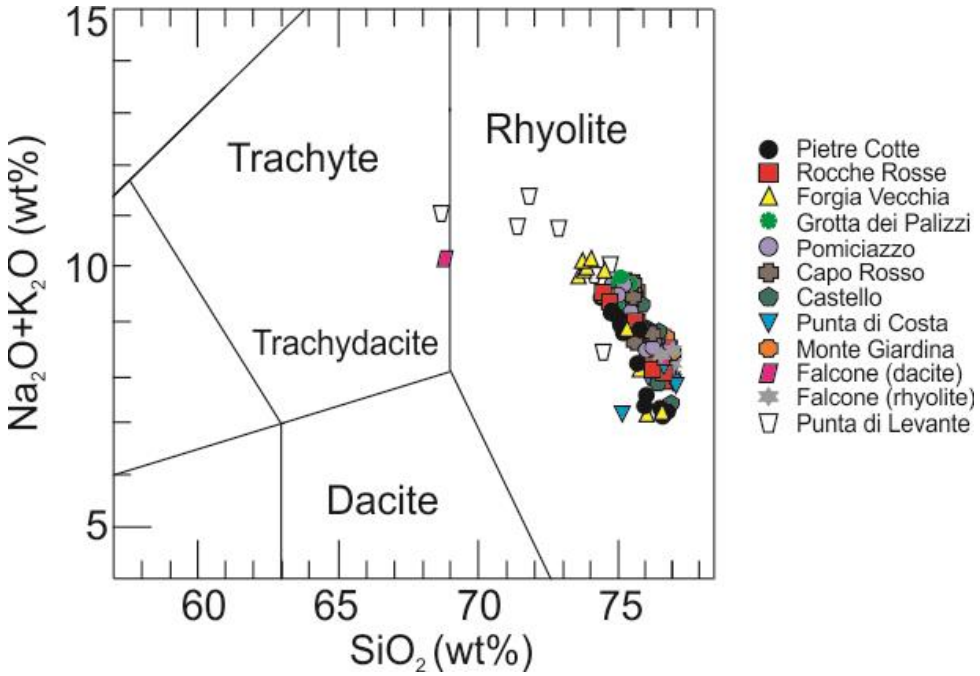

Figure 3.7: Total Alkali-Silica (TAS) diagram (adapted from Le Bas et al., 1986) of glass compositions across sampled lava bodies on Lipari and Vulcano. The majority of points are clustered together at 73-76 wt% SiO_2 and 7-9 wt% $Na_2O + K_2O$. Pietre Cotte plots show typical SiO_2 values of 73-76 wt% and alkali content 7-10 wt%, Rocche Rosse shows SiO_2 values up to 75 wt% and alkali content of 9-10 wt%, and Monte Giardina has SiO_2 content of typically 75-76 wt%, and alkali content of 7-9 wt%.

Table 3.5: Typical geochemical characteristics of the glassy groundmass of sampled lava flows and domes, including geochemical signature of brown rims (where evident) surrounding spherulites.

Flow/dome	**Glass geochemical observations and comments**
Pietre Cotte	SiO_2 compositional range of ~74-77 wt%, with Al_2O_3 content ~13 wt% for all samples, ~2-5 wt% Na_2O and ~3-5 wt% K_2O. The brown rim at the spherulite-glass interface shows a slight SiO_2 depletion compared to the clear obsidian glass (~75 wt compared to ~77 wt%), and an alkali element (Na_2O and K_2O) enrichment (~8.5 wt% compared to ~7 wt%)
Rocche Rosse	SiO_2 content of ~72-75 wt%, and Al_2O_3, Na_2O and K_2O contents of ~3-5 wt%. Unlike the Pietre Cotte obsidian, the brown spherulite rims within the Rocche Rosse obsidian show a slight SiO_2 enrichment (~1 wt% enrichment), with a Na_2O enrichment and K_2O depletion (~0.6 wt% depletion)
Forgia Vecchia	SiO_2 ~76 wt%, ~13-14 wt% Al_2O_3, ~3-4 wt% Na_2O and ~4-6 wt% K_2O
Grotta dei Palizzi	SiO_2 ~73-75 wt%, Al_2O_3 content of ~13 wt%, Na_2O content of ~3-4 wt% and K_2O content of ~5-6 wt%
Pomiciazzo	SiO_2 content of ~75-77 wt%, ~12-13 wt% Al_2O_3, ~3-5 wt% Na_2O, and ~4-6 wt% K_2O. The brown spherulite rims within the Pomiciazzo obsidian show very minor differences compared to the clear glassy groundmass, with minor K_2O depletion and Na_2O enrichment
Capo Rosso	SiO_2 content of ~76-77 wt%, Al_2O_3 content of ~12-13 wt%, Na_2O content of ~3-6 wt%, and a K_2O content of ~3-5 wt%. The brown spherulite rims within the Capo Rosso show Na_2O enrichment (glass ~2 wt% depletion compared to rim) and K_2O depletion (~3 wt% depleted compared to glass)
Castello	SiO_2 content range of ~74-76 wt%, Al_2O_3 content of ~12-14 wt%, Na_2O content of ~3-6 wt%, and K_2O content of ~3-5 wt%. Castello brown rims show a Na_2O enrichment (~2 wt%) compared to the obsidian glass
Punta di Costa	SiO_2 range of ~73-76 wt%, Al_2O_3 range of ~13-14 wt%, ~3-5 wt% Na_2O, and ~4-6 wt% K_2O content
Monte Giardina	SiO_2 ~75-77 wt%, ~12-13 wt% Al_2O, ~3-4 wt% Na_2O, and ~4-5 wt% K_2O
Falcone (rhyolite)	The minimum SiO_2 content is ~68 wt% and the maximum SiO_2 content is ~79 wt%, suggesting considerable compositional variation within this lava dome
Falcone (dacite)	Brown rims found within the dacitic/trachytic Falcone samples show a SiO_2 depletion, compared to a slight enrichment in the rhyolitic Falcone samples, Al_2O_3 is enriched in the brown rims of the dacitic samples (~4 wt% enrichment in rims compared to glass), Na_2O is enriched in both the dacitic (~1 wt% enrichment in rim compared to the glass) and rhyolitic samples, and K_2O is heavily enriched in the rims of the dacitic samples (~3 wt% enrichment in rim) but slightly depleted in the rhyolitic samples

Flow/dome	Glass geochemical observations and comments
Punta di Levante	SiO_2 compositional range of ~66-77 wt% (dacitic/trachytic to rhyolitic), Al_2O_3 range of ~12-18 wt%, Na_2O of ~4-6 wt% and K_2O content range of ~4-8 wt%. Al_2O_3 shows a negative linear correlation with increasing SiO_2 content (see Fig. 3.9)

Selected major and trace element variation diagrams are shown in Figure 3.8. The Punta di Levante lava dome glass shows a considerable compositional range. The Punta di Levante rhyolite has a SiO_2 compositional range of ~66-77 wt% (dacitic/trachytic to rhyolitic), Al_2O_3 range of ~12-18 wt%, Na_2O of ~4-6 wt% and K_2O content range of ~4-8 wt%. Al_2O_3 shows a negative linear correlation with increasing SiO_2 content (see Fig. 3.9). The slight linear regression in the K_2O also indicates K_2O being incorporated into crystalline phases in more evolved lavas (K and Al incorporated into crystallising feldspar phases with magmatic evolution). CaO content generally plateus at 0.5-0.7 wt%, but reaches 1.5 wt% in the Rocche Rosse lava flow. CaO shows a general enrichment in more SiO_2-rich samples. FeO content commonly ranges ~1-2 wt%, with a maximum value of ~4 wt% in the Punta di Levante lava dome.

The Falcone (rhyolite) lava dome shows the lowest FeO content, thus, the two oldest domes show the most considerable FeO content range. P_2O_5, TiO_2 and MgO occur in trace amounts. Maximum P_2O_5 is 0.06 wt%, and TiO_2, though highest in the Punta di Levante lava dome (0.17 wt%) is consistently high in Grotta dei Palizzi samples. MgO is also consistently higher in Grotta dei Palizzi obsidian (maximum 0.1 wt%). F and Cl occur in trace amounts.

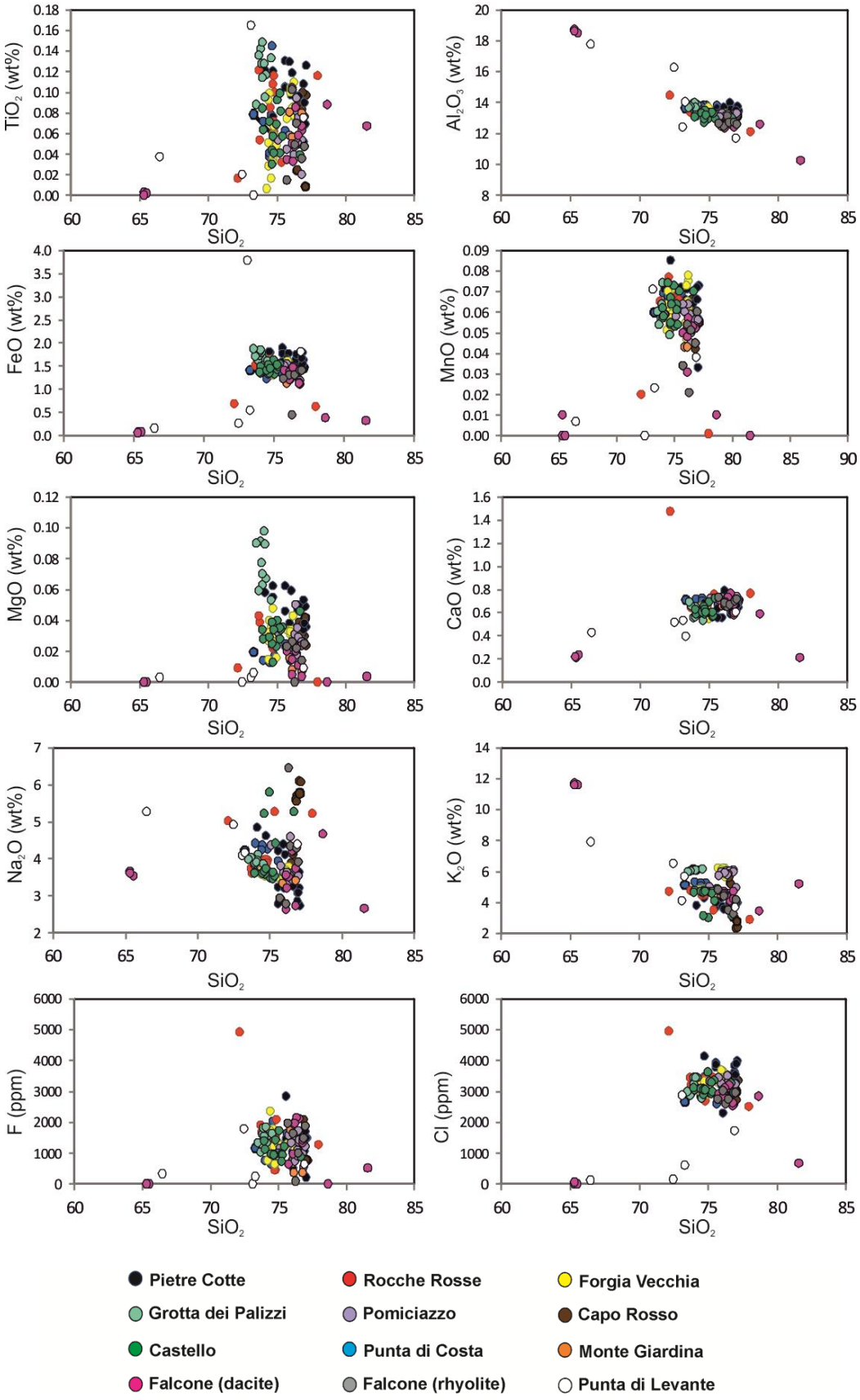

Figure 3.8: Variation diagrams of selected major (wt%) and trace elements (ppm) vs. SiO_2 in analysed glass from the 12 sampled lava bodies on Lipari and Vulcano.

3.5.2 Spherulites

Electron microprobe (EMP) spot analyses reveal a mixture of results, with silica values between ~70 wt% and ~78 wt% (potentially glass), evidence for crystalline silica (e.g. quartz or cristobalite – see XRD and Raman results) with silica content ~99 wt%, and alkali feldspar (silica content 60-67 wt%). Spherulites in the Pietre Cotte obsidian contain alkali feldspar (~67-68 wt% SiO_2, ~17-19 wt% Al_2O_3), and a crystalline silica phase (>99 wt% SiO_2). The Rocche Rosse spherulites also contain alkali feldspar and pure silica. Castello spherulites contain plagioclase, and the Punta di Costa spherulites contain minor Fe-rich clinopyroxene.

Electron microprobe data suggests the presence of plagioclase and alkali feldspar within cryptocrystalline intergrowths that comprise the spherulite (Fig. 3.9; Appendix II). Feldspar identified by EMP is primarily albitic in composition, specifically the anorthoclase and oligoclase end members. These phases were only identified within the youngest Pietre Cotte and Rocche Rosse spherulites (Fig. 3.9). Both the Pietre Cotte and Rocche Rosse obsidian lavas contain rare feldspar phenocrysts, enclave-derived feldspar xenocrysts, and magmatic enclaves within the lavas contain a feldspar groundmass phase. However, the feldspar compositions of the mineral phases within the Pietre Cotte are predominantly sanidine, andesine and labradorite, and phases within the Rocche Rosse are sanidine and andesine. This indicates that the spherulitic feldspar phase is compositionally distinct from phenocrysts, xenocrysts or enclave groundmass feldspar.

Spherulite EMP results also show results which reflect glass composition. However, these results may reflect mixed analyses due to the sub-micron size of individual phases within spherulites. In order to determine the true nature of these results, plots of major element analyses of orthoclase and cristobalite, the two dominant phases within spherulites as

determined by EMP, XRD and Raman spectroscopy (see later), were created, with the unknown phase results also plotted (see Fig. 3.10). Host obsidian glass data was also plotted for comparison.

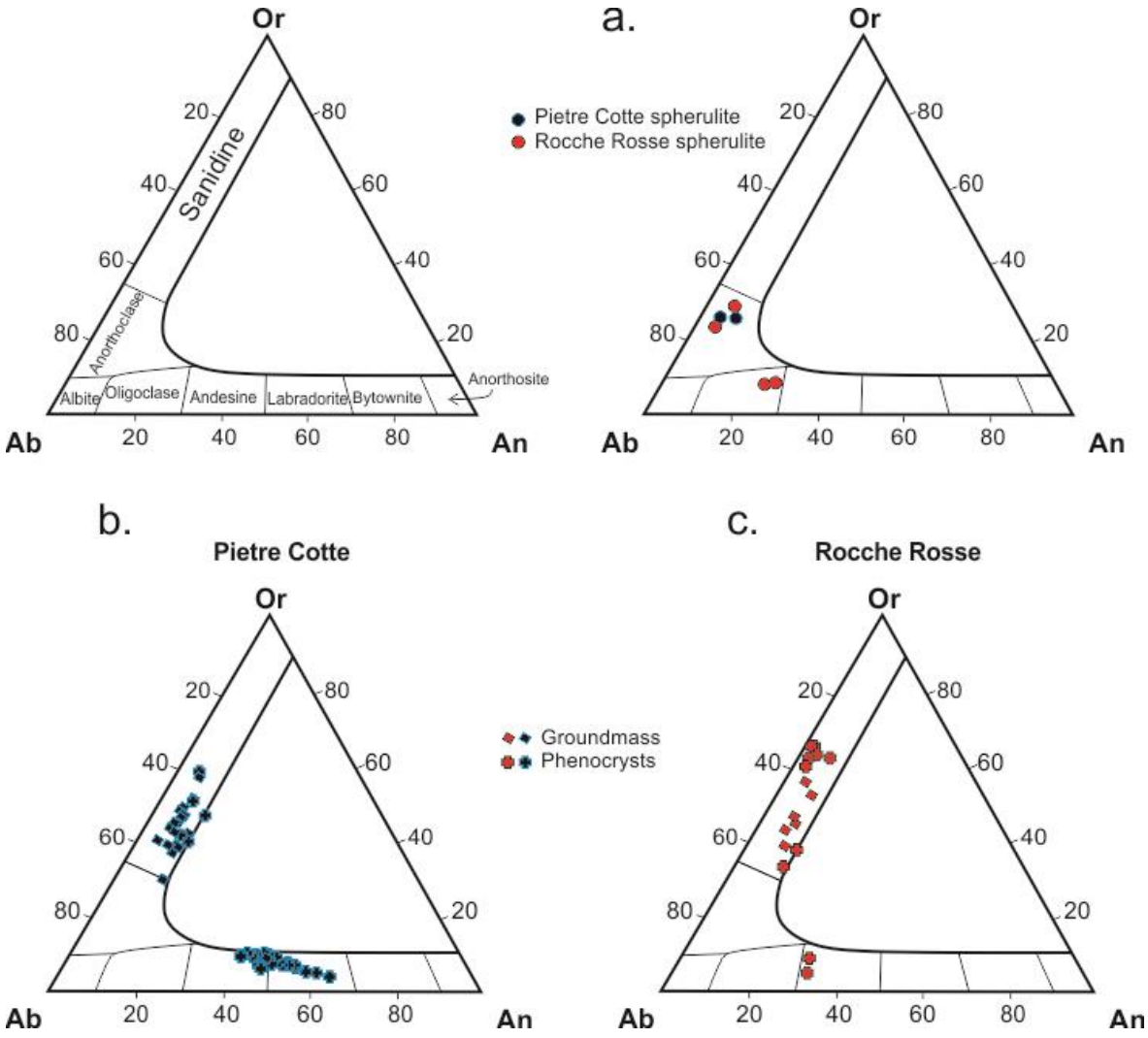

Figure 3.9: (a) Ternary plots of feldspar phase within Pietre Cotte and Rocche Rosse spherulites, showing Pietre Cotte spherulites to include anorthoclase and Rocche Rosse spherulites to contain anorthoclase and oligoclase. (b) Pietre Cotte enclave-derived xenocrysts and enclave groundmass plots, indicating the presence of sanidine, andesine and labradorite, with minor anorthoclase (Appendix III). (c) Rocche Rosse feldspar ternary plots of xenocrysts and enclave groundmass, showing the presence of sanidine and andesine (Appendix IV). Ternary labels also shown.

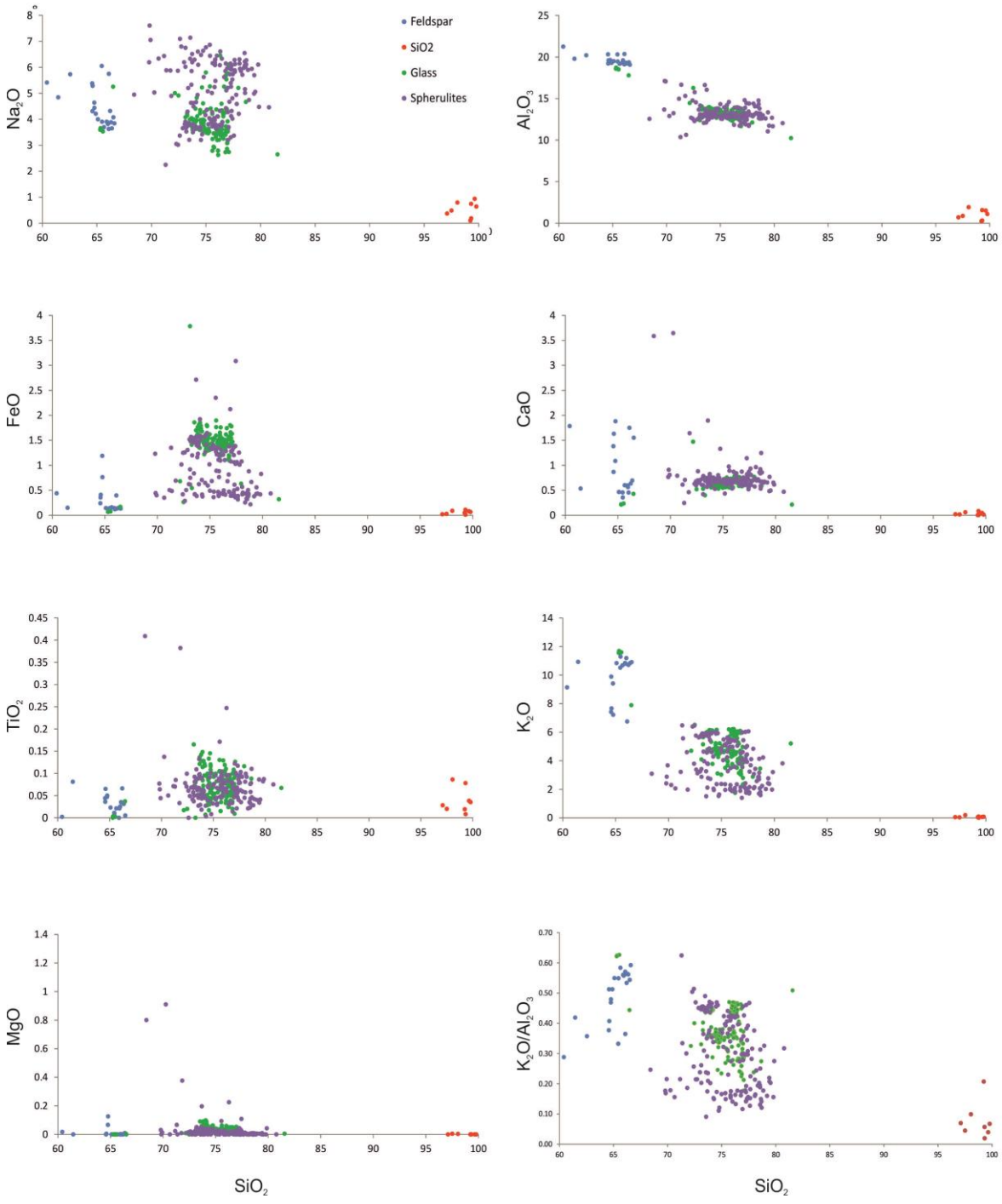

Figure 3.10: Unknown (glass) phase within spherulites plots, showing orthoclase (blue) and cristobalite (red) compositional end members, unknown glass plots (purple) and obsidian glass compositions (green) for comparison.

Clinopyroxene is another phase identified within spherulites from all lava bodies, as well

as a common phase identified within some host obsidian lavas and mafic enclaves. Clinopyroxene and cristobalite phases were also plotted in order to identify or rule out any mixing of phases. If the results reflect a mixture of feldspar (or clinopyroxene) and cristobalite phases, the plots will form a linear trend between these two "end members". If however the unknown phase results plot in a distinct manner, away from this linear trend, then the results may reflect the presence of another phase. If the phase is glass, then the results should compare well to the host glass plots.

Results indicate that the unknown phase plots have a higher Na_2O, FeO, TiO_2 and MgO content than any anticipated mixing trend results for both feldspar-cristobalite phase mixing and clinopyroxene-cristobalite mixing. K_2O content is lower than the mixing trend line for feldspar-cristobalite mixing. Results do however show a relatively linear relationship between end members for Al_2O_3 and CaO. Plots demonstrate no clinopyroxene-cristobalite mixing, and suggest that data does not represent mixing between the dominant alkali feldspar and cristobalite phases. The high silica content and relatively low FeO and TiO_2 content of the unknown phase rules out the suggestion that titanomagnetite has mixed with another phase. Perhaps the highest supporting evidence for the presence of glass within spherulites is the consistent overlapping of the unknown phase plots with host glass plots. These results indicate the presence of amorphous glass within spherulites (supported by Raman and XRD results, see later).

The size of the crystalline phases in the spherulites was often too small to analyse without encountering the problem of mixed analyses. In order to characterise spherulite content, element maps were produced, providing a semi-quantitative assessment of spherulite composition and the effects of their growth on the immediately surrounding glass. Representative spherulites were selected for element mapping based on their textural characteristics, and include a small spherulite without a brown rim, a spherulite with a rim,

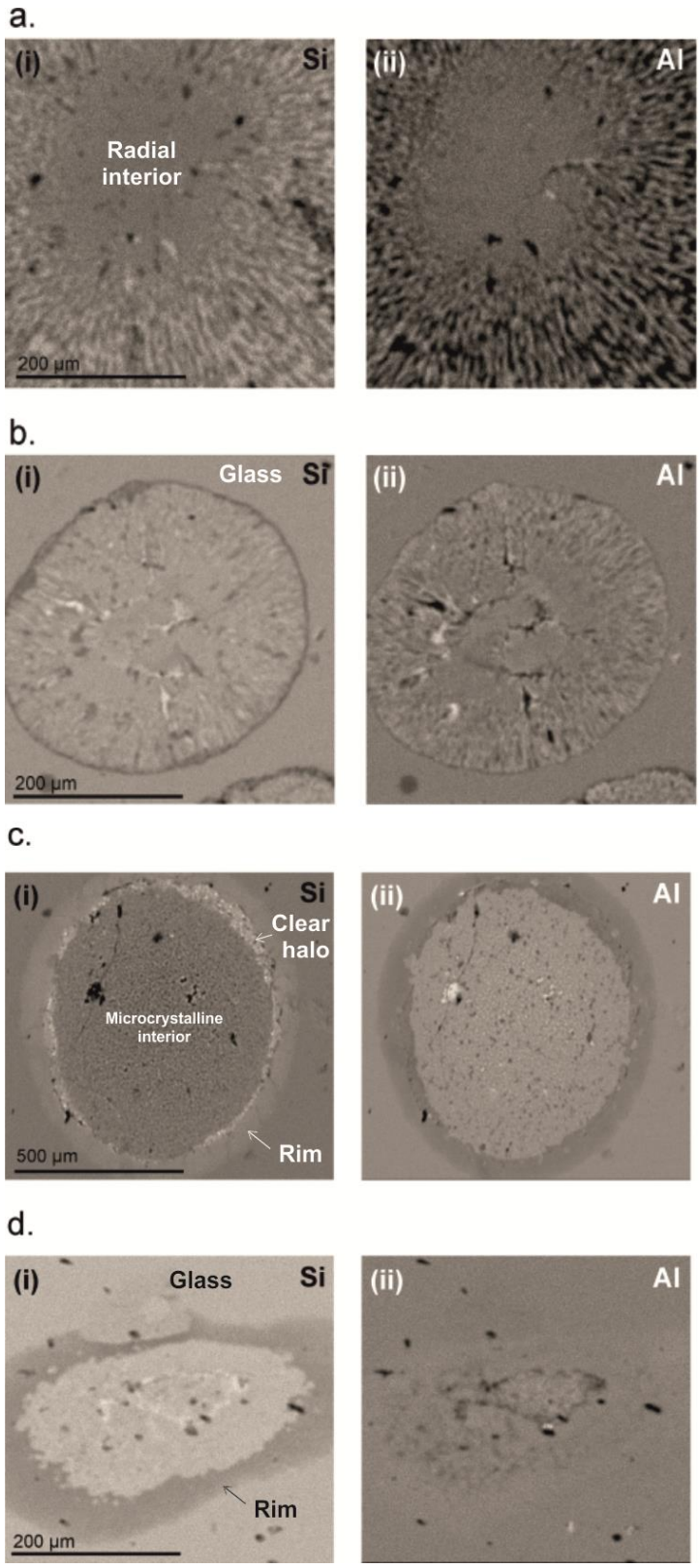

Figure 3.11: X-ray Si, Al and K element maps of spherulites. (a) Radial interior of spherulite (from Rocche Rosse sample). (b) Small spherulite with no surrounding brown zonation, and silica depletion at edge (from Pietre Cotte sample). (c) Large spherulite with surrounding mesh-texture and brown zonation, with silica

enrichment at rim (from Rocche Rosse sample). (d) Elongate spherulite with surrounding brown zonation (from Forgia Vecchia sample).

a stretched spherulite, a spherulite with a microcrystalline texture and a spherulite with a radial texture. Major elements in element mapping included Si Al, K, Ca and Fe. The spherulite element map in Figure 3.11 contains multiple phases, including Si, Al and K. Pure Si occurs in small pockets, and partly defines both a radial and skeletal interior (with Al). Ca and Fe only occur in small, concentrated pockets (and hence are not shown in the figure). Generally, spherulites show a high Si content (indicated by the lighter colour), and a relatively high Al and K content, in specific phases (with a skeletal crystal arrangement of silica polymorph and alkali feldspar). Ca and Fe content are generally low. Despite having no apparent rim optically, the small spherulite with no rim does show K enrichment in the surrounding glassy groundmass. There is a slight K enrichment at the very edge of the spherulite, separating the spherulitic phase from the glass. The spherulite that has a brown rim and no apparent internal radial texture shows Si enrichment at the inner edge (within) of the spherulite (almost pure Si), and a slight enrichment in the surrounding brown rim, and Al depletion in the inner edge and surrounding rim. The interior of the spherulite contains Si, Al and K in a skeletal pattern, and Ca and Fe occur in minor concentrated crystalline phases. The spherulite with the distinct radial interior shows a multi-phase skeletal pattern, containing Si, Al and K, with minor Ca and Fe pockets. The elongate spherulite shows Si depletion in the rim, with high Si content within the spherulite and concentrated in cracks. K also appears to concentrate along fractures. Ca and Fe again concentrate in minor crystalline phases, such as clinopyroxene (as suggested by Punta di Costa EMP results).

3.6 Laser Raman spectroscopy

Raman spectroscopy provides a powerful tool that can probe the structure and bonds in natural glasses, yielding information about the silicate network connectivity and tetrahedral co-ordination. Melts and glasses, containing co-existing structural units, can produce established Raman spectral bands and positions. Obsidian glass can be classified as a partially depolymerised silica network, showing attributes comparable to that of pure silica glass (Bellot-Gurlet et al., 2004), alkali silicate and alkali aluminosilicate glass (White and Minser, 1984). Raman spectroscopy is non-destructive, and also offers rapid identification of crystal chemical properties (Kingma and Hemley, 1994), water content quantification (Di Muro et al., 2006, Mercier et al., 2009), iron-redox state quantification (Di Muro et al., 2009), and structural evolution (Shimoda et al., 2004) of heterogeneous samples, using sensitivity of vibrational frequencies and scattering intensities (slight differences) in chemical structures. As well as glass structure, this method is also well suited for distinguishing between crystalline silica polymorphs within spherulites, and is sample areas capable of analysing as small as ~1 μm (Kingma and Hemley, 1994).

Sixteen obsidian glass samples were analysed using Raman spectroscopy. Results are presented in Figure 3.12, and individual spectra are available in Appendix VII. Examination of Raman spectra for the glassy obsidian groundmass (Fig. 3.12a), spherulites (including the mesh-texture) (Figs. 3.12b, d) and brown rims (Fig. 3.12c) show minimal variation in notable peaks (i.e. Raman response is the same across flows and domes). Spectral results for the haloes (Fig. 3.12e) show some slight variations, whereby peaks do not match, or peaks vary in intensity.

a. Glassy groundmass Raman spectroscopy

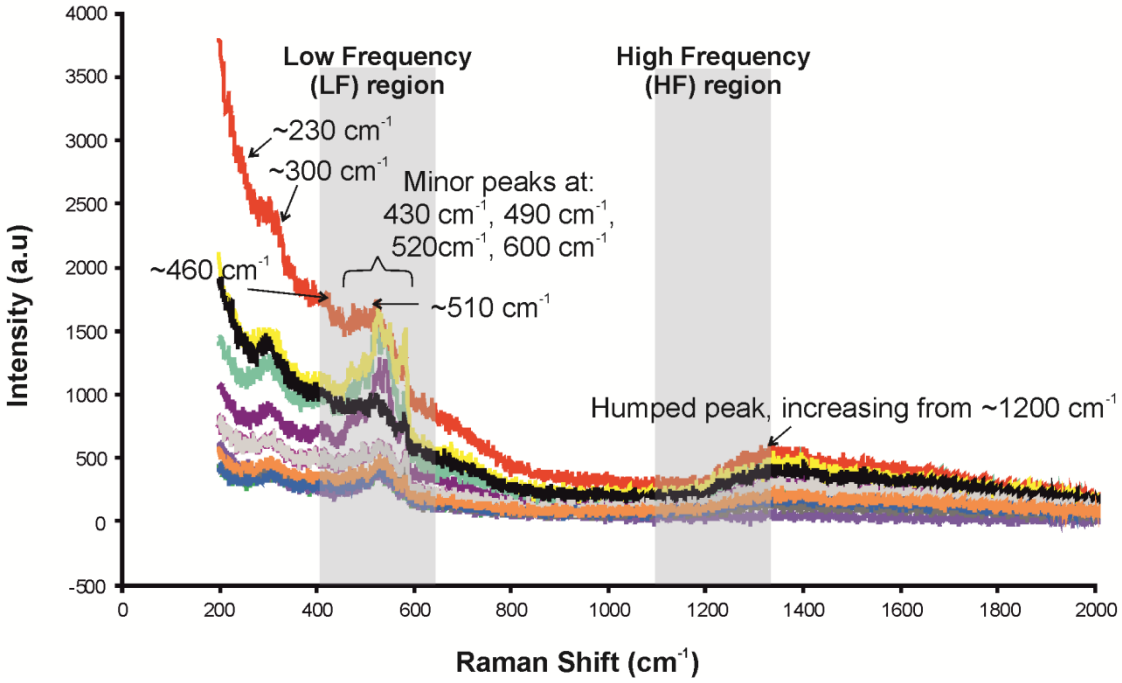

b. Spherulite Raman spectroscopy

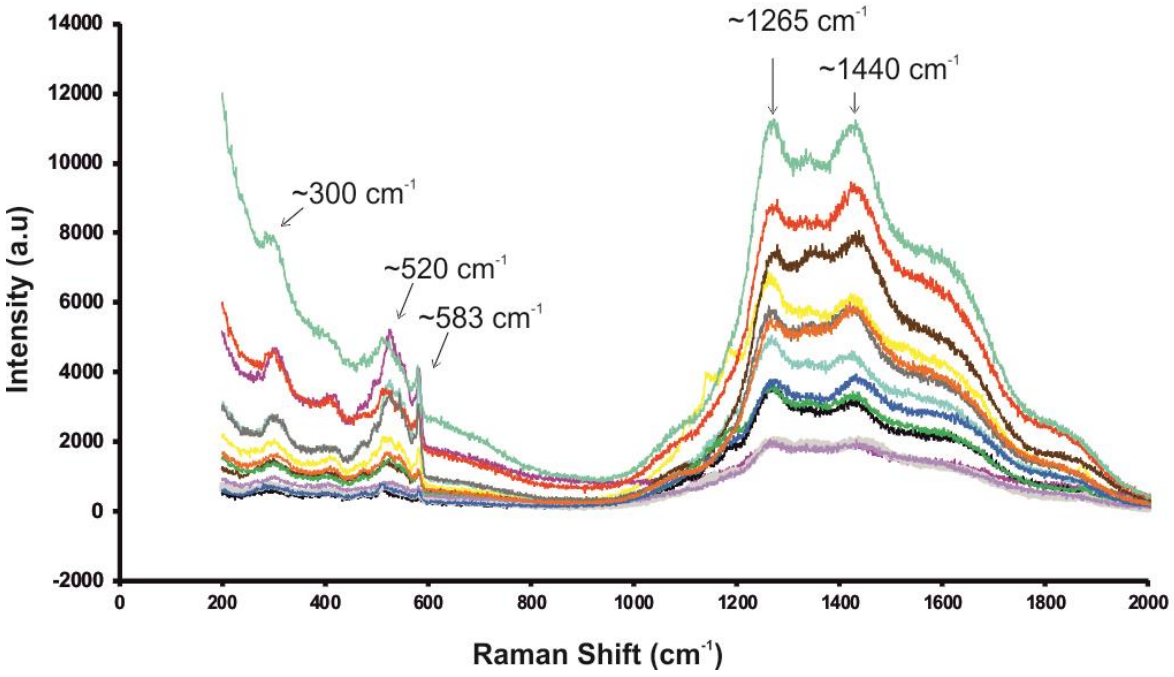

(Image continued on next page)

c. Brown rim Raman spectroscopy

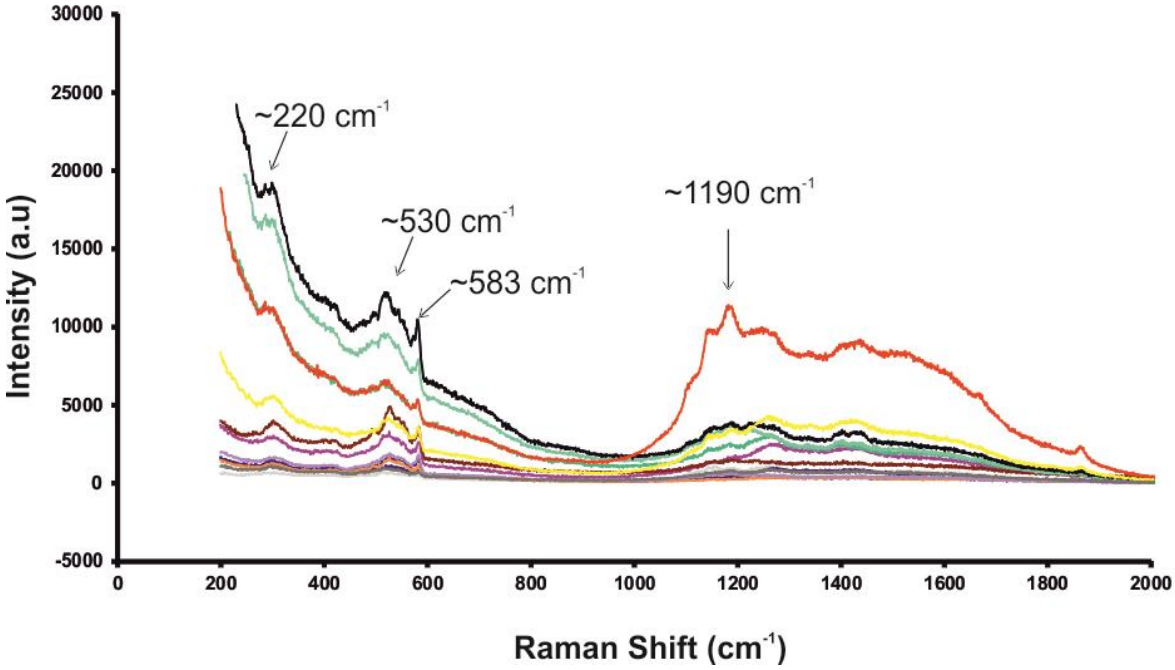

d. Mesh-texture groundmass Raman spectroscopy

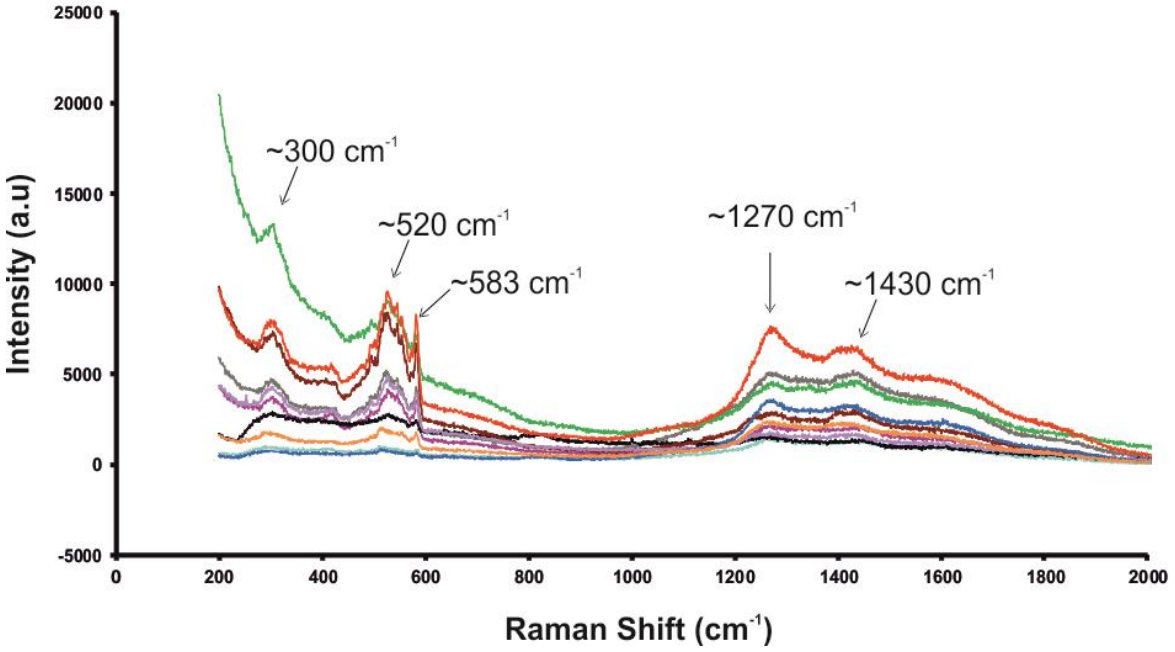

(Image continued on next page)

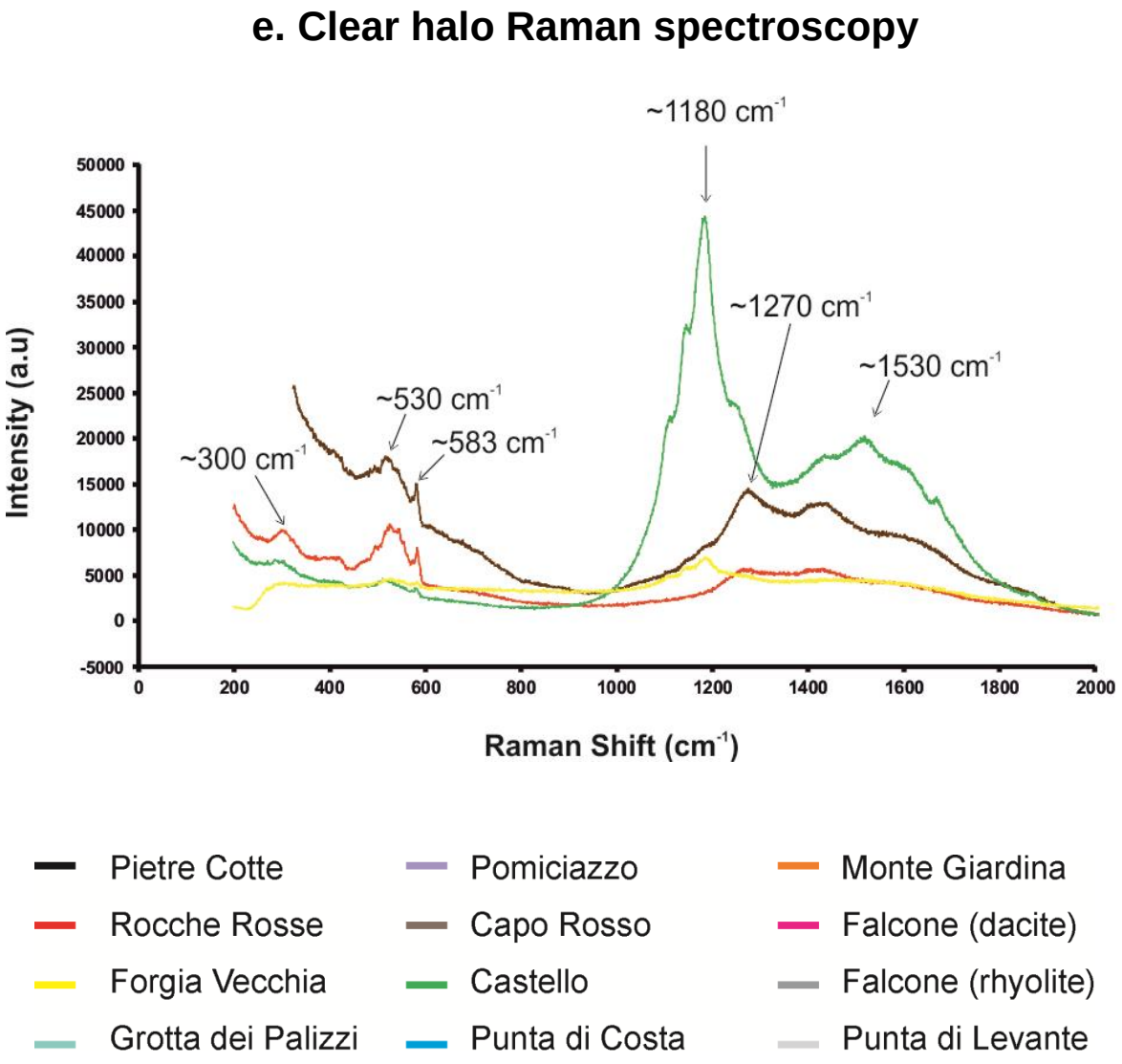

Figure 3.12: Raman spectrum (and notable peaks) for (a) obsidian glassy groundmass, (b) spherulitic interiors, (c) brown rim surrounding spherulites, (d) mesh-like textures found in some spherulites and (e) clear haloes immediately surrounding some spherulites. Key for all spectra shown below (e).

The broad LF spectral response may represent a response to stretch-bend mixed vibrational motions of bridging oxygen ions (White and Minser, 1984; Matson et al., 1986), and may be influenced by systematic variation caused by depolymerisation. Peaks at ~460 cm^{-1} and ~510cm^{-1} indicate the presence of crystalline SiO_2 and alkali feldspar in the glassy groundmass (e.g. microlites). The commonly observed broad spectral response in the HF 1200-1800 cm^{-1} band region may represent a response to luminescence, weak Si-O modes

in the HF region, variable degrees of depolymerisation, bonding angle and composition, or a response to two six-membered, interconnected rings in the three-dimensional network structure (Mysen et al., 1982). See discussion for more detail on peak- and band interpretations.

Raman results show a number of sharp peaks and broad spectral responses, formed by the presence of crystalline phases, and structural modification and instabilities in glass respectively. Generally, there are two broad regions of peaks and humped profiles in the glass results. Despite the differing optical properties (brown material appears more crystalline, with a non-isotropic appearance under crossed polarised light), the brown rims show the characteristic profiles akin to a glass response. Here, glass results include the glassy groundmass and brown rim, and a low frequency (LF) region between 400 cm^{-1} and 650 cm^{-1}, and a high frequency (HF) region between 1200 cm^{-1} and 1800 cm^{-1} have been identified. The main difference between glass and brown rim results is that although the brown rim shows an amorphous hump appearance, peaks tend to be sharper (more akin to crystalline material). Sharp peaks represent the presence of rare crystalline material, and the broad humped regression is characteristic of amorphous material. The LF region has much greater intensity than the HF region. The LF region is characterised by a number of major and minor peaks, whereas the HF region shows a more continuous hump-like appearance. The LF region exhibits two prominent peaks, at ~460 cm^{-1} and ~510 cm^{-1}, accompanied by minor peaks at ~435 cm^{-1}, 490 cm^{-1}, 520 cm^{-1}, 583 cm^{-1} and 600 cm^{-1}. Outlying the LF and HF regions, there are also notable peaks at ~230 cm^{-1} and 300 cm^{-1}, with a relatively flat area between 800 cm^{-1} and 1200 cm^{-1} (see Discussion for peak assignment and what peaks may represent). Though the spectra for brown rims mirror the clear glass in shape, the peaks appear more diluted, suggesting there is a slight difference between the brown zone and the glass.

Spherulites, mesh-textured interiors and surrounding brown zones show a similar trend to the glassy matrix, suggesting the presence of glass in spherulites (supported by EMP results). There are two broad regions of peaks, defined by a LF region (~200-650 cm^{-1}) and a HF region (~1100-2000 cm^{-1}). Spherulite spectra show intense peaks at ~300 cm^{-1} and 520 cm^{-1}, as well as a distinct double-humped banding at ~1265 cm^{-1} and ~1440 cm^{-1}. Mesh-textured interiors exhibit peaks at ~300 cm^{-1}, ~520 cm^{-1}, ~1270 cm^{-1} and ~1430 cm^{-1}. Clear haloes do not show a clearly defined division of peaks between LF and HF regions, and are more sporadically spread at variable intensities. The prominent peaks are at ~300 cm^{-1}, ~530 cm^{-1}, ~583 cm^{-1}, ~1180 cm^{-1}, ~1270 cm^{-1} and 1530 cm^{-1}.

3.7 X-ray diffraction

The principle of the powdered XRD technique is that the resultant diffraction pattern will show sharp distinctive peaks (if associated with crystalline material), and/or a broad or disperse tailing peak (if associated with amorphous material). This is because crystalline materials have a regular array of atoms, producing high intensity, definitive XRD peaks. Amorphous or non-crystalline material, such as glass, does not have a regular array of atoms, and therefore produces a broad "hump" pattern. These humps can also dilute peak intensities derived from crystal components. X-ray diffraction results are displayed in Figure 3.13, and raw data is available in Appendix VIII. The Punta di Levante samples obsidian spherulites were difficult to distinguish from the devitrified groundmass in the coarsely crushed powder. As such, these results better reflect a whole rock component.

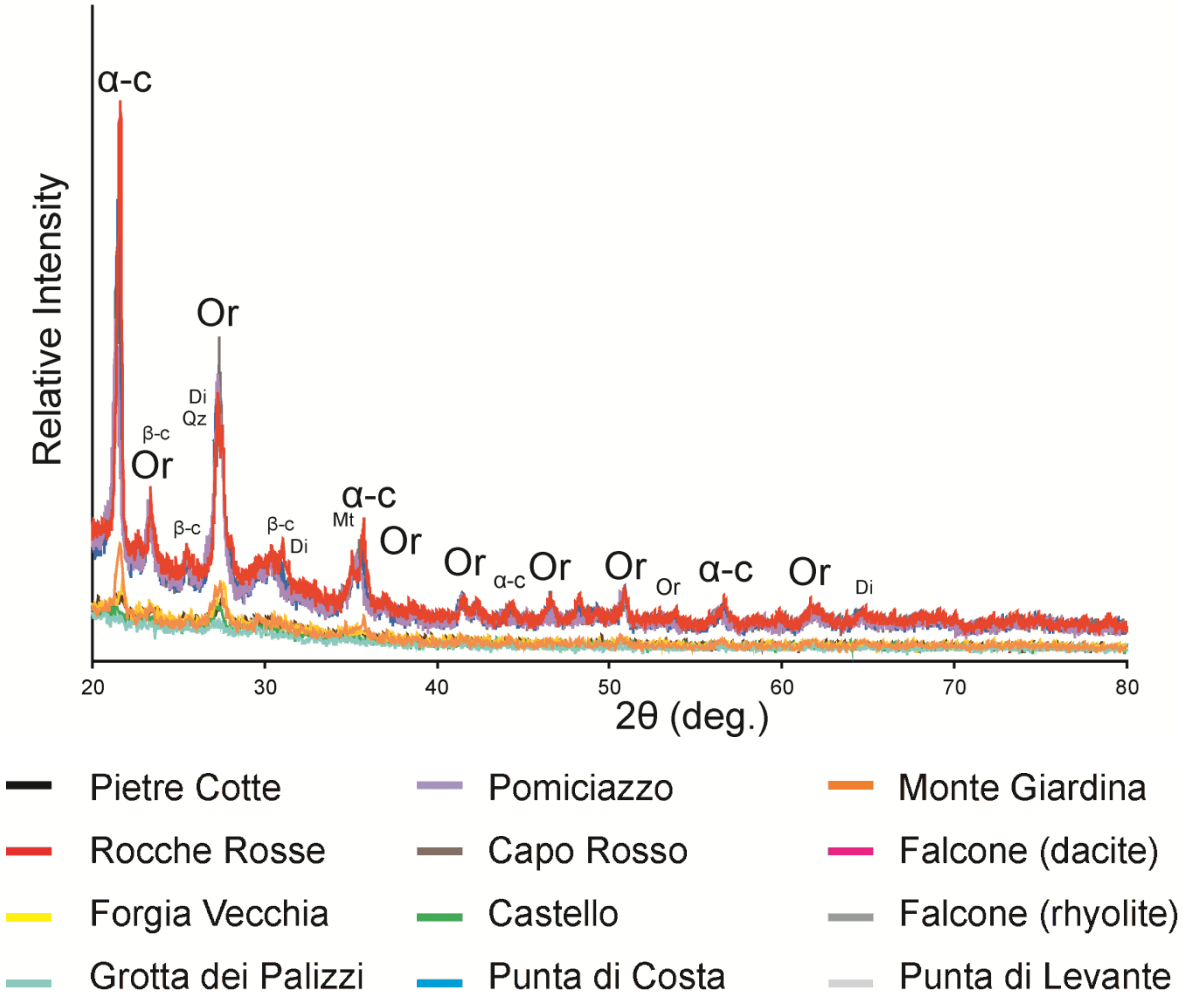

Figure 3.13: X-ray diffraction results (and notable peaks) for spherulites from sampled lava bodies. Notable peaks include several α-cristobalite (α-c) and orthoclase feldspar peaks (Or) (main constituents of spherulites), with minor quartz (Qz), magnetite (Mt), β-cristobalite (β-c) and diopside (Di) peaks.

In general, all samples show 3 to 5 sharp and definitive peaks, with several minor peaks also evident. The two major peaks at 21.6° and 27.3° correspond to α-cristobalite and orthoclase feldspar respectively, with minor peaks representing diopside. There are also peaks suggesting trace amounts of β-cristobalite, quartz and magnetite, though these are absent in a number of samples.

The Punta di Levante sample contains powdered whole rock material, which is reflected in the results (with a more diluted, regressive trend and lack of clearly distinguishable peaks compared to other plots). The Punta di Levante XRD results show a regressive "humped"

trend (akin to amorphous material response), reducing (but not eliminating) crystalline peaks. Peaks reflect the presence of α-cristobalite and orthoclase.

Pietre Cotte spherulites, which are often small, radial and unaltered (no mesh-textures and no rims, see Sample Petrography), contain both α- and β-cristobalite. The Rocche Rosse sample exhibits a number of clear peaks and several minor peaks. There is a clear α-cristobalite peak at 21.6°, and orthoclase peak at 27.3°. There is a number of overlapping peaks from multiple crystal phases (including diopside and quartz), resulting in an enhanced diffraction peak at ~27-30°.

The Forgia Vecchia, Capo Rosso and Castello samples display evidence of a humped amorphous peak, with crystalline peaks superimposed and reduced upon this background pattern (may also reflect glass presence, as suggested by EMP and Raman results). There are 2-4 major (sharp) peaks identified, again representing α-cristobalite and orthoclase, with minor diopside. There is evidence for trace amounts of iron oxide (titanomagnetite), β-cristobalite and quartz in the Castello sample. The Pomiciazzo and Punta di Costa XRD results again show evidence for the glass content. There are a number of large, definitive α-cristobalite and orthoclase peaks, with minor peaks for diopside, and trace amounts of quartz and titanomagnetite apparent. The Monte Giardina sample shows an amorphous hump, with superimposed α-cristobalite and orthoclase feldspar peaks. The Falcone XRD results show several definitive peaks for α-cristobalite, orthoclase and diopside, with minor quartz and magnetite detected.

3.8 Spherulite crystal size distribution and shape morphology

Field and microscopic observations and geochemical characteristics thus far explored allow for a preliminary classification of spherulites. It is hypothesised that these textural heterogeneities are the product of differing nucleation, growth and modification events during ascent, emplacement, deformation and devitrification. Based on textural characteristics and spatial occurrence, spherulites can be classified as five types: Type 1 spherulites are typically small (<0.5 mm), radial, sub-spherical, with a rare surrounding brown rim. Type 2 spherulites also contain a radial interior, are slightly larger (typically 0.5-1.5 mm), and, importantly, occur in close proximity to deformational structures and show an elongate shape. Type 3 spherulites are larger, up to 2 mm, with a radial interior, spherical shape, and often occur individually in zones of apparent low shear. Type 4 spherulites concentrate within fractures and joints, and Type 5 spherulites show a partial or fully microcrystalline interior and a lack of a radial structure. Such textural classifications are important because it allows for further constraints to be placed on spherulite formation and modification by means of crystal size distribution (CSD) methods.

Fifteen CSD plots of spherulites from all lava flows and domes have been produced (Figs. 3.14 and 3.15; key textural parameters are displayed in Table 3.6), with spherulites ranging in size from 0.1 mm (in younger flows), up to 8 mm (in older domes). Generally, the lava bodies host spherulites typically 0.5-3 mm in size. The calculated CSD plots, showing spherulite population density for different spherulite size bins, for all spherulitic lava bodies exhibit negative slopes (with increasing spherulite size), with variable degrees of

complexities highlighted by kinked profiles. The majority of plots show a higher degree of heterogeneity at smaller spherulite sizes, while some plots show little or no deviation from a log-linear profile. Older sampled domes exhibit larger spherulite maximum sizes and wider size ranges. Spherulites below 1 mm in size show a greater degree of complexity, evident by highly non-linear slope regressions. Error bars are generally more significant in the larger spherulite sizes across lava bodies, and do not show considerable errors at smaller spherulite sizes, with minor exceptions (Forgia Vecchia, Grotta dei Palizzi, Pomiciazzo, Punta di Levante). These exceptions do not show significant error which would eradicate the left hand truncation trend.

The CSD plot for the Pietre Cotte lava flow obsidian (Fig. 3.15a) shows an initial steep slope at the lowest spherulite sizes (<0.1 mm, the smallest spherulites in any flow or dome measured). Spherulites larger than 0.1 mm show a relative linear trend, up to the largest spherulites (1 mm). The intercept value (population density) for the Pietre Cotte sample is 4.81, and the R^2 value (correlation coefficient which describes how well the equation describes the data) is 0.96 (parameters calculated using *Microsoft Excel*). The Pietre Cotte sample has a good linear correlation, with a slope value of -8.64 and an R^2 value of 0.96, but there is evidence for two separate slopes, possibly representing two separate spherulite populations (a population <0.1 mm and larger than 0.1 mm in size). This is supported by petrographic observations, with smaller (generally <0.5 mm across samples), sub-spherical spherulites (with no brown rims) and larger, rounded spherulites (with brown rims) observed across samples. Generally, the Rocche Rosse CSD plots (Fig. 3.15b) show a complex regression of up to two or more individual regression slopes.

Table 3.6: Spherulite crystal size distribution (CSD) parameters for sampled lava flows and domes. Calculated growth periods for spherulite growth are also shown in the table (see discussion). Growth period (days) calculations are based on a (temperature dependent) growth rate of 6.33×10^{-7} m s^{-1} (calculated by Castro et al., 2008).

Sample	Lava flow or dome	Number of spherulites	Y intercept	Slope value	R^2 value	Short axis	Int. axis	Long axis	Sphericity (%)	Growth period (days)
VPC	Pietre Cotte	999	4.8186	-8.6421	0.964	1	1.4	2.8	56.3	2
022 (210)	Rocche Rosse	402	1.8993	-2.9169	0.9374	1	1	1.15	91.1	6
96	Rocche Rosse	451	2.9473	-5.2049	0.9234	1	1.05	1.15	92.6	3
398	Rocche Rosse	323	1.8082	-1.3541	0.7954	1	1	1.1	93.8	13
412	Rocche Rosse	212	2.1209	-1.6989	0.9747	1	1.05	1.05	98.4	11
413	Rocche Rosse	154	1.8861	-4.1409	0.9828	1	1.05	1.05	98.4	4
L10-006	Forgia Vecchia	395	1.8111	-4.2732	0.9551	1	1.15	1.25	90.3	4
L10-016	Pomi-ciazzo	255	-2.37	-1.6507	0.9742	1	1.05	1.05	98.4	11
185	Capo Rosso	151	1.7576	-4.9181	0.9268	1	1.1	1.1	96.9	4
186	Capo Rosso	446	1.9945	-4.0199	0.9786	1	1	1.15	91.1	5
Cas 196	Castello	130	1.8541	-4.5033	0.9992	1	1	1	100.0	4
L10-018c	Punta di Costa	431	2.1136	-4.1954	0.9933	1	1.05	1.05	98.4	4
MG3	Monte Giardina	326	2.3264	-2.5891	0.9489	1	1	1	100.0	7
L10-019a	Falcone (Fa2)	576	-0.3493	-2.4533	0.9673	1	1.05	1.1	95.4	7
L10-020	Falcone (Fa3)	1086	-1.2574	-1.485	0.8635	1	1.05	1.05	98.4	12
179	Punta di Levante	156	0.9928	-3.6861	0.9519	1	1	1	100.0	5

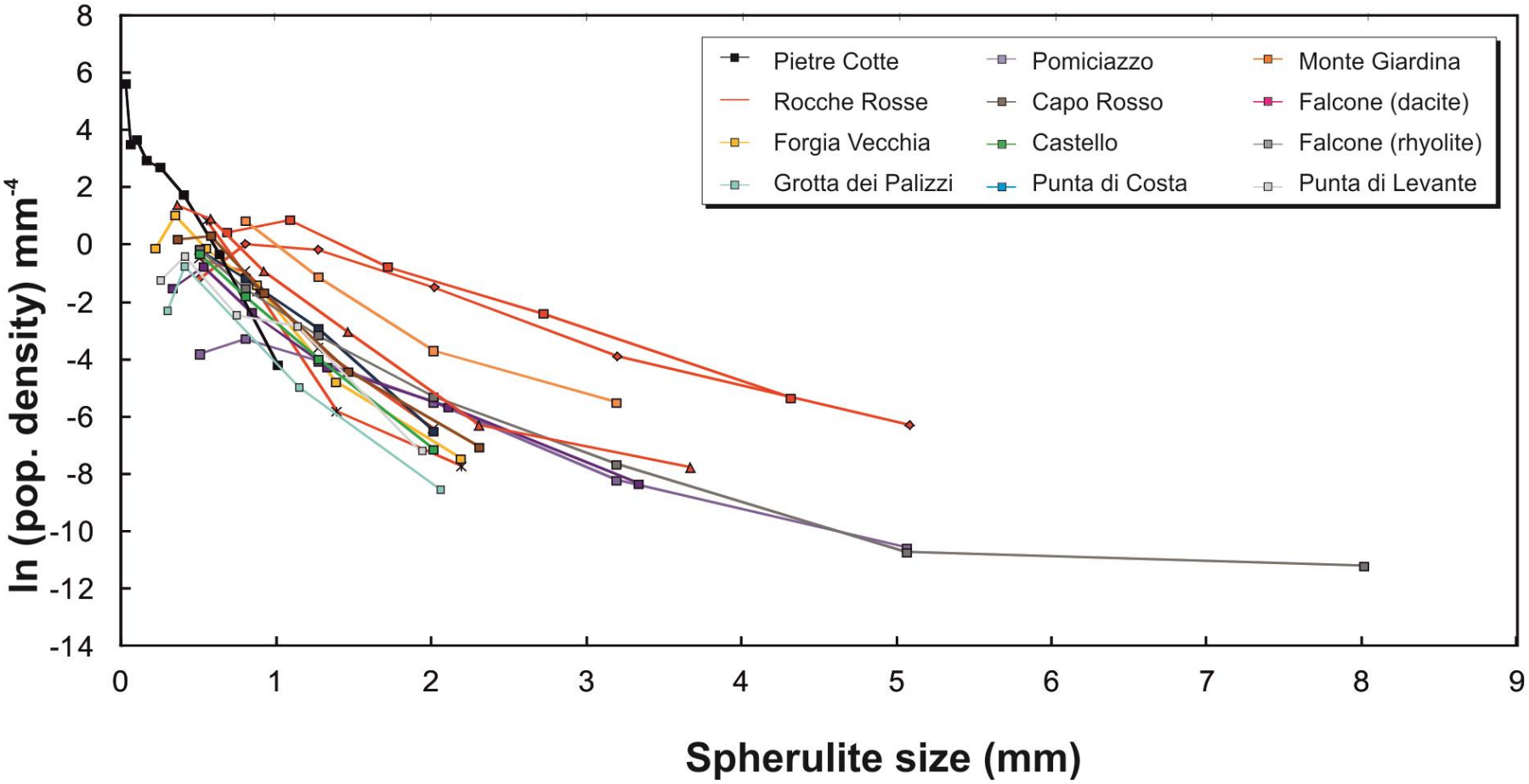

Figure 3.14: Spherulite Crystal size distribution (CSD) plots for all samples. Note higher degree of complexity in slopes at smaller (<1 mm) spherulite sizes, and the general shallowing of slope up to higher spherulite sizes (smaller spherulites more common in younger lava flows, maximum sizes more associated with older dome samples). Rocche Rosse more extensively sampled due to higher variety of spherulite occurrence across exposure.

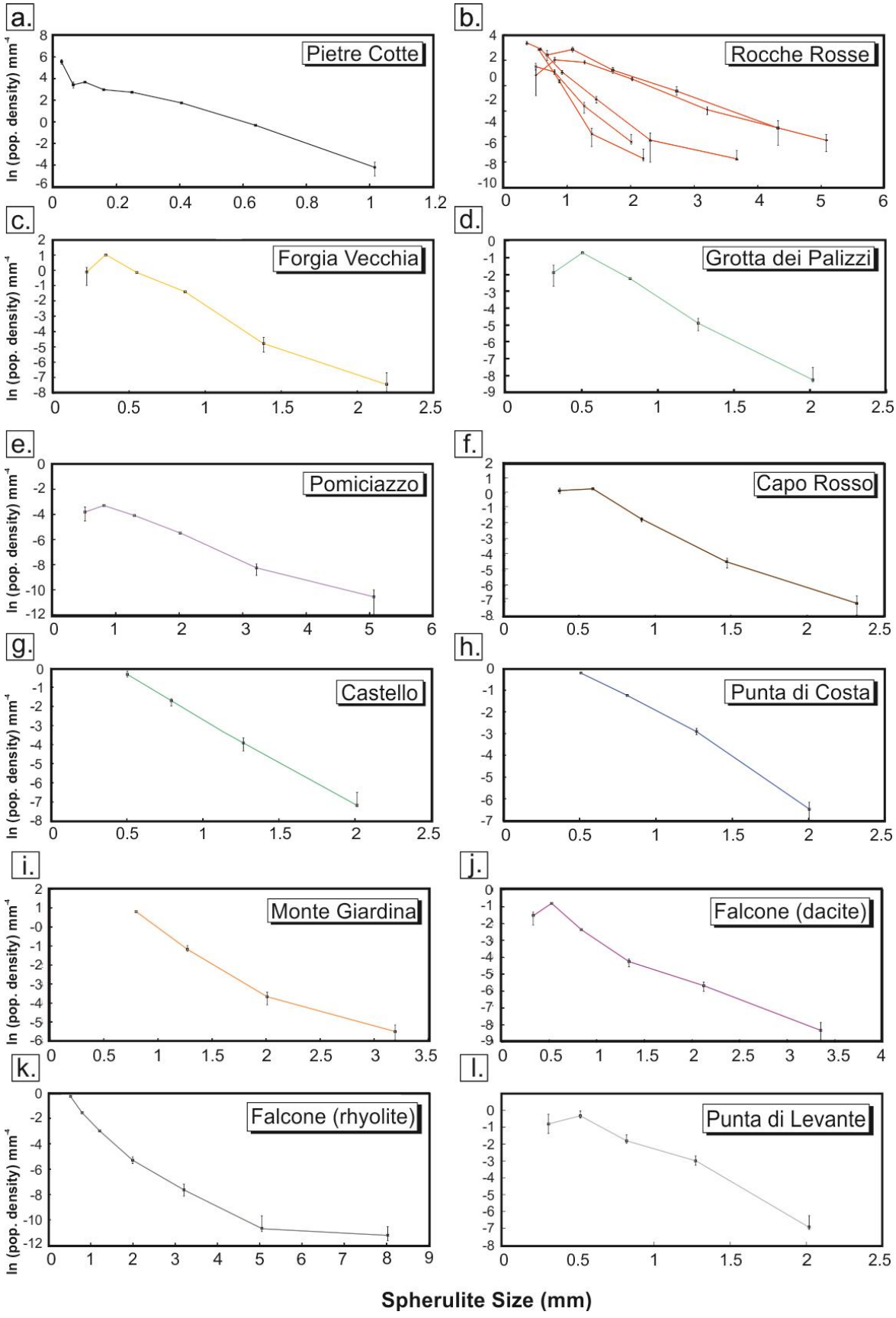

Figure 3.15: Individual spherulite CSD plots for all sampled flows and domes (with associated error bars).

Samples with complex trends show up to three individual and well-defined slope segments (with distinct slope angles), with a slope at lower spherulite sizes (<0.5 mm, showing a steep slope increase or decrease with increasing size), followed by a shallower regression typically up to 1.3 mm in size.

Spherulites range in size from <0.2 mm up to 5 mm, typically 0.5mm to 2 mm. Plots for spherulites smaller than 0.5 mm often shows a deviation from a linear trend, sharply increasing with increasing spherulite size, before decreasing more gradationally to the largest sizes. Forgia Vecchia, Grotta dei Palizzi, Pomiciazzo, Capo Rosso, Falcone (dacite) and Punta di Levante plots (Fig. 3.15c-e; i-j) show a similar trend, with a downturn at lower spherulite sizes (typically 0.5 mm) followed by a linear regression.

The Forgia Vecchia sample (Fig. 3.15c) shows spherulites ranging from 0.2-2.2 mm in size, with a linear regression slope, and an R^2 value of 0.95. However, the regression slope is not perfectly linear, with a left-hand truncation, where the slope kinks at 0.4 mm. There are minor kinks between 0.4 mm and 2.2 mm. The Grotta dei Palizzi CSD plot (Fig. 3.15d) shows a near-identical trend to the Forgia Vecchia CSD plot, with left-hand truncation in the smaller spherulite size range, with spherulites up to 2 mm in size. The Pomiciazzo sample (Fig. 3.15e) shows a very similar trend to the Forgia Vecchia sample, with a relatively linear overall slope regression, indicated by an R^2 value of 0.97. There is a similar, but less-pronounced left-hand truncation at ~0.7 mm size, followed by a continuous regression to the largest spherulites at 5 mm, defining two distinct slopes. The regression is slightly kinked at 3.1 mm. Two Capo Rosso samples were plotted, and again show a minor left-hand truncation, followed by a moderately linear slope regression. Spherulites range in size from <0.2 mm to 2.3 mm, with R^2 values of 0.93 and 0.98, showing at least two distinct slopes. The Castello sample (Fig. 3.15g) shows an almost continuous linear regression, with an R^2 value of 0.99, ranging in size from 0.5 mm to 2

mm. The y-intercept value is 1.85. The Castello sample shows one definitive slope. The Punta di Costa sample (Fig. 3.15h) shows a near-identical trend and size range, with a straight regression (R^2 value - 0.99, y-intercept value - 2.11) between 0.5 mm and 2 mm. There is a minor kink in the Punta di Costa sample at 1.3 mm, but the general trend suggests 1 definitive slope. The Monte Giardina CSD plot (Fig. 3.15i) shows a slight curved profile. Spherulites range in size from 0.7 mm to 3.2 mm, with an R^2 value of 0.94 and y-intercept value of 2.32. There is a pronounced curve to a shallower regression slope at 2 mm. The Falcone lava dome (Fig. 3.15j-k) exhibits the largest spherulite sizes (up to 8 mm), and the largest range of sizes (from the smallest sizes of 0.5 mm to 8 mm). The Falcone (dacite) (Fig. 3.15j) has an R^2 value of 0.96 and y-intercept of -0.34, Falcone (rhyolite) has an R^2 value of 0.86 and y-intercept of -1.25. This sample shows a slight slope deviation at the lowest sizes (<0.7 mm), followed by a kinked profile. The slope angles between 0.7-1.3 mm and 1.3-3.5 mm are comparable, and the Falcone (rhyolite) CSD (Fig. 3.15k) shows a kink at 5 mm to a near-flat trend. The Punta di Levante CSD plot (Fig. 3.15l) shows a typical trend with left-hand truncation below <0.5 mm in size, and spherulites up to 2 mm in size.

Plotting spherulite habit results into an adapted Zingg shape classification scheme (Zingg, 1935; Mock and Jerram, 2005) can yield information such as object shape geometries, including spherical spherulites (ball-shaped), cylindrical or rod-shaped spherulites, disc (oblate) and bladed spherulites (Fig. 3.16). A perfectly spherical object is equidimensional (short, intermediate and long axes equal, S=I=L, giving a ratio of 1:1:1), rod-shaped (S=I≠L), disc-shaped (S≠I=L) and bladed objects (S≠I≠L) show a preferred dimensional length. In general, spherulite populations of the selected lava bodies show strongly spherical shapes (Table 3.6 (sphericity) and Fig. 3.16), with the exception of the Pietre Cotte obsidian sample, which shows a more blade- to disc-like shape. Rocche Rosse

samples show a more spherical shape, but not perfect equidimensional spheroids. The Castello and Monte Giardina obsidian lavas exhibit a perfect spherical population of spherulites (1:1:1 axial ratio), along with one Rocche Rosse obsidian sample. The Pomiciazzo, Punta di Costa and Falcone lava bodies all exhibit the same near-perfect spherical populations of spherulites, and the Rocche Rosse samples also show near-spherical shapes. The Forgia Vecchia and Capo Rosso samples do not show a perfect 1:1:1 sphericity, but still plot within the spherical field.

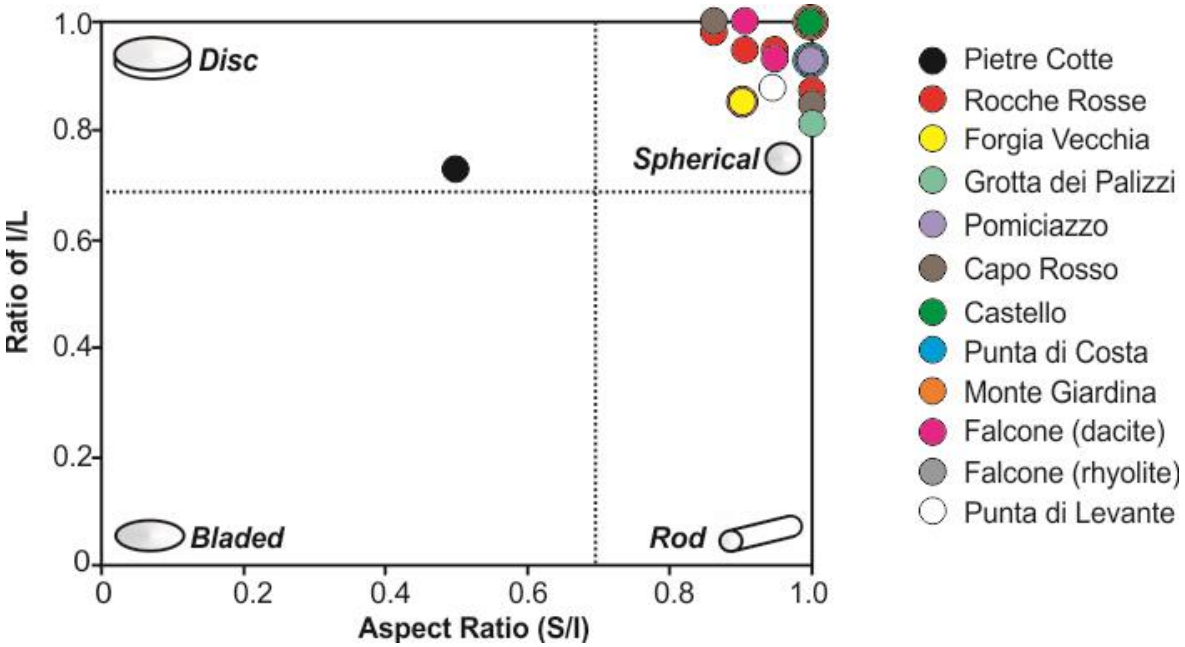

Figure 3.16: Average spherulite shape morphology classification scheme adapted from Zingg, (1935), showing the majority of spherulites are (on average) spherical in shape, with the exception of spherulites in the Pietre Cotte lava flow.

The sphericity of spherulites gives a semi-quantitative indication of the degree of roundness from a 2D projection (Table 3.6). The Castello and Monte Giardina samples are the most spherical, equidimensional spherulites, along with select Rocche Rosse samples. The majority of Rocche Rosse samples, as well as Pomiciazzo, Punta di Costa and Falcone

lavas show near-perfectly spherical populations of spherulites, with the Forgia Vecchia and Capo Rosso samples exhibiting minor variation. The Pietre Cotte lava shows the least spherical-shaped spherulites, with sphericity below 60%. The Pietre Cotte sample agrees in both the Zingg Diagram and sphericity value (~56%, Table 3.6).

As well as average shape parameters for each lava body, individual spherulite area, length, width and characteristic aspect ratio 2 dimensional parameters were also calculated within samples (Fig. 3.17). The total number of spherulites analysed per lava sample (Table 3.7) showed some variation dependent upon spherulite populations within a sample. Ideally, at least ~200-300 crystals would provide a good statistical fit for characteristic dimensions (e.g. Morgan and Jerram, 2006; Preece et al., 2013). This number was achieved for the majority of sampled lava, but was not always possible due to limited spherulites in some older samples (older obsidian may have recrystallised, devitrified, modified or spherulites may not be present).

A total of 4309 individual spherulites were analysed for dimensional data (Figs. 3.17-3.18). Total individual spherulite dimensions from each lava body are shown in Table 3.7. The Falcone rhyolite exhibits the largest area, length and width dimensions, with 2 spherulite outliers, while the Pietre Cotte shows the smallest area and dimensions, forming the base of the graphs in Figure 3.17. Length vs. Width plots (Fig. 3.18) indicate a general pattern of increasing length and width in a linear 1:1 trend, with some scattered distribution in Pietre Cotte, Pomiciazzo, Capo Rosso, Monte Giardina and Falcone dacite samples, particularly clustered in the Capo Rosso and Monte Giardina samples. The Pietre Cotte samples are particularly scattered, with Grotta dei Palizzi, Pomiciazzo and Capo Rosso also slightly scattered. Punta di Levante shows a general lack of any trend, i.e. a completely scattered distribution.

a

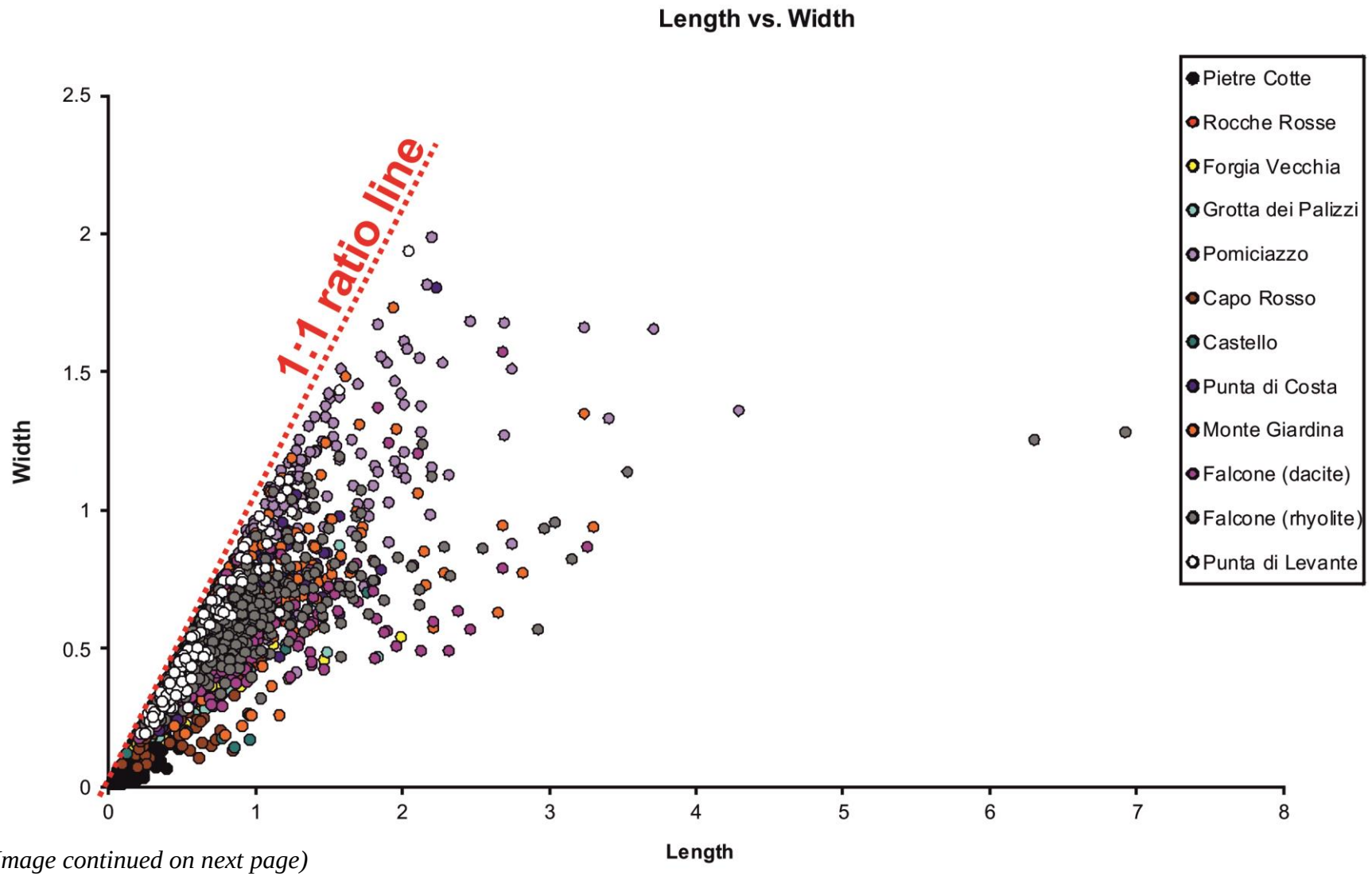

(Image continued on next page)

b

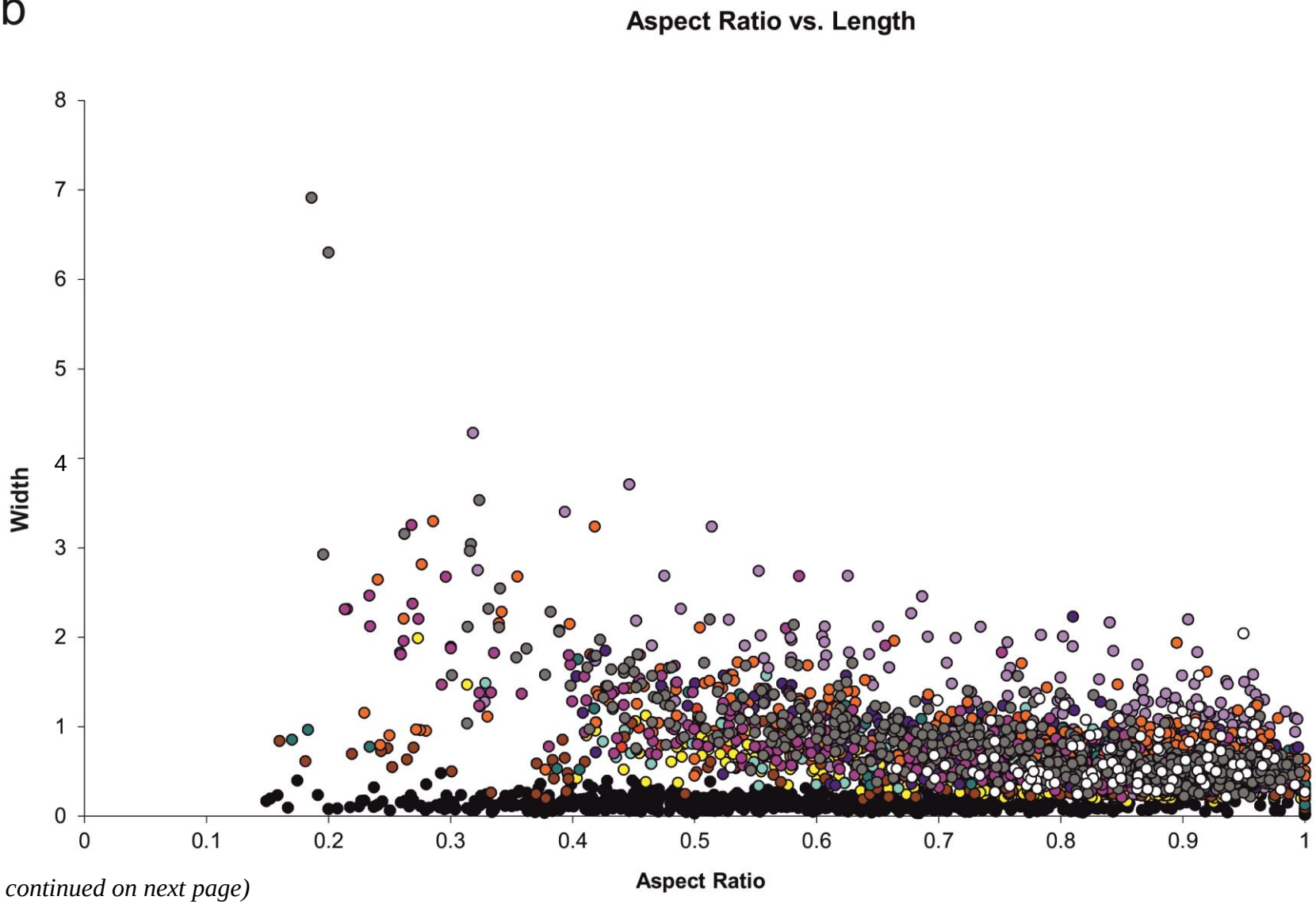

(Image continued on next page)

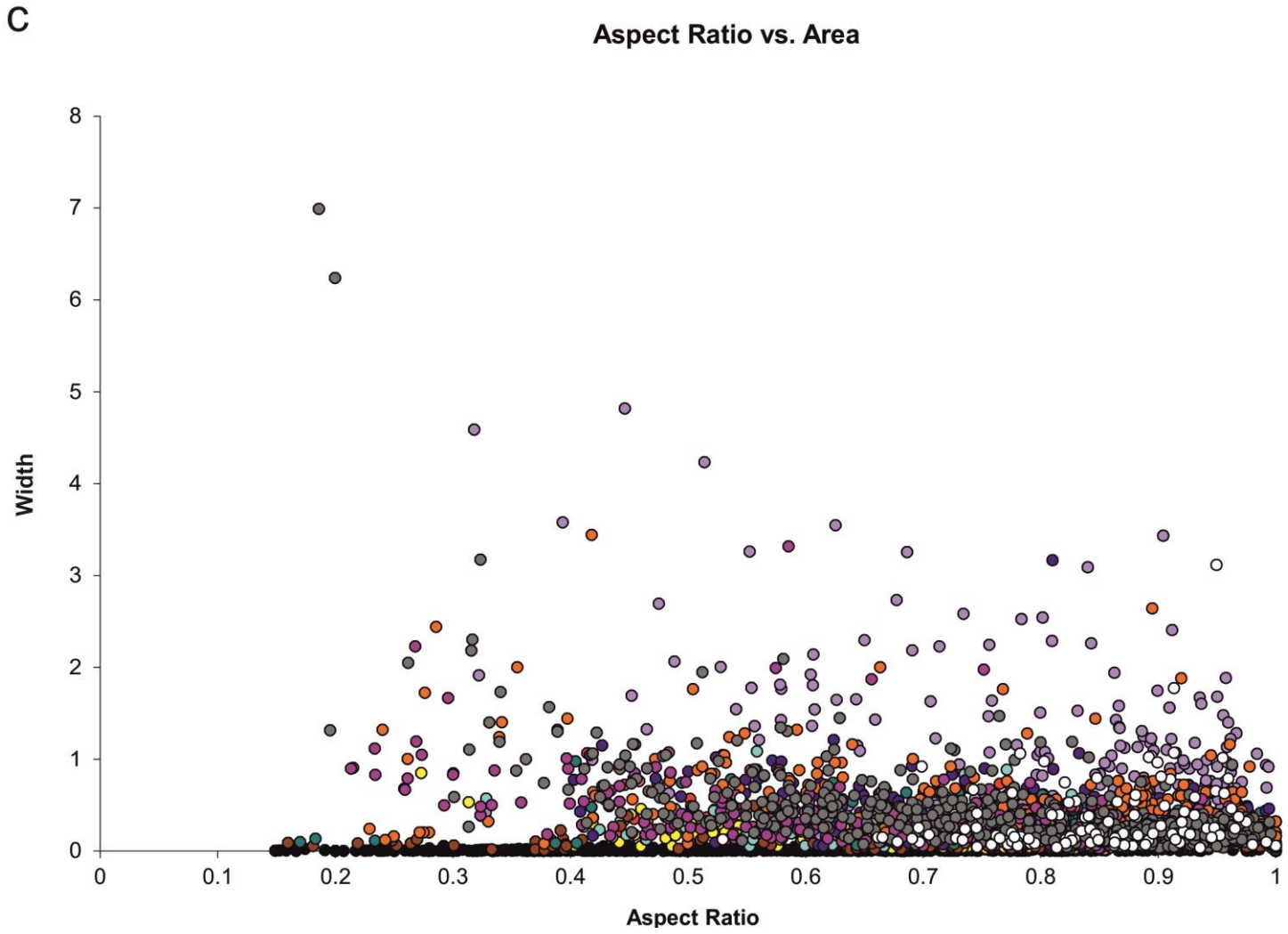

Figure 3.17: (a) Length (mm) vs. Width (mm), (b) Length vs. Aspect Ratio and (c) Area (mm^2) vs. Aspect Ratio plots for all spherulites within sampled lava bodies.

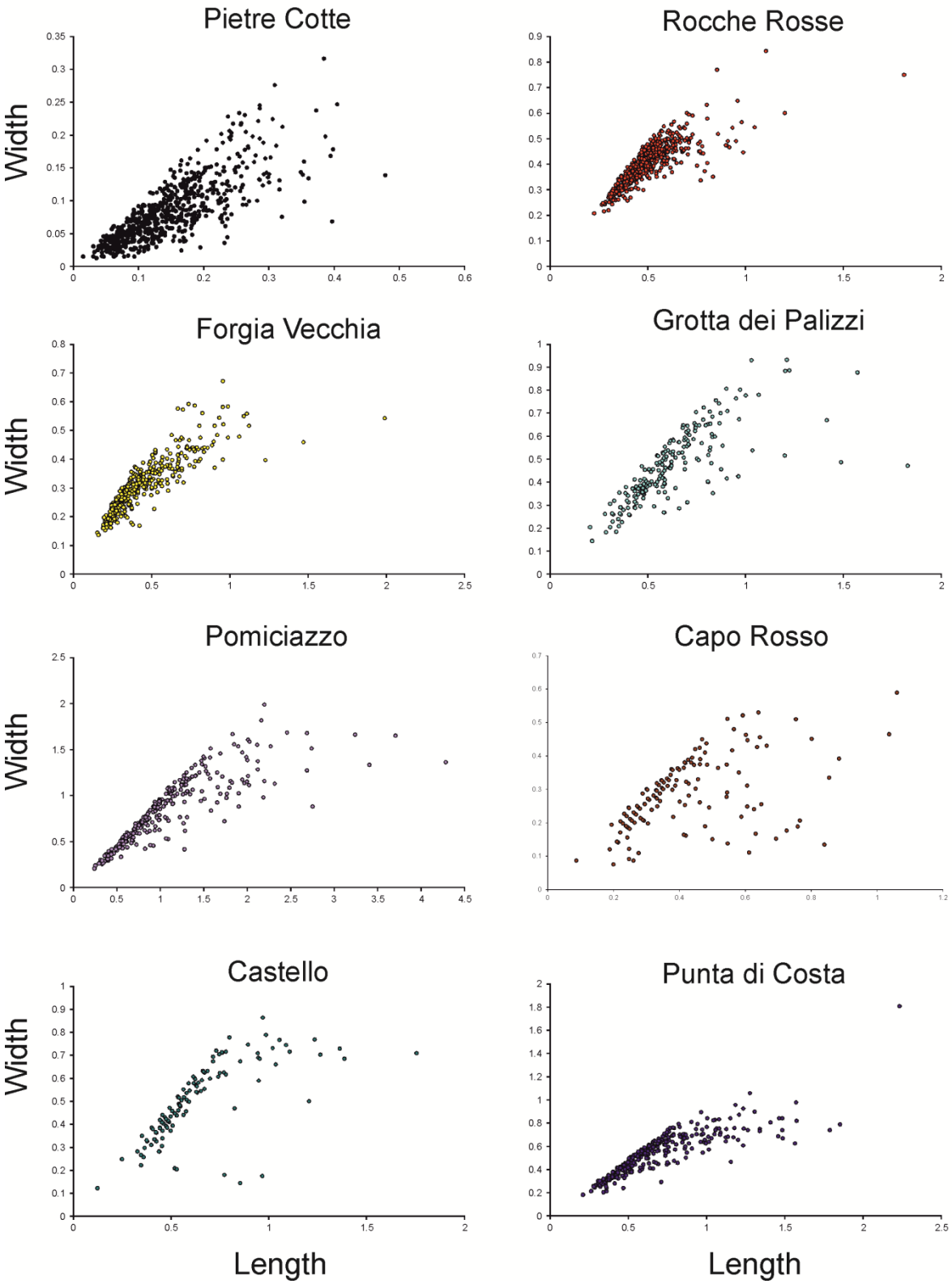

(Image continued on next page)

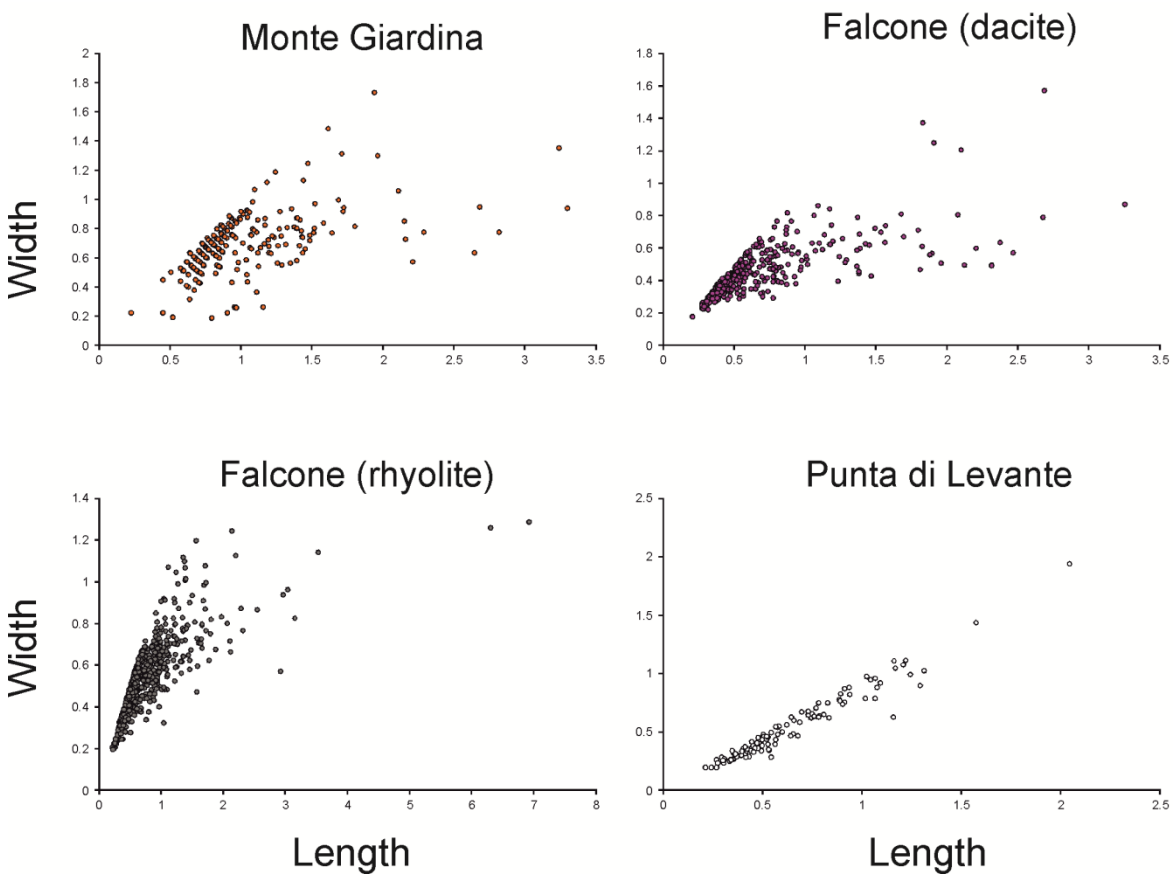

Figure 3.18: Individual spherulite length (mm) vs. width (mm) plots for each sampled lava body.

Table 3.7: Number of individual spherulites analysed in each sampled lava body for length, width and area.

Flow or dome	Number of spherulites analysed
Pietre Cotte	745
Rocche Rosse	450
Forgia Vecchia	382
Grotta dei Palizzi	257
Pomiciazzo	341
Capo Rosso	151
Castello	130
Punta di Costa	334
Monte Giardina	326
Falcone (dacite)	391
Falcone (rhyolite)	686
Punta di Levante	156

3.9 Discussion

3.9.1 Deformation as a trigger for spherulite nucleation

Deformation has been tentatively suggested to play an important role in spherulite nucleation by Clay et al. (2013), and is discussed in further detail here. Field observations show high spherulite concentrations within flow folds, bands and at flow edges, as well as elongate and sheared spherulites, particularly within the heavily deformed Rocche Rosse and Pietre Cotte lava flows (Fig. 3.2d; Fig. 3.3-3.4). Several obsidian lava flows on Lipari and Vulcano show evidence for emplacement-related deformation. For instance, flow folding, brittle fractures and stretching lineations have been observed across the Rocche Rosse lava flow (see Chapter 2; Cas and Wright, 1987; Gottsmann and Dingwell, 2001a; Lucchi et al., 2010; Cabrera et al., 2011; Clay et al., 2013), and the Pietre Cotte lava flow (see Chapter 4, and Piochi et al., 2009). The regular and highly recognisable occurrence of densely spherulitic glass coinciding with flow deformation, and the uniform occurrence of elongate and/or sheared spherulites (see also Chapter 2), suggests a link between flow deformation and spherulite nucleation.

The preservation of deformational structures indicates a degree of compression, shear and elongation within active lava flows or domes. Strain associated with both shear and elongation can enhance crystallisation, with the flow-induced spherulite crystallisation phenomenon particularly well understood in experimental polymer melt studies (e.g. Mackley and Keller, 1975; McHugh, 1995; Doufas et al., 1999; Caroli and Lemaître, 2012; Derakhshandeh and Hatzikiriakos, 2012). Elongation in an extensional flow regime has

been cited as a strong stimulus for polymer crystallisation, causing molecules to orient and stretch in the direction of extension, facilitating the process of flow-induced crystallisation (Swartjes et al., 2003; Janeschitz-Kriegl et al., 2003; Kornfield et al., 2002; Stadlbauer et al., 2004). Shear flow can induce crystallisation, requiring very large generation of strain (Derakhshandeh and Hatzikiriakos, 2012). In polymer bulks, spherulites can also form under no flow conditions, or when deformation rate is low (Monasse, 1995; Pogodina, 2001), and row-like nucleation and anisotropic growth can also occur as the deformation rate increases (Pennings and Kiel, 1965; Pogodina, 2001). Extension and shear flow-related crystallisation may therefore be applicable in highly deformed obsidian lavas, such as the Rocche Rosse and Pietre Cotte lava flows.

Flow-induced crystallisation, also referred to as flow-enhanced nucleation or shear-enhanced nucleation (Kneller, 2002; Graham and Olmsted, 2009), is a well understood phenomenon in polymer sciences as a trigger for spherulite nucleation, but is thus far a neglected concept in a geological context. Though there are molecular, chemical and rheological differences between polymer materials and obsidian, they do share a number of key similarities, most notably an amorphous and semi-crystalline state, and the occurrence of spherulite nucleation. Silicate materials are composed of interlinked tetrahedral molecular chains, and can be classified as polymers (Kneller, 2002). As the silica content increases in silicate systems so does their degree of polymerisation (Kneller, 2002). Rhyolitic lavas are also highly polymerised due to high silica content; hence, acts as an ideal spherulite-forming medium (Keith and Padden, 1963, 1964a, b) much like experimental polymer materials. Polymer crystallisation experiments also account for different degrees of undercooling, temperature changes and changes in strain rate, all processes which also occur within obsidian lavas during emplacement and cooling. These

similarities suggest that polymer crystallisation experiments may form a useful analogue for spherulite crystallisation within obsidian lavas.

In polymer crystallisation studies, it is well established that nucleation of microscopic crystallites in polymer liquids is greatly influenced by flow (e.g. Binsbergen, 1966; Keller and Kolnaar, 1997; Graham and Olmsted, 2009). This is controlled by kinematics, whereby flow enhances nucleation and triggers the formation of elongate crystals (Graham and Olmsted, 2009). After a few seconds of flow in amorphous materials, the timescale of crystallisation is reduced by an order of magnitude for moderate deformation rates (Tribout et al., 1996; Devaux et al., 2004; Housmans et al., 2009), and by several orders of magnitude for high deformation rates (Kornfield et al., 2002; Baert et al., 2006). This significantly increases the number density of spherulites (Tribout et al., 1996; Housmans et al., 2009). Nucleation depends on the change of the free energy difference between the crystal and the melt phases; the degree of order in the melt phase increases under shear conditions, and the free energy difference increases. The entropic penalty for crystallisation is lowered and, therefore, the nucleation rate increases (Keller and Kolnaar, 1997; Coccorullo et al., 2008). This leads to a high number density of spherulites as a result of deformation, which is evident in field observations in obsidian lavas (e.g. the Rocche Rosse lava flow – spherulites concentrated within folds and shear zones; Figs. 3.3-3.4). In polymer experiments, the most pronounced flow-induced effects often occur near the melting point where quiescent crystallisation is considerably slow (e.g. Binsbergen, 1966). An example of such polymer crystallisation experiments includes measurements of nucleation and growth rates of spherulites during continuous and constant steady shear flow (Coccorullo et al., 2008). All tests carried out resulted in a dominant crystalline structure that was fully spherulitic. Nucleation density in quiescent conditions remained constant with time and, under shear flow, an increase of nucleation density with time was

observed (Coccorullo et al., 2008). This may suggest that, in obsidian lavas, spherulite nucleation may increase with flow deformation (during flow), and remain constant in areas of low (or no) strain (e.g. in areas unaffected by strain during flow, or following flow cessation). This results in high spherulite populations in areas of high strain (and spherulites may be sheared or elongate as a result), and lower populations of (undeformed) spherulites in zones of low strain.

Elongate spherulites (elliptical as opposed to bowtie shaped) spatially found within close proximity to deformational structures in sampled flows and domes may have formed while lava was behaving in a ductile manner (within T_g). This is similar to how vesicles and enclaves preserve lava flow strain, based on their shape and size alteration from spherical to elongate (Polacci and Papale, 1997; Rust et al., 2003; Ventura, 2004; Iezzi and Ventura, 2005). The onset of this spherulite nucleation and growth may therefore have been triggered (or enhanced) by flow-induced crystallisation (i.e. as a result of deformation) at high T_g temperatures in the sampled flows and domes. This is supported by polymer experiments whereby flow-induced crystallisation occurs near melting point (above T_g or high T_g transition) (Binsbergen, 1966). Preservation of ductile structures suggests that this occurs at high T_g transition temperatures. Such deformation-triggered crystal growth may result in textural heterogeneities such as concentric compositional zoning (forming by crystallisation pulses and growth phases; Ewart, 1971; Breitkreuz, 2013), sector zoning and lattice constraints within spherulites (Shtukenberg et al., 2012). This has been observed in this study in samples, including in the Rocche Rosse obsidian. The stress created by both spherulite nucleation and that acting due to lava flow emplacement modifies the "ideal" spherulite shape from spherical to elongate. In zones of high strain, such as at flow margins or where individual flow lobes overlap, spherulites are completely sheared into 100% spherulitic bands, or flow bands were microlite-rich (which may have occurred due to

flow-induced crystallisation), which became spherulite-rich due to microlites acting as spherulite nuclei (Figs. 3.2d; 3.3h). There is also clear evidence for spherulites nucleating and growing within brittle fractures, such as conjugate fractures (see Fig. 3.6v) and tension gashes. This suggests that spherulites have preferentially nucleated in these fractures while the flow is behaving in a brittle manner, i.e. below T_g in localised regions of flow or due to high strain rate, as a response to deformation. This indicates that deformation-induced spherulite formation can occur across T_g.

3.9.2 Compositional variations in spherulites and obsidian glass

Spherulite mineralogy, composition and compositional gradients surrounding spherulites preserve a record of the thermal history of obsidian lavas, which may yield information on how spherulites form (Lofgren 1971b; Fenn, 1977; Swanson, 1977; Castro et al., 2008; Watkins et al., 2008; Castro et al., 2009; Gardner et al., 2012; Clay et al., 2013; von Aulock et al., 2013). The presence of α-cristobalite (tetrahedral, low temperature phase) and β-cristobalite (isometric, high temperature phase) within spherulites, for instance, is important for the temperature range in which spherulites form, and glass within spherulites may indicate growth processes (see later). Processes of nucleation, growth and modification of spherulites are also preserved in chemical heterogeneities in the glass surrounding spherulites.

Major element analyses show that spherulites contain a silica polymorph and alkali feldspar (in agreement with XRD results presented for the Rocche Rosse lava flow by Clay et al., 2013). Spherulites often show internal zonation, with a skeletal pattern dominating, often accompanied by a radial texture. Element maps show that Si concentrates within

small crystallites, and within cracks or fractures (Fig. 3.11). High Fe content reflects the presence of an oxide phase within the spherulite, often branching out from the centre, but also occurring as small tabular crystallites (typically <10 μm). Fe and Ca pockets also represent a minor pyroxene phase. Spherulite EMP results also suggest the presence of glass (rhyolitic in composition) within spherulites (see mixing trend Harker diagrams; Fig. 3.10). The presence of glass within spherulites is reported elsewhere (e.g. Richnow, 1999; Ryabov and Grib, 2005; Castro et al., 2008; 2009; Seaman et al., 2009; Gardner et al., 2012). Richnow (1999) reported the presence of glass within spherulites from Ngongotaha Dome (New Zealand), occupying pore space not taken up by silica polymorphs. Ryabov and Grib (2005) identified spherulites of alumosilicic glass, calcite, plagioclase feldspar, mica and amphibole within dykes in the Kamen' alkali mafic province (northern Siberia). Castro et al., (2008; 2009) cite interstitial glass as part of the compositions of spherulites from Icelandic obsidian samples. Seaman et al. (2009) identify rhyolitic glass within spherulites of the Sycamore Canyon lava flow (Arizona, USA). Gardner et al., (2012) describe incompatible elements becoming trapped in the interstitial regions of glass within spherulites from Tequila volcano (Mexico). Seaman et al. (2009) state that large spherulites in their study of the Sycamore Canyon lava flow are mostly glass, possibly a result of devitrification of radiating feldspar crystals. Seaman et al. (2009) conclude that the preservation of glass within spherulites highlights the critical influence of water concentration on the likelihood of quenching versus crystallisation during undercooling of a melt. Sanidine growth in spherulites may have increased water concentration surrounding the growing needle, resulting in local depolymerisation of the melt, lowering of the liquidus of feldspar to the extent that crystallisation of even skeletal crystals is impossible, and quenched glass is formed within the spherulite. Rinds of sanidine crystals and glass may preserve changes in cooling rate of the magma, with the glassy zones containing more

water than sanidine because the glass, responding to more rapid undercooling, overgrew the boundary layer at the tips of the sanidine crystals, where water rejected by the crystals accumulated (Seaman et al., 2009). Richnow (1999) also suggests that the presence of glass within spherulites is an indicator of incomplete crystallisation and spherulite formation above T_g temperatures.

Element maps also sometimes reveal a K depletion and Al enrichment within the spherulite relative to the glassy matrix, and a surrounding rim (typically up to 1 mm in thickness) depleted in Si, Al and K relative to the glassy matrix. However, the surrounding rim also occasionally shows an enrichment of Si and K in some examples, and a thin halo (~1 μm thick) immediately surrounding the spherulite enriched in Si and K. High concentrations of Si at the inner edge of spherulites (creating an internal concentric zonation) and within cracks may represent a later vapour-phase infilling event (Damby et al., 2014; Horwell et al., 2010, 2013, 2014). This is indicated by a surrounding colourless halo with a crystalline interior (e.g. Fig. 3.11c). Following initial spherulite growth, cavities at the interface of the spherulite and surrounding melt may open out, which may act as a nucleation surface for a second phase of crystallisation (Breitkreuz, 2013). Where the surrounding halo does not show a crystalline interior, the surrounding colourless halo may be enriched in OH groups and depleted in ferric iron, produced by a redox front (driven by magnetite crystallisation) that originated from the spherulite margin (Castro et al., 2009). When spherulites begin to form, high-temperature components are incorporated into the crystalline structure. Low-temperature components which are rejected at the crystal-melt interface, assisted by a low diffusion rate, form an impurity layer (Keith and Padden; 1963; Lofgren, 1971b). This impurity layer may be identifiable in Aeolian Islands obsidian samples as the surrounding colourless halo or brown rim evident across all lava bodies. Castro et al. (2009) attribute these brown rims to a solid state redox shift, which grow while the spherulite is also

growing. Gardner et al. (2012) also identify compositional gradients surrounding spherulites, a result of expulsion and slow diffusion of incompatible constituents (H_2O, Rb, and F) away from the spherulite. Generally, obsidian shows relative enrichment or depletion of major element constituents compared to the brown rims surrounding spherulites, and the brown rim also shows enrichment or depletion of elements compared to the interior of spherulites. The relative enrichment and depletion of the brown rims compared to the glass and spherulites indicates that major elements (Si and K) are being used from the glass in spherulite growth. This enrichment and depletion differs across lava bodies. For instance, the Pietre Cotte and dacitic Falcone lavas show Si depletion and alkali (Na and K) enrichment in the brown rim. This indicates that these lavas are using Si from the glass for spherulite growth (crystallising as pure SiO_2 and alkali feldspar), and excess alkali elements are being expelled from the growing spherulitic phase. However, the Rocche Rosse, Falcone (rhyolite) and, to a lesser extent, the Pomiciazzo lavas show Si and Na enrichment in the brown rims, and K depletion. This indicates that excess Si is not being incorporated by the growing spherulite, while K is being used from the glass for spherulite growth (for alkali feldspar crystallisation). Here, and in previous studies (e.g. Morse et al., 1932; Swanson et al., 1989; Breitkreuz, 2001), spherulite growth is considered to initiate while lava is in a highly viscous or rigid state, suggesting that this fractionation of major elements (in particular, alkali elements and Si) is the result of sub-solidus diffusion, occurring in localised areas, i.e. at the edge of growing spherulites with the co-existing glass, resulting in brown rims at the edges and not affecting the bulk composition of the obsidian glass.

As well as composition, spherulite formation is strongly dependent upon other properties. For instance, degree of polymerisation (linked to temperature) is an important property which affects spherulite formation, with a higher degree of polymerisation hindering

phenocryst growth, but promoting spherulite formation (crystallisation kinematics favouring crystallographic orientation and chain crystal structures; see also Keith and Padden, 1963; 1964a, b). Raman spectroscopy provides an opportunity to assess the degree of polymerisation, as well as presence of crystals, in obsidian lava samples. The structure of obsidian glass consists of silicate (or aluminosilicate) tetrahedra linked by network-modifying cations. Significant peaks and broad trend Raman responses are summarised in Table 3.8.

Table 3.8: Summary of common/significant peaks and broad trends identified in Raman spectroscopy.

Raman peak/trend	**Sample spot position**	**Related to**	**Comments/refs**
Broad region - 400-650 cm^{-1}	Glassy groundmass and brown rims	Stretch-bend mixed vibrational motions of bridging oxygen, across the Si-O-Si banded network structure	Observed in other studies of synthetic and natural glass (e.g. Galeener, 1979; Sharma et al., 1983; White and Minser, 1984; Matson et al., 1986; Bellot-Gurlet et al., 2004)
Peak at ~460 cm^{-1}	Glassy groundmass and within spherulites	Crystalline SiO_2, i.e. quartz, typically 464 cm^{-1}	White and Minser, 1984; Matson et al., 1986
Peak at 510 cm^{-1}	Glassy groundmass and within spherulites	Alkali feldspar	White and Minser, 1984; Matson et al., 1986
Minor peaks between 430 and 460 cm^{-1}, 490-495 cm^{-1} and 510-620 cm^{-1}.	Glassy groundmass	Symmetrical stretch-bend vibrations of bridging oxygens and the vibrational mode of tetrahedral structures, decrease from ~430 cm^{-1}, attributed to alkalis being added to the system	Galeener, 1979; Sharma et al., 1983; White and Minser, 1984; Matson et al., 1986; Bellot-Gurlet et al., 2004

Raman peak/trend	Sample spot position	Related to	Comments/refs
Peak at ~583 cm^{-1}	Predominantly present in spherulites and glassy groundmass	Plagioclase (favoured) Olivine Ca-rich sulphides	Chopelas, 1990; Reynard et al., 1999; Fritz et al., 2005; Avril et al., 2013
Peak at 230 cm^{-1}	Predominantly present in spherulites and glassy groundmass	Cristobalite (typically 229 cm^{-1})	Kingma and Hemley, 1994
Peak at 300 cm^{-1}	Predominantly present in spherulites and glassy groundmass	Cristobalite (typically 303 cm^{-1})	Kingma and Hemley, 1994

In the glassy groundmass and brown rims, the Raman LF region (400-650 cm^{-1}) is interpreted as a response to stretch-bend mixed vibrational motions of bridging oxygen, across the Si-O-Si banded network structure. Such Raman features have been observed in other studies of synthetic and natural glass (e.g. Galeener, 1979; Sharma et al., 1983; White and Minser, 1984; Matson et al., 1986; Bellot-Gurlet et al., 2004). The spectral position of this LF region associated with stretch-bend mixed vibration across Si-O-Si bridging bonds varies due to a number of factors. The position varies with various degrees of depolymerisation of the network (combination of monomers to form a polymer), Si-O-Si bridging bond angle, glass composition, conditions of glass formation and thermal history (Mysen et al., 1982; Bellot-Gurlet et al., 2004). The nature of the Raman band is also a function of the type of vibration, scattering geometry and optical properties of the detection system (Mysen et al., 1982). Degree of depolymerisation has a key influence on the Raman spectrum; hence, spectra vary systematically from basalt to rhyolite (increasing SiO_2 content and increasing polymerisation from basalt to rhyolite result in increase in viscosity).

The presence of crystalline material within the glassy groundmass may act as nucleation points for spherulites. The peak at ~460 cm^{-1} may indicate crystalline SiO_2 (i.e. quartz, typically 464 cm^{-1}), and the peak at 510 cm^{-1} suggests the presence of alkali feldspar. The LF region associated with the silica framework gradually decreases from ~430 cm^{-1}, attributed to alkalis being added to the system, a common feature in glass network-forming tetrahedra, and evident in EMP results (high alkali content). Sampled obsidian is rich in aluminium (up to 19 wt%), and increased alumina content results in a decrease in spectral intensity and wavenumber (White and Minser, 1984; Matson et al., 1986). The second prominent feature of the glassy groundmass, brown rims and crystalline features Raman spectra are the humped HF regions, 1200-1800 cm^{-1}. The first suggestion for the origin of this HF region is luminescence, i.e. the result of electronic transitions associated with transition metals present in obsidian (e.g. Ti, Mn, Fe). The luminescence feature originates from an absorption/emission process between different electronic energy levels in the material as a response to illumination by laser. This feature has been observed in a similar region before (spanning from 2100 cm^{-1} to 1150 cm^{-1}; Kelloway et al., 2010), and may mask weak Si-O modes in the HF region. Alternatively, as previously mentioned, Raman position may be affected by a number of parameters, including degree of depolymerisation, bonding angle and composition. The humped HF region could represent a shift of symmetric and anti-symmetric stretching vibrations of silica tetrahedra, with varying numbers (one to four) of non-bridging oxygen ions. This feature is commonly observed between 800 cm^{-1} and 1200 cm^{-1} (Brawer and White, 1975; Verweij, 1979; Furukawa and White, 1980; Mysen et al., 1982; White and Minser, 1984; Shimoda et al., 2004), but appears to be absent in the Lipari and Vulcano obsidian samples in this study. A third option for the observed hump at ~1200 cm^{-1} is a band developed in response to two six-membered, interconnected rings in the three-dimensional network structure (Mysen et al.,

1982). The favoured suggestion is that the hump originates from a shift of symmetric and anti-symmetric stretching vibrations of silica tetrahedral. The differences in geochemistry and glass structure across obsidian samples result in a shift in Raman position towards the HF region (Mysen et al., 1982; White and Minser, 1984; Shimoda et al., 2004). All Raman spectra show a sharp peak at ~583 cm^{-1}. This peak has been previously reported to be a response to olivine (Chopelas, 1990), plagioclase (Reynard et al., 1999; Fritz et al., 2005) and Ca-rich sulphides (Avril et al., 2013). Petrographic observations suggest that this peak likely represents the presence of olivine (enclave-derived) or plagioclase. The consistency of this peak throughout the spectra means that plagioclase is the favoured suggestion of the origin of this peak, as plagioclase is more abundant in the sampled obsidian lavas as both a phenocryst and microlite. The peak may be a response of shock-induced deformation of the plagioclase lattice (Fritz et al., 2005).

Structures with four-membered SiO_4 rings (feldspars) are evident above 500 cm^{-1}, and six-membered rings (quartz and cristobalite) below 480 cm^{-1}. The four main identified phases within spherulites are cristobalite, alkali feldspar, amorphous glass and titanomagnetite. The crystalline phases manifest as fibrous aggregate intergrowths, with an intricate skeletal interlocking structure. These spherulites were likely to begin forming early, at high temperatures, with high temperature β-cristobalite (observed in XRD peaks) converting to low temperature α-cristobalite (in some instances, incomplete conversion resulting in both α- and β- cristobalite), with quartz also crystallising at lower temperatures. As previously stated, Richnow (1999) suggests that the presence of glass within spherulites is an indicator of incomplete crystallisation and spherulite formation above T_g temperatures. The β-α cristobalite transition occurs in the metastable temperature range (~270-250°C), but the precise temperature transition can be altered by the presence of defects such as chemical impurities (Swainson and Dove, 1995). Variations in the intensity and shift of peaks in the

clear surrounding haloes results may suggest some degree of compositional variation (evident in EMP results), and may relate to different processes forming the haloes (e.g. secondary crystallisation infilling (Breitkreuz, 2013), or Fe-redox shift (Castro et al., 2009)).

Microscopic observations indicate that the spherulites in the selected lavas are multi-component, with at least 2 crystal phases identified as regular intergrowth patterns. These phases are ~2-3 microns in length, making it difficult to analyse individual phases by means of electron microprobe. Therefore, XRD provides a practical means of identifying individual crystal phases within spherulites. Crystalline material is defined and characterised by an ordered arrangement of atoms. Such atoms are a periodic array of coherent scatterers, diffracting (bending) x-rays at angles specific to the crystal structure and planes. Therefore, the unique diffraction pattern provides information on the atomic structure within the crystal, therefore allowing the crystal to be identified. The angle at which the x-rays are diffracted is known as the angle of incidence (θ), and the angle of diffraction is the sum of these two angles (2θ). X-ray diffractometers convert these signals in to peaks, used here to identify crystal phases. Glass contributes an amorphous "hump" to the diffraction pattern (background fit), but does not affect the position of crystalline peaks. This response is due to the structural properties of glass, i.e. the lack of long-range order, a random diffraction response and therefore a continuous ("humped") diffraction pattern (Warren, 1934; Leadbetter and Wright, 1972; Wright, 1994).

XRD results suggest that the observed intergrowth texture represents the two main crystal phases: α-cristobalite and orthoclase feldspar. There is also evidence for diopside and magnetite (often forming elongate fibres which define the radial spherulite texture observed under the microscope), as well as an amorphous glass overprint (indicated by a negative linear trend). There are two forms of cristobalite framework, a high temperature

cubic form (β-cristobalite), and a tetragonal form which occurs below 270-250°C (Wright and Leadbetter, 1975; Downs and Palmer, 1994). This β-α transition occurs due to rapid cooling, and any β-cristobalite preserved in the final cooled product occurs when the crystal is fixed in a matrix, preventing strain and the transition of the crystal shape (Downs and Palmer, 1994). The presence of high temperature β-cristobalite suggests that spherulites were forming at least higher than the β-α temperature transition (~270-250°C; Wright and Leadbetter, 1975; Downs and Palmer, 1994; Swainson and Dove, 1994), as a quench phenomenon (Ewart, 1971).

Spherulite and glass composition, as well as glass structural properties, are important as they can provide insights into spherulite formation, growth and modification. Spherulites show distinct compositional variations across, and within, individual lavas. However, a number of key features are common across the Aeolian Islands spherulites. Generally, spherulites contain α- and/or β-cristobalite, orthoclase, titanomagnetite, diopside and glass (evident from EMP, XRD and Raman applications). Some spherulites show K and Al enrichment, with depletion of K and Al in the surrounding rim and occasional evidence of Si and K rim enrichment, potentially a result of sub-solidus diffusion (Castro et al., 2009; Gardner et al., 2012). The presence of glass in spherulites is an indicator of incomplete crystallisation. The obsidian glass shows evidence for vibrational instabilities, evidence for differences in geochemistry, degree of polymerisation and glass structure across samples. The obsidian samples also host crystalline phases (cristobalite, orthoclase and titanomagnetite), which may act as nucleation points for spherulites. The presence of α- and β-cristobalite shows that spherulites were modifying at ~250-270°C as a result of quenching.

3.9.3 Spherulite CSD classification of Aeolian Islands lavas

The CSD theory was developed in chemical engineering (Randolf and Larson, 1971), and can be applied in an igneous context in order to elucidate crystal growth rates, nucleation rates, undercooling and magma residence times (Marsh, 1998; Higgins, 2006). A CSD plot is expressed as number density of a population (amount per unit volume), with sizes expressed as mean, modal or maximum sizes (from longest horizontal dimension) (Higgins, 2006). Simple crystallisation leads to a log-linear CSD plot, as a result of constant nucleation and growth (Marsh, 1998). Kinking of the slope has been attributed to modification of crystal populations, such as crystal accumulation or removal (Marsh, 1998), compaction (Boorman et al., 2004), mixing (Jerram et al., 2003) and Ostwald ripening (Boorman et al., 2004). The CSD theory has been applied in this study in order to identify individual spherulite nucleation and growth events that might result in unique spherulite populations. Applying this methodology to spherulites has the potential to show evidence of differing intensities of deformation affecting spherulites within a lava body. Clay et al., (2013) demonstrate the usefulness of applying the CSD methodology to spherulitic samples from the Rocche Rosse lava flow.

Overall negative slope indicates a similar nucleation and growth relationship to that exhibited in conventional crystallisation magmatic systems. Generally, CSD plots across lava bodies show kinked profiles. The upward kinking profile of the CSD plots indicates increasing heterogeneous spherulite nucleation, e.g. faster or denser spherulite nucleation at a later stage. In some instances, there is evidence for a downturn at the smaller spherulite sizes (e.g. selected Rocche Rosse samples, Forgia Vecchia, Pomiciazzo, Capo Rosso and Falcone samples), while the Pietre Cotte sample shows a steep, short regression at lower sizes. This downturn has been previously attributed the effects of resolution (e.g. Pickering

et al., 1995; Armienti and Tarquini, 2002). However, this is an effect more associated with the applications of CSDs to conventional crystalline systems, and petrographic observations suggest that spherulites do not occur below the resolution limit, and smaller spherulites are optically distinct compared to larger spherulites. Some plots show a shallowing upward-inflection at higher spherulite sizes (e.g. selected Rocche Rosse samples, Forgia Vecchia, Pomiciazzo, Capo Rosso, Monte Giardina, Falcone samples), whilst Castello and Punta di Costa dome samples show a relative log-linear slope. In conventional crystalline systems, an upward inflection (curved CSD) suggests, for instance, accumulation by gravity and a cumulate texture (i.e. large crystals preferentially removed from melt) (Marsh, 1988, 1998; Higgins, 2002). For spherulites, the upward inflection suggests a clustering or coalescence of large spherulites, the result of localised high nucleation rates and/or the product of increasing devitrification. Curvature of the CSD slopes may also suggest the presence of two or more separate (superimposed) slopes. In conventional primary magmatic systems, these kinks may represent a number of magmatic features, such as magma mixing, resorption, fractionation, compaction or fragmentation (Marsh, 1988; Higgins, 2006). Spherulites mainly form due to undercooling and devitrification, so many of these magmatic processes are not appropriate. Instead, such kinks and distinct slopes are likely to reflect individual spherulite populations, nucleating and growing at different times and at different rates. This results in texturally heterogeneous spherulite populations within an obsidian lava flow or dome.

The Pietre Cotte CSD plot shows slope deviation in the lower spherulite size range (<0.2 mm), followed by a steady linear regression to the largest spherulites (1 mm). This indicates two separate spherulite populations – a population of smaller spherulites, and a higher population of larger spherulites. Forgia Vecchia, Pomiciazzo and Capo Rosso domes show a similar CSD slope trend to each other, with a left-hand downturn and a

continuous regression to the larger sizes. This shows that the lava bodies have a lower population of smaller spherulites and a higher population of the largest spherulites. The Falcone lava dome exhibits as many as 3 distinct slopes and, therefore, individual populations of spherulites. The Monte Giardina and Pomiciazzo lavas also show distinct populations of larger (>2 mm) spherulites. In these older domes, there may also be some re-crystallisation of older spherulites (lithophysae). Lithophysae are sub-spherical masses that form in rhyolitic lavas and compacted tuffs, composed of concentric shells of fine-grained silica polymorphs and alkali feldspar separated by empty spaces (Tyrrell, 1926; Kshirsagar et al., 2012). A population of larger spherulites is also indicated in the CSD by the kinked upturn at larger sizes, the result of high nucleation rates. This shallowing of the regression slope is also evident in the older Monte Giardina and Falcone domes.

The extensively sampled Rocche Rosse lava flow shows a range of slope trends, the most common being that similar to the Forgia Vecchia, Pomiciazzo and Capo Rosso lavas, i.e. a left-hand downturn followed by a more continuous regression to larger spherulite sizes. Plots are more complex at smaller sizes. This again indicates a population of smaller and larger spherulites. Later-stage vapour-phase crystallisation has overprinted or re-crystallised earlier formed spherulites, evident by lithophysal textures with an original spherulite in the centre, resulting in a greater population density of larger spherulites. Castello and Punta di Costa lavas show a simple log-linear regression slope. This indicates a single nucleation event, likely to be the result of constant undercooling (i.e. the liquidus and magmatic temperatures vary at the same rate; Clay et al., 2013). The Castello spherulite CSD shows a perfect straight-line regression (Fig. 3.15g). This has been attributed to enhanced undercooling (increasing linearly) in conventional crystalline systems (e.g. crystallisation conditions of anorthosite investigated by Higgins, 1998). As enhanced undercooling due to cooling and degassing may produce spherulites in silicate

melts, the Castello spherulite CSD can be interpreted as the result of enhanced undercooling with the undercooling of the rhyolite increasing linearly. During the period of enhanced undercooling, the growth rate of spherulites within the Castello lava dome was the same, independent of size. Other domes show a similar linear trend, with minor kinks (e.g. Punta di Costa (Fig 3.15h), Monte Giardina (Fig. 3.15i)), suggesting enhanced undercooling may have played a significant role in the formation of spherulites in these lavas, with later spherulite modification (e.g. coarsening with devitrification, increased nucleation with deformation) resulting in a kinked CSD profile. Using this model, the upturn at larger spherulite sizes in the spherulite CSD plots of the Pomiciazzo (Fig. 3.15e), Capo Rosso (Fig. 3.15f), Monte Giardina (Fig. 3.15i) and Falcone (rhyolite) (Fig. 3.15k) lavas may indicate spherulite coarsening, resulting from cavity infilling (vapour-phase secondary crystallisation) and late-stage devitrification. These domes are amongst the oldest sampled obsidian lavas, meaning they have more time for devitrification and spherulite modification processes. As previously mentioned, the Castello lava dome spherulite CSD plot shows evidence for enhanced undercooling at a constant rate. The majority of CSD plots show a kinked regression with a distinct population of smaller spherulites, suggesting multiple nucleation and growth events, and spherulite modification is common in the majority of sampled flows and domes.

CSD plots in a spherulite context may be used to decipher nucleation processes and spherulite modification. For instance, a straight-line regression is attributed to enhanced undercooling (increasing linearly) in conventional crystalline systems (Marsh 1998; Higgins, 1998; 2006), but it can still be attributed to enhanced undercooling as a nucleation stimulus for spherulites (Fig. 3.19a). Kinks in spherulite CSDs may suggest individual spherulite populations. This results from different nucleation events (e.g. deformational trigger) with differing growth rates to spherulites growing as a result of enhanced

undercooling (Fig. 3.19b). Left hand truncation is a common feature in the spherulite CSD plots. This truncation represents a distinct population of small spherulites (Fig. 3.19c). Though it is difficult to identify the nucleation event for certain, this truncation could relate high temperature enhanced undercooling (at a different rate at spherulite growth onset) as suggested by growth theory (resulting in finer spherulites; Lofgren, 1974). Left hand truncation may also represent spherulite nucleation and growth triggered by deformation. The combination of variable degrees of enhanced undercooling, different nucleation events and spherulite modification, as well as a division of smaller and larger spherulites, results in a generalised spherulite CSD plot (Fig. 3.19d), with left hand truncation, a relatively linear regression, and kinks.

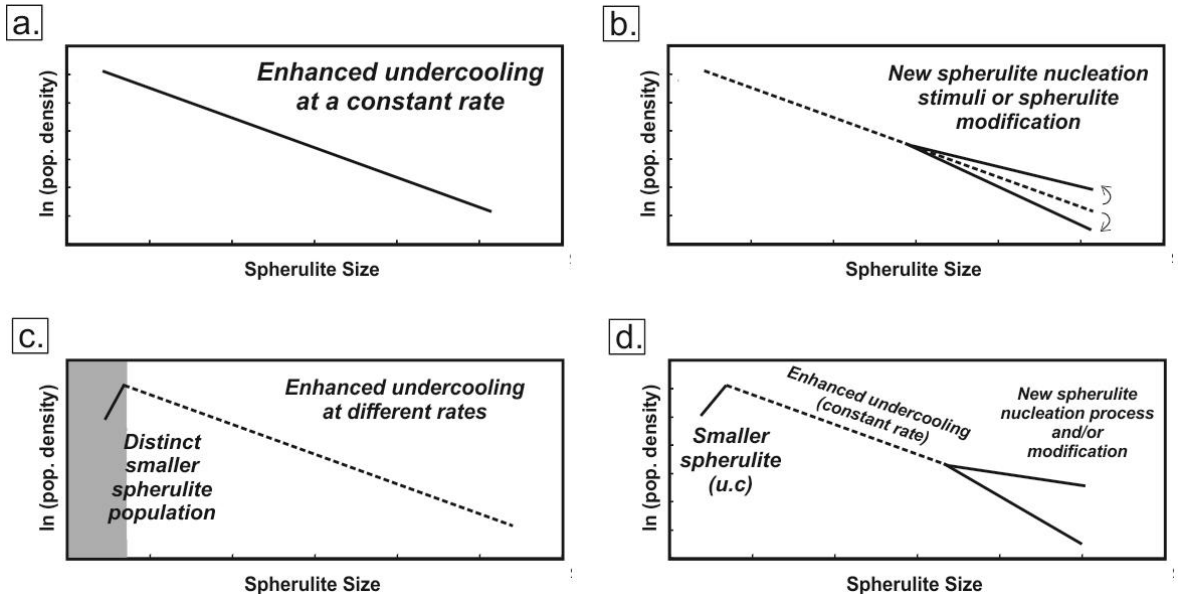

Figure 3.19: Theoretical spherulite CSD plots, based on CSD plots shown in Figs. 3.14 and 3.15, resulting from different nucleation events and modification processes. (a) Spherulite nucleation and growth as a result of a constant rate of enhanced undercooling, producing a straight-line regression. (b) Kinked CSD curve, resulting from different spherulite nucleation stimuli (e.g. deformation-triggered spherulite nucleation), and/or spherulite modification (e.g. re-crystallisation resulting in spherulite coarsening and upward inflection). (c) Sub-division of smaller spherulites, possibly the initial spherulite nucleation onset. (d) Generalised spherulite CSD plot, with a combination of processes.

The growth period of spherulites within obsidian lavas may be important for its effects on the rheological properties of obsidian. Growth of spherulites may lead to the release of latent heat or secondary boiling, leading to a viscosity reduction, vesiculation trigger and may remobilise lava or buffer T_g, allowing for prolonged brittle-ductile deformation (Tuffen et al., 2012). Spherulite CSDs were also used to calculate spherulite growth period in the obsidian domes. Growth period was calculated using the CSD slope value (calculated using *Microsoft Excel* using an interpolated trend line, see Table 3.6), and assuming a constant spherulite growth rate of 6.33×10^{-7} m s^{-1} (calculated by Castro et al. (2008) in obsidian using water concentration profiles). This growth rate has been applied as a constant for broad estimations of spherulite growth periods. However, other studies use different growth rates, suited to a particular suite and study purpose. For instance, Gardner et al. (2012) apply a growth rate at nucleation of 0.25 μm h^{-1}, based on volumetric growth, growth laws and the assumption that spherulite growth is controlled by temperature. Watkins et al. (2008) apply a diffusion-controlled growth model, and show that a spherulite of 2.6 mm requires ~300 days at 800°C, ~10 years at 600°C, or ~300 years at 400°C. The equation for calculating growth period is:

Growth period = -1/ (slope value x growth rate)

(Marsh, 1988, 1998)

Diffusion models of water concentration profiles by Castro et al. (2008) suggest that spherulites may grow according to a size-dependent growth mechanism, and individual spherulites may grow at different rates. Spherulites are likely to grow at a different rate in a melt compared to those growing in a semi-solid or solid obsidian state. However, the growth rate calculated by Castro et al. (2008) provides a good estimation of spherulite growth timescales as spherulites are considered to form in a restricted region of melt, which would experience roughly the same cooling rate. The findings of Castro et al. (2008)

are further substantiated by their comparable results with cooling rates of compositionally similar spherulites calculated by Gottsmann and Dingwell (2001b) of ~0.003–0.0006 °C/s, with timescales of ~20–100 h to cool from 850–650°C. Despite these substantiations, it should still be noted that the growth rate results better reflect spherulite growth from primary crystallisation processes (enhanced undercooling) or as a result of flow deformation at high T_g temperatures. Further support for calculated growth timescales in this study being applicable to high temperature spherulites only is provided by Ar–Ar geochronometry by Clay et al. (2013), with comparable estimated growth rates. Timescale of spherulite formation for the Rocche Rosse lava flow has been previously estimated at ~4 days at high temperatures (≥800°C), comparable to the timescales calculated here (Clay et al., 2013). Spherulite growth at lower temperatures (low or below T_g) is likely to occur on a slower timescale due to the static positioning and rigidity of molecules, atoms and ions in solid materials. Growth below 400°C is also considered prohibitively slow (Clay et al., 2013). Re-crystallisation or modification of spherulites may take place for up to ~400 years (Clay et al., 2013). For this reason, spherulites showing modification textures (e.g. infilled surrounding rim or cavities), a non-radial or lithophysal texture were excluded from growth period calculations.

Growth periods across flows and domes range from 2 days up to 12 days. The average growth period for spherulites in the Rocche Rosse lava flow is 8 days, with a range of 3 days to 13 days. Two Rocche Rosse samples (sample 96 – 3 days; sample 413 – 4 days) give a calculated period that is in relative agreement with the value calculated by Clay et al. (2013) of ~4 days. The Pietre Cotte lava flow exhibits both the smallest spherulites and the lowest growth period (2 days). The Falcone lava dome has the largest spherulites, but the second longest growth period (7 to 12 days). Sample 398 from the Rocche Rosse lava flow has the longest growth period (14 days), indicating significant variation of spherulite

growth periods within the Rocche Rosse lava flow, which may relate to different nucleation events (e.g. from enhanced undercooling and/or deformation). The Forgia Vecchia lava flow has a growth period of 4 days, while the Pomiciazzo lava flow has a longer growth period of 11 days. Capo Rosso (4-5 days), Castello (4 days) and Punta di Costa (4 days) have relatively comparable growth periods to each other, and the Monte Giardina spherulites grew in 7 days. Growth periods calculated for spherulites range from ~2 days to ~14 days (due to dissection of older domes, which are thicker and cooled more slowly). Generally, younger flows have shorter growth periods, and older domes have longer growth periods. This may be a reflection of the size of spherulites being a function of a constant growth rate. However, spherulites are likely to grow at a different rate in a melt compared to those growing in a semi-solid or solid obsidian state. Spherulites may also have grown at different rates from different spherulite-forming processes, i.e. spherulites growing at high temperatures as a response to enhanced undercooling, and spherulites nucleating and growing as a result of deformation. Calculated growth periods for older samples may also take into account the effects of late stage infilling phases (Holzhey, 2001). This indicates that growth periods may be a function of time (older samples result in longer growth periods).

As well as growth period, spherulite physical characteristics may also change with the age of the sampled lava body. The average aspect ratio trends (Fig. 3.20) show a general increase in length, width and area with increasing age of the body (with the Pomiciazzo lava flow providing a variance to the trend; spherulites are larger than older samples). In general, length, width and area dimensions increase with older dome samples. Volume proportion shows increasing volume of spherulites with age, with the Castello lava dome volume proportion remarkably higher than other lavas. Sphericity increases in older samples, from slightly elongate to near-spherical. Older domes generally show more

spherical population of spherulites, and the younger Pietre Cotte shows a more bladed, less spherical population. Spherulites may have simultaneously grown and underwent shear-related deformation (e.g. spherulites within close proximity to shear zones), resulting in a stretched shape morphology, with one dimension longer than the others. Spherulites showing a perfect (or near-perfect) 1:1:1 sphericity may have formed at low T_g transition or below T_g (whereby the flow acts in a brittle state and cannot be deformed in a ductile manner, and also potentially overprinting earlier-formed spherulites), or show flow localisation and formed in areas of low strain.

Individual dimensional plots of spherulites (Figs. 3.17-3.18) indicate that the Pietre Cotte spherulites have the most scattered distribution when plotted against each other. This indicates that spherulites within the youngest flow, the Pietre Cotte lava flow, are more deformed than in the other samples. The majority of other sampled lavas show a more linear distribution of individual dimensional comparisons, indicating a more spherical, less deformed profile. This may indicate that these spherulites formed below T_g, when obsidian no longer behaves in a plastic manner, while the majority of spherulites in the Pietre Cotte were forming above or during T_g, allowing for plastic deformation to alter the spherulite shape from spherical to sub-spherical or a stretched profile. This may be related to the high abundance of mingled mafic enclaves within the Pietre Cotte lava flow compared to the other sampled lavas, resulting in, for instance, variable and localised heating.

3.9.4 Spherulite heterogeneity and model for spherulite formation

All flows and domes show the similar broad features of spherulites within a glassy groundmass. As lava cooled, it passed from a liquid-like behaviour to a solid (glass)-like

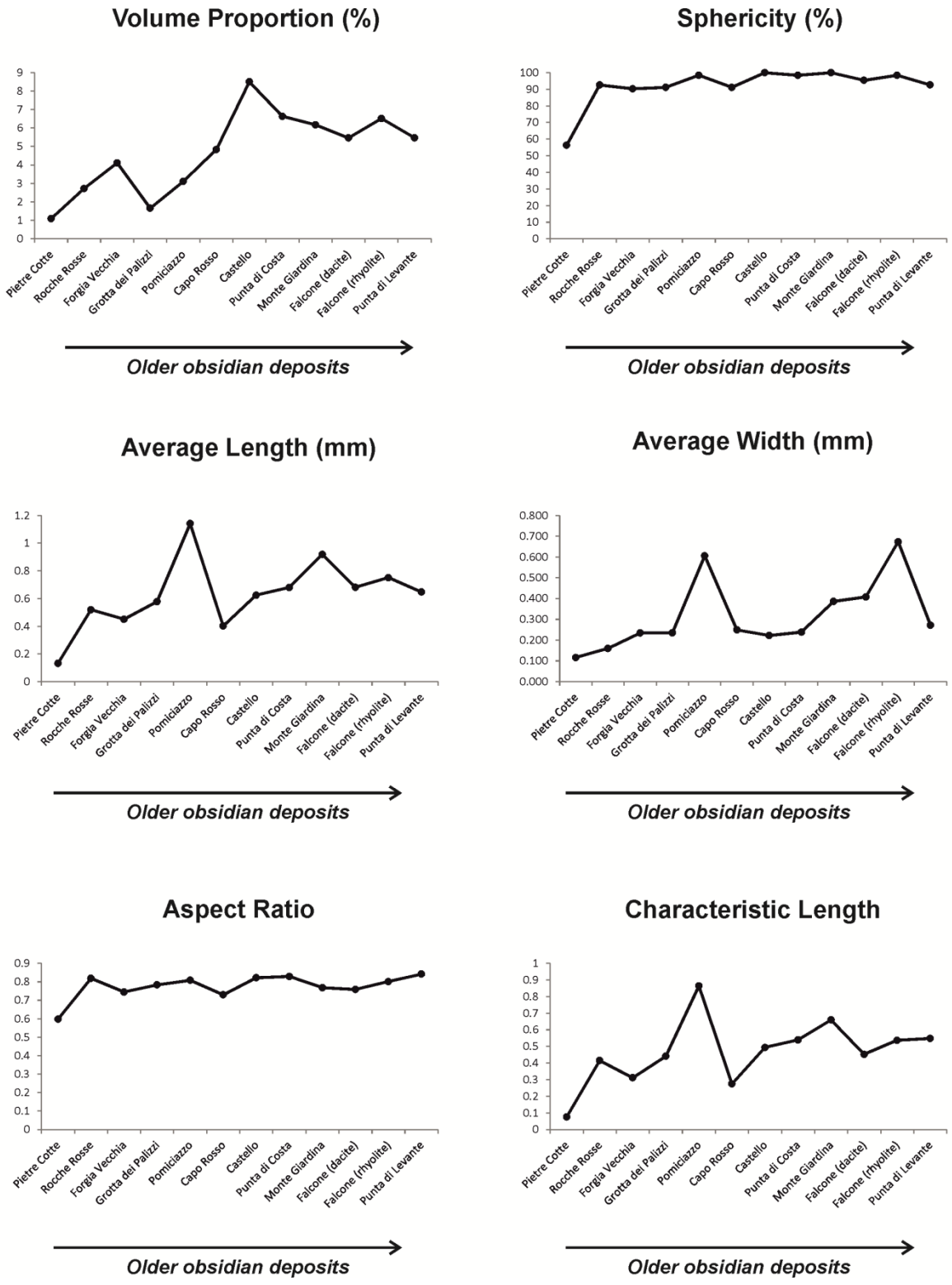

Figure 3.20: Average parameters for each lava body and changing trend through time, indicating that spherulites in the Aeolian Island suite increase in terms of volume, sphericity, and length/width dimensions through time.

behaviour (Gottsmann and Dingwell, 2001b). Nucleation and spherulite formation originally occurred as a response to undercooling, and continued as a down-temperature growth continuum (Clay et al., 2013). Some spherulites show an alignment parallel to flow banding. This may be the result of spherulite growth during a brief period of enhanced undercooling from degassing (resulting in a low population of small spherulites), accentuated by flowage (Davis and McPhie 1995), and supporting the idea that spherulites formed in response to rapid undercooling.

In sampled lavas, microlites grew first and were later overgrown by spherulites. Therefore spherulites formed at lower temperatures than microlite crystallisation. However, many small spherulites sometimes show microlites deflected around them (Fig. 3.6a, d), indicating that spherulites were present when the microlite fabric formed, and therefore spherulites grew at high microlite crystallisation temperatures. Alternatively, microlites may have formed pre- or syn-degassing, with spherulites forming post-degassing but pre-substantial cooling.

Spherulites often show a radial interior, but sometimes show a non-radial skeletal texture, or both textures concentrically zoned. Spherulites with a non-radial interior may reflect a lithophysae texture, whereby cavities and gaps have been later infilled at high to low vapour-phase temperatures. The differing textural observations for larger spherulites (such as those found in the Pomiciazzo obsidian) compared to a more typical spherulite appearance (i.e. lacking the typical radial interior) suggests that these textures may be examples of lithophysae. Lithophysae do not form in the same way as typical spherulites (i.e. outwards from a central nucleus). Instead, lithophysae grow inwards from the outer surface towards the centre of hollows, such as vesicles or hollow spherulites (Von Richthofen, 1860; Iddings, 1887; MacArthur et al., 1998; Breitkreuz, 2001; Smith et al., 2001; Tuffen and Castro, 2009; Kshirsagar et al., 2012). This results in a more mesh-like

(non-radial) microcrystalline texture of silica polymorph and alkali feldspar, either completely filling the hollow, or filling the surrounding cavity around the earlier formed spherulite, resulting in an internal zonation. Spherulites which exhibit a radial centre and non-radial outer zone preserve evidence for both primary spherulite crystallisation (due to enhanced undercooling (Clay et al., 2013)) and lithophysae forming processes. Spherulites are often surrounded by a brown rim, but there are smaller spherulites which do not show this rim. These spherulite rims may have formed within or below T_g as a solid state reaction (Castro et al., 2009). Rim growth ("impurity layer"; Keith and Padden 1963) has been proposed to be driven by volatile loss and localised loss of H_2O and rejection of other "impurities", and changes in Fe-oxidation state (see Keith and Padden; 1963; Lofgren, 1971b; Castro 2008, 2009; Gardner et al., 2012; Clay et al., 2013).

Textural observations, geochemistry and CSD plots suggest that multiple spherulite populations exist across obsidian flows and domes on Lipari and Vulcano. Each population can be classified according to their textural heterogeneity (Figs. 3.21 and 3.22). Initial spherulite nucleation and growth may have been triggered by enhanced undercooling, in a high-temperature bracket above T_g. This results in spherulites with radial interiors (formed due to primary crystallisation). These can be classified as Type 1 spherulites. Type 1 spherulites are comprised of α-cristobalite (converting from high temperature β-cristobalite, which has been identified by XRD, which can still be fixed in the matrix) and orthoclase feldspar, with interstitial glass and minor amounts of titanomagnetite and diopside phases. Microlites form above T_g temperatures, and are therefore affected by high temperature spherulite nucleation and growth. Spherulite nucleation and growth can also be promoted by viscoelastic stresses generated during flow emplacement and deformation. Type 1 spherulites are typically the smallest spherulite types (responsible for left hand truncation in spherulite CSDs); though this size characterisation may not be a key

diagnostic feature of Type 1 spherulites. However, this is tentatively suggested. As degree of undercooling (rate of cooling) increases, spherulites become finer and more compact (based on spherulite growth theory; Lofgren, 1974). Lofgren (1974) found, through isothermal drop experiments in an Ab-An-H_2O system, that there was a progression of spherulite morphology with increased undercooling. Spherulites at low degrees of undercooling are characterised by coarse, open fibre morphology, whilst finer spherulites result from large degrees of undercooling (Lofgren, 1974). This morphological progression is also discussed in other liquid and rhyolitic composition studies (e.g. Lofgren, 1976; Swanson, 1977). This suggests that Type 1 spherulites are typically small as a result of a high degree of undercooling. This is cautiously suggested, however, as spherulite size likely relates to a number of processes acting in a system, both independently and interconnected (e.g. nucleation and growth rate, water concentration, temperature, melt composition, diffusion; Swanson et al., 1989; Castro et al., 2008; Watkins et al., 2009; Gardner et al., 2012; Clay et al., 2013). Spherulites may then continue to form as a result of a constant rate of enhanced undercooling (as suggested by spherulite CSD plots).

The formation of spherulites during emplacement at high T_g transition results in elongate (or completely sheared) spherulites during ductile flow deformation, which are classified here as Type 2 spherulites. The occurrence of isolated, spherical spherulites (larger than Type 1 spherulites), which show a brown rim, suggests that some spherulites may have formed in areas of low strain. These are classified as Type 3 spherulites. Other spherulites grow at temperatures within and below T_g, and concentrate within fractures or bands (deformational trigger), which are classified as Type 4 spherulites. Lithophysal cavities form due to volatile exsolution (Iddings, 1887; Swanson et al., 1989). High-temperature devitrification resulted in spherulite and vesicle modification and an increase in open space due to volume contraction and secondary boiling associated with spherulitic crystallisation

(Iddings, 1887; Swanson et al., 1989). Hollow, partially-hollow, or spherulites containing tensional voids and cavities later become infilled or re-crystallise, resulting in textural and geochemical heterogeneity, including internal spherulite colour zonation and pockets of crystal phases. These are classified as Type 5 spherulites (modification of other spherulite types), and may only partially contain a radial texture (in the centre) or no radial texture at all. These 5 spherulite types form under unique conditions and as a result, exhibit unique spatial occurrence, size, textures and geochemistry. Spherulite types may form concomitantly in different parts of the obsidian lava body, relating to temperature and processes at work (e.g. at higher temperatures in the core of the obsidian lava, as the result of flow-induced crystallisation, see Fig. 3.22). Applying this textural characterisation to the spherulites analysed by EMP, spherulites are more enriched in Si and K in spherulite Types 1 and 2, with the surrounding obsidian glass depleted in Si and K. Type 4 spherulites are more enriched in Al, with the surrounding rim enriched in Si. This indicates that the composition of spherulites and the surrounding melt/glass is altering possibly due to earlier formed spherulites incorporating some major elements and expelling others, possibly differing slightly based on variable geochemistry across lava bodies.

The CSD methodology provides an opportunity to quantify spherulite types. A total of 4261 spherulites were digitised according to their designated type, from samples spanning all sampled lava bodies. Type 3 showed the highest population of spherulites, with more than half of the total spherulites analysed (51.8%). Types 1, 2 and 5 show a similar percentage of the total population (19.3%, 10.1% and 13.4% respectively), and Type 4 was the lowest percentage of the total population (5.3%). Despite Type 3 spherulites having the highest population of spherulites across samples, Type 5 spherulites covered the highest area fraction (43.3%). Types 1 and 4 covered the smallest percentage area fraction (both 3.3%), Type 2 covered 13.3% area fraction and Type 3 covered 36.7% area fraction. These

Type	Microscopic Imagery	Digitized features	Typical Size	Characteristic features	Composition and formation	% of total spherulites	% of total spherulitic area	Typical CSD curve
1	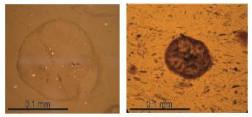	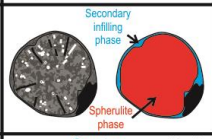	~0.5 mm or smaller	***Radial interior*** (primary spherulitic) Sub-spherical (some slight elongation) Rarely shows clear halo Occssional thin mesh-like texture (secondary modification) Rare brown rim, ***microlites deflected***	***α-β cristobalite transition*** (some β-crist. fixed in matrix), orthoclase, glass, diopside, titanomagnetite Formed by ***enhanced undercooling at high-T temperatures*** above T_g (temperatures similar to microlite crystallisation)	19.3%	3.0%	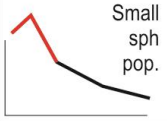
2	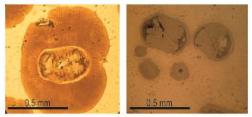	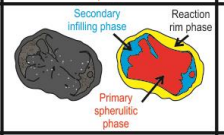	~0.5 mm to 1.5 mm	Vague radial interior (primary spherulitic) ***Elongate shape*** (deformation) Sometimes show clear halo Thin mesh-like texture at edge ***In/close proximity to deformation fabrics*** Brown rim often evident	α cristobalite transition (conversion from β-cristobalite), orthoclase, glass Formed by constant degree of undercooling and ***deformational trigger*** Nucleation during Tg temperatures Zones and pockets of pure crystalline silica	10.2%	13.3%	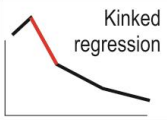
3	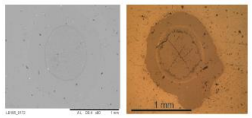	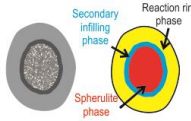	~0.5 mm to 2 mm	Radial interior (primary spherulitic) ***Sub-spherical in zones of low shear*** Sometimes shows clear halo Internal zonation and thin mesh-like texture at edge (secondary modification) Thick brown rim, ***microlites unaffected***	α cristobalite transition (conversion from β-cristobalite), orthoclase, glass Formed by ***constant enhanced undercooling and deformational trigger (low intensity)*** Low to sub-Tg temperatures Zones and pockets of pure crystalline silica	51.9%	39.4%	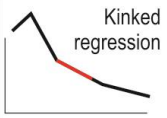
4	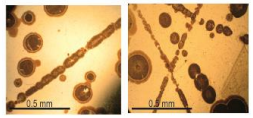	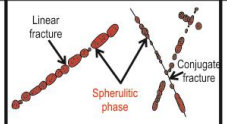	<0.5 mm	Radial interior (primary spherulitic) Sub-spherical, often interjoined No halo or brown rim Relatively consistent internal radial texture and no zonation ***Concentrate within joints and fractures***	α cristobalite, quartz, orthoclase, glass Formed by ***deformation (in the solid state) and preferential nucleation within constrained gaps, cracks, faults and fractures*** Lower temperature (below Tg) nucleation and restricted growth (fracture-controlled)	5.3%	2.8%	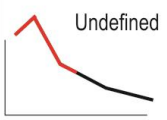
5	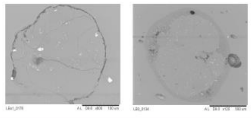	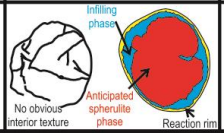	0.5- >1 mm	***Partially radial interior in centre or absent (internal zonation)*** ***Microcrystalline*** internal arrangement Often non-continuous or poorly defined spherulite edge Mesh-like texture evident within interior	α cristobalite, quartz, orthoclase, glass ***Modification of previous Types*** at late-vapour stage temperatures below Tg Texture formed by secondary alteration of spherulites and cavities Otherwise classified as ***Lithophysae***	13.4%	41.7%	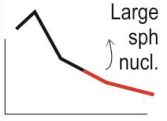

Figure 3.21: Spherulite type classification scheme based on textural characteristics, composition and CSD plots. Five types have been identified, each with a unique history of textural-forming processes. Typical CSD curve indicates position of spherulite type on a typical spherulite CSD plot. Type 1 (high-temperature undercooling) shows a small CSD downturn, indicative of a unique population of small spherulites. Types 2 and 3 (undercooling and flow-induced crystallisation) are typical of sizes ~0.5-1.5 mm, the most common types of spherulite, and result in spherulite CSD kinking. Type 4 (preferentially nucleating in brittle structures) has a less well-defined CSD curve position as the spherulite size is dependent upon the size of the joint or fracture in which the spherulites are able to nucleate and grow. Type 5 spherulites (lithophysae) are the largest spherulite type, and as a result make up the highest percentage of total spherulitic area and force an upward CSD inflection at the higher spherulite sizes.

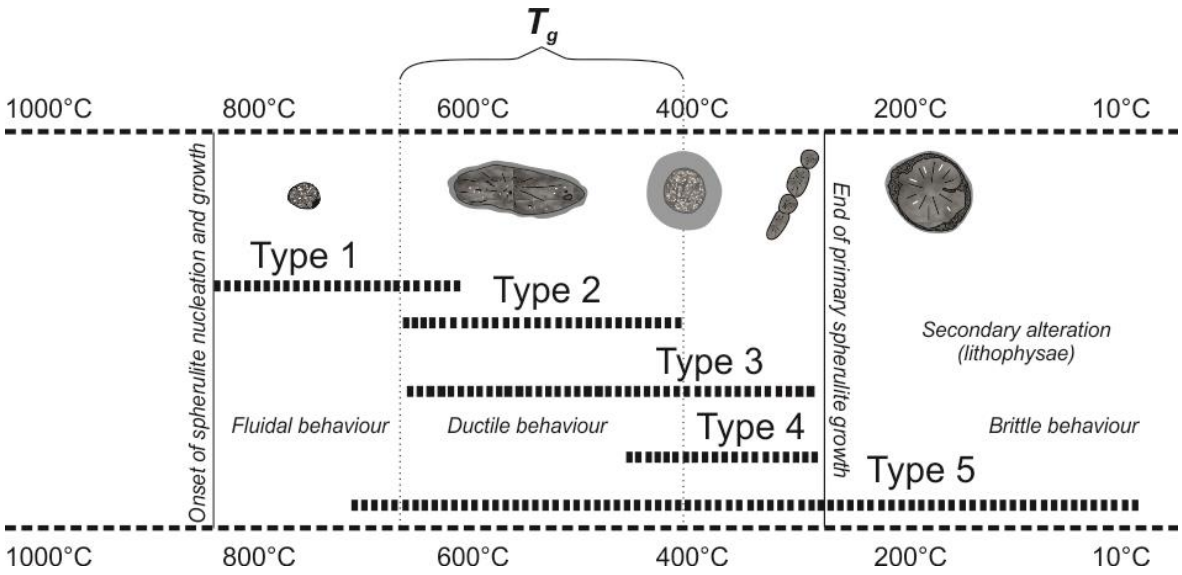

Figure 3.22: Temperature timeline model for the formation of the 5 classified types of spherulites. T_g on the timeline represents the glass transition. Timeline model indicates that spherulite type classification is rheologically controlled rather than time constrained, and spherulite types may form simultaneously in different areas of lava flow/dome (texture process timeline modified from Breitkreuz, 2001 and Wnorowska, 2004).

results show that Types 3 and 5 dominate spherulite populations in obsidian, both in terms of number of spherulites and area (and therefore volume) covered.

Dimensional plots indicate that the Pietre Cotte lava flow hosts relatively deformed spherulites, typical of Types 1 and 2. Radial interior and small size (Type 1) suggests that spherulites may have begun forming due to degassing-driven undercooling at high temperatures. The linear trend at larger spherulite sizes in the older obsidian samples is more akin to Types 3, 4 and 5, forming at low, or below, T_g. Higher volume proportion in older obsidian samples may be the product of exposure, or recrystallisation, modification and devitrification, typical of Type 5 spherulites. Sphericity (and aspect ratio) also increases with age of obsidian lava body, which is also typical of Type 5 spherulites, as well as Type 3. These findings indicate that spherulite Types 3 and 5 are more typical in older obsidian domes, whereas Type 1 spherulites are more typical in younger obsidians.

Petrographic observations support this conclusion, with more lithophysal spherulites evident in older samples, and smaller spherulites in high abundance in Pietre Cotte samples studied here. This occur because older samples are subject to continued modification and recrystallisation as the glass continues to devitrify over time.

Though spherulite formation is a function of processes such as undercooling and deformation, it is unlikely to be fully time constrained. Repeated fracturing and healing of rhyolitic melts have been characterised (Gonnermann and Manga, 2003; Tuffen et al., 2003; Tuffen and Dingwell, 2005), and second boiling or resurgent boiling (separation of a gas from a liquid phase) also occur in rhyolitic melts (Manley and Fink, 1987; Westrich et al., 1988; Sisson and Bacon, 1999; Tuffen et al., 2012) which may re-initiate crystallisation. Therefore, differing spherulite types may nucleate and form simultaneously (Fig. 4.22). As previously stated, rheological properties such as elasticity and temperature are intrinsically linked. For instance, viscosity increases with decreasing temperature. Such rheological parameters will differ across lava flows and domes during and after emplacement. It can therefore be assumed that deformation is intrinsically linked with temperature and different spherulite types form at the same time. In an obsidian flow, for instance, it will be cooler at flow margins and hotter in the centre of the flow. Therefore, spherulites forming via high temperature undercooling in one part of obsidian lava (such as in the hotter core of the flow) do so concomitantly with spherulites forming during T_g in other parts of the lava (by flow-induced crystallisation at margins). Type 5 spherulites, characterised by the filling of cavities and hollows by secondary cristobalite, may occur during and after vapour-activity and fracturing. Such recrystallisation textures may have developed due to primary cooling, and continued to form throughout the cooling history of the lavas (Kneller, 2002). Repeated fracturing and healing also means that Type 4

spherulites cannot be fully time-constrained, but are restricted to areas of flow/dome that are undergoing a brittle flow regime.

3.10 Conclusions

Spherulites from obsidian lavas across the islands of Lipari and Vulcano show a broad range of features, with some variations with age and composition of obsidian lava body sampled. Generally, spherulites are spherical or elongate, contain a radial or non-radial (microcrystalline) interior, with a surrounding thin clear halo (~1 μm thick) and brown rim (up to 10 μm thick). Some spherulites also show pockets of mesh-like crystalline material within the inner spherulite edge. Microlites in the obsidian glass are either unaffected by spherulite presence or deflected around spherulites.

Spatially, spherulites occur individually, often in zones of low shear, or concentrate within bands, folds, faults and fractures (often elongate spherulites concentrate near or within bands and folds). This spatial concentration of spherulites within sheared bands, folds and faults highlights the important role of deformation in the formation of some spherulites in sampled obsidian lavas. Flow-induced crystallisation is well constrained in polymer studies of amorphous and semi-crystalline materials, but is thus far neglected in volcanic glasses. Flow deformation (elongation and shear) may trigger spherulite crystallisation, whereby flow enhances nucleation and triggers the formation of elongate crystals (Graham and Olmsted, 2009), and the entropic penalty for crystallisation is lowered and, therefore, the nucleation rate increases (Keller and Kolnaar, 1997; Coccorullo et al., 2008). This type of spherulite crystallisation may therefore be responsible for deformed spherulites (forming

during deformation), sheared spherulites within bands (formed during deformation), and spherical spherulites concentrated within bands, folds and faults (forming in late stages of, and/or after, deformation).

The composition of spherulites varies across sampled lavas, but commonly contain cristobalite (α and β), orthoclase, minor diopside, titanomagnetite and interstitial glass. The presence of α- and β-cristobalite indicates that spherulites were forming at high temperatures, with α-β cristobalite conversion at ~250-270°C, and the presence of glass suggests incomplete crystallisation. Spherulites are often enriched in Al and K, and rims are often depleted or enriched in K, Al and Si, with variations across lavas. Such variations relate to differing spherulite crystallisation temperatures and variable composition differences across lavas. Diffusion-controlled rejected components form an impurity layer around some spherulites, and gaps and pockets are later filled by SiO_2 (cristobalite). Spherulite CSD plots show an overall trend of a smaller population of spherulites (often complex at lower spherulite sizes <1 mm), and a kinked regression with up to 3 individual slopes. These differences may reflect individual spherulite populations, resulting from different nucleation stimuli and later modification (e.g. re-crystallisation). Small spherulites may have formed earliest as a result of high degrees of undercooling. Largest spherulites may have formed larger sizes due to modification, particularly in older domes with a longer time in which to modify and re-crystallise. Spherulites generally grow from ~2-14 days, but may modify for up to 400 years (Clay et al., 2013).

Based on these observations and interpretations of formation, spherulites can be broadly classified as 5 types. Specifically, this characterisation is based on physical characteristics, spatial distribution, composition and interpretation of nucleation stimuli. Spherulites form across different temperature scales but may form simultaneously in different parts of obsidian from different processes. Spherulite type characterisation is:

- Type 1 spherulites – radial interior, sub-spherical to slight elongate in shape, often small (<1 mm), unaltered by modification, and contain α and β-cristobalite. Microlites are deflected around Type 1 spherulites. Type 1 spherulites form due to high degrees of undercooling at high temperatures (i.e. high T_g or above).
- Type 2 – elongate spherulites, surrounded by a brown rim, show minor alteration, radial interior, and are interpreted as forming due to deformation (tend to form in shear zones) and/or enhanced undercooling.
- Type 3 – Large, radial spherulites, microlites are unaffected and overprinted; tend to form individually in zones of low shear. Type 3 spherulites often show brown rims and clear halos, with minor modification. Type 3 spherulites may form by enhanced undercooling and/or (minor) deformation in low T_g transition or below.
- Type 4 – Spherulites are concentrated within fractures and faults, indicating that these formed during brittle regime. Growth is restricted to faults and fractures.
- Type 5 – partially- or fully-modified spherulites (re-crystallisation) and lithophysae – non-radial interior (microcrystalline), formed by vapour-infilling (low T_g or below), and modifying for long periods of time.

This study provides new results for spherulites in the Aeolian Islands, including EMP data, Raman and XRD spectra and CSD plots. This dataset allowed for the review of spherulite formation in obsidian lavas, the development of CSD applications for spherulite nucleation, growth and modification, and a new classification and timeline model for spherulite types. This study shows that spherulites form due to a number of processes, pre-, syn- and post-flow emplacement, above, during and below T_g. Importantly, deformation may trigger spherulite nucleation, and spherulites may nucleate and grow simultaneously due to different processes.

Chapter 4

Magmatic and post-magmatic history of the Pietre Cotte obsidian lava flow, Vulcano, Aeolian Islands, Italy

Chapter outline

This study provides a new model for the magmatic and post-magmatic processes leading to the development of the texturally-heterogeneous Pietre Cotte obsidian lava flow (Vulcano). The study incorporates a number of petrographic and field observations, structural measurements, glass and mineral compositional data, and thermobarometric methods in order to conceptualise the new model. The pre- and post-extrusive events leading to the final product occur over several stages, creating a number of textures relating to magmatic and post-magmatic evolution. Such textures can be used to assess the relative timing of events, and compositional data can be used in order to quantify intensive variables associated with the Pietre Cotte magmatic system and resultant lava flow.

4.1 Introduction

The Pietre Cotte obsidian lava flow on the northern slope of the Fossa cone (Vulcano, Aeolian Islands, Italy; Fig. 4.1) preserves evidence for several complex stages of pre- and post-eruptive processes. Features which preserve such evidence include widespread mafic enclaves, compositional phenocryst zonation, spherulites and flow deformational structures. Due to its young age (1739 AD - De Fiore, 1922; Keller, 1970; De Astis et al., 2013b) and exceptional exposure, the flow offers an opportunity to reconstruct magmatic and post-magmatic processes which lead to the final solidified lava flow, including crystallisation processes, ascent and eruptive behaviour, flow emplacement mechanisms and post-emplacement modification. Although the magmatic evolution of the Fossa cone is well constrained (e.g. Castellet y Ballarà et al., 1982; Frazzetta et al., 1984b; De Astis et al., 1997; 2013b), currently no model exists that details the story of both pre- and post-extrusive processes, important for a full understanding of the active Fossa magmatic system, eruptive activity and emplacement processes associated with silicic lava flows. At present, only two detailed models exists on the magmatic processes leading to the eruption of the Pietre Cotte lava flow (Perugini et al., 2007; Piochi et al., 2009).

The study of interaction between a felsic and more mafic magma can provide information about the magmatic evolution of a system (e.g. Eichelberger, 1975; Anderson, 1976; Gamble, 1979; Frost and Mahood, 1987; Gioncada et al., 2005; Davì et al., 2009, 2010; Dokukina et al., 2010). Mafic input has the potential to act as an eruption trigger in felsic magma bodies. For instance, the addition of a more mafic magma into a felsic system can cause magma chamber heating or over-pressurisation (e.g. Sparks et al., 1977; Bachmann

and Bergantz, 2003; Pamukcu et al., 2013). As well as the crystallisation and interaction of distinct magma bodies, texture formation and the structural arrangement in silicic lava flows are produced during sequential flow evolution (Fink, 1983; Swanson et al., 1989; Manga, 1998; Castro and Cashman, 1999; Gottsmann and Dingwell, 2001a, b; Tuffen et al., 2013; Clay et al., 2013). For instance, spherulites are considered to progressively nucleate in silicic systems as a down temperature continuum during syn- and post-emplacement cooling (Clay et al., 2013, see also Chapter 3), originally nucleating in response to an enhanced rate of undercooling (Kirkpatrick, 1975; Swanson, 1977; Castro et al., 2009; Clay et al., 2013). Microlite nucleation and growth occurs as a product of rapid isothermal decompression during ascent (Hammer et al., 1999; Cashman and Blundy, 2000; Gonnermann and Manga, 2005; Szramek et al., 2006; Castro et al., 2009). Following extrusion, obsidian lava flow emplacement can take place across both the liquidus (if superheated; Castro et al., 2013) and solidus, progressively deforming (controlled by rheology), resulting in a number of ductile and brittle internal and surface structures. The nature of obsidian lava flow transport and deformation can be inferred from the structures preserved in the rocks (Fink, 1980a, b; Manga, 1998). In this study, petrographic observations, mineral and glass geochemistry, thermobarometry, field observations and structural measurements are combined in order to conceptualise a quantitative sequential process model of the Pietre Cotte lava flow. The study aims to shed light on the magmatic and post-magmatic evolution of the Pietre Cotte obsidian lava flow.

The small volume Pietre Cotte lava flow, which flowed from the active Fossa cone in northern Vulcano (Figs. 4.1 and 4.3), provides an ideal case study for this investigation due to the high abundance of textural variations (Fig. 4.2). The obsidian also preserves mineral assemblages in both mafic enclaves and the rhyolitic host, with some crystals exhibiting disequilibrium textures. Preservation of obsidian glass, olivine, clinopyroxene, plagioclase,

alkali feldspar and titanomagnetite in the Pietre Cotte lava flow allow geochemical analyses of both the rhyolitic host and mafic enclaves to be made, and thermobarometric calculations of multiple distinct magmas crystallising independently prior to mafic-felsic magma interaction to be carried out.

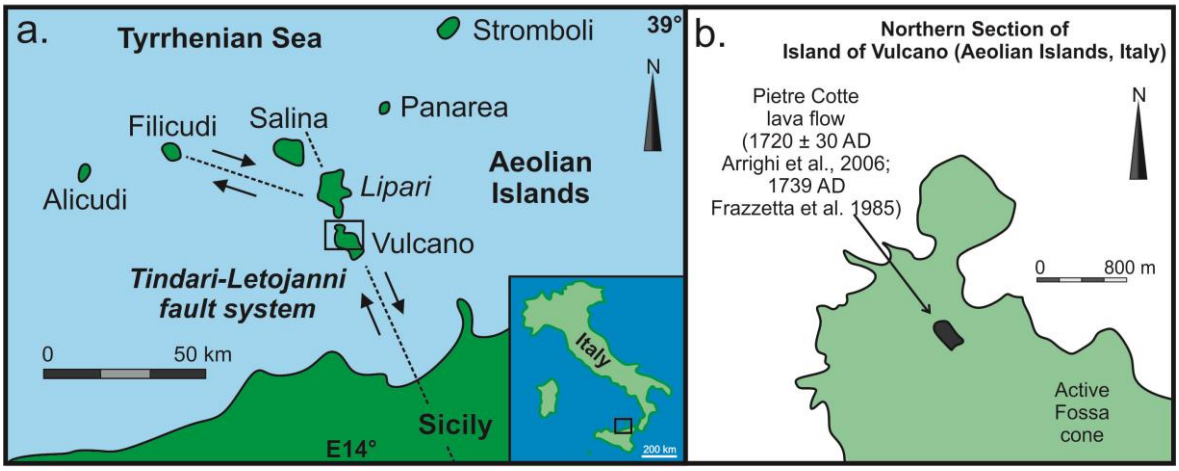

Figure 4.1: (a) Vulcano Island, Aeolian Islands, South Tyrrhenian Sea (Italy), and (b) the Pietre Cotte lava flow on the northern slope of the Fossa cone (After Donato et al., 2006).

Observations suggest a complex relationship between textures, most notably the interaction between a more mafic and felsic magma within the Fossa magmatic system (De Astis et al., 1997; Del Moro et al., 1998; Gioncada et al., 1998; Piochi et al., 2009; 2013). Observations also demonstrate the presence of glomerocrysts in both the mafic magma and the rhyolitic host. This dynamic sequence of events requires a number of thermobarometric applications in order to quantify individual stages of crystallisation.

QUILF thermobarometry provides an opportunity to quantify crystallisation conditions of mafic magma found in the Pietre Cotte obsidian glass, and glomerocrysts within the enclaves and rhyolitic host. *Rhyolite-MELTS* simulations offer crystallisation conditions and a liquidus temperature for the rhyolitic host. The flow is typically spherulitic, and contains abundant microlites and vesicles. Vesicles are often infilled (lithophysal).

Figure 4.2: Characteristic features of the Pietre Cotte lava flow; (a) Field exposure of the Pietre Cotte lava flow, showing foliation planes dipping southerly, and folded foliations. (b) Obsidian containing small spherulites, as well as vesicles (containing fibrous minerals). (c) Abundant mafic enclaves within obsidian host. (d) Mafic enclaves containing large crystals, including plagioclase and pyroxene, as well as olivine, alkali feldspar and titanomagnetite.

The flow is heavily deformed in areas, with multi-scale folds and brittle fractures evident. Deformation is rheologically controlled, as obsidian flows over a large range in rheology, allowing for complex liquid to solid deformation and subsequent structures (Gottsmann and Dingwell, 2001a). These structures were measured and mapped in order to provide insights into flow emplacement mechanisms. Field mapping across the flow was undertaken in order to provide insights into Pietre Cotte eruption and flow emplacement dynamics, necessary in order to fully characterise pre- and post-eruptive flow history.

La Fossa cone successions (Dellino and La Volpe, 1997; De Astis et al., 2006; Piochi et al., 2009)

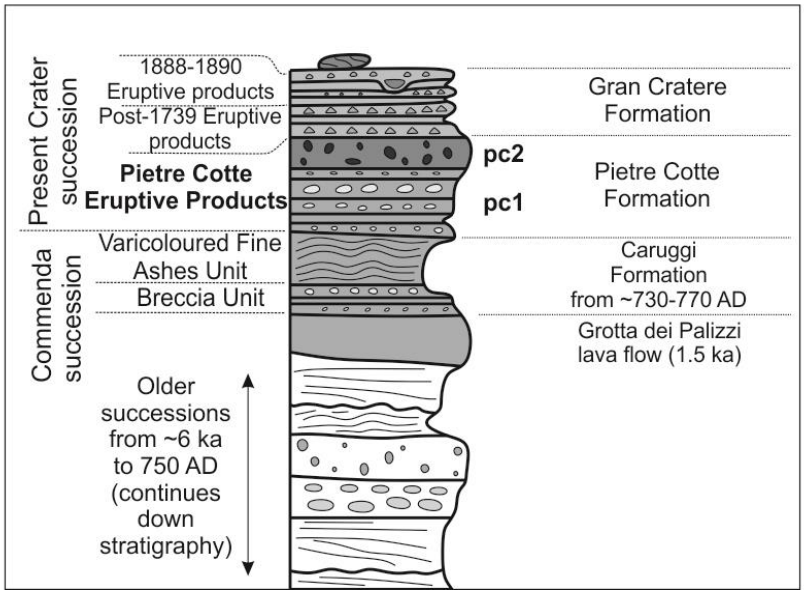

Figure 4.3: Schematic stratigraphic section of La Fossa cone, with the Pietre Cotte sequence subdivided in to pc1 (thinly and plane bedded deposits) and pc2 (Pietre Cotte obsidian lava flow). Majority of stratigraphy consists of pyroclastic products (from Dellino and La Volpe, 1997; De Astis et al., 2006; Piochi et al., 2009).

The nature of obsidian lava flow transport can be inferred from textures and structures preserved in the rocks (Manga, 1998). The structural arrangement of flow foliations preserve a record of deformation associated with flow emplacement (Gonnermann and Manga, 2003), and the analysis of foliation patterns can help to decipher the structural evolution of polyphase-deformed lava flows (e.g. Bastida et al., 1986; Fink, 1980a, b; Forbes et al., 2004; Gregg et al., 1998). Foliation attitude defines the initial configuration of the lava flow, meaning that the final structural arrangement is the product of emplacement and deformational processes.

The observations, results and model presented here provide new quantitative and qualitative information on the systematic evolution of the Pietre Cotte magmatic system and subsequent Pietre Cotte lava flow, including crystallisation conditions and post-extrusive emplacement mechanisms. The new generalised model of magmatic and post-magmatic processes associated with the Pietre Cotte lava flow has been subdivided in to

five stages, including mafic magma crystallisation (with a system temperature of ~1,154°C), trachyte crystallisation (~1,130°C and 853-3,452 bars) and rhyolitic system conditions (~1,033°C at 1-3 km depth), magma mingling, microlite and spherulite formation, flow extrusion and rheologically-controlled flow deformation. These findings place a greater understanding of conditions of crystallisation associated with multiple magmas, applicable to this and other mafic-felsic interaction systems.

4.2 Geological setting

The seven Aeolian Islands form a ring-shaped chain of volcanic islands and seamounts above the south Tyrrhenian subduction zone (Tyrrhenian Sea, southern Italy; Fig. 4.1). The area is tectonically controlled by the African Plate subducting to the northwest beneath the Eurasian Plate (De Astis et al., 2003; Ventura, 2013). The seven islands of the Aeolian Islands are Alicudi, Filicudi, Salina, Lipari, Vulcano, Panarea and Stromboli. Lipari, Vulcano and Stromboli are presently volcanically active (Barberi et al., 1974). The islands of Vulcano and Stromboli give their names to the typical "Vulcanian" and "Strombolian" eruptive styles, first described at these sites. The islands of Salina, Lipari and Vulcano centre on the Tindari-Letojanni Malta tectonic depression (Fig. 4.1; Barberi et al., 1994; Ventura et al., 2013). Vulcano is a relatively young island (~127 ka; Keller, 1980; Francalanci et al., 1989; De Astis et al., 2013b), characterised by a composite volcano, two calderas and a basaltic platform (Vulcanello – connected to the island by ash accumulation around 1550 AD (De Astis et al., 2013b)). The island has four recognisable volcanic centres – Primordial Vulcano (high-K calc-alkaline shoshonitic basalt to andesite), Lentia

Complex (latite to rhyolite), Vulcanello (potassic alkaline shoshonite-trachyte) and the Fossa cone (rhyolite pyroclastics and lavas) (De Astis et al., 1997; 2006; 2013b).

The volcanological history of Vulcano is discussed by Keller (1980) and De Astis et al. (2013b), defining four main epochs of activity. Keller (1980) described the first stage as the evolution of Primordial Vulcano and Piano Caldera magmas (120-20 ka), relating early activity to strike-slip faulting affecting the island (Ventura, 1994; Ventura et al., 2013). The second phase is defined by a 24-15 ka northward-shift in activity, with the formation of the Lentia Complex and associated pyroclastic products and felsic rocks (Keller, 1980). The third epoch is characterised by post-caldera magmas (15-8 ka) with mafic rocks showing a relationship to older 1st stage magmatism. The most recent activity (fourth epoch) has been concentrated at Vulcanello and La Fossa cone (Figs. 4.3-4.5), characterised by intermediate-felsic and coeval mafic products (Di Traglia, 2011; De Astis et al., 2013b). This period of activity includes the extrusion of the Pietre Cotte lava flow (Keller, 1980). More recently, De Astis et al. (2013b) detailed eight main stages of eruptive history, inferred by establishing connections between rock-stratigraphic units and volcanic activity units. The first eruptive epoch (Paleo-Vulcano), beginning at 126.7 ± 6.6 ka (Solìgo et al., 2000), resulted in the extrusion of the Capo Secco lava cone (shoshonitic a'a-type lava flows), followed by the evolution of the Serro di Punta Lunga stratocone (eruptive epoch 2 – Casa Grotta dell'Abate, basaltic to shoshonitic lava flows, fallout and pyroclastic density unit (PDC) units). The third eruptive epoch is defined by Scoglio dell'Arpa shoshonite basaltic and shoshonitic lava flows (99.5 ± 7.0 ka; Gillot, 1987), followed by a series of lava flows, and eruptive fissure and scoria cone development (Rio Grande - eruptive epoch 4). Eruptive epoch 5 (il Piano di Vulcano) is characterised by a northward-shifting series of eruptive fissure, scoria cone and tuff cone development, including the very thickly bedded Pianoconte sequence (shoshonitic to trachytic PDCs).

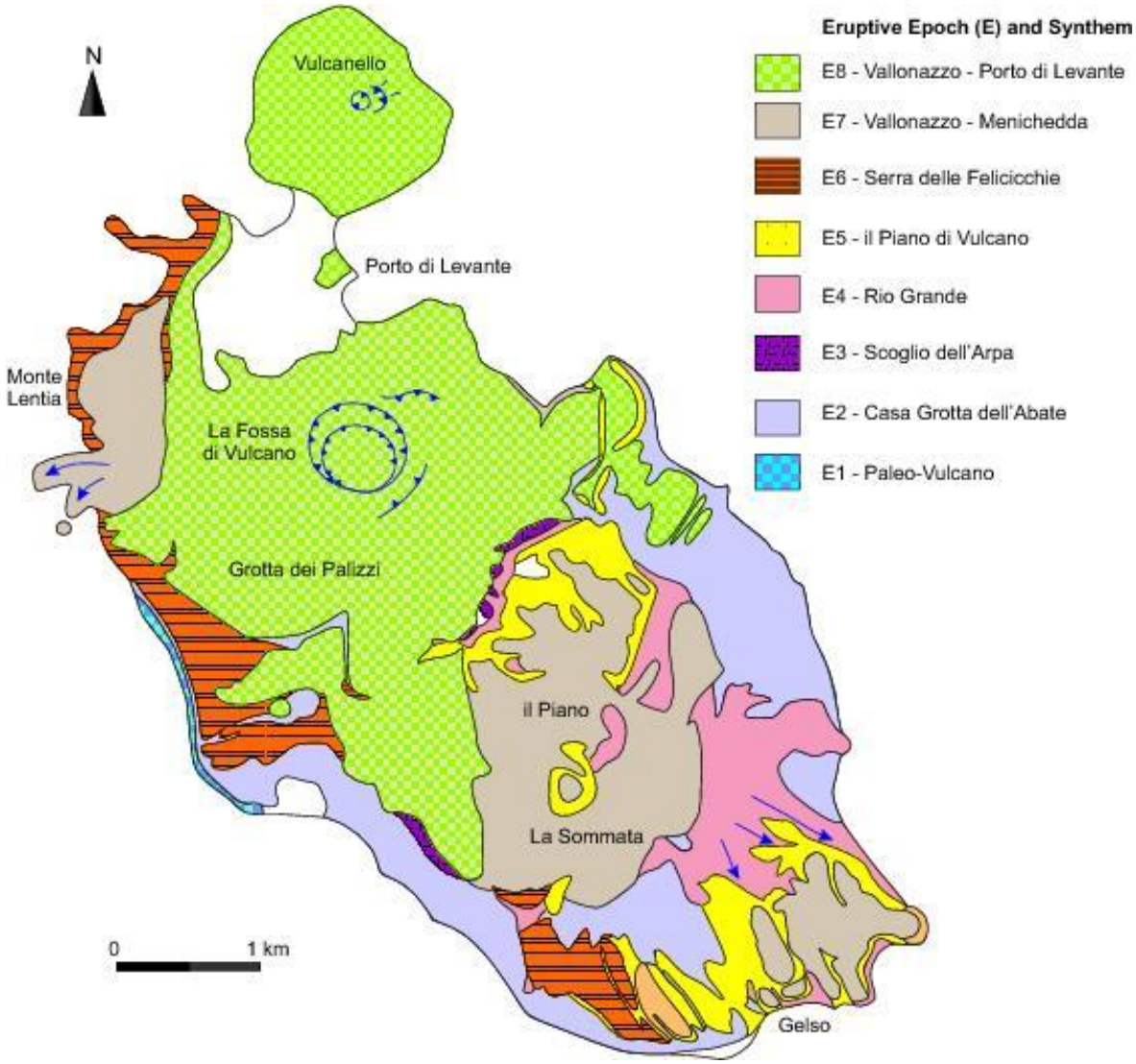

Figure 4.4: Geological sketch map and eruptive epoch and synthems units as mapped and classified according to De Astis et al. (2013a) (after original map by Keller, 1980; re-produced by De Astis et al., 2013a).

At 27.9 ± 6.6 ka (Solìgo et al., 2000), latitic to rhyolitic activity commenced (the Serra delle Felicicchie - eruptive epoch 6), with the extrusion of the lower portion of the Monte Lentia lava domes and flows, Spiaggia Lunga eruptive fissures, the Quadrara eruptive fissure and Punta Bandiera lava flow (stretching along the western coast of Vulcano, to the south eastern edge). Eruptive epoch 7 (Vallonazzo) involved the extrusion of the intermediate portion of the Lentia Complex, as well as the development of the Fossa di

Vulcano tuff cone in northern Vulcano. The most recent eruptive epoch is defined by the continual development of the Gran Cratere di La Fossa (latitic, trachytic and rhyolitic in composition), and the extrusion of the first Vulcanello cone and lava platform (AD 1675 ± 100; Keller, 1980; De Traglia, 2011). Historical records suggest that Vulcanello formed as a new island in 183 BC (Strabo and Plinius writing quoted by De Fiore, 1922; Arrighi et al., 2006; De Astis et al., 2013b), with successive eruptions occurring in the 6th and 17th centuries (Keller, 1980; Di Traglia, 2011; De Astis et al., 2013b).

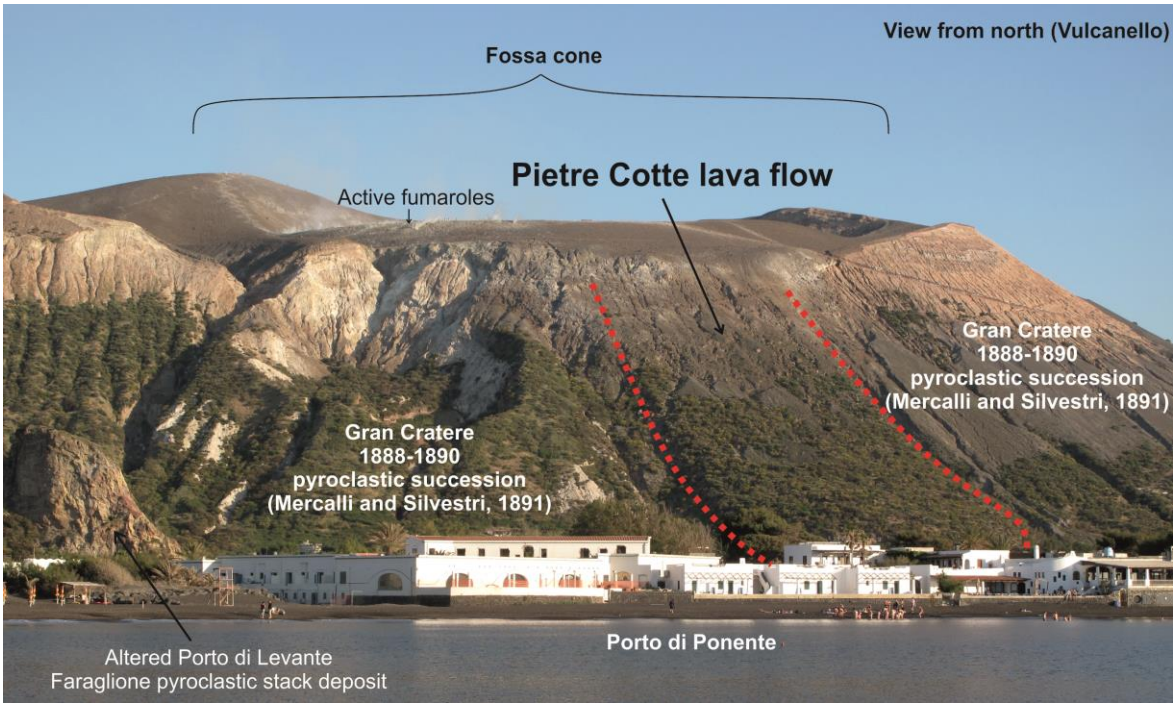

Figure 4.5: Photograph of Pietre Cotte lava flow (taken from the Vulcanello peninsula in northern Vulcano) on north-western side of the active Fossa cone. Surrounding deposits as classified by De Astis et al. (2013a).

Recent cyclicity follows a pattern starting with surge eruptions and ending with effusion of lava from the crater rim, with principle emplacement mechanisms including dry-surge, wet-surge, pyroclastic-fall, lahar, lava-flow, pyroclastic-flow and epiclastic processes (Frazzetta et al., 1984b; Sheridan et al., 1987; Piochi et al., 2009; De Astis et al., 2013b). The active Fossa Cone is located within the Fossa Caldera (N. Vulcano).

The composite Fossa cone has been active for 5.5 ka (Frazzetta et al., 1984b), with at least 15 effusive and explosive eruptions occurring over the last 1000 years (Arrighi et al., 2006; Di Traglia, 2011). The base of the Pietre Cotte cyclic unit consists of latitic ash layers (up to 3 m thick), followed by the Pietre Cotte rhyolitic lava flow, covered sporadically by finely laminated and lenticular massive ash layers (Gran Cratere sequence, 2-4 m thick trachy-rhyolites; De Astis et al., 2013b) (Fig. 4.3). The Pietre Cotte lava flow (Figs. 4.3-4.5) is tongue-like in shape, dated at 1739 AD by historical records (De Fiore, 1922; Keller, 1970; Frazzetta et al., 1984b; De Astis et al., 2013b), in agreement with an age of 1720AD ± 30 by archaeomagnetic dating methods (Arrighi et al., 2006). The flow is up to 20 m in thickness at the flow front, and is characterised by internal banding, flow foliation and folding, a typically blocky surface and includes xenoliths (De Astis et al., 2013b).

Activity within the Fossa Caldera (in the last 15 ka; Laj et al., 1997; De Astis et al., 2013b) shows an increase in K and incompatible trace element concentrations (De Astis et al., 1997; 2013b), with abundant alkali-rich trachytes and rhyolitic products in the last 6 ka (De Astis et al., 1997; 2013b). The last eruption at the Fossa cone occurred 1888-1890 (Mercalli and Silvestri, 1891; Keller, 1980; Dellino and La Volpe, 1997; Peccerillo et al., 2006; De Astis et al., 2013b), with the emission of pyroclastic material (Mercalli and Silvestri, 1891; De Astis et al., 2013b). Intense fumarolic activity then commenced, and periodically continues to modern day (Fig. 4.5). There are few silicic lava flows, with post-750 AD products predominantly pyroclastic (Fig. 4.3).

4.3 Analytical Methods

QUILF thermobarometry (Andersen et al., 1993), clinopyroxene composition barometry

(Nimis and Taylor, 2000; Putirka, 2008), fractional crystallisation trends (*Pele 8.00* calculations, Boudreau, 1999; Ghiorso and Sack, 1995) and *Rhyolite-MELTS* (Gualda et al., 2012) thermobarometric applications have all been utilised in order to place constraints on conditions during the evolution of the Pietre Cotte rhyolitic magma. Field mapping of lava flow structures has also been undertaken in order to constrain syn- and post-eruptive processes.

4.3.1 Electron microprobe analyses

Mineral and glass compositions were determined in polished thin sections. Mineral major element analysis was undertaken at The Open University (UK) using a CAMECA SX 100 electron microprobe. The peak count per element for analyses was 15-30 s using a 10-20 μm defocused beam diameter for glass (a 1 μm wide beam was used for crystals at an extended count time of 40 s), with an acceleration voltage of 15 kV and beam current of 10 nA for glass and crystals. Glass results were regularly checked and systematically controlled against standards, with glass standards and certified values also reported (Appendix V).

4.3.2 QUILF geothermometry

QUILF thermometry was used in order to constrain the temperature conditions of the more mafic magma. QUILF geothermometry was performed using *QUILF95* software (developed by Anderson et al., 1993). The program was used for temperature determinations based on Fe-Mg-Ca exchange between clinopyroxene and olivine in

equilibrium (Frost et al., 1988; Lindsley and Frost, 1992; Frost and Lindsley, 1992; Anderson et al., 1993). Ideally, two-oxide thermometry would allow oxygen fugacity determination. However, only titanomagnetite has been identified in the samples studied here, and as such has been used for oxygen fugacity estimates using clinopyroxene-olivine-titanomagnetite equilibria. QUILF geothermometry has been used to calculate pre-eruptive temperature and oxygen fugacity (fO_2) conditions of the trachytic magma. QUILF geothermometry works on a number of assumptions. QUILF geothermometry assumes that mineral compositions are accurately derived, and effects of components not included in the models can be accounted for. Unaltered (non-exsolved) crystal cores from touching crystals (assumption that neighbouring crystals are in equilibrium) were selected for analysis for equilibrium assemblages, and multiple compositions from the sample were collected to constrain the compositional variation.

4.3.3 Clinopyroxene barometry and phase-liquid equilibrium testing

Clinopyroxene-composition barometry has been applied to determine early pre-eruptive pressure conditions. Clinopyroxene-composition models have been used to calculate and constrain pressure and temperature in hydrous melts, using jadeite-diopside/hedenbergite exchange equilibria, using modelling techniques recalibrated by Putirka (2008) from barometry developed by Nimis (1995) and Nimis and Taylor (2000). Clinopyroxene composition barometry can be applied independently of a co-existing melt for calculations (i.e. only the clinopyroxene composition is needed), which is beneficial in complex systems such as this where disequilibrium textures and multiple magma batches are evident. Putirka (2008) also developed a test for equilibrium between plagioclase,

clinopyroxene and olivine and a co-existing melt by comparing An-Ab exchange (for plagioclase) and Fe-Mg exchange coefficient (for clinopyroxene and olivine) with constant values. These tests were applied to selected phases and melts for equilibrium determination.

4.3.4 Fractional crystallisation modelling

Quantitative fractional crystallisation modelling was developed using *Pele 8.00* software (Boudreau, 1999). The method involves using a hypothetical parental magma (major element composition - weight percent oxides), and the program calculates a computed fractionation trend up to intermediate and felsic magma compositions. Lati-trachytic compositions from previous studies (De Astis et al., 1997, 2013b; Del Moro et al., 1998; Gioncada et al., 1998; Piochi et al., 2009) were selected as parental compositions, as these compositions are the most mafic magmas produced in the most recent Fossa activity (De Astis et al., 2013b). Pressures of 60 MPa, 150 MPa, 210 MPa and 250 MPa were selected for isobaric, closed-system fractional crystallisation simulations in order to cover a wide range of pressures calculated in both previous studies and in this study. A starting temperature of 1,200°C was assumed for all runs. H_2O content and oxygen fugacity (in relation to FMQ buffer reaction) was calculated by *Pele 8.00* for each run. Intermediate (mafic enclave) magma compositions this study and from previous studies (De Astis et al., 1997, 2013b; Del Moro et al., 1998; Gioncada et al., 1998; Piochi et al., 2009) and rhyolitic compositions (from this study) were plotted with computed fractional crystallisation trend lines in variation diagrams in order to assess the role of fractional

crystallisation (and assimilation, see text for discussion) in both mafic enclave magma and rhyolitic host magma evolution.

4.3.5 Pele 8.00 thermometry

Temperature estimates of the trachytic magma was calculated based on the derived glass compositions using the aforementioned *Pele 8.00* software (Boudreau, 1999). Pressure input for calculations was based on values derived through clinopyroxene-composition barometry. The program requires input of weight percent major oxide composition of the glass, as well as a pressure value. Compositional data was normalised, and liquidus temperature was determined. The Pele algorithm works on the same principles as *MELTS* and *Rhyolite-MELTS* thermodynamic modelling (see below).

4.3.6 Rhyolite-MELTS

Rhyolite-MELTS was used to calculate the magmatic temperature and pressure conditions of the rhyolitic host (the latest pre-eruptive magmatic stage). *Rhyolite-MELTS* facilitates thermodynamic modelling of phase equilibria in hydrous silicic systems over a range of temperature 500-2,000°C and pressure 0-2 GPa. *Rhyolite-MELTS* differs from the *MELTS* calibration (Ghiorso and Sack, 1995; Asimow and Ghiorso, 1998) as the enthalpies of formation of quartz and end member $KAlSi_3O_8$ in feldspar solid solution have been adjusted. The program requires input of major oxide composition of glass, as well as an estimation of oxidation state (in relation to the FMQ buffer reaction). *Rhyolite-MELTS*

normalises compositional data, calculates the liquidi temperature and simulates crystallisation at different pre-determined temperature intervals. *Rhyolite-MELTS* was used for the storage conditions of the rhyolitic host, as the method permits more accurate modelling of rhyolitic chemical systems compared to *Pele 8.00* and *MELTS* (see Gualda et al., 2011).

4.3.6 Field Mapping

Field structural mapping was undertaken during the summer of 2012 in order to provide an indication of post-extrusion emplacement mechanisms, flow deformation and late-stage texture formation. This involved field mapping of the main flow structures as well as detailed sampling and observations. Localities were marked by GPS co-ordinates. Flow foliation orientations were mapped and constrained in order to recognise large scale deformation of flow. Foliation attitude was mapped and recorded across flow. Flow foliation was identified as flow bands often defined by the arrangement of spherulites. Foliation attitude was recorded and mapped as strike, dip and dip direction. The primary flow foliation allowed for the identification of flow folding. Folds were measured and described based on their fold axial plane and fold hinge. Wavelength and amplitude were also measured in order to classify scale of folds. Folds were qualitatively characterised based on their closing and facing directions and the vergence of the fold axial plane. Folds were also classified based on the straightness of the hinge line, tightness, roundness and attitude of fold, fold symmetry and harmony. Parasitic folds were noted where observed. Sheath folds were also described, and their trend orientation recorded. Stretching lineations (here defined by a parallel alignment of flattened spherulites, with their long axes stretched

during deformation; Tikoff and Green, 1997) were measured in terms of dip angle and azimuth where lineations were readily accessible and could be seen in three dimensions. As well as flow structures, areas of vegetation cover and urbanised areas were also mapped and highlighted. The topographic baseline map and anticipated lava flow coverage were based on the geological maps produced by Keller (1980) and De Astis et al. (2013a).

4.4 Results

4.4.1 Field and structural features

Field observations

The Pietre Cotte lava flow extends down the northwest portion of the Fossa cone in northern Vulcano, over a relatively steep (~30-35°; Frazzetta et al., 1984a) and uniform topography. The flow section which is most proximal to the crater source is partially destroyed or covered by more recent pyroclastic activity (1880-1890 Gran Cratere sequence – Mercalli and Silvestri, 1891; Dellino and La Volpe, 1997; De Astis et al., 2013b), and is where the flow appears to be the thinnest in thickness (~2-3 m exposure). At the flow front (Fig. 4.6a), the flow reaches a maximum thickness (~15-20 m), coinciding with a break in slope, where the topography completely flattens out. The flow extent is relatively short, approximately 500 m in length, and the flow is ~250 m in width.

The most notable features and textures in the Pietre Cotte obsidian include purple mafic enclaves, rare crystals within the obsidian host, spherulites, flow banding and multi-scale folding. The obsidian host lava is variably glassy and microcrystalline (Figs. 4.6b, c), predominantly displaying a dull black lustre or a light grey (microcrystalline) colour. Glass appears more devitrified in proximal regions, and altered by hydrothermal activity in near-vent regions. Flow banding, often defined by spherulites, is white to light grey in colour and variable in thickness, from less than 1 mm up to 5 mm thick. Flow banding wraps around mafic enclaves. Spherulites (Fig. 4.6c) are generally less than 1 mm in diameter, and variably concentrated (from rare individual spherulites to completely spherulitic intergrowth). Spherulites also concentrate in clusters or within bands, and larger spherulites (1-3 mm in diameter) are evident in upper near-vent flow regions on the northern flank. The host obsidian is vesicular, phenocryst-poor, containing rare plagioclase, pyroxene and olivine. Some vesicles are amygdaloidal, with cristobalite evident on vesicle walls. Stretching lineations are common (Fig. 4.6d), often evident on the underside of foliation planar surfaces. Vesicles often show a degree of lineation (in the direction of flow direction to the NW), and some larger spherulites also show shape modification to a more ellipsoidal shape. Mafic enclaves (Fig. 4.6e) are dark-red to purple in colour, and are typically ellipsoidal in shape (Piochi et al., 2009). Magmatic enclaves vary in size from a few millimetres up to 30 cm in diameter. Some enclaves are slightly elongate (with a skewed aspect ratio). The enclave groundmass is microlitic-diktytaxitic, with feldspar laths and pyroxene phenocrysts and microcrysts apparent. The contact between enclave and glass is sharp, and enclaves are widespread across the flow (Piochi et al., 2009).

A result of obsidian flowing over a large range in flow rheology is a range of liquid- to solid deformational structures, such as multi-scale flow folding and faulting (rheologically-

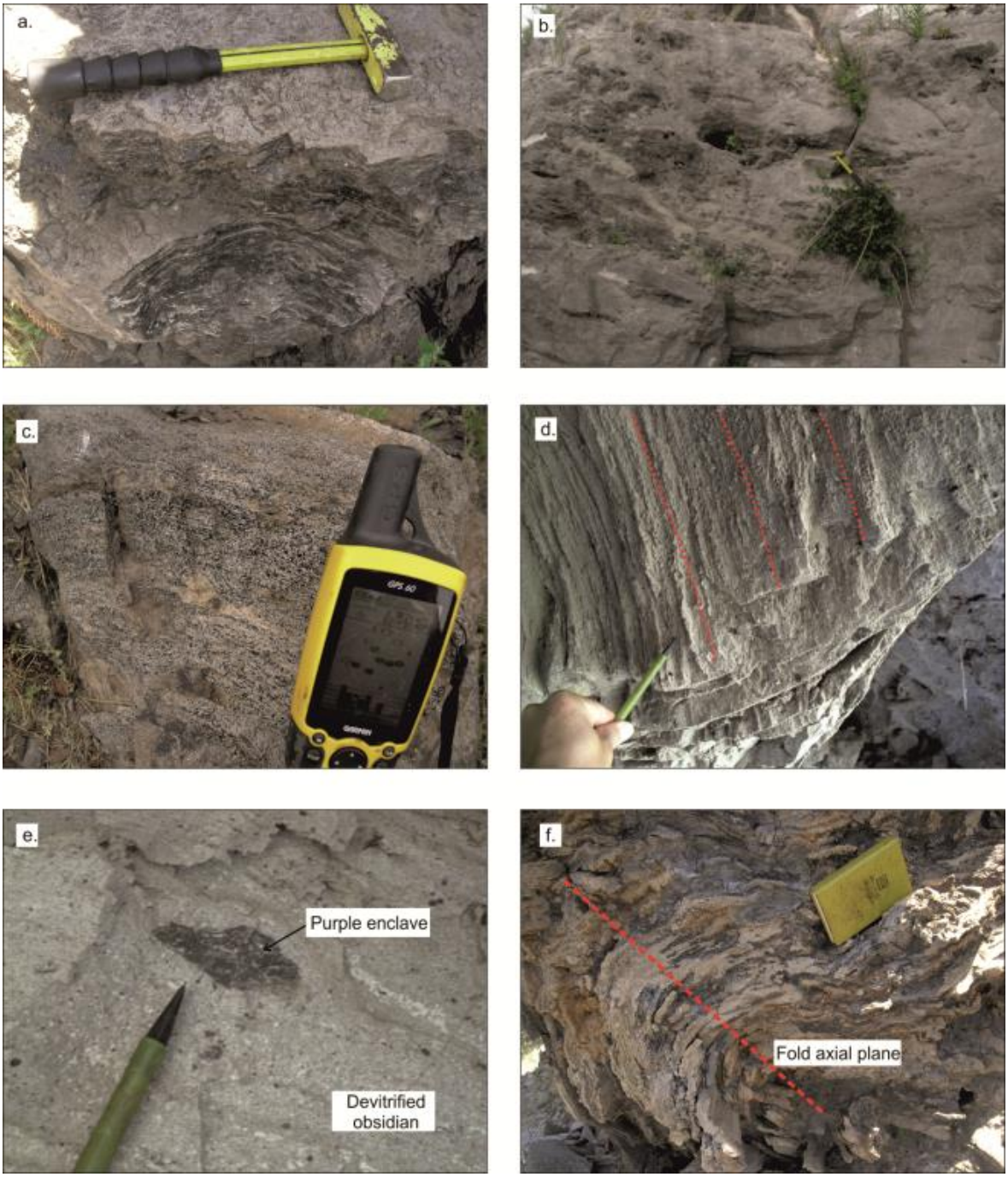

Figure 4.6: Field observations of the Pietre Cotte lava flow. (a) Flow banded obsidian, with devitrified planes. (b) Devitrified obsidian. (c) Heavily spherulitic and banded obsidian. (d) Stretching lineations on underside of planar surface. (e) Purple, slightly deformed enclave in devitrified host. (f) Flow folded obsidian.

controlled – ductile activity above and during glass transition (T_g), brittle behaviour below T_g). Flow folding is common across the flow (Fig. 4.6f), at various scales and attitudes.

Banding is often folded on a millimetre- to centimetre scale, often manifesting as parasitic s- and z-type folding as part of a larger metre-scale fold structure. Folds vary from isoclinal to open folding, and are orientated upright, inclined or recumbently. Glass often appears brown in colour and microcrystalline in the centre of larger scale folds. Sheath folding is also apparent in flow frontal regions, evident by characteristic eye structures. Breadcrust bombs from the 1888-1890 explosive activity phase are found scattered across the flow surface, with a dark, dense exterior rim and a vesicular, lighter core. There is evidence for small scale faulting, particularly in mid-flow regions, where banding shows brittle displacement on a scale of a few centimetres, up to 3-5 metres. Some displacement manifests as flow banding dipping in opposite directions within close proximity. Flow rampart structures are also evident across-flow, with foliations dipping back towards the vent, followed by an abrupt change to more horizontal planes in the distal region. Autobrecciation is apparent at the flow margins, typically a top breccia at the front and basal breccia in near-vent regions, and there are widespread tephra outcrops in middle and upper flow regions. These tephra outcrops are products of the 1888-1890 activity, resulting in a 2 m thick pyroclastic succession of dense lapilli-tuffs with intercalated thinly bedded fallout deposits in upper Pietre Cotte lava flow areas, and scattered breadcrust bombs (De Astis et al., 2013b).

Structural Mapping

Extensive flow exposure allows for the measurement and detailed mapping of various flow structures, including planar igneous foliations (flow banding), stretching lineations, fold hinges and fold axial planes. Important structural features include the attitude of foliations,

the occurrence of folds and stretching lineations, and brittle deformational fabrics. These structures are important as they provide an indication of flow behaviour during emplacement, and rheological controls on structure formation related to emplacement across the solidus. Foliation bands ranging in thickness from less than a millimetre up to several centimetres, defined by spherulite arrangement, make it possible to recognise and measure planar structures in the field. Stretching lineations form a parallel alignment of flattened spherulites, with their long axes stretched during deformation. Stretching lineations are assumed to form parallel to the long axis of the finite strain ellipsoid (Tikoff and Green, 1997). Such structural mapping can provide key insights into lava flow emplacement and associated deformation.

The Pietre Cotte lava flow is relatively short (less than 1 km in length), and advanced over a uniform, steep topography (~30-35°; Frazzetta et al., 1984a) down the north-eastern flank of the Fossa cone. The flow is relatively thin, reaching a maximum of ~20 m thickness at the flow front. Thickness generally increases linearly from upper flow to flow front, but is often masked in areas by younger pyroclastic deposits. The flow shows a single flow direction towards the north, evident by a single, tongue-like lava flow lobe and no breakout lobes evident. The tongue-like shape mirrors the underlying topography. Flow margins run in a parallel NW-SE orientation. The flow terminated at the base of the Fossa cone, where the topography shallows. Structural mapping of foliations, lineations and folding reveals a relatively consistent and uniform arrangement of orientations (Fig. 4.7). Foliations typically dip 30-50° (Fig. 4.8), dipping steeper in higher up the flow (60-80°). Foliations align in a curvilinear pattern across the flow, sub-parallel to the flow front. At the western and eastern flow flanks, foliation strikes and dips vary much more significantly, often dipping westwards, as shallow as 10-12°. Folds are also more prominent at the flow margins, with fold axial planes and fold hinges often orientated N-S and some cases of

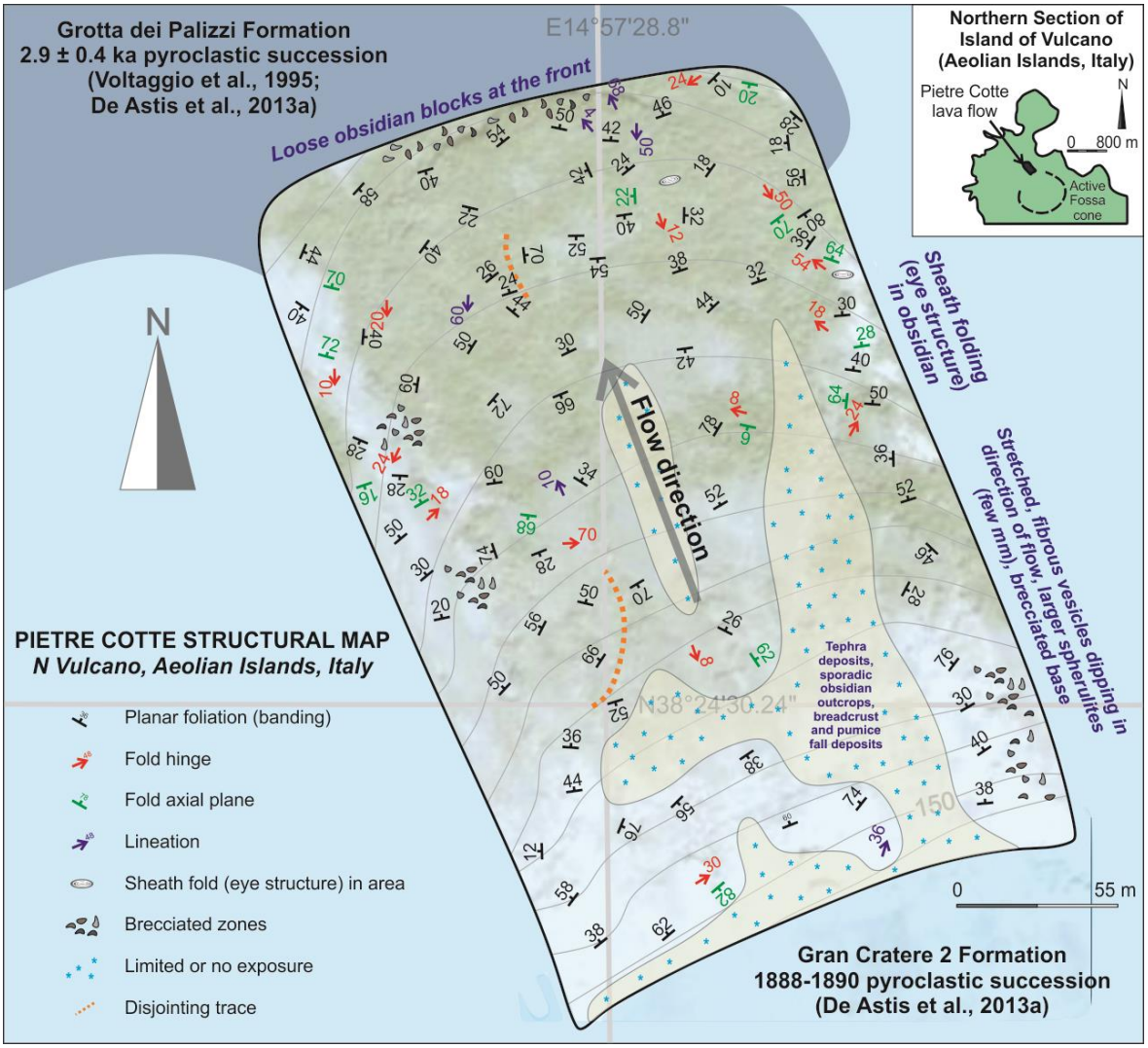

Figure 4.7: Structural map of the Pietre Cotte lava flow, with foliation, fold hinge, fold axial plane and lineation measurements and key structural features highlighted.

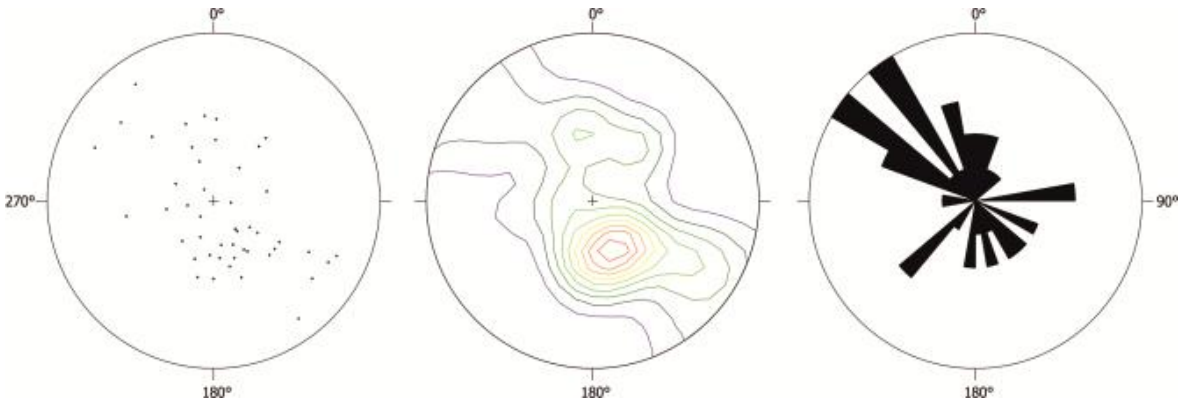

Figure 4.8: Stereographic representation (poles to planes) of Pietre Cotte lava flow foliation structural data; (from left to right) – stereonet, density plot and rose diagram.

NE-SW alignment. The majority of folds were classified as medium scale folding (~44% of 16 measured folds, based on a wavelength and amplitude of ~0.2-2 m), with ~37% of measured folds were classified as small scale folds (<20 cm in wavelength and amplitude). Only ~19% of folds were large scale folds (>2 m in wavelength and amplitude). Sheath folding is evident in the north eastern flow frontal region. There is brittle separation (jointing) of flow units, manifested as foliations dipping in opposite directions significantly within close proximity. Stretching lineations show a relatively uniform alignment, occurring predominantly in mid-flow regions. These are identifiable as sheared or stretched spherulites, and fibrous pumiceous vesicles. Stretching lineations align in a relatively uniform N-S orientation, dipping from shallow (10°) to steep (68°).

4.4.2 Petrography

Microscopic observations show three clear textural subdivisions, including glomerocrysts of mafic mineral assemblage, enclaves with a microlitic-diktytaxitic groundmass and obsidian glass. Glomerocrysts occur in both enclaves and in the obsidian host. Petrographic observations are described in both the obsidian host and in enclaves.

Pietre Cotte obsidian

This section describes the obsidian glass, including crystals that are located within (but not necessarily derived from) the obsidian host. Important features to highlight include the abrupt boundary between the mafic enclaves and the rhyolitic host, phenocryst texture and

zonation, relationships between phenocryst assemblages and the spatial distribution of microlites and spherulites. Such features give a qualitative timeline indication of evolutionary stage divisions (see Discussion and Chapter 5).

Microscopic observations show that the obsidian host lava is variably vesicular (~10% of total volume, varying from vesicle-free to highly vesicular), contains purple mafic enclaves (~4% of the total volume, calculated using *ImageJ* software), and is predominantly crystal-poor (<5% of total volume), with a mineral assemblage of plagioclase (~50% of the total crystals, 1-2 mm in length) (Fig. 4.9c, d), clinopyroxene (~40%. 0.5-1 mm) (Fig. 4.9d, e), olivine (5%, ~0.5 mm) and titanomagnetite (5%, <0.5 mm) (Fig. 4.9d). Plagioclase feldspar often shows clinopyroxene, olivine and titanomagnetite inclusions (Fig. 4.9d), sieve-textured interiors and embayed rims (Fig. 4.9c). Normal zonation and twinning is often disturbed by neighbouring plagioclase crystals. The majority of crystals and glomerocrysts are often surrounded by a thin rim of microcrystalline material, predominantly consisting of interlocking needles of alkali feldspar, plagioclase and clinopyroxene (Figs. 4.9c-e). Crystals found in the obsidian host occur individually, or in crystal clusters (typically 2-4 mm in length), and are wrapped by flow banding textures in the obsidian host (defined by microlites and spherulites). The host obsidian glass varies from completely glassy to completely devitrified, evident by a speckled microcrystalline texture. The groundmass is heavily microlitic (Figs. 4.9a-b, f), with microlites showing a preferred orientation (Figs. 4.9a-b, f), often wrapping around enclaves and crystals (Fig. 4.9c, e). Microlite alignment often defines the primary planar foliation (flow banding) and displays evidence for microscopic folding. Vesicles are elongate, and are often partially or completely infilled with cristobalite.

The glass is predominantly spherulite-rich (~20% of area, calculated using *ImageJ* software), and concentrations of spherulites vary from completely spherulite-free to near-

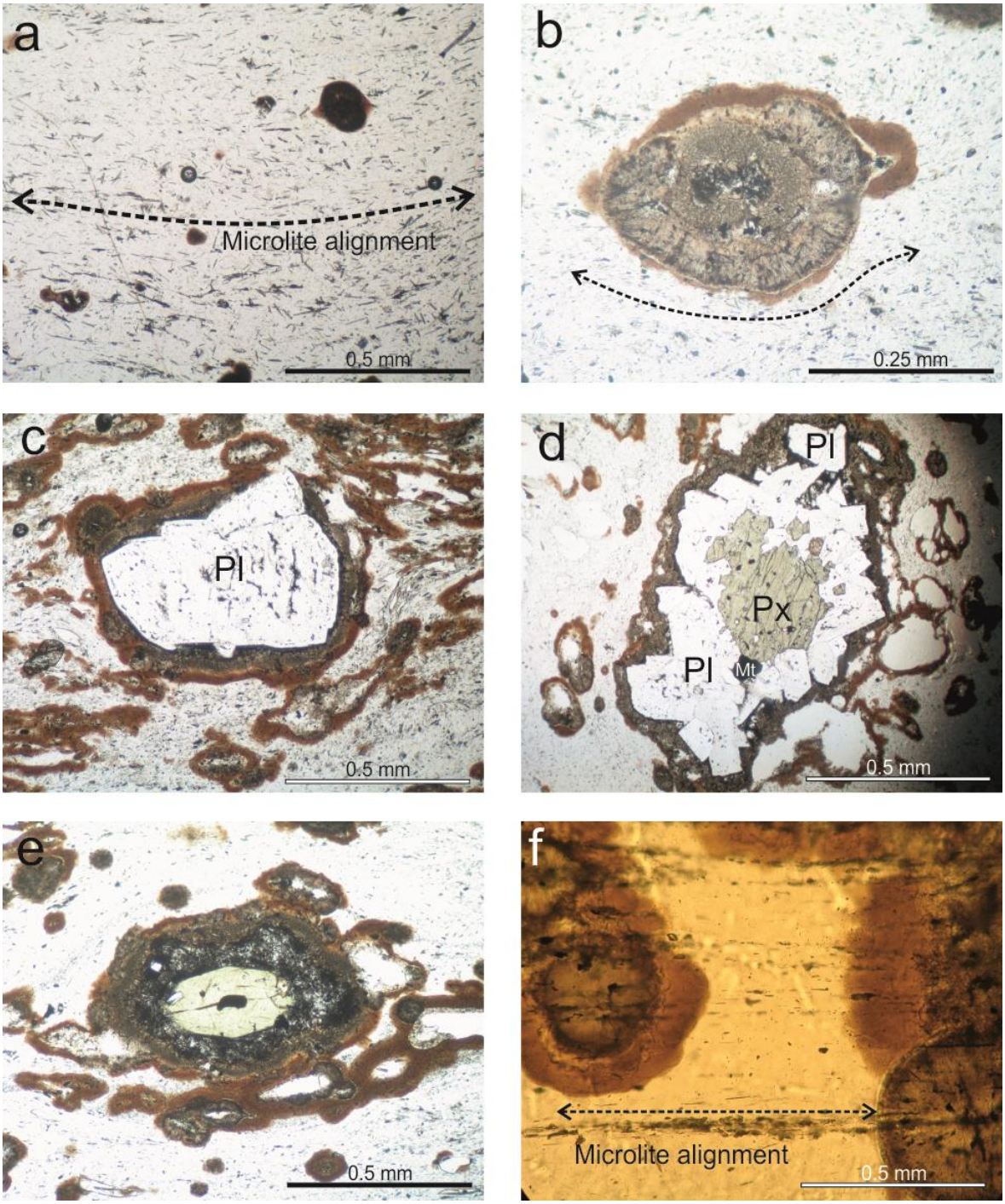

Figure 4.9: Microscopic (plane polarised light) images of crystals and textures within obsidian host. (a) Microlite alignment and spherulites within obsidian. (b) Microlites wrapping around mildly deformed spherulite. (c) Plagioclase showing resorption at edges, surrounded by mafic film. Spherulites nucleate on edge of enclave. (d) Plagioclase and pyroxene glomerocryst. (e) Clinopyroxene showing thick rim of enclave material, with spherulites nucleating at edge and wrapping enclave. (f) Spherulites with microlites overprinted and unaffected.

completely spherulitic. Spherulites often nucleate on crystals and mafic enclaves (Fig. 4.9c, e). Spherulites are sub-spherical, radiating out from the centre, and contain multiple phases, predominantly alkali feldspar and cristobalite, in a skeletal arrangement. Spherulites sometimes show an internal dark/light colour zonation in plane and cross polarised light, reflecting growth rings and compositional variation within spherulites (Ewart, 1971). Spherulites occur individually, in clusters or concentrated in bands. Some spherulites are mildly deformed (Fig. 4.9b), showing a slight elongation parallel to banding and microlite alignment. Microlites are sometimes deflected around spherulites (Fig. 4.9b), or in some cases completely unaffected and are overprinted by microlites (Fig. 4.9f). Spherulites are often surrounded by a zone of brown, non-isotropic amorphous material (Fig. 4.9b, f) and occasionally surrounded by a thin clear halo. These zones also encompass mafic enclaves, crystals, small microlites and vesicles.

Mafic enclaves

Mafic enclaves are surrounded by a thin brown rim (before clear glass – Fig. 4.10a), with spherulites often nucleating at the enclave edges (Fig. 4.9c, e; 4.10a). The enclaves scarcely exhibit vesicles, and contain a phenocryst assemblage of plagioclase (~60% of total observed phenocrysts) (Fig. 4.10c, e), clinopyroxene (~20%) (Figs. 4.10c-e), olivine (~10%) and titanomagnetite (~10%), with minor apatite (see also Piochi et al., 2009). As well as the common purple enclaves, there is minor evidence for patches of a rare finer, brown enclave material, more angular in appearance (Fig. 4.10b). Minerals in these finer enclaves are indiscernible, but sieve-textures are apparent within enclaves.

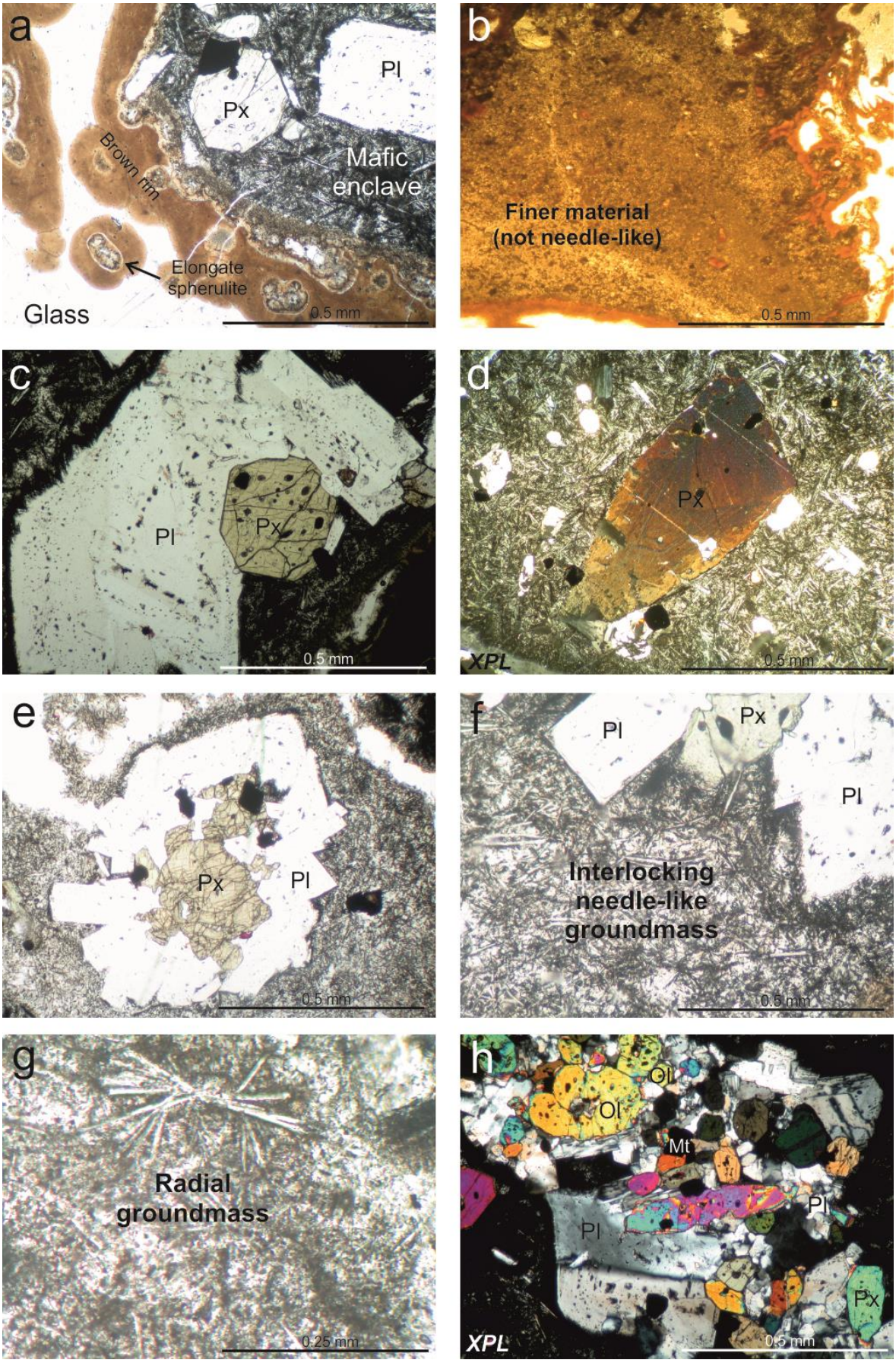

(Image continued on next page)

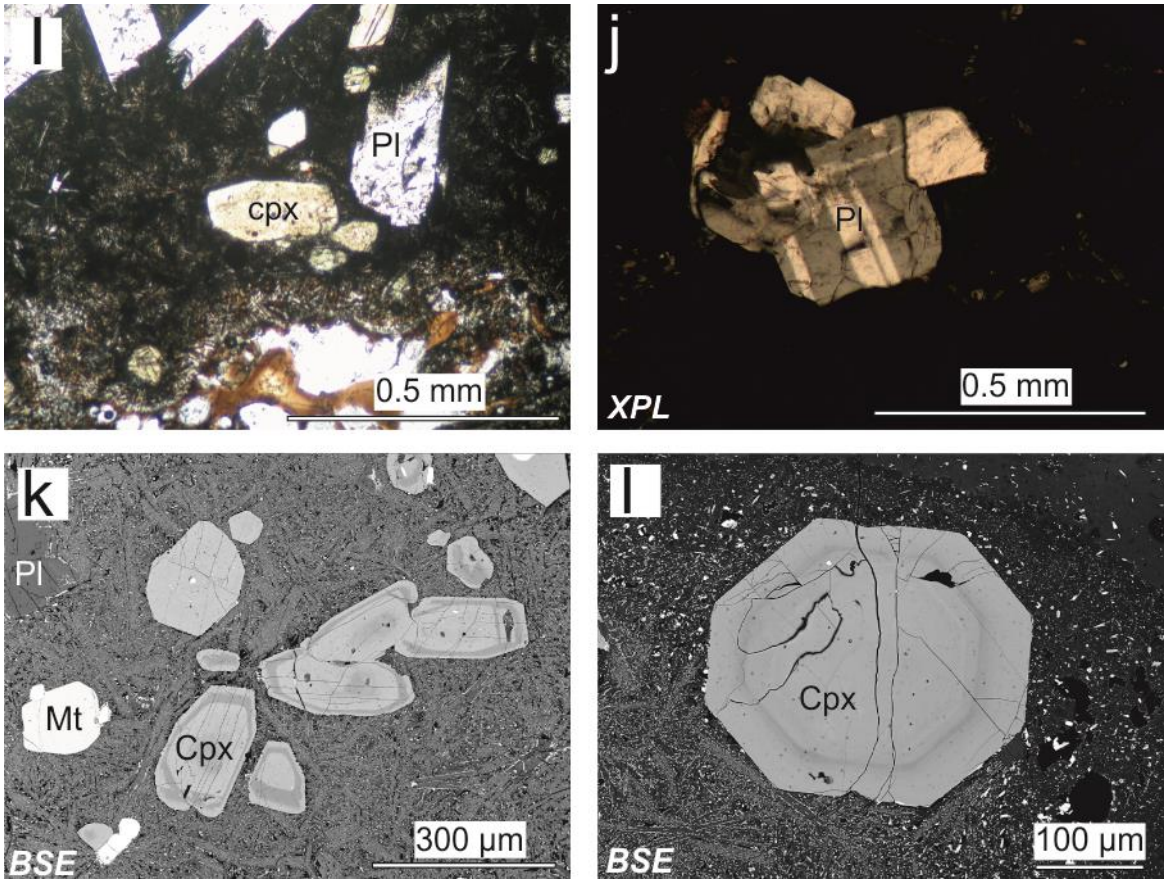

Figure 4.10: Microscopic images of crystals and textures within mafic enclaves. (a) Boundary between a mafic enclave and surrounding obsidian host, with brown rim surrounding both the enclave and spherulites in the host. (b) Finer, brown coloured enclave. (c) Sieve-textured plagioclase and clinopyroxene phenocrysts. (d) Compositionally zoned clinopyroxene. (e) Anhedral clinopyroxene inclusions within plagioclase. (f) Mafic enclave microlitic-diktytaxitic groundmass. (g) Radial textured feldspars in groundmass. (h) Glomerocryst of plagioclase, clinopyroxene, olivine and titanomagnetite. (i) Resorbed clinopyroxene and plagioclase. (j) Cluster of slightly resorbed plagioclase. (k) Clinopyroxene with and without chemical zonation. (l) Compositionally-zoned clinopyroxene.

Scanning Electron Microscopy with energy-dispersive x-ray spectroscopy reveals the presence of aluminium-rich minerals and iron- and magnesium-rich minerals within these enclaves, suggesting the presence of plagioclase and clinopyroxene. There is an abrupt boundary between the finer enclaves and the obsidian glass (Fig. 4.10a). Plagioclase phenocrysts display compositional zoning. Plagioclase phenocrysts also often contain sieve

textures (Fig. 4.10c), and occasional embayed rims (Fig. 4.10i-j). Plagioclase commonly displays euhedral crystal shapes, and is typically 1-2 mm in length. Clinopyroxene is also common, typically 0.5-1 mm in length. Clinopyroxene crystals dominantly display euhedral crystal forms (Fig. 4.10c), with occasional evidence for complex zoning (Fig. 4.10d; k-l) (Piochi et al., 2009), and often occurs as inclusions within plagioclase (Fig. 4.10e). Some clinopyroxene crystals also contain large, abundant melt or glass inclusions (which are slightly crystalline; Fig. 4.10c), as well as apatite inclusions and embayed rims. Titanomagnetite and olivine are often present (<0.5 mm), occurring individually, in clusters, or as inclusions. Crystals separating out into the glassy host are often surrounded by a thin film of enclave groundmass (see text above and Figs. 4.10c-e). The groundmass is microlitic-diktytaxitic (Figs. 4.10e-g), consisting of needle-like feldspar laths (~0.02-0.1 mm in length, Figs. 4.10f-g), with clinopyroxene microphenocrysts, glassy inclusions and titanomagnetite. The groundmass sometimes shows a flow-like arrangement around phenocrysts and glomerocrysts, and occasionally the groundmass also displays a radial-like texture (Fig. 4.10g).

Crystal clusters (herein referred to as glomerocrysts) of plagioclase, clinopyroxene, olivine, titanomagnetite and rare apatite are common within enclaves (Fig. 4.10e, h). Mineral phases in glomerocrysts contain touching crystal frameworks in a cumulus texture, showing euhedral and subhedral individual crystal shapes, and glomerocrysts are relatively coarse (an individual glomerocryst is often 2-4 mm in diameter). Glomerocrysts are often plagioclase-dominated, with coarse plagioclase crystals often completely engulfing smaller clinopyroxene, olivine and titanomagnetite. Plagioclase is the most dominant mineral phase in glomerocrysts, followed by clinopyroxene, forming individual phase clusters or a mixture of the two minerals. The needle-like groundmass wraps around glomerocrysts in a flow-like texture. Glomerocrysts may also separate out into the host obsidian, surrounded

by a thin film of enclave groundmass. Coarse crystals which occur individually rather than as part of a glomerocryst often appear more resorbed and embayed at the crystal edges (the centre of the crystal remains relatively unaffected) compared to crystals within glomerocrysts. Crystals within glomerocrysts sometimes show resorption textures, but this is less common than in individual coarse crystals.

4.4.3 Glass and mineral compositions

All glass and mineral compositional data are reported in Appendices I and III. Glass composition from the obsidian lava host exhibits a SiO_2 range of 74.9-77.1 wt% (all glass data has been recalculated volatile-free to 100 wt%). Al_2O_3 content is relatively uniform, ranging from 13.0 wt% to 13.9 wt%, with Na_2O exhibiting a range from 3 wt% to 4.9 wt%, and K_2O ranging from 3.5 wt% to 4.7 wt%. FeO ranges from 1.4 wt% to 1.9 wt%, CaO ranges from 0.5-0.8 wt%, and TiO_2, MgO, MnO and P_2O_5 all occur in trace amounts (<0.2 wt%). Total alkali (K_2O+Na_2O) and silica content (TAS diagram, Fig. 4.11) reveal that the Pietre Cotte glass is sub-alkaline high-K calc-alkaline (HKCA) rhyolitic in composition (see Fig. 4.12).

Phenocrysts of plagioclase, clinopyroxene, olivine and titanomagnetite have been identified by petrographic observations, and plagioclase has also been identified as part of the (predominantly sanidine) enclave groundmass. Analyses of glassy groundmass within the mafic enclaves reveal a trachytic enclave composition (with one analysis revealing a trachy-andesitic composition) (Fig. 4.13). The compositional data roughly agrees with that of Piochi et al. (2009) (Fig. 4.13). FeO and CaO show notable variations, ranging from ~2.6 wt% to ~6.1 wt% and ~1 wt% to 6 wt% respectively.

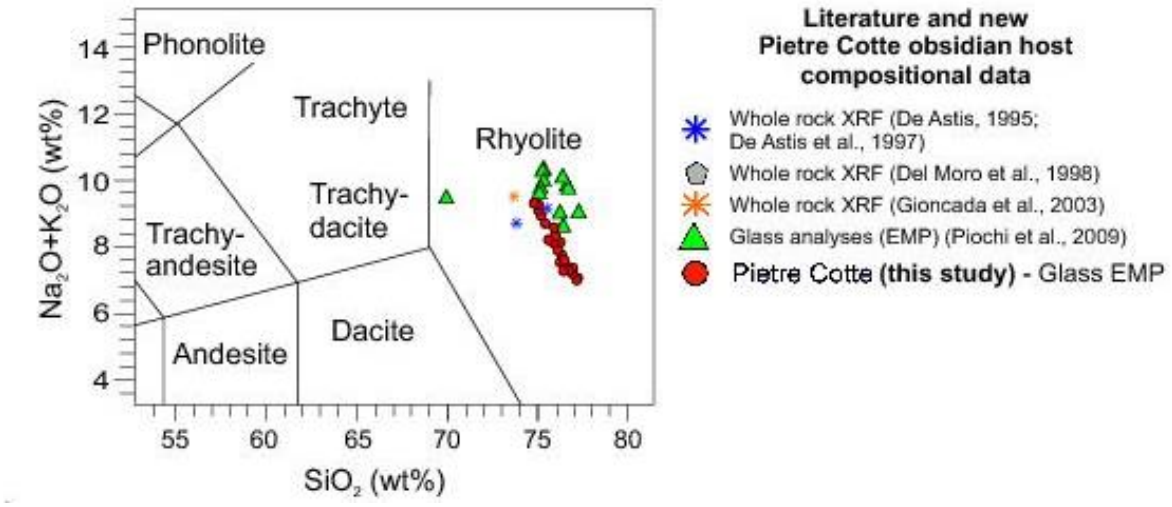

Figure 4.11: Total alkali versus silica (TAS) diagram (adapted from Le Bas et al. 1986) for Pietre Cotte obsidian glass (Electron microprobe (EMP) glass analyses). Includes Pietre Cotte XRF whole rock data from De Astis (1995), De Astis et al. (1997), Del Moro et al. (1998), Gioncada et al. (2003), and glass electron microprobe data from Piochi et al. (2009). All Fe is reported as FeO; data have been recalculated water-free to 100 wt%.

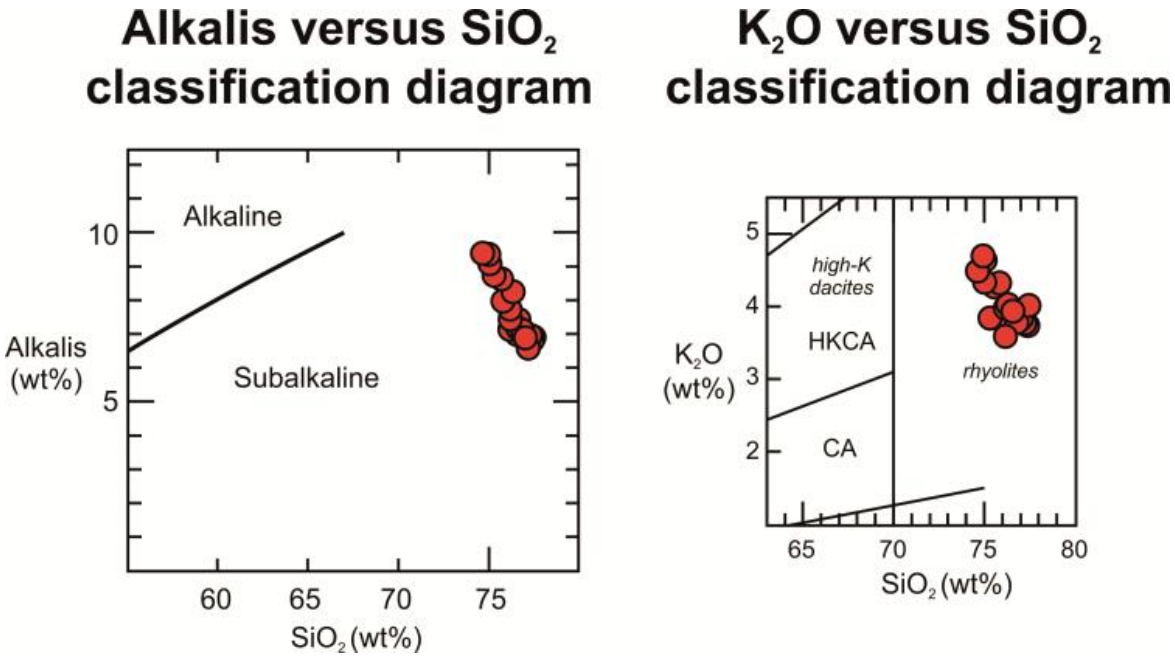

Figure 4.12: Alkalis vs. SiO_2 (wt%) classification diagram (Irvine and Baragar, 1971) and K_2O vs. SiO_2 (wt%) classification diagram (Peccerillo and Taylor, 1976) showing Pietre Cotte obsidian host EMP glass data (normalised volatile-free to 100%).

SiO_2 shows a range of ~60-63 wt%, Al_2O_3 ranges from~18-21 wt%, Na_2O ranges from 4.4-5.8 wt% and K_2O ranges from 3.2-6.3 wt%. MgO ranges from ~0.5 wt to 1.5 wt%, and TiO_2 and MnO occur in trace amounts. Whole rock data from previous studies (recalculated volatile-free to 100 wt%) also indicate that the enclaves are trachytic in composition (trachy-andesitic and trachy-dacitic in some studies; Fig. 4.13) (De Astis et al., 1997; 2013b; Gioncada et al., 1998; Piochi et al., 2009). Plagioclase exhibits a compositional range of An_{5-63} and alkali feldspar shows a range Or_{4-58} (Fig. 4.14). Zoned plagioclase shows some variation from core to rim, with cores slightly more anorthitic, and plagioclase rims more albitic. The majority of plagioclase is classified as labradorite, with andesine also evident. There is also evidence for rare alkali feldspar phenocrysts in the obsidian host (sanidine). Small plagioclase feldspar crystals and microlitic-diktytaxitic laths in the groundmass exhibit a compositional range of An_{5-46} and alkali feldspar groundmass minerals show a range in composition of Or_{9-57} (Fig. 4.14). The majority of feldspar laths in the groundmass are alkali feldspar (sanidine), with occasional plagioclase (anorthoclase and rare labradorite). Piochi et al. (2009) report labradorite compositions from core to rim in feldspars in the Pietre Cotte lava flow (becoming more albitic as also reported here), and labradorite is also reported by De Astis et al. (1997) in La Fossa and Vulcanello mafic products. Clinopyroxene crystals in the Pietre Cotte lava flow show a relatively uniform compositional range of $En_{38-47}Fs_{7-16}Wo_{45-50}$ (calculated from ferric form, Fig. 4.15). There is minor variation from core to the rim, with rims showing slight Fe enrichment compared to the core (on average, 4.1% enrichment at rim compared to core). Al_2O_3 wt% is generally more depleted in the rim compared to the core (on average, 9.3% depletion). MnO wt% is variable from core to rim, but is predominantly enriched in the rim (14% average enrichment from core to rim) and Na_2O also shows enrichment from core to rim (15.8%).

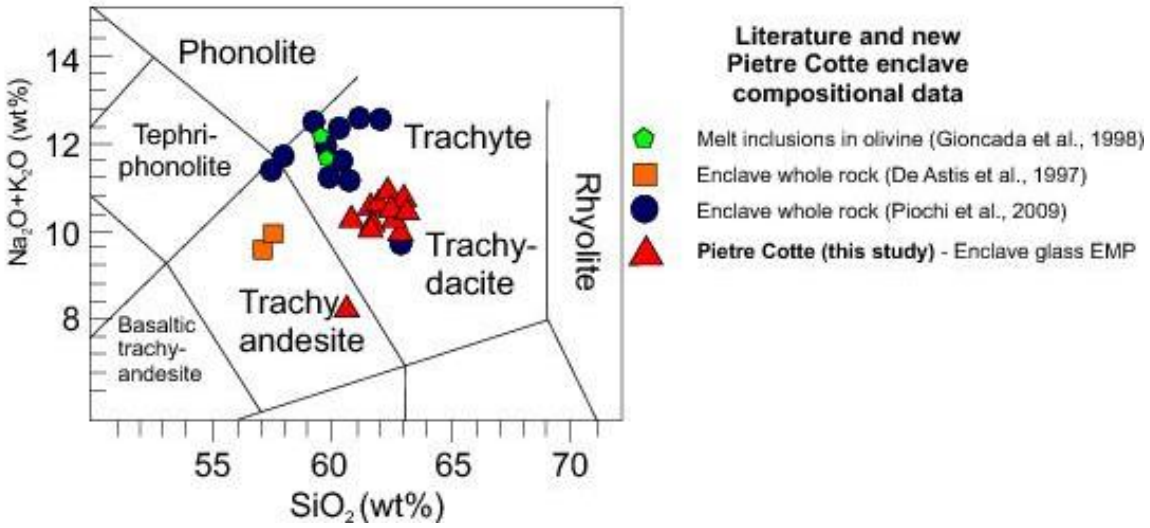

Figure 4.13: Total alkali versus silica (TAS) diagram (adapted from Le Bas et al., 1986) for Pietre Cotte enclave (whole rock, glassy groundmass and melt inclusions). Data from this study represents EMPA of melt inclusions. Literature whole rock and olivine melt inclusion data taken from De Astis et al. (1997), Gioncada et al. (1998) and Piochi et al. (2009) . All Fe as FeO.

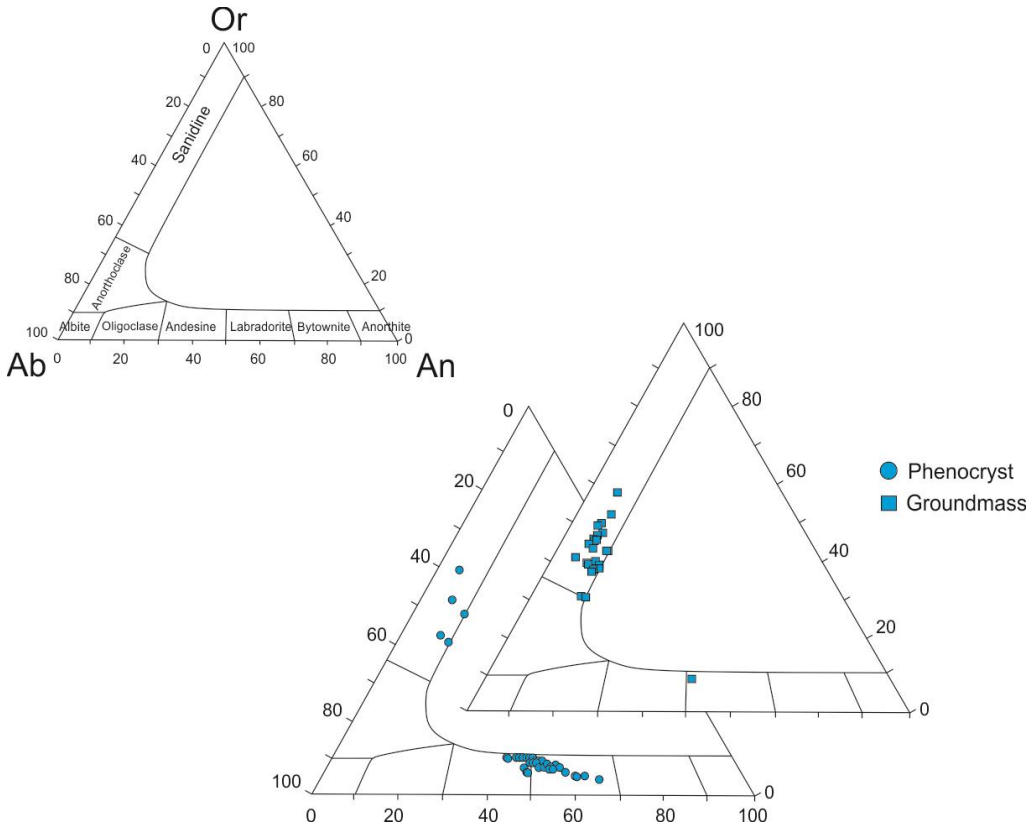

Figure 4.14: Feldspar ternary classification diagrams for Pietre Cotte enclave plagioclase and alkali feldspar phenocrysts and mafic enclave groundmass. Field labels are also shown.

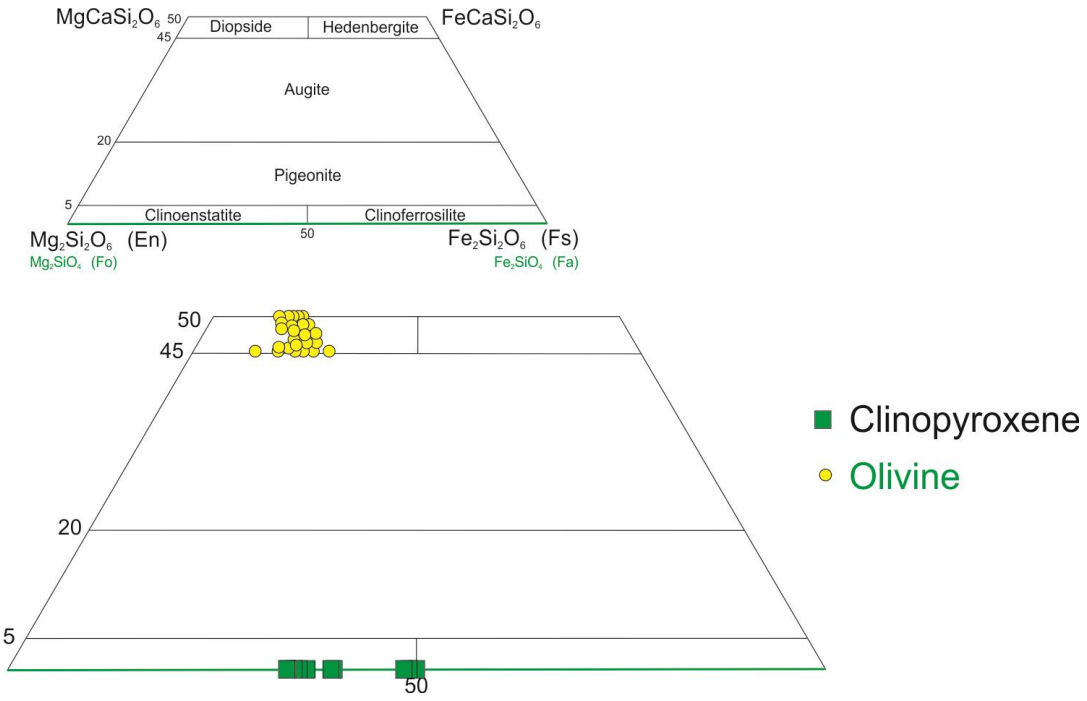

Figure 4.15: Pyroxene ternary classification diagram (Morimoto et al., 1988) for Pietre Cotte enclave clinopyroxene and crystals within obsidian host (yellow circles), and superimposed olivine classification (green boxes and text).

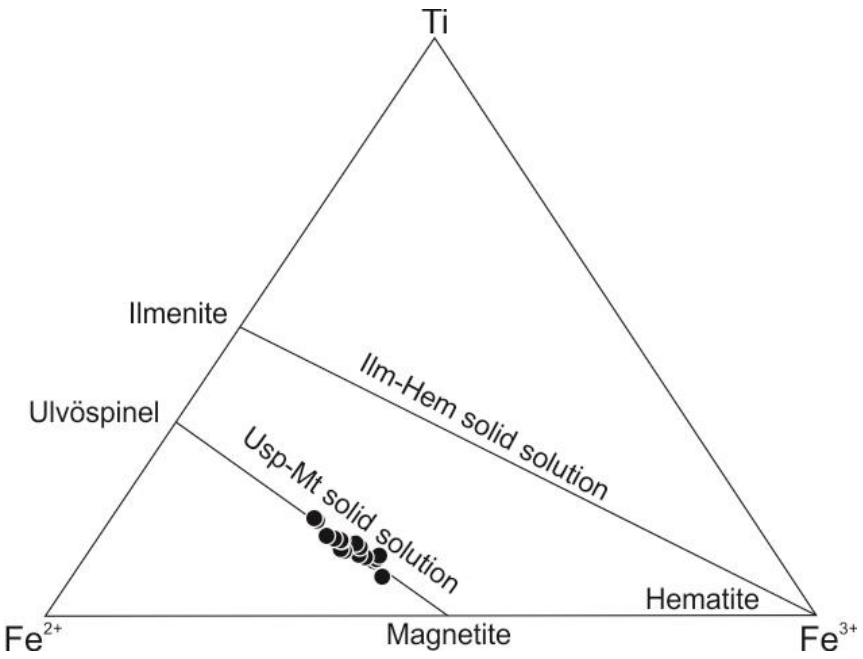

Figure 4.16: Ternary classification of analysed oxide minerals in Pietre Cotte trachytic enclaves and obsidian host.

Other major element oxides (SiO_2, TiO_2, CaO and MgO) show no significant enrichment or depletion trends. Clinopyroxene phenocrysts are exclusively classified as diopside (according to the classification scheme of Morimoto et al., 1988). Olivine is predominantly forsteritic in composition (average Fo_{57}, ranging $Fo_{49\text{-}66}$), with rare fayalitic olivine ($Fa_{34\text{-}51}$). The compositional range of olivine is $Fo_{49\text{-}66}$ (Fig. 4.15). Titanomagnetite shows minor geochemical variation, with a compositional range of $Usp_{7\text{-}26}$ (Fig. 4.16).

4.4.4 Thermobarometry

Preliminary observations and geochemical results suggest that there were up to three magmas involved in the evolution of the Pietre Cotte magmatic system: (1) a more mafic magma, resulting in the glomerocryst-forming crystal assemblage, (2) a trachytic magma, which hosts the glomerocrysts, and (3) a rhyolitic magma, which hosts trachytic enclaves and glomerocrysts (within and separated from trachytic enclaves).

The preservation of the two most distinct magmas (the rhyolitic host and trachytic enclaves) suggests that these two magmas likely formed under different temperature and pressure (depth) conditions, and are calculated as such. The more complex interaction between the trachytic and more mafic magma is more difficult to distinguish from initial observations, and therefore, the conditions of their formation are initially treated as an associated event.

Pressure

Intensive variables of magmatic stages forming sequential parts of the dynamic system associated with the Pietre Cotte pre-eruptive magmatic evolution have been calculated. Pressure estimates are based on previous fluid and melt inclusion studies in mafic enclaves and in the rhyolitic host, and clinopyroxene barometry methods applied here. There have been numerous pressure and depth calculations and constraints placed on the plumbing conditions beneath the Fossa cone (e.g. Clocchiatti et al., 1994; De Astis et al., 1997; 2013; Zanon et al., 2003; Frezzotti et al., 2004; Frezzotti and Peccerillo 2004; Dellino and De Astis 2008; Piochi et al., 2009). However, there are still contrasting intensive variable results and opportunity to more precisely quantify and constrain magmatic storage conditions which ultimately led to the extrusion of the Pietre Cotte lava flow.

Estimations of pressure conditions associated with each magma in the Pietre Cotte plumbing system is complicated by the complexity of the series of processes involved in magma evolution. For instance, a number of pressure calculations have been made based on inclusions within xenoliths (see below). It is difficult to anticipate that the origin of such inclusions within xenoliths precisely reflects the conditions under which their host magma formed. In order to mitigate against such complications, clinopyroxene barometry has been utilised as the method requires the minimal input (and therefore a minimal influence from variables such as crustal contamination sources). Clinopyroxene composition barometry can be applied independently of a co-existing melt for calculations, which is beneficial in complex systems such as this, where disequilibrium textures and multiple magma batches are widespread. Euhedral clinopyroxene phenocrysts with no apparent disequilibrium textures are plausibly the product of a crystallising mafic magma, and therefore the

conditions of their formation reflect their magmatic storage conditions compared to xenolith inclusions of a differing origin.

Pressure of deeper, more mafic magma

Average results from six samples show a pressure of 1,668 bars (~6.2 km depth), but shows a significant range of 853-3,452 bars (~3-13 km depth), and a standard deviation of 975. Despite this significant range, these pressure calculations suggest that the more mafic magma batch may have been crystallising at a shallower depth and lower pressure than that suggested by Zanon et al., (2003), and provides more rigorous constraints than the pressure estimate provided by Frezzotti et al., (2004) and Piochi et al., (2009). Zanon et al., (2003) and Frezzotti et al., (2004) studied fluid inclusion data of Si-rich xenoliths which formed in association with a third, more mafic Fossa system magma (xenoliths are thought to derive from a deeper reservoir and are carried by this third, more mafic magma; Zanon et al., 2003; Frezzotti et al., 2004; Piochi et al., 2009). Zanon et al., (2003) showed that the fluid inclusions yield a pressure of 5,600-3,300 bars relating to xenolith entrapment within magmas, and therefore shows some agreement and overlap with the calculations made in this study. Further previous studies indicate that Si-rich melts formed in association with shoshonitic to latitic magmas at a pressure of >2,200 bars (Zanon et al., 2003; Frezzotti et al., 2004; Piochi et al., 2009), which, though more vague and implicit of the interaction of a Si-rich and more mafic magma, also agrees with calculations made in this study.

Pressure of rhyolitic magma

Pressure and depth of the rhyolitic melt have been made in previous fluid inclusion, barometric and petrological studies. Fluid inclusion studies (Clocchiatti et al., 1994; Zanon et al., 2003) reveal rhyolitic magmas in thermal equilibrium with quartz-rich xenoliths at 300-600 bars (~0.8-1.6 km depth), coinciding with magma-crust interaction (De Astis et al., 1997; Del Moro et al., 1998; Piochi et al., 2009).

Barometric (Zanon et al., 2003) and petrological data (De Astis et al., 1997) constrain the shallower magma ponding system to depths of 4-3 km. De Astis et al., (2013) describe the shallow plumbing system below the Fossa cone, suggesting magmas reside at 5.5-2.8 km, with small batches of latitic magma evolving to trachyte and rhyolite, assimilating low amounts of upper crustal material, with little variation over the past 28 ka (De Astis et al., 1997; 2013).

A shallower magma ponding system has been inferred beneath the Fossa cone by Clocchiatti et al., (1994), at a depth of 1.6 km (De Astis et al., 1997; Del Moro et al., 1998; Piochi et al., 2009) where magma mixing and interaction with seawater also occur (Clocchiatti et al., 1994).

Temperature

Temperature of deeper, more mafic magma

Temperatures determined using QUILF (pyroxene-olivine-titanomagnetite) equilibria (Frost et al., 1988; Lindsley and Frost, 1992; Anderson et al., 1993) have been applied for the temperature conditions of the third, more mafic magma responsible for the crystallisation of the xenocrysts that make up glomerocrysts. Here, a maximum pressure of

3,452 bars is selected based on pressure calculations (above). Cores of touching olivine, clinopyroxene and titanomagnetite crystals, free of resorption and zoning textures, were selected for temperature calculations. QUILF thermometry results presented here are based on an average temperature from 8 runs.

QUILF results suggest a temperature range between 1,115°C and 1,178°C, with an average temperature of 1,154°C. The average error calculated is ±18°C. As well as calculating temperature, an oxygen fugacity (fO_2) was also calculated using QUILF (based on olivine-clinopyroxene-titanomagnetite equilibria). Oxygen fugacity (fO_2) plots approximately 1.5 log units above FMQ. This result agrees with the redox conditions of the Fossa hydrothermal system, which was also computed close to the NNO buffer (Carapezza et al., 1981; Di Liberto et al., 2002).

Temperature of the trachytic magma

Trachytic compositions (determined by glassy inclusions) and pressure calculations were used to estimate the storage temperature conditions of the trachytic magma. A total of twenty four simulations were conducted using *Pele 8.00* thermodynamic calculation software (Boudreau, 1999).

Temperature was calculated for twelve compositions at two different pressures: the minimum calculated pressure of 853 bars and the maximum pressure of 3,452 bars. The average system temperature of the trachyte was 1,132°C, with a range of 1,078-1,171°C and a standard deviation of 27.

Temperature of the rhyolitic magma

Rhyolite-MELTS simulation modelling (Gualda et al., 2012) has been applied in order to decipher rhyolite storage conditions. Twenty four simulations were carried out, with temperature calculations for twelve rhyolitic compositions undertaken at a pressure of 300 bars and a pressure of 600 bars, as previously calculated by fluid inclusion studies (Clocchiatti et al., 1994; Zanon et al., 2003) and supported by other studies (De Astis et al., 1997; 2013; Del Moro et al., 1998; Piochi et al., 2009).

The average temperature for the rhyolitic magma in this pressure bracket is 1,033°C, with a temperature range of 985-1,103°C and a standard deviation of 37.25. This range suggests that the rhyolite is sitting roughly at temperature conditions that may be considered near-liquidus (~1,050°C, Bottinga and Weill, 1972). *Rhyolite-MELTS* also calculated an fO_2 redox value, giving an fO_2 state of ~0.6 units above FMQ for the rhyolitic magma.

4.5 Discussion

The magmatic and post-magmatic evolution of the Pietre Cotte lava flow can be described by a multi-stage evolutionary model, related to process-based stages (determined by field and petrographic observations, and thermobarometric calculations). This includes crystallisation of a trachytic magma (i.e. the mafic enclave magma), the crystallisation of a rhyolitic magma and mingling of the two magmas, late-stage pre- and post-eruptive

microlite and spherulite formation, flow extrusion, rheologically-controlled flow behaviour and post-emplacement processes. These stages of evolution are discussed below.

4.5.1 Intensive parameters and crystallisation conditions of trachytic enclaves

Field and microscopic observations, as well as geochemistry and thermobarometric calculations, suggest that there are up to three magmas interacting in the evolution of the Pietre Cotte magmatic system: (1) A deeper, more mafic magma, (2) a trachytic magma, and (3) a shallower rhyolitic magma.

The glomerocryst assemblage is typically more associated with mafic magmas, yet the enclave groundmass contains crystals more associated with intermediate magmas (plagioclase, alkali feldspar). For instance, De Astis et al., (2013b) cite plagioclase, alkali feldspar and biotite as the generally prevalent phenocryst assemblage in trachytes of Vulcano, while Vulcano mafic rocks display a plagioclase, Ca-rich clinopyroxene, titanomagnetite and olivine mineral assemblage. Therefore, the glomerocrysts and mineral assemblage of olivine, clinopyroxene, plagioclase and titanomagnetite is most likely the product of a more mafic magma. A summary model of the lower magma chamber processes and parameters is shown below in Figure 4.17.

The considerable range in pressure values derived from the glomerocryst-forming minerals may be indicative of the depth variation associated with the more mafic and trachytic magmas. For instance, the plumbing system may exhibit the more mafic magma crystallising at depth within a compositionally zoned magma reservoir, made up of a trachytic magma (at the shallower pressure and depths) and a deeper mafic magma (at the

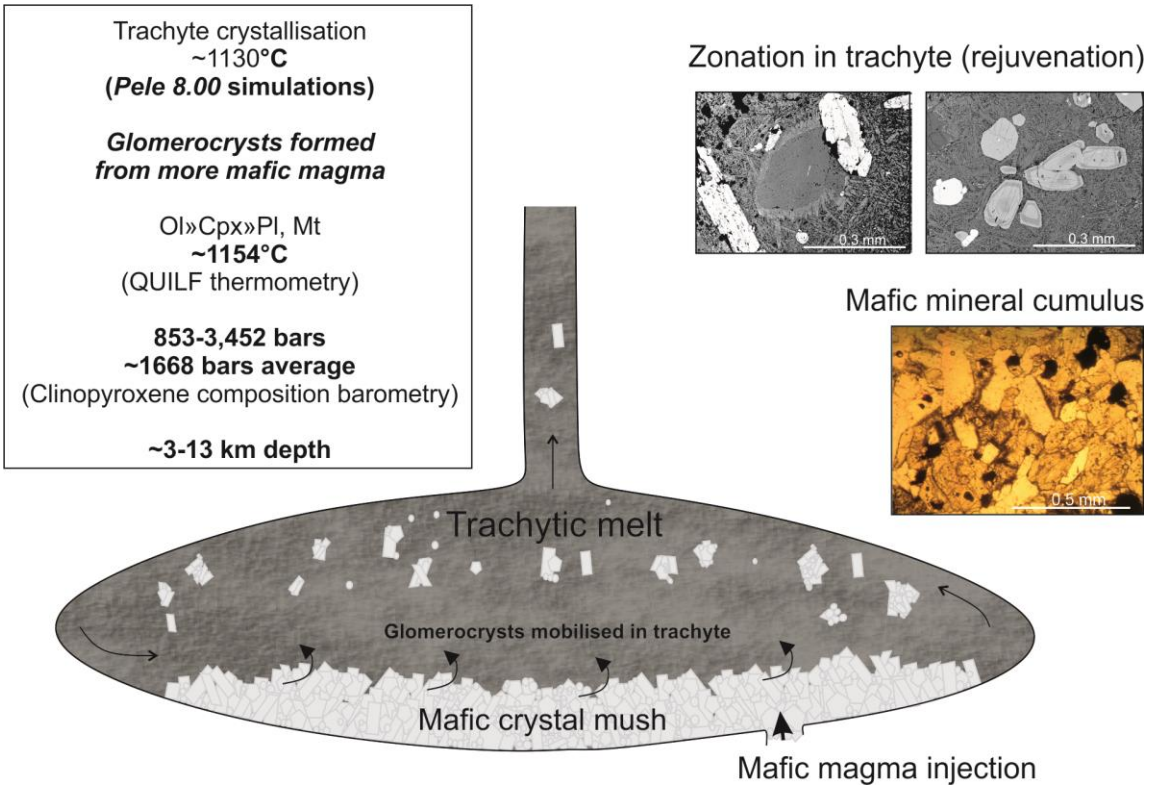

Figure 4.17: Summary model of lower magma chamber and intensive parameters, with 2 early crystallisation stages (indicated by (1) and (2)) of cumulate material and trachytic melt. Glomerocrysts form by remobilisation of a cumulate mush, and the trachytic magma formed by AFC from a more mafic magma.

greater pressure and depths). Compositional zonation arises via fractional crystallisation, with crystals settling out of suspension and forming a crystal mush at the bottom of the reservoir. Injection of a new input of magma from depth may disrupt and mobilise the crystal mush, resulting in glomerocrysts in the trachytic magma. A new input of magma is likely to occur as the plumbing system has been characterised by many small magma batches interacting (Clocchiatti et al., 1994; Del Moro et al., 1998; Zanon et al., 2004; Piochi et al., 2009; De Astis et al., 1997; 2013b). Clinopyroxene exhibits chemical zonation, formed by alterations in composition or temperature of the magmatic system, which may be the product of magma replenishment. The suggestion of a refilling process is also supported by the enrichment of alkali elements, as suggested by Del Moro et al. (1998). Such new magma batch inputs may also result in the glomerocryst-bearing

trachytic magma rising and mingling with the shallower rhyolitic magma, and triggering the eventual eruption. An alternative suggestion for the formation of the glomerocrysts is that closely-spaced crystals resorbed and crystallisation sutured the crystals together (Seaman, 2000). However, the remobilisation theory is preferred due to a lack of disequilibrium textures within glomerocrysts, the distinct differences in the mafic crystal assemblage and trachytic groundmass, the presence of chemical zonation in clinopyroxene, and the refilling/enrichment of alkali elements proposal of Del Moro et al. (1998).

Previous studies identified petrographic (crustal xenoliths) and isotopic evidence of small amounts of crustal assimilation (Clocchiatti et al., 1994; De Astis et al., 1997; 2013b; Del Moro et al., 1998; Piochi et al., 2009). Assimilation and fractional crystallisation (AFC) for the creation of trachyte and rhyolite has been inferred by previous studies (Clocchiatti et al., 1994; De Astis et al., 1997, 2013b; Gioncada et al., 1998; Del Moro et al., 1998; Piochi et al., 2009), specifically latitic magmas evolving to rhyolite through fractional crystallisation from latite and concomitant assimilation of upper crustal rocks. As previously stated, a superimposed refilling process has also been suggested, resulting in the enrichment in alkaline elements (Del Moro et al., 1998). Strontium and lead isotopic data and modelling of De Astis et al., (1997) also supports dominant AFC processes in magma evolution, requiring 60 wt% of crystal fractionation and a ratio between assimilated and crystallised mass ≤0.2 (Piochi et al., 2009). To summarise, these previous studies support the suggestion that the trachyte and rhyolite compositions associated with the Pietre Cotte lava flow were generated from a magma of latitic composition.

Back-mixing of mafic and silicic magmas may also have led to intermediate magmas (De Astis et al., 1997; 2000). In order to make an assessment on the possibility of the trachytic magma being the product of back-mixing between rhyolite and a more mafic (latitic) magma, Harker diagrams have been devised (Fig. 4.18). The latitic end member (based on

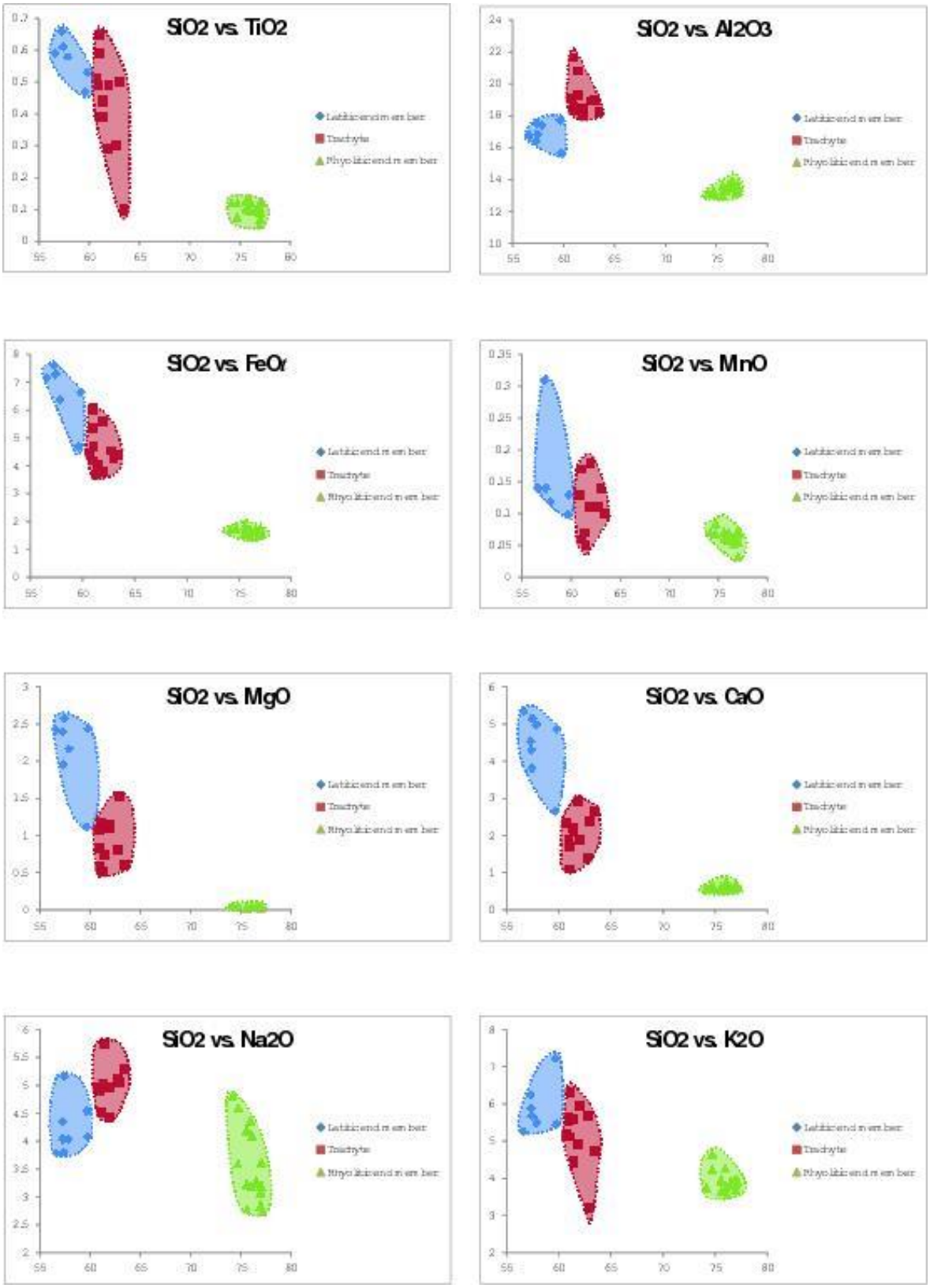

Figure 4.18: Harker diagrams of latitic end-member (from Del Moro et al., 1998), rhyolitic end-member and trachytic compositions plotted in order to assess the potential role of back-mixing (as proposed by De Astis et

al., 1997, 2000). SiO_2 plotted along the base (x-axis) and major element oxides on the y-axis. A mixing trend is observed in SiO_2 versus FeO*t*, MnO and K_2O plots, but is not evident in SiO_2 versus Al_2O_3 and Na_2O plots.

latitic/lati-trachytic compositional data of Del Moro et al., 1998) and the rhyolitic end member (compositional data from this study) were plotted, with trachytic glassy inclusions (from this study) also plotted. If the trachyte is a product of back-mixing of rhyolitic and latitic magmas, the trachytic compositions should plot on along a line between these end members.

Plotting suggests that back-mixing may have produced the trachytic magma. Plots of SiO_2 against FeO*t*, MnO and K_2O effectively show this, while SiO_2 against MgO and CaO are less conclusive, but do not rule this out. However, plots of Al_2O_3 and Na_2O against SiO_2 suggest that the trachytic magma is too enriched in aluminium and sodium to be the product of back-mixing. This may be the result of interaction with another magma (replenishment as previously stated), or crustal material, but this is not known. The plots suggest that the trachyte is may indeed be the product of back-mixing of a rhyolitic and latitic magma, but it is not fully conclusive.

Fractional crystallisation modelling (see Figs. 4.19 and 4.20 and text later) suggests that the trachytic magma was produced by fractional crystallisation processes, with the more mafic crystal assemblage forming early in magma evolution. Smaller glomerocrysts, and, in particular, individual coarse crystals exhibit resorption and compositional zonation (Fig. 4.10k-l). This suggests that the crystal cargo was equilibrated prior to- and during the glomerocrysts-forming process, and crystals underwent resorption and compositional changes under disequilibrium conditions at a later stage. This is likely to have taken place when glomerocrysts and coarse crystals interacted with the rhyolitic host. Conditions of glomerocryst- and coarse crystals were calculated as an average of ~1,154°C (QUILF thermometry; Anderson et al., 1993). *Pele 8.00* simulations indicate a probable sequential

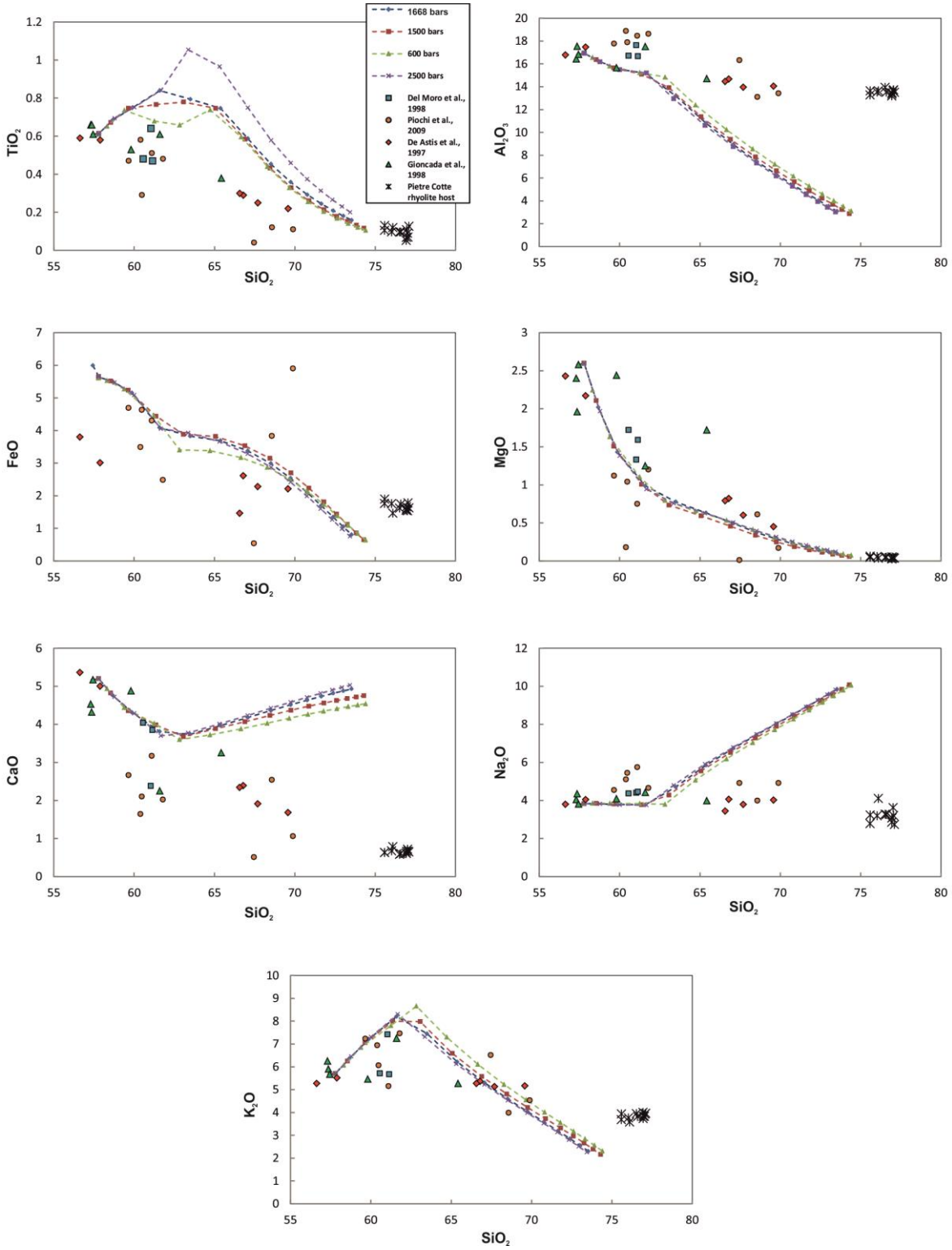

Figure 4.19: Variation diagrams of fractional crystallisation model results from thermodynamic modelling using *Pele 8.00* software, based on a lati-trachytic parental magma from Del Moro et al., 1998. All models were run under the 'Fractionation' flag in an isobaric, closed-system crystallisation model, with H_2O content and oxidation state computed for each pressure input. Dashed lines show modelled evolution, and plot symbols show trachytic mafic enclaves (from literature) and rhyolitic host compositions.

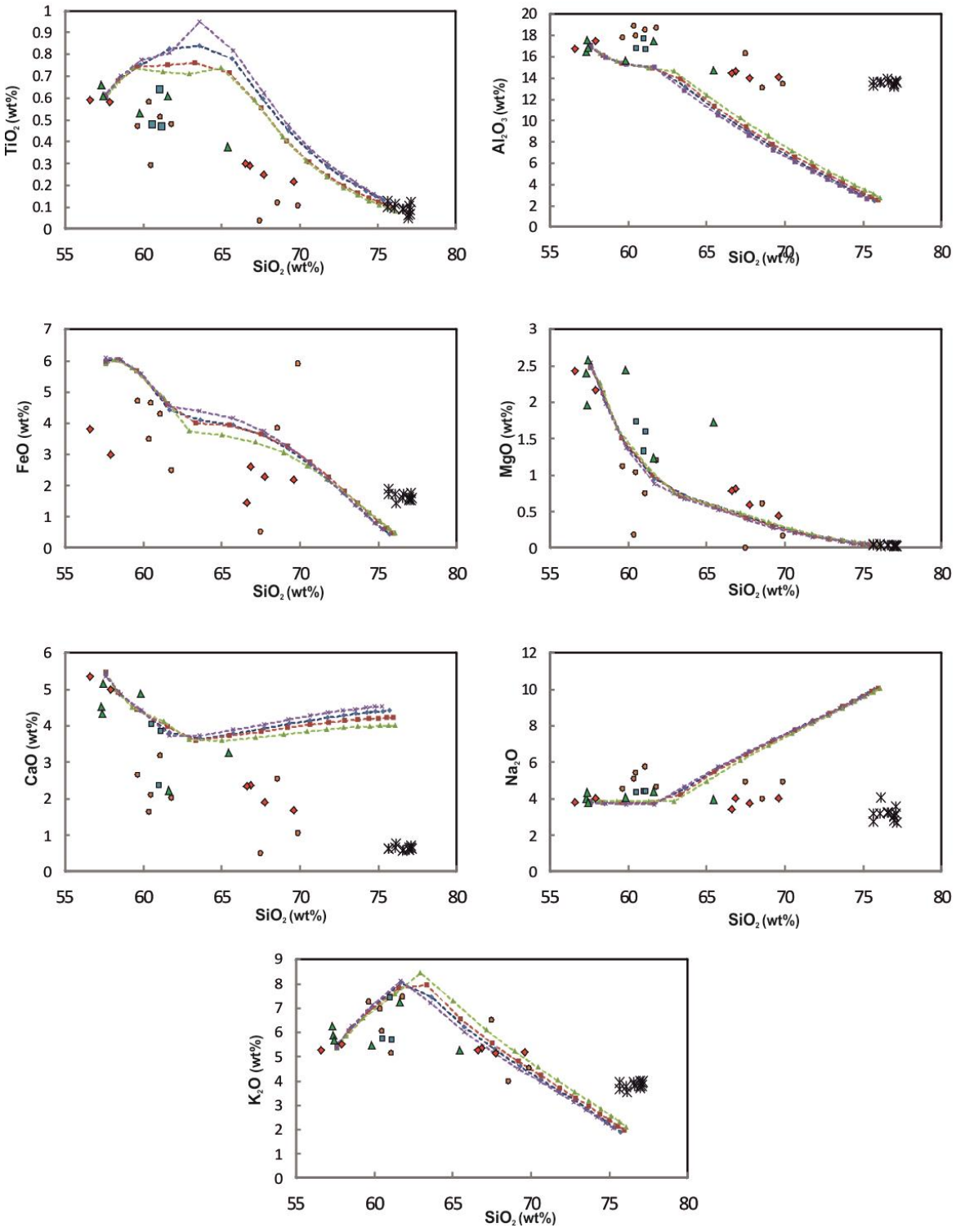

Figure 4.20: Variation diagrams of fractional crystallisation model results from thermodynamic modelling using *Pele 8.00* software, based on a lati-trachytic parental magma from De Astis et al., 1997. See figure 4.19 for model specifications. Figure differs from Fig. 4.19 due to different literature sources for starting compositions.

crystallisation history of the mafic magma of olivine → clinopyroxene → plagioclase. Plagioclase is assumed to either crystallise below the lower clinopyroxene and olivine crystallisation limit, or at a faster growth rate. This is because plagioclase crystals often engulf smaller clinopyroxene and olivine crystals. The mafic melt crystallised at a pressure of ~1,668 bars (clinopyroxene-composition barometry; Putirka, 2008).

The crustal material under Vulcano is Calabrian arc crust (Schütte 1978; Van Dijk and Scheepers 1995), comprised of Hercynian metasediments and metaigneous rocks, with minor Jurassic ophiolitic material and Miocene Quaternary sediments (Honnorez and Keller, 1968; Barberi et al., 1974; Amodio-Morelli et al., 1976; Scandone, 1982; Wang et al., 1989; Ventura et al., 1999; Peccerillo et al., 2006; De Astis et al., 2013b). Depth was calculated as a function of pressure (force per unit area), where force is calculated by mass of the rock (using a continental crustal density of 2.7 g cm^{-3}; Ringwood, 1991; Dobrzhinetskaya and Green, 2007) multiplied by acceleration (gravity at the surface of the earth – 9.8 m/s^2). This gives an average pressure of 260 bars/km, and therefore an estimated average depth of ~6 km for a pressure of 1,668 bars.

In order to assess the role of fractional crystallisation (FC) in the evolution of the trachytic enclave magma (and the rhyolitic host), fractional crystallisation trends have been modelled for major element oxides (wt% of TiO_2, Al_2O_3, FeO, MgO, CaO, Na_2O, K_2O vs. wt% of SiO_2) from more primitive products associated with recent Fossa cone activity (i.e. in the latest epoch of activity at the Fossa cone as defined by De Astis et al., 2013b). Latitrachyte was selected as the starting composition (see equilibrium calculations later), and modelled in variation diagrams as a FC trend at different pressures and fO_2 slightly above FMQ, calculated using *Pele 8.00* software (Ghiorso, 1975; Ghiorso and Sack, 1994). Latitrachyte starting compositions were used from previous whole rock studies (Del Moro et al., 1998; De Astis et al., 1997; 2013b). Trachytic enclaves from whole rock (Del Moro et

al., 1998; De Astis et al., 1997; 2013b; Piochi et al., 2009) and melt inclusion studies (Gioncada et al., 1998 and this study), and rhyolitic magma compositions (from this study) have also been plotted in order to evaluate the role and contribution played by FC of the more primitive lati-trachytic melt in producing the more evolved (intermediate) enclave magma and the rhyolitic host. Harker diagrams are shown in Figs. 4.19 and 4.20.

For all runs, an isobaric, closed system fractional crystallisation trend is modelled, with a starting temperature of 1,200°C. Pressures of 1,668 bars (based on clinopyroxene-composition barometry), 1,500 bars, 600 bars and 2,500 bars were selected in order to cover a wide pressure range. Oxygen fugacity (calculated by *Pele* algorithm; Boudreau, 1999) shows no significant variation relative to FMQ with changing pressure. Variation diagrams of modelled FC trends show enrichment of TiO_2 and K_2O wt% up to ~62-63 wt% SiO_2, where TiO_2 and K_2O become depleted. FeO wt% shows a kinked regression at the same ~62-63 wt% SiO_2. CaO and Na_2O show depletion followed by enrichment at ~62-63 wt% SiO_2 (although glass and whole rock plots suggest a more continuous depletion, suggesting that the model may not work for these elements), and Al_2O_3 and MgO show a continuous depletion trend. FC modelling shows crystallisation of clinopyroxene, albitic plagioclase, alkali feldspar and olivine, consistent with petrological observations. Fractional crystallisation modelling with *Pele* gives a total mass, as well as proportions of mineral phases that are crystallising. The FC model (from lati-trachyte composition of De Astis et al., 1997; 2013b) shows alkali feldspar is the highest mineral volume proportion (~52%), followed by plagioclase (~32%), clinopyroxene (~7%), titanomagnetite (~5%) and olivine (~4%). Although alkali feldspar is identified in petrological observations of the mafic enclaves, its occurrence as a groundmass mineral means that the proportion has not been quantified. If alkali feldspar is excluded from the FC model output, mineral proportions are plagioclase (~66%), clinopyroxene (~15%), titanomagnetite (~11%) and

olivine (~8%). These proportions closely resemble that of petrographic observations made here (plagioclase - 60%, clinopyroxene - 20%, olivine and titanomagnetite – 10%).

Models show a depletion of TiO_2 and K_2O at intermediate compositions (Figs. 4.19 and 4.20). Depletion of TiO_2 and K_2O at intermediate compositions relates to later crystallisation of titanomagnetite (ulvöspinel) and alkali feldspar. Some FC modelling suggests that continual FC of lati-trachyte may lead to trachyte and rhyolite, such as TiO_2, MgO and K_2O plots with minor or no variation from modelled trend. However, plots of other FC modelling failed to reproduce trends indicated by the trachyte and rhyolite plots (which follow a relatively straight trend). Though minor variations may be related to differing pressure and fO_2 parameters, these discrepancies are likely the result of other differentiation processes, such as an increasing role of magma mingling and/or crustal contamination. Observations make it clear that at least two magmas have interacted in the magmatic history of the Pietre Cotte rhyolite, so magma mingling is likely to have played an important role during magmatic evolution. Previous studies also identify petrographic (crustal xenoliths) and isotopic evidence of small amounts of crustal assimilation (Clocchiatti et al., 1994; Del Moro et al., 1998; De Astis et al., 1997, 2013b; Piochi et al., 2009). The significant difference between rhyolite plots and FC modelling trends (compared to that of the trachytic plots and FC trends) suggests that AFC played some role during magma generation.

Putirka (2008) developed a test for equilibrium between plagioclase and a co-existing melt by comparing An-Ab exchange. The equilibrium constant is sensitive to temperatures at T<1,050°C (the output value should be ~0.1±0.11 for temperature systems above 1,050°C, or equal ~0.25±0.05 for temperature systems below 1,050°C). This model has been applied to plagioclase rims and the rhyolitic melt, as well as plagioclase rims and the trachytic melt in order to determine conditions under which plagioclase was crystallising in equilibrium.

The model requires the melt and feldspar compositions (major element wt%), and a pressure estimate (600 bars used for rhyolite equilibrium test, 1,668 bars for trachyte equilibrium test). Results suggest disequilibrium of plagioclase rims and the rhyolitic melt (with some exceptions but at temperatures >1,050°C), but equilibrium is achieved for plagioclase rims and the trachytic glass (observed output values of 0.06-0.09 for four tests), at temperatures below 1,050°C and a pressure of ~1,668 bars.

Putirka (2008) also devised built-in tests for equilibrium for clinopyroxene-liquid and olivine-liquid thermobarometry methods. These tests for equilibrium between clinopyroxene/olivine and a co-existing melt compare observed and predicted values for Fe-Mg exchange coefficient with constant values. These tests have been applied for clinopyroxene and olivine (cores, rims and, where present, groundmass) with a co-existing lati-trachytic melt composition (from Del Moro et al., 1998), as well as the trachytic glass composition from this study. Equilibrium tests for clinopyroxene cores and co-existing lati-trachytic melt indicate a good correlation between predicted and observed component values, suggesting that the clinopyroxene cores were indeed in equilibrium with a lati-trachytic melt (based on based on Equation. 3.2 (EnFs) - Putirka et al., 1996; Putirka, 1999; Putirka, 2008). Clinopyroxene rims also show a correlated component between predicted and observed values, suggesting the rims were also in equilibrium with a lati-trachytic melt. However, clinopyroxene groundmass phases do not show a good correlation, suggesting that the groundmass material is not equilibrated with a lati-trachytic melt, and is instead equilibrated with the trachytic melt (measured groundmass phase correlates well with the trachytic melt). Olivine-liquid equilibrium testing (based on Roeder and Emslie, 1970; Rhodes et al., 1979; Putirka, 2008) reveals similar findings, with a number of olivine (cores and rims) samples correlating within the predicted limits of equilibrium for a lati-trachytic melt, but showing disequilibrium with the trachytic melt. These results indicate

that olivine and clinopyroxene (crystals and within glomerocrysts) crystallised in a more primitive melt, before being incorporated into the trachytic (enclave) magma.

Glass/whole rock plots (lati-trachyte, trachyte and rhyolite) and FC modelling (excluding CaO and Na_2O models which did not work) suggest that the trachyte is genetically related to a more mafic magma (lati-trachyte). Therefore, the origin of individual crystals (olivine, clinopyroxene, plagioclase and titanomagnetite) and glomerocrysts within the trachytic melt may be the result of FC of a lati trachytic melt. One suggestion is that the chamber was characterised by a compositional vertical zonation, with crystals accumulating at the base or margins in a solidification front, with further FC of the remaining lati-trachytic magma to a trachytic magma. Textural observations suggest a cumulate-like formation, with crystals grouped and touching. A rejuvenated crystal mush resulted in the presence of glomerocrysts in the deeper trachytic melt (~6 km depth and ~1,130°C). An alternative suggestion for the formation of the glomerocrysts is that closely-spaced crystals resorbed and crystallisation sutured the crystals together (Seaman, 2000). However, the remobilisation theory is preferred due to a lack of disequilibrium textures within glomerocrysts, and the distinct optical differences in the mafic crystal assemblage and trachytic groundmass.

4.5.2 Trachytic and silicic magma interaction

Field observations indicate that the trachytic magma entered a rhyolitic host, forming (predominantly) ellipsoidal enclaves. Previous studies state that the trachytic magma also contained crustal-derived quartzite xenoliths (Frezzotti et al., 2004; Piochi et al., 2009). Glomerocrysts and individual coarse crystals are evident within the rhyolitic glass as

enclave-derived xenocrysts (surrounded by a thin layer of enclave groundmass). Plagioclase rims within the rhyolitic host show lower An content, which may be the result of minor chemical interaction between the enclave-derived crystals and the Si- and K-rich rhyolite host (although petrological observations suggest there is no chemical mixing, meaning any mixing would likely be minimal).

Trachytic enclave morphology suggests that the enclaves had plastic properties upon mingling with the rhyolitic host, with contrasting magma viscosities. The sharp boundary between some enclaves and rhyolitic host suggests that the enclaves cooled quickly (evident from occasional chilled margins), (evident from occasional chilled margins, Fig. 4.21), resulting in limited diffusion.

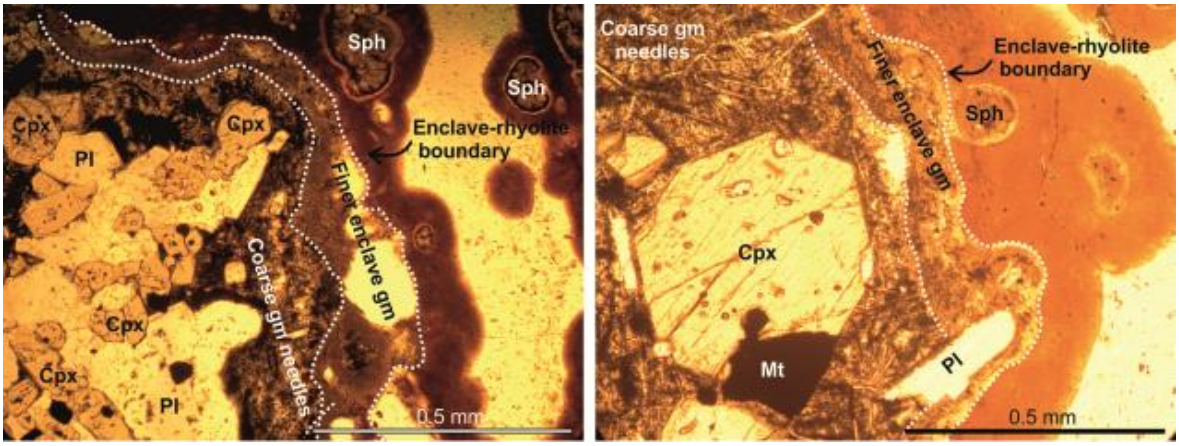

Figure 4.21: Examples of enclave-rhyolite boundaries, showing finer enclave groundmass material at the enclave boundary (indicating a chilled margin and fast cooling). Brown rims surrounding enclaves and spherulites form as a later solid-state modification (see later).

The shallower chamber model of magmatic evolution is summarised in Figure 4.22. *Rhyolite-MELTS* simulations give an average system temperature of ~1,033°C, over a range of 985-1,103°C. The rhyolite storage pressure conditions have been previously

calculated as ~300-600 bars (on the basis of fluid inclusion studies, Clocchiatti et al., 1994; Zanon et al., 2003; Piochi et al., 2009).

The rhyolitic host has been interpreted as the product of an earlier mafic magma undergoing AFC processes, originating from melting of metasomatised residual lithospheric mantle (Del Moro et al., 1998; De Astis et al., 2000; Peccerillo et al., 2006). De Astis et al. (2013b) state that most recent rhyolitic lavas from the Fossa cone originate at mid-crustal levels and reside within the metapelitic basement and/or the transition between the basement and the volcano-sedimentary sequence (5-3 km) (see also Zanon et al., 2003; Dellino and De Astis, 2008). Small magma batches evolved to rhyolite at this depth, and assimilated small amounts of upper crustal material (De Astis et al., 1997; 2013b).

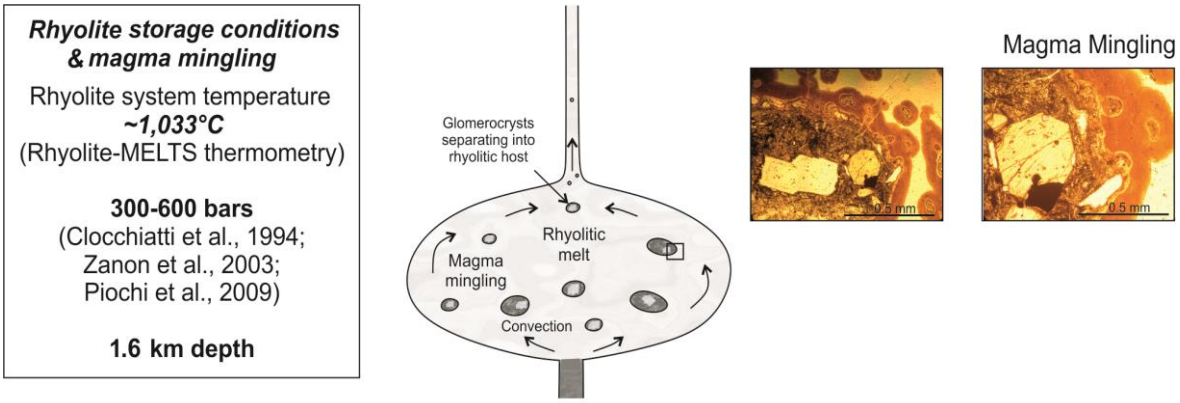

Figure 4.22: Model of upper magma evolution processes, including rhyolite crystallisation and magma mingling of trachytic magma with rhyolitic magma.

In modelling of petrochemical processes, Eu has been used as an indicator of feldspar fractionation or accumulation, and a fO_2 indicator (Möller and Muecke, 1984). For instance, relatively low fO_2 conditions (close to FMQ) were suggested for intermediate enclave and host rhyolite crystallisation conditions in the Rocche Rosse lava flow and other young silicic lava bodies on neighbouring Lipari, based on a negative Eu whole rock

anomaly (Gioncada et al., 2005; Davì, 2007; Davì et al., 2010). Generally, this anomaly is attributed to plagioclase fractionation at low fO_2 conditions, although it may also be the product of assimilation or partial melting of crustal material, as a negative Eu anomaly is also a feature of post-Archean upper continental sediments (Taylor and McLennan, 1985; Rudnick, 1992). This negative Eu anomaly has been identified in younger Vulcano rocks, including evolved samples from the Fossa cone, more pronounced than in older, less evolved rocks (De Astis et al., 2013b). Though an Eu anomaly may partly reflect prevailing fO_2, the role of melt composition also plays an important role in Eu partitioning (Möller and Muecke, 1984). An Eu anomaly has been identified within Fossa samples (De Astis et al., 1997; 2013; Piochi et al., 2009), which may hint at low fO_2 conditions (above FMQ) for this rhyolitic system.

Glomerocrysts and coarse crystals (surrounded by a thin layer of trachytic groundmass) occasionally separate out from the trachytic enclaves in to the rhyolitic host. The estimated depth of rhyolite storage (for a pressure of 300-600 bars) is ~0.8-1.6 km. This depth is in agreement with previous studies (though more specific), estimating a depth of short-lived, shallow reservoirs of less than 3 km (Gioncada et al., 1997; Del Moro et al., 1998). The proposal of back-mixing of the rhyolitic magma and more latitic magma (producing the trachytic magma) suggests that the magmas may have interacted for a considerable time before the eruption. Further injection of the trachytic magma (following replenishment from a deeper source) in to the rhyolite may have acted as an eruption trigger for the Pietre Cotte lava extrusion. Such an interpretation is in agreement with the overall evolution of the Fossa cone, where younger magmas differentiated at intermediate and shallow levels (e.g. 1.6 km depth for AD 1888-1890 pyroclastic products; Clocchiatti et al., 1994) by AFC processes, with mingling of silicic and intermediate melts occurring shortly before eruptions (De Astis et al., 2013b). Trachyte to rhyolite magmas are considered to have

formed at mid-crustal levels through prolonged FC processes (De Astis et al., 1997) as a result of the quiescence in the Vulcano eruptive activity between 50–42 ka and 28 ka (De Astis et al., 2013b).

Isotopic data from previous studies further illustrate magma-crust interaction at shallow depths below the Fossa cone. Recent products (younger than 28 ka) display ranges of $^{87}Sr/^{86}Sr$ (0.704495–0.705879) and $^{143}Nd/^{144}Nd$ (0.512432–0.512671) (De Astis et al., 2013b). The highest $^{87}Sr/^{86}Sr$ and the lowest 143Nd/144Nd ratios correspond to the trachytes and rhyolites of La Fossa cone (De Astis et al., 2013b). Geochemical modelling by De Astis et al., (1997) and Del Moro et al., (1998) indicate that these Sr isotopic signatures of the rhyolite rocks can be modelled with the assumption of AFC processes, with variable rates of assimilation vs. crystallisation. It is concluded that the composition of the assimilated material has no bearing on AFC trends, but the upper crustal rocks used by the modelling of Del Moro et al., (1998) fit the isotopic variation trends well. The low Sr content in late La Fossa rhyolites (compared to older deposits) make the rhyolitic magmas more susceptible to Sr isotopic modification by small amounts of assimilation. Radiogenic isotopic data therefore highlights the occurrence of crustal assimilation in the evolutionary processes that affected the rhyolitic magmas erupted from La Fossa cone, including the Pietre Cotte lava flow (De Astis et al., 2013b).

4.5.3 Extrusion and post-magmatic processes

A summarised model of magma ascent, conduit processes and flow extrusion is shown in Figure 4.23. Following the complex interaction of three texturally- and compositionally-distinct magmas at depth, the rhyolitic magma (containing trachytic enclaves and

glomerocrysts) extruded. Microlites in the rhyolite exhibit slender rod-like crystallite forms. Microlites have been previously reported as sanidine and plagioclase in composition (Piochi et al., 2009). Microlites can crystallise in the conduit (Manga, 1998; Martel et al., 2006; Humphreys et al., 2009), nucleating in response to an increase in liquidus temperature (related to vapour loss) during the initial stages of eruption (Swanson et al., 1989). Microlites, characterised by many nucleation sites and small crystal sizes (due to either a slow growth rate or short period of growth due to cooling; Swanson et al., 1989), are hypothesised to crystallise in silicic melts in response to vapour-phase evolution and magma degassing, typically related to early volatile loss from a system (Swanson et al., 1989). The reported water values of <0.08 wt% in the rhyolite (Piochi et al., 2009) and ~1 wt% in inclusions (Clocchiatti et al., 1994), are consistent with an early volatile loss from the system, and therefore microlite crystallisation in the Pietre Cotte rhyolitic melt o ccurred as a response to magma degassing (decompression-induced crystallisation; Hammer and Rutherford, 2002; Couch et al., 2003; Blundy and Cashman, 2005; Mollard et al., 2012).

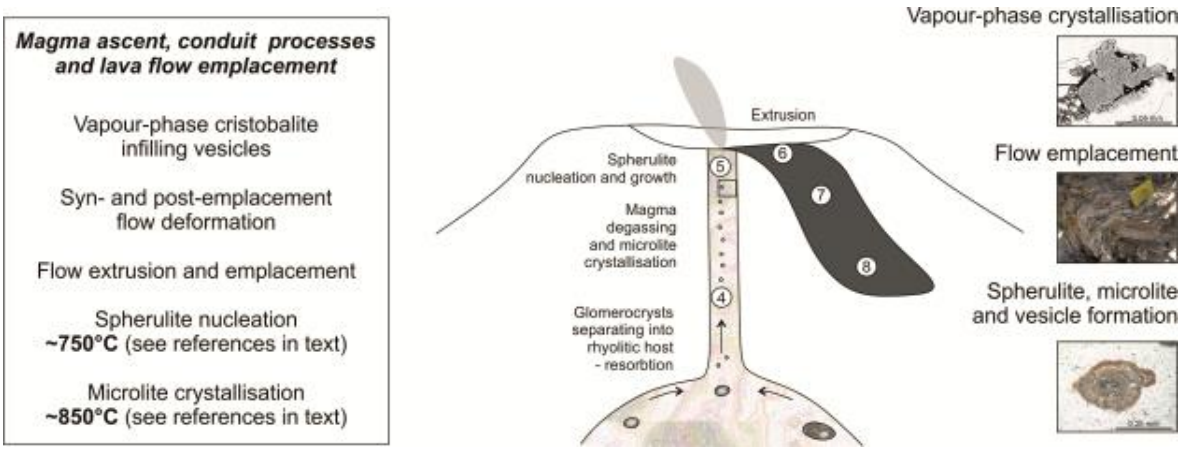

Figure 4.23: Model of magma migration, flow extrusion, emplacement and post-emplacement deformation and modification.

Microlites are rare to abundant in the glass, 1-3 micrometres in length, and showing an alignment (due to flow – suggesting microlites continued to form following eruption). Microlites are deflected around spherulites, or are overprinted by spherulites. Microlites are generally considered to form due to rapid growth during quenching, in undercooling conditions (an observation made for microlites formed in the Monte Guardia activity on Lipari, suggested by De Rosa et al., 2003 and Gioncada et al., 2005). This process of microlite formation is consistent with microlite shape (elongate, skeletal), and the widespread presence of spherulites (considered to form due to enhanced undercooling (Kirkpatrick, 1975; Swanson, 1977; Castro et al., 2009; Clay et al., 2013) and/or enhanced by deformation). Microlites can also form due to magma mingling processes, whereby inclusions disaggregate under conditions of high shear stress during ascent in the conduit, transferring enclave material in to the host (in this case, rhyolite) groundmass (Martel et al., 2006; Humphreys et al., 2009). Mafic enclaves contain a microlitic-diktytaxitic groundmass (forming as a response to rapid undercooling), and these microlites may have transferred from the trachytic enclaves in to the rhyolitic host during mingling. As previously stated, this would require high shear stress, which may occur during ascent through the conduit or upon extrusion and during flow deformation. Microlites in the rhyolitic host are both plagioclase and sanidine (De Astis et al., 1997; Piochi et al., 2009). Clinopyroxene microlites have also been identified, and previously reported (De Astis et al., 2013b). Plagioclase microlites are noted by Piochi et al., (2009) to be similar in composition to plagioclase (enclave) phenocryst rims, while sanidine microlites show no such similarities. This suggests that microlites may have formed due to two processes: (1) degassing-induced crystallisation at large degrees of undercooling (evident by skeletal morphology, presence of spherulites and glassy nature), resulting in sanidine microlites, and (2) disaggregation of trachytic enclaves leading to microlites within the rhyolitic host,

responsible for plagioclase and clinopyroxene microlites. Flow banding, stretching lineations and large scale structures preserved in the Pietre Cotte lava flow suggests that the flow had undergone a high shear stress history, required for such disaggregation processes.

Spherulites in the Pietre Cotte rhyolitic host are slightly ellipsoidal, with a radial interior (see Chapter 3). Spherulites contain alkali feldspar, α-cristobalite and β-cristobalite, and glass (determined by laser Raman spectroscopy and XRD in Chapter 3). The feldspar composition within spherulites is chemically distinct from feldspar phenocrysts, xenocrysts and groundmass phases within the Pietre Cotte enclaves (predominantly sanidine, andesine and labradorite in composition). Spherulite CSD analyses indicate two populations comprising smaller spherulites (<0.1 mm in size) and larger spherulites (>0.1 mm), and spherulites grew in a short period of ~2 days. Glass and β-cristobalite within spherulites, as well as microlite deflection, suggests that spherulites began forming at high temperatures (i.e. above glass transition (T_g) temperatures; Swainson and Dove, 1995; Richnow, 1999). Seaman et al., (2009) showed that the preservation of glass within spherulites highlights the critical influence of water concentration on the likelihood of quenching versus crystallisation during undercooling of a melt. Richnow (1999) also suggests that the presence of glass within spherulites is an indicator of incomplete crystallisation and spherulite formation above T_g temperatures. High temperature β-cristobalite converts to low temperature α-cristobalite. β-α cristobalite transition occurs in the metastable temperature range (~200°C; Damby et al., 2014). Spherulites form at high temperatures (above or at high T_g temperatures), forming due to primary nucleation, with microlites growing concomitantly and deflected around spherulites. Observations also suggest spherulites continued to grow at a later stage. Elongate spherulites may indicate that spherulites formed during flow deformation. Deformation may have triggered or promoted

spherulite crystallisation, or deformation may have been induced due to spherulite crystallisation (Clay et al., 2013; Chapters 2 and 3). Both circumstances, however, suggest that spherulites were forming during flow emplacement, overprinting microlites.

Vesicles formed during the extrusion of magma to the surface. Trachytic enclaves, spherulites and vesicles are generally surrounded by a thin brown rim (see later). Temperature estimates of texture formation in SiO_2-rich volcanics during ascent, eruption, emplacement and cooling (Lofgren, 1971; Eichelberger et al., 1986; Swanson et al., 1989; Davis and McPhie, 1996; Manley, 1996; MacArthur et al., 1998; Breitkreuz, 2001) suggest that microlites crystallise from ~850°C (to the onset of T_g), with primary spherulites nucleating and growing from ~750°C (to lower T_g temperatures; Lofgren, 1971; Swanson, 1977; Castro et al., 2009; Watkins et al., 2009; Gardner et al., 2012; Clay et al., 2013). Angular inclusions have also been identified in microscopic observations, containing altered minerals. These are likely to be modified xenoliths, which have been identified in previous studies (e.g. Frezzotti et al., 2004; Piochi et al., 2009). It has been suggested that these xenoliths have undergone argillic alteration (i.e. transformed by intense hydrothermal activity), which would account for the alteration of minerals and groundmass material within xenoliths (Piochi et al., 2009).

Non-isotropic brown rims commonly surround spherulites in the Pietre Cotte obsidian. Though these rims are non-isotropic, EMP analysis and Raman spectroscopy studies of Pietre Cotte spherulites and rims yield a response akin to glass (rhyolitic glass in composition, with an amorphous humped Raman profile; Chapter 3). These brown rims show a slight enrichment of alkali elements, and Si depletion relative to the surrounding glass, suggesting that Si is being incorporated the during spherulite growth (cristobalite and alkali feldspar crystallisation; Chapter 3). Spherulite growth is considered to initiate while lava is in a highly viscous or rigid state (above or high T_g), suggesting that this

fractionation of major elements (in particular, alkali elements and Si) is the result of sub-solidus diffusion, occurring in localised areas, i.e. at the edge of growing spherulites with the co-existing glass, resulting in brown rims at the edges. Castro et al. (2009) attribute these rims in obsidian lavas to a solid state redox shift, which grow while the spherulite is also growing. Gardner et al. (2012) further describe these rims as compositional gradients surrounding spherulites, a result of expulsion and slow diffusion of incompatible constituents (H_2O, Rb, and F) away from the spherulite. Clay et al. (2013) also suggest that 'oxidised rims' in the Rocche Rosse lava flow on Lipari develop during solid-state modification. Based on these observations and previous interpretations, the brown rims in the Pietre Cotte lava flow are interpreted to form syn- and post-spherulite formation in solid state. Glass colour differences are considered to correspond to different oxidation states of Fe (Galliard et al., 2003), and may also show non-isotropic properties due to unrelaxed stress accumulation during hydration during spherulite growth (Friedman and Smith, 1960; Castro et al., 2008).

Upon extrusion, the flow underwent ductile and brittle deformation, evident by a number of deformational structures preserved within the flow. Obsidian underwent complex rheological change from ductile to brittle during flow. Cooling history is a key control on obsidian flow rheology, and subsequently plays a major role in flow emplacement and the subsequent formation of surface structures (Fink, 1983; Hess and Dingwell, 1996; Gottsmann and Dingwell, 2001b; Gonnermann and Manga, 2003; Castro et al., 2008). Here, the Pietre Cotte lava flow underwent an extensional and compressional regime. This produced stretching lineations and folding. The low volume and thickness of the flow, combined with the single flow directional advance, hindered the development of large scale folding (e.g. widespread folding >5 m in wavelength and amplitude observed on the Rocche Rosse lava flow on Lipari; Chapter 2). Structural mapping of foliations reveals an

overall arrangement of north- and south-dipping orientations, indicating the development of flow ramps and folds during emplacement. Stretching lineations show a relatively uniform alignment, formed due to extensional forces and controlled by flow advance. This suggests a single flow direction towards the north, with no obvious field evidence of multiple flow directions. The overall structural orientations can be attributed to a uniform and steep underlying topography, resulting in relatively weak compressional forces, except at the base of the cone where compression results in flow-frontal folding. Structures which do not show this overall orientation are likely to have been affected by progressive deformation and variations in rheology. Spherulite nucleation and growth continued following extrusion, potentially nucleating in response to deformation (Chapters 2 and 3).

In upper flow regions, there are areas that exhibit a more vesicular texture. These zones are characterised by a dark grey colour, and a sheared and vesicular appearance at the flow surface. The origin of this vesicular unit in the Pietre Cotte lava flow is unknown, though it is speculated that the texture may be a result of either a rising pumice diapir or, (more favourably), rheological contrasts resulting in a silicic foam. Fink (1983) identified rising coarse pumice diapirs from the base of Little Glass Mountain, which disrupted flow configuration. However, the glassy nature of the zone in the Pietre Cotte and the presence of sheared vesicles suggest that this texture may be the product of a silicic foam (i.e. formed during foaming due to higher temperatures). The flow terminated at shallower topographies, whereby the increase in friction and weaker gravitational pull to advance resulted in folding and variable structural orientation patterns observed at the flow front, as well as sheath folding observed in the flow frontal region. Flow deformation culminated with a brittle deformational regime, controlled by cooling and strain rate, with the onset of a brittle regime first occurring in cooler and more highly strained areas of the flow (e.g. flow margins). This brittle deformation resulted in the formation of autobreccia (more

abundant in flow frontal areas likely due to stresses, early cooling and talus production), faulting and fracture development.

4.5.4 Post-emplacement processes

Gottsmann and Dingwell (2001b) modelled the cooling history of the Rocche Rosse obsidian lava flow on Lipari, and show that the flow cooled, remained mobile and actively deformed slowly, lasting for weeks following emplacement, and cooling at a rate of tens of degrees K per day (at a depth of 40-120 cm). This suggests that obsidian flows such as the Pietre Cotte lava flow may have also continued to slowly deform following emplacement. This thermal insulation may have also buffered spherulite growth following emplacement (resulting in smaller, undeformed spherulites). Lithophysae formation, infilling vesicles, re-crystallisation and/or modification of spherulites, gaps and hollows, occurred at lower vapour phase temperatures, with inward crystallite growth (Von Richthofen, 1860; MacArthur et al., 1998; Breitkreuz, 2001; Smith et al., 2001; Tuffen and Castro, 2009). Spherulite growth below 400°C is also considered prohibitively slow, though re-crystallisation or modification of spherulites may take place for up to ~400 years (Clay et al., 2013). The final stage of texture-formation within the Pietre Cotte lava flow was this vapour-phase cristobalite crystallisation partially or completely filling vesicles, formed due to hot magmatic gases derived from gas exsolution. Mesh-like, non-radial (microcrystalline) silica partially, or completely, infilling vesicles and hollows, represents cristobalite crystallising during late-stage vapour crystallisation (<400°C; Rosenberg, 1973; Horwell et al., 2013; Damby et al., 2014). These form due to decompression during degassing (pressure decrease), and vapour crystallising in patches in vesicles. This type of

crystallisation may also suggest slow cooling (Baxter et al., 1999, de Hoog et al., 2005), which may be similar to the slow cooling of days to weeks as suggested for the Rocche Rosse lava flow by Gottsmann and Dingwell (2001b). Spherulites characterised by the filling of cavities and hollows by secondary cristobalite may occur during and after vapour-activity and fracturing. Such re-crystallisation textures developed due to primary cooling, and continued to form throughout the cooling history of the lava (Kneller, 2002). Crystallisation from the glassy state (i.e. devitrification) is the final (ongoing) process occurring in the Pietre Cotte lava flow. Devitrification involves the same atomic rearrangement as is found in melt crystallisation (Marshall, 1961). Devitrification (the product of obsidian hydration) results in further spherulite modification and other secondary fibrous crystallisation development.

4.5.5 Evolutionary model and summary

Currently, there are two previous studies addressing magmatic processes and magma chamber dynamics associated with the evolution of the Pietre Cotte lava flow. Piochi et al. (2009) comprehensively studied the recent plumbing system of the Pietre Cotte lava flow based on textural, petrological and fractal data, and a prior study by Perugini et al. (2007) analysed the size distribution of enclaves in the Pietre Cotte lava flow. Piochi et al. (2009) modelled the processes of magma evolution associated with the Pietre Cotte lava flow, based on field, textural and fractal data, major, trace and volatile element analyses, and incorporated petrological and fluid inclusion data from De Astis et al. (1997), Gioncada et al. (1998), and Frezzotti et al. (2004). This suggests a rhyolite magma uprising in to a lati-trachytic plug (based on whole rock analyses by De Astis et al., 1997), with the trachytic

and rhyolitic melt compositions generated by AFC processes from a less evolved latitic magma (see also Clocchiatti et al., 1994; De Astis et al., 1997; 2013b; Gioncada et al., 1998; Del Moro et al., 1998). The sharp compositional transition across the contact between the rhyolitic host and the enclaves provided evidence for the absence of significant elemental diffusion and mingling between magmas is identified as dominant process (Piochi et al., 2009).

Piochi et al. (2009) attributed chemical variability in the analysed rocks to specific crystallisation histories before interaction. For mafic enclaves, geochemical variations in their glass matrices and the occurrence of clinopyroxene with normal and reverse zoning suggest disequilibrium conditions during crystallisation. The study also concludes that whole trachytic compositions can be considered actually representative of a closed magmatic system, based on the observation of trachytic glass bordering phenocrysts acting as a barrier to chemical exchange with surroundings. The study states that the rhyolitic magma is in thermal equilibrium with quartz-rich xenoliths at 1,000°C and 600–300 bars, and that magma-crust interaction occurred at 600–300 bars in the shallower portion of the volcanic system. The injection of a more mafic magma in to the rhyolitic host proposed in this study is a contrasting model to lati-trachytic magma plug suggested. This magma plug theory is suggested based on a large range of observed textures resulting from specific parts of the lati-trachytic magma body experiencing different thermal histories (and viscosity ratios). A lati-trachytic plug is depicted (variably affected by cooling, crystallisation and degassing processes), with contemporaneous eruption of the lati-trachytic magma and rhyolitic magma caused by the rise of the rhyolitic magma batch. Desegregation of the partially solidified plug accounts for mingling at variable scales and the fragmented nature of the enclaves (Piochi et al., 2009). This model is also favoured by

the study of Piochi et al. (2009) as it accounts for the variable groundmass crystallisation of the enclaves, and the lower volatile content and vesicularity of the trachyte.

Perugini et al. (2007) performed enclave size distribution studies on the mafic enclaves in the Pietre Cotte lava flow in order to provide insights in to magma chamber processes. Perugini et al. (2007) proposed that mafic enclaves formed within the rhyolitic host by injection of the more mafic magma in to the rhyolitic magma. This is suggested based on enclave size distribution analysis, with fragmentation processes produced in response to disruption of viscous fingering morphologies, caused by rheological contrasts associated with the mafic magma entering the rhyolitic magma. A mafic injection of a hotter, intermediate magma in to a cooler rhyolitic magma resulted in cooling of the mafic magma and more solid behaviour, accounting for enclave shape variation (Perugini et al., 2007). Perugini et al. (2007) state a need for further studies to fully evaluate the magma chamber processes. The model suggested in this study provides further substantiation and quantification to this mafic injection hypothesis suggested by Perugini et al. (2007).

The lati-trachytic plug model of Piochi et al. (2009) is in contrast to the model suggested here. The plug model is not favoured in this study based on field and microscopic observations, and thermobarometric estimates. Variable shape (roundness) and size of enclaves is suggested by Piochi et al. (2009) as an indicator of a lati-trachytic plug. Temperature estimates of this study suggest that the deeper, more mafic magma (responsible for the glomerocryst mineral assemblage), crystallised at ~1,154°C, and the glomerocryst-bearing trachytic magma (~1,132°C) entered a slightly cooler rhyolitic magma (~1,033°C) at shallower depths. This temperature contrast (considering the temperature range) would result in some cooling of the mafic magma as it entered the rhyolite, which would result in a more solid-like behaviour of the mafic magma and therefore more angular enclaves. As the system evolved (for instance, some heating of the

rhyolite by the trachytic magma), enclave shape and size may vary, resulting in variable degrees of roundness of enclaves, and variable evidence of chilled margins. This is supported by the results and interpretations of Perugini et al. (2007).

The initial eruptive phase of the Pietre Cotte cycle involved the eruption of wet- and dry-type pyroclastic density currents (PDCs) and fallout interlayered trachy-rhyolite deposits (Roverato, 2008; Lorieri, 2009; Di Traglia, 2011; De Astis et al., 2013b). Roverato (2008) and Lorieri (2009) studied these pre-effusive deposits, describing stratified to laminated pumice and (coarse and fine) ash deposits, rich in scoriaceous and obsidian clasts. No substantial evidence for xenoliths were identified or previously reported. Xenoliths of lati-trachytic origin would likely be abundant in these initial explosive deposits if the eruption was triggered by a rhyolitic magma disrupting a shallower lati-trachytic plug. Based on these observations, the notion of a mafic magma entering a rhyolitic magma is favoured here, and substantiated by field and microscopic observations, and thermobarometric calculations. The new model suggested in this study also addresses the origin of glomerocrysts in enclaves and the rhyolitic host.

Detailed petrographic and textural observations, glass and mineral geochemistry, thermobarometric simulations and structural mapping have been integrated in order to conceptualise a new model of magmatic and post-magmatic processes associated with the Pietre Cotte obsidian lava flow (Fig. 4.24). The timeline of processes has been summarised as five stages, shown in the model in Figs. 4.24a and 4.24b. The mafic mineral assemblage (found in glomerocrysts and individually), the finer trachytic groundmass and the rhyolitic host all have contrasting origins, with some degree of physical and chemical interaction between three distinct magmas in this setting. Glomerocrysts formed from rejuvenation of a mafic crystal mush by the injection of a new pulse of magma. As the mush formed and melt fractionated over time, a trachytic melt was produced, though the melt may have also

a

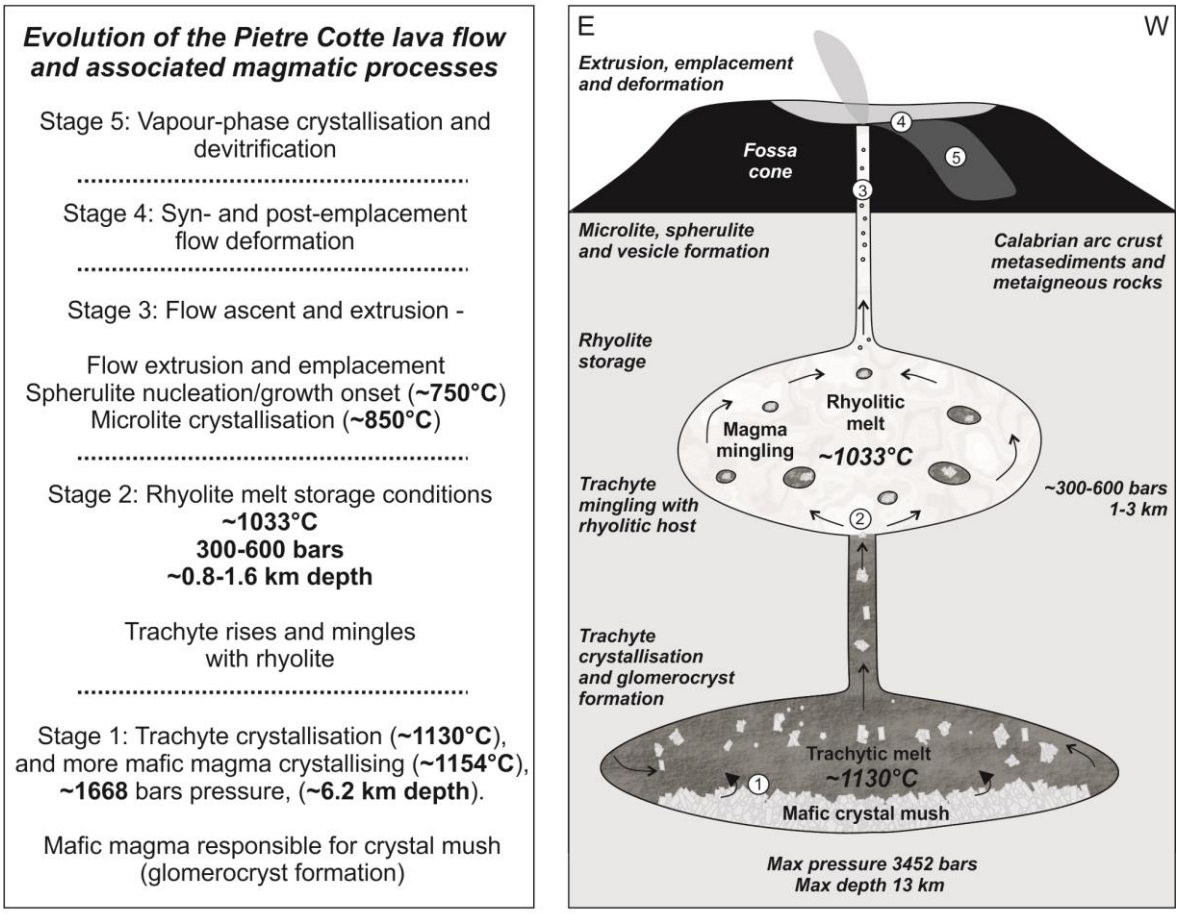

b

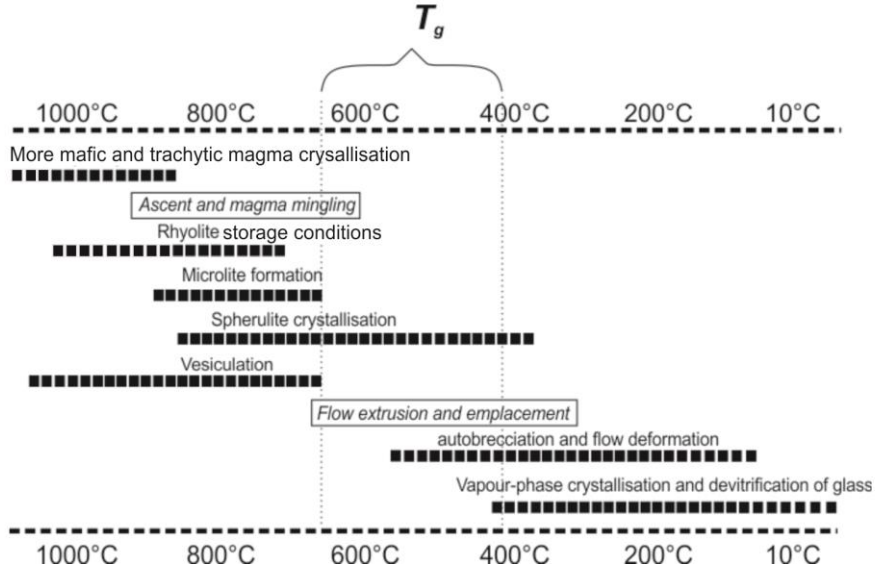

Figure 4.24: (a) Model of magmatic and post-magmatic processes occurring in the Fossa magmatic system, and leading to the final Pietre Cotte lava flow product. (b) Processes of texture formation in the Pietre Cotte lava flow during ascent, eruption, emplacement and cooling. Brittle-ductile transition shown by glass transition (T_g). Figure modified from Breitkreuz (2001) and Wnorowska (2004).

been produced as a hybrid from back-mixing of rhyolite and latitic magmas. The glomerocryst-bearing trachytic magma migrated upwards, injecting trachytic magma in to a rhyolitic magma host. The trachytic magma mingled with the rhyolitic host, forming angular to sub-spherical enclaves, with some disaggregation of enclaves resulting in glomerocrysts and crystals separating in to the rhyolitic host. This magma mingling process may have triggered the eruption, with vesiculation, microlite crystallisation and spherulite nucleation occurring during ascent, upon, and following extrusion. This is evident from the relationship between spherulites and microlites, with microlites wrapping spherulites.

Microlites in the rhyolitic magma may have formed due to decompression-induced crystallisation and due to magma mingling (resulting in two chemically distinct microlite populations). Spherulites nucleated in response to rapid undercooling, and flow deformation may have enhanced nucleation. Brown rims formed during spherulite growth due to sub-solidus diffusion, and show differences in colour and isotropic properties due to differing oxidation state and unrelaxed stress accumulation during spherulite growth. During flow extrusion and advance, the Pietre Cotte lava flow deformed in both a ductile and brittle manner (crossing the ductile-brittle transition), resulting in flow folding, stretching lineations, autobrecciation and fracturing. Following emplacement and upon flow solidification, cristobalite formed within vesicles during the final vapour-phase, and the flow began to devitrify. The final product is a heterogeneous lava flow, preserving evidence for magma mingling processes, spherulite and microlite nucleation, flow deformation and alteration.

4.6 Conclusions

The Pietre Cotte obsidian flow shows a number of distinct and exceptionally-preserved textures that can be used to infer the complete evolution of the final effusive product. The flow is the product of historical activity of the Fossa cone on Vulcano (Aeolian Islands, Italy). The flow is characterised by two key components: rhyolitic glass and dispersed trachytic enclaves, with significant mineralogical and textural variations within each component. The exceptional preservation of several textures allows for a detailed study of all processes leading to the final product. The main aim of this chapter was to develop a model of magmatic and post-magmatic processes (based on these preserved textures) associated with the Pietre Cotte lava flow. This was addressed through a detailed assessment of textural-forming processes by petrographic observations, geochemistry, thermobarometry, field and structural observations.

Field and microscopic observations, coupled with geochemical results, indicate as many as three distinct magmas interacted during early (magmatic) evolution. These include a more mafic (latitic) magma, a trachytic magma, and rhyolitic magma. The more mafic magma produced a mineral assemblage of olivine, clinopyroxene, plagioclase and titanomagnetite, often evident as glomerocrysts within the trachytic magma. The trachytic magma manifests as purple enclaves, characterised by a microlitic-diktytaxitic groundmass of interlocking plagioclase and alkali feldspar microlites. These trachytic enclaves are hosted within a rhyolitic host, forming the obsidian lava in the final product. The trachytic magma crystallised at ~1,668 bars (though showing considerable pressure range of 853-3,452 bars according to clinopyroxene barometry) and a temperature of ~1,130°C (Pele 8.0

thermometry). The more mafic magma crystallised at ~1,154°C (QUILF thermometry), and rhyolite system temperature was ~1,033°C (*Rhyolite-MELTS*).

The final product also hosts microlites, spherulites and deformational structures. Raman spectroscopy and x-ray diffraction reveal spherulites predominantly contain α-cristobalite, orthoclase feldspar and glass, and spherulite crystal size distribution plots indicate distinct spherulite populations <0.1 mm and >0.1 mm, growing over a period of ~2 days (see Chapter 3). Microlites also show distinct populations, with compositions similar to, or distinct from, phenocryst compositions, forming due to both degassing –induced crystallisation and magma mingling processes. Flow deformed upon extrusion across the ductile-brittle transition, resulting in a number of ductile and brittle structures, including stretching lineations, folding and jointing. Flow continued to slowly deform and devitrify following emplacement.

The Pietre Cotte magmatic system and lava flow developed over five stages: (1) Mafic magma crystallisation and the remobilisation of a crystal mush; (2) Mingling of a (glomerocryst-bearing) trachytic magma with a rhyolitic magma; (3) Ascent and extrusion of the (trachytic enclave-bearing) rhyolite accompanied by microlite crystallisation, onset of spherulite nucleation and growth during ascent and extrusion, and extrusion and lava flow emplacement; (4) Flow deformation across the ductile-brittle transition during and following emplacement; and (5) Vapour-phase crystallisation and devitrification late- and post-emplacement. The study shows how the preservation of textures can be used to constrain magmatic and post-magmatic process-timescale information.

Chapter 5

Synthesis and discussion

This chapter focuses on how the new models and findings of this study contribute to our understanding of silicic volcanism and obsidian lava flows, and examines the wider implications for previously developed models relating to obsidian lava emplacement and spherulite formation, the role of underlying topography and comparisons to rheomorphic ignimbrites.

5.1 Obsidian lava flow emplacement

Emplacement mechanisms and rheological properties controlling advance in the Rocche Rosse lava flow have been previously described by Hall (1978) (structural arrangement of flow) and Gottsmann and Dingwell (2001b) (cooling of flow frontal ramps). Hall (1978) described features in the Rocche Rosse obsidian lava flow, including well developed flow foliations developing ramp structures, steep at the top of the flow and curving down towards a flat surface against the base in the up flow direction. A typical compressive regime resulted in the build-up of lava behind a brecciated flow front, which hindered the advancing flow (Hall, 1978). Hall (1978) compared such features to similar structures and stress distributions found in glaciers, with slip or shear planes (ramp structures) inclined back towards the vent. If the flow were to become extensional (e.g. just in front of a sudden increase in slope), shear planes would have the opposite dip. Hall (1978) provided a cross sectional model of the Rocche Rosse, with such compressional and extensional regions, and resultant ramp structures as indicated by flow foliations (Fig. 5.1).

The observations and cross sectional model of the Rocche Rosse developed by Hall (1978) effectively demonstrates the occurrence of flow ramps (often well exposed in flanks), a simplified stratigraphy with a surface breccia, foliated obsidian and basal breccia, and the role of compression and extension in the formation of surface and internal flow structures. The model of Hall (1978) also tentatively highlights the influence of the underlying topography on structure formation, with compression dominating in flatter near-source and distal flow areas, and extension occurring mid-flow over steeper topography (see section 5.4). However, the model and observations of Hall (1978) provides only a simplified

interpretation of events, and does not adequately portray the high complexity of structures and structural orientations in the Rocche Rosse lava flow, the range in scale of structures or the role played by differential flow rheology and progressive deformation.

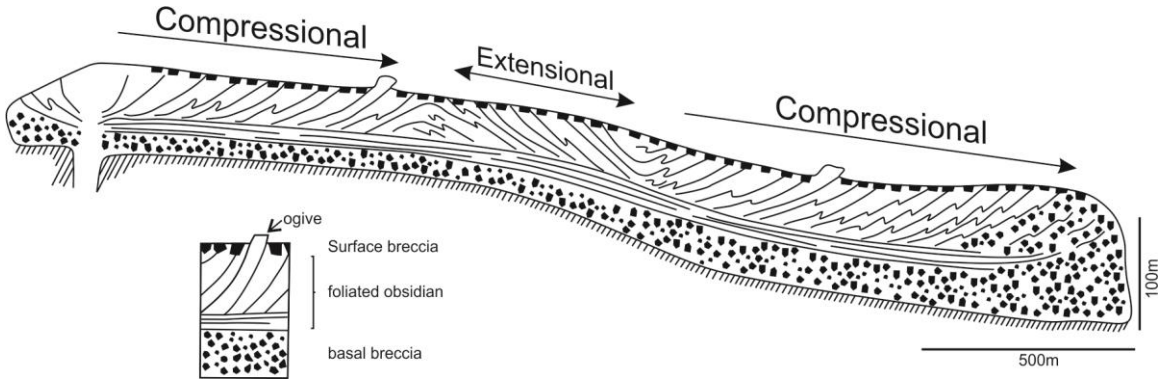

5.1: Simplified cross sectional model of the Rocche Rosse lava flow, with generalised flow foliations defining ramp structures (after Hall, 1978).

Flow rheology of the Rocche Rosse lava flow is discussed by Gottsmann and Dingwell (2001b). Gottsmann and Dingwell (2001b) studied the cooling of the Rocche Rosse frontal flow ramps in order to quantify the cooling history across the glass transition. Thermal history is an important input parameter for modelling the rheology of silica lava flows in order to assess flow propagation and associated hazards. Cooling history and stress regime have a strong control on flow rheology, directly influencing morphologies and structures. For instance, folded flow banding may indicate an increased stress regime as a result of increasing frictional resistance towards the base of the flow ramp, and the sheet-like succession of individual flow units define individual cooling histories. Such cooling rates controlled the latest stage of viscous deformation before the flow ceased. Modelled cooling rates range between 0.2 and 0.03 K min^{-1} (tens of Kelvins per day), dominated by conductive heat loss of individual flow ramps. Importantly, this indicates that flow fronts

may actively deform and remain mobile for days or weeks after effusion has ceased (Gottsmann and Dingwell, 2001b). This likely accounts for structural complexity at the flow front, the abundance of folds and re-folded folds, and significantly contributes to progressive deformation. Castro and Cashman (1999) investigated the constraints on rheology of obsidian lavas based on observations and measurements of mesoscopic folds. Mesoscopic folds form as the result of flow layers, defined by planar variations in microlite content, deforming during flow advance. These were defined by changes in shape and orientation of textural flow layers. The relative thicknesses of pumice and obsidian govern the style of folding, with folds generally increasing in arc wavelength with increasing layer thickness. The folds analysed formed during flow, and as such the rheological contrasts governing their formation may be viewed as viscosity contrasts (Castro and Cashman, 1999). This study further emphasises the role of flow rheology in structural development of obsidian lavas.

Well established obsidian emplacement models include those devised by Fink (1983) and Tuffen et al. (2013). Emplacement models are generally based on flow foliation configuration, identifiable by flow banding and flow stratigraphic units. The flow stratigraphy model of textural units devised by Fink (1983) and Manley and Fink (1987) is also widely cited as a template for interpretation of outcrop stratigraphy (e.g. Branney et al., 1992; Anderson et al., 1998; Wright et al., 2003), and has been used in order to interpret flank and outcrop stratigraphy in this study. The stratigraphy of textural units in a typical rhyolite lava flow (based on the textural stratigraphy of North American Holocene rhyolite lavas and adapted from Fink, 1983; Fink and Manley, 1987; Cas and Wright, 1987, see Fig. 5.2) describes an upper finely vesicular pumice, upper and lower obsidian layers, coarsely vesicular pumice, crystalline rhyolite and a basal breccia. This flow configuration is well constrained across North American Holocene rhyolite lavas (Manley

and Fink, 1987), although the units are not always continuously or widely observed across the Rocche Rosse lava flow.

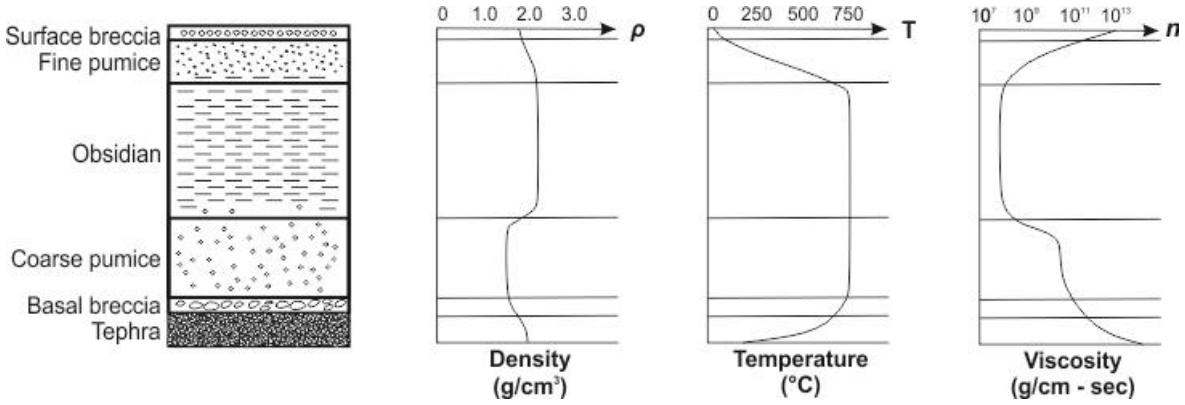

Figure 5.2: Profile of a typical 35 m thick rhyolitic obsidian flow, with density, temperature and viscosity profiles for each stratigraphic unit (from Fink, 1983).

The model established by Fink (1983), and further developed by Fink and Manley (1987), and Manley and Fink (1987), indicates that obsidian flows develop distinctive vertical and lateral zonation (Fig. 5.2). The model of Fink (1983) incorporates flow stratigraphy and pumice diapir and foliation development. The stages of stratigraphic unit development include (a) volatile exsolution and development of a frothy cap as the stratified mass rises, (b) vesiculation which leads to explosive phase(s), (c) the remaining volatile rich magma reaches the surface as highly inflated pumiceous lava, before evolving to a continuous lava flow, (d) the vesicle-free obsidian extrudes over the pumiceous lava, compressing and shearing the underlying pumice into a basal layer of irregular thickness, (e) continual volatile exsolution produces a finely vesicular carapace and promotes insulation, and (f) a more crystalline rhyolite piles up over vent due to higher crystallinity, viscosity and lower emplacement temperature. Pumice diapirs are described as the product of rising coarsely vesicular pumice to the surface due to the density contrast. These diapirs push apart the overlying obsidian and other identifiable units. Foliation attitudes also vary as the viscous

flow emplaced and shallow surface fractures develop and deepen (propagating inward as the lava spreads laterally), with compression during flow leading to folding, and continual rise of lava leading to uplift and outward rotation of blocks (Fig. 5.3).

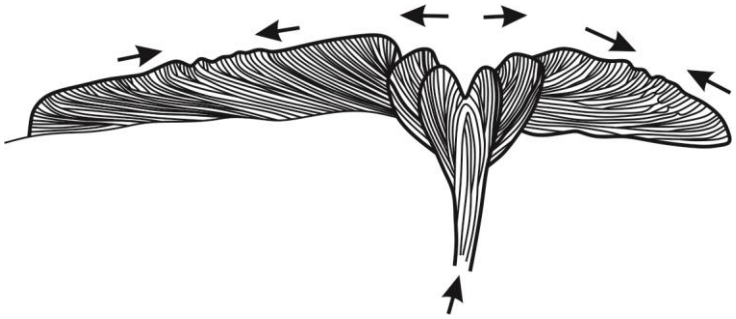

Figure 5.3: Schematic diagram of compression during flow forming surface folds (indicated by foliation attitudes). Figure taken from Fink (1983).

The emplacement model devised by Tuffen et al. (2013) following the extrusion of an obsidian flow at Cordón Caulle volcano in Chile is well constrained, as it is based on real time observations of an active obsidian lava flow. The model also incorporates photo reconstruction techniques and sequential satellite imagery (adopted and adapted in this study of the Rocche Rosse lava flow). The emplacement model details ductile extrusion on shear surfaces extending back into flow interior, with brittle deformation becoming increasingly important as lava cools and inflation triggers fracturing. Localised flow extrusion and stalling results in breakout lobes, and greatly extends flow. These breakout lobes promote internal structural complexity, and greatly boost flow extent. The development of the flow carapace results in insulation, and the thermal efficiency is highlighted as an important process for within-flow horizontal transport.

Both models provide a detailed and suitable model for comparison to the observations and model developed here for the Rocche Rosse lava flow. The model of Fink (1983) provides a relevant model for comparison, as interpretations are based on structures preserved in the

final solidified product, such as flow foliations. The model of Tuffen et al. (2013) has the obvious advantage of direct observations of emplacement, allowing for definitive constraints to be placed upon the formation of comparable structures identified in the Rocche Rosse lava flow (e.g. breakout lobes and shear zones). However, though both models highlight associated structural complexity, detail that could be applicable to other obsidian lava flows is mostly lacking. For instance, Fink (1983) highlights rising pumice diapirs, flow-parallel compression and inward fracture propagation as contributions to observed structural complexity in Little Glass Mountain. Though rising pumice diapirs are noted as a potential contributor here in the Rocche Rosse and Pietre Cotte lava flows, they are not widely described in other studied lava flows, and the occurrence of those observed in this study are not widespread enough to disrupt flow configuration in the complex manner that it shows. These zones are also potentially found in the Pietre Cotte lava flow (forming dark grey pumiceous zones of sheared, glassy and vesicular zones in the Pietre Cotte lava flow), although their obsidianaceous nature and sheared vesicles suggest they may be the product of a silicic foam (foaming due to higher temperatures). Flow compression is noted by Fink (1983) as producing regularly spaced ridges or folds transverse to flow direction. In the Rocche Rosse lava flow, ridges and flows show a highly variable spatial distribution, scaling, vergence and attitude, and sheath folds also occur. A simple compressional stress regime would not produce such a range in folding or multiple folding episodes. The explanation for such structural complexity provided by this study is a significant role played by differences in flow rheology and resultant progressive deformation. This is suggested by Tuffen et al (2013), as thermal efficiency is highlighted as an important factor in prolonging within-flow horizontal transport and greatly increasing flow extent. Increasing flow thickness is also attributed to lava maturity (Tuffen et al., 2013). In this study of the Rocche Rosse, spherulite crystallisation is proposed to play a

role in second heating of lava (enhancing flow mobility), and following spherulite growth, the bulk density increase and rigidity contrast of spherulites contribute to structural development (e.g. development of shear zones). The model presented here also details smaller scale structures (e.g. formation of sub-centimetre folds and faults, significance and origin of elongate spherulites), whereas the models of Fink (1983) and Tuffen et al. (2013) focus on the formation of larger scale features.

5.2 Spherulite formation

The formation of spherulites remains a debated topic in igneous petrology. Spherulites are predominantly considered to crystallise in response to significant undercooling as lava cools (Kirkpatrick, 1975; Swanson, 1977; Fenn, 1977; Swanson et al., 1989; Castro et al., 2009; Gardner et al., 2012), and are also commonly attributed to devitrification processes (Lofgren, 1971b, Swanson et al. 1989). Observations suggest growth both above and below glass transition (T_g) (Dingwell, 1998; Gottsmann et al., 2002). As well as being observed in glassy and devitrified lavas, spherulites are noted in other geological settings (e.g. pseudotachylite veins; Wenk 1978; Wenk and Weiss, 1982; Macaudière et al., 1985; Caggianelli et al., 2005), and in synthetic polymers (Pirsson, 1910; Keith and Padden, 1963; Ryschenkow and Faivre, 1988; Hosier and Bassett, 1995; Magill, 2001). Lofgren (1980) showed that experimental crystallisation from a melt and by lower-temperature devitrification are very similar, which may imply similar processes take place in spherulite crystallisation and devitrification in both natural and crystallisation periods. In order to

fully assess the formation and importance of spherulites in obsidian lavas, this study integrated a number of multi-disciplinary methods and concepts.

The most comprehensive spherulite model for the Rocche Rosse lava flow was developed by Clay et al. (2013). This study is a suitable association as it focuses on spherulites in the Rocche Rosse lava flow, an integral sample locality of this study. Clay et al. (2013) combine petrographic, crystal size distribution and in situ major and volatile elemental analyses to assess the mode, temperature and timescales of spherulite formation in the Rocche Rosse lava flow. Clay et al. (2013) demonstrate a down-temperature continuum model of spherulite formation (Fig. 5.4), with spherulite formation and modification above T_g, during T_g transition and in solid state:

- Above T_g: cristobalite and orthoclase crystallisation (>800°C), enhanced diffusivity and depolymerisation.
- T_g transition: complex deformation, alignment of spherulites.
- Solid state modification: oxidised rim development and development of polygonal texture.

Importantly, Clay et al. (2013) suggest flow deformation as a potential catalyst of progressive nucleation and growth. Widespread evidence for high spherulite nucleation and growth within deformed areas of flow suggests that high-strain zones may have triggered progressive nucleation and growth of further generations of spherulites syn- and post-emplacement cooling. This study complements the findings of Clay et al. (2013), supporting the conclusion of continuum of spherulite crystallisation and growth, and expands on the idea of deformation-triggered spherulite growth and spherulite relationship to deformation, though this hypothesis may require more strenuous study. This study also furthers spherulite CSD interpretations, through more sampled lava flows and domes modelled, and development of spherulite CSD interpretations. Tuffen et al. (2012) suggest

that initial spherulite nucleation only requires undercooling of >100°C, so spherulites can grow at temperatures up to 900°C or in more degassed rhyolite lavas. Importantly, spherulite crystallisation may be a latent heat source, and heating can even lead to exceeding the initial lava temperature (heating in the centre of the lava body and quenching of carapace). This significant temperature fluctuation may be linked to flow deformation (areas of lava with variable temperature promotes variable viscosity, and may lead to preferential or progressive deformation).

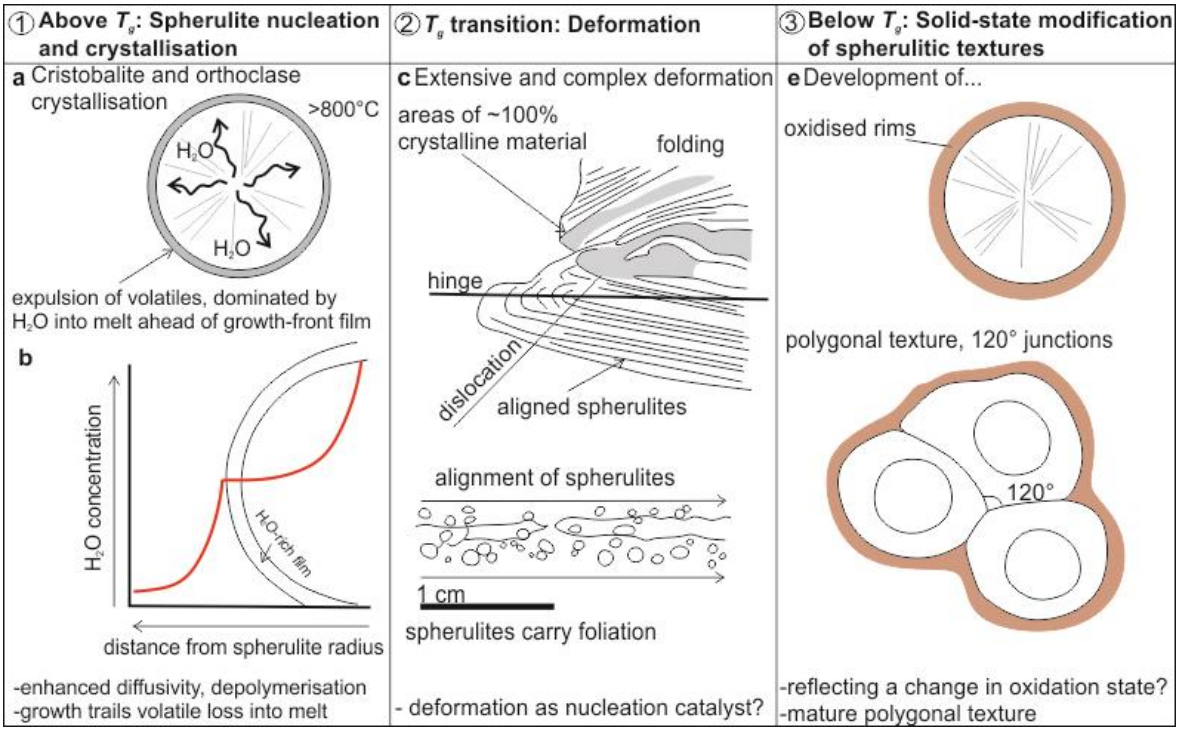

Figure 5.4: Schematic of temperature continuum growth model for the spherulites in the Rocche Rosse obsidian developed by Clay et al. (2013).

These concepts are important findings, as, along with results from this study, observations and interpretations support both spherulite nucleation enhancement by deformation, and deformation enhancement by spherulite presence (density contrast may promote folding, rigidity contrast may promote shearing and lineation formation, evident by high spherulite

population densities in folds, areas of extension and shear zones). Nucleation sites for spherulites may be attained through flow undercooling, and orderly configuration of such nuclei attained through strain, leading to enhancing spherulite formation (with spherulites preferentially orientated in localised areas of flow). Elongation in an extensional flow regime can act as a strong stimulus for polymer crystallisation, causing molecules to orient and stretch in the direction of extension, facilitating the process of flow-induced crystallisation (Swartjes et al., 2003; Janeschitz-Kriegl et al., 2003; Kornfield et al., 2002; Stadlbauer et al., 2004).

Deformational structures in obsidian lavas often suggest that obsidian lava bodies do accommodate high magnitudes of strain, with multi-scale folds at variable attitudes and tightness common across flow. Spherulites often concentrate within folds, faults, fractures and bands in sampled localities in the Aeolian Islands. Spherulites are often deformed (elongate) near shear zones. Qualitative observations indicate a relationship between spherulite nucleation and deformation, i.e. either spherulites nucleate in response to deformation or deformation is promoted/enhanced by spherulites. Both are qualitatively suggested in this study, based on polymer science observations and rheological property contrasts between spherulites and surrounding obsidian (density, rigidity, latent heat). This potential link between deformation and spherulite nucleation may lead to extensive spherulite crystallisation in areas of high strain and deformation.

This study provides new techniques, results and insights into spherulite nucleation and growth processes in obsidian lavas. For instance, the study demonstrates how crystal size distribution (CSD) methods can be effectively applied in a non-conventional crystallisation setting. Spherulite CSD plots can be used for interpreting spherulite nucleation and growth events, including the identification of individual spherulite populations, determination of nucleation processes and enhancement of nucleation events (i.e. enhanced undercooling,

deformational trigger), and estimating spherulite growth rates in obsidian lavas (see Fig. 3.20). Spherulite Preferred Orientation (SPO) methods have also been utilised for the first time, in order to identify localised stress regimes affecting spherulite growth in obsidian lavas, resulting in preferential alignment of spherulites during growth.

New spherulite compositional data for the Aeolian Islands obsidian suite indicates the presence of glass and both α- and β-cristobalite within some spherulites (previously unreported), which both have important implications for determining nucleation and growth processes. The study also places a high emphasis on the link between spherulite nucleation and deformation, with high spherulite population densities seemingly coinciding with deformational structures such as folds, areas of extension and in shear zones in a number of cases (also emphasised by SPO results). This is a well understood concept in polymer sciences, but is relatively neglected in spherulite studies in obsidian lavas, with the exception of the study of Clay et al. (2013) which tentatively suggests the link between spherulite nucleation/growth and deformation in the Rocche Rosse lava flow.

The study also provides the first detailed spherulite classification scheme, based on physical characteristics, spatial occurrence, composition, spherulite CSD plots and interpretations of nucleation and growth. The results of this study, combined with these previous multi-disciplinary models and interpretations, indicate that there is significant complexity involved in spherulite nucleation, growth and modification in obsidian. This study details the differences in spherulite morphology as a response to such processes, and indicates the significant relationship to flow-emplacement.

5.3 Using textures to constrain magmatic and post-magmatic processes

The pre- and post-extrusive processes associated with the Pietre Cotte obsidian lava flow were investigated based on field and petrographic observations, glass and mineral geochemistry and thermobarometric applications. Results led to the development of a new model for the magmatic and post-magmatic evolution of the Pietre Cotte lava flow. The study demonstrates how textures can provide process-timescale information, both qualitatively (i.e. relative timescale of texture-forming processes) and quantitatively. Early crystallisation conditions, processes of magma mixing and/or mingling and magmatic evolution can be inferred from mineral assemblages, including the identification of disequilibrium textures, cumulate textures and their spatial occurrence (e.g. within enclaves, host magma). Mafic enclaves mingled with a more felsic host can also yield information on magmatic processes, based on enclave shape, abundance and separation/disaggregation of crystals in to the host.

The identification of multiple spherulite and microlite populations can also provide constrains upon pre- and post-extrusive processes. Such populations may be identifiable based on their shape, size, orientation and composition. For instance, distinct microlite compositions potentially suggest that microlites formed due to more than one process. Microlite compositions which show correlation to phenocryst compositions within enclaves and/or host magma may point to a mingling origin (Martel et al., 2006; Humphreys et al., 2009), and chemically-distinct microlites with a preferred orientation, elongate or skeletal appearance may form due to rapid growth during quenching, in

undercooling conditions (Kirkpatrick, 1975; Swanson, 1977; De Rosa et al., 2003; Gioncada et al., 2005; Castro et al., 2009). Spherulites that show radial interiors, containing glass and β-cristobalite, are indicative of nucleation and growth above T_g temperatures (Swainson and Dove, 1995; Richnow, 1999), and deformed spherulites may indicate that spherulites formed during flow deformation. Microlite and spherulite relationship to each other also offers insights into timescale information. Spherulites overprinted by microlites indicate that microlites formed first, while microlites deflecting around spherulites suggests that both spherulites and microlites were at least partially forming simultaneously.

The occurrence, distribution and orientation of foliations, lineations, folds and fractures provide details on extrusive and emplacement processes. Textural and structural complexities can serve as a record for magmatic flow and deformation (Castro and Cashman, 1999). Foliation orientations preserve a record of deformation associated with flow emplacement (Gonnermann and Manga, 2003), deforming in response to extension and compression. The final orientation distribution represents initial flow stratigraphy and subsequent deformational processes. Foliation strike direction may also be explained by stages of emplacement, initially impressed with the strike direction of the vent (preserved laterally as near-horizontal), with changes reflecting changes in state of stress during eruption or during hiatus (pulses). Changes may also indicate vent geometry modifications (e.g. obstruction in vent caused by explosion or congealed lava). Recognising such changes in foliation orientation could indicate future extrusive directions or where near-surface magma bodies may reside. Post-emplacement processes can also be recognised through textures such as modification or re-crystallisation of spherulites (lithophysae) and vesicles (e.g. vapour-phase crystallisation).

This study demonstrates how texturally heterogeneous lava flows can be constrained using textural occurrence. Timescales of processes can be inferred from textures based on their relationships to each other, the presence of disequilibrium textures, the distribution of textures, and their physical characteristics (e.g. shape and size, orientation). This provides a means of qualitative timescale information (i.e. texture formation relative to each other based on aforementioned parameters), and can be further quantified based on composition (e.g. thermobarometric methods for mineral assemblages, spherulite and microlite composition). Knowledge of pre-eruptive storage conditions, and mafic magmas and their relationships with the co-erupted rhyolites is important for the understanding of how such magmatic systems work. Eruptive behaviour, emplacement mechanisms and deformation, and post-emplacement processes provide key insights into lava flow behaviour and flow modification. Such textural insights allow for a full reconstruction of silicic lavas and coeval mafic products in active settings. This provides a better understanding of magmatic and post-magmatic processes in silicic systems, which offers vital information for hazard evaluation (eruption and emplacement behaviour) in active silicic volcanic settings.

5.4 Influence of underlying topography

When determining the primary controls on lava flow morphology and structures, it is important to consider the influence of the underlying slope characteristics. Such characteristics include the slope angle (i.e. steep and shallow slopes) and uniformity (uniform and non-uniform or variable slope). Observations of the Rocche Rosse and Pietre Cotte lava flows suggest that structure formation, orientation complexity, flow length and

transport mechanisms may all be influenced by the underlying slope. The 2 km Rocche Rosse lava flow extends over a variable slope (in terms of both angle and mean dip direction), generally covering a slope that varies from shallow in the near-source region, steep in mid-flow regions, and shallow in flow frontal areas. The topography also dips in two dominant directions, to the north and to the north east. By comparison, the <1 km Pietre Cotte lava flow extends over a steeper topography (~30-35°; Frazzetta et al., 1984a), in a north-westerly direction. The Rocche Rosse lava flow exhibits a complex range in structures and structural orientations, with large scale folding, two prominent flow lobes and multiple breakout lobes. The Pietre Cotte lava flow shows a lower degree of complexity (i.e. a more uniform arrangement of foliations and folds), with smaller scale folds, and one prominent lobe and flow direction. The difference in flow structure and underlying topography highlights the potential influence of slope and raises the question: Does slope angle and slope dip direction play a significant role in structure formation and structural complexity?

Gravity is the force that drives flow movement. Non-particulate gravity currents are coherent deforming masses of material moving under the influence of gravity (e.g. due to slope). Examples of non-particulate gravity current-driven movement in a geological setting include movement of ice glaciers, salt glaciers, sedimentary slumps and lavas (Andrews, 2006). Such movement results in a number of structures and structural orientations. For instance, in lava flows, slope-perpendicular, parallel-style folds are characteristic of down-slope flows where deformation is gravity-driven (Ramsey, 1967; Fink, 1980). Lava dome or flow shape may vary due to the underlying slope and conduit geometry, e.g. continued extrusion of a dome on a steep slope may generate a thick lava flow that may travel for several kilometres. A number of investigations of lava flow emplacement (both field- and analogue-based) have been conducted and ascribe underlying

slope characteristics as an influence or control on flow morphology and/or structural development.

The effects of topography are well established in basalts due to an abundance of direct observations. Examples include basaltic flows in San José Valley, USA (Nichols, 1936), whereby topographic restrictions resulted in a narrow flow regime, a greater flow velocity and low number of breakout lobes (Nichols, 1936). Similar observations were made at a basaltic lava flow from the Western Volcanic Zone in Iceland, where a break in slope and topographic steepening enhanced flow velocity, caused the lava to stretch and brecciate in to a'a-type flow (Chevrel et al., 2013). By contrast, shallowing topography led to a waning of flow velocity, pressure ridge formation and inflation features in basaltic lavas (Chevrel et al., 2013). A shallow topography also promotes the formation of breakout lobes. For instance, Walker (1991) found that breakout lobes (tumuli development) tend to form on shallow slopes in lava flows experiencing a modest amount of extension in Hawaii.

The effects of slope characteristics on more silicic lavas have also been carried out (based on field measurements and observations). Observations from the Porri andesitic lava flow on the island of Salina (Aeolian Islands, Italy) indicate a steep (10-30°), uniform slope with no abrupt changes (Iezzi and Ventura, 2000). Structural observations indicate a decrease in fold axial plane dip away from the vent (due to increasing contribution of simple shear to bulk deformation), with gravity-driven mechanisms controlling deformation patterns (Iezzi and Ventura, 2000). These observations and findings support a relatively simple flow regime over a steep, uniform topography. Crease structures tend to form on slopes less than 20°, at the very beginning or end of extrusion of lobes on steeper slopes (e.g. crease structures at Mount St Helens; Anderson and Fink, 1989).

Slope angle and underlying topography has been noted as an influence in the emplacement and structural development of obsidian lava flows. Direct observations of the emplacement

of the obsidian flow at Cordón Caulle volcano in Chile highlights the formation of lava breakout lobes >3 km from the vent area (Tuffen et al., 2013). This emphasises the role of thermal insulation, and Tuffen et al. (2013) note the influence of a downward-sloping underlying topography in enhancing flow mobility. Breakout lobes are noted as longer, more rapidly advancing in the channel to the east because of overtopping a topographic barrier and flow down a steepening slope (Tuffen et al., 2013). The structure of Obsidian Dome (USA) includes large surface fold axes orientated normal to underlying topography (Castro et al., 2002). These folds are formed due to compression of flow by a topographic barrier, which also influences local extension direction, and caused earlier-formed lineations to rotate to present positions (Castro et al., 2002). This further highlights how interaction of flow with topography is important in modifying earlier formed fabrics. In Little Glass Mountain (USA), extension and breakout lobes from flow margins coincide with slope increase (~9° slope), with an overall development of marginal levees and channelled flow also identified (Fink, 1978). Such confinement led to lack of lateral spreading and absence of extensional cracks (Fink, 1978). However, circumferential stretching is identified in Little Glass Mountain. Similarly, the north lobe of Big Glass Mountain moved down a steeper slope and developed marginal levees which channelled the lava and suppressed radial expansion. Consequently the domes on this lobe are less affected by the circumferential stretching seen on Little Glass Mountain (Fink, 1983). To summarise the findings of obsidian lava flow structure and the role of underlying topography, steeper slopes often lead to a channelled flow regime with the development of levees, while a shallower slope promotes radial spreading and lava breakout lobe development.

Gregg and Fink (2000) investigated the effects of slope on the dynamics of lava flow emplacement. This involved simulations with polyethylene glycol extruded at a constant

rate beneath a cold sucrose solution onto a uniform slope, which could be varied between 1° and 60°. To summarise some of the key findings, shallower slopes produced advancing bulbous toes (akin to breakout lobes), while the steepest slopes produced leveed flows which solidified only at margins. These findings support field observations made in this study of the Rocche Rosse and Pietre Cotte lava flows, and in previous studies (see above). Gregg and Fink (2000) found that an increased slope of up to 30° promoted further flow advance. For underlying slopes, gravitational forces caused the surface and marginal crust to break apart, making folded and leveed flows less likely to form.

As well as lava flows, ignimbrite and glacier studies show similar findings in terms of the influence of the underlying slope on flow regime and structural formation. In ignimbrites, non-uniform (variable) flow results from slope changes, with pyroclastic density currents accelerating down steepening slopes, and shallower slopes promoting deceleration (causing flow thickening) (Branney and Kokelaar, 2002). Radial spreading occurs across flat ground or converging into a channel (Branney and Kokelaar, 2002; Andrews, 2006). In glaciers, slope-perpendicular, parallel-style folds in glaciers are generated (Hambrey and Lawson, 2000), typically forming curvilinear ogives.

To summarise, slope characteristics should be considered a key primary control in lava transport, deformation and structural development. Underlying topography may play a significant role in the formation and final configuration of flow structures (see Fig. 5.5). This may be an important consideration for lava flows extruding from source regions such as steep volcano flanks, or shallower vents such as vents confined to craters or from shield volcanoes. It is also important to consider slope uniformity and not just steepness. Observations from Aeolian Islands and in previous studies emphasise that flow transport may be controlled by slope angle. Steeper slopes promote leveed/channelled flow regime and associated structures, while a flatter topography promotes lateral spreading. A

combination of variable slope angle and slope dip direction has associated structural complexity, and may promote lobe and breakout lobe development. Therefore, slope characteristics should be considered an important primary control factor on structural development alongside flow rheology, effusion rate, eruption behaviour and lava volume.

Increasing structural complexity

Schematic cross section	Slope characteristics	Typical flow features	Settings and examples
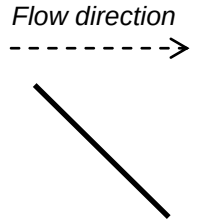	Steep (~>15°), uniform	Levees and channelled flows, stretching lineations, unidirectional flow, relatively uniform structural arrangement	Stratovolcano flanks e.g. Fossa cone (Pietre Cotte lava flow), Italy
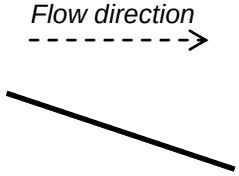	Shallow (~≤15°), uniform dip	Lava domes, Radial spreading short flows, flow ramping, multi-scale folding, relatively uniform structural arrangement	Shield volcanoes, calderas, crater emplacements.
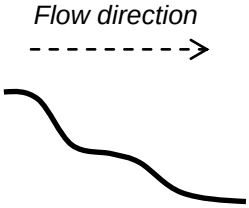	Variable slope angle	Channelled flow and radial spreading, folds and stretching lineations, sporadic structural orientations	Mount St. Helens, USA (Anderson and Fink, 1989)
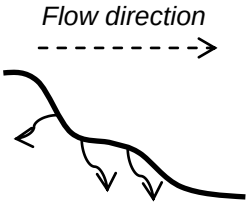	Variable slope angle and slope dip direction	Multiple lobes and breakout lobes, multi-directional flow direction, complex structural arrangement, complex structural distribution	Monte Pilato (Rocche Rosse lava flow), Italy; Cordón Caulle, Chile (Tuffen et al., 2013)

Figure 5.5: Influence of slope angle and slope dip direction on flow structures (with examples of settings and flows). Complexity of structures (in terms of distribution, orientation and scale) increases with increased slope angle and slope directional variability.

5.5 Comparisons to rheomorphic ignimbrites

The origin of extensive silicic sheets that resemble lava flows or non-rheomorphic welded ignimbrites (lacking vitroclastic textures) has been debated and discussed in the past three decades. The descriptive term "lava-like" has been ascribed to rheomorphic ignimbrites that resemble lava flows, i.e. massive and flow-banded lithologies that lack fiamme and vitroclastic textures, and the origin of which (i.e. part of a lava or part of an ignimbrite) is not immediately apparent and may only be deduced from the field relations (Branney et al., 1992; Freundt and Schmincke 1995). Interpretations vary due to the convergence of emplacement-related textures and mechanisms (substantial non-particulate flow), whereby features converge with increasing emplacement temperatures (Branney and Kokelaar, 1992). For instance, coalescence of hot particles during deposition may obliterate original pyroclastic textures (Branney et al., 1992).

Examples of "lava-like" ignimbrites that show (or have been recently been classified as) lava flow characteristics include the Bad Step Tuff in the English Lake District (Branney et al., 1992), the 'TL' ignimbrite on Gran Canaria (Sumner and Branney, 2002), Etive Rhyolites of Glencoe (Moore and Kokelaar, 1998) and in fountain-fed lava flows (Duffield, 1990; Stevenson et al., 1993; Sumner, 1998). The Stockdale Rhyolite member was also previously considered a lava flow (Rutley, 1885; Green, 1915; Marr, 1916; Mitchell, 1934, 1956; Gale et al., 1979), but was re-interpreted as a rheomorphic ignimbrite based on outcrop length and thickness ratios, textural characteristics and associated sedimentary rocks (Millward and Lawrence, 1985). Diagnostic criteria for distinguishing rheomorphic ignimbrites from lava flows include (1) gradation from unambiguous vitroclastic matrix of the basal lithic breccia into central flow-laminated tuff;

(2) only rare autobreccia at the base but ubiquitous autobreccia at the top of the sheet; and (3) close textural similarity with localised, intensely rheomorphic parts of associated ignimbrites that widely display unequivocal vitroclastic textures where rheomorphism is less pronounced (Branney et al., 1992).

The Bad Step Tuff is a lava-like sequence of rheomorphic calc-alkaline rhyolitic ignimbrites emplaced during a caldera-forming eruption episode in the English Lake District (Branney et al., 1992). The deposit is characterised by flow-folded flow-laminations, autobrecciation, and an absence of vitroclastic textures. It therefore shares similar diagnostic features akin to a viscous block-lava flow, and has been considered as such by previous studies (e.g. Millward 1976; Moseley and Millward 1982). The presence of mesobreccia incorporated into the base of the Bad Step Tuff and the preservation of its true pyroclastic nature, alongside the exposure of basal lithic breccia, allowed for the re-classification of the Bad Step Tuff (Branney et al., 1992). The 'TL' ignimbrite on Gran Canaria also locally exhibits features considered to be diagnostic of lava flows (Sumner and Branney, 2002). Again, problems with classification arise due to the convergence of features and related emplacement mechanisms (the first documented example of an ignimbrite that travelled like a lava flow, beyond its original depositional limit; Sumner and Branney, 2002). Based on the aforementioned diagnostic criteria, the 'TL' ignimbrite was described as a "lava-like" ignimbrite (Branney et al., 1992; Sumner and Branney, 2002).

An improved understanding in obsidian transport mechanisms, differential flow regime and post-extrusive deformation makes comparisons to the structures and processes involved in rheomorphic ignimbrites highly relevant. This comparison is justifiable as the physical characteristics of lavas and ignimbrites converge with increasing emplacement temperatures (Branney and Kokelaar, 1992). For instance, Branney et al. (1992) identify a

number of structures in the Bad Step Tuff (English Lake District) that are comparable to those found in obsidian lavas. Specifically, flow laminations, deformed vesicles and micro-fractures are noted as showing a striking similarity to structures identified in obsidian lava flows (compared to structures identified by Fink and Manley, 1987). For silicic bodies of unknown origin, structural analysis can help distinguish between long lavas and unusually high-grade ignimbrites. The term 'rheomorphism' refers to mass flow following post-emplacement welding-compaction (Wolff and Wright, 1981). Branney et al. (1992) reclassified the term 'rheomorphism' to describe all viscous flow structures in extremely high-grade ignimbrites, such as folds, non-particulate lineations, attenuated fabrics, and ramp structures (see Table 5.1), formed both during emplacement and during fault- and gravity-induced hot slumping. Various models of the emplacement of high grade rheomorphic ignimbrites have been proposed.

Schmincke and Swanson (1967) suggested that rapid welding and rheomorphism occur before, and independently of, post-emplacement cooling and welding. This is the result of a decelerating pyroclastic density current becoming a laminar current, which deflates and agglutinates en masse, before finally deforming rheomorphically post-emplacement. Chapin and Lowell (1979) suggested that agglutination and deformation occur during initial emplacement, but propose that the hot agglutinate progressively accrete and shear in a laminar boundary layer at the base and sides of a valley-filling pyroclastic plug flow, followed by hot-state gravitational slumping towards the valley axis. Wolff and Wright (1981) proposed that welding and rheomorphism start after the initial pyroclastic flow had ceased transport and deposition. The flow halts en masse, followed by stationary welding and compaction of the sheet, before the stationary hot deposit remobilises. Branney and Kokelaar (1992) abandoned the en masse deposition model and proposed a model of agglutination and deformation at, and within the base of, a sustained hot pyroclastic

density current. The model suggests a rapid, but sustained aggradation process, whereby any bedding reflects current unsteadiness, and occurs irrespective of welding and does not require valley-confined transport as a dense plug.

Sumner and Branney (2002) detailed a heterogeneous, chemically-zoned lava-like ignimbrite 'TL' on Gran Canaria. This ignimbrite shares similar characteristics to obsidian lava flows, exhibiting lobate margins emplaced during a single event. Eutaxitic features are said to be formed in ignimbrites in a similar manner to their formation in obsidian lava flows; by comminution and viscous shear of hot pumiceous autobreccias (Sumner and Branney, 2002). TL has characteristics diagnostic of lavas, and is a documented example of an ignimbrite that travelled like a true lava flow, beyond its original depositional limit. The TL exhibits imbricated fiamme, rheomorphic lineations, open to isoclinal folds, ramp structures, surface ridges, and boudinage and load structures. Andrews and Branney (2011) investigated the emplacement and rheomorphic deformation of a large, lava-like rhyolitic ignimbrite (Grey's Landing, southern Idaho), and discuss the comparison of such ignimbrites to silicic lavas. Andrews and Branney (2011) state that a comparable detailed study of unequivocal long silicic lava can help distinguish between lava and ignimbrite by structural and kinematic analysis. Shear in ignimbrite affects the thickness, and silicic lavas may inherit flow bands, flow folds, and elongation lineations adjacent to conduit-margin shear. Differences recorded in ignimbrites and lava in relation to structural, textural and kinematic features are stated to require further investigation (Andrews and Branney, 2011). Parameters in Table 5.1 indicate common features or structures found in obsidian lavas and/or rheomorphic ignimbrites. Both lavas and ignimbrites commonly host such features, but may be more abundant or characteristic of one particular origin. For instance, phenocrysts are generally more common in ignimbrites, often rotated and wrapped by banding (relating to shear strain).

Table 5.1: Common features and structures in obsidian lavas and rheomorphic ignimbrites, and the assessment of their occurrence (based on study observations and previous examples from Bonnichsen and Kauffman, 1987; Fink and Manley, 1987; Henry et al., 1990; Branney et al., 1992, 2004; Branney and Kokelaar 1992; Manley, 1996).

Feature or structure	**Obsidian lavas**	**Rheomorphic ignimbrites**
Magmatic enclaves	Variable occurrence	Variable occurrence
Phenocrysts	Predominantly rare	Rare to common
Microlites	Commonly occur	Rare axiolitic
Spherulites	Commonly occur	Variable occurrence
Flow foliations	Commonly occur	Occur in welded ignimbrites
Lineations	Commonly occur	Commonly occur
Folding	Commonly occur	Commonly occur
Sheath folds	Sometimes occur	Commonly occur
Autobrecciation	Top, basal and internal	Top, basal and internal
Faults and fractures	Commonly occur	Commonly occur
Ogives	Commonly occur	Commonly occur
Vesicles	Variable occurrence	Commonly occur
Groundmass material	Glassy/ devitrified	Ash/lapilli - pumice
Groundmass texture	Holohyaline, coherent	Eutaxitic, fragmented glass
Imbricated fragments	Rare	Commonly occur (fiamme)
Channelled flow	Variable occurrence	Topographically controlled
Lobate margins	Commonly occur	Commonly occur
Ramp structures	Commonly occur	Commonly occur

Phenocrysts in obsidian are rare, and may be nucleation sites for spherulites. Microlites are more commonly associated with obsidian lavas, though rare axiolitic microlites may occur within the ignimbrite matrix. Spherulites occur in both obsidian lavas and ignimbrites, but are often more concentrated within ignimbrites compared to obsidian lavas. Flow foliations

are typical of both obsidian lavas and highlight welded ignimbrites, but sheath folds occur more commonly in ignimbrites due to transport, emplacement and post-emplacement mechanisms. Brecciation is common in both obsidian lavas and ignimbrites, but the presence of brecciation incorporated into tuffs may preserve the pyroclastic nature of the ignimbrite, if the matrix is sufficiently cooled. Vesicles occur in concentrated areas in obsidian flow stratigraphy (such as pumiceous zones), but spherical, flattened and highly attenuated vesicles are common in ignimbrites. The groundmass material is often a strong indicator of origin. Obsidian groundmass is often coherent, glassy or devitrified, whereas ignimbrites are often fragmented, clastic and/or eutaxitic. Imbricated fragments are much more common in ignimbrites, and eutaxitic fabrics similar to those found in welded ignimbrites occurring locally in lava flows, by comminution and viscous shear of hot pumiceous autobreccia. For silicic bodies of unknown origin, the criteria in Table 5.1 offers a guide for distinguishing between obsidian lavas and rheomorphic ignimbrites, but is often non-definitive. However, variations in the occurrence of features or structures can help to elucidate the origin. These previous studies demonstrate a number of striking similarities between structures identified in obsidian lava flows and in rheomorphic ignimbrites. Importantly, these structures may relate to comparable processes, and further emphasises the role of thermal insulation, differential flow regimes and progressive deformation in the formation of complex structures in obsidian lava flows. These processes can sustain obsidian flow mobility and deformation for days to weeks following extrusion, comparable to post-depositional remobilisation in rheomorphic ignimbrites (e.g. Wolff and Wright 1981; Branney and Kokelaar 1992; Branney et al., 2004).

Chapter 6

Conclusions and future research

This chapter summarises the initial aims and key findings of this study, recaps new data and models presented, and suggests potential future research as a follow-up to this study.

Conclusions and future research

This study addressed the structure, emplacement and textural evolution of young obsidian lavas in the Aeolian Islands, Italy. Specifically, the study has aimed to investigate the emplacement and deformation of the Rocche Rosse obsidian lava flow (Lipari), address the occurrence of spherulites in obsidian lavas across Lipari and Vulcano, and reconstruct the magmatic and post-magmatic processes of the Pietre Cotte obsidian lava flow (Vulcano). The findings from this study contribute to our understanding of the emplacement behaviour and texture formation associated with obsidian lavas.

The Rocche Rosse lava flow emplaced and deformed over five stages of emplacement, occurring concomitantly, resulting in a number of complex ductile and brittle structures. Such structures are evident in satellite imagery, field observations, structural recordings, and at microscopic-scale. The final lava flow is the product of (1) Initial extrusion, (2) extensional forces over steep topography, (3) compressional forces at the topographic break, (4) progressive deformation and (5) brittle deformation due to cooling. Variable rheology and differential flow regime determined the variable influence of each of these stages, and particularly affected progressive deformation. Such rheological variations resulted in the high degree of observed structural complexity. Rheological estimates vary in terms of H_2O content (up to 0.21 wt%), extrusion temperature (730°C to 763°C), viscosity ($10^{10.5\text{-}11.2}$ Pa s), and SiO_2 (69-76 wt%). Spherulite content also varies and occasionally shows a spatial relationship to structures (high populations of spherulites concentrated within deformational structures), and an observed channelled flow geometry may have also influenced flow configuration and deformation. Flow localisation and non-Newtonian rheology arises from differences in rheology and spherulite content, and was

also partly responsible for flow complexity, a channelled flow regime, flow lobe development and breakout lobes (frontal stalling). The study therefore emphasises the role of differential flow rheology, progressive deformation and channelled flow in the multi-scale structural evolution of the Rocche Rosse lava flow.

Spherulites are widespread across Aeolian obsidian lavas, and show variable textural features in terms of shape, size, physical characteristics, distribution and composition. Spherulite commonly contain cristobalite (α and β), orthoclase, minor diopside, titanomagnetite and glass. In this study, individual spherulite populations were identified, resulting from different nucleation stimuli and later spherulite modification. Spherulites have been classified as five types. Type 1 spherulites are radial, sub-spherical, often small and unaltered, and contain α- and β-cristobalite. Microlites are often deflected around Type 1 spherulites. Type 1 spherulites formed due to high degrees of undercooling at high temperatures at high T_g transition temperatures or above. Type 2 spherulites are elongate, with a brown rim, minor alteration, radial interior, and are interpreted as forming due to deformation (tend to form in shear zones) and/or enhanced undercooling. Type 3 spherulites are large, radial spherulites, often occurring individually in zones of low shear. Type 3 spherulites formed by enhanced undercooling or deformation in low T_g transition or below. Type 4 spherulites concentrated within fractures and faults, indicating that these formed following solid state deformation. Type 5 spherulites are partially- or fully-modified spherulites and lithophysae, with a non-radial interior, formed by vapour-infilling (low T_g transition or below). Flow-induced crystallisation (elongation and shear) may have triggered spherulite crystallisation, aiding the formation of elongate crystals, the entropic penalty for crystallisation was lowered and, therefore, the nucleation rate increases. This type of spherulite crystallisation may therefore have been responsible for deformed spherulites (forming during deformation), sheared spherulites within bands (formed during

deformation), and spherical spherulites concentrated within bands, folds and faults (forming in late stages of deformation and/or after deformation). Spherulites formed due to a number of processes, pre-, syn- and post-flow emplacement, from high to low temperatures (i.e. above, during and below T_g transition). Importantly, deformation may have triggered spherulite nucleation, and/or promoted deformation. Spherulites in Aeolian island obsidian lavas nucleated and grew simultaneously due to a number of different processes, resulting in individual spherulite populations and heterogeneous characteristics.

Magmatic and post-magmatic processes leading to the texturally heterogeneous Pietre Cotte obsidian lava flow were investigated. The study shows three distinct magmas interacting (indicated by a glassy rhyolitic host containing trachytic enclaves, which host a glomerocrysts of a more mafic mineral assemblage), a crystal assemblage of olivine, clinopyroxene, plagioclase and titanomagnetite, with disequilibrium textures, microlites and spherulites, and deformational structures such as multi-scale folding and stretching lineations. Enclaves are trachytic in composition, and crystallised at ~1,130°C and 1,668 bars pressure (8 km depth), with an oxidation state of ~1.5 units above FMQ. The rhyolitic host crystallised at ~1,033°C and 1.6 km depth. The Pietre Cotte magmatic system and lava flow developed over five stages: (1) Mafic magma crystallisation and the remobilisation of a crystal mush; (2) Mingling of a (glomerocryst-bearing) trachytic magma with a rhyolitic magma; (3) Ascent and extrusion of the (trachytic enclave-bearing) rhyolite accompanied by microlite crystallisation, onset of spherulite nucleation and growth during ascent and extrusion, and extrusion and lava flow emplacement; (4) Flow deformation across the ductile-brittle transition during and following emplacement; and (5) Vapour-phase crystallisation and devitrification late- and post-emplacement. This study provides a new model for the Pietre Cotte lava flow evolution, addressing the formation of glomerocrysts, proposing a hotter trachyte entering a rhyolitic host, microlite and

spherulite crystallisation, and culminating in flow deformation and late-stage modification.

A continuation of the work conducted in this study may include a follow-up investigation on the potential origin of pumiceous zones in the Rocche Rosse and Pietre Cotte lava flows. Field observations suggest that pumiceous zones exist at the flow surface and distort the overlying obsidian foliation attitudes. Geochemistry, detailed surface and flank mapping, and Vesicle Size Distribution (VSD) methods of these pumiceous zones and older/spatially related pumice and lava deposits may give an indication of the source or origin of these pumiceous zones, eruption mechanisms and emplacement/remobilisation dynamics, as well as nucleation and deformation stresses. Future research that is more focused on the Aeolian Islands may also include research on the relatively unknown Forgia Vecchia lava flow in E Lipari. Field observations in this study suggest that there are no mafic enclaves within the Forgia Vecchia obsidian lava. However, studies of the other young obsidian lava flows reveal the presence of sparse- to widespread mafic enclaves. It could therefore be assumed that the Forgia Vecchia lava flow does contain mafic enclaves. If no mafic enclaves are identified, does this suggest that the Forgia Vecchia lava flow is the product of a more unique magmatic evolution that does not involve mixing or mingling of a coeval mafic product?

The proposed obsidian emplacement and spherulite formation models emphasise the complexity of obsidian lava flows in multi-scale detail, and the role played by flow rheology, spherulite crystallisation and progressive deformation, and the intrinsic relationship between spherulite crystallisation and flow deformation. Obsidian lava flows also show a number of similarities to ignimbrites, relating to comparable emplacement and deformation processes, and further emphasising the role of progressive deformation. The new magmatic and post-magmatic model for Pietre Cotte lava flow is the first to detail pre- and post-extrusive processes, important for a full understanding of magmatic behaviour

and flow behaviour, addresses the presence of glomerocrysts within Pietre Cotte lava flow, and provides new intensive variable estimates for pressure, temperature and oxygen fugacity conditions. Overall, this study shows that the complex details of obsidian structural and textural evolution can be addressed by multi-disciplinary techniques and approaches, and can be modelled according to their physical characteristics and interpreted processes. The study also emphasises the relationship between spherulites and deformation as proposed previously by Clay et al. (2013), which is well understood in polymer sciences but not in geological context, the role of T_g and progressive deformation in obsidian emplacement and texture evolution, and offers an evaluation of silicic lava generation and emplacement in the Aeolian Islands, which may be applicable to other obsidian lava flows.

References

Abrams, M., Abbott, E., Kahle, A., 1991. Combined Use of Visible, Reflected Infrared, and Thermal Infrared Images for Mapping Hawaiian Lava Flows. Journal of Geophysical Research 96, 475-484.

Alley, R.B., 1992. Flow-law hypotheses for ice-sheet modeling, Journal of Glaciology 38, 245–256, 1992.

Amodio-Morelli, L., Bonardi, G., Colonna, V., Dietrich, D., Giunta, G., Ippolito, F., Liguori, V., Lorenzoni, S., Paglionico, A., Perrone, V., Piccarreta, G., Russo, M., Scandone, P., Zanettin-Lorenzoni, E., Zuppetta, A., 1976. L'arco Calabro-Peloritano nell'orogene appenninico Maghrebide (The Calabrian-Peloritan Arc in the Apennine-Maghrebide orogen). Memorie della Società Geologica Italiana 17, 1–60.

Andersen, D., Lindsley, D.H., Davidson, P.M., 1993. QUILF: A pascal program to assess equilibria among Fe-Mg-Mn-Ti oxides, pyroxenes, olivine, and quartz. Computers & Geosciences 19, 9, 1333-1350.

Anderson, A.T., Jr., 1976, Magma mixing: Petrologic process and volcanological tool. Journal of Volcanology and Geothermal Research l, 3-33.

Anderson, H.J., Jackson, J.A., 1987. The deep seismicity of the Tyrrhenian Sea. Geophysical Journal of the Royal Astronomical Society 91, 613-637.

Anderson, S.W., Fink, J.H., 1989. Hydrogen isotope evidence for extrusion mechanisms of the Mount St. Helens dome. Nature 341, 521–523.

Anderson, S.W., Fink, J.H., 1990. The development and distribution of lava textures at the Mount St. Helens dome. In Fink, J.H., ed., The mechanics of lava flow and dome growth, IAVCEI Proceedings in Volcanology 2, 25–46.

Anderson, S.W., Fink, J.H., 1992. Crease structures as indicators of emplacement rates and surface stress regimes of lava flows. Geological Society of America Bulletin 104, 615–626.

Anderson, S.W., Stofan, E.R., Plaut, J.J., Crown, D.A., 1998. Block size distributions on silicic lava flow surfaces: Implications for emplacement conditions. Geological Society of America Bulletin 110, 1258–1267.

Anderson, S.W., Stofan, E.R., Smrekar, S.E., Guest, J.E., Wood, B., 1999. Pulsed inflation of pahoehoe lava flows: Implications for flood basalt emplacement. Earth and Planetary Science Letters 168, 7-18.

Andrews, G.D.M., 2006. Emplacement and deformation of high-temperature tuffs: a structural analysis of the Grey's landing ignimbrite, Snake River plain, Idaho. PhD thesis, University of Leicester.

Andrews, G.D.M., Branney, M.J., 2011. Emplacement and rheomorphic deformation of a large, lava-like rhyolitic ignimbrite: Grey's Landing, southern Idaho. Geological Society of America Bulletin 123, 725-743.

Anovitz, L.M., Riciputi, L.R., Cole, D.R., Elam, J.M., Gruszkiewicz, M.S., 2006. The effect of changes in relative humidity on the hydration rate of Pachuca obsidian. Journal of Non-Crystalline Solids 352, 5652–5662.

Applegarth, L.J., Pinkerton, H., James, M.R., Calvari, S., 2010. Lava flow superposition: The reactivation of flow units in compound'a'a flows. Journal of Volcanology and Geothermal Research 194, 100-106.

Armienti, P., Tarquini, S., 2002. Power law olivine crystal size distributions in lithospheric mantle xenoliths. Lithos 65, 3-4, 273-285.

Arrighi, S., Tanguy, J., Rosi, M., 2006. Eruptions of the last 2200 years at Vulcano and Vulcanello (Aeolian Islands, Italy) dated by high-accuracy archaeomagnetic. Physics of the Earth and Planetary Interiors 159, 225-233.

Asimow, P.D., Ghiorso, M.S., 1998. Algorithmic modifications extending MELTS to calculate subsolidus phase relations. American Mineralogist 83, 1127-1131.

Avril, C., Malavergne, V., Caracas, R., Zanda, B., Reynard, B., Charon, E., Bobocioiu, E., Brunet, F., Borensztajn, S., Pont, S., Tarrida, M., 2013. Raman spectroscopic properties and Raman identification of CaS–MgS–MnS–FeS–Cr_2FeS_4 sulfides in meteorites and reduced sulfur-rich systems. Meteoritics & Planetary Science 48, 1415–1426.

Azuma, N., Higashi., A., 1985. Formation processes of ice fabric pattern in ice sheets. Annual Glaciology 6, 130-134.

Bachmann, O., Bergantz, G.W., 2003. Rejuvenation of the Fish Canyon magma body: a window into the evolution of large-volume silicic magma systems. Geology 31, 789–792.

Baert, J., Van Puyvelde, P., Langouche, F., 2006. Flow induced crystallization of PB-1: From the low shear rate region up to processing rates. Macromolecules 39, 9215-9222.

Bagdassarov, N.S., Dingwell, D.B., 1993. Frequency dependent rheology of vesicular rhyolite. Journal of Geophysical Research: Solid Earth 98, B4, 6477-6487.

Bain, A.D.N., 1934. The younger intrusive rocks of the Kudaru Hills, Nigeria. Quarterly Journal of the Geological Society 90, 201–239.

Balk, D.C., 1937. Structural behavior of igneous rocks. Geological Society of America Memoir 5, 177.

Barberi, F., Gandino A., Gioncada, A., La Torre, P., Sbrana, A., Zenucchini, C., 1994. The deep structure of the Eolian arc (Filicudi-Panarea-Vulcano sector) in light of gravity, magnetic and volcanological data, Journal of Volcanology and Geothermal Research 61, 189–206.

Barberi, F., Innocenti, F., Ferrara, G., Keller, J., Villari, L., 1974. Evolution of Eolian arc volcanism (South Tyrrhenian Sea). Earth and Planetary Science Letters 21 (3), 269-276.

Barclay, J., Carroll, M.R., Houghton, B.F., Wilson, C.J.N., 1996. Pre-eruptive volatile content and degassing history of an evolving peralkaline volcano. Journal of Volcanology and Geothermal Research 74, 1-2, 75-87.

Bastida, F., Martínez Catalán, J.R., Pulgar, J.A., 1986. Structural, metamorphic and magmatic history of the Mondoñedo nappe (Hercynian belt, NW Spain). Journal of Structural Geology 8, 415-430.

Baxter, P.J., Bonadonna, R., Dupree, R., Hards, V.L., Kohn, S.C., Murphy, M.D., Nichols, A., Nicholson, R.A., Norton, G., Searl, A., Sparks, R.S.J., Vickers, B.P., 1999. Cristobalite in volcanic ash of the Soufriere Hills Volcano, Montserrat, British West Indies. Science 283, 1142-1145.

Befus, K.S., Zinke, R.W., Jordan, J.S., Manga, M., Gardner, J.E., 2014. Pre-eruptive storage conditions and eruption dynamics of a small rhyolite dome: Douglas Knob, Yellowstone volcanic field, USA. Bulletin of Volcanology 76: 808. DOI 10.1007/s00445-014-0808-8.

Bellot-Gurlet L., Le Bourdonnec F.-X., Poupeau G., Dubernet S., 2004. Raman micro-spectroscopy of Western Mediterranean obsidian glass: one step toward provenance studies? Journal of Raman Spectroscopy 35, 671-677.

Bigazzi, G., Bonadonna, F.P., 1973. Fission track dating of the obsidian of Lipari Island (Italy). Nature. 242, 322-323.

Binsbergen, F.L., 1966. Orientation-induced Nucleation in Polymer Crystallization. Letters to Nature 211, 516-517.

Blake, S., Bruno, B.C., 2000. Modelling the emplacement of compound lava flows. Earth and Planetary Science Letters 184, 181–197.

Blundy, J.D., Cashman, K., 2005. Rapid decompression-driven crystallization recorded by melt inclusions from Mount St Helens volcano. Geology 33 (10), 10.2005, 793-796.

Bondre, N., 2003. Analysis of vesicular basalts and lava emplacement processes for application as a paleobarometer/paleoaltimeter: a discussion. The Journal of Geology 111, 499–502.

Bonnichsen, B., Kauffman, D.F., 1987. Physical features of rhyolite lava flows in the Snake River Plain volcanic province, south-western Idaho In Fink, J.H., ed., The emplacement of silicic domes and lava flows, Geological Society of America Special 212, 119–145.

Boorman, S., Boudreau, A., Kruger, F.J., 2004. The lower zone-critical zone transition of the Bushveld Complex: a quantitative textural study. Journal of Petrology. 45, 1209-1235.

Bottinga, Y., Weill, D.F., 1972. The viscosity of magmatic silicate liquids: a model for calculation. American Journal of Science 272, 438-475.

Boudreau, A.E., 1999. PELE—a version of the MELTS software program for the PC platform. Computers and Geoscience 25, 21–203.

Bouška, V., 1993. Natural Glasses. Ellis Horwood and Academia, New York and Prague.

Branca, S., De Beni, E., Proietti, C., 2013. The large and destructive 1669 AD eruption at Etna volcano: reconstruction of the lava flow field evolution and effusion rate trend. Bulletin of Volcanology 75, 694.

Branney, M.J., Barry, T.L., Godchaux, M., 2004. Sheathfolds in rheomorphic ignimbrites. Bulletin of Volcanology 66, 485-491.

Branney, M.J., Kokelaar, B.P., McConnell, B.J., 1992. The Bad Step Tuff: a lava-like ignimbrite in a calc-alkaline piecemeal caldera, English Lake District. Bulletin of Volcanology 54, 187-199.

Branney, M.J., Kokelaar, B.P., 2002. Pyroclastic density currents and the sedimentation of ignimbrites. Geological Society of London, Memoirs 27, 152.

Brawer, S. A., White, W B., 1975. Raman Spectroscopic investigation of the structures of silicate glasses (II). Soda-alkaline earth-alumina ternary and quaternary glasses. Journal of Non-Crystalline Solids 23, 261-278.

Breitkreuz C., 2001., Introduction to physical volcanology and volcanic textures. CVT Short course, TU Bergakademie Freiberg, Germany.

Breitkreuz, C., 2004. Silicic Lava Domes: between Field Observations and Analog Modelling. TU Bergakademie Freiberg, Oberseminar Geologie.

Breitkreuz, C., 2013. Spherulites and lithophysae—200 years of investigation on high-temperature crystallization domains in silica-rich volcanic rocks. Bulletin of Volcanology 75, 1-16.

Brun, J-P., Merle, O., 1988. Experiments on folding in spreading-gliding nappes. Tectonophysics 145, 129–139.

Byrnes, J.M., Crown, D.A., 2001. Relationships between pahoehoe surface units, topography, and lava tubes at Mauna Ulu, Kilauea Volcano, Hawaii. Journal of Geophysical Research: Solid Earth 106, B2, 2139-2151.

Cabrera, A., Weinberg, R.F., Wright, H.M.N., Zlotnik, S., Cas, R.A.F., 2011. Melt fracturing and healing: A mechanism for degassing and origin of silicic obsidian. Geology, 39, 1, 67-70.

Caggianelli, A., de Lorenzo, S., Prosser, G., 2005. Modelling the heat pulses generated on a fault plane during coseismic slip: inferences from the pseudotachylites of the Copanello cliffs (Calabria, Italy). Tectonophysics 405, 99-119.

Calvari, S., Pinkerton, H., 1999. Lava tube morphology on Etna and evidence for lava flow emplacement mechanisms. Journal of Volcanology and Geothermal Research 90, 263-280.

Caputo, M., Panza, G.F., Postpischl, D., 1972. New evidences about the deep structure of the Lipari arc. Tectonophysics 15:219-231.

Carapezza, M., Nuccio, P.M., Valenza, M., 1981. Genesis and Evolution of Fumaroles of Vulcano (Aeolian Islands, Italy): a Geochemical Model. Bulletin of Volcanology 44-3, 547-563.

Carmichael, I.S.E., 1967. The iron-titanium oxides of salic volcanic rocks and their associated ferromagnesian silicates. Contributions to Mineralogy and Petrology 14, 36-64.

Carmichael, I.S.E., 1991. The redox states of basic and silicic magmas: a reflection of their source regions? Contributions to Mineralogy and Petrology 106, 129-141.

Carmichael, I.S.E, Turner, F., Verhoogen, J., 1974. Igneous petrology. McGraw-Hill, New York, p 739.

Caroli, C., Lemaître, A., 2012. Ultrafast spherulitic crystal growth as a stress-induced phenomenon specific of fragile glass-formers. The Journal of Chemical Physics 137, 114506.

Carrichi, L., Burlini, L., Ulmer, P., Gerya, T., Vassalli, M., Papale, P., 2007. Non-Newtonian rheology of crystal-bearing magmas and implications for magma ascent dynamics. Earth and Planetary Science Letters 264, 402-419.

Carrichi, L., Pommier, A., Pistone, M., Castro, J., Burgisser, A., Perugini, D., 2011. Strain-induced magma degassing: insights from simple-shear experiments on bubble bearing melts. Bulletin of Volcanology 73, 1245-1257.

Cas, R.A.F., Wright, J.V. (eds), 1987. Volcanic Successions. Modern and Ancient. Allen and Unwin, London, UK. 528 pp.

Cashman, K., Blundy, J., 2000. Degassing and crystallization of ascending andesite. Philosophical Transactions of the Royal Society 358, 1487-1513.

Cashman, K.V., Kauahikaua, J.P., Thornber, C., 1999. Cooling and crystallization of lava in open channels, and the transition of pahoehoe lava to a'a. Bulletin of Volcanology 61, 306–323.

Castellet y Ballarà, G., Crescenzi, R., Pompili, A., Trigila, R., 1982. A petrological model on magma evolution of Vulcano eruptive complex (Aeolian Islands—Italy). In: Coradini, A. & Fulchignoni, M. (eds) The Comparative Study of Planets. NATO Advanced Study Institutes Series, D. Dordrecht: Reidel, 459–476.

Castro, J.M., 1999. Textural and structural development of obsidian lavas. Ph.D. dissertation. University of Oregon, USA, 163 pp.

Castro, J.M., Cashman, K.V., 1999. Constraints on rheology of obsidian lavas based on mesoscopic folds. Journal of Structural Geology 21, 807-819.

Castro, J.M., Beck, P., Tuffen, H., Nichols, A.R.L., Martin, M., 2008. Timescales of spherulite crystallization in obsidian inferred from water concentration profiles. American Mineralogist 93, 1816–1822.

Castro, J.M., Cottrell, E., Tuffen, H., Logan, A.V., Kelley, K.A., 2009. Spherulite crystallisation induces Fe-redox redistribution in silicic melt. Chemical Geology 268, 272-280.

Castro, J.M., Manga, M., Cashman, K., 2002. Dynamics of obsidian flows inferred from microstructures: insights from microlite preferred orientations. Earth and Planetary Science Letters 199 (1-2), 211-226.

Castro, J.M., Mercer, C.N., 2004. Microlite textures and volatile contents of obsidian from the Inyo volcanic chain, California. Geophysical Research Letters 31(L18605): doi: 10.1029/2004GL02489.

Castro, J.M., Schipper, C.I., Mueller, S., Militzer, A., Amigo, A., Parejas, C.S., Jacob, D., 2013. Storage and eruption of near-liquidus rhyolite magma at Cordón Caulle, Chile. Bulletin of Volcanology 75, 702-719.

Chapin, C.E., Lowell, G.R., 1979. Primary and secondary flow structures in ash-flow tuffs of the Gribbles Run paleovalley, central Colorado. Geology Society of America Special Paper 180, 137–154.

Chevrel, M.O., Platz, T., Hauber, E., Baratoux, D., Lavallée, Y., Dingwell, D.B., 2013. Lava flow rheology: A comparison of morphological and petrological methods. Earth and Planetary Science Letters 384, 109-120.

Chopelas, A., 1990. Thermal properties of forsterite at mantle pressures derived from vibrational spectroscopy. Physics and Chemistry of Minerals 17, 149-156.

Christiansen, R.L., Lipman, P.W., 1966. Emplacement and Thermal History of a Rhyolite Lava Flow near Fortymile Canyon, Southern Nevada. Geological Society of America Bulletin 77; 7; 671-684.

Cioni, R., Funedda, A., 2005. Structural geology of crystal-rich, silicic lava flows: A case study from San Pietro Island (Sardinia, Italy), In: Manga, M., Ventura, G., (eds), Kinematics and Dynamics of Lava Flows. Geological Society of America Special Paper 396, 1-14.

Clay, P.L., O'Driscoll, B., Gertisser, R., Busemann, H., Sherlock, S.C., Kelley, S.P., 2013. Textural characterization, major and volatile element quantification and Ar–Ar systematics of spherulites in the Rocche Rosse obsidian flow, Lipari, Aeolian Islands: a temperature continuum growth model. Contributions to Mineralogy and Petrology 165, 2, 373-395.

Clocchiatti, R., Del Moro, A., Gioncada, A., Joron, J.L., Mosbah, M., Pinarelli, L., Sbrana, A., 1994. Assessment of a shallow magmatic system: the 1888–90 eruption, Vulcano Island, Italy. Bulletin of Volcanology, 56, 466–486.

Coccorullo, I., Pantani, R., Titomanlio, G., 2008. Spherulitic nucleation and growth rates in an iPP under continuous shear flow. Macromolecules 41, 9214–9223.

Cole, G.A.J., 1886. On the Alteration of coarsely Spherulitic Rocks. Quarterly Journal of the Geological Society 42, 183-191.

Cortese, M., Frazzetta, G., La Volpe, L., 1986. Volcanic history of Lipari (Aeolian Islands, Italy) during the last 10,000 years. Journal of Volcanology and Geothermal Research 1-2, 117-133.

Costa, A., Macedonio, G., 2003. Viscous heating in fluids with temperature-dependent viscosity: implications for magma flows. Nonlinear Processes in Geophysics 10, 545–555.

Couch, S., Sparks, R.S.J., Carroll, M.R., 2003. The kinetics of degassing-induced crystallization at Soufrière Hills Volcano, Montserrat. Journal of Petrology 44, 1477-1502.

Crisci, G.M., De Rosa, R., Lanzafame, G., Mazzuoli, R., Sheridan, M.F., Zuffa, G.G., 1981. Monte Guardia sequence: a late Pleistocene eruptive cycle on Lipari (Italy). Bulletin of Volcanology. 44, 3, 241-255.

Crisci G.M., Delibrias G., De Rosa R., Mazzuoli R., Sheridan M.F., 1983. Age and Petrology of the Late-Pleistocene Brown Tuffs on Lipari, Italy. Bulletin of Volcanology 53, 207-221.

Crisci, G.M., De Rosa, R., Esperanca, S., Mazzuoli, R., Sonnino, M., 1991. Temporal evolution of a three component volcanological system: the Island of Lipari (Aeolian Arc, Southern Italy). Bulletin of Volcanology 53, 207–221.

Damby, D,E., Llewellin, E.W., Horwell, C.J., Williamson, b.J., Najorka, J., Cressey, G., Carpenter, M., 2014. The α–β phase transition in volcanic cristobalite. Journal of Applied Crystallography 47 (4), 1205-1215.

Davì, M., 2007. The Rocche Rosse rhyolitic lava flow (Lipari, Aeolian Islands): magmatological and volcanological aspects. Plinius 33, 1-7.

Davì, M., De Rosa, R., Barca, D., 2009. A LA-ICP-MS study of minerals in the Rocche Rosse magmatic enclaves: Evidence of a mafic input triggering the latest silicic eruption of Lipari Island (Aeolian Arc, Italy). Journal of Volcanology and Geothermal Research 182, 45-56.

Davì, M., De Rosa, R., Donato, P., Sulpizio, R., 2011. The Lami pyroclastic succession (Lipari, Aeolian Islands): a clue for unravelling the eruptive dynamics of the Monte Pilato rhyolitic pumice cone. Journal of Volcanology and Geothermal Research 201, 285–300.

Davì, M., De Rosa, R., Holtz, F., 2010. Mafic enclaves in the rhyolitic products of Lipari historical eruptions; relationships with the coeval Vulcano magmas (Aeolian Islands, Italy). Bulletin of Volcanology 72, 991-1008.

Davis, B., McPhie, J., 1996. Spherulites, quench fractures and relict perlite in a Late Devonian rhyolite dyke, Queensland, Australia. Journal of Volcanology and Geothermal Research 71, 1–11.

De Astis, G., 1995. Evoluzione vulcanologicae magmatological dell'isola di Vulcano (Isole Eolie), Ph.D. thesis, Dip. Geomineral., University of Bari, Bari, Italy.

De Astis, G., Dellino, P., La Volpe, L., Lucchi, F., Tranne, C.A., 2006. Geological map of the island of Vulcano (Aeolian Islands), scale 1:10,000, edited by L. La Volpe and G. De Astis, Litographia Artistica Cartographica, Florence, Italy. University of Bari, University of Bologna and INGV. LAC, Firenze, Italy.

De Astis, G., La Volpe, L., Peccerillo, A., Civetta, L., 1997. Volcanological and petrological evolution of Vulcano island (Aeolian Arc, southern Tyrrhenian Sea). Journal of Geophysical Research. 102, 8021-8050.

De Astis, G., Lucchi, F., Dellino, P., La Volpe, L., Tranne, C.A., Frezzotti, M.L., Peccerillo, A., 2013. Geology, volcanic history and petrology of Vulcano (central Aeolian archipelago). In: Lucchi, F., Peccerillo, A., Keller, J., Tranne, C.A., Rossi, P.L. (eds). The Aeolian Islands Volcanoes. Geological Society, London, Memoirs 37, 281-349.

De Astis, G., Peccerillo, A., Kempton, P.D., La Volpe, L., Wu, T.W., 2000. Calcalkaline to potassium-rich magmatism in the Aeolian Arc: geochemical and Sr, Nd, Pb isotopic constraints from the Island of Vulcano (Aeolian arc). Contributions to Mineralogy and Petrology 139, 684-703.

De Astis, G., Ventura, G., Vilardo, G., 2003. Geodynamic significance of the Aeolian volcanism (Southern Tyrrhenian Sea, Italy) in light of structural, seismological, and geochemical data. Tectonics 22, 1040, doi: 10.1029/2003TC001506.

De Fiore, O., 1922. Vulcano (Isole Eolie). Monografia – Zeitschrift fur Vulkanologie 3, 3–393. (Rep. Swets and Zeitlinger N. V., Amsterdam, 1969).

de Hoog, J.C.M., van Bergen, M.J., Jacobs, M.H.G., 2005. Vapour-phase crystallisation of silica from SiF4-bearing volcanic gases. Annals of Geophysics 48, 4/5, 775-785.

De Rosa, R., Donato, P., Gioncada, A., Masetti, M., Santacroce, R., 2003. The Monte Guardia eruption (Lipari, Aeolian Islands): an unusual example of magma mixing sequence. Bulletin of Volcanology 65, 530–543.

De Rosa, R., Sheridan, M.F., 1983. Evidence for magma mixing in the surge deposits of the Monte Guardia sequence, Lipari. Journal of Volcanology and Geothermal Research 17, 313-328.

de Silva, S.L., Self, S., Francis, P.W., Drake, R.E., Carlos, R.R., 1994. Effusive silicic volcanism in the Central Andes: The Chao dacite and other young lavas of the Altiplano-Puna Volcanic Complex. Journal of Geophysical Research: Solid Earth 99, B9, 17805-17825.

Del Moro, A., Gioncada, A., Pinarelli, L., Sbrana, A., Joron, J.L., 1998. Sr, Nd, and Pb isotope evidence for open system evolution at Vulcano, Aeolian Arc, Italy. Lithos 43, 81-106.

Dell'ertole, D., Schellart, W.P., 2013. The development of sheath folds in viscously stratified materials in simple shear conditions: an analogue approach. Journal of Structural Geology 56, 129-141.

Dellino, P., De Astis, G., 2008. Relazione scientifica per la predisposizione del piano di emergenza vulcanica all'isola di Vulcano. INGV-DPC Projects 2005–2007, Final report on Project V3_5 –Vulcano, pp. 1–64.

Dellino, P., La Volpe, L., 1995. Fragmentation versus transportation mechanism in the pyroclastic sequence of Monte Pilato-Rocche Rosse (Lipari, Italy). Journal of Volcanology and Geothermal Research 64, 211-231.

Dellino, P., La Volpe, L., 1997. Stratigrafia, dinamiche eruttive e deposizionali, scenario eruttivo e valutazioni di pericolosità La Fossa di Vulcano, C.N.R. Gruppo Nazionale per la Vulcanologia, volume speciale Vulcano, pp. 207–213, Felici Editore, Pisa, Italy.

Derakhshandeh, M., **Hatzikiriakos, S.G., 2012.** Flow-Induced Crystallization of High-Density Polyethylene: The Effects of Shear & Uniaxial Extension, Rheologica Acta 51, 315-327.

Devaux, N., Monasse, B., Haudin, J.M., Moldenaers, P., Vermant, J., 2004. Rheooptical study of the early stages of flow enhanced crystallization in isotactic polypropylene. Rheologica Acta 43(3), 210-222.

Di Liberto V., Nuccio P. M, Paonita A., 2002. Genesis of chlorine and sulfur in fumarolic emissions at Vulcano Island (Italy): assessment of pH and redox conditions in the hydrothermal system. Journal of Volcanology and Geothermal Research 116, 137–150.

Di Muro, A., Villemant, B., Montagnac, G., Sciallet, B., Reynard, B., 2006. Quantification of water content and speciation in natural silicic glasses (phonolite, dacite, rhyolite) by confocal micro-Raman spectrometry. Geochimica et Cosmochimica Acta. 70, 2868–2884.

Di Muro, A., Métrich, N., Mercier, M., Giordano, D., Massare, D., Montagnac, G., 2009. Micro-Raman determination of iron redox state in dry natural glasses: Application to peralkaline rhyolites and basalts. Chemical Geology. 259, 78-88.

Di Traglia, F., 2011. The last 1000 years of eruptive activity at the Fossa Cone (Island of Vulcano, Southern Italy). PhD thesis, Università degli Studi di Pisa, Italy.

Di Traglia, F., Del Ventisette, C., Rosi, M., Mugnai, F., Intrieri, E., Moretti, S., Casagli N., 2013. Ground-based InSAR reveals conduit pressurization pulses at Stromboli volcano. Terra Nova doi: 10.1111/ter.12020.

Dingwell, D.B., 1995. Relaxation in silicate melts: Applications. In J. Stebbins, P.F. McMillan and D.B. Dingwell, ed., Structure, Dynamics and Properties of Silicate Melts, Reviews in Mineralogy, Mineralogical Society of America 32, 21–66.

Dingwell, D.B., 1996. Volcanic dilemma: Flow or blow? Science 273, 1054-1055 doi:10.1126/science.273.5278.1054.

Dingwell, D.B., 1998. The glass transition in hydrous granitic melts. Physics of the Earth and Planetary Interiors 107, 1-8.

Dobrzhinetskaya, L.F., Green, H.W., 2007. Experimental studies of mineralogical assemblages of metasedimentary rocks at Earth's mantle transition zone conditions. Journal of Metamorphic Geology 25, 2, 83-96.

Dokukina, K.A., Konilov, A.N., Kaulina, T.V., Vladimorov, V.G., 2010. Interaction between mafic and felsic magmas in subvolcanic environment (Tastau igneous complex, eastern Kazakhstan). Russian Geology and Geophysics 51, 625-643.

Donato, P., Behrens, H., De Rosa, R., Holtz, F., Parat, F., 2006. Crystallization conditions in the Upper Pollara magma chamber, Salina Island, Southern Tyrrhenian Sea. Mineralogy and Petrology. 86, 89-108.

Doufas, A.K., Dairanieh, I.S., McHugh, A.J., 1999. A continuum model for flow-induced crystallization of polymer melts. Journal of Rheology 43, 85-109.

Downs, R.T., 2006. The RRUFF Project: an integrated study of the chemistry, crystallography, Raman and infrared spectroscopy of minerals. Program and Abstracts of the 19th General Meeting of the International Mineralogical Association in Kobe, Japan. O03-13.

Downs, R.T., Palmer, D.C., 1994. The pressure behavior of α cristobalite. American Mineralogist 7 (9), 9-14.

Dragoni, M., 1993. Modelling the rheology and cooling of lava flows. In: Kilburn, C.R.J., Luongo, G. (eds), Active Lavas: Monitoring and Modelling. University College of London Press, 235-261.

Dragoni, M., 1997. Physical modelling of lava flows. Annali Di Geofisica 40, 5, 1179-1187.

Dragoni, M., Pondrelli, S., Tallarico, A., 1992. Longitudinal deformation of a lava flow: the influence of Bingham rheology. Journal of Volcanology and Geothermal Research 52:247–254.

Dragoni, M., Tallarico, A., 1994. The effect of crystallization on the rheology and dynamics of lava flows. Journal of Volcanology and Geothermal Research 59, 3, 241-252.

Duffield, W.A., 1990. Eruptive fountains of silicic magma and their possible effects on the tin content of fountain-fed lavas, Taylor Creek Rhyolite, New Mexico. Geological Society of America Special Paper 246, 251-261.

Eichelberger, J.C., 1975. Origin of andesite and dacite: Evidence of mixing at Glass Mountain in California and at other circum-Pacific volcanoes. Geological Society of America Bulletin 86, 1381–1391.

Eichelberger, J.C., Carrigan, C.R., Westrich, H.R., Price, R.H., 1986. Non-explosive silicic volcanism. Nature 323, 598–602, doi: 10.1038/323598a0.

Ekren, E.B., Mclntyre, D.H., Bennet, E.H., 1984. High-temperature large-volume, lava like ash-flow tuffs without calderas in southwestern Idaho. US Geological Survey Professional Paper 1272, 1-76.

El Hadani, D., 1997. Remote Sensing and Geographic Information Systems for the management and water research. Geo-Observer. The Thematic Report 1, 28.

Elkins, L., Grove, T.L., 1990. Ternary feldspar experiments and thermodynamic models. American Mineralogist 75, 5–6, 544–559.

Elliot, C.G., Williams, P.F., 1988. Sediment slump structures: a review of diagnostic criteria and application to an example from Newfoundland. Journal of Structural Geology 10, 171-182.

Elliot, D., 1976. The motion of thrust sheets. Journal of Geophysical Reviews 81, 949-963.

Elston, W.E., Smith, E.I., 1970. Determination of flow direction of rhyolite ash-flow tuffs from fluidal textures. Geological Society of America Bulletin 81, 3393-3406.

Ewart, A., 1971. Chemical changes accompanying spherulitic crystallization in rhyolitic lavas, central volcanic region, New Zealand. Mineralogical Magazine 38, 424-434.

Ez, V., 2000. When shearing is a cause of folding. Earth Science Reviews 51 (1-4), 155-172.

Farrell, S.G., 1984. A dislocation model applied to slump structures, Ainsa Basin, South Central Pyrenees. Journal of Structural Geology 6, 727–736.

Fenn, P., 1977. The nucleation and growth of alkali feldspars from hydrous melts. Canadian Mineralogist 15, 135–161.

Finetti, I., Morelli, C., 1973. Geophysical exploration of the Mediterranean Sea. Bollettino di Geofisica Teorica e Applicata 15, 263-344.

Fink, J.H., 1978. Surface structures on obsidian flows. PhD thesis, Stanford University, USA.

Fink, J.H., 1980a. Gravity instability in the Holocene Big and Little Glass Mountain rhyolitic obsidian flows, northern California. Tectonophysics 66, 144-166.

Fink, J. H., 1980b. Surface folding and viscosity of rhyolite flows. Geology 8, 250-254.

Fink, J.H., 1983. Structure and emplacement of a rhyolitic obsidian flow: Little Glass Mountain, Medicine Lake Highland, northern California. Geological Society of America Bulletin 94, 362-380.

Fink, J.H., 1984. Structural geologic constraints on the rheology of rhyolitic obsidian. Journal of Non-Crystalline Solids 67, 135-146.

Fink, J.H., Bridges, N.T., 1995. Effects of eruption history and cooling rate on lava dome growth. Bulletin of Volcanology 57, 4, 229-239.

Fink, J.H., Fletcher, R.C., 1978. Ropy pahoehoe: Surface folding of a viscous fluid. Journal of Volcanology and Geothermal Research 4, 151-170.

Fink, J.H., Griffiths, R.W., 1998. Morphology, eruption rates, and rheology of lava domes: Insights from laboratory models. Journal of Geophysical Research 103: doi: 10.1029/97JB02838.

Fink J. H., Manley C. R., 1987. Origin of pumiceous and glassy textures in rhyolite flows and domes. Special Paper Geological Society of America 212, 77-88.

Flinn, D., 1962. On folding during three-dimensional progressive deformation. Quarterly Journal of Geological Society of London 118, 385–433.

Forbes, J.D., 1900. Travels through the Alps. London, Adam and Charles Black (new edition revised and annotated by W.A.B. Coolidge).

Forbes, C.J., Betts, P.G., Lister, G.S., 2004. Synchronous development of type 2 and type 3 fold interference patterns: evidence for recumbent sheath folds in the Allendale Area, Broken Hill, NSW, Australia. Journal of Structural Geology 26, 1,113-126.

Forni, F., Lucchi, F., Peccerillo, A., Tranne, C.A., Rossi, P.L., Frezzotti, M.L., 2013. Stratigraphy and geological evolution of the Lipari volcanic complex (central Aeolian archipelago). In: Lucchi, F., Peccerillo, A., Keller, J., Tranne, C.A., Rossi, P.L. (eds). The Aeolian Islands Volcanoes. Geological Society, London, Memoirs 37, 395-469.

Francalanci, L., Manetti, P., Peccerillo, A., 1989. Volcanological and magmatological evolution of Stromboli volcano (Aeolian Islands): the roles of fractional crystallization magma mixing, crustal contamination and source heterogeneity. Bulletin of Volcanology 51, 355–378.

Frazzetta, G., Gillot, P.Y., La Volpe, L., Sheridan, M.F., 1984a. Volcanic Hazards at Fossa of Vulcano: Data from the last 6,000 years. Bulletin of Volcanology 47-1, 106-124.

Frazzetta, G., La Volpe, L., Sheridan, M.F., 1984b. Evolution of the Fossa cone, Vulcano. Journal of Volcanology and Geothermal Research 17, 329–360.

Freebody, N.A., Vaughan, A.S., Macdonald, A.M., 2010. On optical depth profiling using confocal Raman spectroscopy. *Analytical and Bioanalytical Chemistry* 396, (8), 2813-2823.

Frezzotti, M.L., Peccerillo, A., 2004. Fluid inclusion and petrological studies elucidate reconstruction of magma conduits. Transactions American Geophysical Union, 85, 157, doi: 10.1029/2004EO160001.

Frezzotti, M.L., Peccerillo, A., Zanon, V., Nikogosian, I., 2004. Silica-rich Melts in Quartz Xenoliths from Vulcano Island and their Bearing on Processes of Crustal Anatexis

and Crust–Magma Interaction beneath the Aeolian Arc, Southern Italy. Journal of Petrology 45, 3–26, doi:10.1093/petrology/egg080.

Freundt, A., Schmincke, H.U., 1995. Petrogenesis of rhyolite–trachyte–basalt composite ignimbrite P1, Gran Canaria, Canary Islands. Journal of Geophysical Research 100, 455–474.

Friedman, I., Long, W., 1984. Volcanic glasses, their origins and alteration processes. Journal of Non-Crystalline Solids 67,127-133.

Friedman, I., Long, W., Smith, R.L., 1963. Viscosity and water content of rhyolite glasses. Journal of Geophysical Research 68, 6523-6535.

Fritz, J., Greshake, A., Stöffler, D., 2005. Micro-Raman spectroscopy of plagioclase and maskelynite in Martian meteorites: Evidence of progressive shock metamorphism. Antarctica Meteorite Research 18, 96-116.

Frost, B.R., Lindsley, D.H., 1992. Equilibria among Fe-Ti oxides, pyroxenes, olivine, and quartz: Part II Application. American Mineralogist 77, 1004- 1020.

Frost, B.R., Lindsley, D.H., Andersen, D.J., 1988. Fe–Ti oxide–silicate equilibria: assemblages with fayalitic olivine. American Mineralogist 73, 727–740.

Frost, T.P., Mahood, G.A., 1987. Style of mafic-felsic magma interaction: The Lamarck Granodiorite, Sierra Nevada, California. Geological Society of America Bulletin 99, 272-291.

Fuhrman, M.L., Lindsley, D.H., 1988. Ternary-feldspar modeling and thermometry. American Mineralogist 73, 20l-215.

Furukawa, T., White, W.B., 1980. Raman spectroscopic investigation of the structure of silicate glasses III. Alkali-silicogermanates. Journal of Chemical Physics 95, 776.

Gale, N. H., Beckinsale, R. D., Wadge, A. J., 1979. A Rb-Sr whole-rock isochron for the Stockdale Rhyolite of the English Lake District and a revised Mid-Palaeozoic time-scale. Journal of the Geological Society of London 136, 235–42.

Galeener, F.L., 1979. Band limits and vibrational spectra of tetrahedral glasses. Physical Review B, 19, 42924297.

Gamble, J., 1979. Some relationships between coexisting granitic and basaltic magmas and the genesis of hybrid rocks in the Tertiary central complex of Slieve Gullion, northeast Ireland. Journal of Volcanology and Geothermal Research 5, 297–316.

Gardner, J.E., Befus, K.S., Watkins, J., Hesse, M., Miller, N., 2012. Compositional gradients surrounding spherulites in obsidian and their relationship to spherulite growth and lava cooling. Bulletin of Volcanology 74, 8, 1865-1879.

Gasparini, C., Iannaccone, G., Scandone, P., Scarpa, R., 1982. Seismotectonics of the Calabrian arc. Tectonophysics 84, 267-286.

Gasparini, C., Iannaccone, G., Scarpa, R., 1985. Fault-plane solutions and seismicity of the Italian peninsula. Tectonophysics 110, 59-78.

Ghiorso, M.S., 1984. Activity/composition relations in the ternary feldspars. Contributions to Mineralogy and Petrology 87, 182-296.

Ghiorso, M.S., Sack, R.O., 1991. Fe-Ti oxide geothermometry: thermodynamic formulation and the estimation of intensive variables in silicic magmas. Contributions to Mineralogy and Petrology 108, 485-510.

Ghiorso, M.S., Sack, R.O., 1995. Chemical Mass Transfer in Magmatic Processes. IV. A Revised and Internally Consistent Thermodynamic Model for the Interpolation and Extrapolation of Liquid-Solid Equilibria in Magmatic Systems at Elevated Temperatures and Pressures. Contributions to Mineralogy and Petrology 119, 197-212.

Ghisetti, F., 1979. Relations between structure and transcurrent and distensive phases in the Messina-Fiumefreddo, Tindari-Letojanni and Alia-Malvagna systems (north-eastern Sicily); a microtectonic study. Geologica Romana 18, 23–58.

Gill, W. D., 1979. Syndepositional sliding and slumping in the West Clare Namurian Basin, Ireland. Geological Survey of Ireland Special Paper 4.

Gillot, P.Y., 1987. Histoire volcanique des iles Eoliennes: arc insulaire ou complexe orogeenique annulaire? Documents et Travaux de l'Institut Geologique Albert de l'Apparent 11, 35-42.

Gillot, P.Y., Villari, L., 1981. K-Ar dating of the Aeolian Islands volcanism (Southern Tyrrhenian Sea, Italy). 7° ECOG, Jerusalem, Terra Cognita 2, 1, 56.

Gioncada, A., Clocchiatti, R., Sbrana, A., Bottazzi, P., Massare, D., Ottolini, L., 1998. A study of melt inclusions at Vulcano (Aeolian Islands, Italy): insights on the primitive magmas and on the volcanic feeding system. Bulletin of Volcanology 60, 286-306.

Gioncada, A., Mazzuoli, R., Bisson, M., Pareschi, M.T., 2003. Petrology of volcanic products younger than 42 ka on the Lipari-Vulcano complex (Aeolian Islands, Italy): An example of volcanism controlled by tectonics. Journal of Volcanology and Geothermal Research 122, 91-220.

Gioncada, A., Mazzuoli, R., Milton, A., 2005. Magma mixing at Lipari (Aeolian Islands, Italy): insights from textural and compositional features of phenocrysts. Journal of Volcanology and Geothermal Research 145 1–2, 97–118.

Goguel, J., 1948. Introduction a` l'e´tude me´canique des de´formations de l'e´corce terrestre 1948. 530pp.

Giordano, D., Russell, J. K., Dingwell, D. B., 2008. Viscosity of magmatic liquids: a model. Earth and Planetary Science Letters 271, 123–134.

Gonnermann, H.M., Manga, M., 2003. Flow banding in obsidian: A record of evolving textural heterogeneity during magma deformation. Earth and Planetary Science Letters 236, 135-147.

Gonnermann, H. M., Manga, M., 2005. Nonequilibrium magma degassing: results from modeling of the ca. 1340A.D. eruption of Mono Craters, California. Earth and Planetary Science Letters 238, 1-16.

Gottsmann, J., Dingwell, D.B., 2001a. Cooling dynamics of phonolitic rheomorphic fall-out deposits on Tenerife, Canary Islands. Journal of Volcanology and Geothermal Research 105, 323-342.

Gottsmann, J., Dingwell, D.B., 2001b. The cooling of frontal flow ramps: a calorimetric study on the Rocche Rosse rhyolite flow, Lipari, Aeolian Island, Italy. Terra Nova 13, 157-164.

Gottsmann, J., Giordano, D., Dingwell, D.B., 2002. Predicting shear viscosity during volcanic processes at the glass transition: A calorimetric calibration. Earth and Planetary Science Letters 198, 417-427.

Graham, R. S., Olmsted, P.D., 2010. Coarse-grained simulations of flow-induced nucleation in semicrystalline polymers. Physical Review Letters 103, 115702.

Green, J.F.N., 1915. The structure of the eastern part of the Lake District. Proceedings of the Geologists' Association 26, 195–223.

Green, N.L., Usdansky, S.I., 1986. Ternary-feldspar mixing relations and thermobarometry. American Mineralogist 71, 1100-1108.

Gregg, T.K.P., 1995. Quantification of lava flow morphologies through analog experiments. PhD thesis, Arizona State University Tempe, 1995.

Gregg, T.K.P., Fink, J.H., 2000. A laboratory investigation into the effects of slope on lava flow morphology. Journal of Volcanology and Geothermal Research 96, 145-159.

Gregg, T.K.P., Fink, J.H., Griffiths, R.W., 1998. The formation of multiple fold generations on lava flow surfaces: influence of strain rate, cooling rate, and lava composition. Journal of Volcanology and Geothermal Research 80, 281-292.

Griffiths, R.W., 2000. The dynamics of lava flows. Annual Review of Fluid Mechanics 32, 477-518.

Griffiths, R.W., Fink, J.H., 1992. The morphology of lava flows in planetary environments: Predictions from analog experiments. Journal of Geophysical Research 97, B13, 19739-19748.

Gualda, G.A.R., Ghiorso, M.S., Lemons, R.V., Carley, TL., 2012. Rhyolite-MELTS: A modified calibration of MELTS optimized for silica-rich, fluid-bearing magmatic systems. Journal of Petrology DOI: 10.1093/petrology/egr080.

Guest, J.E., Sanchez, J., 1969. A large dacitic lava flow in Northern Chile. Bulletin of Volcanology 33, 778-790.

Guilbaud, M-N., Self, S., Thordarson, T., Blake, S., 2005. Morphology, surface structures and emplacement of lavas produced by Laki, AD 1783–1874. In: Manga, M., Ventura, G. (eds), Kinematics and dynamics of lava flows. Geological Society of America Special Paper, 396, 81–102.

Gurevich, V.L., Parshin, D.A., Schober, H.R., 2002. On the theory of Boson Peaks in glasses. Journal of Experimental and Theoretical Physics Letters 76, 9, 553-557.

Gvirtzman, Z., Nur, A., 2001. Residual topography, lithospheric thickness, and sunken slabs in the central Mediterranean. Earth and Planetary Science Letters 187, 117-130.

Hall, S.H., 1978. The stratigraphy of Northern Lipari and the structure of the Rocche Rosse rhyolite lava flow and its implications [B.S thesis]: Leeds, University of Leeds, pp 89.

Hambrey, M.J., 1991. Structure and dynamics of the Lambert Glacier-Amery Ice Shelf system: implications for the origin of Prydz Bay sediments. In Barron, J., Larsen, B., and Shipboard Scientific Party, Proceedings of the Ocean Drilling Program, Scientific Results 119, 61-75.

Hammer, J.E., Cashman, K.V., Hoblitt, R.P., Newman, S., 1999. Degassing and microlite crystallization during pre-climactic events of the 1991 eruption of Mt. Pinatubo, Philippines. Bulletin of Volcanology 60, 355-380.

Hammer, J.E., Rutherford, M.J., 2002. An experimental study of the kinetics of decompression-induced crystallization in silicic melt. Journal of Geophysical Research 107, B1, 2101, 0.1029/2001JB000281.

Harris, A.J.L., 2013. Thermal Remote Sensing of Active Volcanoes: A User's Manual. Cambridge University Press 728 pp.

Harris, A.J.L., Steffke, A., Calvari, S., Spampinato, L., 2011. Thirty years of satellite-derived lava discharge rates at Etna: implications for steady volumetric output. Journal of Geophysical Research: Solid Earth 116, B08204, doi: 10.1029/2011JB008237.

Henry, C.D., Price, J.G., Rubin, J.N., Laubach, S.E., 1990. Case study of an extensive silicic lava: the Bracks Rhyolite, Trans-Pecos Texas. Journal of Volcanology and Geothermal Research 43, 113-132.

Hess, K.U., Dingwell, D.B., 1996. Viscosities of hydrous leucogranitic melts: A non-Arrhenian model. American Mineralogist 81, 1297–1300.

Hess, K.U., Dingwell, D.B., Webb, S.L., 1995. The influence of excess alkalis on the viscosity of a haplogranitic melt. American Mineralogist 80, 297–304.

Higgins, M.D., 1998. Origin of anorthosite by textural coarsening: Quantitative measurements of a natural sequence of textural development. Journal of Petrology 39, 1307–1325.

Higgins, M.D., 2000. Measurement of Crystal size distributions. American Mineralogist 85, 1105-1116.

Higgins, M.D., 2002. Closure in crystal size distributions (CSD), verification of CSD calculations, and the significance of CSD fans. American Mineralogist. 87, 171-175.

Higgins, M.D., 2006. Quantitative textural measurements in igneous and metamorphic petrology. 1st edition. Cambridge University Press, Cambridge, 270.

Holzhey, G., 2001. Contribution to petrochemical-mineralogical characterization of alteration processes within the marginal facies of rhyolitic volcanics of Lower Permian age, Thuringian Forest, Germany. Chemie der Erde 61, 149–186.

Honda, K., Nagai, M., 2002. Real-time volcano activity mapping using ground-based digital imagery. ISPRS Journal of Photogrammetry and Remote Sensing 57, 159-168.

Honnorez, J., Keller, J., 1968. Xenolithe in Vulkanischen Gesteinen der Aolischen Inseln (Sizilien). Geologische Rundschau 57, 719-736.

Horbach, J., Kob, W., Binder, K., 2001 High frequency sound and the boson peak in amorphous silica. European Physics Journal B 19, 531–543.

Horwell, C.J., Hillman, S.E., Cole, P.D., Loughlin, S.C., Llewellin, E.W., Damby, D.E., Christopher, T., 2014. Controls on variations in cristobalite abundance in ash generated by the Soufrière Hills volcano, Montserrat in the period 1997–2010. Memoir of the Geological Society of London 39, 399-406.

Horwell, C.J., Le Blond, J.S., Michnowicz, S.A.K., Cressey, G., 2010. Cristobalite in a rhyolitic lava dome: evolution of ash hazard. Bulletin of Volcanology 72, 249–253.

Horwell, C.J., Williamson, B.J., Llwellin, E.W., Damby, D.E., Le Blond, J.S., 2013. The nature and formation of cristobalite at the Soufrière Hills volcano, Montserrat: implications for the petrology and stability of silicic lava domes. Bulletin of Volcanology 75, 696. DOI 10.1007/s00445-013-0696-3.

Hosier, I.L., Bassett, D.C., 1995. On the morphology of polyethylene crystallized from a sheared melt. Polymer 36, 22, 4197-4202.

Housmans, J.W., Steenbakkers, R.J.A., Roozemond, P.C., Peters, G.W.M., Meijer, H.E.H., 2009. Saturation of Pointlike Nuclei and the Transition to Oriented Structures in Flow Induced Crystallization of Isotactic Polypropylene. Macromolecules 42, 5728-5740.

Hudleston, P. J., 1980. The progressive development of inhomogeneous shear and crystallographic fabric in glacial ice. Journal of Structural Geology 2: 189-196.

Huddleston, P.J., 1983. Strain patterns in an ice cap and implications for strain variations in shear zones. Journal of Structural Geology 5, 455-463.

Huddleston, P.J., 1989. The association of folds and veins in shear zones. Journal of Structural Geology 11, 949-957.

Hulme, G., 1974. The interpretation of lava flow morphology. Royal Astronomical Society. Geophysical Supplement 39, 361-383.

Humphreys, M.C.S., Christopher, T., Hards, V., 2009. Microlite transfer by disaggregation of mafic inclusions following magma mixing at Soufrière Hills volcano, Montserrat. Contributions to Mineralogy and Petrology 157, 609-624.

Hutton, D.H.W., 1988. Granite emplacement mechanisms and tectonics controls: inferences from deformation studies. Transactions of the Royal Society of Edinburgh 79, 249-255.

Iddings, J.P., 1887. The nature and origin of lithophysae and the lamination of acid lavas. American Journal of Science 33, 36–45.

Iezzi G., Ventura G., 2000. Kinematics of lava flows based on folds analysis. Geophysical Research Letters 27 (8), 1227-1231.

Iezzi, G., Ventura, G., 2005. The kinematics of lava flows inferred from structural analysis of enclaves: a review. In: Kinematics and dynamics of lava flows. Manga M., Ventura G. (Eds). Geological Society of America Special Paper 396, 15-28.

Irvine, T.N., Baragar, W.R.A., 1971. A guide to the chemical classification of the common volcanic rocks. Canadian Journal of Earth Sciences 8, 523-548.

IUPAC, 1997. Compendium of Chemical Terminology, 2nd ed. (the "Gold Book"). Compiled by A. D. McNaught and A. Wilkinson. Blackwell Scientific Publications, Oxford. XML on-line corrected version: http://goldbook.iupac.org (2006-) created by M. Nic, J. Jirat, B. Kosata; updates compiled by A. Jenkins. ISBN 0-9678550-9-8. doi:10.1351/goldbook.

Janeschitz-Kriegl, H., Ratajski, E., Stadlbauer, M., 2003. Flow as an effective promoter of nucleation in polymer melts: A quantitative evaluation. Rheologica Acta 42, 355–364.

Jerram, D.A., 2002. Volcanology and facies architecture of flood basalts. Geological Society of America Special Papers 362, 119-132.

Jerram, D.A., Cheadle, M.C., Philpotts, A.R., 2003. Quantifying the building blocks of igneous rocks: are clustered crystal frameworks the foundation? Journal of Petrology 44, 2033–2051.

Judd, J., 1888. On the volcanic phenomena of the eruption, and on the nature and distribution of the ejected materials, Part I. In: Symons GJ (ed) The eruption of Krakatoa committee of the royal society. Harrison & Son, London, pp 1–46.

Kassou, A., Essahlaoui, A., Aissa, M., 2012. Extraction of Structural Lineaments from Satellite Images Landsat 7 ETM+ of Tighza Mining District (Central Morocco). Research Journal of Earth Sciences 4, 2, 44-48.

Keith, H.D., Padden, F.J., 1963. A Phenomenological Theory of Spherulitic Crystallization: Journal of Applied Physics 34, 2409-2421.

Keith, H. D., Padden, F. J. 1964a, Spherulitic Crystallization from melt. I. Fractionation and impurity segregation and their influence on crystalline morphology: Journal of Applied Physics 34, 1270-1285.

Keith, H. D., Padden, F. J., 1964b. Spherulitic crystallization from melt. II. Influence of fractionation and impurity segregation on the kinetics of crystallization: Journal of Applied Physics 35, 1286-1296.

Keller, A., Kolnaar, H.W., 1997. Flow induced orientation and structure formation. In: Meijer HEH (ed) Processing of polymers 18. VCH, New York, 189–268.

Keller, J., 1970. Die historischen Eruptionen von Vulcano und Lipari. Zeitschrift Deutschen Geologischen Gesellschaft 121, 179–185.

Keller J., 1980. The island of Vulcano. Rendiconti Società Italiana di Mineralogia e Petrologia, 36 (1), 369-414.

Keller, J., 1982. Mediterranean island arcs. In: Thorpe, R.S. (ed), Andesites. Wiley, Chichester, 307-325.

Keller, J., 2002. Lipari's fiery past: dating the medieval pumice eruption of Monte Pilato: International Conference 'The fire between air and water', UNESCO-Regione Siciliana, Lipari, September 29th–October 2nd, oral presentation.

Kelloway, S.A., Kononenko, N., Torrence, R., Carter, E.A., 2010. Assessing the viability of portable Raman spectroscopy for determining the geological source of obsidian. Vibrational Spectroscopy 53 (1), 88-96.

Kesler, S.E., Weiblen, P.W., 1968. Distribution of elements in a spherulitic andesite. American Mineralogist 53, 2025-2035.

Keszthelyi, L, Self, S., 1998. Some physical requirements for the emplacement of long basaltic lava flows. Journal of Geophysical Research 103, 27447-27464.

Kilburn, C.R.J., 2000, Lava flows and flow fields. In: Sigurdsson, H. (Editor-in Chief). Encyclopaedia of Volcanoes, Academic Press, San Diego, 291-305.

Kilburn, C.R.J., Guest, J.E., 1993. Aa lavas of Mount Etna, Sicily. In: Active Lavas: Monitoring and Modelling, edited by C.R.J. Kilburn and G. Luongo (University College of London Press), 73-106.

Kilburn, C.R.J., Mcguire, W., 2001. Italian Volcanoes. Classic Geology in Europe Series Volume 1. Harpenden: Terra Publishing. vii 166 pp.

Kingsbury, C.G., 2012. Physical volcanology of Obsidian Dome, California: A complex record of emplacement of a youthful lava dome. MSc thesis, University of Ottawa, Canada.

Kingma, K.J., Hemley, R.J., 1994. Raman spectroscopic study of microcrystalline silica. American Mineralogist. 79, 269-273.

Kirkpatrick, R., 1975. Crystal growth from the melt: a review. American Mineralogist 60 (9–10), 798–814.

Kneller, E.A., 2002. Preliminary Textural Study of the Proterozoic, Red, Rhyolitic Lava from the St. Francois Mountains, Southeastern Missouri: Textural Description, Origin, & Chronology. Bsc thesis, University of Toledo, USA.

Kornfield, J.A., Kumaraswamy, G., Issaian, A.M., 2002. Recent advances in understanding flow effects on polymer crystallization. Industrial & Engineering Chemistry Research 41, 6383-6392.

Kraml, M., Keller, J., Henjes-Kunst, F., 1997. Dating of Upper Quaternary deep-sea sediments from the Ionian Sea (Eastern Mediterranean) with laser $^{40}Ar/^{39}Ar$ analyses on prominent tephra layers. EUG 9 (European Union of Geosciences), Strasbourg (France) 23–27 March 1997, Terra Nova 9, Abstract Supplement 1, 406.

Krauskopf, K. B., 1948. Lava movement at Paricutin Volcano, Mexico. Geological Society of America Bulletin 59, 1267-1284.

Kshirsagar, P.V., Sheth, H.C., Seaman, S.J., Shaikh, B., Mohite, P., Gurav, T., Chandrasekharam, D., 2012. Spherulites and thundereggs from pitchstones of the Deccan Traps: geology, petrochemistry, and emplacement environments. Bulletin of Volcanology 74, 559-577.

Laj, C., Rais, A., Surmont, J., Gillot, P. Y., Guillou, H., Kissel,C., Zanella, E., 1997. Changes of the geomagnetic field vector obtained from lava sequences on the island of Vulcano (Aeolian Islands, Sicily). Physics of the Earth and Planetary Interiors 99, 161–177.

Launeau, P., Archanjo, C.J., Picard, D., Arbaret, L., Robin, P-Y.F., 2010. Two- and three-dimensional shape fabric analysis by the intercept method in grey levels Tectonophysics 492, 230-239.

Launeau, P., Bouchez, J.L., Keith, B., 1990. Shape preferred orientation of object population: automatic analysis of digitized images. Tectonophysics 180, 201–211.

Launeau, P., Robin, P.-Y.F., 1996. Fabric analysis using the intercept method. Tectonophysics 267, 91-119.

Lawson, W.J., Sharp, M.J., Hambrey, M.J., 2000. Deformation histories and structural assemblages of glacier ice in a non-steady flow regime. In: Maltman, A.J., Hambrey, M.J., Hubbard, B. (eds). Deformation of Glacial Material. Geological Society, London, Special Publications 176.

Le Bas, M.J., Lemaitre, R.W., Streckeisen, A., Zanettin, B., 1986. A Chemical Classification of Volcanic-Rocks Based on the Total Alkali Silica Diagram. Journal of Petrology 27, 3, 745-750.

Leadbetter, A.J., Wright, A.C., 1972. Diffraction studies of glass structure: I. Theory and quasi-crystalline model. Journal of Non-Crystalline Solids 7 (1), 23-36.

Legelay-Padovanie, A., Mering, C., Guillande, R., Huaman, D., 1997. Mapping of lava flows through SPOT images - an example of the Sabancaya volcano (Peru), International Journal Remote Sensing 18 (15), 3111-3133.

Leocat, E., Gillot, P.Y., Peccerillo, A., 2010. Eruptive history of western and central Aeolian volcanoes (south Tyrrhenian Sea): insights from K/Ar dating. 44th Annual conference of the Volcanic and Magmatic Studies Group (VMSG), Geological Society of London and Mineralogical Society, 4th-6th January 2010, abstract volume.

Lejeune, A-M., Richet, P.R., 1995. Rheology of crystal-bearing silicate melts: An experimental study at high viscosities. Journal of Geophysical Research: Solid Earth 100, B3, 4215-4229.

Lindsley, D.H., Frost, B.R., 1992. Equilibria among Fe-Ti oxides, pyroxenes, olivine, and quartz: Part l. Theory. American Mineralogist 77, 987-1003.

Lindsley, D.H., Nekvasil, H., 1989. A ternary feldspar model for all reasons. EOS Transactions, American Geophysical Union 70, 15, 506.

Llewellin, E. W., Manga, M., 2005. Bubble suspension rheology and implications for conduit flow. Journal of Volcanology and Geothermal Research 143, 205–217.

Lofgren, G.E., 1971a. Experimentally produced devitrification textures in natural rhyolite glass. Geological Society of America Bulletin 82, 111-124.

Lofgren, G.E., 1971b. Spherulitic textures in glassy and crystalline rocks: Journal of Geophysical Research 76, 23, 5635-5648.

Lofgren, G.E., 1974. An experimental study of plagioclase crystal morphology: isothermal crystallization. American Journal of Science 274, 243-273.

Lofgren, G.E., 1976. Nucleation and growth of feldspar in dynamic crystallization (abstract): Geological Society of America Abstract with Programs 7, 982.

Lofgren, G.E., 1980. Experimental studies on the dynamic crystallisation of silicate melts. In: R.B. Hargraves (ed.): Physics of Magmatic Processes. Princeton University Press, Princeton, New Jersey: pp. 487-552.

Lorieri, L., 2009. Le eruzioni Upper Pietre Cotte ed Intermedia de La Fossa di Vulcano (Isole Eolie) (The Upper Pietre Cotte and the Intermediate eruptions of the La Fossa di Vulcano – Aeolian Islands). MSc Thesis, Univesity of Pisa, Unpublished.

Lu, Z., Rykhus, R., Masterlark, T., Dean, K.G., 2004. Mapping recent lava flows at Westdahl Volcano, Alaska, using radar and optical satellite imagery. Remote Sensing of Environment 91, 345-353.

Lucchi, F., Tranne, C.A., Forni, F., Rossi, P. L., 2013. Geological map of the island of Lipari, scale 1:10 000 (Aeolian archipelago). In: Lucchi, F., Peccerillo, A., Keller, J., Tranne, C.A., Rossi, P. L. (eds), The Aeolian Islands Volcanoes. Geological Society, London, Memoirs 37.

Lucchi, F., Tranne, C.A., Rossi, P.L., 2010. Stratigraphic approach to geological mapping of the late Quaternary volcanic island of Lipari (Aeolian Archipelago, southern Italy). The Geological Society of America 464, 1-33.

MacArthur, A.N., Cas, R.A.F., Orton, G.J., 1998. Distribution and significance of crystalline, perlitic and vesicular textures in the Ordovician Garth Tuff (Wales). Bulletin of Volcanology 60, 260–285.

Macaudière, J., Brown, L.W., and Ohnenstetter, D. (1985) Microcrystalline textures resulting from rapid crystallization in a pseudotachylite melt in a meta-anorthosite. Contributions to Mineralogy and Petrology 89, 39–51.

Macdonald, G.A., 1972. Volcanoes. Prentice-Hall Inc., Englewood-Cliffs, New Jersey. 510 pp.

Mackley, M.R., Keller, A., 1975. Flow-induced crystallization of polyethylene melts. Journal of Material Sciences 10, 1501-1509.

Magill, J. H., 2001. Spherulites: a personal perspective. Journal of Material Sciences 36, 3143–3164.

Maltman, A.J., Hubbard, A.J., Hambrey, M.J., (eds)., 2000. Deformation of Glacial Materials, Geological Society, London, Special Publications 176, 59-83.

Mandal, N., Mitra, A.K., Sakar, S., Chakraborty, C., 2009. Numerical estimations of the initial hinge-line irregularity required for the development of sheath folds: a pure shear model. Journal of Structural Geology 31 (10), 1161-1173.

Manga, M., 1998. Orientation distribution of microlites in obsidian. Journal of Volcanology and Geothermal Research 86, 107-115.

Manga, M., Castro, J., Cashman, K., Loewenberg, M., 1998. Rheology of bubble-bearing magmas. Journal of Volcanology and Geothermal Research 87, 15-28.

Manley, C.H., 1992. Extended cooling and viscous flow of large, hot rhyolite lavas: implications of numerical modeling results. Journal of Volcanology and Geothermal Research 53, 27–46.

Manley, C.H., 1996. In situ formation of welded tuff-like textures in the carapace of a voluminous silicic lava flow, Owyhee County, SW Idaho. Bulletin of Volcanology 57, 672-686.

Manley, C.H., Fink, J. H., 1987. Internal textures of rhyolite flows as revealed by research drilling. Geology (Boulder) 15, 6, 549-552.

Marr, J. E., 1916. The geology of the Lake District and the scenery as influenced by Geological structure. Cambridge University Press, Cambridge, pp. 220.

Marsh, B.D., 1988. Crystal size distributions (CSD) in rocks and the kinetics and dynamics of crystallization I: Theory. Contributions to Mineralogy and Petrology 99, 277–291.

Marsh, B.D., 1998. On the interpretations of Crystal Size Distributions in Magmatic Systems. Journal of Petrology 39, 4, 553-599.

Marshall, R., 1961. Devitrification of natural glass. Bulletin of the Geological Society of America 72, 1493-1520.

Martel, C., Radadi Ali, A., Poussineau, S., Gourgaud, A., Pichavant, M., 2006. Basalt-inherited microlites in silicic magmas: Evidence from Mount Pelée (Martinique, French West Indies). Geology 34,905-908.

Martinsen, O.J., 1994. Mass movements. In Maltman, A. (ed.), The Geological Deformation of Sediments. Chapman & Hall, London, 127–165.

Martinsen, O. J., Bakken, B., 1990. Extensional and compressional zones in slumps and slides in the Namurian of County Clare, Ireland. Journal Geological Society of London 147, 153–164.

Matson, D.W., Sharma, S.K., Philpotts, J.A., 1986. Raman spectra of some tectosilicates and of glasses along the orthoclase-anorthite and nepheline-anorthite joins. American Mineralogist 71, 694-704.

Marruzzo, A., Schirmacher, W., Fratalocchi, A., Ruocco, G., 2013. Heterogeneous shear elasticity of glasses: the origin of the boson peak. Nature Scientific Reports 3, 1407, doi:10.1038/srep01407.

McHugh, A.J., in: Lyngaae-Jorgenson, J., Sandergaard, K. (Eds.), 1995. Flow induced crystallization in polymers. Rheo-physics of Multiphase Polymeric Systems, Technomic Publishing Co., Lancaster, PA, 227-267.

McMillan, P.F., 1989. Raman Spectrometry in Mineralogy and Geochemistry. Annual Review of Earth Planetary Sciences. 17, 255-283.

McPhie, J., Doyle, M., Allen. R., 1993. Volcanic textures – A guide to the interpretation of textures in volcanic rocks. Centre for Ore Deposit and Exploration Studies. University of Tasmania, 196 pp.

Mercalli, G., Silvestri, O., 1891. Le eruzioni dell'isola di Vulcano, incominciate il 3 Agosto 1888 e terminate il 22 Marzo 1890. Relazione Scientifica. Annali dell'Ufficio Centrale di Meteorologia e Geodinamica 10, 4, 1-213.

Mercier, M., Di Muro, A., Giordano, D., Métrich, N., Lesne, P., Pichavante, M., Sciallet, B., Clocchiatti, R., Montagnac, G., 2009. Influence of glass polymerisation and oxidation on micro-Raman water analysis in alumino-silicate glasses. Geochimica et Cosmochimica Acta. 73, 197–217.

Merle, O., 1998. Internal strain within lava flows from analogue modelling. Journal of Volcanology and Geothermal Research 81, 189-206.

Millward, D., 1976. The Borrowdale Volcanics of the English Lake District: a study of the petrology, volcanicity and geochemistry of selected areas with particular reference

to ignimbrites. Unpublished PhD thesis, University of Birmingham, United Kingdom.

Millward, D., Lawrence, D.J.D., 1985. The Stockdale (Yarlside) Rhyolite – a rheomorphic ignimbrite? Proceedings of the Yorkshire Geological Society 45, 299-306.

Mitchell, G.H., 1934. The Borrowdale Volcanic Series of the country between Longsleddale and Shap. Quarterly Journal of the Geological Society of London 90, 418–444.

Mitchell, G.H., 1956. The geological history of the Lake District. Proceedings of the Yorkshire Geological Society 30, 407–463.

Mock, A., Jerram, D. A., 2005. Crystal size distributions (CSD) in three dimensions: insights from the 3D reconstruction of a highly porphyritic rhyolite. Journal of Petrology 46 (8),1525-1541.

Mollard, E., Martel, C., Bourdier, J.-L., 2012. Decompression-induced crystallization in hydrated silica-rich melts: empirical models of experimental plagioclase nucleation and growth kinetics. Journal of Petrology 53, 1743–1766.

Möller, P., Muecke, G.K., 1984. Significance of Europium anomalies in silicate melts and crystal-melt equilibria: a re-evaluation. Contributions to Mineralogy and Petrology 87, 242-250.

Monasse, B., 1995. Nucleation and anisotropic crystalline growth of polyethylene under shear. Journal of Material Sciences 30, 5002-5012.

Moore, I., Kokelaar, P., Tectonically controlled piecemeal caldera collapse: A case study of Glencoe volcano, Scotland. Geological Society of America Bulletin 110, 11, 1448-1466.

Morgan, D.J. Jerram, D.A., 2006. On estimating crystal shape for crystal size distribution analysis. Journal of Volcanology and Geothermal Research. 154, 1-7.

Morimoto, N., Fabries, J., Ferguson, A.K., Ginzburg, I.V., Ross, M., Seifert, F.A., Zussman, J., Aoki, K., Gottardi, D., 1988. Nomenclature of pyroxenes. American Mineralogist 73, 9-10, 1123-1133.

Morse, H.W., Warren, C.H., Donnay, J.D.H., 1932. Artificial spherulites and related aggregates. American Journal of Science 23, 421-439.

Moseley, F., Millward, D., 1982. Ordovician volcanicity in the English Lake District. In: Sutherland, D.S., (ed), Igneous rocks of the British Isles. Wiley, Chichester, United Kingdom, pp 93-111.

Murase, T., McBirney, A.R., 1973. Properties of some common igneous rocks and their melts at high temperatures. Geological Society of America Bulletin 84, 3563–3592.

Mysen, B.O., Finger, L W., Seifert, F.A., Virgo, D., 1982. Curve- fitting of Raman spectra of amorphous materials. American Mineralogist 67, 686-696.

Nekvasil, H., Burnham, C.W., 1987. The calculated individual effects of pressure and water content on phase equilibria in the granite system. In B.O. Mysen, (ed.), Magmatic processes: Physicochemical principles. Geochemical Society Special Publication 1, 433-445.

Nichols, R.L., 1936. Flow-units in basalt. Journal of Geology 44, 617-630.

Nimis, P., 1995. A clinopyroxene geobarometer for basaltic systems based on crystal structure modeling. Contributions to Mineralogy and Petrology 121, 115–125.

Nimis, P., Taylor, W.R., 2000. Single clinopyroxene thermobarometry for garnet peridotites. Part I. Calibration and testing of a Cr-in-Cpx barometer and an enstatite-in-Cpx thermometer. Contributions to Mineralogy and Petrology 139, 541–544.

Nye, J.F., 1952. A method for calculating the thickness of ice-sheets. Nature 169, 4300, 529-530.

Pamukcu, A.S., Carley, T.L., Gualda, G.A.R., Miller, C.F., Ferguson, C.A., 2013. The evolution of the Peach Spring Tuff giant magma body: evidence from accessory mineral textures and compositions, bulk pumice and glass geochemistry, and rhyolite MELTS modeling. Journal of Petrology 54, 6, 1109-1148.

Park, R.G., 1989. Foundations of Structural Geology, 2nd ed. xii + 148 pp. Glasgow, London: Blackie; New York: Chapman & Hall.

Park, S., Iversen, J.D., 1984. Dynamics of lava flow: Thickness growth characteristics of steady two-dimensional flow. Geophysical Research Letters 11, 641-644.

Passey, S., Bell, B., 2007. Morphologies and emplacement mechanisms of the lava flows of the Faroe Islands Basalt Group, Faroe Islands, NE Atlantic Ocean. Bulletin of Volcanology 70, 2, 139-156.

Paterson, S.R., Fowler, T.K., Schmidt, K.L., Yoshinobu, A.S., Yuan, E.S., Miller, R.B., 1998. Interpreting magmatic fabric patterns in plutons. Lithos 44, 53-82.

Paterson, S.R., Tobisch, O.T., 1993. Pre-lithification structures, deformation mechanisms, and fabric ellipsoids in slumped turbidites from the Pigeon Point Formation, California. Tectonophysics 222, 135–149.

Peccerillo, A., 2005. Plio-Quaternary volcanism in Italy. Petrology, Geochemistry, Geodynamics. Springer, Heidelberg, 365 pp.

Peccerillo, A., Frezzotti, M.L., De Astis, G., Ventura, G., 2006. Modeling the magma plumbing system of Vulcano (Aeolian Islands, Italy) by integrated fluid-inclusion geobarometry, petrology, and geophysics. Geology 34, 1, 17–20.

Peccerillo, A., Taylor, S.R., 1976. Geochemistry of Eocene calcalkaline volcanic rocks of the Kastamonu area northern Turkey. Contribution to Mineralogy and Petrology 58, 63–81.

Pennings, A.J., Kiel, A.M., 1965. Fractionation of Polymers by Crystallization from Solution, III. On the Morphology of Fibrillar Polyethylene Crystals Grown in Solution. Kolloid-Zeitschrift & Zeitschrift Für Polymere 205, 2, 160-162.

Perugini, D., Valentini, L., Poli, G., 2007. Insights into magma chamber processes from the analysis of size distribution of enclaves in lava flows: A case study from Vulcano Island (Southern Italy). Journal of Volcanology and Geothermal Research 166, 193-203.

Phillips, W.A. (editor), 1981. Amorphous Solids: Low-Temperature Properties (Berlin: Springer).

Pichler, H., 1976. Carta geologica dell'Isola di Lipari (scala 1:10,000). Firenze, Litografia Artistica Cartografica.

Pichler, H., 1980. The Island of Lipari. Rendiconti della Società Italiana di Mineralogia e Petrologia 36, 1, 415-440.

Pichler, H., 1990. Italienische Vulkan-Gebiete III: Lipari, Vulcano, Stromboli, Tyrrhenisches Meer. Sammlung Geologischer Führer 69, 272 pp.

Pickering, G., Bull, J.M., Sanderson, D.J., 1995. Sampling Power-law distributions. Tectonophysics 248, 1-20.

Piochi, M., De Astis, G., Petrelli, M., Ventura, G., Sulpizio, R., Zanetti A., 2009. Constraining the recent plumbing system of Vulcano (Aeolian Arc, Italy) by textural, petrological, and fractal analysis: The 1739 A.D. Pietre Cotte lava flow. Geochemistry, Geophysics, Geosystems. 10, No Q01009.

Pinkerton, H., Norton, G., 1995. Rheological properties of basaltic lavas at sub-liquidus temperatures: laboratory and field measurements on lavas from Mount Ethna. Journal of Volcanology and Geothermal Research 68, 307−323.

Pinkerton, H., Sparks, R.S.J., 1978. Field measurements of the rheology of lava. Nature Letters 276, 382-385.

Pirsson, L.V., 1910. On an artificial lava-flow and its spherulitic crystallization. American Journal of Science (4), 30, 97-114.

Pogodina, N., 2001. Rheology and Structure of Isotactic Polypropylene near the Gel Point: Quiescent and Shear-induced Crystallization. Polymer 42, 21, 9031-043.

Polacci, M., Papale, P., 1997. The evolution of lava flows from ephemeral vents at Mount Etna: insights from vesicle distribution and morphological studies. Journal of Volcanology and Geothermal Research 76, 1–17.

Preece, K., Barclay, J., Gertisser, R., Herd, R.A., 2013. Textural and micro-petrological variations in the eruptive products of the 2006 dome-forming eruption of Merapi volcano, Indonesia: Implications for sub-surface processes. Journal of Volcanology and Geothermal Research 261, 98-120.

Putirka, K.D., 2000. Igneous thermometers and barometers based on plagioclase + liquid equilibria: tests of some existing models and new calibrations. American Mineralogist 90, 336–346.

Putirka, K.D., 2008. Thermometers and barometers for volcanic systems. Reviews in Mineralogy and Geochemistry 69, 61–120.

Putirka, K.D., Mikaelian, H., Ryerson, F., Shaw, H., 2003. New clinopyroxene-liquid thermobarometers for mafic, evolved, and volatile-bearing lava compositions, with applications to lavas from Tibet and the Sanke River Plain, Idaho. American Mineralogist 88,1542–1554.

Ramberg, H., 1977. Some Remarks on the Mechanism of Nappe Movement. Geol. Foremingen, Stockholm Forhandlingar pp. 110–117.

Ramsay, D.M., 1979. Analysis of rotation of folds during progressive deformation. Geological Society of America Bulletin 98 (8), 732-738.

Ramsay, J.G., 1967. Folding and fracturing of rocks, McGraw Hill, New York, 568 p.

Ramsay, J.G., 1980. The crack-seal mechanism of rock deformation. Nature 284, 135-139.

Ramsay, J.G., 1989. Emplacement kinematics of a granite diapir – The Chindamora batholith, Zimbabwe. Journal of Structural Geology 11, 191-210.

Randolph, A.D., Larson, M.A., 1971. Theory of particulate processes: Analysis and techniques of continuous crystallization. Academic Press, New York, USA.

Raymond, C.F., Echelmayer, K.A., Whillians, M., Doake, C.S.M., 2001. Ice stream shear margins. The West Antarctic Ice Sheet: Behavior and Environment, Antarctic Research Series 77, 137-155.

Reber, J.E., Dabrowski, M., Galland, O., Schmid, D.W., 2013. Sheath fold morphology in simple shear. Journal of Structural Geology 53, 15-26.

Ren, M., Omenda, P.A., Anthony, E.Y., White, J.C., Macdonald, R.., Bailey, D.K., 2006. Application of the QUILF thermobarometer to the peralkaline trachytes and pantellerites of the Eburru volcanic complex, East African Rift, Kenya. Lithos 91, 109–124.

Reynard, B., Okuno, M., Shimada, Y., Syono, Y., Willaime, C., 1999. A Raman spectroscopic study of shock-wave densification of anorthite ($CaAl_2Si_2O_8$) glass. Physics and Chemistry of Minerals 26, 432-436.

Reynolds, M.A., Best, J.G., Johnson, R.W., 1980. 1953–1957 eruption of Tuluman volcano: rhyolitic volcanic activity in the northern Bismarck Sea. Geological Survey of Papua New Guinea Memoir 7.

Richnow, J., 1999. Eruptional and post-eruptional processes in rhyolite domes. Published PhD thesis, University of Canterbury, New Zealand.

Ringwood, A.E., 1991. Phase transformations and their bearing on the constitution and dynamics of the mantle. Geochim Cosmochim Acta 55, 2083–2110.

Röller, K., Trepmann, C., 2008. Stereo32 Version 1.01. <http://www.ruhr-uni-bochum.de/hardrock/downloads.htm>.

Ross, C.S., 1962. Microlites in glassy volcanic rocks. American Mineralogist 47, 723-740.

Rossano, S., Mysen, B., 2012. Raman spectroscopy of silicate glasses and melts in geological systems. Raman Spectroscopy Applied to Earth Sciences and Cultural Heritage, J. Dubessy, M.-C. Caumon, and F. Rull, eds., pp. 321-366, EMU Notes in Mineralogy, Vol. 12, European Mineralogical Union and Mineralogical Society of Great Britain & Ireland, Twickenham, United Kingdom.

Roverato, M., 2008. Ricostruzione tephro-cronologica dei depositi recenti del cono della Fossa di Vulcano e della penisola di Vulcanello (isole Eolie). MSc Thesis, University of Pisa, unpublished.

Rudnick, R.L., 1992. Restites, Eu anomalies and the lower continental crust. Geochimica et Cosmochimica Acta 56, 963-970.

Ruland, W., 1964. The separation of coherent and incoherent Compton x-ray scattering. British Journal of Applied Physics 15, 1301–07.

Rust, A.C., Manga, M., Cashman K.V., 2003. Determining flow type, shear rate and shear stress in magmas from bubble shapes and orientations. Journal of Volcanology and Geothermal Research 122, 111-132.

Rutley, F., 1885. On strain in connexion with crystallisation and the development of perlitic structure. Journal of the Geological Society of London 40, 340–347.

Ryabov, V.V., Grib, D.E., 2005. Multiphase dykes: Signature of diverse spreading in the Northern Siberian Craton. Russian Geology and Geophysics 46, 5, 471-485.

Ryan, M, Sammis, C., 1981. The glass transition in basalt. Journal of Geophysical Research 86, 9515–9535.

Ryschenkow, G., Faivre, G., 1988. Bulk crystallization of liquid selenium Primary nucleation, growth kinetics and modes of crystallization. Journal of Crystal Growth 87 (2-3), 221, DOI: 10.1016/0022-0248(88)90169-8. .

Sakka, S., Mackenzie, J.D., 1971. Relation between apparent glass transition temperature and liquidus temperature for inorganic glasses. Journal of Non-Crystalline Solids 6, 145-62.

Sakuma, S., 1951. Elastic and viscous properties of volcanic rocks at elevated temperatures, Part II. Bulletin of the Earthquake Research Institute 31, 63-70.

Sampson, D. E., 1987, Textural heterogeneities and vent area structures in the 600-year-old lavas of the Inyo volcanic chain, eastern California. In Fink, J. H., ed., The emplacement of silicic domes and lava flows, Geological Society of America Special 212, 89–100.

Scandone, P., 1982. Structure and evolution of Calabrian arc. Earth-Evolution Sciences 3, 172-180.

Schmincke, H.U., Swanson, D.A., 1967. Laminar viscous flowage structures in ash-flow tuffs from Gran Canaria, Canary Islands. The Journal of Geology, 75, 6, 641-664.

Schneider, C.A., Rasband, W.S., Eliceiri, K.W., 2012. NIH Image to ImageJ: 25 years of image analysis. Nature Methods 9, 671-675, 2012.

Schütte, K.G., 1978. Crustal structure of southern Italy. In: Closs, H., Roeder, D., Schmidt, K. (eds), Alps, Apennines, Hellenides. Schweizerbart, Stuttgart, 315-321.

Seaman, S.J., 2000. Crystal clusters, feldspar glomerocrysts, and magma envelopes in the Atascosa Lookout lava flow, southern Arizona, USA: recorders of magmatic events. Journal of Petrology 41, 693-716.

Seaman, S.J., Dyar, M., Marinkovic, N., 2009. The effects of heterogeneity in magma water concentration on the development of flow banding and spherulites in rhyolitic lava. Journal of Volcanology and Geothermal Research 183, 157–169.

Self, S., Thordarson, T., Keszthelyi, L., 1997. Emplacement of continental flood basalt lava flows. American Geophysical Union Monograph 100, 381-410.

Self, S., Thordarson, T., Keszthelyi, L., Walker, G.P.L., Hon, K., Murphy, M.T., Long, P.E., Finnemore, S., 1996. A new model for the emplacement of Columbia River basalt as large inflated pahoehoe lava sheets. Geophysical Research Letters 23, 2689-2692.

Schneider, C.A., Rasband, W.S., Eliceiri, K.W., 2012. NIH Image to ImageJ: 25 years of image analysis. Nature Methods 671, doi: doi:10.1038/nmeth.2089.

Schroeder, J., Wu, W., Apkarian, J.L., Lee, M., Hwa, L.G., Moynihan, C.T., 2004. Raman scattering and Boson peaks in glasses: temperature and pressure effects. Journal of Non-Crystalline Solids 349, 88-97.

Shaw, H.R., 1963. Obsidian viscosities at 1000 and 2000 bars in the temperature range 700°-900°C. Journal of Geophysical Research 68, 6337-6343.

Shaw, H.R., 1972. Viscosities of magmatic silicate liquids: An empirical method of prediction. American Journal of Science 272, 870-893.

Sharma, S.K., Simons, B., Yoder, H.S., Jr., 1983. Raman study of anorthite, calcium Tschermak's pyroxene and gehlenite in crystalline and glassy states. American Mineralogist 68, 1113-1125.

Shelley, D., 1985. Determining paleo-flow directions from groundmass fabrics in the Lyttelton radial dikes, New Zealand. Journal of Volcanology and Geothermal Research 25, 69-79.

Sheridan, M.F., Frazzetta, G., La Volpe, L., 1987. Eruptive histories of Lipari and Vulcano, Italy, during the past 22,000 years. In Fink, J. H., ed., The emplacement of silicic domes and lava flows, Geological Society of America Special 212, 29–34.

Shimoda, K., Okuno, M., Syono, Y., Kikuchi, M., Fukuoka, K., Koyano, M., Katayama, S., 2004. Structural evolutions of an obsidian and its fused glass by shock-wave compression. Physics and Chemistry of Minerals 31, 532-542.

Shtukenberg, A.G., Punin, Y.O., Gunn, E., Kahr, B., 2012. Spherulites. Chemical Reviews 112, 1805-1838.

Sisson, T.W., Bacon, C.R., 1999. Gas-driven filter-pressing in magmas: Geology 27, 613–616.

Smith, J.V., 2000. Flow pattern within a Permian submarine slump recorded by oblique folds and deformed fossils, Ulladulla, south-eastern Australia. Sedimentology 47, 357-366.

Smith, J.V., Yamauchi, S., Miyake, Y., 1994. Coaxial progressive deformation textures in extrusive and shallow intrusive rocks, southwest Japan. Journal of Structural Geology 16, 315-322.

Smith, R., Tremallo, R., Lofgren, G., 2001. Growth of megaspherulites in a rhyolitic vitrophyre. American Mineralogist 86, 589–600.

Smythe, D.K., 1971. Viscous theory of angular folding by flexural flow. Tectonophysics 12, 415-430.

Solìgo, M., De Astis, G., Delitala, M.C., La Volpe, L., Taddeucci, A., Tuccimei, P., 2000. Uranium-series disequilibria in the products from Vulcano Island (Sicily, Italy): Isotopic Chronology and magmatological implications. Acta Vulcanologica 12, 1-2.

Sparks, R.S.J., Sigurdsson, H., Wilson, L., 1977. Magma mixing: a mechanism for triggering acid explosive eruptions. Nature 267, 315-318.

Spera, F.J., Borgia, A., Strimple, J., Feigenson, M., 1988. Rheology of melts and magmatic suspensions. 1. Design and calibration of concentric cylinder viscometer with application to rhyolitic magma. Journal of Geophysical Research B93, 10273-10294.

Stadlbauer, M., Janeschitz-Kriegl, H., Eder, G., Ratajski, E., 2004. New extensional rheometer for creep flow at high tensile stress. Part II. Flow induced nucleation for the crystallization of iPP. Journal of Rheology 48, 631-639.

Stein, D.J., Spera, F.J., 1992. Rheology and microstructure of magmatic emulsions – Theory and experiments. Journal of Volcanology and Geothermal Research 49, 157-174.

Stevenson, R.J., Briggs, R.M., Hodder, P.W., 1993. Emplacement history of a low-viscosity, fountain-fed pantelleritic lava flow. Journal of Volcanology and Geothermal Research 57, 39-56.

Stevenson, R.J., Briggs, R.M., Hodder, A.P.W., 1994a. Physical volcanology and emplacement history of the Ben Lomond rhyolite lava flow, Taupo Volcanic Centre, New Zealand. New Zealand Journal of Geology and Geophysics 37, 345-358.

Stevenson, R.J., Hodder, A.P.W., Briggs, R.M., 1994b. Rheological estimates of rhyolite lava flows from the Okataina Volcanic Centre, New Zealand. New Zealand Journal of Geology and Geophysics 37, 211-221.

Sumner, J. M., Formation of clastogenic lava flows during fissure eruption and scoria cone collapse: the 1986 eruption of Izu-Oshima Volcano, eastern Japan. Bulletin of Volcanology 60, 195-212.

Sumner, J.M., Branney, M.J., 2002. The emplacement history of a remarkable heterogeneous, chemically zoned, rheomorphic and locally lava-like ignimbrite:

'TL' on Gran Canaria. Journal of Volcanology and Geothermal Research 115, 109-138.

Swainson, I.P., Dove, M.T., 1995. Molecular dynamics simulation of alpha- and beta-cristobalite. Journal of Physics: Condensed Matter 7, 1771-1788, 1995.

Swanson, S., 1977. Relation of nucleation and crystal-growth rate to the development of granitic textures. American Mineralogist 62, 966–978.

Swanson, S., Naney, M., Westrich, H., Eichelberger, J., 1989. Crystallization history of Obsidian Dome, Inyo Domes, California. Bulletin of Volcanology 51, 161–176.

Swartjes, F.H.M., Peters, G.W.M., Rastogi, S., Mejer, H.E.H., 2003. Stress induced crystallization in elongational flow. International Polymer Processing 18, 53-66.

Szramek, L., Gardner, J.E., Larsen, J., 2006. Degassing and microlite crystallization of basaltic andesite magma erupting at Arenal volcano, Costa Rica. Journal of Volcanology and Geothermal Research 157, 182–201.

Tanguy, J.C., Le Goff, M., Principe, C., Arrighi, S., Chillemi, V., Paiotti, A., La Delfa, S., Patanè, G., 2003. Archaeomagnetic dating of Mediterranean volcanics of the last 2100 years: validity and limits. Earth and Planetary Science Letters 211, 111–124.

Taylor, S.R., McLennan, S.M., 1985. The continental crust: its composition and evolution. Blackwell Scientific Publishing, Oxford 312 pp.

Tikoff, B., Green, D., 1997. Stretching lineations in transpressional shear zones: an example from the Sierra Nevada Batholith, California. Journal of Structural Geology 19, 1, 29-39.

Tobisch, O.T., 1984. Development of foliation and fold interference patterns produced by sedimentary processes. Geology 12, 441-444.

Tranne, C.A., Lucchi, F., Calanchi, N., Lanzafame, G., Rossi, P.L., 2002. Geological map of the Island of Lipari. (Aeolian Islands), Scale 1:10.000. University of Bologna and INGV, LAC, Firenze.

Tribout, C., Monasse, B., Haud, J.M., 1996. Experimental Study of Shear-Induced Crystallization of an Impact Polypropylene Copolymer. Colloid and Polymer Science 274, 3, 197-208.

Tuffen, H., Castro, J.M., 2008. Brittle-ductile rheology, foam collapse and latent heat: the story of obsidian lava emplacement at Krafla volcano, Iceland. Abstract from IAVCEI 2008 General Assembly, Reykjavik, Iceland.

Tuffen, H., Castro, J.M., 2009. The emplacement of an obsidian dyke through thin ice: Hrafntinnuhryggur, Krafla, Iceland. Journal of Volcanology and Geothermal Research 185, 352-366.

Tuffen, H., Dingwell, D.B., Pinkerton, H., 2003. Repeated fracture and healing of silicic magma generate flow banding and earthquakes? Geology 31, 12, 1089-1092.

Tuffen, H., James, M., Castro, J.M., Schipper, I., 2012. Observations of obsidian lava flow emplacement at Puyehue-Cordón Caulle, Chile. Poster session presented at EGU General Assembly 2012, Vienna, Austria.

Tuffen H., James. M., Castro, J.M., Schipper, I., 2013. Exceptional mobility of an advancing rhyolitic obsidian flow at Cordón Caulle volcano in Chile. Nature Communications 4. ISSN 2041-1723.

Tyndall, J., 1859. On the veined structure of glaciers, with observations on white seams, air bubbles and dirt bands. Philosophical Transactions of the Royal Society of London 149, 279-307.

Tyrrell, G.W., 1926. The principles of petrology. Methuen, London, 349p.

van Dijk, J.P., Scheepers, P.J.J., 1995. Neogene rotations in the Calabrian Arc. Implications for a Pliocene-Recent geodynamic scenario for the Central Mediterranean. Earth Science Reviews 39, 207-246.

Ventura, G., 1994. Tectonics, structural evolution and caldera formation on Vulcano Island (Aeolian Archipelago, Southern Tyrrhenian Sea). Journal of Volcanology and Geothermal Research 60, 207–224.

Ventura, G., 2001. The strain path and emplacement mechanism of lava flows: an example from Salina (Southern Tyrrhenian Sea, Italy). Earth and Planetary Science Letters 188, 229-240.

Ventura, G., 2004. The strain path and kinematics of lava domes: an example from Lipari (Aeolian Islands, Southern Tyrrhenian Sea, Italy). Journal of Geophysical Research 109, No.B1, DOI: B01203 10.1029/2003JB002740.

Ventura, G., 2013. Kinematics of the Aeolian volcanism (Southern Tyrrhenian Sea) from geophysical and geological data. In: Lucchi, F., Peccerillo, A., Keller, J., Tranne, C.A., Rossi, P. L. (eds), The Aeolian Islands Volcanoes. Geological Society, London, Memoirs 37, 3–11.

Ventura, G., De Rossa, R., Colletta, E., Mazzuoli, R., 1996. Deformation patterns in a high-viscosity lava flow inferred from the crystal preferred orientation and imbrication structures: an example from Salina. Bulletin of Volcanology 57, 555-562.

Ventura, G., Vilardo, G., Milano, G., Pino, N.A., 1999. Relationships among crustal structure, volcanism and strike-slip tectonics in the Lipari-Vulcano volcanic complex (Aeolian Islands, Southern Tyrrhenian Sea, Italy). Physics of the Earth and Planetary Interiors 116, 31–52.

Verweij, H., 1979. The Structure of Lithium, Sodium and Potassium Germanate Glasses, Studied by Raman Scattering. Journal of Non-Crystalline Solids 34 (1), 81-99.

Vicari, A., Ciraudo, A., Del Negro, C., Herault, A., Fortuna, L., 2009. Lava flow simulations using discharge rates from thermal infrared satellite imagery during the 2006 Etna eruption. Natural Hazards 50, 539-550.

Voltaggio, M., Branca, M., Tuccimei, P., Tecce, F., 1995. Leaching procedure used in dating young potassic volcanic rocks by the $^{226}Ra/^{230}Th$ method. Earth and Planetary Science Letters 136, 123–131.

von Aulock, F.W., Nichols, A.R.L., Kennedy, B.M., Oze, C., 2013. Timescales of the texture development in a cooling lava dome. Geochimica et Cosmochimica Acta 114, 72-80.

Von Richthofen, F. 1860. Studien aus den ungarisch-siebenbürgischen Trachytgebirgen. Jahrbuch der Geologischen Reichsanstalt 11, 180–182.

Walcott, C.D., 1896. The Cambrian rocks of Pennsylvania. USGS Bulletin: 134.

Walker, G.P.L., 1983. Ignimbrite types and ignimbrite problems: Journal of Volcanology and Geothermal Research 17, 65-88.

Walker, G.P.L., 1991. Structure and origin by injection of lava under surface crust, of tumuli, “lava rises”, “lava-rise pits”, and “lava-inflation clefts” in Hawaii. Bulletin of Volcanology 53, 546-558.

Wang, C. Y., Hwang, W.T., Shi, Y., 1989. Thermal evolution of a rift basin: The Tyrrhenian Sea. Journal of Geophysical Research 94, 3991–4006.

Warren, B.E., 1934. The diffraction of x-rays in glass. Physical Review Letters 45, 657.

Watkins, J., Manga, M., Huber, C., Martin, M., 2008. Diffusion-controlled spherulite growth in obsidian inferred from H_2O concentration profiles. Contributions to Mineralogy and Petrology 157, 2, 163-172.

Welhan, J.A., Johannesen, C.M., Reeves, K.S., Clemo, T.M., Glover, J.A., Bosworth, K.W., 2002. Morphology of inflated pahoehoe lavas and spatial architecture of their porous and permeable zones, eastern Snake River Plain, Idaho. In: Link, P.K., Mink, L.L. (Eds.), Geology, Hydrogeology, and Environmental Remediation, Idaho National Engineering and Environmental Laboratory, Eastern Snake River Plain, Idaho. Geological Society of America Special Paper 353, 135–150.

Wen, S., Nekvasil, H., 1994. SOLVCALC: an interactive graphics program for calculating the ternary feldspar solvus and for two-feldspar geothermometry. Computers and Geosciences 20, 1025–1040.

Wenk, H.R., 1978. Are pseudotachylites products of fracture or fusion? Geology 6, 507-511.

Wenk, H.R., Weiss, L.E., 1982. Al-rich calcic pyroxene in pseudotachylite: an indicator of high pressure and high temperature? Tectonophysics 84, 329–341.

Westrich, H., Stockman, H., Eichelberger, J., 1988. Degassing of rhyolitic magma during ascent and emplacement. Journal of Geophysical Research 93, 6503-6511.

White W.B., Minser D. G., 1984. Raman spectra and structure of natural glasses. Journal of Non-Crystalline Solids 67, 45–59.

Wilding, M.C., Webb, S.L., Dingwell, D.B., 1995. Evaluation of a relaxation geospeedometer for volcanic glasses. Chemical Geology 125, 137–148.

Williams, H., McBirney, A.R., 1979. Volcanology. Freeman, Cooper and Co, San Francisco Publishing, Berkeley, CA, 397 pp.

Wilson, L., Head, J. W., 2008. Eruption rates of mare lava flows on the Moon and implications for mantle melt volumes and dike geometries. Geophysical Research Letters 35, L23205 , doi:10.1029/2008GL0356.

Wnorowska, U., 2004. SiO_2–rich lava complexes: Textures in SiO_2-rich lava complexes. Oberseminar Geologie WS 2003/04, Technische Universität Bergakademie Freiberg, Institut für Geologie, Freiberg, Germany.

Wolff, J.A., Wright, J.V., 1981. Rheomorphism of welded tuffs. Journal of Volcanology and Geothermal Research 10, 13–34.

Wright, A.C., 1994. Neutron scattering from vitreous silica. V. The structure of vitreous silica: what have we learned from 60 years of diffraction studies? Journal of Non-Crystallien Solids 179, 84-115.

Wright, A.C., Leadbetter, A.J., 1975. The structures of the β-cristobalite phases SiO_2 and $AlPO_4$. Philosophical Magazine 31, 1391-1401.

Wright, H.M.N., Folks, C.B., Cas, R.A.F., Cashman, K.V., 2011. Heterogeneous pumice populations in the 2.08-Ma Cerro Galán Ignimbrite: implications for magma recharge and ascent preceding a large-volume silicic eruption. Bulletin of Volcanology 73, 1513-1533.

Wright, I.C., Gamble, J.A., Shane, P.A.R., 2003. Submarine silicic volcanism of the Healy caldera, southern Kermadec arc (SW Pacific): I - volcanology and eruption mechanisms. Bulletin of Volcanology 65, 15-29.

Zanchetta, G., Sulpizio, R., Roberts, N., Coini, R., Eastwood, W.J., Siani, G., Caron, B., Paterne, M., Santacroce, R., 2011. Tephrostratigraphy , chronology and climatic events of the Mediterranean basin during the Holocene: An overview. The Holocene 21, 33-52.

Zanon, V., Frezzotti, M., Peccerillo, A., 2003. Magmatic feeding system and crustal magma accumulation beneath Vulcano Island (Italy): Evidence from CO_2 fluid inclusions in quartz xenoliths. Journal of Geophysical Research 108: doi: 10.1029/2002JB002140.

Zingg T., 1935. Beitrag zur Schotteranalyse, Schweizerische. Mineralogische und Petrographische Mitteilungen 15, 39-140.

Appendices

Appendix I – Electron microprobe – Rhyolitic glass compositional data

Pietre Cotte

	P. Cotte	P. Cotte	P. Cotte	P. Cotte	P. Cotte	P. Cotte	P. Cotte	P. Cotte	P. Cotte	P. Cotte	P. Cotte	P. Cotte	P. Cotte	P. Cotte	P. Cotte	P. Cotte	P. Cotte
Major elements (wt%)																	
SiO_2	77.11	76.94	76.95	75.60	75.59	76.03	77.03	77.05	76.53	76.60	76.96	76.10	75.95	74.74	75.59	74.70	74.16
TiO_2	0.13	0.05	0.07	0.13	0.11	0.10	0.09	0.07	0.10	0.10	0.11	0.12	0.13	0.12	0.10	0.08	0.12
Al_2O_3	13.51	13.19	13.35	13.63	13.28	13.53	13.65	13.73	13.94	13.52	13.47	13.64	13.29	13.06	12.99	13.26	13.14
FeO*	1.63	1.55	1.59	1.90	1.76	1.76	1.54	1.78	1.62	1.74	1.66	1.47	1.65	1.78	1.59	1.80	1.73
MnO	0.07	0.06	0.07	0.06	0.06	0.07	0.03	0.06	0.05	0.06	0.07	0.06	0.07	0.07	0.07	0.09	0.07
MgO	0.04	0.03	0.03	0.06	0.05	0.06	0.04	0.05	0.05	0.05	0.05	0.04	0.04	0.06	0.02	0.06	0.06
CaO	0.65	0.61	0.61	0.63	0.63	0.68	0.72	0.67	0.59	0.60	0.66	0.79	0.56	0.59	0.56	0.68	0.59
Na_2O	2.74	2.86	3.08	3.24	2.79	3.20	3.62	3.21	3.28	3.26	3.08	4.10	4.38	4.61	4.21	3.60	4.83
K_2O	3.96	4.00	3.73	3.94	3.68	3.76	3.83	3.93	3.95	3.82	3.83	3.58	4.28	4.68	3.98	4.26	3.77
P_2O_5	0.02	0.01	0.00	0.03	0.02	0.00	0.01	0.03	0.01	0.01	0.01	0.02	0.01	0.03	0.00	0.01	0.04
Total	100.39	99.79	99.96	99.75	98.51	99.63	100.95	101.10	100.63	100.25	100.42	100.20	100.81	100.23	99.78	99.06	99.00
FeO = all iron as FeO*																	
Volatile concentrations (ppm)																	
F	1490	1390	1080	1440	1450	1040	220	1490	1560	1510	1690	530	1380	710	2850	1700	1660
Cl	3970	3630	3820	3770	3910	3450	3280.	3880	3450	3380	3520	2310	3190.	4130	3870	3470	3250

Rocche Rosse

	R. Rosse	R. Rosse	R. Rosse	R. Rosse	R. Rosse	R. Rosse	R. Rosse	R. Rosse	R. Rosse	R. Rosse	R. Rosse	R. Rosse	R. Rosse	R. Rosse	R. Rosse	R. Rosse
Major elements (wt%)																
SiO_2	75.36	77.97	72.16	73.77	74.85	73.68	74.82	74.74	74.77	74.75	74.67	74.51	74.85	74.75	74.72	74.77
TiO_2	0.03	0.12	0.02	0.05	0.10	0.12	0.06	0.11	0.07	0.12	0.03	0.09	0.07	0.07	0.06	0.06
Al_2O_3	13.05	12.12	14.46	13.31	13.37	13.35	13.35	13.37	13.48	13.46	13.31	13.16	13.30	13.33	13.31	13.49
FeO*	1.53	0.63	0.68	1.60	1.60	1.50	1.30	1.50	1.50	1.57	1.57	1.55	1.55	1.53	1.65	1.62
MnO	0.07	0.00	0.02	0.07	0.07	0.05	0.06	0.06	0.06	0.07	0.05	0.08	0.07	0.07	0.07	0.06
MgO	0.04	0.00	0.01	0.04	0.04	0.04	0.03	0.02	0.02	0.04	0.03	0.03	0.03	0.03	0.04	0.04
CaO	0.75	0.77	1.47	0.64	0.62	0.64	0.62	0.63	0.63	0.63	0.63	0.65	0.65	0.60	0.63	0.63
Na_2O	5.26	5.20	5.00	3.60	3.68	3.73	3.67	3.76	3.82	3.85	3.80	3.97	3.95	3.98	3.69	3.87
K_2O	3.50	2.88	4.70	4.78	4.70	4.79	4.74	4.59	4.63	4.53	4.54	4.48	4.51	4.52	4.48	4.54
P_2O_5	0.03	0.01	0.00	0.01	0.01	0.00	0.02	0.02	0.03	0.01	0.00	0.00	0.02	0.03	0	0.03
Total	100.07	99.70	98.51	98.37	99.58	98.45	98.99	99.23	99.51	99.47	99.14	98.97	99.39	99.28	99.15	99.61
Volatile concentrations (ppm)																
F	1150	1290	4930	1670	2100	1900	470	1120	1520	1370	1470	1190	970	450	1580	1720
Cl	3440	2510	4960	3190	3270	3450	2700	2990	3360	3180	3420	3330	3030	3030	3420	3030

Forgia Vecchia

	F. Vecch	F. Vecch	F. Vecch	F. Vecch	F. Vecch	F. Vecch	F. Vecch	F. Vecch	F. Vecch	F. Vecch	F. Vecch	F. Vecch	F. Vecch	F. Vecch	F. Vecch	F. Vecch
Major elements (wt%)																
SiO_2	76.01	76.19	76.29	76.19	76.11	76.21	76.18	75.71	76.06	75.96	74.57	74.72	74.24	74.44	74.42	74.40
TiO_2	0.10	0.09	0.04	0.08	0.08	0.11	0.08	0.07	0.06	0.10	0.02	0.04	0.01	0.10	0.09	0.05
Al_2O_3	13.28	13.27	13.27	13.24	13.31	13.26	13.29	13.19	13.25	13.26	13.31	13.43	13.33	13.49	13.40	13.32
FeO*	1.41	1.53	1.34	1.51	1.54	1.52	1.29	1.45	1.51	1.60	1.39	1.45	1.68	1.48	1.50	1.55
MnO	0.05	0.08	0.06	0.08	0.07	0.06	0.06	0.06	0.07	0.06	0.05	0.07	0.06	0.06	0.06	0.05
MgO	0.03	0.04	0.03	0.03	0.03	0.03	0.03	0.03	0.03	0.03	0.04	0.03	0.03	0.04	0.02	0.03
CaO	0.72	0.73	0.69	0.73	0.72	0.74	0.67	0.72	0.73	0.73	0.61	0.63	0.62	0.65	0.65	0.63
Na_2O	3.51	3.74	3.78	3.54	3.68	3.61	3.50	3.45	3.45	3.47	3.58	3.56	3.63	3.59	3.59	3.61
K_2O	6.09	5.70	5.82	6.01	5.86	5.85	6.22	6.20	6.21	6.10	4.84	4.87	4.82	4.81	4.79	4.85
P_2O_5	0.01	0.01	0.01	0.03	0.03	0.02	0.02	0.00	0.00	0.00	0.00	0.00	0.01	0.02	0.02	0.00
Total	101.76	101.80	101.72	101.88	101.91	101.89	101.77	101.34	101.81	101.86	98.93	99.24	98.83	99.11	98.96	99.04
Volatile concentrations (ppm)																
F	1880	930	930	1030	1340	1180	1130	1300	720	1830	1780	1200	770	1140	990	2350
Cl	3450	3360	3120	3520	3440	3370	3070	3300	3640	3680	3270	3190	3260	3070	3050	2990

	Forgia Vecchia	Forgia Vecchia	Forgia Vecchia	Forgia Vecchia	Forgia Vecchia	Forgia Vecchia
Major elements (wt%)						
SiO_2	74.41	74.78	74.69	74.79	74.98	74.73
TiO_2	0.03	0.06	0.03	0.07	0.05	0.06
Al_2O_3	13.25	13.12	13.40	13.30	13.64	13.14
FeO*	1.44	1.62	1.51	1.61	1.31	1.57
MnO	0.07	0.06	0.06	0.06	0.05	0.05
MgO	0.03	0.04	0.05	0.04	0.02	0.03
CaO	0.61	0.64	0.63	0.61	0.55	0.60
Na_2O	3.69	3.58	3.54	3.58	3.60	3.55
K_2O	4.82	4.80	4.78	4.79	4.84	4.82
P_2O_5	0.00	0.00	0.00	0.00	0.00	0.00
Total	98.83	99.15	99.13	99.21	99.46	98.94
Volatile concentrations (ppm)						
F	1720	1260	1210	650	1320	650
Cl	3060	3310	3100	3060	2910	3320

Grotta dei Palizzi

	Grotta dei Palizzi	Grotta dei Palizzi	Grotta dei Palizzi	Grotta dei Palizzi	Grotta dei Palizzi	Grotta dei Palizzi	Grotta dei Palizzi	Grotta dei Palizzi	Grotta dei Palizzi	Grotta dei Palizzi
Major elements (wt%)										
SiO_2	74.20	73.84	73.87	73.96	74.14	73.96	74.07	74.56	73.68	73.52
TiO_2	0.12	0.14	0.13	0.11	0.10	0.15	0.13	0.13	0.14	0.09
Al_2O_3	13.68	13.63	13.91	13.68	13.83	13.96	13.68	13.44	13.73	13.64
FeO*	1.68	1.76	1.63	1.72	1.79	1.81	1.85	1.61	1.70	1.86
MnO	0.06	0.06	0.06	0.07	0.06	0.06	0.06	0.05	0.05	0.06
MgO	0.07	0.09	0.08	0.06	0.09	0.07	0.10	0.05	0.06	0.09
CaO	0.58	0.65	0.56	0.56	0.63	0.65	0.62	0.53	0.66	0.69
Na_2O	4.11	3.97	3.99	3.84	3.95	3.88	3.91	3.87	4.04	3.99
K_2O	6.07	6.07	6.15	6.13	6.11	6.07	6.07	6.16	6.02	5.94
P_2O_5	0.01	0.00	0.01	0.00	0.03	0.04	0.06	0.03	0.02	0.02
Total	101.08	100.66	100.87	100.64	101.15	101.13	101.06	100.88	100.49	100.33
Volatile concentrations (ppm)										
F	1550	1600	1820	1440	1350	1560	1860	1630	1030	1330
Cl	3430	2960	3030	3440	3100	3240	3430	2790	2860	3000

Pomiciazzo

	Pomic.	Pomic.	Pomic.	Pomic.	Pomic.	Pomic.	Pomic.	Pomic.	Pomic.	Pomic.	Pomic.	Pomic.	Pomic.
Major elements (wt%)													
SiO_2	76.46	76.31	76.79	76.54	76.84	76.47	76.39	75.93	77.01	76.22	75.76	76.43	75.10
TiO_2	0.08	0.05	0.05	0.08	0.02	0.05	0.05	0.06	0.08	0.04	0.05	0.09	0.05
Al_2O_3	12.93	13.18	13.16	13.10	13.24	13.21	13.26	13.28	13.31	13.11	13.04	13.11	13.17
FeO*	1.51	1.40	1.20	1.48	1.19	1.33	1.49	1.54	1.43	1.38	1.50	1.50	1.43
MnO	0.05	0.06	0.06	0.05	0.05	0.05	0.06	0.06	0.06	0.06	0.06	0.05	0.06
MgO	0.02	0.03	0.03	0.03	0.03	0.04	0.05	0.02	0.03	0.02	0.02	0.02	0.03
CaO	0.73	0.72	0.70	0.73	0.70	0.71	0.75	0.73	0.74	0.71	0.72	0.75	0.72
Na_2O	3.43	3.38	3.47	3.43	3.57	3.61	3.54	3.62	3.53	3.62	3.80	4.59	4.37
K_2O	6.03	6.01	6.09	6.05	5.94	5.87	5.77	5.98	4.96	5.94	5.70	4.59	5.01
P_2O_5	0.01	0.04	0.04	0.00	0.02	0.00	0.02	0.01	0.00	0.03	0.02	0.02	0.02
Total	101.72	101.70	101.99	101.93	101.95	101.87	101.82	101.71	101.59	101.51	101.18	101.58	100.41
Volatile concentrations (ppm)													
F	1370	2030	1000	1430	560	1740	1110	1350	1220	740	1580	910	1160
Cl	3510	3190	3000	3100	2940	3340	3160	3260	3220	2910	3430	3500	3320

Capo Rosso

	Capo Rosso	Capo Rosso	Capo Rosso	Capo Rosso	Capo Rosso	Capo Rosso	Capo Rosso	Capo Rosso	Capo Rosso	Capo Rosso	Capo Rosso
Major elements (wt%)											
SiO_2	76.01	76.45	76.59	76.65	76.49	76.84	77.03	77.04	76.79	77.15	76.87
TiO_2	0.08	0.02	0.09	0.05	0.03	0.07	0.07	0.01	0.08	0.10	0.10
Al_2O_3	12.93	13.11	13.01	13.04	13.23	13.46	13.18	13.19	13.20	13.42	13.20
FeO*	1.23	1.51	1.43	1.50	1.48	1.10	1.42	1.47	1.56	1.47	1.52
MnO	0.05	0.06	0.06	0.04	0.07	0.04	0.06	0.06	0.06	0.06	0.07
MgO	0.01	0.03	0.03	0.04	0.03	0.04	0.03	0.04	0.03	0.02	0.04
CaO	0.68	0.74	0.70	0.72	0.70	0.64	0.70	0.70	0.72	0.71	0.72
Na_2O	3.67	3.78	4.11	4.22	3.89	5.69	6.10	5.76	5.59	6.07	5.53
K_2O	5.91	5.84	5.27	5.19	5.58	3.03	2.33	2.80	3.13	2.39	3.06
P_2O_5	0.00	0.00	0.00	0.01	0.02	0.02	0.03	0.00	0.00	0.01	0.04
Total	100.96	101.99	101.78	101.92	101.93	101.39	101.29	101.45	101.66	101.81	101.60
Volatile concentrations (ppm)											
F	780	1220	1570	1300	1100	2080	800	800	1630	780	1330
Cl	2820	3280	3290	3230	3080	2560	2720	3000	3390	3350	3110

Castello

	Castello	Castello	Castello	Castello	Castello	Castello	Castello	Castello	Castello	Castello	Castello	Castello	Castello	Castello
Major elements (wt%)														
SiO_2	74.99	74.64	75.43	76.66	75.04	75.22	75.31	75.23	74.02	74.69	73.97	74.48	74.64	74.77
TiO_2	0.07	0.03	0.06	0.04	0.09	0.10	0.08	0.04	0.06	0.06	0.08	0.07	0.04	0.04
Al_2O_3	12.92	12.67	12.93	13.03	13.39	13.28	13.30	13.35	13.15	13.45	13.06	13.30	12.93	13.17
FeO*	1.62	1.32	1.55	1.42	1.33	1.42	1.50	1.53	1.48	1.35	1.36	1.41	1.52	1.44
MnO	0.07	0.05	0.07	0.07	0.05	0.06	0.05	0.06	0.06	0.07	0.06	0.07	0.06	0.06
MgO	0.02	0.03	0.04	0.05	0.04	0.03	0.03	0.04	0.03	0.01	0.03	0.03	0.04	0.03
CaO	0.69	0.66	0.73	0.72	0.60	0.56	0.57	0.60	0.59	0.59	0.63	0.61	0.63	0.61
Na_2O	5.80	5.22	4.41	5.26	3.48	3.46	3.52	3.63	3.62	3.58	3.61	3.60	3.65	3.74
K_2O	3.02	3.11	4.09	3.14	4.69	4.65	4.69	4.60	4.74	4.74	4.65	4.72	4.66	4.70
P_2O_5	0.01	0.03	0.00	0.00	0.01	0.00	0.01	0.02	0.00	0.02	0.04	0.02	0.02	0.00
Total	99.68	98.18	99.76	100.80	99.20	99.17	99.45	99.50	98.16	98.95	97.95	98.70	98.59	99.01
Volatile concentrations (ppm)														
F	1000	990	1230	880	1740	990	940	750	1120	950	1400	970	950	1440
Cl	3620	3070	3350	3250	2960	2920	3000	3300	3040	2910	3120	3070	3050	3040

Punta di Costa

	Punta di Costa	Punta di Costa	Punta di Costa	Punta di Costa	Punta di Costa	Punta di Costa	Punta di Costa	Punta di Costa
Major elements (wt%)								
SiO_2	74.84	73.27	74.61	74.04	74.68	75.61	74.47	74.46
TiO_2	0.06	0.08	0.08	0.07	0.15	0.06	0.04	0.04
Al_2O_3	13.78	13.66	13.77	13.75	13.79	13.79	13.74	13.73
FeO*	1.36	1.41	1.32	1.35	1.38	1.33	1.42	1.22
MnO	0.06	0.06	0.05	0.07	0.06	0.07	0.07	0.07
MgO	0.02	0.02	0.01	0.01	0.02	0.03	0.01	0.03
CaO	0.69	0.71	0.68	0.72	0.68	0.68	0.72	0.70
Na_2O	4.27	4.22	3.79	4.41	3.91	3.94	4.35	4.23
K_2O	5.22	5.15	4.82	5.32	4.78	4.89	5.22	5.09
P_2O_5	0.01	0.02	0.01	0.00	0.00	0.02	0.00	0.02
Total	100.78	98.99	99.66	100.13	99.88	100.84	100.39	99.98
Volatile concentrations (ppm)								
F	1890	1190	2040	780	1480	1650	650	1190
Cl	3220	2680	3140	3160	2820	2600	2830	2910

Monte Giardina

	Monte Giardina	Monte Giardina	Monte Giardina
Major elements (wt%)			
SiO_2	75.91	76.80	76.14
TiO_2	0.08	0.08	0.06
Al_2O_3	12.46	12.43	12.55
FeO*	1.13	1.14	1.31
MnO	0.04	0.05	0.04
MgO	0.02	0.01	0.01
CaO	0.66	0.58	0.66
Na_2O	3.33	3.40	3.53
K_2O	4.50	4.24	4.59
P_2O_5	0.00	0.01	0.03
Total	98.58	99.05	99.24
Volatile concentrations (ppm)			
F	1770	370	370
Cl	2740	2640	2840

Falcone

	Falcone	Falcone	Falcone	Falcone	Falcone	Falcone	Falcone	Falcone	Falcone	Falcone	Falcone	Falcone
Major elements (wt%)												
SiO_2	75.75	76.12	76.79	76.56	76.34	76.20	76.82	76.11	78.67	65.33	65.55	65.30
TiO_2	0.04	0.10	0.06	0.06	0.09	0.03	0.07	0.05	0.09	0.00	0.00	0.00
Al_2O_3	12.61	12.53	12.46	12.57	12.61	12.50	12.39	12.31	12.58	18.73	18.51	18.59
FeO*	1.40	1.36	1.13	1.38	1.46	1.21	1.13	1.20	0.38	0.07	0.08	0.07
MnO	0.05	0.05	0.05	0.05	0.05	0.06	0.05	0.03	0.01	0.00	0.00	0.01
MgO	0.02	0.01	0.02	0.01	0.02	0.03	0.00	0.02	0.00	0.00	0.00	0.00
CaO	0.71	0.69	0.67	0.76	0.74	0.69	0.60	0.67	0.58	0.21	0.23	0.22
Na_2O	2.91	2.63	2.73	4.22	3.51	3.21	3.72	3.55	4.67	3.65	3.53	3.59
K_2O	4.78	4.69	4.70	4.11	4.47	4.60	4.19	4.55	3.45	11.69	11.60	11.56
P_2O_5	0.00	0.01	0.00	0.01	0.01	0.00	0.02	0.03	0.00	0.01	0.02	0.01
Total	98.63	98.68	99.00	100.27	99.79	99.03	99.39	98.91	100.71	99.70	99.51	99.35
Volatile concentrations (ppm)												
F	650	1940	1330	2130	2160	1980	1430	980	1120	1560	980	1150
Cl	2900	2900	2540	3190	2780	3100	2620	2810	2850	3000	2200	2510

	Falcone	Falcone	Falcone	Falcone	Falcone	Falcone	Falcone	Falcone	Falcone	Falcone	Falcone
Major elements (wt%)											
SiO_2	76.11	76.47	76.84	76.98	75.71	76.31	76.11	76.47	76.84	76.98	75.71
TiO_2	0.10	0.07	0.04	0.05	0.02	0.05	0.10	0.07	0.04	0.05	0.02
Al_2O_3	12.45	12.68	12.68	12.56	12.62	13.12	12.45	12.68	12.68	12.56	12.62
FeO*	1.31	1.30	1.40	1.40	1.23	0.45	1.31	1.30	1.40	1.40	1.23
MnO	0.05	0.05	0.05	0.06	0.03	0.02	0.05	0.05	0.05	0.06	0.03
MgO	0.03	0.02	0.01	0.03	0.02	0.00	0.03	0.02	0.01	0.03	0.02
CaO	0.68	0.67	0.70	0.72	0.73	0.65	0.68	0.67	0.70	0.72	0.73
Na_2O	2.79	4.34	4.28	3.92	2.94	3.45	2.79	4.34	4.28	3.92	2.94
K_2O	4.37	3.51	3.28	4.18	4.81	4.74	4.37	3.51	3.28	4.18	4.81
P_2O_5	0.00	0.00	0.01	0.00	0.01	0.01	0.02	0.03	0.00	0.01	0.02
Total	98.36	99.48	99.73	100.37	98.57	99.06	98.36	99.48	99.73	100.37	98.57
Volatile concentrations (ppm)											
F	1630	1010	1480	1880	1970	1990	1630	1010	1480	1880	1970
Cl	3030	2750	2950	2970	2760	2590	3030	2750	2950	2970	2760

Punta di Levante

	Punta di Levante	Punta di Levante	Punta di Levante	Punta di Levante	Punta di Levante
Major elements (wt%)					
SiO_2	66.49	73.12	73.28	72.49	76.93
TiO_2	0.04	0.17	0.00	0.02	0.08
Al_2O_3	17.79	12.40	14.04	16.28	11.68
FeO*	0.17	3.78	0.54	0.26	1.80
MnO	0.01	0.07	0.02	0.00	0.04
MgO	0.00	0.00	0.01	0.00	0.01
CaO	0.43	0.53	0.40	0.52	0.60
Na_2O	5.25	4.08	4.15	4.91	4.39
K_2O	7.89	4.10	5.65	6.51	3.68
P_2O_5	0.03	0.03	0.00	0.02	0.03
Total	98.14	98.56	98.18	101.20	99.47
Volatile concentrations (ppm)					
F	1350	1550	1240	1780	1650
Cl	1130	2860	1630	1160	1730

Appendix II – Mineral compositional data – Spherulites

Feldspar in spherulites data

	P Cotte	P Cotte	P Cotte	R Rosse	R Rosse	R Rosse
SiO_2	65.76	66.66	66.01	66.35	62.01	62.30
TiO_2	0.11	0.07	0.52	0.04	0.00	0.03
Al_2O_3	17.08	19.27	19.43	18.57	23.79	24.21
FeO	4.63	0.60	0.02	0.37	0.25	0.27
MnO	0.00	0.00	0.17	0.01	0.00	0.00
MgO	0.00	0.00	0.90	0.00	0.00	0.00
CaO	0.92	1.65	1.11	0.95	5.21	5.61
Na_2O	7.33	7.18	7.38	7.90	7.93	7.57
K_2O	5.00	5.54	5.21	5.86	1.41	1.41
Total	100.84	100.96	100.74	100.04	100.60	101.40
Si	2.971	2.959	2.929	2.977	2.749	2.740
Al	0.910	1.008	1.016	0.982	1.243	1.255
Ti	0.004	0.002	0.017	0.001	0.000	0.001
Mg	0.000	0.000	0.060	0.000	0.000	0.000
Fe	0.175	0.022	0.001	0.014	0.009	0.010
Mn	0.000	0.000	0.007	0.000	0.000	0.000
Ca	0.045	0.079	0.053	0.046	0.248	0.264
Na	0.642	0.618	0.634	0.688	0.682	0.645
K	0.288	0.313	0.295	0.335	0.080	0.079
Sum	5.035	5.001	5.011	5.042	5.010	4.994
An (mol%)	4.9	8.4	4.8	24.5	26.7	6.9
Ab (mol%)	70.0	66.0	72.1	67.6	65.3	64.8
Or (mol%)	25.2	25.6	23.2	7.9	8.0	28.3

Glass in spherulites data

Pietre Cotte

	Pietre Cotte	Pietre Cotte	Pietre Cotte	Pietre Cotte	Pietre Cotte	Pietre Cotte	Pietre Cotte	Pietre Cotte	Pietre Cotte	Pietre Cotte
Major elements (wt%)										
SiO_2	76.64	75.43	70.27	73.42	76.30	76.27	73.57	75.61	76.99	78.58
TiO_2	0.08	0.09	0.14	0.07	0.06	0.25	0.03	0.17	0.05	0.04
Al_2O_3	13.79	14.44	12.90	14.77	13.89	11.84	16.63	14.20	12.76	12.63
FeO*	0.50	0.36	6.28	0.42	0.50	4.44	0.42	0.89	0.39	0.39
MnO	0.02	0.00	0.50	0.00	0.02	0.15	0.00	0.04	0.00	0.03
MgO	0.00	0.00	0.91	0.02	0.00	0.23	0.02	0.02	0.00	0.00
CaO	1.25	0.52	3.64	0.68	0.61	0.84	1.89	0.89	0.60	0.59
Na_2O	6.03	5.53	5.03	5.87	5.25	4.33	7.14	6.16	5.20	5.16
K_2O	2.06	4.44	2.30	3.79	4.12	3.58	1.51	3.27	3.55	3.16
P_2O_5	b.d	b.d	b.d	b.d	b.d	b.d	b.d	b.d	b.d	b.d
Total	100.37	100.79	101.96	99.02	100.75	101.92	101.20	101.25	99.53	100.57

FeO = all iron as FeO*

Rocche Rosse

	R Rosse	R Rosse	R Rosse	R Rosse	R Rosse	R Rosse	R Rosse	R Rosse	R Rosse	R Rosse	R Rosse	R Rosse
Major elements (wt%)												
SiO_2	74.66	74.49	74.50	73.89	73.20	74.06	74.10	73.89	74.10	73.56	75.87	72.74
TiO_2	0.09	0.07	0.07	0.09	0.08	0.06	0.06	0.04	0.05	0.05	0.05	0.05
Al_2O_3	12.87	13.14	12.93	12.78	13.04	13.02	12.84	12.68	13.03	13.74	12.71	14.54
FeO*	1.41	1.57	1.58	1.57	1.53	1.92	1.59	1.38	1.51	0.42	0.76	0.50
MnO	0.06	0.08	0.07	0.06	0.07	0.06	0.07	0.07	0.07	0.03	0.05	0.03
MgO	0.02	0.04	0.03	0.03	0.05	0.04	0.04	0.04	0.03	0.00	0.00	0.00
CaO	0.75	0.74	0.75	0.76	0.76	0.70	0.75	0.70	0.75	0.64	0.53	0.65
Na_2O	3.42	3.69	3.62	3.67	3.52	3.72	3.64	3.62	4.66	6.33	5.48	6.80
K_2O	5.92	5.98	5.90	5.90	5.91	5.90	5.98	5.97	4.60	3.26	3.49	3.12
P_2O_5	0.00	0.01	0.01	0.00	0.01	0.02	0.01	0.01	0.00	0.01	0.01	0.00
Total	99.74	100.32	100.00	99.31	98.78	100.01	99.66	99.00	99.46	98.63	99.90	98.73

	R Rosse	R Rosse	R Rosse	R Rosse	R Rosse	R Rosse	R Rosse	R Rosse	R Rosse	R Rosse	R Rosse	R Rosse
Major elements (wt%)												
SiO_2	77.66	77.26	76.82	77.21	74.55	76.01	73.95	76.79	76.27	73.13	73.00	76.46
TiO_2	0.09	0.06	0.03	0.06	0.04	0.07	0.05	0.08	0.10	0.07	0.04	0.10
Al_2O_3	11.84	12.15	12.34	12.07	13.65	13.29	13.49	11.72	12.78	14.15	13.66	13.25
FeO*	0.32	0.44	0.47	0.39	0.65	0.43	0.62	0.81	0.42	0.75	0.62	0.41
MnO	0.00	0.03	0.02	0.02	0.02	0.02	0.03	0.08	0.01	0.05	0.04	0.01
MgO	0.00	0.00	0.00	0.00	0.00	0.00	0.00	0.01	0.00	0.00	0.00	0.01
CaO	0.61	0.70	0.74	0.70	0.80	0.87	0.72	0.87	0.79	0.79	0.61	0.68
Na_2O	5.83	5.93	6.15	5.73	6.47	6.45	6.29	5.85	6.08	6.75	6.19	6.33
K_2O	2.15	2.09	2.14	2.14	2.36	1.87	2.73	1.89	2.08	2.87	3.25	2.35
P_2O_5	0.00	0.00	0.00	0.00	0.00	0.00	0.00	0.01	0.00	0.00	0.00	0.00
Total	98.68	99.08	99.32	98.96	98.91	99.21	98.34	98.85	98.86	99.30	98.22	99.87

	R Rosse	R Rosse	R Rosse	R Rosse	R Rosse	R Rosse	R Rosse	R Rosse	R Rosse	R Rosse	R Rosse	R Rosse
Major elements (wt%)												0.09
Al_2O_3	13.31	13.09	15.76	12.60	13.27	12.82	13.10	12.83	12.95	12.81	12.89	12.82
FeO*	1.40	0.61	0.29	0.22	0.26	1.46	1.56	1.57	1.48	1.55	1.45	1.54
MnO	0.06	0.05	0.00	0.00	0.01	0.07	0.06	0.06	0.06	0.08	0.06	0.07
MgO	0.01	0.00	0.01	0.00	0.01	0.02	0.04	0.04	0.05	0.04	0.04	0.03
CaO	0.78	0.60	0.88	0.65	0.72	0.73	0.73	0.76	0.75	0.73	0.73	0.75
Na_2O	6.19	6.02	7.09	5.90	5.71	5.20	5.33	3.67	3.67	3.85	3.80	3.79
K_2O	2.78	3.42	3.38	2.23	2.57	3.97	3.81	5.84	5.87	5.84	5.81	5.80
P_2O_5	0.00	0.01	b.d	b.d	0.01	0.02	b.d	0.01	0.02	0.01	b.d	0.03
Total	98.96	97.67	100.14	100.52	101.04	98.32	98.96	98.55	98.49	98.75	98.90	98.81

	R Rosse	R Rosse	R Rosse	R Rosse	R Rosse	R Rosse	R Rosse	R Rosse	R Rosse	R Rosse	R Rosse	R Rosse
Major elements (wt%)												
SiO_2	73.63	73.30	73.06	73.46	73.64	78.13	69.79	75.86	77.13	76.31	76.67	75.67
TiO_2	0.10	0.08	0.06	0.06	0.13	0.10	0.08	0.09	0.08	0.06	0.04	0.04
Al_2O_3	12.90	12.89	12.76	13.08	13.12	13.05	13.67	13.10	12.89	13.90	13.91	14.40
FeO*	1.45	1.56	1.52	1.54	1.46	0.45	1.23	0.88	0.46	0.50	0.68	0.39
MnO	0.06	0.07	0.07	0.07	0.07	0.05	0.03	0.02	0.00	0.03	0.02	0.01
MgO	0.04	0.04	0.02	0.04	0.05	0.00	0.03	0.01	0.00	0.01	0.00	0.00
CaO	0.72	0.72	0.74	0.74	0.74	0.96	0.77	0.65	0.56	0.77	0.61	0.81
Na_2O	3.80	3.74	3.81	3.84	3.81	5.94	6.19	6.29	5.83	6.61	5.62	6.12
K_2O	5.77	5.75	5.75	5.76	5.78	2.15	2.42	2.29	2.35	1.84	3.80	3.24
P_2O_5	b.d	b.d	b.d	0.03	b.d	b.d	b.d	0.01	b.d	b.d	b.d	b.d
Total	98.87	98.66	98.32	99.10	99.27	100.82	94.20	99.41	99.30	100.03	101.35	100.67

	Rocche Rosse	Rocche Rosse	Rocche Rosse	Rocche Rosse	Rocche Rosse	Rocche Rosse
Major elements (wt%)						
SiO_2	75.48	73.74	76.87	75.79	75.55	71.38
TiO_2	0.04	0.05	0.01	0.07	0.09	0.09
Al_2O_3	14.05	16.06	13.80	14.58	13.57	16.66
FeO*	0.33	0.39	0.46	0.47	2.35	0.48
MnO	0.01	0.01	0.02	0.03	0.10	0.04
MgO	0.00	0.00	0.00	0.00	0.09	0.00
CaO	0.86	0.82	0.65	0.61	0.97	0.71
Na_2O	5.98	6.51	5.11	5.24	5.01	5.88
K_2O	2.85	3.78	4.09	4.96	4.24	5.57
P_2O_5	b.d	b.d	b.d	b.d	b.d	b.d
Total	99.59	101.35	101.02	101.74	101.97	100.80

Forgia Vecchia

	Forgia Vecchia	Forgia Vecchia
Major elements (wt%)		
SiO_2	77.34	78.07
TiO_2	0.06	0.08
Al_2O_3	13.02	13.00
FeO*	0.61	0.57
MnO	0.03	0.02
MgO	0.00	0.00
CaO	0.78	0.74
Na_2O	5.91	6.30
K_2O	1.96	2.08
P_2O_5	b.d	b.d
Total	99.70	100.85

Castello

	Castello	Castello	Castello	Castello	Castello	Castello	Castello	Castello	Castello	Castello	Castello
Major elements (wt%)											
SiO_2	75.38	77.64	75.36	75.84	75.83	75.83	75.17	73.11	73.86	73.82	73.63
TiO_2	0.03	0.10	0.03	0.07	0.05	0.10	0.04	0.07	0.02	0.09	0.05
Al_2O_3	13.10	11.71	13.93	12.85	12.90	12.73	12.55	12.76	12.92	12.93	13.05
FeO*	0.47	0.38	0.36	0.39	0.41	0.41	0.68	0.92	1.23	1.45	1.50
MnO	0.03	0.01	0.01	0.03	0.02	0.04	0.02	0.05	0.05	0.07	0.05
MgO	0.00	0.00	0.00	0.00	0.00	0.00	0.00	0.00	0.02	0.03	0.02
CaO	0.64	0.64	0.60	0.68	0.68	0.66	0.43	0.42	0.59	0.66	0.68
Na_2O	6.44	5.88	6.86	6.29	6.08	6.16	5.08	3.90	4.49	4.62	4.63
K_2O	1.95	1.78	2.35	1.98	2.03	2.06	4.04	5.69	4.86	4.74	4.57
P_2O_5	0.03	0.00	0.03	0.00	0.01	0.03	0.00	0.00	0.00	0.01	0.00
Total	98.46	98.56	99.76	98.52	98.40	98.37	98.34	97.34	98.44	98.89	98.57

Monte Giardina

	Monte Giardina	Monte Giardina
Major elements (wt%)		
SiO_2	78.56	79.87
TiO_2	0.03	0.09
Al_2O_3	13.02	11.66
FeO*	0.46	0.83
MnO	0.04	0.03
MgO	0.00	0.04
CaO	0.92	0.61
Na_2O	6.22	4.47
K_2O	1.70	3.20
P_2O_5	b.d	b.d
Total	100.94	100.80

Falcone (dacite)

	Falcone (dacite)	Falcone (dacite)	Falcone (dacite)	Falcone (dacite)	Falcone (dacite)	Falcone (dacite)	Falcone (dacite)	Falcone (dacite)	Falcone (dacite)	Falcone (dacite)	Falcone (dacite)	Falcone (dacite)
Major elements (wt%)												
SiO_2	77.07	77.36	77.16	77.82	77.56	77.02	72.88	73.32	78.01	77.31	77.43	76.51
TiO_2	0.12	0.12	0.10	0.06	0.08	0.06	0.07	0.07	0.05	0.10	0.04	0.03
Al_2O_3	12.75	12.72	13.20	13.00	12.96	12.90	12.49	12.72	12.86	12.87	12.83	12.74
FeO*	1.27	1.39	1.31	1.01	1.06	1.28	1.31	1.20	1.08	1.06	1.03	1.28
MnO	0.06	0.05	0.03	0.04	0.05	0.08	0.06	0.03	0.03	0.01	0.03	0.06
MgO	0.03	0.01	0.03	0.01	0.01	0.02	0.01	0.03	0.00	0.02	0.00	0.02
CaO	0.69	0.72	0.72	0.69	0.61	0.70	0.71	0.69	0.57	0.63	0.55	0.63
Na_2O	3.70	4.32	4.67	4.59	3.37	4.27	3.65	4.29	4.21	4.12	4.02	3.89
K_2O	5.43	4.38	3.93	4.11	6.06	4.61	5.63	4.64	4.84	4.93	5.03	5.05
P_2O_5	b.d	b.d	b.d	b.d	b.d	b.d	b.d	b.d	b.d	b.d	b.d	b.d
Total	101.12	101.06	101.15	101.32	101.77	100.93	96.81	96.98	101.64	101.04	100.97	100.21

	Falcone (dacite)	Falcone (dacite)	Falcone (dacite)
Major elements (wt%)			
SiO_2	77.46	79.21	78.71
TiO_2	0.08	0.04	0.05
Al_2O_3	12.46	12.60	13.20
FeO*	3.08	0.38	0.88
MnO	0.24	0.02	0.03
MgO	0.11	0.00	0.01
CaO	0.87	0.66	0.86
Na_2O	5.73	5.94	6.27
K_2O	1.94	2.01	1.59
P_2O_5	b.d	b.d	b.d
Total	101.97	100.86	101.59

Falcone (rhyolite)

	Falcone (rhyolite)	Falcone (rhyolite)	Falcone (rhyolite)	Falcone (rhyolite)	Falcone (rhyolite)	Falcone (rhyolite)	Falcone (rhyolite)	Falcone (rhyolite)	Falcone (rhyolite)	Falcone (rhyolite)	Falcone (rhyolite)	Falcone (rhyolite)
Major elements (wt%)												
SiO_2	75.76	75.65	75.22	75.57	76.05	75.32	75.37	75.81	75.50	75.58	76.26	75.90
TiO_2	0.10	0.05	0.10	0.07	0.08	0.05	0.07	0.05	0.08	0.08	0.07	0.07
Al_2O_3	12.97	12.89	12.95	12.76	12.79	12.92	12.93	12.91	12.81	12.68	12.88	12.84
FeO*	1.35	1.22	1.33	1.31	1.31	1.41	1.38	1.11	1.35	1.27	1.21	1.19
MnO	0.06	0.08	0.07	0.04	0.05	0.07	0.07	0.04	0.04	0.05	0.04	0.04
MgO	0.01	0.01	0.03	0.02	0.01	0.02	0.03	0.01	0.01	0.02	0.01	0.03
CaO	0.71	0.67	0.70	0.69	0.71	0.71	0.71	0.65	0.72	0.67	0.70	0.71
Na_2O	4.04	3.76	3.80	3.72	4.11	4.04	4.01	3.97	3.89	4.27	3.77	3.80
K_2O	4.93	5.44	5.48	5.62	4.97	5.13	5.08	5.28	5.20	4.64	5.39	5.47
P_2O_5	b.d	b.d	b.d	b.d	b.d	b.d	b.d	b.d	b.d	b.d	b.d	b.d
Total	99.93	99.77	99.66	99.80	100.09	99.66	99.65	99.83	99.60	99.27	100.33	100.04

	Falcone (rhyolite)	Falcone (rhyolite)	Falcone (rhyolite)	Falcone (rhyolite)	Falcone (rhyolite)	Falcone (rhyolite)	Falcone (rhyolite)	Falcone (rhyolite)	Falcone (rhyolite)	Falcone (rhyolite)	Falcone (rhyolite)	Falcone (rhyolite)
Major elements (wt%)												
SiO_2	76.41	76.00	75.88	77.77	77.28	76.99	77.42	76.83	75.06	74.55	74.96	79.53
TiO_2	0.08	0.06	0.08	0.09	0.05	0.05	0.09	0.08	0.08	0.07	0.03	0.04
Al_2O_3	12.73	12.88	12.84	13.07	13.06	13.13	13.22	13.01	12.57	12.80	12.90	11.74
FeO*	1.10	1.09	1.22	1.25	1.36	1.08	1.38	1.38	1.34	1.26	1.02	0.43
MnO	0.04	0.06	0.03	0.03	0.06	0.04	0.05	0.03	0.04	0.04	0.06	0.01
MgO	0.02	0.02	0.01	0.01	0.02	0.02	0.03	0.02	0.01	0.01	0.02	0.00
CaO	0.67	0.66	0.70	0.69	0.72	0.67	0.72	0.71	0.72	0.67	0.64	0.50
Na_2O	3.74	3.62	3.68	4.94	3.30	3.20	4.81	4.42	4.36	3.20	4.16	5.06
K_2O	5.41	5.44	5.37	3.68	6.01	5.98	3.92	4.51	4.63	6.01	4.85	2.38
P_2O_5	b.d	b.d	b.d	b.d	b.d	b.d	b.d	b.d	b.d	b.d	b.d	b.d
Total	100.21	99.83	99.80	101.54	101.86	101.15	101.64	100.99	98.81	98.60	98.63	99.68

	Falcone (rhyolite)	Falcone (rhyolite)	Falcone (rhyolite)	Falcone (rhyolite)	Falcone (rhyolite)
Major elements (wt%)					
SiO_2	75.00	76.94	79.80	77.28	78.69
TiO_2	0.07	0.07	0.08	0.07	0.11
Al_2O_3	14.32	12.02	12.68	12.59	12.75
FeO*	0.49	2.12	0.42	1.20	0.43
MnO	0.01	0.16	0.01	0.06	0.01
MgO	0.00	0.02	0.00	0.04	0.00
CaO	0.66	0.76	0.65	0.82	0.67
Na_2O	6.77	5.96	6.10	5.39	6.11
K_2O	2.37	1.40	1.97	2.42	1.80
P_2O_5	b.d	b.d	b.d	b.d	b.d
Total	99.70	99.45	101.71	99.86	100.56

Appendix III –Pietre Cotte lava flow – Mineral and enclave glass data

Feldspar data

	Vulc-pl1	Vulc-pl2	Vulc-pl5	Vulc-fsp1	Vulc-fsp2	Vulc-fsp3	Vulc-fsp4	Vulc-fsp5	PCMfsp3-phc	PCMfsp9-phr	PCM2fsp22-phr	PCM2fsp6-phr	PCM2fsp10-phc
SiO_2	57.93	54.12	54.81	56.69	57.48	56.82	57.20	56.84	54.76	56.92	57.49	55.54	56.53
TiO_2	0.01	0.09	0.06	0.02	0.01	0.04	0.07	0.07	0.04	0.02	0.04	0.00	0.06
Al_2O_3	26.83	29.43	28.90	27.71	26.91	27.69	27.35	27.18	28.68	27.20	26.68	27.69	27.81
FeO	0.61	0.68	0.85	0.63	0.59	0.63	0.61	0.61	0.62	0.63	0.61	0.98	0.82
MnO	0.00	0.01	0.00	0.00	0.00	0.00	0.02	0.00	0.02	0.00	0.01	0.00	0.00
MgO	0.07	0.07	0.08	0.06	0.05	0.06	0.06	0.07	0.06	0.05	0.04	0.06	0.04
CaO	8.78	11.79	11.29	9.62	8.87	9.67	9.23	9.20	8.65	8.50	8.90	9.55	7.95
Na_2O	5.36	4.27	4.49	5.03	5.23	5.07	5.14	5.09	5.06	5.27	5.31	4.84	5.24
K_2O	1.92	0.89	1.09	1.57	1.87	1.51	1.69	1.74	1.15	1.53	1.61	1.38	1.94
Total	101.51	101.35	101.57	101.32	101.01	101.49	101.37	100.80	99.03	100.14	100.70	100.03	100.37
Structural formula based on 8 oxygens (ferrous)													
Si	2.578	2.427	2.453	2.531	2.571	2.532	2.550	2.550	2.492	2.562	2.577	2.514	2.542
Al	1.407	1.555	1.524	1.458	1.419	1.455	1.437	1.437	1.538	1.443	1.409	1.477	1.474
Ti	0.000	0.003	0.002	0.001	0.000	0.001	0.002	0.002	0.002	0.001	0.001	0.000	0.002
Mg	0.005	0.005	0.005	0.004	0.004	0.004	0.004	0.005	0.004	0.004	0.003	0.004	0.003
Fe	0.023	0.026	0.032	0.023	0.022	0.024	0.023	0.023	0.024	0.024	0.023	0.037	0.031
Mn	0.000	0.000	0.000	0.000	0.000	0.000	0.001	0.000	0.001	0.000	0.000	0.000	0.000
Ca	0.419	0.567	0.541	0.460	0.425	0.462	0.441	0.442	0.422	0.410	0.428	0.463	0.383
Na	0.462	0.372	0.390	0.435	0.453	0.438	0.444	0.443	0.447	0.460	0.461	0.425	0.457
K	0.109	0.051	0.062	0.089	0.107	0.086	0.096	0.100	0.067	0.088	0.092	0.080	0.111
Sum	5.003	5.004	5.009	5.001	5.000	5.001	4.999	5.001	4.994	4.990	4.994	5.000	5.003
An (mol%)	42.3	57.3	54.5	46.7	43.1	46.9	44.9	44.9	45.1	42.8	43.6	47.8	40.3
Ab (mol%)	46.7	37.6	39.2	44.2	46.0	44.4	45.3	45.0	47.8	48.0	47.0	43.9	48.0
Or (mol%)	11.0	5.2	6.3	9.1	10.8	8.7	9.8	10.1	7.1	9.2	9.4	8.2	11.7

	PC11 phc	PCM 22hr	PCfsp -1	OPCfsp -2	OPCfsp -3	OPCfsp -4	OPCfsp-4b	OPCfsp -5	OPCfsp -6	OPCfsp -7	OPCfsp -9	OPCfsp 10	OPCfsp 11
SiO_2	56.82	57.09	55.57	57.40	51.82	56.97	57.27	54.43	55.88	55.74	54.82	57.05	55.99
TiO_2	0.00	0.04	0.00	0.00	0.00	0.00	0.00	0.00	0.00	0.00	0.00	0.00	0.00
Al_2O_3	27.14	27.68	27.65	26.15	30.25	26.75	26.35	27.53	26.69	27.25	27.84	26.66	27.12
FeO	0.91	0.61	0.62	0.61	0.60	0.59	0.59	0.62	0.59	0.61	0.64	0.60	0.64
MnO	0.00	0.01	0.07	0.05	0.06	0.08	0.04	0.15	0.07	0.05	0.05	0.05	0.05
MgO	0.06	0.04	0.00	0.00	0.00	0.00	0.00	0.00	0.00	0.00	0.00	0.00	0.00
CaO	9.28	8.00	9.94	8.19	13.12	8.81	8.47	10.08	9.19	9.42	10.35	8.65	9.43
Na_2O	5.10	5.51	4.88	5.20	3.73	5.19	5.27	4.81	5.06	4.90	4.68	5.21	4.92
K_2O	1.34	1.61	1.46	2.27	0.70	1.85	2.08	1.37	1.66	1.52	1.27	2.00	1.64
Total	100.65	100.60	100.19	99.87	100.27	100.24	100.07	98.99	99.14	99.50	99.65	100.21	99.79
Structural formula based on 8 oxygens (ferrous)													
Si	2.551	2.556	2.513	2.597	2.358	2.568	2.586	2.495	2.550	2.533	2.494	2.573	2.539
Al	1.436	1.460	1.474	1.394	1.623	1.421	1.402	1.487	1.435	1.460	1.493	1.417	1.449
Ti	0.000	0.001	0.000	0.000	0.000	0.000	0.000	0.000	0.000	0.000	0.000	0.000	0.000
Mg	0.004	0.003	0.000	0.000	0.000	0.000	0.000	0.000	0.000	0.000	0.000	0.000	0.000
Fe	0.034	0.023	0.023	0.023	0.023	0.022	0.022	0.024	0.023	0.023	0.024	0.022	0.024
Mn	0.000	0.000	0.003	0.002	0.002	0.003	0.001	0.006	0.003	0.002	0.002	0.002	0.002
Ca	0.446	0.384	0.482	0.397	0.640	0.426	0.410	0.495	0.449	0.459	0.504	0.418	0.458
Na	0.444	0.478	0.428	0.456	0.329	0.454	0.461	0.428	0.448	0.432	0.413	0.456	0.433
K	0.077	0.092	0.084	0.131	0.040	0.106	0.120	0.080	0.097	0.088	0.074	0.115	0.095
Sum	4.992	4.998	5.006	5.000	5.015	5.001	5.003	5.015	5.004	4.997	5.003	5.004	5.000
An (mol%)	46.2	40.2	48.5	40.3	63.4	43.2	41.4	49.4	45.2	46.9	50.9	42.3	46.5
Ab (mol%)	45.9	50.1	43.1	46.3	32.6	46.0	46.6	42.6	45.1	44.1	41.7	46.1	43.9
Or (mol%)	7.9	9.7	8.5	13.3	4.0	10.8	12.1	8.0	9.7	9.0	7.4	11.6	9.6

	OPCfsp12	OPCfsp13	OPCfsp14	OPCfsp15	OPCfsp16	OPCfsp17	OPCfsp18	OPCfsp19	OPCfsp20	OPCfsp21	OPCfsp22	OPCfsp23	OPCfsp24	OPCfsp25
SiO_2	56.43	56.33	55.93	54.90	55.30	55.08	55.74	56.46	55.62	56.09	54.22	57.48	53.59	55.21
TiO_2	0.00	0.00	0.00	0.00	0.00	0.00	0.00	0.00	0.00	0.00	0.00	0.00	0.00	0.00
Al_2O_3	26.56	27.44	27.43	28.05	28.08	27.43	27.38	26.83	27.51	27.23	28.20	25.81	28.85	28.80
FeO	0.60	0.36	0.47	0.55	0.56	0.72	0.46	0.49	0.44	0.80	0.62	0.62	0.64	0.67
MnO	0.05	0.02	0.03	0.05	0.05	0.01	0.06	0.05	0.05	0.00	0.05	0.06	0.07	0.06
MgO	0.00	0.00	0.00	0.00	0.00	0.00	0.00	0.00	0.00	0.00	0.00	0.00	0.00	0.00
CaO	8.75	9.80	9.36	10.23	10.31	8.04	9.66	9.21	9.71	9.91	10.43	7.81	10.74	9.16
Na_2O	5.17	5.12	5.20	4.82	4.74	5.12	4.89	5.04	4.94	4.84	4.47	5.07	4.40	5.22
K_2O	1.85	1.36	1.58	1.25	1.35	1.70	1.47	1.81	1.55	1.62	1.32	2.16	1.19	0.99
Total	99.42	100.43	100.00	99.85	100.39	98.11	99.67	99.89	99.82	100.49	99.31	99.01	99.48	100.10
Structural formula based on 8 oxygens (ferrous)														
Si	2.566	2.534	2.530	2.491	2.496	2.533	2.529	2.556	2.521	2.530	2.476	2.615	2.446	2.489
Al	1.423	1.455	1.462	1.500	1.494	1.487	1.464	1.432	1.470	1.448	1.518	1.384	1.552	1.530
Ti	0.000	0.000	0.000	0.000	0.000	0.000	0.000	0.000	0.000	0.000	0.000	0.000	0.000	0.000
Mg	0.000	0.000	0.000	0.000	0.000	0.000	0.000	0.000	0.000	0.000	0.000	0.000	0.000	0.000
Fe	0.023	0.013	0.018	0.021	0.021	0.028	0.018	0.019	0.017	0.030	0.024	0.024	0.024	0.025
Mn	0.002	0.001	0.001	0.002	0.002	0.001	0.002	0.002	0.002	0.000	0.002	0.002	0.003	0.002
Ca	0.426	0.472	0.454	0.497	0.499	0.396	0.470	0.447	0.472	0.479	0.510	0.381	0.525	0.442
Na	0.456	0.447	0.456	0.424	0.415	0.457	0.430	0.442	0.434	0.423	0.396	0.447	0.389	0.456
K	0.107	0.078	0.091	0.072	0.078	0.100	0.085	0.105	0.090	0.093	0.077	0.125	0.070	0.057
Sum	5.004	5.001	5.012	5.007	5.004	5.001	4.997	5.002	5.006	5.004	5.002	4.979	5.008	5.002
An (mol%)	43.1	47.4	45.3	50.0	50.3	41.6	47.7	45.0	47.4	48.1	51.9	39.9	53.4	46.3
Ab (mol%)	46.1	44.8	45.6	42.7	41.9	47.9	43.7	44.5	43.6	42.5	40.3	46.9	39.6	47.7
Or (mol%)	10.8	7.8	9.1	7.3	7.8	10.5	8.6	10.5	9.0	9.4	7.8	13.2	7.1	6.0

	OPCfsp26	OPCfsp27	OPCfsp28	OPCfsp29	OPCfsp30	OPCfsp31	OPCfsp32	OPCfsp33	OPCfsp34	OPCfsp35	OPCfsp36	OPCfsp37	OPCfsp38	OPCfsp39
SiO_2	51.39	56.06	55.44	56.96	57.04	57.15	54.86	57.49	55.60	56.05	56.63	55.80	55.18	55.22
TiO_2	0.00	0.00	0.00	0.00	0.00	0.00	0.00	0.00	0.00	0.00	0.00	0.00	0.00	0.00
Al_2O_3	29.44	26.15	27.59	26.28	26.59	26.45	28.31	26.33	27.37	27.38	26.77	27.89	27.07	27.35
FeO	0.62	0.63	0.61	0.57	0.55	0.61	0.59	0.63	0.64	0.60	0.61	0.60	0.66	0.66
MnO	0.07	0.06	0.05	0.05	0.05	0.06	0.06	0.04	0.05	0.05	0.05	0.06	0.02	0.05
MgO	0.00	0.00	0.00	0.00	0.00	0.00	0.00	0.00	0.00	0.00	0.00	0.00	0.00	0.00
CaO	12.04	8.81	10.04	8.30	8.78	8.44	10.57	8.53	9.79	9.52	9.04	9.88	10.61	9.25
Na_2O	3.91	5.30	4.83	5.20	5.12	5.21	4.66	5.22	4.78	5.00	5.26	4.91	4.63	4.91
K_2O	0.82	1.78	1.47	2.14	1.89	1.99	1.24	2.05	1.51	1.64	1.79	1.48	1.26	1.55
Total	98.29	98.78	100.03	99.50	100.02	99.91	100.28	100.29	99.74	100.23	100.15	100.61	99.43	98.99
Structural formula based on 8 oxygens (ferrous)														
Si	2.382	2.568	2.512	2.586	2.576	2.583	2.480	2.590	2.524	2.531	2.559	2.511	2.516	2.524
Al	1.608	1.412	1.473	1.406	1.415	1.409	1.509	1.398	1.464	1.457	1.425	1.479	1.455	1.473
Ti	0.000	0.000	0.000	0.000	0.000	0.000	0.000	0.000	0.000	0.000	0.000	0.000	0.000	0.000
Mg	0.000	0.000	0.000	0.000	0.000	0.000	0.000	0.000	0.000	0.000	0.000	0.000	0.000	0.000
Fe	0.024	0.024	0.023	0.022	0.021	0.023	0.022	0.024	0.024	0.023	0.023	0.022	0.025	0.025
Mn	0.003	0.002	0.002	0.002	0.002	0.002	0.002	0.002	0.002	0.002	0.002	0.002	0.001	0.002
Ca	0.598	0.432	0.487	0.404	0.425	0.409	0.512	0.412	0.476	0.461	0.438	0.476	0.518	0.453
Na	0.351	0.471	0.424	0.458	0.448	0.457	0.409	0.456	0.421	0.438	0.461	0.428	0.409	0.435
K	0.048	0.104	0.085	0.124	0.109	0.115	0.072	0.118	0.087	0.094	0.103	0.085	0.073	0.090
Sum	5.014	5.013	5.006	5.002	4.995	4.998	5.005	4.998	4.998	5.006	5.011	5.005	4.998	5.003
An (mol%)	59.9	42.9	48.9	41.0	43.3	41.7	51.6	41.8	48.4	46.4	43.7	48.1	51.8	46.3
Ab (mol%)	35.2	46.7	42.6	46.5	45.7	46.6	41.2	46.3	42.7	44.1	46.0	43.3	40.9	44.5
Or (mol%)	4.8	10.3	8.5	12.6	11.1	11.7	7.2	12.0	8.9	9.5	10.3	8.6	7.3	9.2

	OPCfsp40	OPCfsp41	OPCfsp42	OPCfsp43	OPCfsp44
SiO_2	55.64	54.62	56.04	55.88	57.23
TiO_2	0.00	0.00	0.00	0.00	0.00
Al_2O_3	27.55	28.32	27.17	27.42	26.39
FeO	0.67	0.61	0.77	0.62	0.60
MnO	0.05	0.06	0.01	0.07	0.05
MgO	0.00	0.00	0.00	0.00	0.00
CaO	9.80	10.71	9.86	9.72	8.57
Na_2O	4.96	4.58	4.83	4.99	5.21
K_2O	1.50	1.22	1.60	1.55	2.16
Total	100.18	100.12	100.28	100.25	100.21
Structural formula based on 8 oxygens (ferrous)					
Si	2.517	2.475	2.532	2.525	2.583
Al	1.469	1.512	1.447	1.460	1.404
Ti	0.000	0.000	0.000	0.000	0.000
Mg	0.000	0.000	0.000	0.000	0.000
Fe	0.025	0.023	0.029	0.024	0.023
Mn	0.002	0.002	0.001	0.003	0.002
Ca	0.475	0.520	0.477	0.471	0.414
Na	0.435	0.402	0.423	0.437	0.456
K	0.087	0.071	0.092	0.089	0.124
Sum	5.010	5.005	5.002	5.008	5.006
An (mol%)	47.7	52.4	48.1	47.2	41.7
Ab (mol%)	43.7	40.5	42.6	43.8	45.8
Or (mol%)	8.7	7.1	9.3	9.0	12.5

Glass inclusion (from mafic enclaves) data

	TR1-M38	TR22	TR23	TR21	TR25	TR19	TR18	TR31	TR17	TR26	TR30	TR31
SiO_2	63.01	63.46	62.77	61.96	61.46	61.91	60.96	61.10	61.00	60.70	60.94	61.37
TiO_2	0.50	0.10	0.30	0.49	0.39	0.29	0.59	0.65	0.39	0.51	0.49	0.44
Al_2O_3	19.00	18.25	18.91	17.98	19.27	18.45	21.67	18.49	18.64	19.17	18.35	20.83
FeO *	4.26	4.39	4.55	5.60	4.02	3.80	4.18	4.67	6.05	4.47	5.36	3.68
MnO	0.14	0.10	0.11	0.18	0.05	0.11	0.06	0.06	0.17	0.13	0.13	0.07
MgO	1.52	0.61	0.80	1.09	0.74	1.15	0.58	1.19	1.07	1.08	0.83	0.51
CaO	2.41	2.67	1.41	1.90	2.14	2.94	1.89	1.11	1.71	2.35	1.75	2.19
Na_2O	5.05	5.31	5.13	4.43	5.76	4.98	4.89	4.52	4.94	4.96	4.92	5.04
K_2O	3.22	4.75	5.70	5.98	4.46	4.93	5.55	6.32	5.14	5.17	5.65	5.59
P_2O_5	b.d	b.d	b.d	b.d	b.d	b.d	b.d	b.d	b.d	b.d	b.d	b.d
Total	99.11	99.64	99.68	99.61	98.28	98.56	100.37	98.09	99.10	98.53	98.42	99.72

FeO = all iron as FeO*

Feldspar microlitic groundmass (from mafic enclaves) data

	VB1-M9	OPCfspgm-1	OPCfspgm-2	OPCfspgm-3	OPCfspgm-4	OPCfspgm-5	OPCfspgm-6	OPCfspgm-7	OPCfspgm-8	OPCfspg9	OPCfspgm-10	OPCfspgm-11	OPCfspgm-12
SiO_2	60.61	62.31	62.82	64.36	65.70	65.10	64.49	65.24	65.52	64.78	62.24	66.34	66.43
TiO_2	0.04	0.00	0.00	0.00	0.00	0.00	0.00	0.00	0.00	0.00	0.00	0.00	0.00
Al_2O_3	23.33	20.28	19.14	19.87	18.49	20.11	20.69	19.87	20.29	20.09	19.08	18.75	19.01
FeO	0.64	1.06	1.08	0.70	0.74	0.36	0.59	0.49	0.36	0.61	0.94	0.45	0.48
MnO	0.01	0.00	0.00	0.00	0.00	0.00	0.00	0.00	0.00	0.00	0.00	0.00	0.00
MgO	0.07	0.03	0.02	0.11	0.05	0.02	0.01	0.00	0.00	0.01	0.03	0.00	0.01
CaO	9.55	1.67	1.85	1.54	1.67	1.28	1.53	1.27	1.25	1.51	1.57	1.39	1.42
Na_2O	5.08	5.94	5.94	4.64	5.81	5.91	5.49	4.24	5.27	5.33	5.90	5.82	5.71
K_2O	1.54	8.68	9.20	8.69	7.44	7.65	7.71	9.81	8.30	7.99	9.80	7.65	7.93
Total	100.87	99.97	100.06	99.91	99.91	100.43	100.51	100.91	100.99	100.32	99.57	100.40	100.99
Structural formula based on 8 oxygens (ferrous)													
Si	2.539	2.826	2.888	2.921	2.970	2.925	2.899	2.936	2.929	2.920	2.883	2.978	2.969
Al	1.445	1.056	1.037	1.063	0.985	1.065	1.096	1.054	1.069	1.067	1.042	0.992	1.001
Ti	0.001	0.010	0.000	0.000	0.000	0.000	0.000	0.000	0.000	0.000	0.000	0.000	0.000
Mg	0.004	0.079	0.002	0.007	0.004	0.002	0.001	0.000	0.000	0.001	0.002	0.000	0.001
Fe	0.024	0.146	0.042	0.027	0.028	0.013	0.022	0.018	0.014	0.023	0.037	0.017	0.018
Mn	0.001	0.004	0.000	0.000	0.000	0.000	0.000	0.000	0.000	0.000	0.000	0.000	0.000
Ca	0.459	0.145	0.091	0.075	0.081	0.062	0.074	0.061	0.060	0.073	0.078	0.067	0.068
Na	0.442	0.445	0.529	0.408	0.509	0.515	0.479	0.370	0.457	0.466	0.530	0.507	0.495
K	0.088	0.290	0.540	0.503	0.429	0.438	0.442	0.563	0.473	0.459	0.579	0.438	0.452
Sum	5.002	5.003	5.128	5.004	5.006	5.019	5.013	5.003	5.002	5.009	5.151	4.998	5.004
An (mol%)	46.4	16.5	7.9	7.6	7.9	6.1	7.4	6.1	6.0	7.3	6.6	6.6	6.7
Ab (mol%)	44.7	50.5	45.6	41.4	50.0	50.7	48.1	37.2	46.1	46.7	44.6	50.1	48.8
Or (mol%)	8.9	33.0	46.5	51.0	42.1	43.2	44.5	56.6	47.8	46.0	48.8	43.3	44.5

Pyroxene Phenocryst Data

	VB1-M8	VB1-M11	VB1-M28	VB1-M35	VB1-M43	VB1-M47	VB1-M50	VB1-M58	VB1-M62	VB1-M64	PCMfsp 1-phc	PCMfsp 1-phr	PCMfsp 2-phc	PCMfsp 2-phr	PCMfsp 1-phc
SiO_2	51.58	51.07	52.20	51.82	51.30	51.67	51.51	51.31	51.81	51.49	51.75	51.38	51.26	50.67	51.91
TiO_2	0.52	0.59	0.51	0.46	0.57	0.53	0.69	0.65	0.59	0.60	0.58	0.34	0.54	0.36	0.57
Al_2O_3	3.20	4.00	3.17	2.52	3.56	3.23	3.74	3.27	3.45	3.61	3.90	2.43	3.67	2.68	3.60
Cr_2O_3	0.02	0.04	0.00	0.01	0.03	0.02	0.01	0.00	0.03	0.03	b.d	b.d	b.d	b.d	b.d
FeO	8.60	7.82	9.28	7.90	8.34	8.74	8.82	8.55	8.61	8.48	8.72	9.10	8.53	8.96	8.66
MnO	0.27	0.19	0.30	0.21	0.27	0.30	0.20	0.28	0.24	0.26	0.26	0.30	0.23	0.27	0.22
MgO	14.15	14.21	13.84	14.68	13.85	13.94	13.59	13.77	13.94	13.92	13.72	14.23	13.95	14.28	13.70
NiO	0.02	0.01	0.00	0.01	0.00	0.01	0.00	0.00	0.01	0.02	b.d	b.d	b.d	b.d	b.d
CaO	21.97	22.12	21.56	22.25	22.08	21.90	21.61	22.17	21.99	22.04	20.92	20.18	20.48	20.30	20.78
Na_2O	0.45	0.37	0.46	0.37	0.48	0.45	0.48	0.43	0.47	0.46	0.43	0.43	0.47	0.48	0.46
K_2O	0.00	0.00	0.00	0.00	0.01	0.00	0.00	0.00	0.00	0.00	0.00	0.00	0.00	0.00	0.00
Total	100.78	100.42	101.31	100.22	100.49	100.77	100.66	100.44	101.12	100.90	100.28	98.39	99.12	97.99	99.90
Ferrous Form															
Si	1.909	1.890	1.922	1.923	1.903	1.912	1.906	1.907	1.909	1.902	1.916	1.943	1.918	1.926	1.928
Al	0.140	0.174	0.137	0.110	0.155	0.141	0.163	0.143	0.150	0.157	0.170	0.108	0.162	0.120	0.157
Ti	0.015	0.016	0.014	0.013	0.016	0.015	0.019	0.018	0.016	0.017	0.016	0.010	0.015	0.010	0.016
Cr	0.001	0.001	0.000	0.000	0.001	0.001	0.000	0.000	0.001	0.001	0.000	0.000	0.000	0.000	0.000
Mg	0.781	0.784	0.760	0.812	0.766	0.769	0.750	0.763	0.766	0.766	0.757	0.802	0.778	0.809	0.758
Fe 2+	0.266	0.242	0.286	0.245	0.259	0.270	0.273	0.266	0.265	0.262	0.270	0.288	0.267	0.285	0.269
Mn	0.008	0.006	0.009	0.006	0.008	0.009	0.006	0.009	0.007	0.008	0.008	0.010	0.007	0.009	0.007
Ni	0.001	0.000	0.000	0.000	0.000	0.000	0.000	0.000	0.000	0.000	0.000	0.000	0.000	0.000	0.000
Ca	0.871	0.877	0.850	0.885	0.877	0.868	0.857	0.883	0.868	0.872	0.830	0.817	0.821	0.827	0.827
Na	0.032	0.027	0.033	0.026	0.034	0.032	0.034	0.031	0.034	0.033	0.031	0.031	0.034	0.035	0.033
K	0.000	0.000	0.000	0.000	0.001	0.000	0.000	0.000	0.000	0.000	0.000	0.000	0.000	0.000	0.000
Sum	4.023	4.019	4.012	4.022	4.020	4.018	4.010	4.019	4.016	4.019	3.998	4.009	4.003	4.021	3.995

Continued

Ferric Form

Si	1.898	1.881	1.916	1.913	1.893	1.904	1.902	1.898	1.901	1.893	1.917	1.938	1.917	1.916	1.930
Al	0.139	0.174	0.137	0.110	0.155	0.140	0.163	0.143	0.149	0.156	0.170	0.108	0.162	0.119	0.158
Ti	0.014	0.016	0.014	0.013	0.016	0.015	0.019	0.018	0.016	0.017	0.016	0.010	0.015	0.010	0.016
Cr	0.001	0.001	0.000	0.000	0.001	0.001	0.000	0.000	0.001	0.001	0.000	0.000	0.000	0.000	0.000
Fe3+	0.068	0.056	0.035	0.066	0.061	0.054	0.029	0.057	0.048	0.056	0.000	0.027	0.008	0.063	0.000
Mg	0.776	0.780	0.758	0.808	0.762	0.766	0.748	0.759	0.762	0.763	0.757	0.800	0.778	0.805	0.759
Fe	0.197	0.185	0.250	0.178	0.196	0.215	0.243	0.208	0.216	0.204	0.270	0.260	0.259	0.220	0.269
Mn	0.008	0.006	0.009	0.006	0.008	0.009	0.006	0.009	0.007	0.008	0.008	0.009	0.007	0.009	0.007
Ni	0.001	0.000	0.000	0.000	0.000	0.000	0.000	0.000	0.000	0.000	0.000	0.000	0.000	0.000	0.000
Ca	0.866	0.873	0.848	0.880	0.873	0.864	0.855	0.878	0.865	0.868	0.830	0.816	0.820	0.822	0.828
Na	0.032	0.027	0.033	0.026	0.034	0.032	0.034	0.031	0.034	0.033	0.031	0.031	0.034	0.035	0.033
K	0.000	0.000	0.000	0.000	0.001	0.000	0.000	0.000	0.000	0.000	0.000	0.000	0.000	0.000	0.000
Sum	4.000	4.000	4.000	4.000	4.000	4.000	4.000	4.000	4.000	4.000	4.000	4.000	4.000	4.000	4.000
Wo (mol%)	49.4	50.3	47.5	49.1	50.2	49.0	48.4	49.9	49.1	49.7	46.4	44.7	45.9	46.4	45.9
En (mol%)	40.3	40.2	39.5	41.7	39.6	39.8	39.0	39.3	39.7	39.6	39.5	41.7	40.6	42.1	39.9
Fs (mol%)	10.2	9.5	13.0	9.2	10.2	11.2	12.7	10.8	11.2	10.6	14.1	13.6	13.5	11.5	14.2

End members calculated from ferric form

	PCMfsp1-phr	OPC-px1	OPC-px2	OPC-px3	OPC-px4	OPC-px5	OPC-px6	OPC-px7	OPC-px9	OPC-px10	OPC-px11	OPC-px12
SiO_2	52.08	53.10	52.07	51.11	51.62	52.22	50.90	52.42	50.97	50.66	52.97	52.84
TiO_2	0.38	0.47	0.40	0.52	0.47	0.40	0.53	0.46	0.51	0.53	0.41	0.37
Al_2O_3	2.55	3.21	2.01	2.96	2.53	2.46	2.91	3.92	2.88	3.43	2.90	2.87
Cr_2O_3	0.00	0.19	0.06	0.00	0.00	0.00	0.02	0.11	0.04	0.00	0.42	0.26
FeO	9.02	7.09	9.66	9.06	9.16	9.78	9.51	6.00	9.38	9.33	4.61	5.93
MnO	0.30	0.15	0.46	0.35	0.36	0.35	0.32	0.13	0.31	0.35	0.08	0.18
MgO	14.27	14.17	14.04	13.67	13.98	13.05	13.83	14.73	13.89	13.58	16.22	15.57
NiO	b.d	0.00	0.00	0.02	0.00	0.00	0.01	0.00	0.01	0.00	0.02	0.01
CaO	20.88	21.37	21.04	21.30	21.48	21.75	21.22	21.06	21.59	21.35	21.13	21.59
Na_2O	0.43	0.31	0.47	0.51	0.47	0.58	0.48	0.51	0.51	0.46	0.28	0.25
K_2O	0.00	0.01	0.00	0.03	0.02	0.06	0.02	0.00	0.00	0.03	0.00	0.00
Total	99.90	100.07	100.22	99.53	100.08	100.64	99.75	99.34	100.09	99.72	99.03	99.87
Ferrous Form												
Si	1.940	1.952	1.943	1.918	1.927	1.943	1.911	1.933	1.908	1.901	1.947	1.941
Al	0.112	0.139	0.088	0.131	0.111	0.108	0.129	0.170	0.127	0.152	0.126	0.124
Ti	0.011	0.013	0.011	0.015	0.013	0.011	0.015	0.013	0.014	0.015	0.011	0.010
Cr	0.000	0.006	0.002	0.000	0.000	0.000	0.001	0.003	0.001	0.000	0.012	0.007
Mg	0.792	0.777	0.781	0.765	0.778	0.724	0.774	0.810	0.775	0.760	0.889	0.853
Fe	0.281	0.218	0.301	0.284	0.286	0.304	0.299	0.185	0.294	0.293	0.142	0.182
Mn	0.009	0.005	0.015	0.011	0.011	0.011	0.010	0.004	0.010	0.011	0.002	0.006
Ni	0.000	0.000	0.000	0.001	0.000	0.000	0.000	0.000	0.000	0.000	0.001	0.000
Ca	0.833	0.842	0.841	0.857	0.859	0.867	0.854	0.832	0.866	0.859	0.832	0.850
Na	0.031	0.022	0.034	0.037	0.034	0.042	0.035	0.037	0.037	0.033	0.020	0.018
K	0.000	0.000	0.000	0.001	0.001	0.003	0.001	0.000	0.000	0.001	0.000	0.000
Sum	4.009	3.974	4.018	4.020	4.021	4.014	4.027	3.986	4.032	4.025	3.982	3.991

Continued

Ferric Form

Si	1.935	1.965	1.935	1.909	1.917	1.937	1.898	1.939	1.893	1.889	1.956	1.945
Al	0.112	0.140	0.088	0.130	0.111	0.108	0.128	0.171	0.126	0.151	0.126	0.125
Ti	0.011	0.013	0.011	0.015	0.013	0.011	0.015	0.013	0.014	0.015	0.011	0.010
Cr	0.000	0.006	0.002	0.000	0.000	0.000	0.001	0.003	0.001	0.000	0.012	0.007
Fe3+	0.028	0.000	0.052	0.061	0.063	0.041	0.081	0.000	0.096	0.075	0.000	0.000
Mg	0.791	0.782	0.778	0.761	0.774	0.722	0.769	0.812	0.769	0.755	0.893	0.855
Fe	0.253	0.219	0.248	0.222	0.221	0.262	0.215	0.186	0.195	0.216	0.142	0.183
Mn	0.009	0.005	0.015	0.011	0.011	0.011	0.010	0.004	0.010	0.011	0.002	0.006
Ni	0.000	0.000	0.000	0.001	0.000	0.000	0.000	0.000	0.000	0.000	0.001	0.000
Ca	0.831	0.847	0.838	0.852	0.855	0.864	0.848	0.835	0.859	0.853	0.836	0.852
Na	0.031	0.022	0.034	0.037	0.034	0.042	0.035	0.037	0.037	0.033	0.020	0.018
K	0.000	0.000	0.000	0.001	0.001	0.003	0.001	0.000	0.000	0.001	0.000	0.000
Sum	4.000	4.000	4.000	4.000	4.000	4.000	4.000	4.000	4.000	4.000	4.000	4.000
Wo (mol%)	45.7	46.4	46.3	48.5	48.0	48.1	48.6	46.8	49.7	49.4	45.5	46.2
En (mol%)	41.2	41.9	40.7	39.9	40.4	38.0	40.2	43.3	40.2	39.4	47.0	44.4
Fs (mol%)	13.2	11.8	13.0	11.6	11.6	13.8	11.2	9.9	10.2	11.3	7.5	9.5

	OPC-px13	OPC-px14	OPC-px15	OPC-px16	OPC-px17	OPC-px19	OPC-px20	OPC-px21	OPC-px22	OPC-px23	OPC-px24	OPC-px25	OPC-px26
SiO_2	51.68	52.16	51.73	51.06	51.60	51.04	51.66	51.18	50.65	51.03	51.50	51.78	52.60
TiO_2	0.42	0.41	0.38	0.52	0.40	0.40	0.54	0.44	0.62	0.49	0.45	0.42	0.44
Al_2O_3	2.80	1.93	1.99	2.87	2.59	2.94	2.65	2.85	3.35	3.70	2.57	2.34	2.20
Cr_2O_3	0.00	0.05	0.09	0.01	0.01	0.00	0.00	0.00	0.02	0.04	0.00	0.04	0.00
FeO	8.99	9.75	9.44	9.23	8.96	8.12	9.35	9.22	9.55	8.01	8.40	9.95	10.21
MnO	0.35	0.45	0.43	0.35	0.33	0.25	0.28	0.33	0.33	0.23	0.30	0.37	0.33
MgO	14.25	14.23	14.18	13.76	14.10	14.53	14.08	14.20	13.46	13.97	14.50	13.39	12.97
NiO	0.03	0.01	0.02	0.01	0.05	0.04	0.00	0.00	0.04	0.00	0.00	0.00	0.04
CaO	21.34	20.96	20.73	21.30	21.35	21.67	21.42	21.21	21.27	22.01	21.98	21.32	21.36
Na_2O	0.50	0.46	0.47	0.47	0.41	0.40	0.40	0.44	0.50	0.31	0.41	0.47	0.57
K_2O	0.02	0.01	0.00	0.03	0.02	0.00	0.02	0.00	0.00	0.02	0.02	0.01	0.00
Total	100.37	100.42	99.47	99.61	99.81	99.38	100.40	99.87	99.79	99.81	100.13	100.09	100.72
Ferrous Form													
Si	1.921	1.943	1.943	1.917	1.929	1.912	1.923	1.915	1.902	1.902	1.918	1.938	1.956
Al	0.123	0.085	0.088	0.127	0.114	0.130	0.116	0.126	0.148	0.163	0.113	0.103	0.096
Ti	0.012	0.011	0.011	0.015	0.011	0.011	0.015	0.012	0.018	0.014	0.013	0.012	0.012
Cr	0.000	0.002	0.003	0.000	0.000	0.000	0.000	0.000	0.001	0.001	0.000	0.001	0.000
Mg	0.790	0.790	0.794	0.770	0.786	0.811	0.781	0.792	0.753	0.776	0.805	0.747	0.719
Fe	0.280	0.304	0.297	0.290	0.280	0.254	0.291	0.288	0.300	0.250	0.262	0.312	0.317
Mn	0.011	0.014	0.014	0.011	0.010	0.008	0.009	0.010	0.011	0.007	0.009	0.012	0.010
Ni	0.001	0.000	0.001	0.000	0.002	0.001	0.000	0.000	0.001	0.000	0.000	0.000	0.001
Ca	0.850	0.837	0.834	0.857	0.855	0.870	0.854	0.850	0.856	0.879	0.877	0.855	0.851
Na	0.036	0.033	0.034	0.034	0.029	0.029	0.029	0.032	0.037	0.023	0.030	0.034	0.041
K	0.001	0.001	0.000	0.002	0.001	0.000	0.001	0.000	0.000	0.001	0.001	0.000	0.000
Sum	4.024	4.019	4.018	4.023	4.018	4.027	4.019	4.026	4.025	4.014	4.028	4.015	4.004

Continued

Ferric Form													
Si	1.910	1.934	1.934	1.906	1.920	1.899	1.914	1.903	1.890	1.895	1.905	1.931	1.953
Al	0.122	0.084	0.088	0.126	0.114	0.129	0.116	0.125	0.147	0.162	0.112	0.103	0.096
Ti	0.012	0.011	0.011	0.015	0.011	0.011	0.015	0.012	0.017	0.014	0.012	0.012	0.012
Cr	0.000	0.002	0.003	0.000	0.000	0.000	0.000	0.000	0.001	0.001	0.000	0.001	0.000
Fe3+	0.071	0.058	0.054	0.067	0.053	0.079	0.057	0.077	0.074	0.043	0.083	0.044	0.013
Mg	0.785	0.786	0.790	0.766	0.782	0.806	0.777	0.787	0.749	0.773	0.800	0.745	0.718
Fe	0.207	0.244	0.241	0.221	0.226	0.173	0.233	0.210	0.224	0.205	0.176	0.266	0.304
Mn	0.011	0.014	0.014	0.011	0.010	0.008	0.009	0.010	0.011	0.007	0.009	0.012	0.010
Ni	0.001	0.000	0.001	0.000	0.002	0.001	0.000	0.000	0.001	0.000	0.000	0.000	0.001
Ca	0.845	0.833	0.830	0.852	0.851	0.864	0.850	0.845	0.850	0.876	0.871	0.852	0.850
Na	0.036	0.033	0.034	0.034	0.029	0.029	0.029	0.032	0.036	0.023	0.029	0.034	0.041
K	0.001	0.001	0.000	0.002	0.001	0.000	0.001	0.000	0.000	0.001	0.001	0.000	0.000
Sum	4.000	4.000	4.000	4.000	4.000	4.000	4.000	4.000	4.000	4.000	4.000	4.000	4.000
Wo (mol%)	48.1	46.0	46.0	48.4	47.5	49.3	47.5	48.1	49.1	49.7	49.4	47.2	46.3
En (mol%)	41.1	41.2	41.4	40.0	40.7	41.8	40.4	41.0	39.1	39.8	41.5	38.9	37.8
Fs (mol%)	10.8	12.8	12.6	11.6	11.7	9.0	12.1	10.9	11.7	10.6	9.2	13.9	16.0

	OPC-px28	OPC-px29	OPC-px30	OPC-px31	OPC-px32	OPC-px33	OPC-px34	OPC-px35	OPC-px36	OPC-px37	OPC-px38	OPC-px39	OPC-px40	OPC-px41	OPC-px42
SiO_2	52.22	51.52	51.16	50.31	51.18	50.38	50.72	51.25	50.77	50.99	50.83	51.64	51.23	51.22	51.65
TiO_2	0.34	0.39	0.51	0.64	0.53	0.59	0.60	0.29	0.60	0.51	0.59	0.43	0.52	0.39	0.49
Al_2O_3	1.89	3.03	2.84	3.74	2.94	3.40	3.17	3.63	3.59	3.26	2.99	2.60	2.76	2.50	2.75
Cr_2O_3	0.03	0.04	0.05	0.02	0.00	0.00	0.03	0.06	0.00	0.01	0.02	0.00	0.02	0.04	0.01
FeO	9.40	7.86	9.19	9.14	9.13	8.95	9.40	9.96	9.53	9.05	9.75	9.04	8.91	8.81	9.16
MnO	0.40	0.27	0.30	0.29	0.28	0.30	0.32	0.13	0.31	0.30	0.32	0.33	0.34	0.33	0.31
MgO	14.44	14.48	13.91	13.60	13.95	13.93	13.71	13.83	13.51	13.99	13.81	13.94	14.12	14.30	13.78
NiO	0.02	0.00	0.02	0.00	0.00	0.01	0.00	0.02	0.00	0.00	0.03	0.01	0.02	0.00	0.00
CaO	20.85	21.99	21.53	21.41	21.37	21.50	21.63	21.05	21.57	21.46	21.32	21.26	21.74	21.72	21.29
Na_2O	0.44	0.40	0.45	0.46	0.44	0.47	0.48	0.19	0.48	0.43	0.45	0.44	0.44	0.43	0.48
K_2O	0.00	0.01	0.00	0.01	0.01	0.02	0.00	0.00	0.03	0.00	0.05	0.01	0.03	0.00	0.00
Total	100.03	99.99	99.96	99.62	99.83	99.54	100.06	100.41	100.39	100.00	100.17	99.70	100.12	99.73	99.92

Ferrous Form

Si	1.948	1.916	1.914	1.889	1.915	1.893	1.900	1.907	1.895	1.905	1.903	1.932	1.913	1.919	1.929
Al	0.083	0.133	0.125	0.166	0.130	0.151	0.140	0.159	0.158	0.144	0.132	0.115	0.121	0.110	0.121
Ti	0.010	0.011	0.014	0.018	0.015	0.017	0.017	0.008	0.017	0.014	0.017	0.012	0.015	0.011	0.014
Cr	0.001	0.001	0.002	0.001	0.000	0.000	0.001	0.002	0.000	0.000	0.001	0.000	0.001	0.001	0.000
Mg	0.803	0.803	0.776	0.761	0.778	0.780	0.766	0.767	0.752	0.779	0.771	0.778	0.786	0.799	0.767
Fe	0.293	0.244	0.288	0.287	0.286	0.281	0.294	0.310	0.297	0.283	0.305	0.283	0.278	0.276	0.286
Mn	0.013	0.008	0.010	0.009	0.009	0.009	0.010	0.004	0.010	0.009	0.010	0.011	0.011	0.010	0.010
Ni	0.001	0.000	0.001	0.000	0.000	0.000	0.000	0.001	0.000	0.000	0.001	0.000	0.001	0.000	0.000
Ca	0.833	0.876	0.863	0.861	0.857	0.866	0.868	0.839	0.863	0.859	0.855	0.852	0.870	0.872	0.852
Na	0.032	0.029	0.032	0.033	0.032	0.034	0.035	0.014	0.035	0.031	0.033	0.032	0.032	0.031	0.035
K	0.000	0.001	0.000	0.001	0.001	0.001	0.000	0.000	0.002	0.000	0.002	0.000	0.001	0.000	0.000
Sum	4.016	4.021	4.024	4.026	4.021	4.033	4.031	4.011	4.027	4.024	4.031	4.015	4.028	4.030	4.014

Continued

Ferric Form															
Si	1.940	1.905	1.903	1.877	1.905	1.878	1.885	1.902	1.882	1.893	1.889	1.925	1.900	1.905	1.922
Al	0.083	0.132	0.124	0.164	0.129	0.149	0.139	0.159	0.157	0.143	0.131	0.114	0.121	0.110	0.121
Ti	0.009	0.011	0.014	0.018	0.015	0.016	0.017	0.008	0.017	0.014	0.017	0.012	0.014	0.011	0.014
Cr	0.001	0.001	0.001	0.001	0.000	0.000	0.001	0.002	0.000	0.000	0.001	0.000	0.001	0.001	0.000
Fe3+	0.049	0.064	0.072	0.079	0.064	0.097	0.091	0.034	0.081	0.073	0.093	0.044	0.083	0.088	0.041
Mg	0.800	0.798	0.771	0.756	0.774	0.774	0.760	0.765	0.747	0.774	0.765	0.775	0.781	0.793	0.765
Fe	0.243	0.179	0.213	0.206	0.221	0.182	0.201	0.276	0.214	0.208	0.210	0.238	0.193	0.186	0.244
Mn	0.013	0.008	0.010	0.009	0.009	0.009	0.010	0.004	0.010	0.009	0.010	0.010	0.011	0.010	0.010
Ni	0.001	0.000	0.001	0.000	0.000	0.000	0.000	0.001	0.000	0.000	0.001	0.000	0.001	0.000	0.000
Ca	0.830	0.871	0.858	0.856	0.852	0.859	0.861	0.837	0.857	0.854	0.849	0.849	0.864	0.865	0.849
Na	0.032	0.029	0.032	0.033	0.031	0.034	0.035	0.014	0.034	0.031	0.033	0.032	0.031	0.031	0.035
K	0.000	0.001	0.000	0.001	0.001	0.001	0.000	0.000	0.001	0.000	0.002	0.000	0.001	0.000	0.000
Sum	4.000	4.000	4.000	4.000	4.000	4.000	4.000	4.000	4.000	4.000	4.000	4.000	4.000	4.000	4.000
Wo (mol%)	45.5	49.4	48.8	50.0	48.2	50.2	50.0	46.8	49.9	49.0	49.1	47.2	49.3	49.2	47.3
En (mol%)	41.8	41.4	40.1	39.3	40.3	40.3	39.6	39.1	38.9	40.2	39.9	40.4	40.6	41.2	39.9
Fs (mol%)	12.7	9.3	11.1	10.7	11.5	9.5	10.5	14.1	11.2	10.8	11.0	12.4	10.0	9.6	12.7

Olivine Phenocryst Data

	VB1-M12	VB1-M13	VB1-M19	VB1-M20	VB1-M21	VB1-M22	VB1-M30	VB1-M33	VB1-M59	VB1-M65	PCM1-phc	PCM1-phr	PCM6-phc
SiO_2	37.64	37.79	37.72	38.00	37.89	37.93	38.02	37.85	37.17	37.25	36.16	35.04	35.96
TiO_2	0.00	0.00	0.03	0.02	0.04	0.06	0.00	0.01	0.01	0.00	0.00	0.00	0.00
FeO	31.53	31.95	31.67	31.77	31.64	31.97	31.88	32.04	33.87	33.67	31.75	31.55	30.80
MnO	0.77	0.76	0.73	0.75	0.77	0.79	0.77	0.77	0.69	0.66	0.75	0.77	0.72
MgO	30.86	30.86	30.75	30.76	30.27	30.83	31.11	30.79	28.23	28.63	33.02	33.19	31.91
NiO	0.31	0.31	0.31	0.29	0.35	0.32	0.29	0.29	0.34	0.37	0.00	0.00	0.00
K_2O	0.01	0.00	0.00	0.00	0.00	0.00	0.00	0.00	0.00	0.00	0.00	0.00	0.00
Total	101.31	101.74	101.30	101.70	101.04	101.97	102.12	101.83	101.34	100.63	100.93	100.83	99.70
Ferrous Form													
Si	1.012	1.013	1.014	1.017	1.021	1.014	1.014	1.013	1.034	1.032	1.034	1.033	1.061
Ti	0.000	0.000	0.001	0.000	0.001	0.001	0.000	0.000	0.000	0.000	0.000	0.000	0.000
Mg	1.237	1.233	1.232	1.227	1.216	1.228	1.237	1.229	1.140	1.151	0.971	0.978	0.942
Fe	0.709	0.716	0.712	0.711	0.713	0.715	0.711	0.717	0.767	0.760	0.934	0.930	0.909
Mn	0.017	0.017	0.017	0.017	0.017	0.018	0.017	0.017	0.016	0.015	0.022	0.023	0.021
Ni	0.007	0.007	0.007	0.006	0.007	0.007	0.006	0.006	0.007	0.008	0.000	0.000	0.000
K	0.000	0.000	0.000	0.000	0.000	0.000	0.000	0.000	0.000	0.000	0.001	0.000	0.000
Sum	2.991	2.988	2.986	2.983	2.979	2.985	2.987	2.987	2.966	2.968	2.969	2.971	2.943
Fo (mol%)	63.6	63.3	63.4	63.3	63.0	63.2	63.5	63.1	59.8	60.2	51.0	51.3	50.9
Fa (mol%)	36.4	36.7	36.6	36.7	37.0	36.8	36.5	36.9	40.2	39.8	49.0	48.7	49.1

	PCMmaf37-phc	PCMmaf38-phc	PCMmaf39-phc	PCM2fsp6-phc	PCM2fsp7-phc	PCM2fsp7-phr	PCM2fsp8-phr	PCM2fsp9-phc	PCM2fsp9-phr	PCM2maf2-phc	PCM2maf2-phr	PCM2maf5-phc	PCM2maf5-phr
SiO_2	36.14	36.21	36.08	36.41	36.23	36.24	36.08	36.24	36.22	36.17	36.25	36.21	36.23
TiO_2	0.05	0.04	0.00	0.00	0.04	0.01	0.02	0.02	0.02	0.00	0.00	0.00	0.02
FeO	31.80	31.82	31.74	31.66	32.18	32.20	32.29	31.67	32.22	31.75	31.80	31.77	31.77
MnO	0.80	0.78	0.73	0.76	0.80	0.81	0.78	0.77	0.75	0.80	0.76	0.77	0.82
MgO	31.99	31.88	32.02	32.07	32.03	31.51	31.46	31.99	31.92	31.83	31.96	32.13	31.99
NiO	0.00	0.00	0.00	0.00	0.00	0.00	0.00	0.00	0.00	0.00	0.00	0.00	0.00
K_2O	0.00	0.00	0.00	0.00	0.00	0.00	0.00	0.00	0.00	0.00	0.00	0.00	0.00
Total	101.07	100.99	100.83	101.18	101.52	101.02	100.91	100.95	101.38	100.80	101.04	101.14	101.09
Ferrous Form													
Si	1.054	1.056	1.055	1.060	1.053	1.057	1.054	1.057	1.054	1.057	1.057	1.055	1.056
Ti	0.001	0.001	0.000	0.000	0.001	0.000	0.001	0.001	0.000	0.000	0.000	0.000	0.001
Mg	0.933	0.930	0.936	0.933	0.931	0.919	0.919	0.933	0.929	0.930	0.932	0.937	0.933
Fe	0.928	0.928	0.928	0.921	0.935	0.939	0.943	0.924	0.937	0.928	0.927	0.926	0.926
Mn	0.023	0.023	0.021	0.022	0.023	0.023	0.023	0.022	0.022	0.023	0.022	0.023	0.024
Ni	0.000	0.000	0.000	0.000	0.000	0.000	0.000	0.000	0.000	0.000	0.000	0.000	0.000
K	0.001	0.000	0.000	0.001	0.000	0.000	0.001	0.001	0.000	0.000	0.001	0.000	0.001
Sum	2.948	2.946	2.949	2.944	2.950	2.946	2.949	2.945	2.950	2.946	2.947	2.948	2.947
Fo (mol%)	50.2	50.0	50.2	50.3	49.9	49.5	49.4	50.2	49.8	50.1	50.1	50.3	50.2
Fa (mol%)	49.8	50.0	49.8	49.7	50.1	50.5	50.6	49.8	50.2	49.9	49.9	49.7	49.8

	PCM21phr	OPCol 1	OPCol2	OPCol3	OPCol4	OPCol5	OPCol6	OPCol7	OPCol8	OPCol9	OPCol10
SiO_2	36.11	37.37	36.28	36.44	36.95	37.00	37.37	37.28	36.44	37.10	37.20
TiO_2	0.02	0.00	0.01	0.00	0.00	0.01	0.00	0.01	0.00	0.00	0.00
FeO	31.92	30.37	30.17	30.71	30.67	30.99	30.37	30.17	30.71	30.89	30.51
MnO	0.76	0.85	0.70	0.84	0.85	0.77	0.85	0.80	0.84	0.82	0.85
MgO	31.76	32.22	32.59	31.94	31.99	31.69	32.22	30.59	31.94	32.18	32.25
NiO	0.00	0.00	0.00	0.00	0.00	0.00	0.00	0.00	0.00	0.00	0.00
K_2O	0.00	0.00	0.14	0.04	0.02	0.00	0.00	0.14	0.04	0.00	0.00
Total	100.86	101.19	101.37	100.47	100.88	100.81	101.19	100.47	100.47	101.39	101.21
Ferrous Form											
Si	1.055	1.001	0.972	0.988	0.996	0.998	1.001	1.005	0.988	0.995	0.998
Al	0.001	0.001	0.027	0.004	0.000	0.001	0.001	0.028	0.004	0.001	0.001
Ti	0.001	0.000	0.000	0.000	0.000	0.000	0.000	0.000	0.000	0.000	0.000
Cr	0.000	0.000	0.000	0.000	0.000	0.000	0.000	0.000	0.000	0.000	0.001
Mg	0.928	1.287	1.302	1.291	1.285	1.275	1.287	1.230	1.291	1.287	1.289
Fe	0.933	0.680	0.676	0.696	0.691	0.699	0.680	0.680	0.696	0.693	0.684
Mn	0.022	0.019	0.016	0.019	0.019	0.018	0.019	0.018	0.019	0.019	0.019
Ni	0.000	0.000	0.000	0.000	0.000	0.000	0.000	0.000	0.000	0.000	0.000
Ca	0.000	0.009	0.012	0.009	0.009	0.009	0.009	0.012	0.009	0.010	0.009
Na	0.007	0.001	0.011	0.003	0.004	0.000	0.001	0.011	0.003	0.001	0.002
K	0.000	0.000	0.005	0.001	0.001	0.000	0.000	0.005	0.001	0.000	0.000
Sum	2.947	2.999	3.022	3.012	3.006	3.001	2.999	2.989	3.012	3.005	3.003
Fo (mol%)	49.9	65.4	65.8	65.0	65.0	64.6	65.4	64.4	65.0	65.0	65.3
Fa (mol%)	50.1	34.6	34.2	35.0	35.0	35.4	34.6	35.6	35.0	35.0	34.7

Oxide Phenocryst Data

	VB1-M3	VB1-M7	VB1-M10	VB1-M14	VB1-M15	VB1-M16	VB1-M17	VB1-M18	VB1-M23	VB1-M24	VB1-M25	VB1-M26	VB1-M27
TiO_2	3.50	7.82	6.17	7.90	8.05	8.14	8.02	7.62	8.30	8.00	8.29	8.11	8.28
Al_2O_3	10.45	4.47	4.45	4.14	4.47	4.71	4.55	4.39	4.98	4.85	4.82	4.63	4.59
Cr_2O_3	6.71	0.20	0.83	0.29	0.31	0.32	0.31	0.36	0.36	0.37	0.33	0.20	0.16
FeO	68.51	78.01	78.57	77.45	77.10	76.23	77.57	77.03	76.83	76.80	77.00	77.26	77.08
MnO	0.38	0.39	0.44	0.39	0.34	0.46	0.40	0.33	0.49	0.41	0.45	0.46	0.40
MgO	5.30	2.94	2.93	2.63	2.76	2.73	2.82	2.82	2.72	2.88	2.71	3.19	3.16
NiO	0.08	0.03	0.00	0.03	0.03	0.03	0.04	0.03	0.05	0.04	0.02	0.04	0.03
CaO	0.07	0.01	0.23	0.10	0.11	0.10	0.08	0.08	0.05	0.05	0.04	0.01	0.01
Total	95.16	94.07	93.83	93.14	93.33	93.05	93.98	92.98	94.01	93.56	93.82	94.07	93.93
Ferric Form (Fe corrected)													
Al	0.429	0.194	0.193	0.182	0.196	0.206	0.198	0.193	0.216	0.211	0.210	0.200	0.199
Ti	0.092	0.216	0.171	0.221	0.225	0.228	0.222	0.213	0.230	0.222	0.230	0.224	0.229
Cr	0.185	0.006	0.024	0.008	0.009	0.009	0.009	0.011	0.010	0.011	0.010	0.006	0.005
Fe3+	1.198	1.357	1.430	1.356	1.339	1.314	1.342	1.350	1.304	1.324	1.311	1.343	1.330
Mg	0.275	0.161	0.161	0.146	0.153	0.151	0.155	0.157	0.149	0.158	0.149	0.175	0.173
Fe2+	0.798	1.044	0.989	1.059	1.056	1.057	1.048	1.049	1.061	1.050	1.067	1.028	1.040
Mn	0.011	0.012	0.014	0.012	0.011	0.014	0.012	0.010	0.015	0.013	0.014	0.014	0.013
Ni	0.002	0.001	0.000	0.001	0.001	0.001	0.001	0.001	0.002	0.001	0.001	0.001	0.001
Ca	0.003	0.001	0.009	0.004	0.004	0.004	0.003	0.003	0.002	0.002	0.002	0.000	0.000
Sum	3.000	3.000	3.000	3.000	3.000	3.000	3.000	3.000	3.000	3.000	3.000	3.000	3.000
Usp (mol %)	25.6	13.4	14.0	12.1	12.6	12.5	12.9	13.0	12.3	13.1	12.3	14.5	14.3
Mt (mol %)	74.4	86.6	86.0	87.9	87.4	87.5	87.1	87.0	87.7	86.9	87.7	85.5	85.7

	VB1-M29	VB1-M31	VB1-M34	VB1-M48	VB1-M49	VB1-M53	PCM4-ox1	PCM4-ox2	PCM4-ox3	PCM4-ox4	PC17-ox5	PCf17-ox6	PCf17-ox7
TiO_2	8.02	8.11	7.01	6.59	6.97	6.42	7.70	7.79	7.81	7.78	7.51	7.47	7.69
Al_2O_3	4.50	4.07	4.33	6.08	5.13	5.68	5.20	5.15	5.34	5.35	4.93	4.99	5.10
Cr_2O_3	0.29	0.20	0.20	0.22	0.20	0.21	0.24	0.22	0.22	0.19	0.24	0.22	0.21
FeO	79.08	80.00	77.40	76.75	77.28	78.10	76.22	76.26	76.88	77.24	79.00	77.44	77.95
MnO	0.47	0.54	0.48	0.40	0.56	0.39	0.42	0.46	0.38	0.37	0.41	0.35	0.36
MgO	2.45	1.79	4.45	3.44	2.49	3.90	3.16	2.41	2.09	1.71	3.24	3.14	3.18
NiO	0.02	0.02	0.03	0.02	0.02	0.04	0.05	0.04	0.00	0.03	0.06	0.07	0.00
CaO	0.08	0.00	0.02	0.03	0.04	0.00	0.05	0.02	0.00	0.00	0.01	0.00	0.02
Total	95.07	94.88	95.55	93.65	92.80	94.83	93.17	92.50	92.84	92.77	95.53	93.82	94.65
Ferric Form (Fe corrected)													
Al	0.194	0.177	0.182	0.262	0.225	0.241	0.227	0.227	0.236	0.237	0.210	0.216	0.219
Ti	0.221	0.225	0.188	0.181	0.196	0.174	0.214	0.220	0.220	0.220	0.204	0.207	0.211
Cr	0.008	0.006	0.006	0.006	0.006	0.006	0.007	0.006	0.007	0.006	0.007	0.007	0.006
Fe3+	1.351	1.360	1.322	1.361	1.370	1.398	1.329	1.316	1.311	1.309	1.369	1.355	1.343
Mg	0.134	0.099	0.237	0.188	0.139	0.210	0.174	0.135	0.116	0.095	0.174	0.172	0.173
Fe 2+	1.067	1.110	0.989	0.983	1.041	0.955	1.028	1.074	1.094	1.116	1.017	1.026	1.032
Mn	0.015	0.017	0.014	0.012	0.018	0.012	0.013	0.015	0.012	0.012	0.013	0.011	0.011
Ni	0.001	0.001	0.001	0.001	0.001	0.001	0.002	0.001	0.000	0.001	0.002	0.002	0.000
Ca	0.003	0.000	0.001	0.001	0.002	0.000	0.002	0.001	0.000	0.000	0.000	0.000	0.001
Sum	3.000	3.000	3.000	3.000	3.000	3.000	3.000	3.000	3.000	3.000	3.000	3.000	3.000
Usp (mol %)	11.1	8.2	19.3	16.0	11.8	18.0	14.5	11.1	9.6	7.9	14.6	14.4	14.3
Mt (mol %)	88.9	91.8	80.7	84.0	88.2	82.0	85.5	88.9	90.4	92.1	85.4	85.6	85.7

	PCMmaf17-ox8	PCMmaf17-ox9	PCMmaf17-ox10	PCMmaf29-ox11	PCMmaf34-ox13	PCMmaf35-ox14	PCM2maf16-ox	PCM2maf18-ox	PCM2maf19-ox	PCM2maf20-ox	OPCmafox-1	OPCmafox-2	OPCmafox-3
TiO_2	7.43	7.75	9.68	7.71	7.54	7.75	7.59	7.27	7.22	7.32	8.79	9.03	8.96
Al_2O_3	5.00	5.15	4.81	5.20	5.21	5.31	5.19	5.24	4.93	5.37	5.21	5.29	5.13
Cr_2O_3	0.25	0.18	0.24	0.26	0.29	0.25	0.25	0.21	0.18	0.26	0.17	0.21	0.21
FeO	76.70	76.43	75.47	77.20	77.14	77.23	76.24	76.56	78.42	76.47	76.11	73.29	73.45
MnO	0.37	0.41	0.39	0.44	0.34	0.34	0.35	0.39	0.40	0.36	0.56	0.47	0.48
MgO	3.17	3.07	1.58	1.69	1.81	1.68	3.24	3.20	3.08	3.24	3.20	4.43	3.31
NiO	0.02	0.02	0.01	0.01	0.01	0.02	0.01	0.00	0.02	0.07	0.03	0.03	0.02
CaO	0.01	0.01	0.05	0.03	0.01	0.01	0.01	0.01	0.05	0.02	0.00	0.00	0.00
Total	93.04	93.13	92.36	92.64	92.47	92.72	93.02	92.99	94.42	93.22	94.29	92.87	91.75
Ferric Form (Fe corrected)													
Al	0.218	0.225	0.215	0.231	0.231	0.235	0.226	0.228	0.212	0.233	0.225	0.229	0.227
Ti	0.207	0.216	0.276	0.218	0.214	0.219	0.211	0.202	0.198	0.203	0.242	0.250	0.253
Cr	0.007	0.005	0.007	0.008	0.008	0.007	0.007	0.006	0.005	0.007	0.005	0.006	0.006
Fe3+	1.354	1.332	1.219	1.316	1.324	1.309	1.336	1.352	1.376	1.344	1.271	1.257	1.247
Mg	0.175	0.169	0.089	0.095	0.101	0.094	0.179	0.176	0.168	0.178	0.174	0.243	0.185
Fe2+	1.022	1.035	1.174	1.113	1.105	1.118	1.023	1.018	1.021	1.015	1.057	0.996	1.059
Mn	0.012	0.013	0.012	0.014	0.011	0.011	0.011	0.012	0.012	0.011	0.017	0.015	0.015
Ni	0.001	0.001	0.000	0.000	0.000	0.001	0.000	0.000	0.000	0.002	0.001	0.001	0.001
Ca	0.001	0.000	0.002	0.001	0.000	0.000	0.000	0.000	0.002	0.001	0.000	0.000	0.000
Sum	3.000	3.000	3.000	3.000	3.000	3.000	3.000	3.000	3.000	3.000	3.000	3.000	3.000
Usp (mol %)	14.6	14.0	7.0	7.8	8.4	7.8	14.9	14.8	14.1	14.9	14.2	19.6	14.9
Mt (mol %)	85.4	86.0	93.0	92.2	91.6	92.2	85.1	85.2	85.9	85.1	85.8	80.4	85.1

	OPCmafox-4	OPCmafox-5	OPCmafox-7	OPCmafox-8	OPCmafox-9	OPCmafox-10	OPCmafox-11	OPCmafox-12	OPCmafox-14	OPCmafox-15	OPCmafox-16
TiO_2	9.01	9.04	7.27	11.59	8.14	8.19	6.59	8.66	9.04	11.99	8.57
Al_2O_3	5.21	5.98	4.71	5.42	3.89	6.26	6.17	4.86	4.90	5.27	5.11
Cr_2O_3	0.17	0.00	0.17	0.17	0.16	0.16	0.17	0.14	0.16	0.15	0.00
FeO	73.17	73.56	76.34	71.83	77.06	73.30	73.90	74.12	74.57	71.53	74.67
MnO	0.50	1.15	0.46	0.41	0.39	0.36	0.49	0.53	0.35	0.44	0.62
MgO	3.35	3.13	3.03	3.22	2.59	3.10	4.71	3.11	3.09	3.31	3.11
NiO	0.03	0.00	0.02	0.03	0.03	0.01	0.02	0.05	0.03	0.03	0.00
CaO	0.00	0.00	0.00	0.00	0.00	0.00	0.00	0.00	0.00	0.00	0.00
Total	91.59	93.56	92.12	92.82	92.49	91.51	92.19	91.62	92.26	92.88	92.89
Ferric Form (Fe corrected)											
Al	0.231	0.259	0.208	0.238	0.173	0.277	0.267	0.216	0.216	0.231	0.223
Ti	0.255	0.250	0.205	0.324	0.230	0.231	0.182	0.245	0.255	0.335	0.239
Cr	0.005	0.000	0.005	0.005	0.005	0.005	0.005	0.004	0.005	0.004	0.000
Fe3+	1.243	1.191	1.368	1.098	1.345	1.247	1.354	1.278	1.260	1.082	1.239
Mg	0.188	0.171	0.169	0.179	0.145	0.173	0.258	0.175	0.172	0.184	0.172
Fe2+	1.056	1.068	1.025	1.137	1.081	1.051	0.914	1.058	1.075	1.143	1.078
Mn	0.016	0.036	0.015	0.013	0.012	0.011	0.015	0.017	0.011	0.014	0.019
Ni	0.001	0.000	0.001	0.001	0.001	0.000	0.001	0.001	0.001	0.001	0.000
Ca	0.000	0.000	0.000	0.000	0.000	0.000	0.000	0.000	0.000	0.000	0.000
Sum	3.000	3.000	3.000	3.000	3.000	3.000	3.000	3.000	3.000	3.000	3.000
Usp (mol %)	15.1	13.8	14.2	13.6	11.9	14.2	22.0	14.2	13.8	13.8	13.8
Mt (mol %)	84.9	86.2	85.8	86.4	88.1	85.8	78.0	85.8	86.2	86.2	86.2

	OPCmafox-17	OPCmafox-18	OPCmafox-19	OPCmafox-20	OPCmafox-21	OPCmafox-22	OPCmafox-23	OPCmafox-24	OPCmafox-25
TiO_2	7.95	8.14	8.41	8.23	8.57	8.41	8.46	8.45	8.55
Al_2O_3	4.75	4.68	4.70	4.81	4.92	4.81	4.82	4.79	4.97
Cr_2O_3	0.15	0.15	0.18	0.14	0.13	0.14	0.12	0.03	0.00
FeO	78.95	79.15	77.14	77.97	76.70	78.69	78.43	79.27	78.45
MnO	0.52	0.53	0.41	0.47	0.47	0.42	0.43	0.74	0.83
MgO	3.11	3.12	2.10	3.35	3.38	3.48	3.35	3.12	3.21
NiO	0.02	0.03	0.03	0.03	0.02	0.05	0.02	0.01	0.00
CaO	0.00	0.00	0.00	0.00	0.00	0.00	0.00	0.00	0.00
Total	95.54	95.94	93.09	95.13	94.31	96.07	95.73	96.83	96.75
Ferric Form (Fe corrected)									
Al	0.203	0.199	0.207	0.206	0.212	0.204	0.205	0.201	0.209
Ti	0.216	0.221	0.237	0.224	0.236	0.227	0.229	0.227	0.229
Cr	0.004	0.004	0.005	0.004	0.004	0.004	0.003	0.001	0.000
Fe3+	1.353	1.345	1.306	1.332	1.304	1.334	1.325	1.313	1.279
Mg	0.168	0.168	0.117	0.181	0.184	0.186	0.180	0.166	0.171
Fe2+	1.036	1.041	1.110	1.033	1.041	1.029	1.040	1.054	1.060
Mn	0.016	0.016	0.013	0.014	0.015	0.013	0.013	0.022	0.025
Ni	0.001	0.001	0.001	0.001	0.001	0.001	0.001	0.000	0.000
Ca	0.000	0.000	0.000	0.000	0.000	0.000	0.000	0.000	0.000
Sum	3.000	3.000	3.000	3.000	3.000	3.000	3.000	3.000	3.000
Usp (mol %)	13.9	13.9	9.6	14.9	15.0	15.3	14.8	13.6	13.9
Mt (mol %)	86.1	86.1	90.4	85.1	85.0	84.7	85.2	86.4	86.1

Appendix IV – Rocche Rosse lava flow mineral chemical data

Feldspar data

	058rrm-21	058rrm-23	058r-40	058r-41	058r-42	058r-43	058r-44	099r-pl1	099r-pl2	099r-pl3	099r-pl4	099pl-13
SiO_2	60.43	59.05	59.63	61.12	60.35	64.90	64.59	61.20	61.58	66.09	66.51	66.30
TiO_2	0.00	0.01	0.06	0.07	0.04	0.04	0.04	0.01	0.06	0.01	0.01	0.03
Al_2O_3	24.70	24.98	24.86	23.83	23.79	19.29	19.21	24.12	24.64	19.12	19.35	19.20
FeO	0.66	0.80	0.56	0.53	0.63	0.36	0.35	0.29	0.28	0.13	0.14	0.15
MnO	0.01	0.01	0.00	0.00	0.01	0.00	0.02	0.00	0.00	0.04	0.00	0.00
MgO	0.01	0.03	0.03	0.01	0.01	0.00	0.00	0.01	0.02	0.00	0.00	0.01
CaO	6.64	6.93	6.46	5.86	5.91	0.87	0.87	6.17	6.12	1.55	0.46	0.69
Na_2O	7.47	5.96	6.64	7.05	6.56	4.21	4.31	7.09	7.08	3.62	4.07	3.88
K_2O	0.91	2.52	1.50	1.78	1.81	9.88	9.85	1.60	1.59	10.90	10.51	10.83
Total	100.84	100.29	99.74	100.25	99.11	99.55	99.24	100.49	101.37	101.46	101.05	101.09
Structural formula based on 8 oxygens (ferrous)												
Si	2.685	2.657	2.678	2.729	2.724	2.957	2.954	2.723	2.714	2.966	2.981	2.977
Al	1.293	1.325	1.316	1.254	1.266	1.036	1.036	1.265	1.280	1.011	1.022	1.016
Ti	0.000	0.000	0.002	0.002	0.001	0.001	0.001	0.000	0.002	0.000	0.000	0.001
Mg	0.001	0.002	0.002	0.001	0.001	0.000	0.000	0.001	0.001	0.000	0.000	0.001
Fe	0.024	0.030	0.021	0.020	0.024	0.014	0.013	0.011	0.010	0.005	0.005	0.006
Mn	0.000	0.000	0.000	0.000	0.000	0.000	0.001	0.000	0.000	0.002	0.000	0.000
Ca	0.316	0.334	0.311	0.280	0.286	0.042	0.043	0.294	0.289	0.075	0.022	0.033
Na	0.644	0.520	0.578	0.610	0.574	0.372	0.382	0.612	0.605	0.315	0.354	0.338
K	0.051	0.144	0.086	0.101	0.104	0.574	0.575	0.091	0.089	0.624	0.601	0.620
Sum	5.015	5.013	4.994	4.998	4.981	4.997	5.005	4.996	4.991	4.998	4.985	4.993
An (mol%)	31.2	33.5	31.9	28.3	29.6	4.3	4.3	29.5	29.4	7.4	2.3	3.3
Ab (mol%)	63.7	52.1	59.3	61.5	59.5	37.6	38.2	61.4	61.5	31.1	36.2	34.1
Or (mol%)	5.1	14.5	8.8	10.2	10.8	58.1	57.5	9.1	9.1	61.6	61.5	62.6

	099rrm-pl4	099-pl-13	099-pl-15	099rrm-fsp1	139rrm-fsp1	139rrm-fsp2	139rrm-fsp3	139-fsp4	139-fsp5	139-fsp6	099-22
SiO_2	65.51	66.30	65.10	66.22	66.61	65.47	65.65	66.02	65.90	65.96	65.24
TiO_2	0.01	0.03	0.07	0.00	0.01	0.02	0.03	0.00	0.02	0.08	0.06
Al_2O_3	19.35	19.23	19.50	19.29	19.06	19.45	19.18	19.36	19.28	19.59	21.28
FeO	0.14	0.15	0.14	0.13	0.11	0.16	0.13	0.14	0.12	0.15	0.36
MnO	0.00	0.00	0.00	0.04	0.00	0.00	0.01	0.00	0.00	0.00	0.00
MgO	0.00	0.01	0.00	0.00	0.00	0.00	0.00	0.00	0.00	0.00	0.00
CaO	0.46	0.70	0.63	0.61	0.36	0.60	0.45	0.59	0.56	0.53	2.53
Na_2O	4.07	3.88	4.00	4.32	3.84	3.90	3.69	3.82	3.90	3.88	6.55
K_2O	10.52	10.84	10.71	10.29	11.29	10.68	11.19	10.84	10.80	10.92	5.90
Total	100.06	101.14	100.14	100.89	101.27	100.28	100.33	100.77	100.58	101.12	101.95
Structural formula based on 8 oxygens (ferrous)											
Si	2.969	2.976	2.955	2.975	2.988	2.964	2.975	2.973	2.974	2.963	2.878
Al	1.033	1.017	1.043	1.021	1.008	1.038	1.024	1.028	1.025	1.037	1.106
Ti	0.000	0.001	0.002	0.000	0.000	0.001	0.001	0.000	0.001	0.003	0.002
Mg	0.000	0.001	0.000	0.000	0.000	0.000	0.000	0.000	0.000	0.000	0.000
Fe	0.005	0.006	0.005	0.005	0.004	0.006	0.005	0.005	0.005	0.006	0.013
Mn	0.000	0.000	0.000	0.001	0.000	0.000	0.000	0.000	0.000	0.000	0.000
Ca	0.022	0.033	0.031	0.029	0.017	0.029	0.022	0.029	0.027	0.026	0.120
Na	0.358	0.338	0.352	0.376	0.334	0.342	0.324	0.333	0.341	0.338	0.560
K	0.608	0.621	0.620	0.590	0.646	0.617	0.647	0.623	0.622	0.626	0.332
Sum	4.997	4.993	5.008	4.997	4.998	4.996	4.998	4.991	4.994	4.998	5.013
An (mol%)	2.2%	3.4%	3.1%	2.9%	1.7%	2.9%	2.2%	2.9%	2.7%	2.6%	11.8%
Ab (mol%)	36.2%	34.1%	35.1%	37.8%	33.5%	34.6%	32.7%	33.8%	34.5%	34.2%	55.4%
Or (mol%)	61.5%	62.6%	61.8%	59.3%	64.8%	62.4%	65.1%	63.2%	62.8%	63.2%	32.8%

	139rfsp4	139rfsp5	139rfsp6	139rfsp-2
SiO_2	66.01	65.9	65.96	60.84
TiO_2	0.00	0.02	0.08	0.15
Al_2O_3	19.36	19.28	19.59	22.58
FeO	0.14	0.12	0.15	0.95
MnO	0.00	0.00	0.00	0.02
MgO	0.00	0.00	0.00	0.32
CaO	0.59	0.56	0.53	5.38
Na_2O	3.82	3.9	3.88	6.77
K_2O	10.84	10.8	10.92	3.04
Total	100.77	100.58	101.11	100.05
Structural formula based on 8 oxygens (ferrous)				
Si	2.973	2.974	2.963	2.744
Al	1.028	1.025	1.037	1.200
Ti	0.000	0.001	0.003	0.005
Mg	0.000	0.000	0.000	0.022
Fe	0.005	0.005	0.006	0.036
Mn	0.000	0.000	0.000	0.001
Ca	0.028	0.027	0.026	0.260
Na	0.334	0.341	0.338	0.592
K	0.623	0.622	0.626	0.175
Sum	4.991	4.994	4.998	5.034
An (mol%)	2.9	2.7	2.6	25.3
Ab (mol%)	33.9	34.5	34.2	57.6
Or (mol%)	63.2	62.8	63.3	17.0

Feldspar microlitic groundmass (from mafic enclaves) data

	099rpl8gm	099rpl9gm	099rpl10gm	139rfsp4gm	139rfsp9gm	139rfsp10gm
SiO_2	66.1	64.57	64.62	61.46	64.77	64.76
TiO_2	0.04	0.06	0.08	0.20	0.05	0.00
Al_2O_3	20.36	20.32	19.59	19.78	19.64	19.49
FeO	0.24	0.41	0.59	2.78	1.19	0.44
MnO	b.d	0.01	0.02	0.04	0.02	0.01
MgO	b.d	b.d	0.10	0.35	0.07	0.02
CaO	1.38	1.63	1.41	1.57	1.08	1.78
Na_2O	5.75	5.38	5.28	4.84	4.44	4.64
K_2O	7.42	7.66	7.97	8.28	9.41	9.14
Total	101.29	100.04	99.66	99.3	100.67	100.28
Structural formula based on 8 oxygens (ferrous)						
Si	2.934	2.913	2.931	2.847	2.929	2.933
Al	1.065	1.080	1.047	1.080	1.047	1.040
Ti	0.001	0.002	0.003	0.007	0.002	0.000
Mg	0.000	0.000	0.007	0.024	0.005	0.001
Fe	0.009	0.015	0.022	0.108	0.045	0.017
Mn	0.000	0.000	0.001	0.002	0.001	0.000
Ca	0.066	0.079	0.069	0.078	0.052	0.086
Na	0.495	0.471	0.464	0.435	0.389	0.407
K	0.420	0.441	0.461	0.489	0.543	0.528
Sum	4.990	5.001	5.005	5.069	5.012	5.014
An (mol%)	6.7	8.0	6.9	7.8	5.3	8.5
Ab (mol%)	50.5	47.5	46.7	43.4	39.5	39.9
Or (mol%)	42.8	44.5	46.4	48.8	55.1	51.7

Appendix V - Standard oxide values and average microprobe oxide values from this study for VG-568 and KN-18 natural high-silica glass standards

	Standard VG-568	Standard KN-18	VG-568 (measured here**)	KN-18 (measured here***)	Standard deviation VG-568	Standard deviation KN-18
SiO_2	76.71	74.6	76.64	74.63	0.05	0.02
TiO_2	0.12	0.18	0.06	0.16	0.04	0.01
Al_2O_3	12.06	10.53	12.32	10.67	0.18	0.10
FeO*	1.24	3.45	1.1	3.57	0.10	0.08
MnO	0.03	0.01	0.02	0.05	0.01	0.03
MgO	0.1	0.06	0.02	0	0.06	0.04
CaO	0.5	0.15	0.44	0.1	0.04	0.04
Na_2O	3.75	5.68	4.01	5.68	0.18	0.00
K_2O	4.89	4.39	4.94	4.51	0.04	0.08
P_2O_5	< 0.01	< 0.01	b.d	b.d	-	-

*** Based on an average of 3 runs*

**** Based on an average of 2 runs*

Appendix VI – Literature examples of Raman spectral response to glass and minerals

(a.u = arbitrary units)

Glass

(i) Libyan Desert Glass (Clayton and Spencer, 1934; Faulques et al., 2001)

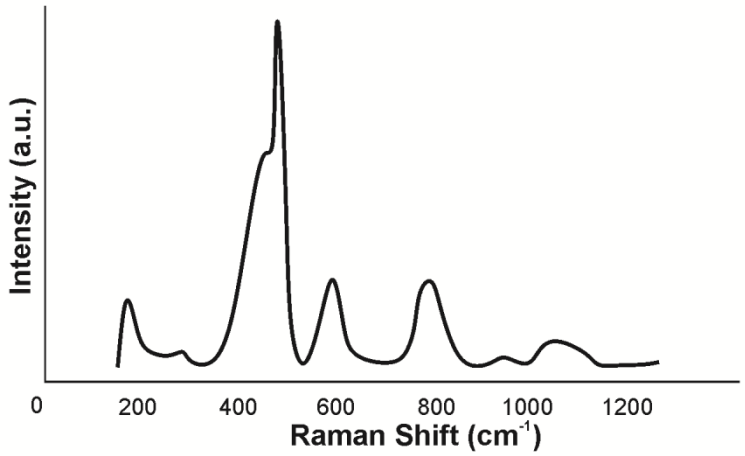

(ii) Iceland obsidian (source undefined) (Zotov, 2003)

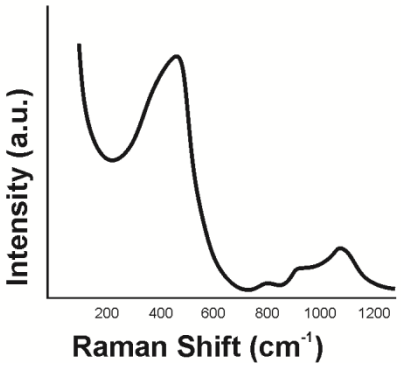

(iii) Lipari obsidian (source undefined) (Bellot-Gurlet et al., 2004)

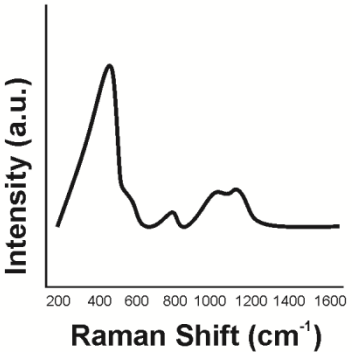

(i) Orthoclase peaks
(after Coombs, 1954; Harris et al., 1989;
Freeman et al., 2010)

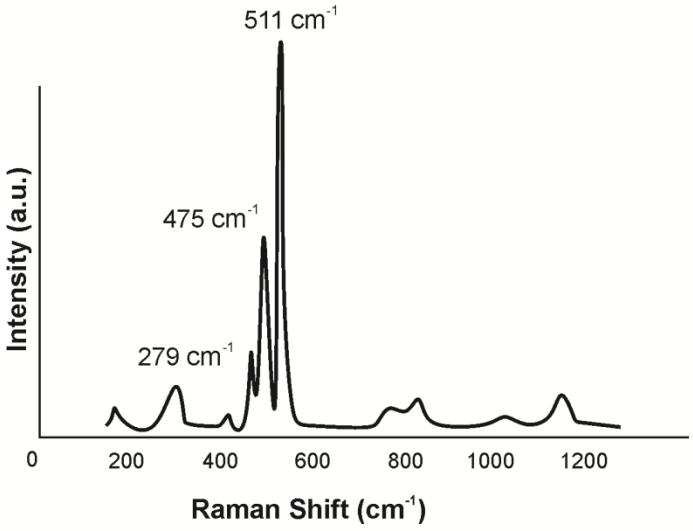

(ii) SiO_2 and plagioclase peaks
(after Gage and Farwell, 1981)

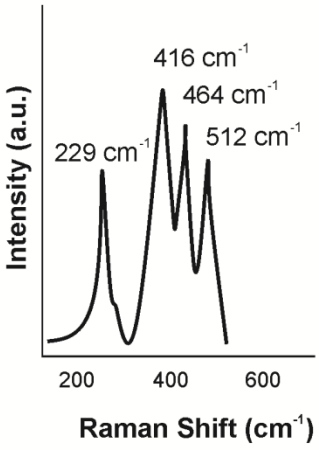

(iii) Magnetite peaks
(after Shebanova and Lazor, 2003;
Kelloway et al., 2010)

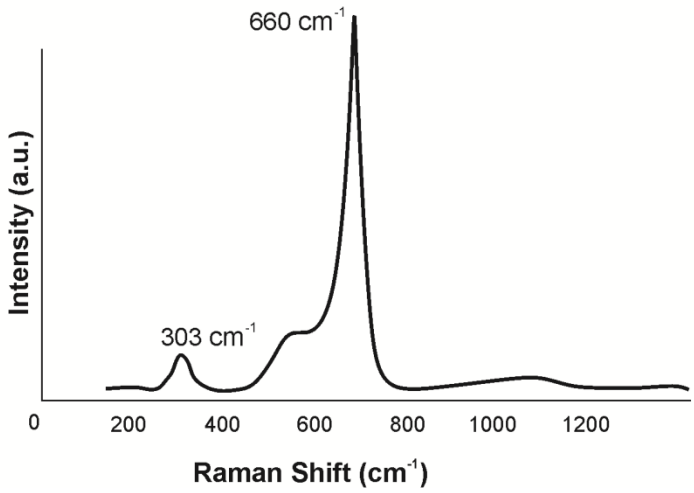

Appendix VII – Individual Raman Spectra Results

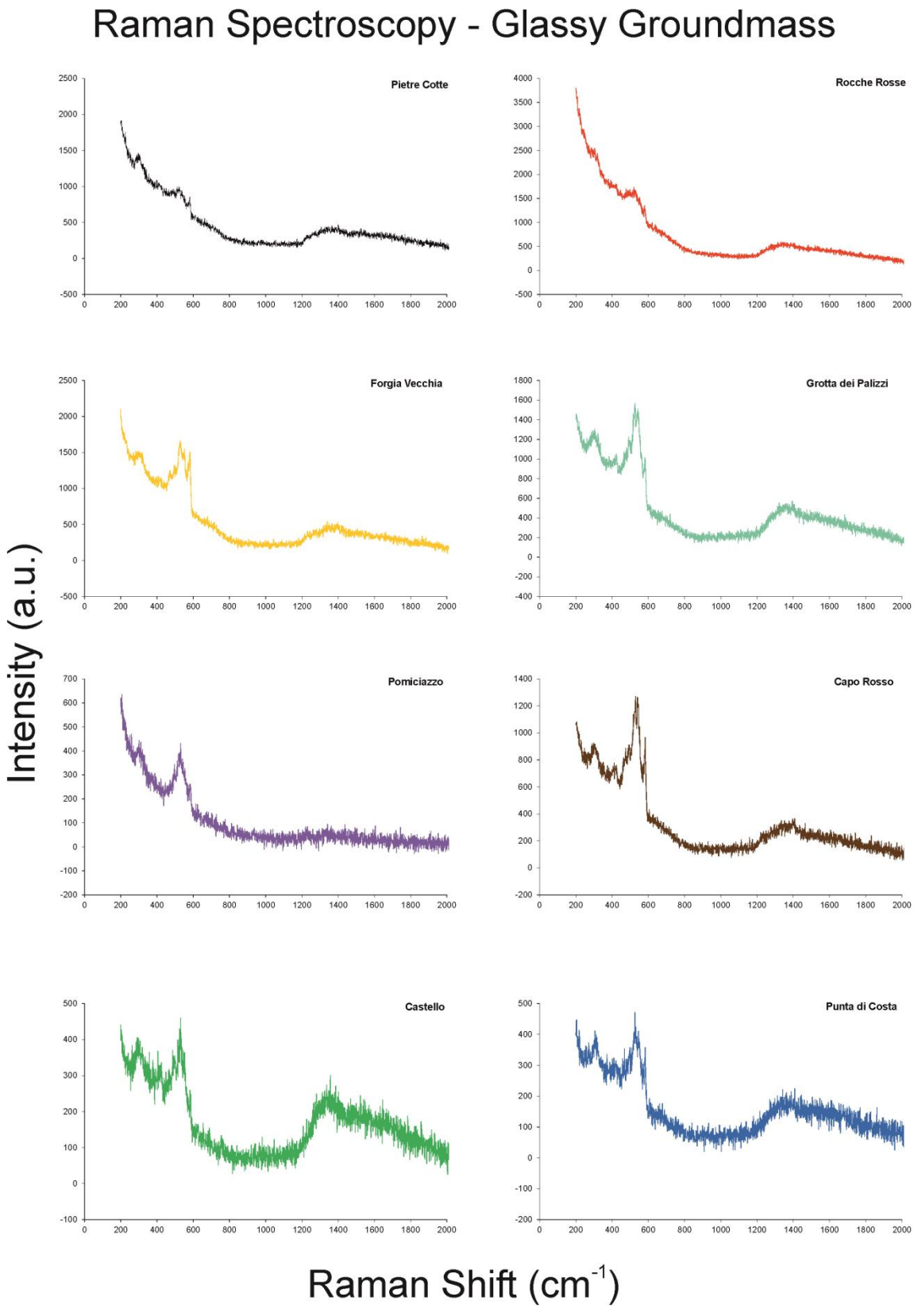

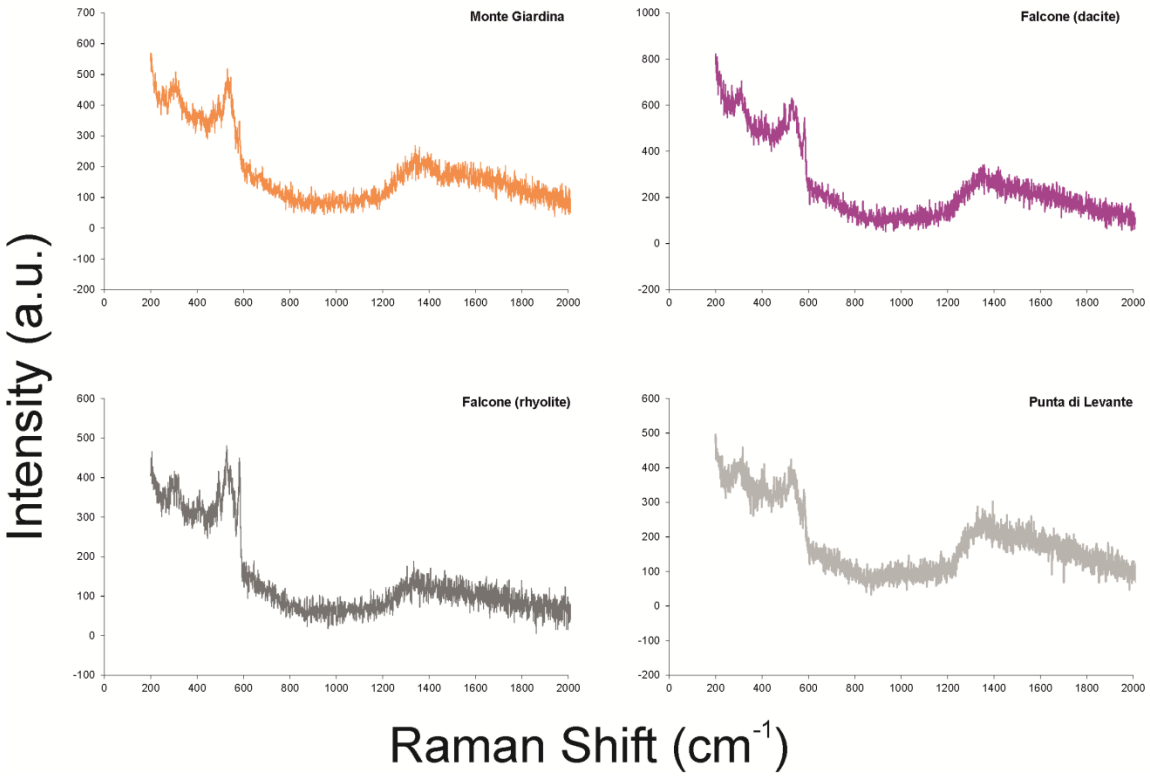
Monte Giardina
Falcone (dacite)
Falcone (rhyolite)
Punta di Levante
Intensity (a.u.)
Raman Shift (cm-1)

Raman Spectroscopy - Spherulites

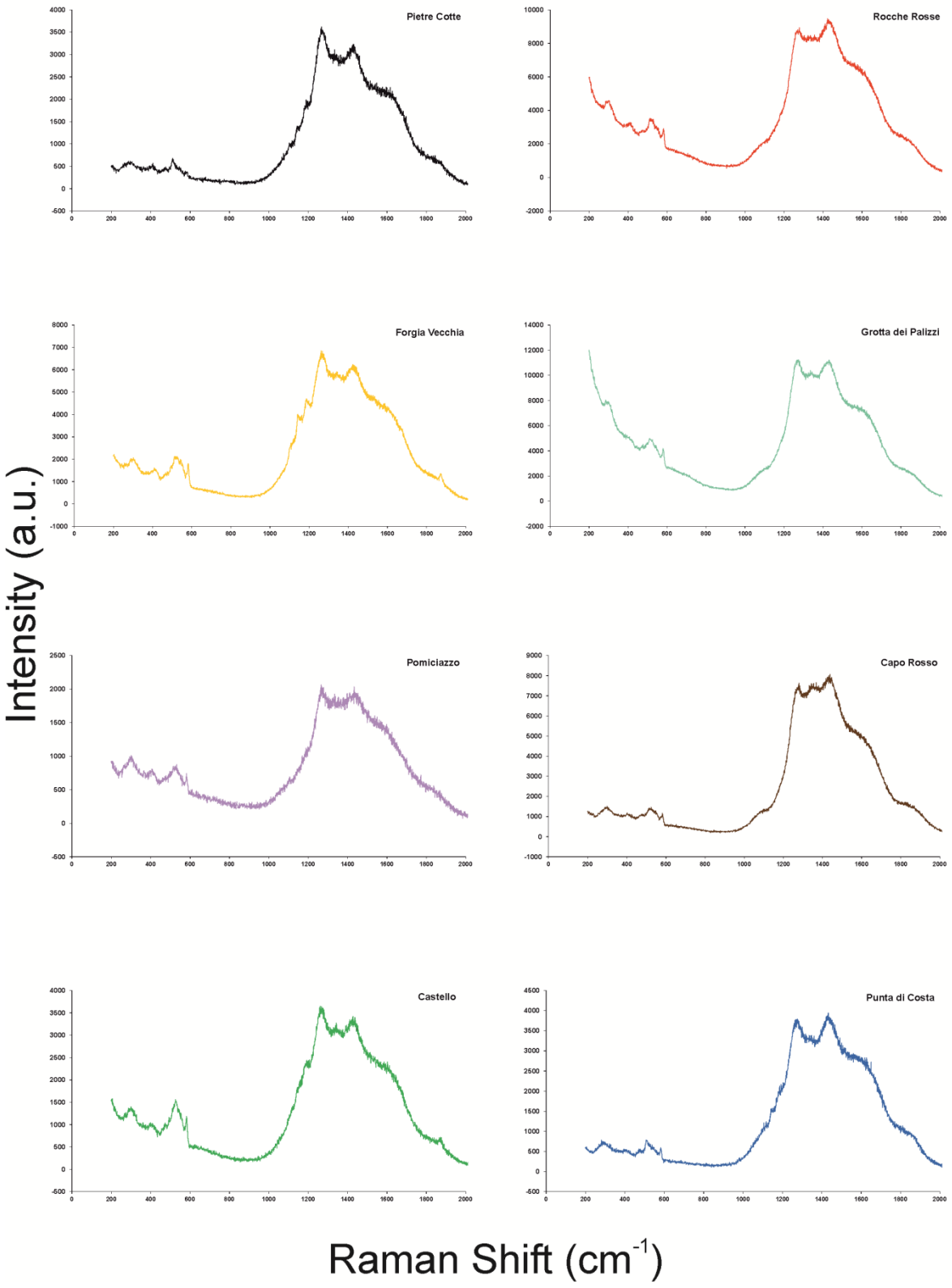

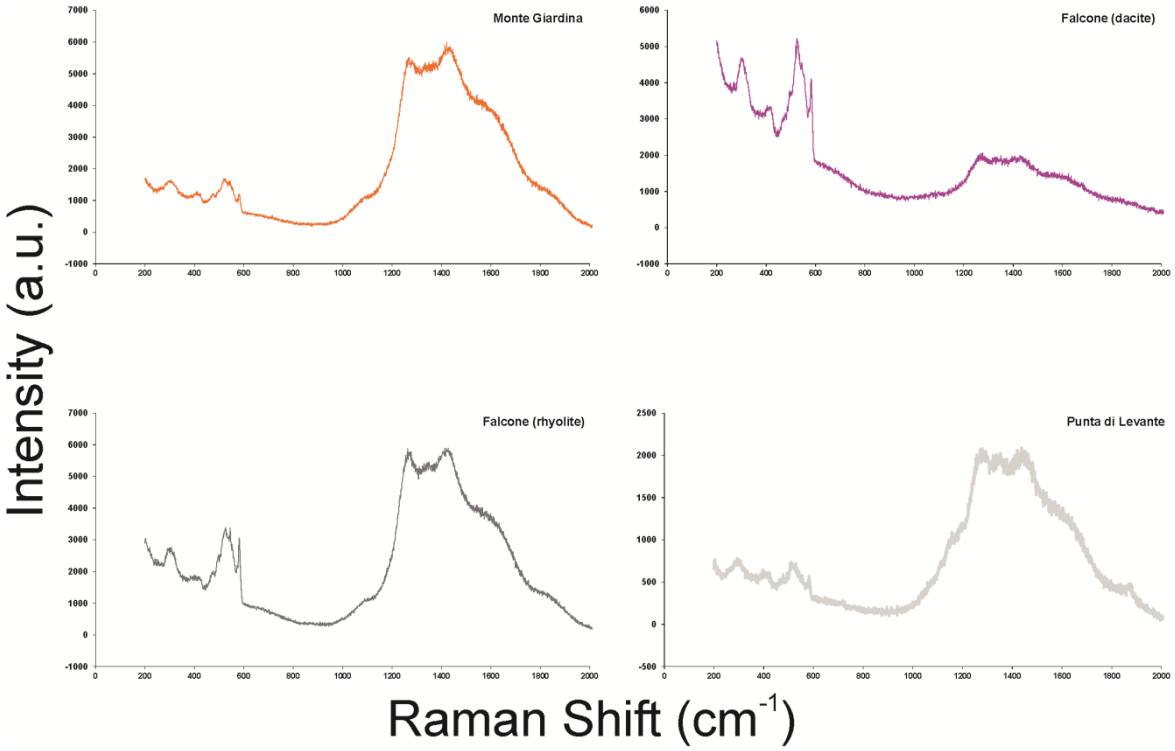
Monte Giardina
Falcone (dacite)
Falcone (rhyolite)
Punta di Levante
Intensity (a.u.)
Raman Shift (cm-1)

Raman Spectroscopy - Brown Reaction Zone

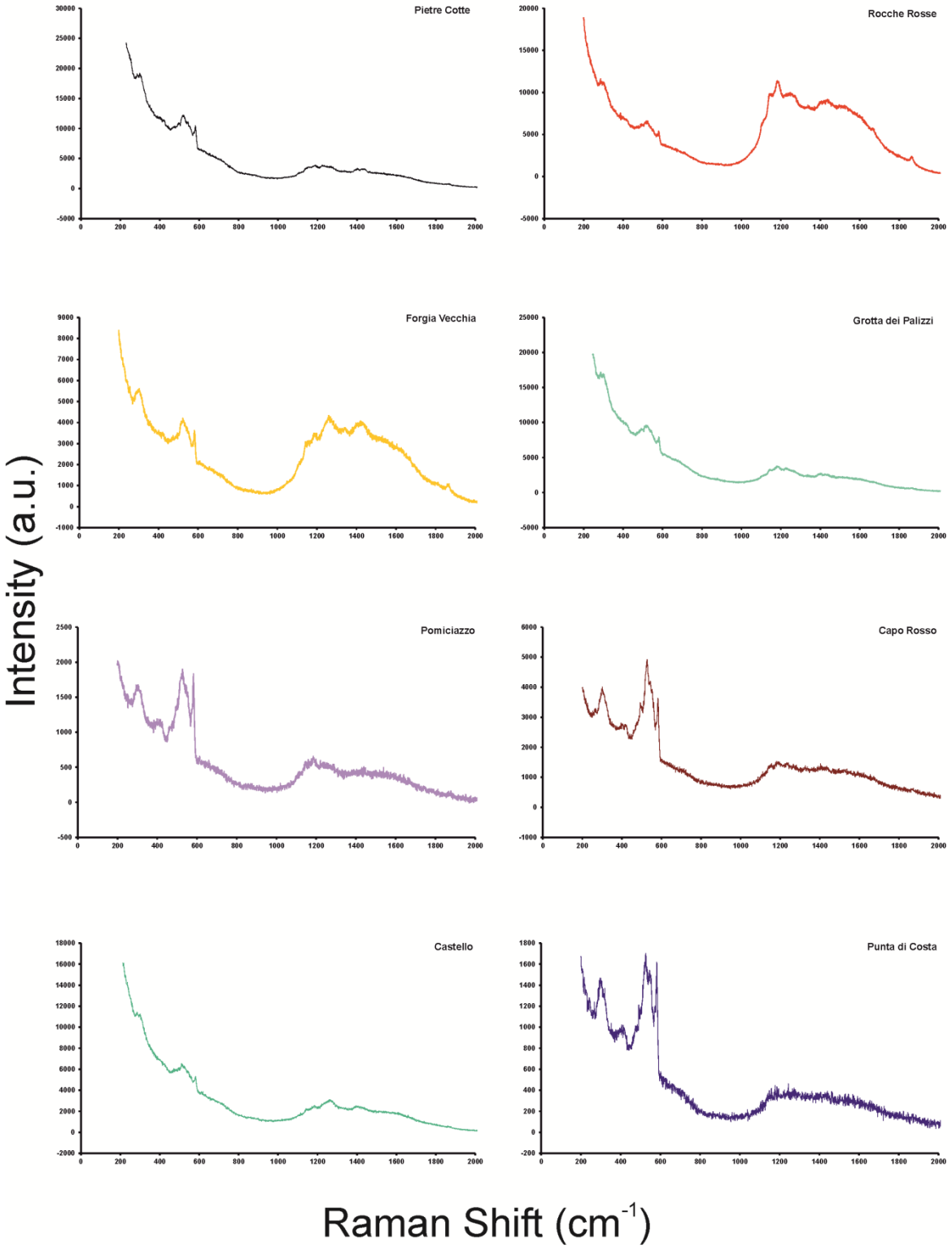

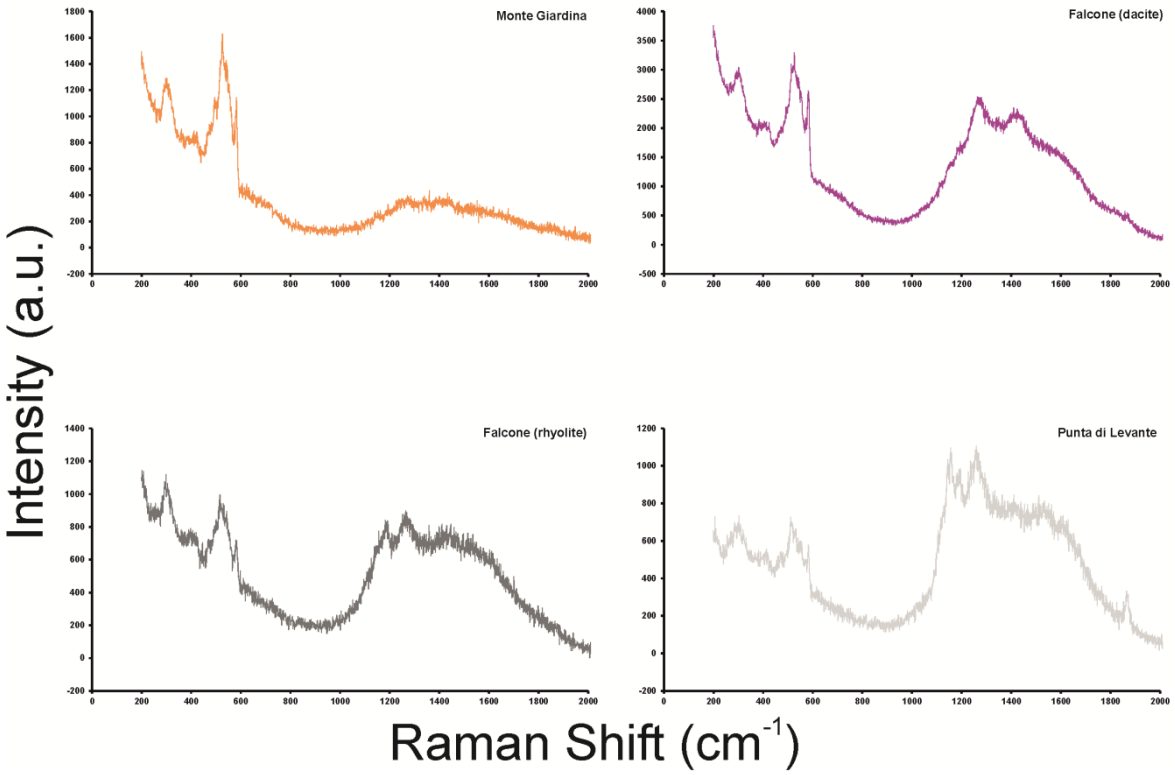
Monte Giardina
Falcone (dacite)
Falcone (rhyolite)
Punta di Levante
Intensity (a.u.)
Raman Shift (cm-1)

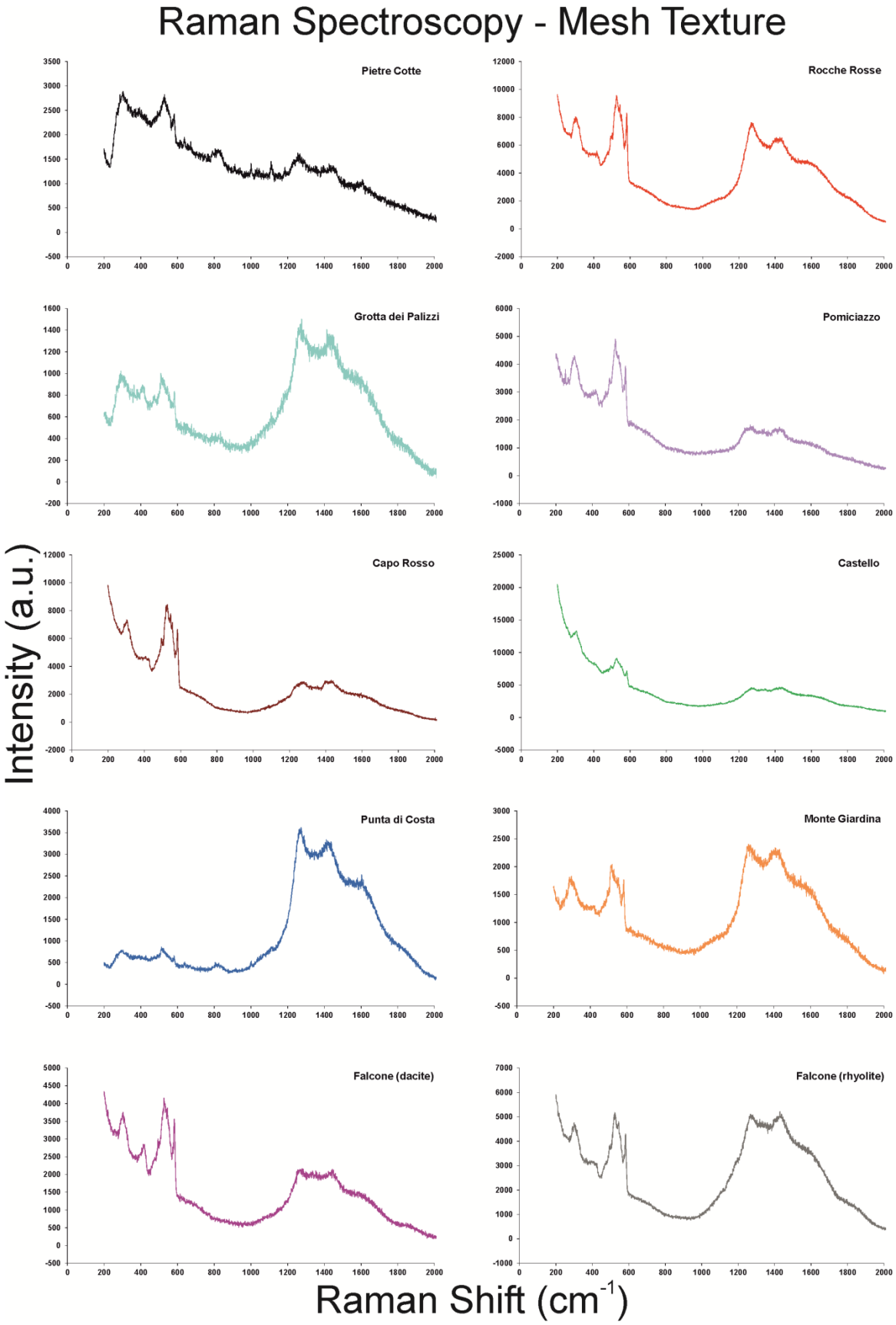
Raman Spectroscopy - Mesh Texture
Pietre Cotte
Rocche Rosse
Grotta dei Palizzi
Pomiciazzo
Capo Rosso
Castello
Punta di Costa
Monte Giardina
Falcone (dacite)
Falcone (rhyolite)
Intensity (a.u.)
Raman Shift (cm-1)

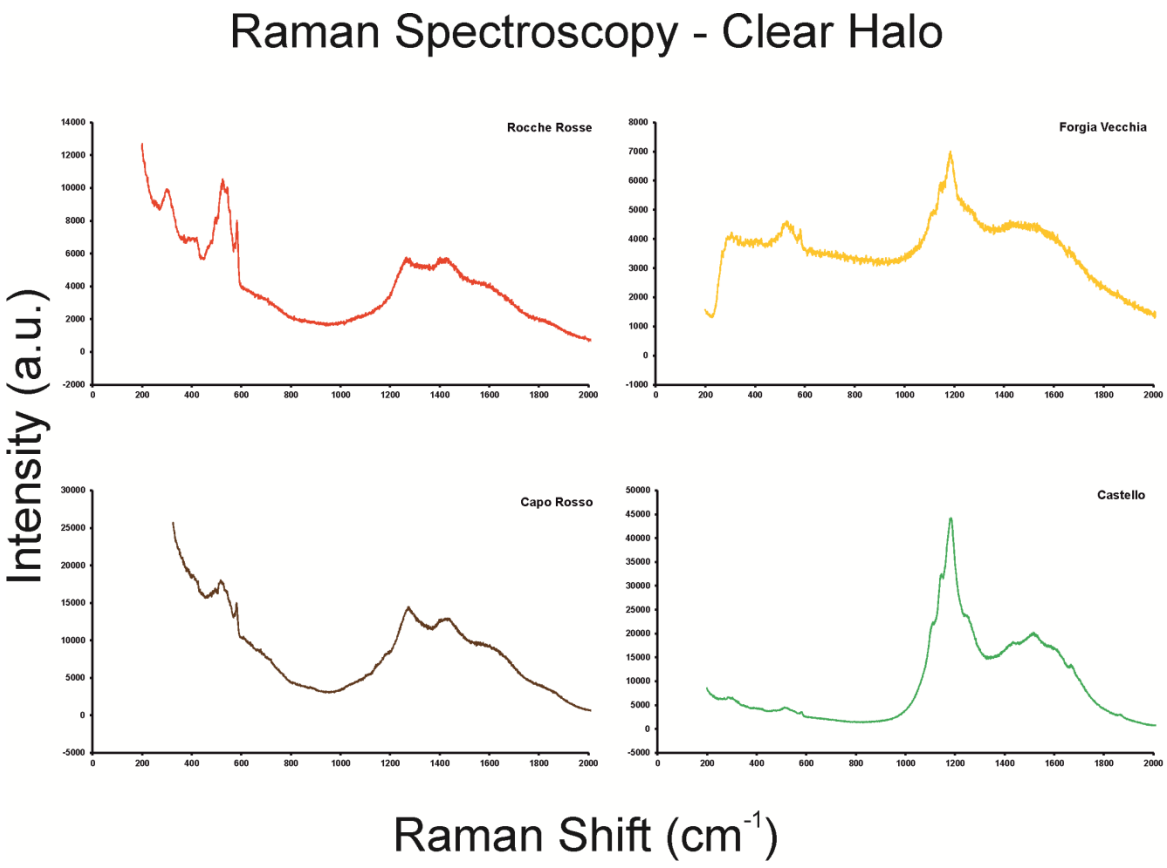
Raman Spectroscopy - Clear Halo
Rocche Rosse
Forgia Vecchia
Capo Rosso
Castello
Intensity (a.u.)
Raman Shift (cm-1)

Appendix VIII – Spherulite x-ray diffraction raw data - Pietre Cotte lava flow

Angle	R.Int	Angle	R.Int	Angle	R.Int	Angle	R.Int	Angle	R.Int	Angle	R.Int	Angle	R.Int	Angle	R.Int	Angle	R.Int	Angle	R.Int
20	203	22.05	142	24.1	152	26.15	132	28.2	108	30.25	114	32.3	93	34.35	96	36.4	87	38.45	84	40.5	69
20.05	182	22.1	167	24.15	130	26.2	131	28.25	145	30.3	124	32.35	88	34.4	94	36.45	78	38.5	69	40.55	71
20.1	188	22.15	155	24.2	121	26.25	135	28.3	117	30.35	133	32.4	97	34.45	89	36.5	80	38.55	73	40.6	68
20.15	207	22.2	141	24.25	161	26.3	139	28.35	121	30.4	132	32.45	101	34.5	108	36.55	77	38.6	76	40.65	73
20.2	175	22.25	165	24.3	130	26.35	118	28.4	141	30.45	103	32.5	97	34.55	102	36.6	85	38.65	81	40.7	86
20.25	185	22.3	167	24.35	122	26.4	140	28.45	135	30.5	111	32.55	86	34.6	105	36.65	82	38.7	99	40.75	78
20.3	200	22.35	156	24.4	130	26.45	136	28.5	142	30.55	119	32.6	97	34.65	95	36.7	76	38.75	78	40.8	71
20.35	194	22.4	161	24.45	147	26.5	124	28.55	117	30.6	107	32.65	108	34.7	88	36.75	81	38.8	67	40.85	88
20.4	188	22.45	169	24.5	127	26.55	132	28.6	127	30.65	109	32.7	105	34.75	93	36.8	72	38.85	67	40.9	83
20.45	183	22.5	178	24.55	140	26.6	132	28.65	124	30.7	117	32.75	101	34.8	107	36.85	83	38.9	79	40.95	62
20.5	177	22.55	131	24.6	140	26.65	145	28.7	116	30.75	101	32.8	110	34.85	96	36.9	91	38.95	68	41	73
20.55	187	22.6	151	24.65	118	26.7	132	28.75	139	30.8	116	32.85	89	34.9	93	36.95	75	39	76	41.05	75
20.6	200	22.65	138	24.7	131	26.75	145	28.8	130	30.85	114	32.9	94	34.95	97	37	87	39.05	71	41.1	76
20.65	186	22.7	155	24.75	136	26.8	145	28.85	132	30.9	135	32.95	106	35	110	37.05	80	39.1	78	41.15	86
20.7	189	22.75	173	24.8	140	26.85	140	28.9	118	30.95	117	33	91	35.05	86	37.1	81	39.15	70	41.2	84
20.75	196	22.8	169	24.85	142	26.9	155	28.95	131	31	108	33.05	110	35.1	98	37.15	77	39.2	60	41.25	78
20.8	185	22.85	135	24.9	131	26.95	162	29	114	31.05	118	33.1	98	35.15	86	37.2	80	39.25	77	41.3	86
20.85	163	22.9	158	24.95	143	27	163	29.05	111	31.1	108	33.15	101	35.2	90	37.25	73	39.3	77	41.35	84
20.9	193	22.95	149	25	135	27.05	167	29.1	134	31.15	116	33.2	94	35.25	94	37.3	72	39.35	83	41.4	83
20.95	174	23	171	25.05	137	27.1	143	29.15	142	31.2	124	33.25	108	35.3	106	37.35	84	39.4	71	41.45	68
21	158	23.05	204	25.1	133	27.15	152	29.2	120	31.25	109	33.3	98	35.35	84	37.4	82	39.45	72	41.5	70
21.05	146	23.1	157	25.15	129	27.2	173	29.25	125	31.3	117	33.35	84	35.4	90	37.45	83	39.5	79	41.55	77
21.1	182	23.15	140	25.2	146	27.25	141	29.3	129	31.35	107	33.4	85	35.45	92	37.5	80	39.55	77	41.6	79
21.15	181	23.2	142	25.25	146	27.3	151	29.35	178	31.4	101	33.45	89	35.5	92	37.55	67	39.6	71	41.65	87
21.2	171	23.25	166	25.3	138	27.35	176	29.4	134	31.45	113	33.5	90	35.55	78	37.6	78	39.65	71	41.7	73
21.25	191	23.3	170	25.35	149	27.4	145	29.45	152	31.5	104	33.55	91	35.6	85	37.65	77	39.7	71	41.75	86
21.3	179	23.35	151	25.4	135	27.45	143	29.5	119	31.55	120	33.6	77	35.65	92	37.7	79	39.75	72	41.8	81
21.35	170	23.4	146	25.45	151	27.5	142	29.55	130	31.6	98	33.65	93	35.7	89	37.75	81	39.8	72	41.85	70
21.4	185	23.45	162	25.5	147	27.55	160	29.6	149	31.65	107	33.7	104	35.75	84	37.8	71	39.85	72	41.9	61
21.45	171	23.5	164	25.55	164	27.6	152	29.65	132	31.7	134	33.75	82	35.8	92	37.85	82	39.9	78	41.95	83
21.5	189	23.55	152	25.6	134	27.65	126	29.7	139	31.75	121	33.8	97	35.85	76	37.9	81	39.95	64	42	63
21.55	160	23.6	103	25.65	137	27.7	126	29.75	131	31.8	98	33.85	99	35.9	72	37.95	83	40	89	42.05	65
21.6	169	23.65	114	25.7	127	27.75	141	29.8	108	31.85	101	33.9	100	35.95	95	38	72	40.05	79	42.1	78
21.65	163	23.7	150	25.75	133	27.8	143	29.85	124	31.9	126	33.95	93	36	80	38.05	64	40.1	74	42.15	74
21.7	189	23.75	136	25.8	142	27.85	139	29.9	125	31.95	90	34	80	36.05	92	38.1	73	40.15	85	42.2	75
21.75	174	23.8	152	25.85	153	27.9	115	29.95	131	32	112	34.05	102	36.1	90	38.15	78	40.2	77	42.25	69
21.8	165	23.85	140	25.9	131	27.95	119	30	171	32.05	107	34.1	95	36.15	86	38.2	67	40.25	72	42.3	62
21.85	149	23.9	156	25.95	129	28	141	30.05	133	32.1	102	34.15	79	36.2	80	38.25	67	40.3	71	42.35	69
21.9	154	23.95	138	26	131	28.05	137	30.1	126	32.15	98	34.2	107	36.25	93	38.3	83	40.35	87	42.4	57
21.95	134	24	136	26.05	136	28.1	129	30.15	119	32.2	81	34.25	92	36.3	91	38.35	77	40.4	63	42.45	80
22	153	24.05	145	26.1	125	28.15	117	30.2	117	32.25	89	34.3	94	36.35	82	38.4	87	40.45	82	42.5	80

Angle	R.Int	Angle	R.Int	Angle	R.Int	Angle	R.Int	Angle	R.Int	Angle	R.Int	Angle	R.Int	Angle	R.Int	Angle	R.Int	Angle	R.Int
42.55	66	44.6	73	46.65	63	48.7	75	50.75	59	52.8	66	54.85	63	56.9	61	58.95	63	61	64	63.05	70
42.6	80	44.65	76	46.7	66	48.75	70	50.8	57	52.85	59	54.9	73	56.95	65	59	64	61.05	55	63.1	63
42.65	72	44.7	74	46.75	58	48.8	66	50.85	72	52.9	69	54.95	70	57	67	59.05	75	61.1	71	63.15	65
42.7	65	44.75	75	46.8	74	48.85	69	50.9	63	52.95	67	55	56	57.05	63	59.1	67	61.15	67	63.2	61
42.75	66	44.8	70	46.85	60	48.9	68	50.95	69	53	62	55.05	71	57.1	59	59.15	59	61.2	59	63.25	53
42.8	71	44.85	82	46.9	66	48.95	79	51	62	53.05	64	55.1	68	57.15	65	59.2	53	61.25	57	63.3	55
42.85	66	44.9	82	46.95	60	49	62	51.05	72	53.1	71	55.15	59	57.2	61	59.25	63	61.3	70	63.35	58
42.9	62	44.95	65	47	61	49.05	60	51.1	65	53.15	72	55.2	57	57.25	54	59.3	73	61.35	55	63.4	64
42.95	66	45	67	47.05	68	49.1	69	51.15	60	53.2	62	55.25	62	57.3	64	59.35	73	61.4	71	63.45	52
43	70	45.05	73	47.1	75	49.15	54	51.2	79	53.25	70	55.3	72	57.35	61	59.4	52	61.45	69	63.5	64
43.05	69	45.1	59	47.15	49	49.2	64	51.25	78	53.3	56	55.35	71	57.4	60	59.45	58	61.5	65	63.55	69
43.1	49	45.15	68	47.2	77	49.25	70	51.3	62	53.35	70	55.4	64	57.45	59	59.5	67	61.55	80	63.6	73
43.15	64	45.2	70	47.25	67	49.3	73	51.35	51	53.4	55	55.45	59	57.5	64	59.55	62	61.6	81	63.65	69
43.2	62	45.25	66	47.3	72	49.35	92	51.4	76	53.45	57	55.5	65	57.55	66	59.6	62	61.65	76	63.7	57
43.25	66	45.3	68	47.35	66	49.4	57	51.45	70	53.5	59	55.55	54	57.6	59	59.65	80	61.7	64	63.75	70
43.3	75	45.35	70	47.4	58	49.45	63	51.5	57	53.55	60	55.6	64	57.65	64	59.7	72	61.75	60	63.8	69
43.35	77	45.4	63	47.45	59	49.5	66	51.55	64	53.6	66	55.65	63	57.7	76	59.75	56	61.8	72	63.85	65
43.4	66	45.45	73	47.5	69	49.55	67	51.6	62	53.65	64	55.7	84	57.75	64	59.8	53	61.85	66	63.9	66
43.45	68	45.5	68	47.55	78	49.6	66	51.65	71	53.7	55	55.75	56	57.8	68	59.85	68	61.9	76	63.95	69
43.5	62	45.55	61	47.6	64	49.65	49	51.7	69	53.75	66	55.8	64	57.85	76	59.9	63	61.95	75	64	61
43.55	74	45.6	70	47.65	78	49.7	57	51.75	65	53.8	66	55.85	60	57.9	56	59.95	56	62	58	64.05	63
43.6	71	45.65	63	47.7	73	49.75	65	51.8	72	53.85	63	55.9	78	57.95	71	60	75	62.05	62	64.1	57
43.65	73	45.7	72	47.75	74	49.8	71	51.85	72	53.9	53	55.95	63	58	71	60.05	71	62.1	60	64.15	74
43.7	63	45.75	71	47.8	61	49.85	81	51.9	64	53.95	64	56	70	58.05	64	60.1	74	62.15	63	64.2	61
43.75	67	45.8	63	47.85	56	49.9	72	51.95	46	54	57	56.05	66	58.1	67	60.15	68	62.2	77	64.25	77
43.8	75	45.85	58	47.9	77	49.95	65	52	63	54.05	70	56.1	76	58.15	63	60.2	65	62.25	58	64.3	65
43.85	84	45.9	79	47.95	74	50	64	52.05	67	54.1	62	56.15	62	58.2	66	60.25	71	62.3	70	64.35	65
43.9	74	45.95	70	48	50	50.05	72	52.1	79	54.15	57	56.2	80	58.25	54	60.3	66	62.35	72	64.4	63
43.95	72	46	83	48.05	52	50.1	57	52.15	68	54.2	61	56.25	71	58.3	64	60.35	63	62.4	54	64.45	69
44	76	46.05	69	48.1	65	50.15	67	52.2	67	54.25	54	56.3	64	58.35	67	60.4	61	62.45	52	64.5	67
44.05	86	46.1	86	48.15	70	50.2	62	52.25	76	54.3	61	56.35	56	58.4	74	60.45	73	62.5	67	64.55	57
44.1	66	46.15	64	48.2	55	50.25	64	52.3	58	54.35	65	56.4	82	58.45	60	60.5	54	62.55	64	64.6	66
44.15	73	46.2	63	48.25	66	50.3	71	52.35	57	54.4	64	56.45	76	58.5	64	60.55	76	62.6	57	64.65	65
44.2	84	46.25	64	48.3	67	50.35	74	52.4	70	54.45	63	56.5	64	58.55	49	60.6	66	62.65	60	64.7	61
44.25	73	46.3	63	48.35	74	50.4	76	52.45	69	54.5	68	56.55	77	58.6	59	60.65	62	62.7	61	64.75	68
44.3	75	46.35	60	48.4	76	50.45	65	52.5	62	54.55	62	56.6	74	58.65	60	60.7	59	62.75	69	64.8	79
44.35	62	46.4	72	48.45	64	50.5	71	52.55	74	54.6	65	56.65	70	58.7	62	60.75	65	62.8	55	64.85	63
44.4	65	46.45	59	48.5	59	50.55	65	52.6	66	54.65	71	56.7	68	58.75	55	60.8	66	62.85	74	64.9	75
44.45	71	46.5	71	48.55	64	50.6	97	52.65	69	54.7	58	56.75	49	58.8	62	60.85	57	62.9	61	64.95	64
44.5	62	46.55	70	48.6	83	50.65	76	52.7	67	54.75	73	56.8	69	58.85	56	60.9	68	62.95	56	65	74
44.55	62	46.6	60	48.65	71	50.7	66	52.75	62	54.8	63	56.85	69	58.9	64	60.95	69	63	56	65.05	79

Angle	R.Int	Angle	R.Int	Angle	R.Int	Angle	R.Int	Angle	R.Int	Angle	R.Int	Angle	R.Int
65.1	74	67.3	67	69.5	67	71.7	72	73.9	73	76.1	53	78.3	55
65.15	61	67.35	59	69.55	59	71.75	62	73.95	67	76.15	65	78.35	63
65.2	69	67.4	72	69.6	72	71.8	80	74	65	76.2	58	78.4	53
65.25	62	67.45	64	69.65	68	71.85	56	74.05	59	76.25	65	78.45	53
65.3	75	67.5	64	69.7	60	71.9	60	74.1	53	76.3	64	78.5	57
65.35	74	67.55	57	69.75	73	71.95	63	74.15	54	76.35	57	78.55	55
65.4	62	67.6	62	69.8	71	72	68	74.2	74	76.4	53	78.6	54
65.45	62	67.65	72	69.85	78	72.05	68	74.25	59	76.45	51	78.65	57
65.5	57	67.7	53	69.9	67	72.1	69	74.3	63	76.5	51	78.7	59
65.55	64	67.75	64	69.95	68	72.15	54	74.35	74	76.55	51	78.75	45
65.6	77	67.8	61	70	65	72.2	50	74.4	54	76.6	53	78.8	62
65.65	60	67.85	58	70.05	59	72.25	80	74.45	57	76.65	50	78.85	72
65.7	76	67.9	68	70.1	58	72.3	59	74.5	63	76.7	60	78.9	49
65.75	59	67.95	56	70.15	70	72.35	71	74.55	77	76.75	65	78.95	61
65.8	62	68	67	70.2	62	72.4	64	74.6	67	76.8	74	79	69
65.85	63	68.05	56	70.25	62	72.45	55	74.65	80	76.85	64	79.05	68
65.9	64	68.1	65	70.3	53	72.5	54	74.7	59	76.9	54	79.1	60
65.95	67	68.15	59	70.35	70	72.55	61	74.75	62	76.95	61	79.15	53
66	68	68.2	55	70.4	53	72.6	68	74.8	61	77	58	79.2	76
66.05	64	68.25	65	70.45	64	72.65	70	74.85	55	77.05	57	79.25	76
66.1	66	68.3	67	70.5	67	72.7	63	74.9	69	77.1	73	79.3	58
66.15	55	68.35	59	70.55	78	72.75	69	74.95	68	77.15	56	79.35	52
66.2	74	68.4	59	70.6	60	72.8	61	75	72	77.2	59	79.4	56
66.25	61	68.45	67	70.65	62	72.85	64	75.05	77	77.25	59	79.45	64
66.3	58	68.5	59	70.7	61	72.9	58	75.1	72	77.3	77	79.5	68
66.35	53	68.55	54	70.75	75	72.95	58	75.15	59	77.35	56	79.55	59
66.4	59	68.6	64	70.8	73	73	60	75.2	65	77.4	62	79.6	63
66.45	67	68.65	59	70.85	65	73.05	65	75.25	61	77.45	76	79.65	75
66.5	70	68.7	66	70.9	56	73.1	61	75.3	57	77.5	64	79.7	64
66.55	70	68.75	62	70.95	66	73.15	68	75.35	85	77.55	61	79.75	67
66.6	54	68.8	60	71	64	73.2	64	75.4	65	77.6	59	79.8	59
66.65	52	68.85	63	71.05	67	73.25	54	75.45	53	77.65	58	79.85	58
66.7	65	68.9	72	71.1	64	73.3	53	75.5	67	77.7	50	79.9	60
66.75	92	68.95	66	71.15	49	73.35	61	75.55	63	77.75	52	79.95	55
66.8	65	69	72	71.2	55	73.4	55	75.6	58	77.8	66	80	58
66.85	67	69.05	57	71.25	50	73.45	73	75.65	65	77.85	52		
66.9	54	69.1	74	71.3	66	73.5	54	75.7	65	77.9	63		
66.95	59	69.15	72	71.35	55	73.55	66	75.75	66	77.95	58		
67	62	69.2	60	71.4	57	73.6	62	75.8	61	78	58		
67.05	61	69.25	56	71.45	55	73.65	57	75.85	80	78.05	59		
67.1	50	69.3	68	71.5	58	73.7	68	75.9	65	78.1	74		
67.15	68	69.35	69	71.55	48	73.75	72	75.95	68	78.15	53		
67.2	64	69.4	68	71.6	61	73.8	47	76	68	78.2	64		
67.25	43	69.45	72	71.65	59	73.85	67	76.05	65	78.25	63		

Rocche Rosse lava flow

Angle	R.Int	Angle	R.Int	Angle	R.Int	Angle	R.Int	Angle	R.Int	Angle	R.Int	Angle	R.Int	Angle	R.Int	Angle	R.Int	Angle	R.Int
20	462	20.82	527	21.64	2068	22.46	395	23.28	513	24.1	377	24.92	350	25.74	374	26.56	338	27.38	858	28.2	431
20.02	521	20.84	511	21.66	1829	22.48	415	23.3	545	24.12	355	24.94	338	25.76	375	26.58	325	27.4	796	28.22	360
20.04	540	20.86	466	21.68	1611	22.5	453	23.32	541	24.14	334	24.96	341	25.78	405	26.6	348	27.42	792	28.24	331
20.06	473	20.88	487	21.7	1346	22.52	470	23.34	591	24.16	371	24.98	314	25.8	369	26.62	361	27.44	777	28.26	343
20.08	504	20.9	502	21.72	1092	22.54	481	23.36	564	24.18	370	25	324	25.82	391	26.64	341	27.46	861	28.28	371
20.1	516	20.92	514	21.74	924	22.56	460	23.38	660	24.2	387	25.02	363	25.84	332	26.66	363	27.48	897	28.3	364
20.12	508	20.94	522	21.76	793	22.58	452	23.4	570	24.22	371	25.04	332	25.86	404	26.68	358	27.5	851	28.32	332
20.14	515	20.96	481	21.78	668	22.6	469	23.42	592	24.24	336	25.06	320	25.88	371	26.7	349	27.52	841	28.34	376
20.16	484	20.98	520	21.8	608	22.62	495	23.44	568	24.26	380	25.08	355	25.9	346	26.72	389	27.54	850	28.36	340
20.18	491	21	535	21.82	591	22.64	451	23.46	552	24.28	367	25.1	318	25.92	337	26.74	373	27.56	862	28.38	352
20.2	505	21.02	541	21.84	551	22.66	434	23.48	540	24.3	410	25.12	340	25.94	341	26.76	367	27.58	816	28.4	348
20.22	526	21.04	521	21.86	515	22.68	438	23.5	506	24.32	343	25.14	328	25.96	344	26.78	369	27.6	798	28.42	316
20.24	496	21.06	543	21.88	514	22.7	465	23.52	533	24.34	391	25.16	365	25.98	358	26.8	390	27.62	808	28.44	356
20.26	475	21.08	552	21.9	506	22.72	445	23.54	521	24.36	361	25.18	362	26	329	26.82	390	27.64	709	28.46	329
20.28	496	21.1	500	21.92	516	22.74	462	23.56	466	24.38	399	25.2	347	26.02	336	26.84	408	27.66	643	28.48	341
20.3	513	21.12	571	21.94	466	22.76	415	23.58	463	24.4	338	25.22	360	26.04	345	26.86	372	27.68	578	28.5	351
20.32	533	21.14	538	21.96	481	22.78	434	23.6	478	24.42	343	25.24	345	26.06	366	26.88	373	27.7	556	28.52	311
20.34	516	21.16	554	21.98	440	22.8	422	23.62	467	24.44	385	25.26	367	26.08	387	26.9	398	27.72	554	28.54	328
20.36	486	21.18	611	22	465	22.82	474	23.64	498	24.46	340	25.28	331	26.1	337	26.92	447	27.74	543	28.56	318
20.38	499	21.2	617	22.02	426	22.84	419	23.66	444	24.48	352	25.3	367	26.12	357	26.94	401	27.76	504	28.58	300
20.4	498	21.22	659	22.04	433	22.86	435	23.68	414	24.5	314	25.32	413	26.14	309	26.96	428	27.78	507	28.6	320
20.42	519	21.24	678	22.06	450	22.88	457	23.7	476	24.52	355	25.34	349	26.16	373	26.98	477	27.8	481	28.62	329
20.44	505	21.26	729	22.08	411	22.9	397	23.72	399	24.54	365	25.36	398	26.18	322	27	492	27.82	473	28.64	326
20.46	511	21.28	734	22.1	410	22.92	414	23.74	446	24.56	344	25.38	415	26.2	366	27.02	547	27.84	481	28.66	320
20.48	482	21.3	919	22.12	425	22.94	417	23.76	386	24.58	328	25.4	390	26.22	332	27.04	527	27.86	440	28.68	351
20.5	512	21.32	838	22.14	415	22.96	422	23.78	431	24.6	337	25.42	439	26.24	343	27.06	593	27.88	447	28.7	294
20.52	517	21.34	939	22.16	406	22.98	419	23.8	410	24.62	381	25.44	391	26.26	356	27.08	674	27.9	438	28.72	329
20.54	549	21.36	1037	22.18	444	23	436	23.82	420	24.64	343	25.46	398	26.28	335	27.1	629	27.92	471	28.74	325
20.56	534	21.38	1011	22.2	446	23.02	437	23.84	375	24.66	355	25.48	444	26.3	327	27.12	768	27.94	431	28.76	348
20.58	521	21.4	1139	22.22	418	23.04	415	23.86	401	24.68	357	25.5	411	26.32	351	27.14	778	27.96	436	28.78	292
20.6	511	21.42	1269	22.24	434	23.06	408	23.88	384	24.7	319	25.52	423	26.34	341	27.16	828	27.98	459	28.8	331
20.62	496	21.44	1401	22.26	426	23.08	412	23.9	407	24.72	333	25.54	429	26.36	343	27.18	836	28	447	28.82	336
20.64	491	21.46	1447	22.28	440	23.1	440	23.92	391	24.74	338	25.56	397	26.38	357	27.2	961	28.02	459	28.84	318
20.66	514	21.48	1568	22.3	448	23.12	430	23.94	376	24.76	350	25.58	390	26.4	315	27.22	964	28.04	449	28.86	329
20.68	512	21.5	1645	22.32	415	23.14	430	23.96	381	24.78	357	25.6	353	26.42	335	27.24	974	28.06	459	28.88	345
20.7	493	21.52	1811	22.34	422	23.16	411	23.98	397	24.8	313	25.62	418	26.44	334	27.26	945	28.08	479	28.9	315
20.72	495	21.54	1926	22.36	454	23.18	426	24	339	24.82	317	25.64	375	26.46	331	27.28	964	28.1	432	28.92	327
20.74	538	21.56	2055	22.38	435	23.2	467	24.02	334	24.84	396	25.66	362	26.48	345	27.3	1019	28.12	452	28.94	350
20.76	506	21.58	2070	22.4	433	23.22	468	24.04	361	24.86	350	25.68	392	26.5	344	27.32	975	28.14	418	28.96	310
20.78	510	21.6	2135	22.42	386	23.24	521	24.06	385	24.88	361	25.7	363	26.52	346	27.34	878	28.16	411	28.98	326
20.8	506	21.62	2105	22.44	443	23.26	517	24.08	404	24.9	332	25.72	390	26.54	366	27.36	861	28.18	362	29	324

Angle	R.Int	Angle	R.Int	Angle	R.Int	Angle	R.Int	Angle	R.Int	Angle	R.Int	Angle	R.Int	Angle	R.Int	Angle	R.Int	Angle	R.Int	Angle	R.Int
29.02	344	29.84	379	30.66	392	31.48	305	32.3	274	33.12	228	33.94	218	34.76	287	35.58	425	36.4	186	37.22	232
29.04	314	29.86	379	30.68	410	31.5	296	32.32	245	33.14	256	33.96	214	34.78	257	35.6	447	36.42	210	37.24	206
29.06	324	29.88	362	30.7	375	31.52	288	32.34	297	33.16	269	33.98	247	34.8	305	35.62	429	36.44	225	37.26	215
29.08	311	29.9	360	30.72	377	31.54	283	32.36	248	33.18	244	34	237	34.82	274	35.64	479	36.46	206	37.28	229
29.1	293	29.92	358	30.74	390	31.56	279	32.38	303	33.2	266	34.02	269	34.84	276	35.66	480	36.48	226	37.3	175
29.12	363	29.94	369	30.76	334	31.58	256	32.4	276	33.22	245	34.04	236	34.86	312	35.68	497	36.5	234	37.32	218
29.14	314	29.96	357	30.78	366	31.6	308	32.42	256	33.24	241	34.06	221	34.88	292	35.7	484	36.52	212	37.34	222
29.16	344	29.98	369	30.8	341	31.62	283	32.44	262	33.26	226	34.08	238	34.9	317	35.72	544	36.54	236	37.36	198
29.18	332	30	383	30.82	385	31.64	314	32.46	303	33.28	256	34.1	188	34.92	319	35.74	502	36.56	225	37.38	218
29.2	362	30.02	389	30.84	378	31.66	281	32.48	268	33.3	241	34.12	225	34.94	326	35.76	504	36.58	215	37.4	206
29.22	343	30.04	389	30.86	346	31.68	313	32.5	297	33.32	223	34.14	223	34.96	360	35.78	427	36.6	201	37.42	208
29.24	365	30.06	406	30.88	419	31.7	277	32.52	258	33.34	236	34.16	218	34.98	345	35.8	453	36.62	232	37.44	213
29.26	361	30.08	380	30.9	398	31.72	300	32.54	252	33.36	224	34.18	243	35	342	35.82	420	36.64	227	37.46	193
29.28	350	30.1	393	30.92	405	31.74	276	32.56	282	33.38	224	34.2	238	35.02	332	35.84	381	36.66	202	37.48	191
29.3	322	30.12	354	30.94	392	31.76	295	32.58	249	33.4	225	34.22	238	35.04	340	35.86	381	36.68	235	37.5	211
29.32	345	30.14	336	30.96	393	31.78	299	32.6	266	33.42	221	34.24	225	35.06	339	35.88	370	36.7	207	37.52	171
29.34	360	30.16	389	30.98	437	31.8	271	32.62	287	33.44	228	34.26	219	35.08	419	35.9	316	36.72	221	37.54	221
29.36	362	30.18	380	31	395	31.82	263	32.64	265	33.46	219	34.28	235	35.1	358	35.92	322	36.74	202	37.56	190
29.38	372	30.2	363	31.02	436	31.84	302	32.66	259	33.48	264	34.3	203	35.12	381	35.94	309	36.76	220	37.58	210
29.4	349	30.22	384	31.04	467	31.86	272	32.68	273	33.5	241	34.32	260	35.14	346	35.96	287	36.78	208	37.6	207
29.42	388	30.24	409	31.06	435	31.88	271	32.7	292	33.52	243	34.34	222	35.16	326	35.98	342	36.8	213	37.62	181
29.44	359	30.26	415	31.08	458	31.9	260	32.72	271	33.54	278	34.36	221	35.18	333	36	319	36.82	217	37.64	209
29.46	317	30.28	391	31.1	401	31.92	284	32.74	241	33.56	225	34.38	227	35.2	319	36.02	317	36.84	260	37.66	185
29.48	381	30.3	392	31.12	411	31.94	269	32.76	266	33.58	240	34.4	186	35.22	323	36.04	285	36.86	198	37.68	176
29.5	396	30.32	381	31.14	406	31.96	278	32.78	252	33.6	208	34.42	219	35.24	314	36.06	304	36.88	247	37.7	185
29.52	344	30.34	386	31.16	376	31.98	272	32.8	260	33.62	192	34.44	206	35.26	335	36.08	266	36.9	255	37.72	170
29.54	352	30.36	422	31.18	363	32	304	32.82	267	33.64	228	34.46	254	35.28	346	36.1	278	36.92	223	37.74	208
29.56	377	30.38	440	31.2	376	32.02	312	32.84	293	33.66	250	34.48	229	35.3	332	36.12	241	36.94	226	37.76	187
29.58	347	30.4	413	31.22	371	32.04	297	32.86	303	33.68	216	34.5	235	35.32	302	36.14	253	36.96	240	37.78	168
29.6	394	30.42	438	31.24	349	32.06	261	32.88	280	33.7	250	34.52	230	35.34	335	36.16	236	36.98	254	37.8	187
29.62	384	30.44	406	31.26	350	32.08	292	32.9	265	33.72	215	34.54	251	35.36	327	36.18	239	37	218	37.82	180
29.64	405	30.46	422	31.28	356	32.1	278	32.92	211	33.74	247	34.56	247	35.38	314	36.2	212	37.02	214	37.84	198
29.66	399	30.48	414	31.3	355	32.12	268	32.94	271	33.76	232	34.58	262	35.4	322	36.22	245	37.04	214	37.86	186
29.68	394	30.5	356	31.32	333	32.14	296	32.96	309	33.78	225	34.6	247	35.42	347	36.24	215	37.06	255	37.88	182
29.7	394	30.52	410	31.34	350	32.16	287	32.98	274	33.8	218	34.62	284	35.44	329	36.26	228	37.08	248	37.9	194
29.72	394	30.54	416	31.36	340	32.18	289	33	258	33.82	234	34.64	253	35.46	314	36.28	235	37.1	206	37.92	216
29.74	357	30.56	407	31.38	381	32.2	299	33.02	281	33.84	225	34.66	234	35.48	307	36.3	246	37.12	221	37.94	216
29.76	378	30.58	376	31.4	357	32.22	318	33.04	240	33.86	248	34.68	278	35.5	358	36.32	211	37.14	219	37.96	215
29.78	386	30.6	337	31.42	321	32.24	261	33.06	264	33.88	253	34.7	249	35.52	364	36.34	247	37.16	220	37.98	180
29.8	388	30.62	374	31.44	307	32.26	280	33.08	274	33.9	252	34.72	279	35.54	389	36.36	217	37.18	199	38	174
29.82	365	30.64	384	31.46	335	32.28	247	33.1	239	33.92	220	34.74	296	35.56	379	36.38	229	37.2	216	38.02	193

Angle	R.Int	Angle	R.Int	Angle	R.Int	Angle	R.Int	Angle	R.Int	Angle	R.Int	Angle	R.Int	Angle	R.Int	Angle	R.Int	Angle	R.Int
38.04	168	38.92	190	39.8	153	40.68	195	41.56	200	42.44	188	43.32	138	44.2	223	45.08	178	45.96	166	46.84	187
38.06	177	38.94	164	39.82	168	40.7	147	41.58	211	42.46	175	43.34	162	44.22	200	45.1	172	45.98	148	46.86	183
38.08	205	38.96	185	39.84	164	40.72	162	41.6	254	42.48	227	43.36	167	44.24	206	45.12	163	46	171	46.88	183
38.1	185	38.98	162	39.86	176	40.74	169	41.62	210	42.5	213	43.38	169	44.26	204	45.14	174	46.02	157	46.9	170
38.12	184	39	187	39.88	155	40.76	164	41.64	214	42.52	183	43.4	161	44.28	202	45.16	172	46.04	144	46.92	189
38.14	186	39.02	185	39.9	158	40.78	168	41.66	179	42.54	185	43.42	164	44.3	213	45.18	166	46.06	183	46.94	165
38.16	169	39.04	158	39.92	162	40.8	170	41.68	221	42.56	189	43.44	161	44.32	222	45.2	152	46.08	171	46.96	182
38.18	206	39.06	159	39.94	170	40.82	154	41.7	238	42.58	180	43.46	182	44.34	227	45.22	188	46.1	161	46.98	201
38.2	159	39.08	187	39.96	185	40.84	170	41.72	194	42.6	177	43.48	166	44.36	225	45.24	182	46.12	192	47	134
38.22	167	39.1	194	39.98	198	40.86	167	41.74	196	42.62	147	43.5	162	44.38	185	45.26	174	46.14	156	47.02	159
38.24	166	39.12	166	40	179	40.88	186	41.76	197	42.64	192	43.52	138	44.4	214	45.28	179	46.16	175	47.04	162
38.26	178	39.14	212	40.02	162	40.9	171	41.78	187	42.66	185	43.54	141	44.42	176	45.3	171	46.18	178	47.06	151
38.28	184	39.16	178	40.04	168	40.92	159	41.8	195	42.68	194	43.56	172	44.44	198	45.32	130	46.2	175	47.08	170
38.3	194	39.18	171	40.06	178	40.94	164	41.82	187	42.7	166	43.58	160	44.46	224	45.34	154	46.22	170	47.1	163
38.32	186	39.2	172	40.08	164	40.96	162	41.84	184	42.72	195	43.6	156	44.48	197	45.36	169	46.24	188	47.12	150
38.34	244	39.22	178	40.1	169	40.98	178	41.86	176	42.74	192	43.62	156	44.5	204	45.38	157	46.26	196	47.14	166
38.36	207	39.24	170	40.12	166	41	183	41.88	200	42.76	199	43.64	145	44.52	185	45.4	171	46.28	192	47.16	175
38.38	219	39.26	212	40.14	195	41.02	164	41.9	195	42.78	178	43.66	169	44.54	180	45.42	184	46.3	191	47.18	153
38.4	224	39.28	166	40.16	156	41.04	173	41.92	179	42.8	166	43.68	134	44.56	190	45.44	164	46.32	181	47.2	161
38.42	200	39.3	163	40.18	170	41.06	172	41.94	172	42.82	159	43.7	153	44.58	184	45.46	175	46.34	187	47.22	161
38.44	223	39.32	169	40.2	167	41.08	166	41.96	197	42.84	190	43.72	157	44.6	169	45.48	158	46.36	196	47.24	153
38.46	181	39.34	159	40.22	193	41.1	176	41.98	202	42.86	161	43.74	158	44.62	180	45.5	135	46.38	199	47.26	158
38.48	208	39.36	151	40.24	174	41.12	158	42	195	42.88	165	43.76	165	44.64	162	45.52	159	46.4	216	47.28	163
38.5	204	39.38	193	40.26	151	41.14	181	42.02	173	42.9	179	43.78	161	44.66	169	45.54	166	46.42	232	47.3	143
38.52	209	39.4	165	40.28	156	41.16	151	42.04	184	42.92	161	43.8	179	44.68	155	45.56	129	46.44	217	47.32	150
38.54	206	39.42	158	40.3	152	41.18	177	42.06	206	42.94	159	43.82	156	44.7	144	45.58	161	46.46	233	47.34	157
38.56	189	39.44	160	40.32	181	41.2	159	42.08	196	42.96	150	43.84	165	44.72	159	45.6	144	46.48	217	47.36	155
38.58	220	39.46	181	40.34	191	41.22	174	42.1	204	42.98	166	43.86	159	44.74	188	45.62	174	46.5	229	47.38	162
38.6	203	39.48	157	40.36	187	41.24	171	42.12	203	43	144	43.88	153	44.76	166	45.64	146	46.52	202	47.4	157
38.62	228	39.5	173	40.38	197	41.26	180	42.14	218	43.02	150	43.9	193	44.78	170	45.66	133	46.54	245	47.42	157
38.64	178	39.52	159	40.4	165	41.28	201	42.16	177	43.04	155	43.92	184	44.8	164	45.68	152	46.56	208	47.44	153
38.66	229	39.54	165	40.42	185	41.3	186	42.18	213	43.06	176	43.94	165	44.82	150	45.7	175	46.58	262	47.46	173
38.68	184	39.56	190	40.44	164	41.32	196	42.2	207	43.08	165	43.96	165	44.84	157	45.72	172	46.6	221	47.48	174
38.7	209	39.58	146	40.46	179	41.34	198	42.22	216	43.1	159	43.98	148	44.86	154	45.74	145	46.62	208	47.5	169
38.72	192	39.6	172	40.48	159	41.36	212	42.24	227	43.12	167	44	135	44.88	154	45.76	148	46.64	216	47.52	170
38.74	177	39.62	175	40.5	183	41.38	235	42.26	243	43.14	152	44.02	208	44.9	141	45.78	162	46.66	220	47.54	141
38.76	178	39.64	172	40.52	179	41.4	209	42.28	209	43.16	146	44.04	215	44.92	167	45.8	147	46.68	213	47.56	157
38.78	196	39.66	177	40.54	187	41.42	228	42.3	220	43.18	161	44.06	179	44.94	140	45.82	173	46.7	221	47.58	187
38.8	214	39.68	170	40.56	171	41.44	233	42.32	237	43.2	144	44.08	178	44.96	159	45.84	143	46.72	220	47.6	158
38.82	188	39.7	164	40.58	182	41.46	220	42.34	200	43.22	141	44.1	171	44.98	150	45.86	160	46.74	220	47.62	160
38.84	192	39.72	166	40.6	172	41.48	240	42.36	210	43.24	170	44.12	187	45	160	45.88	164	46.76	231	47.64	177
38.86	186	39.74	190	40.62	180	41.5	227	42.38	180	43.26	187	44.14	182	45.02	160	45.9	141	46.78	229	47.66	148
38.88	201	39.76	169	40.64	172	41.52	241	42.4	207	43.28	140	44.16	186	45.04	161	45.92	165	46.8	196	47.68	172
38.9	211	39.78	158	40.66	150	41.54	236	42.42	207	43.3	129	44.18	192	45.06	174	45.94	176	46.82	192	47.7	145

Angle	R.Int	Angle	R.Int	Angle	R.Int	Angle	R.Int	Angle	R.Int	Angle	R.Int	Angle	R.Int	Angle	R.Int	Angle	R.Int	Angle	R.Int	Angle	R.Int
47.72	158	48.56	175	49.4	155	50.24	160	51.08	216	51.92	164	52.76	171	53.6	154	54.44	134	55.28	118	56.12	157
47.74	156	48.58	175	49.42	197	50.26	176	51.1	209	51.94	149	52.78	152	53.62	183	54.46	138	55.3	131	56.14	142
47.76	165	48.6	192	49.44	186	50.28	174	51.12	222	51.96	162	52.8	162	53.64	162	54.48	119	55.32	145	56.16	176
47.78	165	48.62	176	49.46	172	50.3	148	51.14	168	51.98	159	52.82	171	53.66	166	54.5	160	55.34	159	56.18	177
47.8	178	48.64	167	49.48	149	50.32	209	51.16	182	52	184	52.84	154	53.68	172	54.52	129	55.36	141	56.2	171
47.82	162	48.66	193	49.5	179	50.34	186	51.18	149	52.02	168	52.86	164	53.7	187	54.54	158	55.38	135	56.22	166
47.84	170	48.68	141	49.52	151	50.36	159	51.2	188	52.04	178	52.88	154	53.72	176	54.56	134	55.4	139	56.24	191
47.86	191	48.7	166	49.54	169	50.38	201	51.22	161	52.06	173	52.9	206	53.74	179	54.58	130	55.42	122	56.26	177
47.88	187	48.72	193	49.56	172	50.4	181	51.24	160	52.08	124	52.92	152	53.76	196	54.6	157	55.44	145	56.28	197
47.9	191	48.74	182	49.58	193	50.42	174	51.26	166	52.1	131	52.94	193	53.78	175	54.62	127	55.46	137	56.3	169
47.92	183	48.76	177	49.6	161	50.44	197	51.28	155	52.12	150	52.96	163	53.8	171	54.64	144	55.48	127	56.32	197
47.94	171	48.78	153	49.62	186	50.46	166	51.3	148	52.14	161	52.98	149	53.82	169	54.66	170	55.5	120	56.34	179
47.96	165	48.8	142	49.64	202	50.48	193	51.32	181	52.16	183	53	147	53.84	172	54.68	137	55.52	126	56.36	182
47.98	170	48.82	157	49.66	177	50.5	193	51.34	152	52.18	150	53.02	146	53.86	186	54.7	146	55.54	153	56.38	174
48	203	48.84	145	49.68	154	50.52	162	51.36	168	52.2	164	53.04	148	53.88	209	54.72	145	55.56	142	56.4	193
48.02	192	48.86	207	49.7	180	50.54	173	51.38	153	52.22	171	53.06	171	53.9	181	54.74	134	55.58	145	56.42	207
48.04	227	48.88	170	49.72	167	50.56	200	51.4	126	52.24	153	53.08	147	53.92	170	54.76	133	55.6	133	56.44	206
48.06	203	48.9	164	49.74	161	50.58	187	51.42	150	52.26	159	53.1	165	53.94	187	54.78	129	55.62	151	56.46	185
48.08	218	48.92	174	49.76	171	50.6	204	51.44	151	52.28	154	53.12	139	53.96	168	54.8	140	55.64	130	56.48	164
48.1	217	48.94	164	49.78	133	50.62	217	51.46	162	52.3	159	53.14	172	53.98	152	54.82	141	55.66	127	56.5	200
48.12	234	48.96	153	49.8	170	50.64	176	51.48	169	52.32	161	53.16	160	54	156	54.84	120	55.68	165	56.52	204
48.14	215	48.98	155	49.82	153	50.66	183	51.5	158	52.34	156	53.18	150	54.02	168	54.86	128	55.7	143	56.54	211
48.16	240	49	152	49.84	166	50.68	222	51.52	163	52.36	142	53.2	169	54.04	143	54.88	146	55.72	141	56.56	197
48.18	239	49.02	164	49.86	182	50.7	202	51.54	158	52.38	161	53.22	151	54.06	156	54.9	123	55.74	171	56.58	208
48.2	239	49.04	164	49.88	169	50.72	231	51.56	164	52.4	163	53.24	150	54.08	154	54.92	159	55.76	152	56.6	211
48.22	246	49.06	184	49.9	196	50.74	216	51.58	190	52.42	183	53.26	159	54.1	164	54.94	156	55.78	174	56.62	244
48.24	258	49.08	184	49.92	186	50.76	223	51.6	153	52.44	160	53.28	161	54.12	143	54.96	140	55.8	193	56.64	251
48.26	263	49.1	181	49.94	183	50.78	257	51.62	161	52.46	159	53.3	148	54.14	135	54.98	133	55.82	170	56.66	242
48.28	244	49.12	188	49.96	162	50.8	262	51.64	174	52.48	168	53.32	183	54.16	138	55	150	55.84	150	56.68	221
48.3	248	49.14	176	49.98	173	50.82	278	51.66	160	52.5	169	53.34	170	54.18	129	55.02	145	55.86	150	56.7	228
48.32	232	49.16	193	50	177	50.84	263	51.68	164	52.52	152	53.36	158	54.2	144	55.04	144	55.88	148	56.72	217
48.34	210	49.18	190	50.02	163	50.86	279	51.7	147	52.54	176	53.38	147	54.22	155	55.06	132	55.9	145	56.74	206
48.36	218	49.2	185	50.04	178	50.88	263	51.72	160	52.56	159	53.4	172	54.24	120	55.08	153	55.92	168	56.76	239
48.38	238	49.22	196	50.06	169	50.9	277	51.74	155	52.58	176	53.42	167	54.26	169	55.1	156	55.94	144	56.78	207
48.4	209	49.24	188	50.08	151	50.92	248	51.76	166	52.6	147	53.44	178	54.28	143	55.12	120	55.96	152	56.8	204
48.42	208	49.26	191	50.1	176	50.94	223	51.78	149	52.62	196	53.46	185	54.3	145	55.14	117	55.98	148	56.82	193
48.44	180	49.28	180	50.12	151	50.96	247	51.8	164	52.64	165	53.48	180	54.32	150	55.16	116	56	159	56.84	201
48.46	197	49.3	182	50.14	167	50.98	253	51.82	144	52.66	173	53.5	144	54.34	140	55.18	129	56.02	155	56.86	195
48.48	194	49.32	174	50.16	171	51	229	51.84	163	52.68	164	53.52	181	54.36	145	55.2	143	56.04	164	56.88	182
48.5	205	49.34	204	50.18	144	51.02	202	51.86	155	52.7	152	53.54	151	54.38	131	55.22	135	56.06	165	56.9	178
48.52	182	49.36	190	50.2	192	51.04	213	51.88	149	52.72	171	53.56	171	54.4	167	55.24	128	56.08	152	56.92	175
48.54	194	49.38	166	50.22	171	51.06	239	51.9	135	52.74	137	53.58	166	54.42	142	55.26	151	56.1	159	56.94	173

Angle	R.Int	Angle	R.Int	Angle	R.Int	Angle	R.Int	Angle	R.Int	Angle	R.Int	Angle	R.Int	Angle	R.Int	Angle	R.Int	Angle	R.Int
56.96	171	57.8	135	58.64	155	59.48	146	60.32	172	61.16	165	62	188	62.84	137	63.68	141	64.52	180	65.36	179
56.98	152	57.82	120	58.66	128	59.5	135	60.34	133	61.18	155	62.02	200	62.86	163	63.7	136	64.54	182	65.38	177
57	172	57.84	138	58.68	157	59.52	144	60.36	138	61.2	149	62.04	202	62.88	136	63.72	160	64.56	173	65.4	144
57.02	167	57.86	134	58.7	162	59.54	150	60.38	138	61.22	166	62.06	198	62.9	183	63.74	190	64.58	179	65.42	172
57.04	182	57.88	141	58.72	160	59.56	157	60.4	143	61.24	152	62.08	178	62.92	160	63.76	163	64.6	183	65.44	161
57.06	163	57.9	148	58.74	170	59.58	161	60.42	153	61.26	185	62.1	221	62.94	155	63.78	155	64.62	179	65.46	146
57.08	170	57.92	132	58.76	152	59.6	145	60.44	142	61.28	173	62.12	202	62.96	155	63.8	156	64.64	176	65.48	155
57.1	161	57.94	128	58.78	170	59.62	159	60.46	128	61.3	164	62.14	184	62.98	140	63.82	144	64.66	173	65.5	161
57.12	165	57.96	141	58.8	147	59.64	126	60.48	136	61.32	156	62.16	178	63	143	63.84	170	64.68	180	65.52	176
57.14	169	57.98	147	58.82	150	59.66	173	60.5	148	61.34	163	62.18	212	63.02	128	63.86	135	64.7	207	65.54	170
57.16	160	58	170	58.84	130	59.68	157	60.52	154	61.36	162	62.2	191	63.04	141	63.88	138	64.72	201	65.56	189
57.18	151	58.02	136	58.86	158	59.7	168	60.54	124	61.38	188	62.22	198	63.06	132	63.9	150	64.74	188	65.58	156
57.2	171	58.04	132	58.88	155	59.72	146	60.56	126	61.4	190	62.24	185	63.08	157	63.92	150	64.76	199	65.6	155
57.22	161	58.06	150	58.9	171	59.74	189	60.58	159	61.42	172	62.26	195	63.1	134	63.94	163	64.78	187	65.62	160
57.24	170	58.08	134	58.92	164	59.76	181	60.6	141	61.44	169	62.28	193	63.12	141	63.96	156	64.8	190	65.64	165
57.26	127	58.1	159	58.94	151	59.78	156	60.62	143	61.46	181	62.3	183	63.14	162	63.98	154	64.82	171	65.66	140
57.28	155	58.12	144	58.96	145	59.8	158	60.64	119	61.48	185	62.32	195	63.16	125	64	148	64.84	197	65.68	151
57.3	154	58.14	153	58.98	139	59.82	179	60.66	121	61.5	160	62.34	156	63.18	149	64.02	126	64.86	159	65.7	155
57.32	154	58.16	152	59	160	59.84	156	60.68	133	61.52	183	62.36	172	63.2	136	64.04	150	64.88	217	65.72	183
57.34	164	58.18	158	59.02	159	59.86	203	60.7	129	61.54	205	62.38	178	63.22	159	64.06	138	64.9	167	65.74	146
57.36	156	58.2	141	59.04	145	59.88	165	60.72	139	61.56	155	62.4	160	63.24	171	64.08	161	64.92	193	65.76	172
57.38	151	58.22	157	59.06	152	59.9	153	60.74	121	61.58	175	62.42	165	63.26	158	64.1	162	64.94	149	65.78	152
57.4	133	58.24	145	59.08	146	59.92	173	60.76	157	61.6	201	62.44	155	63.28	143	64.12	162	64.96	173	65.8	156
57.42	140	58.26	154	59.1	137	59.94	172	60.78	151	61.62	211	62.46	187	63.3	146	64.14	146	64.98	175	65.82	176
57.44	142	58.28	139	59.12	147	59.96	175	60.8	165	61.64	223	62.48	173	63.32	140	64.16	147	65	169	65.84	176
57.46	135	58.3	168	59.14	142	59.98	148	60.82	125	61.66	243	62.5	177	63.34	147	64.18	157	65.02	169	65.86	143
57.48	164	58.32	176	59.16	153	60	158	60.84	129	61.68	204	62.52	163	63.36	156	64.2	159	65.04	159	65.88	141
57.5	110	58.34	173	59.18	131	60.02	186	60.86	150	61.7	219	62.54	177	63.38	153	64.22	156	65.06	185	65.9	166
57.52	141	58.36	154	59.2	149	60.04	170	60.88	150	61.72	210	62.56	166	63.4	141	64.24	142	65.08	173	65.92	149
57.54	141	58.38	152	59.22	144	60.06	172	60.9	156	61.74	208	62.58	174	63.42	121	64.26	176	65.1	177	65.94	149
57.56	120	58.4	152	59.24	141	60.08	160	60.92	143	61.76	212	62.6	153	63.44	137	64.28	153	65.12	181	65.96	150
57.58	152	58.42	154	59.26	133	60.1	149	60.94	121	61.78	210	62.62	159	63.46	132	64.3	168	65.14	163	65.98	164
57.6	152	58.44	139	59.28	156	60.12	171	60.96	150	61.8	203	62.64	165	63.48	148	64.32	165	65.16	160	66	155
57.62	121	58.46	173	59.3	146	60.14	175	60.98	136	61.82	203	62.66	156	63.5	112	64.34	171	65.18	146	66.02	145
57.64	150	58.48	158	59.32	138	60.16	143	61	155	61.84	185	62.68	168	63.52	128	64.36	181	65.2	158	66.04	166
57.66	142	58.5	153	59.34	145	60.18	138	61.02	134	61.86	204	62.7	154	63.54	155	64.38	167	65.22	171	66.06	159
57.68	136	58.52	146	59.36	147	60.2	131	61.04	133	61.88	188	62.72	157	63.56	124	64.4	157	65.24	189	66.08	143
57.7	145	58.54	154	59.38	143	60.22	149	61.06	157	61.9	205	62.74	173	63.58	133	64.42	181	65.26	162	66.1	151
57.72	144	58.56	155	59.4	142	60.24	157	61.08	135	61.92	195	62.76	146	63.6	148	64.44	166	65.28	174	66.12	148
57.74	135	58.58	163	59.42	172	60.26	146	61.1	147	61.94	181	62.78	154	63.62	122	64.46	174	65.3	161	66.14	157
57.76	158	58.6	182	59.44	155	60.28	147	61.12	136	61.96	189	62.8	175	63.64	159	64.48	178	65.32	147	66.16	140
57.78	151	58.62	172	59.46	142	60.3	152	61.14	175	61.98	208	62.82	144	63.66	132	64.5	189	65.34	149	66.18	162

Angle	R.Int	Angle	R.Int	Angle	R.Int	Angle	R.Int	Angle	R.Int	Angle	R.Int	Angle	R.Int	Angle	R.Int	Angle	R.Int	Angle	R.Int
66.2	158	67.04	153	67.88	166	68.72	145	69.56	155	70.4	139	71.24	148	72.08	128	72.92	162	73.76	139	74.6	160
66.22	160	67.06	134	67.9	183	68.74	146	69.58	158	70.42	132	71.26	130	72.1	151	72.94	145	73.78	162	74.62	142
66.24	166	67.08	168	67.92	160	68.76	168	69.6	145	70.44	144	71.28	141	72.12	148	72.96	157	73.8	168	74.64	130
66.26	162	67.1	140	67.94	171	68.78	186	69.62	144	70.46	157	71.3	148	72.14	133	72.98	138	73.82	164	74.66	152
66.28	166	67.12	121	67.96	161	68.8	157	69.64	150	70.48	144	71.32	139	72.16	164	73	139	73.84	145	74.68	157
66.3	182	67.14	146	67.98	182	68.82	155	69.66	149	70.5	117	71.34	140	72.18	164	73.02	162	73.86	160	74.7	138
66.32	146	67.16	164	68	177	68.84	159	69.68	155	70.52	145	71.36	140	72.2	176	73.04	135	73.88	159	74.72	154
66.34	147	67.18	144	68.02	154	68.86	148	69.7	169	70.54	129	71.38	148	72.22	156	73.06	143	73.9	159	74.74	148
66.36	166	67.2	156	68.04	156	68.88	151	69.72	164	70.56	132	71.4	136	72.24	164	73.08	157	73.92	140	74.76	170
66.38	174	67.22	146	68.06	166	68.9	162	69.74	146	70.58	135	71.42	127	72.26	152	73.1	150	73.94	149	74.78	154
66.4	180	67.24	140	68.08	185	68.92	172	69.76	168	70.6	123	71.44	159	72.28	157	73.12	150	73.96	127	74.8	165
66.42	141	67.26	141	68.1	178	68.94	148	69.78	136	70.62	105	71.46	145	72.3	187	73.14	163	73.98	145	74.82	161
66.44	165	67.28	145	68.12	167	68.96	177	69.8	154	70.64	138	71.48	147	72.32	146	73.16	156	74	158	74.84	152
66.46	171	67.3	143	68.14	171	68.98	182	69.82	138	70.66	135	71.5	134	72.34	148	73.18	147	74.02	124	74.86	155
66.48	165	67.32	152	68.16	177	69	158	69.84	147	70.68	116	71.52	150	72.36	146	73.2	144	74.04	169	74.88	190
66.5	196	67.34	137	68.18	141	69.02	167	69.86	170	70.7	141	71.54	147	72.38	145	73.22	157	74.06	176	74.9	158
66.52	149	67.36	159	68.2	194	69.04	160	69.88	139	70.72	130	71.56	134	72.4	153	73.24	157	74.08	151	74.92	167
66.54	169	67.38	143	68.22	178	69.06	193	69.9	155	70.74	130	71.58	140	72.42	157	73.26	183	74.1	124	74.94	174
66.56	190	67.4	158	68.24	180	69.08	173	69.92	157	70.76	115	71.6	108	72.44	137	73.28	144	74.12	148	74.96	142
66.58	168	67.42	151	68.26	166	69.1	162	69.94	139	70.78	142	71.62	164	72.46	138	73.3	169	74.14	153	74.98	137
66.6	168	67.44	166	68.28	172	69.12	157	69.96	164	70.8	138	71.64	148	72.48	152	73.32	133	74.16	146	75	167
66.62	145	67.46	171	68.3	183	69.14	203	69.98	166	70.82	120	71.66	156	72.5	136	73.34	175	74.18	153	75.02	162
66.64	148	67.48	155	68.32	186	69.16	168	70	148	70.84	129	71.68	131	72.52	158	73.36	138	74.2	156	75.04	167
66.66	153	67.5	160	68.34	158	69.18	154	70.02	165	70.86	148	71.7	139	72.54	150	73.38	155	74.22	137	75.06	173
66.68	136	67.52	161	68.36	179	69.2	167	70.04	151	70.88	126	71.72	149	72.56	164	73.4	152	74.24	158	75.08	141
66.7	158	67.54	142	68.38	170	69.22	168	70.06	180	70.9	133	71.74	152	72.58	134	73.42	168	74.26	148	75.1	170
66.72	145	67.56	151	68.4	182	69.24	175	70.08	164	70.92	140	71.76	128	72.6	128	73.44	152	74.28	155	75.12	141
66.74	153	67.58	171	68.42	163	69.26	156	70.1	192	70.94	131	71.78	158	72.62	150	73.46	184	74.3	159	75.14	166
66.76	139	67.6	135	68.44	162	69.28	165	70.12	147	70.96	137	71.8	135	72.64	159	73.48	149	74.32	129	75.16	126
66.78	138	67.62	131	68.46	179	69.3	171	70.14	152	70.98	120	71.82	152	72.66	148	73.5	173	74.34	183	75.18	175
66.8	164	67.64	179	68.48	132	69.32	146	70.16	155	71	132	71.84	152	72.68	145	73.52	162	74.36	164	75.2	128
66.82	150	67.66	154	68.5	158	69.34	156	70.18	174	71.02	135	71.86	126	72.7	150	73.54	169	74.38	150	75.22	163
66.84	157	67.68	162	68.52	171	69.36	190	70.2	154	71.04	137	71.88	139	72.72	155	73.56	160	74.4	157	75.24	160
66.86	164	67.7	166	68.54	153	69.38	176	70.22	154	71.06	131	71.9	126	72.74	163	73.58	166	74.42	161	75.26	136
66.88	149	67.72	145	68.56	167	69.4	157	70.24	143	71.08	138	71.92	134	72.76	131	73.6	160	74.44	164	75.28	150
66.9	135	67.74	160	68.58	176	69.42	183	70.26	150	71.1	130	71.94	147	72.78	150	73.62	160	74.46	160	75.3	154
66.92	156	67.76	167	68.6	168	69.44	174	70.28	153	71.12	107	71.96	136	72.8	151	73.64	180	74.48	169	75.32	152
66.94	146	67.78	185	68.62	150	69.46	167	70.3	140	71.14	120	71.98	160	72.82	150	73.66	158	74.5	140	75.34	139
66.96	153	67.8	144	68.64	161	69.48	126	70.32	146	71.16	126	72	146	72.84	128	73.68	193	74.52	156	75.36	146
66.98	164	67.82	171	68.66	164	69.5	180	70.34	152	71.18	123	72.02	156	72.86	148	73.7	172	74.54	160	75.38	147
67	151	67.84	171	68.68	145	69.52	148	70.36	142	71.2	129	72.04	151	72.88	151	73.72	153	74.56	146	75.4	141
67.02	143	67.86	167	68.7	164	69.54	150	70.38	130	71.22	127	72.06	171	72.9	118	73.74	172	74.58	166	75.42	150

Angle	R.Int	Angle	R.Int	Angle	R.Int	Angle	R.Int	Angle	R.Int	Angle	R.Int
75.44	137	76.28	154	77.12	150	77.96	116	78.8	135	79.64	131
75.46	139	76.3	146	77.14	149	77.98	115	78.82	150	79.66	138
75.48	143	76.32	161	77.16	146	78	138	78.84	159	79.68	126
75.5	148	76.34	154	77.18	147	78.02	135	78.86	175	79.7	143
75.52	120	76.36	148	77.2	126	78.04	133	78.88	146	79.72	147
75.54	158	76.38	141	77.22	137	78.06	116	78.9	184	79.74	126
75.56	151	76.4	131	77.24	123	78.08	129	78.92	128	79.76	116
75.58	147	76.42	137	77.26	116	78.1	119	78.94	136	79.78	139
75.6	157	76.44	131	77.28	158	78.12	138	78.96	166	79.8	128
75.62	137	76.46	120	77.3	154	78.14	116	78.98	160	79.82	142
75.64	130	76.48	137	77.32	125	78.16	141	79	149	79.84	116
75.66	143	76.5	141	77.34	139	78.18	113	79.02	159	79.86	129
75.68	118	76.52	149	77.36	151	78.2	121	79.04	161	79.88	127
75.7	145	76.54	127	77.38	152	78.22	127	79.06	155	79.9	125
75.72	136	76.56	134	77.4	149	78.24	134	79.08	182	79.92	120
75.74	144	76.58	158	77.42	154	78.26	123	79.1	137	79.94	121
75.76	131	76.6	144	77.44	140	78.28	130	79.12	146	79.96	153
75.78	146	76.62	140	77.46	171	78.3	131	79.14	167	79.98	135
75.8	121	76.64	140	77.48	128	78.32	115	79.16	140	80	115
75.82	134	76.66	132	77.5	158	78.34	122	79.18	131		
75.84	131	76.68	134	77.52	154	78.36	145	79.2	144		
75.86	141	76.7	137	77.54	172	78.38	160	79.22	138		
75.88	135	76.72	145	77.56	118	78.4	100	79.24	133		
75.9	141	76.74	133	77.58	152	78.42	134	79.26	151		
75.92	125	76.76	135	77.6	131	78.44	110	79.28	157		
75.94	144	76.78	148	77.62	135	78.46	127	79.3	165		
75.96	151	76.8	165	77.64	171	78.48	145	79.32	131		
75.98	142	76.82	164	77.66	136	78.5	124	79.34	136		
76	117	76.84	139	77.68	174	78.52	129	79.36	133		
76.02	149	76.86	145	77.7	163	78.54	128	79.38	110		
76.04	134	76.88	133	77.72	141	78.56	142	79.4	132		
76.06	130	76.9	145	77.74	143	78.58	130	79.42	160		
76.08	136	76.92	162	77.76	148	78.6	132	79.44	132		
76.1	114	76.94	142	77.78	147	78.62	128	79.46	132		
76.12	158	76.96	133	77.8	148	78.64	139	79.48	145		
76.14	141	76.98	135	77.82	155	78.66	148	79.5	140		
76.16	137	77	146	77.84	135	78.68	162	79.52	148		
76.18	147	77.02	160	77.86	146	78.7	144	79.54	147		
76.2	138	77.04	146	77.88	114	78.72	129	79.56	123		
76.22	140	77.06	143	77.9	133	78.74	136	79.58	134		
76.24	135	77.08	138	77.92	119	78.76	131	79.6	141		
76.26	141	77.1	144	77.94	125	78.78	158	79.62	136		

Forgia Vecchia lava flow

Angle	R.Int	Angle	R.Int	Angle	R.Int	Angle	R.Int	Angle	R.Int	Angle	R.Int	Angle	R.Int	Angle	R.Int	Angle	R.Int	Angle	R.Int
20	219	22.05	199	24.1	160	26.15	149	28.2	162	30.25	145	32.3	112	34.35	102	36.4	94	38.45	87	40.5	74
20.05	196	22.1	195	24.15	158	26.2	162	28.25	147	30.3	151	32.35	121	34.4	105	36.45	93	38.5	80	40.55	82
20.1	223	22.15	197	24.2	172	26.25	139	28.3	132	30.35	146	32.4	133	34.45	111	36.5	87	38.55	101	40.6	56
20.15	189	22.2	182	24.25	151	26.3	154	28.35	138	30.4	155	32.45	121	34.5	127	36.55	81	38.6	83	40.65	87
20.2	216	22.25	184	24.3	168	26.35	173	28.4	144	30.45	141	32.5	110	34.55	115	36.6	85	38.65	73	40.7	95
20.25	201	22.3	151	24.35	148	26.4	157	28.45	169	30.5	143	32.55	122	34.6	117	36.65	87	38.7	84	40.75	79
20.3	211	22.35	196	24.4	143	26.45	146	28.5	148	30.55	186	32.6	123	34.65	111	36.7	100	38.75	82	40.8	95
20.35	188	22.4	186	24.45	189	26.5	142	28.55	146	30.6	154	32.65	148	34.7	111	36.75	83	38.8	83	40.85	79
20.4	225	22.45	184	24.5	149	26.55	164	28.6	144	30.65	134	32.7	116	34.75	135	36.8	74	38.85	110	40.9	87
20.45	193	22.5	189	24.55	162	26.6	171	28.65	153	30.7	146	32.75	134	34.8	121	36.85	88	38.9	95	40.95	75
20.5	220	22.55	211	24.6	167	26.65	174	28.7	174	30.75	157	32.8	111	34.85	130	36.9	97	38.95	95	41	73
20.55	228	22.6	187	24.65	168	26.7	152	28.75	155	30.8	144	32.85	134	34.9	95	36.95	89	39	96	41.05	78
20.6	204	22.65	169	24.7	176	26.75	171	28.8	141	30.85	166	32.9	123	34.95	98	37	85	39.05	78	41.1	84
20.65	193	22.7	226	24.75	157	26.8	187	28.85	123	30.9	140	32.95	120	35	129	37.05	91	39.1	79	41.15	78
20.7	207	22.75	174	24.8	156	26.85	178	28.9	152	30.95	167	33	125	35.05	113	37.1	76	39.15	74	41.2	90
20.75	195	22.8	194	24.85	163	26.9	192	28.95	146	31	154	33.05	134	35.1	100	37.15	85	39.2	83	41.25	98
20.8	215	22.85	186	24.9	143	26.95	169	29	144	31.05	118	33.1	134	35.15	116	37.2	112	39.25	78	41.3	69
20.85	196	22.9	195	24.95	155	27	190	29.05	137	31.1	153	33.15	102	35.2	106	37.25	84	39.3	76	41.35	81
20.9	231	22.95	184	25	157	27.05	212	29.1	146	31.15	122	33.2	106	35.25	137	37.3	90	39.35	78	41.4	93
20.95	234	23	166	25.05	176	27.1	222	29.15	154	31.2	172	33.25	123	35.3	142	37.35	92	39.4	83	41.45	79
21	220	23.05	197	25.1	143	27.15	219	29.2	135	31.25	135	33.3	109	35.35	102	37.4	110	39.45	80	41.5	97
21.05	232	23.1	192	25.15	129	27.2	215	29.25	143	31.3	147	33.35	110	35.4	119	37.45	101	39.5	88	41.55	85
21.1	216	23.15	170	25.2	158	27.25	251	29.3	151	31.35	152	33.4	112	35.45	106	37.5	70	39.55	72	41.6	81
21.15	223	23.2	200	25.25	153	27.3	252	29.35	144	31.4	129	33.45	118	35.5	103	37.55	75	39.6	64	41.65	87
21.2	233	23.25	192	25.3	145	27.35	283	29.4	135	31.45	140	33.5	112	35.55	127	37.6	94	39.65	71	41.7	93
21.25	221	23.3	235	25.35	138	27.4	288	29.45	149	31.5	132	33.55	113	35.6	113	37.65	64	39.7	95	41.75	86
21.3	246	23.35	197	25.4	168	27.45	304	29.5	158	31.55	131	33.6	101	35.65	113	37.7	93	39.75	96	41.8	72
21.35	228	23.4	204	25.45	176	27.5	283	29.55	129	31.6	139	33.65	102	35.7	110	37.75	99	39.8	89	41.85	75
21.4	213	23.45	218	25.5	168	27.55	288	29.6	167	31.65	126	33.7	108	35.75	109	37.8	83	39.85	76	41.9	79
21.45	226	23.5	217	25.55	168	27.6	300	29.65	180	31.7	134	33.75	103	35.8	104	37.85	102	39.9	65	41.95	91
21.5	247	23.55	188	25.6	175	27.65	275	29.7	172	31.75	129	33.8	118	35.85	111	37.9	96	39.95	74	42	73
21.55	262	23.6	188	25.65	176	27.7	285	29.75	174	31.8	136	33.85	106	35.9	115	37.95	78	40	82	42.05	77
21.6	260	23.65	173	25.7	197	27.75	215	29.8	153	31.85	126	33.9	99	35.95	98	38	92	40.05	57	42.1	70
21.65	258	23.7	164	25.75	159	27.8	222	29.85	163	31.9	130	33.95	99	36	82	38.05	96	40.1	79	42.15	78
21.7	270	23.75	204	25.8	174	27.85	199	29.9	156	31.95	126	34	108	36.05	91	38.1	98	40.15	72	42.2	92
21.75	311	23.8	209	25.85	131	27.9	197	29.95	149	32	132	34.05	106	36.1	94	38.15	84	40.2	52	42.25	83
21.8	289	23.85	162	25.9	135	27.95	176	30	162	32.05	143	34.1	103	36.15	98	38.2	80	40.25	83	42.3	67
21.85	238	23.9	177	25.95	138	28	162	30.05	162	32.1	128	34.15	100	36.2	93	38.25	78	40.3	68	42.35	69
21.9	230	23.95	191	26	141	28.05	160	30.1	155	32.15	109	34.2	104	36.25	98	38.3	76	40.35	95	42.4	87
21.95	242	24	166	26.05	141	28.1	175	30.15	137	32.2	124	34.25	116	36.3	90	38.35	89	40.4	73	42.45	83
22	191	24.05	174	26.1	168	28.15	162	30.2	142	32.25	121	34.3	132	36.35	106	38.4	84	40.45	85	42.5	84

Angle	R.Int	Angle	R.Int	Angle	R.Int	Angle	R.Int	Angle	R.Int	Angle	R.Int	Angle	R.Int	Angle	R.Int	Angle	R.Int	Angle	R.Int
42.55	84	44.6	71	46.65	77	48.7	68	50.75	62	52.75	73	54.8	55	56.85	73	58.9	59	60.95	67	63	50
42.6	76	44.65	76	46.7	69	48.75	70	50.8	89	52.8	63	54.85	63	56.9	56	58.95	53	61	42	63.05	56
42.65	81	44.7	70	46.75	82	48.8	85	50.85	83	52.85	60	54.9	66	56.95	50	59	63	61.05	63	63.1	53
42.7	82	44.75	75	46.8	78	48.85	74	50.9	88	52.9	55	54.95	54	57	62	59.05	61	61.1	66	63.15	67
42.75	91	44.8	60	46.85	71	48.9	69	50.95	92	52.95	84	55	60	57.05	64	59.1	66	61.15	58	63.2	54
42.8	80	44.85	72	46.9	72	48.95	64	51	91	53	56	55.05	65	57.1	57	59.15	76	61.2	80	63.25	66
42.85	65	44.9	61	46.95	89	49	58	51.05	78	53.05	54	55.1	60	57.15	54	59.2	52	61.25	65	63.3	70
42.9	74	44.95	73	47	69	49.05	55	51.1	83	53.1	76	55.15	53	57.2	71	59.25	57	61.3	70	63.35	63
42.95	98	45	84	47.05	71	49.1	79	51.15	65	53.15	73	55.2	52	57.25	69	59.3	75	61.35	55	63.4	76
43	78	45.05	62	47.1	68	49.15	68	51.2	64	53.2	79	55.25	68	57.3	53	59.35	54	61.4	73	63.45	64
43.05	87	45.1	72	47.15	83	49.2	71	51.25	62	53.25	66	55.3	48	57.35	59	59.4	65	61.45	60	63.5	62
43.1	65	45.15	57	47.2	72	49.25	78	51.3	58	53.3	69	55.35	53	57.4	61	59.45	72	61.5	61	63.55	70
43.15	69	45.2	62	47.25	76	49.3	76	51.35	54	53.35	79	55.4	60	57.45	56	59.5	58	61.55	60	63.6	56
43.2	70	45.25	83	47.3	68	49.35	72	51.4	59	53.4	61	55.45	45	57.5	64	59.55	53	61.6	71	63.65	61
43.25	63	45.3	63	47.35	67	49.4	91	51.45	51	53.45	65	55.5	57	57.55	67	59.6	59	61.65	73	63.7	58
43.3	62	45.35	57	47.4	67	49.45	66	51.5	69	53.5	56	55.55	66	57.6	61	59.65	59	61.7	60	63.75	64
43.35	79	45.4	76	47.45	75	49.5	63	51.55	63	53.55	61	55.6	54	57.65	59	59.7	50	61.75	67	63.8	50
43.4	75	45.45	64	47.5	48	49.55	70	51.6	57	53.6	51	55.65	50	57.7	46	59.75	53	61.8	78	63.85	69
43.45	65	45.5	69	47.55	67	49.6	63	51.65	55	53.65	68	55.7	59	57.75	57	59.8	54	61.85	77	63.9	47
43.5	61	45.55	61	47.6	59	49.65	65	51.7	73	53.7	68	55.75	67	57.8	54	59.85	51	61.9	80	63.95	55
43.55	80	45.6	76	47.65	70	49.7	68	51.75	62	53.75	60	55.8	65	57.85	72	59.9	49	61.95	68	64	65
43.6	68	45.65	56	47.7	50	49.75	60	51.8	62	53.8	65	55.85	53	57.9	49	59.95	64	62	64	64.05	58
43.65	65	45.7	59	47.75	83	49.8	67	51.85	74	53.85	51	55.9	59	57.95	56	60	60	62.05	58	64.1	74
43.7	88	45.75	56	47.8	70	49.85	65	51.9	64	53.9	67	55.95	59	58	61	60.05	57	62.1	76	64.15	63
43.75	70	45.8	86	47.85	49	49.9	74	51.95	51	53.95	53	56	59	58.05	56	60.1	45	62.15	70	64.2	62
43.8	92	45.85	65	47.9	58	49.95	60	52	57	54	56	56.05	57	58.1	63	60.15	40	62.2	64	64.25	55
43.85	57	45.9	72	47.95	58	50	67	52.05	56	54.05	76	56.1	63	58.15	69	60.2	81	62.25	69	64.3	53
43.9	61	45.95	73	48	62	50.05	70	52.1	60	54.1	67	56.15	64	58.2	63	60.25	56	62.3	65	64.35	51
43.95	68	46	79	48.05	79	50.1	57	52.15	53	54.15	56	56.2	72	58.25	66	60.3	57	62.35	75	64.4	58
44	77	46.05	75	48.1	71	50.15	82	52.2	65	54.2	67	56.25	66	58.3	44	60.35	60	62.4	59	64.45	75
44.05	71	46.1	80	48.15	69	50.2	86	52.25	53	54.25	71	56.3	59	58.35	43	60.4	54	62.45	63	64.5	44
44.1	81	46.15	75	48.2	70	50.25	77	52.3	74	54.3	60	56.35	70	58.4	69	60.45	54	62.5	65	64.55	68
44.15	73	46.2	46	48.25	72	50.3	74	52.35	63	54.35	58	56.4	71	58.45	54	60.5	64	62.55	70	64.6	56
44.2	62	46.25	79	48.3	68	50.35	66	52.4	58	54.4	52	56.45	65	58.5	43	60.55	58	62.6	60	64.65	76
44.25	91	46.3	84	48.35	61	50.4	80	52.45	52	54.45	63	56.5	52	58.55	48	60.6	59	62.65	68	64.7	66
44.3	78	46.35	70	48.4	80	50.45	63	52.5	79	54.5	59	56.55	81	58.6	59	60.65	54	62.7	71	64.75	55
44.35	80	46.4	64	48.45	71	50.5	79	52.55	77	54.55	61	56.6	55	58.65	57	60.7	66	62.75	59	64.8	76
44.4	82	46.45	77	48.5	64	50.55	78	52.6	63	54.6	65	56.65	78	58.7	64	60.75	50	62.8	65	64.85	59
44.45	79	46.5	72	48.55	79	50.6	79	52.65	58	54.65	60	56.7	69	58.75	62	60.8	55	62.85	64	64.9	65
44.5	82	46.55	67	48.6	65	50.65	89	52.7	58	54.7	61	56.75	59	58.8	45	60.85	60	62.9	47	64.95	64
44.55	69	46.6	64	48.65	62	50.7	87	52.75	73	54.75	70	56.8	68	58.85	83	60.9	53	62.95	58	65	60

Angle	R.Int	Angle	R.Int	Angle	R.Int	Angle	R.Int	Angle	R.Int	Angle	R.Int	Angle	R.Int
65.05	52	67.25	83	69.45	54	71.65	37	73.85	70	76.05	45	78.25	63
65.1	70	67.3	63	69.5	58	71.7	55	73.9	54	76.1	58	78.3	62
65.15	67	67.35	52	69.55	63	71.75	54	73.95	57	76.15	68	78.35	57
65.2	65	67.4	69	69.6	71	71.8	50	74	73	76.2	52	78.4	58
65.25	74	67.45	58	69.65	68	71.85	42	74.05	74	76.25	49	78.45	46
65.3	62	67.5	60	69.7	46	71.9	76	74.1	51	76.3	66	78.5	56
65.35	58	67.55	70	69.75	53	71.95	59	74.15	67	76.35	64	78.55	49
65.4	66	67.6	57	69.8	51	72	57	74.2	50	76.4	58	78.6	40
65.45	53	67.65	84	69.85	62	72.05	64	74.25	70	76.45	59	78.65	60
65.5	57	67.7	50	69.9	63	72.1	52	74.3	47	76.5	68	78.7	69
65.55	35	67.75	75	69.95	44	72.15	54	74.35	64	76.55	49	78.75	58
65.6	69	67.8	58	70	57	72.2	57	74.4	61	76.6	49	78.8	52
65.65	53	67.85	37	70.05	57	72.25	65	74.45	58	76.65	49	78.85	59
65.7	70	67.9	58	70.1	59	72.3	60	74.5	77	76.7	64	78.9	51
65.75	55	67.95	54	70.15	75	72.35	85	74.55	58	76.75	64	78.95	55
65.8	62	68	70	70.2	57	72.4	62	74.6	70	76.8	54	79	48
65.85	51	68.05	67	70.25	58	72.45	69	74.65	50	76.85	57	79.05	51
65.9	81	68.1	64	70.3	57	72.5	65	74.7	62	76.9	64	79.1	56
65.95	50	68.15	71	70.35	60	72.55	51	74.75	59	76.95	44	79.15	56
66	67	68.2	60	70.4	57	72.6	53	74.8	60	77	52	79.2	56
66.05	62	68.25	54	70.45	58	72.65	58	74.85	56	77.05	54	79.25	64
66.1	74	68.3	59	70.5	53	72.7	43	74.9	69	77.1	51	79.3	59
66.15	58	68.35	49	70.55	59	72.75	73	74.95	73	77.15	64	79.35	54
66.2	55	68.4	62	70.6	64	72.8	48	75	83	77.2	57	79.4	62
66.25	60	68.45	47	70.65	79	72.85	63	75.05	62	77.25	68	79.45	56
66.3	68	68.5	70	70.7	48	72.9	67	75.1	58	77.3	61	79.5	62
66.35	59	68.55	46	70.75	77	72.95	62	75.15	68	77.35	66	79.55	45
66.4	58	68.6	54	70.8	52	73	52	75.2	46	77.4	61	79.6	68
66.45	60	68.65	68	70.85	42	73.05	49	75.25	70	77.45	58	79.65	54
66.5	47	68.7	56	70.9	52	73.1	46	75.3	62	77.5	51	79.7	60
66.55	61	68.75	53	70.95	54	73.15	55	75.35	61	77.55	46	79.75	59
66.6	59	68.8	50	71	53	73.2	65	75.4	63	77.6	52	79.8	40
66.65	52	68.85	64	71.05	63	73.25	53	75.45	49	77.65	40	79.85	45
66.7	55	68.9	56	71.1	53	73.3	54	75.5	60	77.7	63	79.9	63
66.75	53	68.95	51	71.15	59	73.35	69	75.55	61	77.75	64	79.95	53
66.8	66	69	61	71.2	59	73.4	63	75.6	58	77.8	57	80	39
66.85	54	69.05	59	71.25	51	73.45	62	75.65	60	77.85	55		
66.9	55	69.1	63	71.3	66	73.5	57	75.7	50	77.9	47		
66.95	61	69.15	64	71.35	58	73.55	70	75.75	78	77.95	47		
67	62	69.2	58	71.4	63	73.6	54	75.8	74	78	67		
67.05	49	69.25	66	71.45	56	73.65	78	75.85	62	78.05	66		
67.1	51	69.3	68	71.5	61	73.7	70	75.9	76	78.1	58		
67.15	64	69.35	76	71.55	57	73.75	48	75.95	57	78.15	59		
67.2	69	69.4	65	71.6	57	73.8	59	76	51	78.2	47		

Grotta dei Palizzi lava flow

Angle	R.Int	Angle	R.Int	Angle	R.Int	Angle	R.Int	Angle	R.Int	Angle	R.Int	Angle	R.Int	Angle	R.Int	Angle	R.Int	Angle	R.Int
20	185	22.05	128	24.1	137	26.15	117	28.2	94	30.25	99	32.3	76	34.35	79	36.4	72	38.45	70	40.5	54
20.05	165	22.1	153	24.15	116	26.2	116	28.25	130	30.3	110	32.35	70	34.4	80	36.45	63	38.5	54	40.55	57
20.1	174	22.15	141	24.2	107	26.25	121	28.3	102	30.35	116	32.4	80	34.45	74	36.5	66	38.55	58	40.6	53
20.15	192	22.2	127	24.25	147	26.3	124	28.35	107	30.4	114	32.45	87	34.5	93	36.55	62	38.6	62	40.65	58
20.2	160	22.25	150	24.3	116	26.35	103	28.4	124	30.45	86	32.5	82	34.55	88	36.6	70	38.65	66	40.7	72
20.25	171	22.3	152	24.35	108	26.4	126	28.45	117	30.5	97	32.55	71	34.6	90	36.65	68	38.7	84	40.75	61
20.3	185	22.35	142	24.4	116	26.45	119	28.5	125	30.55	104	32.6	83	34.65	80	36.7	61	38.75	64	40.8	53
20.35	179	22.4	147	24.45	133	26.5	109	28.55	103	30.6	92	32.65	93	34.7	74	36.75	66	38.8	50	40.85	71
20.4	174	22.45	155	24.5	110	26.55	118	28.6	112	30.65	95	32.7	90	34.75	78	36.8	58	38.85	49	40.9	69
20.45	168	22.5	164	24.55	122	26.6	115	28.65	109	30.7	102	32.75	87	34.8	92	36.85	66	38.9	62	40.95	47
20.5	162	22.55	114	24.6	123	26.65	130	28.7	102	30.75	86	32.8	95	34.85	82	36.9	73	38.95	54	41	58
20.55	173	22.6	133	24.65	104	26.7	118	28.75	124	30.8	102	32.85	74	34.9	76	36.95	58	39	61	41.05	61
20.6	183	22.65	121	24.7	116	26.75	128	28.8	115	30.85	99	32.9	80	34.95	79	37	73	39.05	56	41.1	61
20.65	168	22.7	141	24.75	121	26.8	130	28.85	118	30.9	120	32.95	89	35	93	37.05	65	39.1	64	41.15	71
20.7	172	22.75	158	24.8	126	26.85	126	28.9	103	30.95	103	33	73	35.05	72	37.1	66	39.15	55	41.2	70
20.75	182	22.8	154	24.85	127	26.9	138	28.95	116	31	91	33.05	93	35.1	83	37.15	63	39.2	45	41.25	63
20.8	170	22.85	121	24.9	116	26.95	147	29	99	31.05	100	33.1	84	35.15	71	37.2	65	39.25	63	41.3	71
20.85	148	22.9	143	24.95	129	27	149	29.05	96	31.1	91	33.15	86	35.2	76	37.25	58	39.3	62	41.35	70
20.9	179	22.95	134	25	120	27.05	150	29.1	119	31.15	102	33.2	79	35.25	79	37.3	58	39.35	68	41.4	66
20.95	159	23	157	25.05	122	27.1	128	29.15	127	31.2	109	33.25	94	35.3	91	37.35	69	39.4	57	41.45	50
21	143	23.05	189	25.1	119	27.15	138	29.2	105	31.25	94	33.3	83	35.35	70	37.4	67	39.45	55	41.5	53
21.05	132	23.1	142	25.15	112	27.2	156	29.25	110	31.3	103	33.35	69	35.4	75	37.45	69	39.5	61	41.55	63
21.1	167	23.15	126	25.2	128	27.25	127	29.3	114	31.35	92	33.4	71	35.45	77	37.5	63	39.55	60	41.6	64
21.15	166	23.2	125	25.25	129	27.3	136	29.35	163	31.4	86	33.45	74	35.5	78	37.55	49	39.6	57	41.65	72
21.2	157	23.25	148	25.3	124	27.35	161	29.4	119	31.45	99	33.5	75	35.55	61	37.6	61	39.65	56	41.7	59
21.25	174	23.3	153	25.35	134	27.4	131	29.45	137	31.5	89	33.55	77	35.6	67	37.65	63	39.7	56	41.75	71
21.3	161	23.35	136	25.4	120	27.45	128	29.5	104	31.55	105	33.6	60	35.65	75	37.7	64	39.75	58	41.8	66
21.35	153	23.4	131	25.45	137	27.5	127	29.55	115	31.6	84	33.65	75	35.7	75	37.75	66	39.8	57	41.85	56
21.4	171	23.45	147	25.5	132	27.55	146	29.6	134	31.65	90	33.7	87	35.75	69	37.8	57	39.85	57	41.9	46
21.45	156	23.5	149	25.55	149	27.6	137	29.65	118	31.7	116	33.75	68	35.8	77	37.85	67	39.9	64	41.95	68
21.5	174	23.55	137	25.6	120	27.65	111	29.7	122	31.75	104	33.8	82	35.85	62	37.9	66	39.95	49	42	49
21.55	146	23.6	88	25.65	122	27.7	112	29.75	113	31.8	84	33.85	84	35.9	57	37.95	69	40	74	42.05	48
21.6	155	23.65	99	25.7	112	27.75	124	29.8	91	31.85	86	33.9	86	35.95	80	38	57	40.05	65	42.1	60
21.65	149	23.7	135	25.75	119	27.8	125	29.85	110	31.9	111	33.95	78	36	66	38.05	49	40.1	57	42.15	57
21.7	175	23.75	121	25.8	125	27.85	122	29.9	110	31.95	76	34	65	36.05	77	38.1	59	40.15	67	42.2	61
21.75	160	23.8	138	25.85	135	27.9	101	29.95	116	32	97	34.05	88	36.1	75	38.15	61	40.2	60	42.25	54
21.8	151	23.85	123	25.9	114	27.95	104	30	157	32.05	92	34.1	80	36.15	72	38.2	49	40.25	58	42.3	47
21.85	135	23.9	138	25.95	115	28	126	30.05	118	32.1	88	34.15	64	36.2	63	38.25	50	40.3	56	42.35	55
21.9	140	23.95	121	26	116	28.05	123	30.1	111	32.15	83	34.2	93	36.25	75	38.3	69	40.35	72	42.4	42
21.95	120	24	122	26.05	121	28.1	114	30.15	105	32.2	66	34.25	75	36.3	74	38.35	62	40.4	49	42.45	65
22	139	24.05	130	26.1	111	28.15	102	30.2	102	32.25	75	34.3	76	36.35	68	38.4	72	40.45	67	42.5	66

Angle	R.Int	Angle	R.Int	Angle	R.Int	Angle	R.Int	Angle	R.Int	Angle	R.Int	Angle	R.Int	Angle	R.Int	Angle	R.Int	Angle	R.Int	Angle	R.Int
42.55	51	44.6	59	46.65	45	48.7	61	50.75	44	52.8	51	54.85	49	56.9	46	58.95	46	61	47	63.05	55
42.6	65	44.65	59	46.7	49	48.75	55	50.8	43	52.85	44	54.9	58	56.95	51	59	46	61.05	41	63.1	48
42.65	58	44.7	56	46.75	44	48.8	51	50.85	57	52.9	55	54.95	55	57	50	59.05	58	61.1	56	63.15	51
42.7	48	44.75	58	46.8	59	48.85	55	50.9	48	52.95	52	55	42	57.05	45	59.1	53	61.15	52	63.2	46
42.75	48	44.8	56	46.85	45	48.9	53	50.95	55	53	47	55.05	54	57.1	42	59.15	44	61.2	45	63.25	38
42.8	54	44.85	67	46.9	52	48.95	64	51	47	53.05	50	55.1	50	57.15	51	59.2	38	61.25	42	63.3	41
42.85	52	44.9	67	46.95	45	49	48	51.05	57	53.1	54	55.15	42	57.2	46	59.25	49	61.3	55	63.35	43
42.9	47	44.95	51	47	46	49.05	45	51.1	51	53.15	54	55.2	43	57.25	39	59.3	58	61.35	41	63.4	49
42.95	51	45	52	47.05	54	49.1	54	51.15	43	53.2	45	55.25	47	57.3	50	59.35	58	61.4	56	63.45	38
43	56	45.05	58	47.1	60	49.15	40	51.2	61	53.25	56	55.3	57	57.35	46	59.4	38	61.45	54	63.5	47
43.05	54	45.1	45	47.15	34	49.2	47	51.25	61	53.3	41	55.35	57	57.4	45	59.45	43	61.5	51	63.55	51
43.1	34	45.15	53	47.2	63	49.25	52	51.3	48	53.35	55	55.4	49	57.45	45	59.5	52	61.55	63	63.6	56
43.15	50	45.2	55	47.25	50	49.3	56	51.35	36	53.4	41	55.45	44	57.5	49	59.55	48	61.6	63	63.65	55
43.2	47	45.25	52	47.3	54	49.35	78	51.4	61	53.45	42	55.5	51	57.55	51	59.6	45	61.65	59	63.7	42
43.25	51	45.3	51	47.35	49	49.4	42	51.45	56	53.5	44	55.55	39	57.6	45	59.65	62	61.7	50	63.75	55
43.3	61	45.35	52	47.4	44	49.45	48	51.5	42	53.55	46	55.6	49	57.65	47	59.7	55	61.75	45	63.8	55
43.35	60	45.4	46	47.45	44	49.5	52	51.55	49	53.6	51	55.65	49	57.7	58	59.75	42	61.8	57	63.85	50
43.4	48	45.45	59	47.5	54	49.55	52	51.6	48	53.65	49	55.7	67	57.75	47	59.8	38	61.85	52	63.9	51
43.45	51	45.5	53	47.55	64	49.6	51	51.65	56	53.7	41	55.75	38	57.8	54	59.85	53	61.9	61	63.95	55
43.5	48	45.55	46	47.6	49	49.65	35	51.7	54	53.75	49	55.8	47	57.85	61	59.9	49	61.95	60	64	46
43.55	59	45.6	56	47.65	63	49.7	42	51.75	51	53.8	48	55.85	46	57.9	41	59.95	41	62	44	64.05	48
43.6	56	45.65	48	47.7	59	49.75	50	51.8	55	53.85	46	55.9	63	57.95	57	60	60	62.05	47	64.1	43
43.65	59	45.7	57	47.75	59	49.8	57	51.85	54	53.9	39	55.95	48	58	56	60.05	57	62.1	45	64.15	57
43.7	48	45.75	57	47.8	46	49.85	64	51.9	47	53.95	49	56	56	58.05	49	60.1	59	62.15	49	64.2	43
43.75	52	45.8	48	47.85	42	49.9	54	51.95	32	54	42	56.05	51	58.1	53	60.15	53	62.2	60	64.25	60
43.8	61	45.85	43	47.9	60	49.95	48	52	48	54.05	56	56.1	61	58.15	48	60.2	51	62.25	40	64.3	51
43.85	69	45.9	65	47.95	56	50	50	52.05	52	54.1	47	56.15	48	58.2	51	60.25	54	62.3	53	64.35	50
43.9	59	45.95	53	48	33	50.05	57	52.1	65	54.15	42	56.2	65	58.25	40	60.3	48	62.35	58	64.4	48
43.95	58	46	65	48.05	38	50.1	42	52.15	53	54.2	47	56.25	56	58.3	47	60.35	46	62.4	39	64.45	55
44	59	46.05	52	48.1	50	50.15	53	52.2	52	54.25	39	56.3	50	58.35	49	60.4	47	62.45	37	64.5	52
44.05	68	46.1	72	48.15	55	50.2	47	52.25	62	54.3	46	56.35	39	58.4	57	60.45	58	62.5	53	64.55	42
44.1	49	46.15	49	48.2	41	50.25	49	52.3	43	54.35	51	56.4	64	58.45	46	60.5	39	62.55	49	64.6	52
44.15	59	46.2	48	48.25	51	50.3	57	52.35	42	54.4	47	56.45	59	58.5	49	60.55	62	62.6	42	64.65	50
44.2	69	46.25	50	48.3	52	50.35	59	52.4	56	54.45	45	56.5	50	58.55	34	60.6	51	62.65	46	64.7	46
44.25	58	46.3	48	48.35	60	50.4	61	52.45	52	54.5	51	56.55	62	58.6	45	60.65	47	62.7	46	64.75	54
44.3	61	46.35	45	48.4	61	50.45	51	52.5	44	54.55	48	56.6	59	58.65	45	60.7	45	62.75	54	64.8	62
44.35	47	46.4	58	48.45	49	50.5	54	52.55	57	54.6	50	56.65	56	58.7	47	60.75	50	62.8	41	64.85	45
44.4	50	46.45	44	48.5	45	50.55	47	52.6	52	54.65	56	56.7	53	58.75	41	60.8	51	62.85	57	64.9	58
44.45	57	46.5	56	48.55	47	50.6	80	52.65	54	54.7	44	56.75	34	58.8	47	60.85	43	62.9	43	64.95	50
44.5	47	46.55	56	48.6	65	50.65	62	52.7	52	54.75	58	56.8	55	58.85	41	60.9	51	62.95	39	65	59
44.55	47	46.6	43	48.65	54	50.7	51	52.75	48	54.8	48	56.85	54	58.9	50	60.95	51	63	42	65.05	64

Angle	R.Int	Angle	R.Int	Angle	R.Int	Angle	R.Int	Angle	R.Int	Angle	R.Int	Angle	R.Int
65.1	60	67.3	52	69.5	53	71.7	57	73.9	58	76.1	38	78.3	41
65.15	46	67.35	45	69.55	44	71.75	48	73.95	52	76.15	50	78.35	46
65.2	54	67.4	55	69.6	57	71.8	65	74	51	76.2	43	78.4	38
65.25	48	67.45	46	69.65	54	71.85	41	74.05	44	76.25	51	78.45	39
65.3	60	67.5	47	69.7	45	71.9	46	74.1	38	76.3	49	78.5	40
65.35	59	67.55	43	69.75	58	71.95	46	74.15	40	76.35	42	78.55	40
65.4	48	67.6	47	69.8	57	72	50	74.2	57	76.4	39	78.6	39
65.45	45	67.65	57	69.85	63	72.05	51	74.25	42	76.45	36	78.65	43
65.5	39	67.7	39	69.9	52	72.1	55	74.3	46	76.5	36	78.7	44
65.55	47	67.75	49	69.95	54	72.15	39	74.35	57	76.55	37	78.75	30
65.6	63	67.8	46	70	48	72.2	35	74.4	36	76.6	38	78.8	48
65.65	45	67.85	44	70.05	41	72.25	66	74.45	40	76.65	35	78.85	57
65.7	61	67.9	53	70.1	41	72.3	44	74.5	49	76.7	46	78.9	35
65.75	45	67.95	41	70.15	56	72.35	56	74.55	62	76.75	50	78.95	46
65.8	47	68	53	70.2	47	72.4	50	74.6	52	76.8	56	79	51
65.85	48	68.05	39	70.25	47	72.45	40	74.65	66	76.85	47	79.05	51
65.9	50	68.1	47	70.3	39	72.5	39	74.7	44	76.9	40	79.1	46
65.95	52	68.15	42	70.35	55	72.55	47	74.75	47	76.95	46	79.15	38
66	53	68.2	41	70.4	38	72.6	51	74.8	47	77	43	79.2	58
66.05	50	68.25	50	70.45	50	72.65	52	74.85	40	77.05	43	79.25	59
66.1	49	68.3	52	70.5	52	72.7	45	74.9	54	77.1	58	79.3	44
66.15	37	68.35	45	70.55	63	72.75	51	74.95	50	77.15	41	79.35	37
66.2	57	68.4	44	70.6	46	72.8	43	75	54	77.2	45	79.4	41
66.25	47	68.45	52	70.65	45	72.85	47	75.05	59	77.25	44	79.45	50
66.3	43	68.5	45	70.7	43	72.9	44	75.1	54	77.3	62	79.5	53
66.35	38	68.55	39	70.75	58	72.95	43	75.15	41	77.35	42	79.55	44
66.4	45	68.6	49	70.8	59	73	45	75.2	47	77.4	45	79.6	49
66.45	52	68.65	45	70.85	50	73.05	51	75.25	44	77.45	58	79.65	60
66.5	55	68.7	49	70.9	41	73.1	46	75.3	43	77.5	46	79.7	49
66.55	56	68.75	44	70.95	52	73.15	53	75.35	70	77.55	43	79.75	53
66.6	39	68.8	43	71	49	73.2	50	75.4	50	77.6	41	79.8	42
66.65	37	68.85	49	71.05	52	73.25	39	75.45	39	77.65	41	79.85	41
66.7	51	68.9	57	71.1	50	73.3	38	75.5	52	77.7	36	79.9	43
66.75	75	68.95	51	71.15	34	73.35	47	75.55	48	77.75	37	79.95	38
66.8	47	69	58	71.2	40	73.4	38	75.6	44	77.8	51	80	40
66.85	50	69.05	42	71.25	36	73.45	58	75.65	50	77.85	38		
66.9	40	69.1	59	71.3	49	73.5	40	75.7	50	77.9	48		
66.95	44	69.15	58	71.35	37	73.55	49	75.75	51	77.95	43		
67	47	69.2	45	71.4	40	73.6	47	75.8	46	78	44		
67.05	47	69.25	41	71.45	41	73.65	40	75.85	65	78.05	44		
67.1	35	69.3	54	71.5	43	73.7	54	75.9	50	78.1	59		
67.15	53	69.35	52	71.55	33	73.75	57	75.95	53	78.15	39		
67.2	50	69.4	50	71.6	47	73.8	32	76	53	78.2	47		
67.25	28	69.45	55	71.65	44	73.85	53	76.05	50	78.25	48		

Pomiciazzo lava flow

Angle	R.Int	Angle	R.Int	Angle	R.Int	Angle	R.Int	Angle	R.Int	Angle	R.Int	Angle	R.Int	Angle	R.Int	Angle	R.Int	Angle	R.Int	Angle	R.Int
20	439	20.82	573	21.64	706	22.46	369	23.28	596	24.1	291	24.92	297	25.74	288	26.56	383	27.38	938	28.2	291
20.02	454	20.84	546	21.66	642	22.48	383	23.3	540	24.12	323	24.94	275	25.76	301	26.58	386	27.4	940	28.22	267
20.04	428	20.86	570	21.68	567	22.5	413	23.32	569	24.14	334	24.96	287	25.78	318	26.6	439	27.42	904	28.24	285
20.06	464	20.88	609	21.7	564	22.52	391	23.34	536	24.16	342	24.98	323	25.8	341	26.62	393	27.44	924	28.26	292
20.08	473	20.9	567	21.72	525	22.54	406	23.36	520	24.18	355	25	307	25.82	310	26.64	435	27.46	796	28.28	238
20.1	461	20.92	578	21.74	484	22.56	355	23.38	471	24.2	343	25.02	320	25.84	311	26.66	413	27.48	805	28.3	274
20.12	451	20.94	529	21.76	503	22.58	404	23.4	459	24.22	368	25.04	270	25.86	294	26.68	472	27.5	787	28.32	270
20.14	465	20.96	598	21.78	477	22.6	386	23.42	499	24.24	320	25.06	274	25.88	294	26.7	427	27.52	808	28.34	235
20.16	461	20.98	601	21.8	459	22.62	422	23.44	454	24.26	332	25.08	301	25.9	310	26.72	442	27.54	793	28.36	262
20.18	439	21	605	21.82	478	22.64	383	23.46	446	24.28	349	25.1	314	25.92	300	26.74	444	27.56	704	28.38	278
20.2	484	21.02	583	21.84	458	22.66	415	23.48	418	24.3	313	25.12	271	25.94	333	26.76	443	27.58	777	28.4	258
20.22	441	21.04	652	21.86	429	22.68	393	23.5	464	24.32	327	25.14	327	25.96	320	26.78	446	27.6	667	28.42	277
20.24	461	21.06	640	21.88	420	22.7	397	23.52	412	24.34	340	25.16	281	25.98	347	26.8	406	27.62	632	28.44	256
20.26	466	21.08	683	21.9	395	22.72	384	23.54	430	24.36	316	25.18	288	26	323	26.82	477	27.64	624	28.46	267
20.28	471	21.1	749	21.92	386	22.74	376	23.56	398	24.38	325	25.2	342	26.02	310	26.84	478	27.66	572	28.48	238
20.3	449	21.12	719	21.94	417	22.76	346	23.58	400	24.4	320	25.22	319	26.04	316	26.86	500	27.68	526	28.5	278
20.32	440	21.14	808	21.96	430	22.78	380	23.6	420	24.42	320	25.24	346	26.06	290	26.88	492	27.7	470	28.52	284
20.34	444	21.16	791	21.98	388	22.8	377	23.62	364	24.44	278	25.26	382	26.08	297	26.9	514	27.72	493	28.54	251
20.36	436	21.18	857	22	392	22.82	353	23.64	383	24.46	333	25.28	352	26.1	306	26.92	501	27.74	446	28.56	243
20.38	433	21.2	981	22.02	384	22.84	395	23.66	343	24.48	305	25.3	352	26.12	286	26.94	517	27.76	410	28.58	280
20.4	429	21.22	995	22.04	385	22.86	347	23.68	358	24.5	277	25.32	376	26.14	296	26.96	550	27.78	439	28.6	294
20.42	503	21.24	1092	22.06	379	22.88	385	23.7	361	24.52	275	25.34	387	26.16	311	26.98	532	27.8	405	28.62	249
20.44	443	21.26	1067	22.08	348	22.9	377	23.72	346	24.54	289	25.36	363	26.18	276	27	605	27.82	412	28.64	274
20.46	462	21.28	1124	22.1	377	22.92	355	23.74	349	24.56	293	25.38	397	26.2	290	27.02	633	27.84	417	28.66	270
20.48	425	21.3	1195	22.12	397	22.94	396	23.76	373	24.58	337	25.4	414	26.22	320	27.04	588	27.86	366	28.68	255
20.5	446	21.32	1193	22.14	376	22.96	395	23.78	344	24.6	294	25.42	427	26.24	308	27.06	692	27.88	398	28.7	279
20.52	459	21.34	1301	22.16	388	22.98	372	23.8	385	24.62	290	25.44	372	26.26	300	27.08	682	27.9	370	28.72	261
20.54	488	21.36	1264	22.18	380	23	431	23.82	344	24.64	305	25.46	411	26.28	287	27.1	737	27.92	345	28.74	278
20.56	484	21.38	1245	22.2	381	23.02	449	23.84	366	24.66	345	25.48	391	26.3	302	27.12	791	27.94	378	28.76	311
20.58	464	21.4	1234	22.22	378	23.04	420	23.86	327	24.68	322	25.5	383	26.32	323	27.14	793	27.96	331	28.78	286
20.6	474	21.42	1211	22.24	420	23.06	420	23.88	344	24.7	306	25.52	395	26.34	326	27.16	870	27.98	297	28.8	221
20.62	486	21.44	1172	22.26	432	23.08	480	23.9	341	24.72	330	25.54	381	26.36	314	27.18	893	28	329	28.82	276
20.64	484	21.46	1199	22.28	399	23.1	495	23.92	383	24.74	323	25.56	363	26.38	335	27.2	906	28.02	350	28.84	278
20.66	494	21.48	1096	22.3	387	23.12	469	23.94	349	24.76	293	25.58	326	26.4	369	27.22	956	28.04	305	28.86	288
20.68	561	21.5	984	22.32	447	23.14	475	23.96	337	24.78	289	25.6	368	26.42	360	27.24	1062	28.06	316	28.88	275
20.7	537	21.52	994	22.34	427	23.16	526	23.98	322	24.8	311	25.62	348	26.44	362	27.26	994	28.08	335	28.9	270
20.72	546	21.54	892	22.36	383	23.18	554	24	345	24.82	304	25.64	319	26.46	344	27.28	1042	28.1	324	28.92	290
20.74	513	21.56	822	22.38	435	23.2	611	24.02	300	24.84	296	25.66	347	26.48	362	27.3	1088	28.12	311	28.94	280
20.76	587	21.58	815	22.4	347	23.22	547	24.04	334	24.86	304	25.68	320	26.5	331	27.32	1022	28.14	320	28.96	266
20.78	569	21.6	836	22.42	402	23.24	566	24.06	352	24.88	316	25.7	322	26.52	408	27.34	1005	28.16	276	28.98	310
20.8	550	21.62	700	22.44	373	23.26	545	24.08	338	24.9	294	25.72	328	26.54	358	27.36	943	28.18	272	29	277

Angle	R.Int	Angle	R.Int	Angle	R.Int	Angle	R.Int	Angle	R.Int	Angle	R.Int	Angle	R.Int	Angle	R.Int	Angle	R.Int	Angle	R.Int	Angle	R.Int
29.02	267	29.84	312	30.66	339	31.48	280	32.3	231	33.12	247	33.94	188	34.76	203	35.58	334	36.4	180	37.22	180
29.04	268	29.86	333	30.68	324	31.5	232	32.32	227	33.14	200	33.96	213	34.78	229	35.6	317	36.42	176	37.24	202
29.06	284	29.88	322	30.7	306	31.52	240	32.34	223	33.16	221	33.98	203	34.8	233	35.62	335	36.44	204	37.26	194
29.08	258	29.9	311	30.72	309	31.54	277	32.36	226	33.18	211	34	218	34.82	241	35.64	317	36.46	200	37.28	211
29.1	277	29.92	343	30.74	357	31.56	244	32.38	214	33.2	195	34.02	193	34.84	243	35.66	323	36.48	182	37.3	196
29.12	286	29.94	305	30.76	345	31.58	218	32.4	227	33.22	208	34.04	217	34.86	260	35.68	304	36.5	194	37.32	185
29.14	272	29.96	345	30.78	348	31.6	245	32.42	210	33.24	194	34.06	193	34.88	285	35.7	278	36.52	198	37.34	176
29.16	302	29.98	329	30.8	291	31.62	227	32.44	214	33.26	191	34.08	232	34.9	277	35.72	268	36.54	198	37.36	172
29.18	302	30	303	30.82	297	31.64	228	32.46	239	33.28	191	34.1	194	34.92	276	35.74	253	36.56	193	37.38	186
29.2	318	30.02	334	30.84	318	31.66	253	32.48	248	33.3	229	34.12	220	34.94	316	35.76	275	36.58	193	37.4	195
29.22	285	30.04	334	30.86	285	31.68	244	32.5	222	33.32	188	34.14	210	34.96	288	35.78	214	36.6	181	37.42	194
29.24	312	30.06	338	30.88	283	31.7	271	32.52	218	33.34	197	34.16	210	34.98	311	35.8	247	36.62	192	37.44	187
29.26	301	30.08	343	30.9	303	31.72	259	32.54	202	33.36	221	34.18	238	35	291	35.82	231	36.64	194	37.46	178
29.28	278	30.1	319	30.92	249	31.74	258	32.56	221	33.38	181	34.2	223	35.02	331	35.84	222	36.66	186	37.48	192
29.3	336	30.12	336	30.94	281	31.76	241	32.58	212	33.4	208	34.22	217	35.04	320	35.86	239	36.68	192	37.5	174
29.32	309	30.14	358	30.96	277	31.78	242	32.6	206	33.42	207	34.24	240	35.06	329	35.88	226	36.7	228	37.52	180
29.34	291	30.16	346	30.98	280	31.8	271	32.62	220	33.44	197	34.26	196	35.08	348	35.9	199	36.72	219	37.54	182
29.36	340	30.18	376	31	257	31.82	246	32.64	213	33.46	208	34.28	211	35.1	385	35.92	229	36.74	235	37.56	203
29.38	321	30.2	335	31.02	253	31.84	232	32.66	214	33.48	161	34.3	231	35.12	349	35.94	208	36.76	204	37.58	167
29.4	318	30.22	354	31.04	295	31.86	246	32.68	225	33.5	192	34.32	237	35.14	357	35.96	208	36.78	187	37.6	180
29.42	368	30.24	380	31.06	270	31.88	245	32.7	208	33.52	185	34.34	222	35.16	345	35.98	233	36.8	200	37.62	172
29.44	323	30.26	354	31.08	285	31.9	248	32.72	186	33.54	190	34.36	218	35.18	376	36	182	36.82	197	37.64	186
29.46	345	30.28	372	31.1	236	31.92	243	32.74	202	33.56	217	34.38	214	35.2	390	36.02	213	36.84	235	37.66	166
29.48	349	30.3	366	31.12	258	31.94	241	32.76	236	33.58	208	34.4	193	35.22	378	36.04	208	36.86	226	37.68	153
29.5	363	30.32	356	31.14	249	31.96	266	32.78	209	33.6	186	34.42	250	35.24	350	36.06	196	36.88	194	37.7	177
29.52	370	30.34	373	31.16	252	31.98	227	32.8	244	33.62	180	34.44	257	35.26	351	36.08	207	36.9	211	37.72	158
29.54	384	30.36	386	31.18	252	32	267	32.82	234	33.64	172	34.46	255	35.28	400	36.1	213	36.92	209	37.74	171
29.56	341	30.38	398	31.2	264	32.02	298	32.84	217	33.66	185	34.48	252	35.3	408	36.12	225	36.94	207	37.76	167
29.58	347	30.4	363	31.22	256	32.04	258	32.86	239	33.68	205	34.5	259	35.32	404	36.14	189	36.96	193	37.78	153
29.6	316	30.42	373	31.24	235	32.06	268	32.88	206	33.7	213	34.52	282	35.34	399	36.16	210	36.98	198	37.8	168
29.62	361	30.44	360	31.26	238	32.08	244	32.9	224	33.72	189	34.54	255	35.36	399	36.18	208	37	224	37.82	172
29.64	346	30.46	327	31.28	229	32.1	267	32.92	209	33.74	187	34.56	276	35.38	367	36.2	172	37.02	188	37.84	154
29.66	356	30.48	352	31.3	251	32.12	258	32.94	206	33.76	186	34.58	248	35.4	355	36.22	210	37.04	182	37.86	166
29.68	349	30.5	341	31.32	272	32.14	249	32.96	201	33.78	189	34.6	273	35.42	372	36.24	190	37.06	193	37.88	175
29.7	358	30.52	377	31.34	256	32.16	214	32.98	227	33.8	179	34.62	234	35.44	377	36.26	189	37.08	170	37.9	142
29.72	359	30.54	371	31.36	249	32.18	262	33	198	33.82	188	34.64	255	35.46	380	36.28	208	37.1	208	37.92	161
29.74	318	30.56	342	31.38	253	32.2	240	33.02	190	33.84	211	34.66	261	35.48	379	36.3	191	37.12	192	37.94	143
29.76	333	30.58	337	31.4	281	32.22	248	33.04	239	33.86	209	34.68	238	35.5	370	36.32	212	37.14	197	37.96	141
29.78	311	30.6	341	31.42	255	32.24	232	33.06	185	33.88	214	34.7	266	35.52	361	36.34	193	37.16	187	37.98	161
29.8	313	30.62	334	31.44	242	32.26	220	33.08	217	33.9	194	34.72	248	35.54	354	36.36	185	37.18	180	38	150
29.82	343	30.64	320	31.46	271	32.28	214	33.1	221	33.92	182	34.74	262	35.56	314	36.38	154	37.2	199	38.02	140

Angle	R.Int	Angle	R.Int	Angle	R.Int	Angle	R.Int	Angle	R.Int	Angle	R.Int	Angle	R.Int	Angle	R.Int	Angle	R.Int	Angle	R.Int
38.04	165	38.92	129	39.8	144	40.68	160	41.56	219	42.44	162	43.32	131	44.2	138	45.08	170	45.96	154	46.84	159
38.06	147	38.94	164	39.82	137	40.7	172	41.58	196	42.46	185	43.34	134	44.22	147	45.1	188	45.98	162	46.86	154
38.08	160	38.96	178	39.84	161	40.72	149	41.6	224	42.48	168	43.36	153	44.24	153	45.12	152	46	157	46.88	157
38.1	147	38.98	185	39.86	142	40.74	155	41.62	240	42.5	154	43.38	170	44.26	149	45.14	153	46.02	167	46.9	132
38.12	170	39	169	39.88	132	40.76	135	41.64	183	42.52	200	43.4	152	44.28	174	45.16	148	46.04	173	46.92	185
38.14	140	39.02	160	39.9	148	40.78	157	41.66	205	42.54	159	43.42	144	44.3	157	45.18	201	46.06	182	46.94	149
38.16	148	39.04	142	39.92	151	40.8	166	41.68	190	42.56	174	43.44	156	44.32	145	45.2	152	46.08	157	46.96	155
38.18	193	39.06	182	39.94	154	40.82	124	41.7	158	42.58	171	43.46	163	44.34	150	45.22	127	46.1	161	46.98	165
38.2	165	39.08	175	39.96	127	40.84	152	41.72	178	42.6	159	43.48	155	44.36	141	45.24	154	46.12	159	47	154
38.22	135	39.1	157	39.98	143	40.86	155	41.74	180	42.62	159	43.5	180	44.38	162	45.26	133	46.14	137	47.02	148
38.24	147	39.12	168	40	132	40.88	136	41.76	161	42.64	169	43.52	159	44.4	163	45.28	146	46.16	159	47.04	134
38.26	162	39.14	155	40.02	146	40.9	154	41.78	188	42.66	155	43.54	140	44.42	159	45.3	149	46.18	151	47.06	176
38.28	145	39.16	140	40.04	144	40.92	158	41.8	176	42.68	155	43.56	169	44.44	172	45.32	147	46.2	155	47.08	185
38.3	158	39.18	161	40.06	149	40.94	158	41.82	163	42.7	155	43.58	159	44.46	154	45.34	142	46.22	145	47.1	141
38.32	164	39.2	120	40.08	141	40.96	134	41.84	166	42.72	148	43.6	168	44.48	164	45.36	143	46.24	180	47.12	165
38.34	184	39.22	164	40.1	152	40.98	132	41.86	155	42.74	162	43.62	172	44.5	142	45.38	149	46.26	154	47.14	160
38.36	156	39.24	143	40.12	155	41	166	41.88	173	42.76	154	43.64	148	44.52	143	45.4	159	46.28	176	47.16	158
38.38	144	39.26	151	40.14	164	41.02	156	41.9	172	42.78	174	43.66	175	44.54	161	45.42	139	46.3	171	47.18	179
38.4	144	39.28	136	40.16	148	41.04	158	41.92	172	42.8	156	43.68	194	44.56	163	45.44	166	46.32	164	47.2	174
38.42	172	39.3	158	40.18	141	41.06	170	41.94	184	42.82	145	43.7	173	44.58	141	45.46	160	46.34	161	47.22	168
38.44	168	39.32	154	40.2	149	41.08	170	41.96	198	42.84	161	43.72	163	44.6	143	45.48	145	46.36	175	47.24	157
38.46	176	39.34	150	40.22	162	41.1	188	41.98	169	42.86	156	43.74	177	44.62	169	45.5	130	46.38	142	47.26	184
38.48	181	39.36	151	40.24	171	41.12	162	42	187	42.88	134	43.76	186	44.64	158	45.52	140	46.4	170	47.28	144
38.5	179	39.38	159	40.26	122	41.14	171	42.02	166	42.9	153	43.78	176	44.66	154	45.54	134	46.42	168	47.3	154
38.52	183	39.4	152	40.28	136	41.16	154	42.04	171	42.92	142	43.8	190	44.68	148	45.56	157	46.44	158	47.32	162
38.54	171	39.42	139	40.3	147	41.18	161	42.06	174	42.94	168	43.82	185	44.7	148	45.58	161	46.46	184	47.34	166
38.56	156	39.44	150	40.32	137	41.2	175	42.08	169	42.96	138	43.84	183	44.72	149	45.6	129	46.48	173	47.36	154
38.58	178	39.46	156	40.34	146	41.22	169	42.1	171	42.98	135	43.86	167	44.74	181	45.62	151	46.5	175	47.38	162
38.6	188	39.48	110	40.36	147	41.24	193	42.12	203	43	134	43.88	166	44.76	143	45.64	133	46.52	135	47.4	126
38.62	194	39.5	137	40.38	145	41.26	202	42.14	170	43.02	147	43.9	169	44.78	164	45.66	160	46.54	180	47.42	161
38.64	182	39.52	137	40.4	149	41.28	185	42.16	193	43.04	143	43.92	150	44.8	167	45.68	144	46.56	176	47.44	165
38.66	185	39.54	161	40.42	171	41.3	219	42.18	191	43.06	140	43.94	186	44.82	152	45.7	147	46.58	199	47.46	152
38.68	180	39.56	171	40.44	134	41.32	217	42.2	196	43.08	149	43.96	175	44.84	140	45.72	164	46.6	190	47.48	141
38.7	176	39.58	142	40.46	164	41.34	220	42.22	203	43.1	147	43.98	166	44.86	156	45.74	163	46.62	169	47.5	172
38.72	164	39.6	157	40.48	136	41.36	231	42.24	194	43.12	155	44	170	44.88	144	45.76	152	46.64	176	47.52	139
38.74	183	39.62	186	40.5	141	41.38	239	42.26	204	43.14	169	44.02	190	44.9	148	45.78	142	46.66	181	47.54	151
38.76	197	39.64	127	40.52	160	41.4	256	42.28	207	43.16	131	44.04	173	44.92	142	45.8	157	46.68	170	47.56	173
38.78	181	39.66	139	40.54	158	41.42	248	42.3	215	43.18	144	44.06	150	44.94	172	45.82	151	46.7	144	47.58	144
38.8	174	39.68	144	40.56	165	41.44	225	42.32	189	43.2	157	44.08	179	44.96	169	45.84	124	46.72	158	47.6	160
38.82	166	39.7	141	40.58	138	41.46	224	42.34	164	43.22	133	44.1	178	44.98	157	45.86	176	46.74	180	47.62	155
38.84	177	39.72	131	40.6	152	41.48	221	42.36	204	43.24	124	44.12	139	45	130	45.88	150	46.76	197	47.64	164
38.86	164	39.74	151	40.62	149	41.5	227	42.38	207	43.26	124	44.14	164	45.02	165	45.9	171	46.78	158	47.66	166
38.88	168	39.76	156	40.64	137	41.52	230	42.4	179	43.28	154	44.16	156	45.04	182	45.92	139	46.8	173	47.68	154
38.9	183	39.78	137	40.66	134	41.54	225	42.42	170	43.3	138	44.18	151	45.06	183	45.94	141	46.82	157	47.7	165

Angle	R.Int	Angle	R.Int	Angle	R.Int	Angle	R.Int	Angle	R.Int	Angle	R.Int	Angle	R.Int	Angle	R.Int	Angle	R.Int	Angle	R.Int	Angle	R.Int
47.72	142	48.56	146	49.4	173	50.24	173	51.08	174	51.92	148	52.76	155	53.6	137	54.44	132	55.28	151	56.12	184
47.74	170	48.58	162	49.42	192	50.26	172	51.1	176	51.94	150	52.78	154	53.62	147	54.46	118	55.3	126	56.14	191
47.76	136	48.6	152	49.44	168	50.28	178	51.12	168	51.96	165	52.8	140	53.64	140	54.48	145	55.32	123	56.16	168
47.78	156	48.62	181	49.46	186	50.3	186	51.14	178	51.98	138	52.82	149	53.66	126	54.5	128	55.34	135	56.18	177
47.8	172	48.64	167	49.48	169	50.32	173	51.16	173	52	146	52.84	169	53.68	149	54.52	136	55.36	137	56.2	180
47.82	186	48.66	181	49.5	190	50.34	185	51.18	148	52.02	142	52.86	139	53.7	129	54.54	147	55.38	127	56.22	198
47.84	128	48.68	157	49.52	161	50.36	202	51.2	131	52.04	120	52.88	131	53.72	126	54.56	136	55.4	135	56.24	163
47.86	138	48.7	141	49.54	192	50.38	173	51.22	145	52.06	157	52.9	168	53.74	149	54.58	141	55.42	137	56.26	184
47.88	169	48.72	155	49.56	146	50.4	159	51.24	167	52.08	112	52.92	145	53.76	131	54.6	150	55.44	123	56.28	172
47.9	159	48.74	170	49.58	190	50.42	204	51.26	163	52.1	109	52.94	182	53.78	135	54.62	143	55.46	128	56.3	205
47.92	155	48.76	163	49.6	179	50.44	197	51.28	185	52.12	144	52.96	131	53.8	133	54.64	126	55.48	140	56.32	176
47.94	147	48.78	152	49.62	172	50.46	192	51.3	168	52.14	146	52.98	158	53.82	126	54.66	135	55.5	141	56.34	182
47.96	162	48.8	167	49.64	176	50.48	166	51.32	154	52.16	132	53	160	53.84	135	54.68	142	55.52	141	56.36	188
47.98	163	48.82	150	49.66	162	50.5	197	51.34	169	52.18	160	53.02	162	53.86	133	54.7	128	55.54	124	56.38	188
48	175	48.84	176	49.68	163	50.52	197	51.36	148	52.2	122	53.04	160	53.88	137	54.72	142	55.56	151	56.4	182
48.02	164	48.86	153	49.7	179	50.54	186	51.38	162	52.22	156	53.06	162	53.9	119	54.74	123	55.58	139	56.42	173
48.04	150	48.88	146	49.72	179	50.56	222	51.4	144	52.24	164	53.08	171	53.92	118	54.76	121	55.6	134	56.44	187
48.06	169	48.9	175	49.74	155	50.58	220	51.42	164	52.26	134	53.1	181	53.94	116	54.78	149	55.62	133	56.46	184
48.08	157	48.92	170	49.76	170	50.6	267	51.44	157	52.28	133	53.12	163	53.96	134	54.8	122	55.64	143	56.48	176
48.1	160	48.94	154	49.78	148	50.62	211	51.46	162	52.3	145	53.14	141	53.98	126	54.82	145	55.66	145	56.5	186
48.12	135	48.96	165	49.8	159	50.64	252	51.48	152	52.32	152	53.16	146	54	137	54.84	122	55.68	150	56.52	172
48.14	150	48.98	175	49.82	157	50.66	235	51.5	139	52.34	154	53.18	141	54.02	120	54.86	124	55.7	168	56.54	183
48.16	174	49	163	49.84	156	50.68	238	51.52	160	52.36	164	53.2	163	54.04	121	54.88	135	55.72	134	56.56	156
48.18	146	49.02	159	49.86	142	50.7	254	51.54	152	52.38	146	53.22	165	54.06	105	54.9	129	55.74	159	56.58	143
48.2	159	49.04	162	49.88	166	50.72	248	51.56	154	52.4	138	53.24	153	54.08	142	54.92	141	55.76	137	56.6	168
48.22	184	49.06	156	49.9	153	50.74	252	51.58	138	52.42	152	53.26	136	54.1	129	54.94	123	55.78	138	56.62	184
48.24	156	49.08	143	49.92	154	50.76	260	51.6	141	52.44	143	53.28	168	54.12	141	54.96	121	55.8	150	56.64	172
48.26	153	49.1	185	49.94	157	50.78	258	51.62	135	52.46	147	53.3	164	54.14	117	54.98	148	55.82	148	56.66	167
48.28	153	49.12	153	49.96	156	50.8	238	51.64	155	52.48	170	53.32	125	54.16	132	55	133	55.84	136	56.68	157
48.3	146	49.14	185	49.98	141	50.82	232	51.66	152	52.5	140	53.34	140	54.18	109	55.02	146	55.86	140	56.7	172
48.32	153	49.16	186	50	160	50.84	216	51.68	149	52.52	126	53.36	151	54.2	131	55.04	129	55.88	161	56.72	171
48.34	154	49.18	186	50.02	173	50.86	269	51.7	143	52.54	160	53.38	143	54.22	122	55.06	105	55.9	173	56.74	137
48.36	146	49.2	178	50.04	157	50.88	217	51.72	165	52.56	155	53.4	148	54.24	131	55.08	152	55.92	146	56.76	140
48.38	158	49.22	201	50.06	160	50.9	271	51.74	160	52.58	135	53.42	164	54.26	123	55.1	139	55.94	150	56.78	150
48.4	147	49.24	183	50.08	179	50.92	240	51.76	132	52.6	155	53.44	142	54.28	140	55.12	127	55.96	153	56.8	149
48.42	153	49.26	186	50.1	143	50.94	214	51.78	157	52.62	155	53.46	138	54.3	159	55.14	146	55.98	169	56.82	158
48.44	159	49.28	188	50.12	150	50.96	220	51.8	143	52.64	144	53.48	147	54.32	124	55.16	137	56	164	56.84	159
48.46	156	49.3	161	50.14	185	50.98	219	51.82	134	52.66	118	53.5	151	54.34	121	55.18	111	56.02	174	56.86	143
48.48	179	49.32	175	50.16	168	51	221	51.84	134	52.68	171	53.52	144	54.36	145	55.2	133	56.04	169	56.88	132
48.5	189	49.34	178	50.18	154	51.02	171	51.86	144	52.7	152	53.54	154	54.38	131	55.22	148	56.06	192	56.9	123
48.52	159	49.36	184	50.2	150	51.04	216	51.88	129	52.72	158	53.56	137	54.4	125	55.24	150	56.08	171	56.92	145
48.54	140	49.38	167	50.22	156	51.06	186	51.9	151	52.74	145	53.58	149	54.42	132	55.26	137	56.1	165	56.94	135

Angle	R.Int	Angle	R.Int	Angle	R.Int	Angle	R.Int	Angle	R.Int	Angle	R.Int	Angle	R.Int	Angle	R.Int	Angle	R.Int	Angle	R.Int	Angle	R.Int
56.96	135	57.8	126	58.64	159	59.48	143	60.32	152	61.16	142	62	169	62.84	148	63.68	166	64.52	160	65.36	146
56.98	145	57.82	158	58.66	174	59.5	142	60.34	140	61.18	118	62.02	168	62.86	147	63.7	150	64.54	171	65.38	143
57	134	57.84	123	58.68	153	59.52	142	60.36	132	61.2	163	62.04	164	62.88	147	63.72	142	64.56	147	65.4	151
57.02	139	57.86	143	58.7	132	59.54	143	60.38	139	61.22	152	62.06	189	62.9	137	63.74	147	64.58	170	65.42	149
57.04	147	57.88	144	58.72	148	59.56	138	60.4	146	61.24	136	62.08	149	62.92	143	63.76	173	64.6	155	65.44	142
57.06	130	57.9	139	58.74	137	59.58	134	60.42	148	61.26	165	62.1	159	62.94	152	63.78	122	64.62	173	65.46	156
57.08	118	57.92	137	58.76	146	59.6	109	60.44	147	61.28	156	62.12	208	62.96	158	63.8	135	64.64	165	65.48	152
57.1	138	57.94	146	58.78	153	59.62	113	60.46	147	61.3	191	62.14	182	62.98	166	63.82	138	64.66	162	65.5	140
57.12	142	57.96	134	58.8	155	59.64	131	60.48	136	61.32	163	62.16	195	63	143	63.84	148	64.68	156	65.52	147
57.14	137	57.98	140	58.82	151	59.66	133	60.5	152	61.34	141	62.18	178	63.02	146	63.86	162	64.7	154	65.54	133
57.16	149	58	154	58.84	138	59.68	138	60.52	137	61.36	162	62.2	132	63.04	131	63.88	154	64.72	173	65.56	159
57.18	132	58.02	150	58.86	142	59.7	111	60.54	128	61.38	177	62.22	161	63.06	149	63.9	138	64.74	143	65.58	113
57.2	139	58.04	141	58.88	170	59.72	114	60.56	112	61.4	136	62.24	133	63.08	141	63.92	149	64.76	167	65.6	132
57.22	126	58.06	137	58.9	145	59.74	133	60.58	114	61.42	147	62.26	153	63.1	144	63.94	160	64.78	152	65.62	162
57.24	138	58.08	154	58.92	163	59.76	141	60.6	136	61.44	150	62.28	166	63.12	145	63.96	145	64.8	161	65.64	143
57.26	139	58.1	119	58.94	142	59.78	139	60.62	140	61.46	145	62.3	155	63.14	128	63.98	169	64.82	145	65.66	168
57.28	129	58.12	122	58.96	133	59.8	149	60.64	117	61.48	146	62.32	162	63.16	136	64	153	64.84	152	65.68	129
57.3	114	58.14	141	58.98	137	59.82	123	60.66	122	61.5	148	62.34	149	63.18	135	64.02	166	64.86	150	65.7	161
57.32	114	58.16	136	59	184	59.84	130	60.68	158	61.52	187	62.36	156	63.2	148	64.04	150	64.88	164	65.72	158
57.34	140	58.18	158	59.02	139	59.86	129	60.7	138	61.54	172	62.38	151	63.22	143	64.06	171	64.9	146	65.74	136
57.36	148	58.2	123	59.04	158	59.88	102	60.72	129	61.56	179	62.4	144	63.24	133	64.08	175	64.92	158	65.76	140
57.38	129	58.22	154	59.06	119	59.9	135	60.74	148	61.58	184	62.42	149	63.26	142	64.1	141	64.94	151	65.78	154
57.4	131	58.24	144	59.08	137	59.92	134	60.76	130	61.6	169	62.44	158	63.28	147	64.12	171	64.96	164	65.8	140
57.42	133	58.26	148	59.1	156	59.94	156	60.78	117	61.62	178	62.46	177	63.3	148	64.14	156	64.98	131	65.82	125
57.44	127	58.28	122	59.12	142	59.96	142	60.8	150	61.64	204	62.48	127	63.32	144	64.16	168	65	139	65.84	135
57.46	129	58.3	141	59.14	138	59.98	129	60.82	149	61.66	155	62.5	162	63.34	132	64.18	155	65.02	138	65.86	129
57.48	106	58.32	135	59.16	118	60	132	60.84	150	61.68	167	62.52	151	63.36	160	64.2	134	65.04	159	65.88	146
57.5	130	58.34	140	59.18	136	60.02	128	60.86	130	61.7	151	62.54	170	63.38	139	64.22	152	65.06	149	65.9	163
57.52	124	58.36	150	59.2	152	60.04	149	60.88	110	61.72	166	62.56	168	63.4	143	64.24	174	65.08	151	65.92	135
57.54	137	58.38	132	59.22	124	60.06	126	60.9	113	61.74	147	62.58	133	63.42	153	64.26	148	65.1	152	65.94	151
57.56	102	58.4	151	59.24	114	60.08	146	60.92	126	61.76	154	62.6	142	63.44	138	64.28	143	65.12	157	65.96	141
57.58	119	58.42	139	59.26	140	60.1	131	60.94	160	61.78	177	62.62	168	63.46	133	64.3	164	65.14	165	65.98	149
57.6	117	58.44	145	59.28	135	60.12	115	60.96	133	61.8	174	62.64	144	63.48	155	64.32	160	65.16	168	66	154
57.62	132	58.46	168	59.3	133	60.14	130	60.98	166	61.82	216	62.66	168	63.5	141	64.34	167	65.18	134	66.02	147
57.64	143	58.48	153	59.32	129	60.16	141	61	125	61.84	173	62.68	143	63.52	157	64.36	137	65.2	127	66.04	136
57.66	115	58.5	154	59.34	124	60.18	133	61.02	137	61.86	162	62.7	136	63.54	156	64.38	173	65.22	157	66.06	141
57.68	131	58.52	148	59.36	126	60.2	130	61.04	144	61.88	196	62.72	138	63.56	111	64.4	159	65.24	124	66.08	125
57.7	145	58.54	139	59.38	138	60.22	134	61.06	149	61.9	196	62.74	139	63.58	138	64.42	143	65.26	161	66.1	147
57.72	156	58.56	142	59.4	120	60.24	144	61.08	149	61.92	180	62.76	161	63.6	143	64.44	169	65.28	143	66.12	134
57.74	121	58.58	141	59.42	106	60.26	141	61.1	137	61.94	168	62.78	157	63.62	149	64.46	131	65.3	137	66.14	163
57.76	121	58.6	148	59.44	131	60.28	148	61.12	137	61.96	168	62.8	179	63.64	124	64.48	155	65.32	145	66.16	140
57.78	138	58.62	142	59.46	127	60.3	132	61.14	137	61.98	183	62.82	156	63.66	160	64.5	169	65.34	152	66.18	123

Angle	R.Int	Angle	R.Int	Angle	R.Int	Angle	R.Int	Angle	R.Int	Angle	R.Int	Angle	R.Int	Angle	R.Int	Angle	R.Int	Angle	R.Int	Angle	R.Int
66.2	145	67.04	126	67.88	142	68.72	152	69.56	141	70.4	149	71.24	110	72.08	143	72.92	129	73.76	130	74.6	122
66.22	126	67.06	140	67.9	159	68.74	140	69.58	136	70.42	122	71.26	134	72.1	115	72.94	149	73.78	140	74.62	164
66.24	129	67.08	126	67.92	154	68.76	154	69.6	136	70.44	126	71.28	109	72.12	105	72.96	140	73.8	138	74.64	136
66.26	144	67.1	124	67.94	160	68.78	149	69.62	161	70.46	147	71.3	144	72.14	139	72.98	144	73.82	152	74.66	142
66.28	152	67.12	155	67.96	146	68.8	148	69.64	144	70.48	139	71.32	117	72.16	119	73	165	73.84	148	74.68	124
66.3	129	67.14	126	67.98	147	68.82	133	69.66	155	70.5	126	71.34	133	72.18	133	73.02	127	73.86	156	74.7	147
66.32	147	67.16	131	68	132	68.84	157	69.68	159	70.52	100	71.36	101	72.2	109	73.04	148	73.88	128	74.72	144
66.34	122	67.18	124	68.02	150	68.86	162	69.7	130	70.54	127	71.38	125	72.22	138	73.06	150	73.9	132	74.74	150
66.36	133	67.2	141	68.04	150	68.88	138	69.72	144	70.56	117	71.4	133	72.24	137	73.08	152	73.92	152	74.76	146
66.38	160	67.22	156	68.06	158	68.9	160	69.74	136	70.58	112	71.42	143	72.26	121	73.1	140	73.94	134	74.78	160
66.4	165	67.24	123	68.08	159	68.92	157	69.76	171	70.6	121	71.44	117	72.28	119	73.12	127	73.96	126	74.8	146
66.42	128	67.26	150	68.1	144	68.94	181	69.78	125	70.62	136	71.46	125	72.3	128	73.14	139	73.98	152	74.82	139
66.44	158	67.28	119	68.12	145	68.96	146	69.8	124	70.64	111	71.48	127	72.32	113	73.16	141	74	137	74.84	147
66.46	118	67.3	159	68.14	163	68.98	150	69.82	140	70.66	109	71.5	138	72.34	140	73.18	134	74.02	148	74.86	177
66.48	155	67.32	137	68.16	141	69	148	69.84	139	70.68	132	71.52	103	72.36	120	73.2	128	74.04	125	74.88	141
66.5	148	67.34	136	68.18	159	69.02	159	69.86	135	70.7	87	71.54	128	72.38	105	73.22	149	74.06	126	74.9	135
66.52	154	67.36	137	68.2	125	69.04	161	69.88	122	70.72	121	71.56	114	72.4	129	73.24	151	74.08	141	74.92	162
66.54	133	67.38	158	68.22	150	69.06	151	69.9	150	70.74	123	71.58	135	72.42	142	73.26	153	74.1	144	74.94	168
66.56	140	67.4	136	68.24	150	69.08	150	69.92	126	70.76	137	71.6	120	72.44	122	73.28	152	74.12	120	74.96	140
66.58	146	67.42	152	68.26	174	69.1	162	69.94	151	70.78	138	71.62	141	72.46	123	73.3	152	74.14	126	74.98	165
66.6	132	67.44	147	68.28	154	69.12	150	69.96	141	70.8	126	71.64	118	72.48	140	73.32	144	74.16	132	75	153
66.62	144	67.46	134	68.3	136	69.14	147	69.98	131	70.82	134	71.66	130	72.5	121	73.34	149	74.18	150	75.02	153
66.64	146	67.48	147	68.32	150	69.16	164	70	141	70.84	102	71.68	129	72.52	156	73.36	143	74.2	153	75.04	153
66.66	133	67.5	150	68.34	156	69.18	162	70.02	141	70.86	125	71.7	126	72.54	139	73.38	157	74.22	124	75.06	139
66.68	148	67.52	152	68.36	162	69.2	154	70.04	130	70.88	132	71.72	126	72.56	122	73.4	163	74.24	136	75.08	153
66.7	137	67.54	177	68.38	176	69.22	157	70.06	135	70.9	120	71.74	134	72.58	113	73.42	137	74.26	138	75.1	157
66.72	127	67.56	156	68.4	148	69.24	131	70.08	125	70.92	151	71.76	127	72.6	136	73.44	141	74.28	122	75.12	157
66.74	136	67.58	121	68.42	151	69.26	162	70.1	91	70.94	119	71.78	136	72.62	153	73.46	141	74.3	147	75.14	159
66.76	133	67.6	157	68.44	147	69.28	151	70.12	135	70.96	129	71.8	150	72.64	157	73.48	148	74.32	157	75.16	157
66.78	139	67.62	148	68.46	160	69.3	139	70.14	137	70.98	125	71.82	145	72.66	145	73.5	150	74.34	164	75.18	141
66.8	133	67.64	134	68.48	144	69.32	164	70.16	119	71	151	71.84	137	72.68	141	73.52	150	74.36	141	75.2	141
66.82	134	67.66	164	68.5	141	69.34	136	70.18	113	71.02	144	71.86	146	72.7	133	73.54	128	74.38	139	75.22	150
66.84	136	67.68	142	68.52	152	69.36	148	70.2	121	71.04	137	71.88	138	72.72	117	73.56	159	74.4	151	75.24	155
66.86	124	67.7	155	68.54	155	69.38	137	70.22	128	71.06	127	71.9	131	72.74	129	73.58	139	74.42	145	75.26	108
66.88	155	67.72	147	68.56	164	69.4	147	70.24	128	71.08	143	71.92	129	72.76	126	73.6	138	74.44	145	75.28	151
66.9	139	67.74	157	68.58	163	69.42	130	70.26	123	71.1	153	71.94	165	72.78	141	73.62	125	74.46	147	75.3	143
66.92	144	67.76	147	68.6	167	69.44	151	70.28	117	71.12	127	71.96	135	72.8	145	73.64	164	74.48	173	75.32	164
66.94	139	67.78	141	68.62	154	69.46	139	70.3	98	71.14	118	71.98	135	72.82	146	73.66	141	74.5	127	75.34	141
66.96	150	67.8	149	68.64	140	69.48	126	70.32	126	71.16	129	72	125	72.84	140	73.68	152	74.52	128	75.36	140
66.98	131	67.82	157	68.66	153	69.5	149	70.34	112	71.18	113	72.02	146	72.86	141	73.7	124	74.54	156	75.38	152
67	117	67.84	156	68.68	169	69.52	144	70.36	124	71.2	107	72.04	125	72.88	134	73.72	162	74.56	138	75.4	165
67.02	138	67.86	134	68.7	149	69.54	149	70.38	116	71.22	131	72.06	132	72.9	140	73.74	175	74.58	147	75.42	149

Angle	R.Int	Angle	R.Int	Angle	R.Int	Angle	R.Int	Angle	R.Int	Angle	R.Int
75.44	140	76.28	149	77.12	110	77.96	130	78.8	140	79.64	102
75.46	147	76.3	128	77.14	142	77.98	122	78.82	137	79.66	147
75.48	140	76.32	130	77.16	140	78	139	78.84	133	79.68	126
75.5	138	76.34	122	77.18	115	78.02	120	78.86	148	79.7	125
75.52	150	76.36	139	77.2	104	78.04	128	78.88	132	79.72	127
75.54	143	76.38	136	77.22	135	78.06	117	78.9	154	79.74	120
75.56	126	76.4	111	77.24	134	78.08	115	78.92	112	79.76	116
75.58	165	76.42	124	77.26	98	78.1	140	78.94	112	79.78	136
75.6	142	76.44	148	77.28	111	78.12	110	78.96	131	79.8	118
75.62	168	76.46	131	77.3	137	78.14	119	78.98	114	79.82	126
75.64	150	76.48	133	77.32	121	78.16	123	79	140	79.84	131
75.66	149	76.5	144	77.34	122	78.18	108	79.02	142	79.86	127
75.68	119	76.52	119	77.36	129	78.2	105	79.04	122	79.88	150
75.7	149	76.54	139	77.38	137	78.22	99	79.06	131	79.9	135
75.72	136	76.56	119	77.4	125	78.24	123	79.08	129	79.92	140
75.74	128	76.58	144	77.42	122	78.26	118	79.1	117	79.94	123
75.76	160	76.6	109	77.44	110	78.28	127	79.12	128	79.96	116
75.78	148	76.62	125	77.46	134	78.3	113	79.14	146	79.98	124
75.8	137	76.64	126	77.48	136	78.32	126	79.16	138	80	125
75.82	117	76.66	121	77.5	125	78.34	116	79.18	131		
75.84	144	76.68	110	77.52	123	78.36	121	79.2	111		
75.86	130	76.7	114	77.54	142	78.38	124	79.22	117		
75.88	146	76.72	110	77.56	119	78.4	129	79.24	141		
75.9	124	76.74	144	77.58	122	78.42	130	79.26	149		
75.92	132	76.76	119	77.6	147	78.44	124	79.28	126		
75.94	123	76.78	132	77.62	114	78.46	116	79.3	140		
75.96	121	76.8	127	77.64	130	78.48	127	79.32	130		
75.98	147	76.82	116	77.66	148	78.5	142	79.34	135		
76	132	76.84	124	77.68	117	78.52	122	79.36	129		
76.02	131	76.86	127	77.7	130	78.54	118	79.38	100		
76.04	123	76.88	128	77.72	118	78.56	128	79.4	121		
76.06	149	76.9	139	77.74	120	78.58	106	79.42	109		
76.08	136	76.92	135	77.76	127	78.6	102	79.44	112		
76.1	140	76.94	114	77.78	138	78.62	127	79.46	127		
76.12	128	76.96	131	77.8	131	78.64	138	79.48	110		
76.14	144	76.98	90	77.82	145	78.66	155	79.5	123		
76.16	136	77	115	77.84	157	78.68	130	79.52	106		
76.18	121	77.02	141	77.86	130	78.7	127	79.54	119		
76.2	123	77.04	127	77.88	145	78.72	135	79.56	128		
76.22	172	77.06	125	77.9	119	78.74	113	79.58	127		
76.24	127	77.08	108	77.92	131	78.76	137	79.6	146		
76.26	145	77.1	141	77.94	124	78.78	120	79.62	133		

Capo Rosso lava dome

Angle	R.Int	Angle	R.Int	Angle	R.Int	Angle	R.Int	Angle	R.Int	Angle	R.Int	Angle	R.Int	Angle	R.Int	Angle	R.Int	Angle	R.Int
20	198	22.05	191	24.1	162	26.15	163	28.2	157	30.25	125	32.3	130	34.35	116	36.4	95	38.45	84	40.5	79
20.05	215	22.1	183	24.15	163	26.2	161	28.25	156	30.3	146	32.35	126	34.4	98	36.45	90	38.5	88	40.55	95
20.1	209	22.15	163	24.2	141	26.25	144	28.3	160	30.35	169	32.4	118	34.45	116	36.5	81	38.55	91	40.6	62
20.15	207	22.2	202	24.25	158	26.3	150	28.35	140	30.4	146	32.45	112	34.5	111	36.55	101	38.6	89	40.65	62
20.2	219	22.25	203	24.3	168	26.35	148	28.4	140	30.45	137	32.5	96	34.55	96	36.6	89	38.65	66	40.7	85
20.25	203	22.3	192	24.35	167	26.4	148	28.45	157	30.5	117	32.55	131	34.6	103	36.65	100	38.7	72	40.75	71
20.3	218	22.35	157	24.4	154	26.45	137	28.5	135	30.55	150	32.6	113	34.65	105	36.7	90	38.75	87	40.8	73
20.35	247	22.4	169	24.45	173	26.5	145	28.55	144	30.6	162	32.65	104	34.7	101	36.75	86	38.8	82	40.85	91
20.4	200	22.45	180	24.5	149	26.55	173	28.6	136	30.65	142	32.7	108	34.75	102	36.8	92	38.85	94	40.9	72
20.45	190	22.5	172	24.55	173	26.6	164	28.65	167	30.7	143	32.75	107	34.8	99	36.85	107	38.9	74	40.95	95
20.5	179	22.55	182	24.6	162	26.65	162	28.7	155	30.75	140	32.8	107	34.85	115	36.9	77	38.95	65	41	75
20.55	210	22.6	207	24.65	153	26.7	158	28.75	162	30.8	139	32.85	110	34.9	120	36.95	89	39	70	41.05	86
20.6	215	22.65	202	24.7	149	26.75	177	28.8	160	30.85	123	32.9	105	34.95	94	37	98	39.05	94	41.1	75
20.65	186	22.7	185	24.75	144	26.8	158	28.85	129	30.9	134	32.95	107	35	110	37.05	83	39.1	88	41.15	70
20.7	191	22.75	154	24.8	154	26.85	153	28.9	168	30.95	136	33	123	35.05	121	37.1	92	39.15	85	41.2	81
20.75	230	22.8	179	24.85	163	26.9	161	28.95	156	31	121	33.05	129	35.1	104	37.15	78	39.2	63	41.25	93
20.8	211	22.85	160	24.9	137	26.95	174	29	150	31.05	115	33.1	100	35.15	117	37.2	97	39.25	87	41.3	88
20.85	219	22.9	200	24.95	156	27	195	29.05	142	31.1	153	33.15	112	35.2	103	37.25	64	39.3	79	41.35	73
20.9	189	22.95	179	25	146	27.05	180	29.1	137	31.15	133	33.2	119	35.25	105	37.3	67	39.35	98	41.4	79
20.95	219	23	184	25.05	170	27.1	172	29.15	153	31.2	154	33.25	111	35.3	122	37.35	99	39.4	70	41.45	68
21	188	23.05	165	25.1	162	27.15	174	29.2	145	31.25	125	33.3	114	35.35	113	37.4	80	39.45	66	41.5	83
21.05	154	23.1	178	25.15	161	27.2	190	29.25	161	31.3	151	33.35	96	35.4	129	37.45	83	39.5	79	41.55	82
21.1	217	23.15	191	25.2	164	27.25	194	29.3	146	31.35	132	33.4	95	35.45	99	37.5	82	39.55	76	41.6	68
21.15	199	23.2	180	25.25	173	27.3	217	29.35	142	31.4	134	33.45	110	35.5	119	37.55	90	39.6	82	41.65	86
21.2	210	23.25	204	25.3	185	27.35	202	29.4	176	31.45	136	33.5	112	35.55	120	37.6	84	39.65	74	41.7	91
21.25	240	23.3	185	25.35	161	27.4	217	29.45	137	31.5	130	33.55	106	35.6	118	37.65	85	39.7	104	41.75	71
21.3	216	23.35	194	25.4	175	27.45	226	29.5	145	31.55	123	33.6	113	35.65	109	37.7	91	39.75	82	41.8	73
21.35	261	23.4	192	25.45	131	27.5	232	29.55	147	31.6	123	33.65	111	35.7	103	37.75	91	39.8	72	41.85	93
21.4	243	23.45	188	25.5	170	27.55	230	29.6	121	31.65	140	33.7	104	35.75	101	37.8	102	39.85	76	41.9	87
21.45	247	23.5	205	25.55	176	27.6	221	29.65	165	31.7	132	33.75	123	35.8	109	37.85	83	39.9	80	41.95	78
21.5	240	23.55	194	25.6	155	27.65	206	29.7	148	31.75	149	33.8	78	35.85	93	37.9	77	39.95	61	42	73
21.55	222	23.6	196	25.65	173	27.7	204	29.75	144	31.8	119	33.85	110	35.9	87	37.95	76	40	73	42.05	87
21.6	239	23.65	193	25.7	181	27.75	208	29.8	160	31.85	124	33.9	116	35.95	104	38	83	40.05	68	42.1	71
21.65	235	23.7	203	25.75	136	27.8	192	29.85	122	31.9	117	33.95	100	36	93	38.05	81	40.1	70	42.15	72
21.7	255	23.75	201	25.8	149	27.85	174	29.9	151	31.95	137	34	120	36.05	109	38.1	73	40.15	83	42.2	71
21.75	228	23.8	163	25.85	158	27.9	182	29.95	116	32	126	34.05	105	36.1	88	38.15	88	40.2	79	42.25	91
21.8	226	23.85	194	25.9	166	27.95	174	30	158	32.05	124	34.1	90	36.15	109	38.2	77	40.25	82	42.3	74
21.85	212	23.9	198	25.95	153	28	149	30.05	168	32.1	113	34.15	98	36.2	90	38.25	104	40.3	74	42.35	71
21.9	212	23.95	161	26	160	28.05	159	30.1	135	32.15	137	34.2	112	36.25	89	38.3	86	40.35	88	42.4	72
21.95	200	24	176	26.05	176	28.1	168	30.15	131	32.2	114	34.25	87	36.3	90	38.35	77	40.4	86	42.45	70
22	200	24.05	156	26.1	176	28.15	170	30.2	167	32.25	111	34.3	97	36.35	93	38.4	92	40.45	69	42.5	84

Angle	R.Int	Angle	R.Int	Angle	R.Int	Angle	R.Int	Angle	R.Int	Angle	R.Int	Angle	R.Int	Angle	R.Int	Angle	R.Int	Angle	R.Int
42.55	70	44.6	60	46.65	63	48.7	69	50.75	80	52.8	53	54.85	61	56.9	50	58.95	66	61	34	63.05	54
42.6	85	44.65	74	46.7	65	48.75	64	50.8	67	52.85	70	54.9	68	56.95	63	59	56	61.05	69	63.1	70
42.65	78	44.7	62	46.75	69	48.8	67	50.85	85	52.9	65	54.95	64	57	54	59.05	69	61.1	67	63.15	58
42.7	78	44.75	72	46.8	63	48.85	67	50.9	66	52.95	66	55	61	57.05	58	59.1	59	61.15	57	63.2	73
42.75	80	44.8	85	46.85	67	48.9	80	50.95	77	53	78	55.05	69	57.1	76	59.15	47	61.2	63	63.25	73
42.8	71	44.85	66	46.9	80	48.95	66	51	78	53.05	74	55.1	61	57.15	45	59.2	72	61.25	48	63.3	79
42.85	75	44.9	80	46.95	58	49	69	51.05	76	53.1	67	55.15	70	57.2	61	59.25	61	61.3	44	63.35	73
42.9	74	44.95	69	47	62	49.05	59	51.1	68	53.15	71	55.2	53	57.25	66	59.3	51	61.35	43	63.4	61
42.95	91	45	61	47.05	69	49.1	73	51.15	80	53.2	61	55.25	65	57.3	62	59.35	53	61.4	72	63.45	57
43	79	45.05	56	47.1	60	49.15	62	51.2	61	53.25	58	55.3	61	57.35	63	59.4	70	61.45	60	63.5	58
43.05	96	45.1	65	47.15	67	49.2	53	51.25	67	53.3	87	55.35	72	57.4	63	59.45	49	61.5	53	63.55	67
43.1	70	45.15	81	47.2	52	49.25	66	51.3	62	53.35	60	55.4	59	57.45	48	59.5	63	61.55	66	63.6	78
43.15	68	45.2	70	47.25	67	49.3	80	51.35	66	53.4	69	55.45	67	57.5	62	59.55	69	61.6	54	63.65	67
43.2	63	45.25	67	47.3	68	49.35	68	51.4	62	53.45	65	55.5	67	57.55	54	59.6	47	61.65	62	63.7	61
43.25	71	45.3	66	47.35	76	49.4	85	51.45	60	53.5	71	55.55	51	57.6	63	59.65	55	61.7	75	63.75	64
43.3	74	45.35	82	47.4	51	49.45	64	51.5	80	53.55	46	55.6	58	57.65	70	59.7	55	61.75	51	63.8	66
43.35	65	45.4	68	47.45	55	49.5	74	51.55	75	53.6	66	55.65	59	57.7	62	59.75	64	61.8	66	63.85	62
43.4	74	45.45	73	47.5	65	49.55	100	51.6	51	53.65	72	55.7	55	57.75	75	59.8	65	61.85	55	63.9	70
43.45	83	45.5	61	47.55	61	49.6	71	51.65	66	53.7	64	55.75	60	57.8	44	59.85	53	61.9	65	63.95	73
43.5	55	45.55	58	47.6	68	49.65	59	51.7	63	53.75	69	55.8	68	57.85	54	59.9	60	61.95	59	64	49
43.55	60	45.6	71	47.65	65	49.7	60	51.75	65	53.8	72	55.85	61	57.9	50	59.95	46	62	68	64.05	51
43.6	74	45.65	71	47.7	57	49.75	63	51.8	64	53.85	53	55.9	42	57.95	57	60	47	62.05	57	64.1	64
43.65	57	45.7	62	47.75	64	49.8	70	51.85	70	53.9	71	55.95	65	58	66	60.05	58	62.1	71	64.15	54
43.7	64	45.75	71	47.8	57	49.85	59	51.9	73	53.95	58	56	51	58.05	49	60.1	68	62.15	68	64.2	68
43.75	80	45.8	65	47.85	66	49.9	66	51.95	55	54	66	56.05	71	58.1	49	60.15	64	62.2	70	64.25	63
43.8	79	45.85	59	47.9	59	49.95	63	52	59	54.05	50	56.1	60	58.15	68	60.2	77	62.25	61	64.3	46
43.85	73	45.9	75	47.95	67	50	64	52.05	57	54.1	58	56.15	61	58.2	58	60.25	54	62.3	72	64.35	75
43.9	57	45.95	77	48	68	50.05	72	52.1	62	54.15	66	56.2	44	58.25	55	60.3	63	62.35	68	64.4	72
43.95	85	46	60	48.05	54	50.1	67	52.15	70	54.2	59	56.25	51	58.3	64	60.35	52	62.4	51	64.45	61
44	76	46.05	72	48.1	70	50.15	68	52.2	61	54.25	70	56.3	66	58.35	49	60.4	66	62.45	64	64.5	50
44.05	65	46.1	67	48.15	61	50.2	74	52.25	79	54.3	83	56.35	64	58.4	56	60.45	56	62.5	64	64.55	60
44.1	70	46.15	63	48.2	63	50.25	61	52.3	74	54.35	56	56.4	68	58.45	72	60.5	61	62.55	59	64.6	62
44.15	76	46.2	65	48.25	66	50.3	78	52.35	61	54.4	51	56.45	57	58.5	63	60.55	60	62.6	81	64.65	72
44.2	61	46.25	51	48.3	61	50.35	70	52.4	65	54.45	81	56.5	55	58.55	63	60.6	61	62.65	67	64.7	72
44.25	70	46.3	62	48.35	66	50.4	49	52.45	48	54.5	52	56.55	66	58.6	52	60.65	72	62.7	62	64.75	71
44.3	64	46.35	82	48.4	70	50.45	67	52.5	52	54.55	50	56.6	72	58.65	48	60.7	59	62.75	53	64.8	56
44.35	66	46.4	78	48.45	63	50.5	69	52.55	69	54.6	55	56.65	82	58.7	79	60.75	56	62.8	72	64.85	72
44.4	74	46.45	80	48.5	66	50.55	63	52.6	59	54.65	69	56.7	62	58.75	72	60.8	59	62.85	54	64.9	61
44.45	67	46.5	74	48.55	72	50.6	70	52.65	59	54.7	57	56.75	59	58.8	49	60.85	63	62.9	72	64.95	61
44.5	69	46.55	82	48.6	65	50.65	61	52.7	73	54.75	59	56.8	65	58.85	48	60.9	65	62.95	54	65	69
44.55	58	46.6	79	48.65	59	50.7	80	52.75	74	54.8	47	56.85	59	58.9	53	60.95	55	63	52	65.05	70

Angle	R.Int	Angle	R.Int	Angle	R.Int	Angle	R.Int	Angle	R.Int	Angle	R.Int	Angle	R.Int
65.1	62	67.3	78	69.5	76	71.7	65	73.9	67	76.1	60	78.3	59
65.15	68	67.35	63	69.55	58	71.75	49	73.95	35	76.15	43	78.35	55
65.2	57	67.4	70	69.6	66	71.8	51	74	56	76.2	60	78.4	56
65.25	60	67.45	59	69.65	53	71.85	64	74.05	37	76.25	63	78.45	54
65.3	52	67.5	70	69.7	65	71.9	50	74.1	74	76.3	55	78.5	70
65.35	65	67.55	65	69.75	58	71.95	64	74.15	58	76.35	56	78.55	73
65.4	47	67.6	58	69.8	46	72	53	74.2	51	76.4	43	78.6	41
65.45	56	67.65	56	69.85	72	72.05	50	74.25	41	76.45	54	78.65	54
65.5	58	67.7	66	69.9	45	72.1	64	74.3	66	76.5	53	78.7	43
65.55	54	67.75	57	69.95	53	72.15	72	74.35	61	76.55	66	78.75	50
65.6	61	67.8	64	70	70	72.2	61	74.4	54	76.6	64	78.8	52
65.65	72	67.85	71	70.05	39	72.25	57	74.45	71	76.65	54	78.85	49
65.7	51	67.9	58	70.1	51	72.3	54	74.5	52	76.7	67	78.9	54
65.75	73	67.95	56	70.15	63	72.35	39	74.55	59	76.75	51	78.95	53
65.8	66	68	52	70.2	55	72.4	59	74.6	77	76.8	44	79	45
65.85	55	68.05	57	70.25	58	72.45	63	74.65	66	76.85	52	79.05	49
65.9	79	68.1	50	70.3	46	72.5	48	74.7	63	76.9	66	79.1	55
65.95	66	68.15	59	70.35	62	72.55	54	74.75	53	76.95	50	79.15	50
66	61	68.2	73	70.4	50	72.6	64	74.8	59	77	49	79.2	45
66.05	58	68.25	70	70.45	54	72.65	55	74.85	68	77.05	48	79.25	56
66.1	61	68.3	59	70.5	64	72.7	61	74.9	66	77.1	39	79.3	50
66.15	63	68.35	43	70.55	72	72.75	51	74.95	65	77.15	45	79.35	55
66.2	52	68.4	57	70.6	61	72.8	48	75	73	77.2	53	79.4	55
66.25	60	68.45	65	70.65	64	72.85	46	75.05	48	77.25	54	79.45	52
66.3	57	68.5	69	70.7	58	72.9	58	75.1	67	77.3	53	79.5	61
66.35	72	68.55	55	70.75	67	72.95	53	75.15	55	77.35	65	79.55	70
66.4	53	68.6	57	70.8	66	73	53	75.2	59	77.4	60	79.6	53
66.45	48	68.65	56	70.85	61	73.05	49	75.25	69	77.45	66	79.65	48
66.5	54	68.7	66	70.9	71	73.1	49	75.3	60	77.5	61	79.7	52
66.55	52	68.75	61	70.95	56	73.15	50	75.35	52	77.55	49	79.75	59
66.6	61	68.8	66	71	68	73.2	55	75.4	68	77.6	56	79.8	52
66.65	72	68.85	62	71.05	69	73.25	37	75.45	57	77.65	37	79.85	60
66.7	78	68.9	64	71.1	62	73.3	69	75.5	57	77.7	67	79.9	55
66.75	51	68.95	65	71.15	57	73.35	48	75.55	60	77.75	45	79.95	53
66.8	40	69	60	71.2	64	73.4	52	75.6	54	77.8	56	80	57
66.85	45	69.05	55	71.25	62	73.45	61	75.65	62	77.85	59		
66.9	55	69.1	60	71.3	59	73.5	56	75.7	51	77.9	37		
66.95	68	69.15	70	71.35	59	73.55	62	75.75	55	77.95	45		
67	61	69.2	53	71.4	58	73.6	56	75.8	45	78	57		
67.05	64	69.25	67	71.45	61	73.65	63	75.85	51	78.05	53		
67.1	57	69.3	44	71.5	59	73.7	60	75.9	61	78.1	59		
67.15	67	69.35	72	71.55	63	73.75	57	75.95	72	78.15	55		
67.2	62	69.4	68	71.6	57	73.8	65	76	46	78.2	48		
67.25	52	69.45	49	71.65	67	73.85	52	76.05	50	78.25	51		

Castello lava dome

Angle	R.Int	Angle	R.Int	Angle	R.Int	Angle	R.Int	Angle	R.Int	Angle	R.Int	Angle	R.Int	Angle	R.Int	Angle	R.Int	Angle	R.Int
20	194	22.05	178	24.1	159	26.15	143	28.2	124	30.25	121	32.3	122	34.35	93	36.4	79	38.45	49	40.5	76
20.05	186	22.1	154	24.15	146	26.2	143	28.25	139	30.3	125	32.35	100	34.4	96	36.45	76	38.5	83	40.55	63
20.1	199	22.15	144	24.2	141	26.25	127	28.3	129	30.35	113	32.4	123	34.45	104	36.5	89	38.55	69	40.6	63
20.15	202	22.2	152	24.25	153	26.3	123	28.35	116	30.4	127	32.45	101	34.5	92	36.55	75	38.6	71	40.65	71
20.2	222	22.25	159	24.3	155	26.35	121	28.4	109	30.45	121	32.5	102	34.55	116	36.6	71	38.65	77	40.7	50
20.25	188	22.3	151	24.35	142	26.4	119	28.45	137	30.5	141	32.55	95	34.6	82	36.65	76	38.7	76	40.75	75
20.3	163	22.35	164	24.4	111	26.45	158	28.5	120	30.55	118	32.6	96	34.65	77	36.7	88	38.75	68	40.8	65
20.35	180	22.4	152	24.45	143	26.5	133	28.55	120	30.6	120	32.65	101	34.7	89	36.75	78	38.8	58	40.85	60
20.4	193	22.45	163	24.5	142	26.55	152	28.6	148	30.65	126	32.7	104	34.75	96	36.8	72	38.85	71	40.9	75
20.45	165	22.5	155	24.55	160	26.6	128	28.65	126	30.7	110	32.75	101	34.8	73	36.85	74	38.9	93	40.95	73
20.5	179	22.55	172	24.6	159	26.65	139	28.7	136	30.75	120	32.8	96	34.85	112	36.9	81	38.95	46	41	63
20.55	210	22.6	167	24.65	143	26.7	139	28.75	132	30.8	113	32.85	99	34.9	84	36.95	60	39	59	41.05	54
20.6	185	22.65	167	24.7	148	26.75	162	28.8	137	30.85	108	32.9	85	34.95	100	37	87	39.05	81	41.1	79
20.65	204	22.7	148	24.75	121	26.8	165	28.85	121	30.9	120	32.95	88	35	96	37.05	62	39.1	60	41.15	70
20.7	211	22.75	137	24.8	153	26.85	152	28.9	131	30.95	98	33	93	35.05	94	37.1	67	39.15	56	41.2	60
20.75	174	22.8	160	24.85	159	26.9	164	28.95	143	31	105	33.05	105	35.1	95	37.15	61	39.2	61	41.25	77
20.8	176	22.85	149	24.9	137	26.95	197	29	114	31.05	110	33.1	92	35.15	109	37.2	64	39.25	78	41.3	71
20.85	178	22.9	161	24.95	137	27	156	29.05	101	31.1	111	33.15	80	35.2	93	37.25	73	39.3	58	41.35	76
20.9	217	22.95	147	25	130	27.05	187	29.1	117	31.15	104	33.2	93	35.25	97	37.3	67	39.35	66	41.4	70
20.95	225	23	146	25.05	135	27.1	198	29.15	114	31.2	106	33.25	75	35.3	102	37.35	68	39.4	65	41.45	82
21	171	23.05	162	25.1	127	27.15	213	29.2	112	31.25	110	33.3	100	35.35	71	37.4	73	39.45	72	41.5	85
21.05	228	23.1	175	25.15	110	27.2	223	29.25	122	31.3	103	33.35	73	35.4	102	37.45	81	39.5	72	41.55	69
21.1	192	23.15	179	25.2	152	27.25	199	29.3	120	31.35	110	33.4	99	35.45	81	37.5	65	39.55	67	41.6	70
21.15	174	23.2	159	25.25	123	27.3	222	29.35	127	31.4	91	33.45	69	35.5	84	37.55	84	39.6	63	41.65	57
21.2	195	23.25	169	25.3	122	27.35	195	29.4	122	31.45	108	33.5	96	35.55	90	37.6	80	39.65	66	41.7	79
21.25	201	23.3	156	25.35	146	27.4	204	29.45	126	31.5	115	33.55	72	35.6	76	37.65	92	39.7	74	41.75	53
21.3	179	23.35	168	25.4	148	27.45	194	29.5	133	31.55	107	33.6	106	35.65	83	37.7	83	39.75	70	41.8	67
21.35	204	23.4	148	25.45	165	27.5	196	29.55	133	31.6	97	33.65	91	35.7	81	37.75	88	39.8	65	41.85	75
21.4	221	23.45	139	25.5	140	27.55	175	29.6	125	31.65	96	33.7	103	35.75	67	37.8	64	39.85	56	41.9	67
21.45	198	23.5	167	25.55	123	27.6	162	29.65	129	31.7	116	33.75	87	35.8	84	37.85	71	39.9	65	41.95	70
21.5	192	23.55	171	25.6	133	27.65	146	29.7	121	31.75	77	33.8	81	35.85	78	37.9	67	39.95	70	42	66
21.55	175	23.6	169	25.65	164	27.7	156	29.75	122	31.8	99	33.85	89	35.9	79	37.95	82	40	67	42.05	55
21.6	182	23.65	167	25.7	142	27.75	116	29.8	132	31.85	100	33.9	95	35.95	79	38	71	40.05	46	42.1	73
21.65	183	23.7	176	25.75	155	27.8	135	29.85	129	31.9	100	33.95	85	36	77	38.05	60	40.1	74	42.15	73
21.7	164	23.75	137	25.8	137	27.85	134	29.9	122	31.95	88	34	95	36.05	78	38.1	77	40.15	78	42.2	64
21.75	182	23.8	140	25.85	125	27.9	130	29.95	140	32	125	34.05	97	36.1	72	38.15	54	40.2	80	42.25	81
21.8	166	23.85	149	25.9	123	27.95	136	30	134	32.05	84	34.1	74	36.15	81	38.2	62	40.25	66	42.3	56
21.85	176	23.9	151	25.95	119	28	117	30.05	99	32.1	95	34.15	81	36.2	84	38.25	66	40.3	60	42.35	63
21.9	148	23.95	133	26	147	28.05	115	30.1	121	32.15	122	34.2	85	36.25	83	38.3	76	40.35	67	42.4	78
21.95	173	24	127	26.05	136	28.1	113	30.15	123	32.2	90	34.25	101	36.3	64	38.35	65	40.4	59	42.45	78
22	162	24.05	135	26.1	146	28.15	123	30.2	132	32.25	98	34.3	98	36.35	76	38.4	81	40.45	87	42.5	79

Angle	R.Int	Angle	R.Int	Angle	R.Int	Angle	R.Int	Angle	R.Int	Angle	R.Int	Angle	R.Int	Angle	R.Int	Angle	R.Int	Angle	R.Int
42.55	72	44.6	63	46.65	61	48.7	65	50.75	84	52.8	58	54.85	59	56.9	54	58.95	64	61	64	63.05	56
42.6	49	44.65	51	46.7	53	48.75	55	50.8	68	52.85	55	54.9	47	56.95	55	59	64	61.05	48	63.1	58
42.65	58	44.7	61	46.75	47	48.8	73	50.85	65	52.9	72	54.95	55	57	56	59.05	67	61.1	69	63.15	59
42.7	56	44.75	61	46.8	79	48.85	65	50.9	81	52.95	61	55	48	57.05	51	59.1	51	61.15	56	63.2	52
42.75	61	44.8	69	46.85	58	48.9	53	50.95	64	53	73	55.05	49	57.1	60	59.15	55	61.2	60	63.25	61
42.8	76	44.85	60	46.9	57	48.95	60	51	65	53.05	68	55.1	54	57.15	58	59.2	46	61.25	48	63.3	42
42.85	77	44.9	58	46.95	53	49	71	51.05	46	53.1	54	55.15	70	57.2	63	59.25	59	61.3	64	63.35	63
42.9	75	44.95	63	47	60	49.05	49	51.1	66	53.15	43	55.2	56	57.25	53	59.3	65	61.35	66	63.4	56
42.95	55	45	71	47.05	79	49.1	67	51.15	61	53.2	68	55.25	59	57.3	60	59.35	45	61.4	60	63.45	54
43	60	45.05	72	47.1	82	49.15	59	51.2	75	53.25	56	55.3	49	57.35	56	59.4	75	61.45	56	63.5	60
43.05	51	45.1	63	47.15	49	49.2	70	51.25	62	53.3	60	55.35	50	57.4	54	59.45	68	61.5	76	63.55	52
43.1	71	45.15	81	47.2	60	49.25	62	51.3	57	53.35	46	55.4	59	57.45	56	59.5	53	61.55	65	63.6	61
43.15	64	45.2	58	47.25	46	49.3	57	51.35	78	53.4	60	55.45	61	57.5	53	59.55	43	61.6	72	63.65	66
43.2	72	45.25	71	47.3	66	49.35	52	51.4	56	53.45	67	55.5	42	57.55	51	59.6	46	61.65	65	63.7	47
43.25	56	45.3	58	47.35	68	49.4	71	51.45	58	53.5	66	55.55	61	57.6	60	59.65	36	61.7	55	63.75	59
43.3	59	45.35	71	47.4	74	49.45	69	51.5	51	53.55	59	55.6	65	57.65	56	59.7	61	61.75	60	63.8	49
43.35	54	45.4	57	47.45	55	49.5	62	51.55	51	53.6	49	55.65	59	57.7	62	59.75	51	61.8	56	63.85	53
43.4	48	45.45	61	47.5	46	49.55	65	51.6	52	53.65	65	55.7	50	57.75	54	59.8	43	61.85	62	63.9	46
43.45	89	45.5	58	47.55	52	49.6	60	51.65	55	53.7	56	55.75	53	57.8	59	59.85	67	61.9	47	63.95	60
43.5	54	45.55	60	47.6	58	49.65	60	51.7	51	53.75	50	55.8	63	57.85	74	59.9	52	61.95	56	64	80
43.55	64	45.6	57	47.65	62	49.7	75	51.75	59	53.8	58	55.85	47	57.9	74	59.95	53	62	55	64.05	41
43.6	54	45.65	68	47.7	50	49.75	70	51.8	59	53.85	60	55.9	60	57.95	64	60	53	62.05	65	64.1	40
43.65	51	45.7	63	47.75	60	49.8	67	51.85	66	53.9	57	55.95	73	58	64	60.05	59	62.1	58	64.15	53
43.7	63	45.75	53	47.8	48	49.85	48	51.9	67	53.95	59	56	74	58.05	53	60.1	50	62.15	58	64.2	61
43.75	66	45.8	67	47.85	53	49.9	65	51.95	57	54	58	56.05	49	58.1	62	60.15	56	62.2	47	64.25	53
43.8	61	45.85	55	47.9	50	49.95	72	52	55	54.05	65	56.1	64	58.15	41	60.2	44	62.25	57	64.3	50
43.85	65	45.9	64	47.95	62	50	61	52.05	63	54.1	64	56.15	56	58.2	66	60.25	66	62.3	74	64.35	69
43.9	70	45.95	72	48	67	50.05	63	52.1	61	54.15	61	56.2	52	58.25	59	60.3	70	62.35	57	64.4	48
43.95	59	46	69	48.05	69	50.1	45	52.15	60	54.2	68	56.25	60	58.3	55	60.35	56	62.4	56	64.45	56
44	69	46.05	60	48.1	65	50.15	66	52.2	36	54.25	63	56.3	65	58.35	61	60.4	65	62.45	66	64.5	70
44.05	77	46.1	61	48.15	45	50.2	63	52.25	49	54.3	72	56.35	57	58.4	62	60.45	52	62.5	55	64.55	46
44.1	53	46.15	61	48.2	57	50.25	60	52.3	49	54.35	61	56.4	64	58.45	67	60.5	69	62.55	45	64.6	51
44.15	63	46.2	56	48.25	43	50.3	54	52.35	46	54.4	57	56.45	58	58.5	51	60.55	46	62.6	56	64.65	54
44.2	59	46.25	58	48.3	52	50.35	75	52.4	57	54.45	62	56.5	71	58.55	56	60.6	69	62.65	55	64.7	53
44.25	61	46.3	53	48.35	59	50.4	56	52.45	59	54.5	51	56.55	51	58.6	49	60.65	63	62.7	61	64.75	51
44.3	64	46.35	65	48.4	50	50.45	60	52.5	70	54.55	67	56.6	62	58.65	64	60.7	71	62.75	53	64.8	57
44.35	79	46.4	71	48.45	67	50.5	66	52.55	51	54.6	65	56.65	64	58.7	55	60.75	64	62.8	64	64.85	53
44.4	56	46.45	56	48.5	61	50.55	58	52.6	57	54.65	62	56.7	54	58.75	61	60.8	60	62.85	60	64.9	51
44.45	60	46.5	57	48.55	69	50.6	57	52.65	65	54.7	58	56.75	67	58.8	59	60.85	52	62.9	63	64.95	51
44.5	69	46.55	58	48.6	61	50.65	78	52.7	70	54.75	52	56.8	58	58.85	59	60.9	47	62.95	58	65	63
44.55	75	46.6	77	48.65	64	50.7	62	52.75	58	54.8	57	56.85	55	58.9	58	60.95	52	63	48	65.05	66

Angle	R.Int	Angle	R.Int	Angle	R.Int	Angle	R.Int	Angle	R.Int	Angle	R.Int	Angle	R.Int
65.1	62	67.3	70	69.5	52	71.7	50	73.9	58	76.1	46	78.3	60
65.15	68	67.35	56	69.55	48	71.75	54	73.95	57	76.15	50	78.35	53
65.2	54	67.4	46	69.6	40	71.8	48	74	58	76.2	42	78.4	44
65.25	56	67.45	38	69.65	56	71.85	53	74.05	53	76.25	66	78.45	51
65.3	58	67.5	52	69.7	67	71.9	51	74.1	50	76.3	49	78.5	42
65.35	47	67.55	55	69.75	52	71.95	59	74.15	47	76.35	54	78.55	49
65.4	54	67.6	45	69.8	69	72	43	74.2	58	76.4	58	78.6	56
65.45	53	67.65	72	69.85	51	72.05	54	74.25	54	76.45	51	78.65	63
65.5	74	67.7	44	69.9	60	72.1	68	74.3	48	76.5	45	78.7	60
65.55	41	67.75	56	69.95	56	72.15	45	74.35	59	76.55	61	78.75	48
65.6	54	67.8	61	70	62	72.2	61	74.4	65	76.6	53	78.8	48
65.65	46	67.85	68	70.05	52	72.25	66	74.45	65	76.65	47	78.85	51
65.7	63	67.9	61	70.1	58	72.3	49	74.5	51	76.7	42	78.9	55
65.75	49	67.95	37	70.15	46	72.35	50	74.55	29	76.75	62	78.95	56
65.8	52	68	52	70.2	52	72.4	70	74.6	52	76.8	59	79	49
65.85	48	68.05	49	70.25	64	72.45	54	74.65	61	76.85	66	79.05	41
65.9	41	68.1	46	70.3	49	72.5	50	74.7	54	76.9	66	79.1	48
65.95	63	68.15	48	70.35	65	72.55	54	74.75	53	76.95	61	79.15	46
66	41	68.2	39	70.4	51	72.6	54	74.8	54	77	44	79.2	51
66.05	52	68.25	47	70.45	63	72.65	51	74.85	54	77.05	50	79.25	46
66.1	62	68.3	62	70.5	58	72.7	49	74.9	70	77.1	50	79.3	48
66.15	59	68.35	47	70.55	50	72.75	46	74.95	56	77.15	63	79.35	58
66.2	50	68.4	67	70.6	58	72.8	53	75	39	77.2	44	79.4	54
66.25	41	68.45	52	70.65	50	72.85	45	75.05	52	77.25	48	79.45	55
66.3	67	68.5	38	70.7	46	72.9	44	75.1	58	77.3	45	79.5	51
66.35	54	68.55	48	70.75	45	72.95	50	75.15	62	77.35	56	79.55	54
66.4	54	68.6	52	70.8	54	73	73	75.2	67	77.4	66	79.6	54
66.45	67	68.65	55	70.85	52	73.05	55	75.25	64	77.45	41	79.65	49
66.5	46	68.7	38	70.9	49	73.1	47	75.3	50	77.5	57	79.7	45
66.55	72	68.75	49	70.95	63	73.15	55	75.35	47	77.55	54	79.75	46
66.6	71	68.8	51	71	47	73.2	38	75.4	45	77.6	60	79.8	64
66.65	52	68.85	56	71.05	53	73.25	65	75.45	64	77.65	53	79.85	48
66.7	67	68.9	40	71.1	48	73.3	45	75.5	56	77.7	55	79.9	33
66.75	54	68.95	56	71.15	51	73.35	53	75.55	46	77.75	58	79.95	50
66.8	51	69	50	71.2	51	73.4	48	75.6	49	77.8	55	80	63
66.85	54	69.05	41	71.25	56	73.45	52	75.65	53	77.85	43		
66.9	54	69.1	70	71.3	60	73.5	57	75.7	43	77.9	55		
66.95	57	69.15	67	71.35	51	73.55	54	75.75	47	77.95	51		
67	62	69.2	56	71.4	62	73.6	50	75.8	51	78	47		
67.05	51	69.25	38	71.45	51	73.65	63	75.85	44	78.05	38		
67.1	58	69.3	49	71.5	46	73.7	58	75.9	54	78.1	53		
67.15	63	69.35	49	71.55	49	73.75	61	75.95	57	78.15	53		
67.2	79	69.4	51	71.6	52	73.8	56	76	54	78.2	61		
67.25	41	69.45	60	71.65	45	73.85	46	76.05	43	78.25	44		

Punta di Costa lava dome

Angle	R.Int	Angle	R.Int	Angle	R.Int	Angle	R.Int	Angle	R.Int	Angle	R.Int	Angle	R.Int	Angle	R.Int	Angle	R.Int	Angle	R.Int
20	458	20.82	490	21.64	1116	22.46	394	23.28	565	24.1	315	24.92	299	25.74	318	26.56	341	27.38	936	28.2	286
20.02	444	20.84	477	21.66	963	22.48	412	23.3	592	24.12	324	24.94	305	25.76	318	26.58	333	27.4	934	28.22	309
20.04	428	20.86	515	21.68	852	22.5	414	23.32	609	24.14	339	24.96	270	25.78	292	26.6	308	27.42	860	28.24	305
20.06	418	20.88	495	21.7	730	22.52	417	23.34	597	24.16	297	24.98	278	25.8	287	26.62	350	27.44	829	28.26	294
20.08	468	20.9	532	21.72	669	22.54	408	23.36	577	24.18	331	25	285	25.82	312	26.64	358	27.46	808	28.28	307
20.1	439	20.92	478	21.74	560	22.56	417	23.38	609	24.2	332	25.02	290	25.84	308	26.66	359	27.48	897	28.3	283
20.12	441	20.94	539	21.76	581	22.58	421	23.4	576	24.22	318	25.04	270	25.86	316	26.68	391	27.5	875	28.32	294
20.14	442	20.96	512	21.78	499	22.6	389	23.42	584	24.24	325	25.06	310	25.88	333	26.7	369	27.52	873	28.34	271
20.16	392	20.98	544	21.8	541	22.62	394	23.44	515	24.26	311	25.08	273	25.9	285	26.72	344	27.54	861	28.36	253
20.18	407	21	517	21.82	466	22.64	399	23.46	491	24.28	330	25.1	324	25.92	326	26.74	408	27.56	808	28.38	276
20.2	430	21.02	556	21.84	467	22.66	381	23.48	506	24.3	304	25.12	291	25.94	286	26.76	408	27.58	819	28.4	294
20.22	461	21.04	561	21.86	459	22.68	429	23.5	521	24.32	333	25.14	299	25.96	296	26.78	434	27.6	752	28.42	281
20.24	436	21.06	585	21.88	452	22.7	406	23.52	419	24.34	346	25.16	325	25.98	272	26.8	418	27.62	730	28.44	264
20.26	444	21.08	559	21.9	437	22.72	351	23.54	492	24.36	315	25.18	287	26	275	26.82	403	27.64	650	28.46	292
20.28	450	21.1	608	21.92	431	22.74	395	23.56	438	24.38	345	25.2	293	26.02	293	26.84	436	27.66	607	28.48	270
20.3	451	21.12	628	21.94	402	22.76	383	23.58	398	24.4	338	25.22	324	26.04	298	26.86	423	27.68	532	28.5	290
20.32	438	21.14	691	21.96	416	22.78	412	23.6	435	24.42	337	25.24	295	26.06	311	26.88	433	27.7	498	28.52	280
20.34	402	21.16	660	21.98	408	22.8	409	23.62	420	24.44	310	25.26	317	26.08	343	26.9	446	27.72	505	28.54	280
20.36	408	21.18	685	22	381	22.82	335	23.64	397	24.46	271	25.28	343	26.1	277	26.92	458	27.74	483	28.56	257
20.38	420	21.2	774	22.02	385	22.84	359	23.66	379	24.48	282	25.3	302	26.12	309	26.94	470	27.76	404	28.58	287
20.4	407	21.22	778	22.04	391	22.86	345	23.68	389	24.5	329	25.32	372	26.14	341	26.96	538	27.78	421	28.6	288
20.42	429	21.24	768	22.06	371	22.88	369	23.7	410	24.52	325	25.34	364	26.16	294	26.98	579	27.8	421	28.62	255
20.44	438	21.26	911	22.08	388	22.9	403	23.72	401	24.54	316	25.36	371	26.18	304	27	570	27.82	391	28.64	278
20.46	433	21.28	936	22.1	374	22.92	353	23.74	347	24.56	293	25.38	357	26.2	296	27.02	580	27.84	428	28.66	242
20.48	404	21.3	1074	22.12	362	22.94	371	23.76	362	24.58	312	25.4	415	26.22	307	27.04	624	27.86	486	28.68	279
20.5	454	21.32	1172	22.14	374	22.96	369	23.78	347	24.6	288	25.42	351	26.24	305	27.06	688	27.88	412	28.7	279
20.52	450	21.34	1249	22.16	385	22.98	399	23.8	355	24.62	304	25.44	374	26.26	266	27.08	784	27.9	411	28.72	226
20.54	454	21.36	1238	22.18	341	23	394	23.82	357	24.64	301	25.46	401	26.28	301	27.1	840	27.92	413	28.74	268
20.56	462	21.38	1372	22.2	322	23.02	368	23.84	390	24.66	281	25.48	399	26.3	301	27.12	839	27.94	379	28.76	268
20.58	468	21.4	1475	22.22	376	23.04	436	23.86	332	24.68	291	25.5	429	26.32	289	27.14	903	27.96	378	28.78	293
20.6	459	21.42	1540	22.24	369	23.06	379	23.88	384	24.7	293	25.52	365	26.34	296	27.16	942	27.98	429	28.8	269
20.62	445	21.44	1590	22.26	385	23.08	476	23.9	342	24.72	295	25.54	405	26.36	331	27.18	1026	28	389	28.82	254
20.64	452	21.46	1644	22.28	382	23.1	441	23.92	309	24.74	317	25.56	325	26.38	309	27.2	1052	28.02	411	28.84	278
20.66	445	21.48	1760	22.3	370	23.12	459	23.94	316	24.76	281	25.58	381	26.4	285	27.22	1014	28.04	353	28.86	276
20.68	415	21.5	1657	22.32	381	23.14	442	23.96	350	24.78	308	25.6	339	26.42	307	27.24	1056	28.06	356	28.88	276
20.7	473	21.52	1644	22.34	373	23.16	455	23.98	321	24.8	293	25.62	354	26.44	313	27.26	1004	28.08	320	28.9	271
20.72	462	21.54	1689	22.36	381	23.18	505	24	292	24.82	294	25.64	379	26.46	316	27.28	1052	28.1	370	28.92	281
20.74	465	21.56	1682	22.38	399	23.2	543	24.02	347	24.84	297	25.66	338	26.48	298	27.3	943	28.12	332	28.94	264
20.76	461	21.58	1553	22.4	380	23.22	494	24.04	346	24.86	299	25.68	315	26.5	366	27.32	965	28.14	299	28.96	305
20.78	446	21.6	1412	22.42	414	23.24	524	24.06	319	24.88	266	25.7	302	26.52	300	27.34	944	28.16	353	28.98	263
20.8	489	21.62	1286	22.44	397	23.26	551	24.08	300	24.9	284	25.72	294	26.54	299	27.36	915	28.18	313	29	284

Angle	R.Int	Angle	R.Int	Angle	R.Int	Angle	R.Int	Angle	R.Int	Angle	R.Int	Angle	R.Int	Angle	R.Int	Angle	R.Int	Angle	R.Int	Angle	R.Int
29.02	281	29.84	318	30.66	350	31.48	261	32.3	238	33.12	215	33.94	178	34.76	246	35.58	395	36.4	211	37.22	198
29.04	263	29.86	323	30.68	342	31.5	256	32.32	225	33.14	198	33.96	173	34.78	272	35.6	404	36.42	210	37.24	193
29.06	246	29.88	354	30.7	355	31.52	258	32.34	221	33.16	176	33.98	194	34.8	262	35.62	426	36.44	190	37.26	170
29.08	280	29.9	318	30.72	313	31.54	261	32.36	218	33.18	218	34	182	34.82	273	35.64	425	36.46	230	37.28	184
29.1	265	29.92	308	30.74	331	31.56	258	32.38	239	33.2	188	34.02	190	34.84	293	35.66	430	36.48	170	37.3	189
29.12	265	29.94	306	30.76	332	31.58	251	32.4	226	33.22	195	34.04	206	34.86	277	35.68	369	36.5	189	37.32	153
29.14	303	29.96	361	30.78	382	31.6	248	32.42	247	33.24	201	34.06	188	34.88	307	35.7	403	36.52	188	37.34	164
29.16	254	29.98	313	30.8	336	31.62	217	32.44	235	33.26	190	34.08	189	34.9	284	35.72	375	36.54	189	37.36	200
29.18	302	30	336	30.82	350	31.64	244	32.46	217	33.28	224	34.1	191	34.92	328	35.74	360	36.56	182	37.38	193
29.2	288	30.02	323	30.84	329	31.66	253	32.48	238	33.3	223	34.12	203	34.94	311	35.76	362	36.58	175	37.4	137
29.22	288	30.04	303	30.86	376	31.68	243	32.5	222	33.32	200	34.14	187	34.96	274	35.78	361	36.6	186	37.42	176
29.24	304	30.06	313	30.88	336	31.7	236	32.52	231	33.34	221	34.16	202	34.98	309	35.8	286	36.62	198	37.44	182
29.26	277	30.08	335	30.9	320	31.72	236	32.54	238	33.36	211	34.18	203	35	348	35.82	272	36.64	195	37.46	170
29.28	283	30.1	298	30.92	326	31.74	259	32.56	240	33.38	208	34.2	200	35.02	355	35.84	296	36.66	162	37.48	192
29.3	313	30.12	338	30.94	361	31.76	246	32.58	223	33.4	195	34.22	175	35.04	330	35.86	298	36.68	197	37.5	183
29.32	305	30.14	345	30.96	350	31.78	256	32.6	222	33.42	196	34.24	192	35.06	345	35.88	259	36.7	181	37.52	188
29.34	312	30.16	350	30.98	350	31.8	266	32.62	232	33.44	188	34.26	215	35.08	345	35.9	281	36.72	180	37.54	153
29.36	284	30.18	352	31	312	31.82	235	32.64	212	33.46	181	34.28	212	35.1	347	35.92	255	36.74	197	37.56	173
29.38	308	30.2	330	31.02	351	31.84	196	32.66	249	33.48	202	34.3	232	35.12	350	35.94	254	36.76	219	37.58	182
29.4	302	30.22	370	31.04	373	31.86	230	32.68	230	33.5	202	34.32	190	35.14	395	35.96	246	36.78	190	37.6	164
29.42	305	30.24	368	31.06	332	31.88	254	32.7	233	33.52	202	34.34	245	35.16	312	35.98	256	36.8	227	37.62	182
29.44	314	30.26	401	31.08	312	31.9	263	32.72	231	33.54	208	34.36	193	35.18	340	36	222	36.82	212	37.64	189
29.46	330	30.28	383	31.1	307	31.92	253	32.74	215	33.56	189	34.38	236	35.2	343	36.02	233	36.84	215	37.66	203
29.48	342	30.3	389	31.12	328	31.94	254	32.76	248	33.58	181	34.4	198	35.22	349	36.04	244	36.86	255	37.68	170
29.5	309	30.32	413	31.14	288	31.96	261	32.78	234	33.6	184	34.42	200	35.24	345	36.06	228	36.88	248	37.7	150
29.52	347	30.34	396	31.16	292	31.98	235	32.8	240	33.62	211	34.44	235	35.26	348	36.08	235	36.9	219	37.72	187
29.54	313	30.36	356	31.18	271	32	267	32.82	237	33.64	177	34.46	211	35.28	341	36.1	222	36.92	208	37.74	186
29.56	344	30.38	414	31.2	266	32.02	218	32.84	251	33.66	203	34.48	205	35.3	323	36.12	229	36.94	200	37.76	175
29.58	360	30.4	366	31.22	303	32.04	240	32.86	225	33.68	215	34.5	252	35.32	347	36.14	220	36.96	210	37.78	155
29.6	361	30.42	386	31.24	277	32.06	240	32.88	265	33.7	205	34.52	225	35.34	343	36.16	223	36.98	227	37.8	209
29.62	375	30.44	345	31.26	250	32.08	257	32.9	265	33.72	171	34.54	234	35.36	352	36.18	214	37	194	37.82	187
29.64	363	30.46	361	31.28	231	32.1	255	32.92	213	33.74	195	34.56	232	35.38	280	36.2	199	37.02	218	37.84	205
29.66	340	30.48	371	31.3	283	32.12	243	32.94	197	33.76	210	34.58	238	35.4	323	36.22	198	37.04	237	37.86	182
29.68	318	30.5	358	31.32	287	32.14	258	32.96	200	33.78	195	34.6	273	35.42	331	36.24	194	37.06	201	37.88	164
29.7	353	30.52	380	31.34	234	32.16	229	32.98	243	33.8	175	34.62	265	35.44	337	36.26	219	37.08	195	37.9	172
29.72	374	30.54	395	31.36	262	32.18	259	33	201	33.82	207	34.64	232	35.46	335	36.28	178	37.1	203	37.92	162
29.74	372	30.56	374	31.38	253	32.2	227	33.02	221	33.84	204	34.66	258	35.48	339	36.3	195	37.12	204	37.94	175
29.76	365	30.58	318	31.4	268	32.22	248	33.04	209	33.86	207	34.68	270	35.5	340	36.32	230	37.14	205	37.96	171
29.78	339	30.6	332	31.42	277	32.24	253	33.06	194	33.88	181	34.7	250	35.52	370	36.34	214	37.16	194	37.98	173
29.8	333	30.62	361	31.44	243	32.26	225	33.08	210	33.9	196	34.72	269	35.54	383	36.36	172	37.18	204	38	169
29.82	341	30.64	335	31.46	266	32.28	225	33.1	191	33.92	211	34.74	220	35.56	395	36.38	197	37.2	187	38.02	166

Angle	R.Int	Angle	R.Int	Angle	R.Int	Angle	R.Int	Angle	R.Int	Angle	R.Int	Angle	R.Int	Angle	R.Int	Angle	R.Int	Angle	R.Int	Angle	R.Int
38.04	179	38.92	170	39.8	133	40.68	140	41.56	199	42.44	197	43.32	156	44.2	169	45.08	140	45.96	164	46.84	171
38.06	169	38.94	177	39.82	135	40.7	155	41.58	203	42.46	174	43.34	124	44.22	183	45.1	183	45.98	140	46.86	189
38.08	160	38.96	169	39.84	140	40.72	162	41.6	192	42.48	187	43.36	147	44.24	171	45.12	161	46	167	46.88	176
38.1	130	38.98	154	39.86	177	40.74	162	41.62	238	42.5	188	43.38	121	44.26	167	45.14	160	46.02	167	46.9	186
38.12	148	39	150	39.88	162	40.76	170	41.64	209	42.52	161	43.4	125	44.28	190	45.16	180	46.04	167	46.92	165
38.14	155	39.02	178	39.9	161	40.78	161	41.66	216	42.54	162	43.42	136	44.3	178	45.18	167	46.06	163	46.94	148
38.16	149	39.04	178	39.92	151	40.8	141	41.68	178	42.56	176	43.44	189	44.32	168	45.2	150	46.08	182	46.96	187
38.18	163	39.06	159	39.94	151	40.82	165	41.7	188	42.58	169	43.46	145	44.34	183	45.22	179	46.1	156	46.98	150
38.2	153	39.08	164	39.96	134	40.84	176	41.72	190	42.6	179	43.48	135	44.36	197	45.24	151	46.12	158	47	148
38.22	158	39.1	151	39.98	151	40.86	126	41.74	191	42.62	172	43.5	152	44.38	191	45.26	179	46.14	172	47.02	161
38.24	170	39.12	175	40	166	40.88	156	41.76	186	42.64	164	43.52	132	44.4	178	45.28	166	46.16	152	47.04	158
38.26	177	39.14	186	40.02	149	40.9	149	41.78	178	42.66	136	43.54	154	44.42	175	45.3	154	46.18	167	47.06	171
38.28	167	39.16	152	40.04	150	40.92	168	41.8	180	42.68	169	43.56	150	44.44	193	45.32	151	46.2	168	47.08	139
38.3	169	39.18	164	40.06	151	40.94	149	41.82	154	42.7	154	43.58	167	44.46	178	45.34	141	46.22	173	47.1	162
38.32	170	39.2	157	40.08	143	40.96	146	41.84	162	42.72	164	43.6	138	44.48	190	45.36	138	46.24	149	47.12	161
38.34	173	39.22	169	40.1	160	40.98	134	41.86	187	42.74	167	43.62	160	44.5	170	45.38	141	46.26	156	47.14	163
38.36	146	39.24	156	40.12	146	41	174	41.88	157	42.76	154	43.64	148	44.52	163	45.4	153	46.28	207	47.16	147
38.38	172	39.26	163	40.14	172	41.02	144	41.9	186	42.78	135	43.66	144	44.54	164	45.42	136	46.3	195	47.18	149
38.4	177	39.28	153	40.16	181	41.04	161	41.92	158	42.8	174	43.68	165	44.56	160	45.44	185	46.32	167	47.2	154
38.42	180	39.3	152	40.18	144	41.06	157	41.94	176	42.82	140	43.7	155	44.58	162	45.46	149	46.34	173	47.22	149
38.44	173	39.32	146	40.2	130	41.08	138	41.96	198	42.84	146	43.72	170	44.6	144	45.48	155	46.36	199	47.24	151
38.46	167	39.34	149	40.22	145	41.1	152	41.98	189	42.86	164	43.74	192	44.62	166	45.5	150	46.38	168	47.26	148
38.48	188	39.36	140	40.24	174	41.12	212	42	202	42.88	157	43.76	193	44.64	162	45.52	142	46.4	191	47.28	162
38.5	180	39.38	164	40.26	164	41.14	152	42.02	156	42.9	154	43.78	146	44.66	128	45.54	162	46.42	195	47.3	132
38.52	174	39.4	160	40.28	167	41.16	137	42.04	196	42.92	140	43.8	169	44.68	170	45.56	137	46.44	162	47.32	141
38.54	191	39.42	138	40.3	156	41.18	159	42.06	210	42.94	159	43.82	153	44.7	147	45.58	135	46.46	200	47.34	136
38.56	197	39.44	146	40.32	135	41.2	189	42.08	175	42.96	155	43.84	185	44.72	147	45.6	144	46.48	203	47.36	168
38.58	179	39.46	147	40.34	150	41.22	160	42.1	166	42.98	137	43.86	182	44.74	130	45.62	153	46.5	196	47.38	157
38.6	181	39.48	135	40.36	167	41.24	174	42.12	182	43	155	43.88	151	44.76	154	45.64	157	46.52	181	47.4	159
38.62	204	39.5	159	40.38	156	41.26	191	42.14	160	43.02	145	43.9	150	44.78	158	45.66	153	46.54	188	47.42	169
38.64	183	39.52	140	40.4	124	41.28	206	42.16	167	43.04	164	43.92	145	44.8	146	45.68	117	46.56	260	47.44	161
38.66	193	39.54	136	40.42	169	41.3	213	42.18	207	43.06	139	43.94	170	44.82	168	45.7	155	46.58	230	47.46	160
38.68	196	39.56	137	40.44	159	41.32	228	42.2	193	43.08	160	43.96	191	44.84	140	45.72	148	46.6	216	47.48	152
38.7	204	39.58	148	40.46	156	41.34	225	42.22	225	43.1	155	43.98	166	44.86	142	45.74	142	46.62	206	47.5	152
38.72	183	39.6	157	40.48	141	41.36	217	42.24	201	43.12	159	44	154	44.88	149	45.76	141	46.64	182	47.52	187
38.74	186	39.62	144	40.5	159	41.38	246	42.26	193	43.14	153	44.02	184	44.9	140	45.78	145	46.66	186	47.54	137
38.76	183	39.64	155	40.52	138	41.4	247	42.28	207	43.16	155	44.04	177	44.92	136	45.8	166	46.68	183	47.56	177
38.78	180	39.66	157	40.54	131	41.42	256	42.3	220	43.18	141	44.06	197	44.94	163	45.82	146	46.7	212	47.58	160
38.8	144	39.68	164	40.56	155	41.44	236	42.32	197	43.2	151	44.08	176	44.96	154	45.84	154	46.72	177	47.6	184
38.82	174	39.7	143	40.58	165	41.46	199	42.34	198	43.22	145	44.1	162	44.98	155	45.86	133	46.74	181	47.62	171
38.84	169	39.72	162	40.6	155	41.48	259	42.36	176	43.24	154	44.12	191	45	145	45.88	169	46.76	151	47.64	169
38.86	168	39.74	166	40.62	155	41.5	261	42.38	184	43.26	129	44.14	165	45.02	146	45.9	142	46.78	171	47.66	148
38.88	180	39.76	140	40.64	160	41.52	233	42.4	175	43.28	147	44.16	183	45.04	158	45.92	139	46.8	169	47.68	185
38.9	156	39.78	154	40.66	172	41.54	251	42.42	181	43.3	145	44.18	187	45.06	166	45.94	160	46.82	166	47.7	138

Angle	R.Int	Angle	R.Int	Angle	R.Int	Angle	R.Int	Angle	R.Int	Angle	R.Int	Angle	R.Int	Angle	R.Int	Angle	R.Int	Angle	R.Int	Angle	R.Int
47.72	186	48.56	157	49.4	165	50.24	153	51.08	178	51.92	134	52.76	155	53.6	141	54.44	130	55.28	147	56.12	175
47.74	166	48.58	191	49.42	169	50.26	160	51.1	190	51.94	136	52.78	129	53.62	146	54.46	123	55.3	117	56.14	156
47.76	158	48.6	159	49.44	174	50.28	148	51.12	152	51.96	156	52.8	179	53.64	168	54.48	130	55.32	115	56.16	138
47.78	151	48.62	179	49.46	181	50.3	148	51.14	180	51.98	132	52.82	152	53.66	180	54.5	120	55.34	116	56.18	152
47.8	148	48.64	174	49.48	175	50.32	161	51.16	153	52	147	52.84	161	53.68	157	54.52	126	55.36	137	56.2	167
47.82	176	48.66	168	49.5	159	50.34	180	51.18	148	52.02	150	52.86	142	53.7	159	54.54	137	55.38	139	56.22	152
47.84	173	48.68	158	49.52	169	50.36	162	51.2	158	52.04	140	52.88	163	53.72	161	54.56	156	55.4	121	56.24	160
47.86	177	48.7	167	49.54	189	50.38	172	51.22	154	52.06	147	52.9	183	53.74	174	54.58	132	55.42	138	56.26	146
47.88	193	48.72	174	49.56	182	50.4	183	51.24	159	52.08	148	52.92	157	53.76	174	54.6	133	55.44	140	56.28	177
47.9	173	48.74	169	49.58	165	50.42	168	51.26	123	52.1	125	52.94	141	53.78	164	54.62	135	55.46	137	56.3	186
47.92	171	48.76	168	49.6	177	50.44	157	51.28	126	52.12	154	52.96	155	53.8	154	54.64	133	55.48	135	56.32	164
47.94	177	48.78	152	49.62	178	50.46	179	51.3	151	52.14	132	52.98	165	53.82	156	54.66	120	55.5	112	56.34	181
47.96	185	48.8	145	49.64	145	50.48	206	51.32	160	52.16	152	53	166	53.84	161	54.68	141	55.52	148	56.36	193
47.98	152	48.82	156	49.66	164	50.5	167	51.34	132	52.18	164	53.02	151	53.86	140	54.7	135	55.54	137	56.38	162
48	185	48.84	185	49.68	144	50.52	173	51.36	137	52.2	154	53.04	153	53.88	157	54.72	142	55.56	133	56.4	192
48.02	175	48.86	169	49.7	138	50.54	143	51.38	110	52.22	155	53.06	171	53.9	137	54.74	137	55.58	149	56.42	176
48.04	181	48.88	163	49.72	147	50.56	186	51.4	147	52.24	179	53.08	163	53.92	156	54.76	131	55.6	125	56.44	192
48.06	187	48.9	201	49.74	175	50.58	188	51.42	151	52.26	136	53.1	164	53.94	154	54.78	128	55.62	130	56.46	192
48.08	182	48.92	168	49.76	188	50.6	191	51.44	129	52.28	159	53.12	135	53.96	140	54.8	115	55.64	139	56.48	209
48.1	185	48.94	163	49.78	145	50.62	210	51.46	163	52.3	157	53.14	142	53.98	148	54.82	133	55.66	120	56.5	196
48.12	175	48.96	180	49.8	156	50.64	194	51.48	136	52.32	176	53.16	147	54	112	54.84	133	55.68	114	56.52	213
48.14	197	48.98	137	49.82	177	50.66	204	51.5	149	52.34	168	53.18	171	54.02	121	54.86	134	55.7	144	56.54	207
48.16	202	49	163	49.84	167	50.68	233	51.52	146	52.36	162	53.2	161	54.04	116	54.88	133	55.72	126	56.56	199
48.18	194	49.02	175	49.86	152	50.7	242	51.54	155	52.38	143	53.22	132	54.06	129	54.9	120	55.74	133	56.58	184
48.2	211	49.04	166	49.88	168	50.72	257	51.56	170	52.4	136	53.24	151	54.08	126	54.92	139	55.76	161	56.6	162
48.22	188	49.06	198	49.9	159	50.74	238	51.58	139	52.42	147	53.26	179	54.1	158	54.94	124	55.78	153	56.62	204
48.24	192	49.08	168	49.92	162	50.76	248	51.6	154	52.44	151	53.28	153	54.12	110	54.96	126	55.8	146	56.64	203
48.26	187	49.1	182	49.94	140	50.78	259	51.62	148	52.46	125	53.3	178	54.14	119	54.98	143	55.82	150	56.66	192
48.28	172	49.12	174	49.96	166	50.8	248	51.64	152	52.48	142	53.32	139	54.16	130	55	124	55.84	155	56.68	188
48.3	190	49.14	160	49.98	172	50.82	258	51.66	145	52.5	138	53.34	152	54.18	121	55.02	120	55.86	154	56.7	176
48.32	188	49.16	164	50	188	50.84	244	51.68	160	52.52	167	53.36	156	54.2	121	55.04	124	55.88	148	56.72	199
48.34	215	49.18	201	50.02	178	50.86	250	51.7	140	52.54	130	53.38	115	54.22	119	55.06	129	55.9	140	56.74	173
48.36	166	49.2	192	50.04	156	50.88	231	51.72	165	52.56	142	53.4	122	54.24	148	55.08	128	55.92	163	56.76	190
48.38	175	49.22	161	50.06	155	50.9	288	51.74	170	52.58	167	53.42	161	54.26	137	55.1	124	55.94	153	56.78	169
48.4	180	49.24	156	50.08	171	50.92	260	51.76	132	52.6	139	53.44	139	54.28	117	55.12	129	55.96	152	56.8	164
48.42	149	49.26	184	50.1	146	50.94	248	51.78	149	52.62	158	53.46	167	54.3	140	55.14	124	55.98	154	56.82	144
48.44	161	49.28	159	50.12	168	50.96	241	51.8	126	52.64	145	53.48	139	54.32	127	55.16	149	56	155	56.84	192
48.46	184	49.3	220	50.14	169	50.98	242	51.82	140	52.66	122	53.5	169	54.34	126	55.18	125	56.02	144	56.86	123
48.48	155	49.32	170	50.16	172	51	191	51.84	161	52.68	156	53.52	123	54.36	133	55.2	137	56.04	181	56.88	128
48.5	155	49.34	185	50.18	159	51.02	216	51.86	143	52.7	164	53.54	180	54.38	122	55.22	152	56.06	133	56.9	117
48.52	182	49.36	149	50.2	162	51.04	189	51.88	145	52.72	140	53.56	145	54.4	125	55.24	157	56.08	157	56.92	140
48.54	167	49.38	162	50.22	163	51.06	180	51.9	144	52.74	173	53.58	156	54.42	145	55.26	110	56.1	162	56.94	156

Angle	R.Int	Angle	R.Int	Angle	R.Int	Angle	R.Int	Angle	R.Int	Angle	R.Int	Angle	R.Int	Angle	R.Int	Angle	R.Int	Angle	R.Int
56.96	148	57.8	131	58.64	158	59.48	143	60.32	122	61.16	139	62	187	62.84	150	63.68	121	64.52	168	65.36	122
56.98	134	57.82	119	58.66	140	59.5	138	60.34	147	61.18	150	62.02	176	62.86	150	63.7	165	64.54	165	65.38	140
57	160	57.84	100	58.68	143	59.52	114	60.36	137	61.2	145	62.04	216	62.88	163	63.72	149	64.56	168	65.4	134
57.02	145	57.86	151	58.7	159	59.54	127	60.38	131	61.22	135	62.06	159	62.9	172	63.74	134	64.58	199	65.42	147
57.04	145	57.88	145	58.72	140	59.56	142	60.4	125	61.24	151	62.08	181	62.92	153	63.76	153	64.6	170	65.44	146
57.06	164	57.9	156	58.74	143	59.58	152	60.42	118	61.26	174	62.1	204	62.94	129	63.78	143	64.62	184	65.46	167
57.08	125	57.92	133	58.76	143	59.6	127	60.44	125	61.28	140	62.12	191	62.96	120	63.8	154	64.64	172	65.48	149
57.1	145	57.94	151	58.78	143	59.62	153	60.46	117	61.3	157	62.14	214	62.98	142	63.82	138	64.66	206	65.5	145
57.12	141	57.96	122	58.8	130	59.64	159	60.48	136	61.32	174	62.16	202	63	138	63.84	113	64.68	189	65.52	157
57.14	151	57.98	144	58.82	142	59.66	159	60.5	146	61.34	167	62.18	179	63.02	131	63.86	137	64.7	170	65.54	139
57.16	135	58	144	58.84	168	59.68	139	60.52	145	61.36	176	62.2	171	63.04	143	63.88	125	64.72	170	65.56	139
57.18	139	58.02	127	58.86	148	59.7	122	60.54	132	61.38	158	62.22	169	63.06	148	63.9	137	64.74	164	65.58	123
57.2	143	58.04	143	58.88	123	59.72	145	60.56	143	61.4	176	62.24	185	63.08	158	63.92	115	64.76	147	65.6	151
57.22	153	58.06	151	58.9	146	59.74	143	60.58	139	61.42	153	62.26	168	63.1	140	63.94	136	64.78	158	65.62	139
57.24	127	58.08	137	58.92	154	59.76	128	60.6	126	61.44	159	62.28	164	63.12	163	63.96	149	64.8	160	65.64	139
57.26	142	58.1	142	58.94	139	59.78	154	60.62	119	61.46	162	62.3	178	63.14	130	63.98	122	64.82	166	65.66	166
57.28	129	58.12	127	58.96	135	59.8	132	60.64	108	61.48	168	62.32	168	63.16	117	64	124	64.84	165	65.68	127
57.3	161	58.14	149	58.98	139	59.82	149	60.66	148	61.5	169	62.34	179	63.18	142	64.02	149	64.86	149	65.7	150
57.32	119	58.16	137	59	144	59.84	135	60.68	123	61.52	181	62.36	185	63.2	145	64.04	153	64.88	155	65.72	181
57.34	127	58.18	135	59.02	166	59.86	140	60.7	143	61.54	154	62.38	159	63.22	130	64.06	148	64.9	153	65.74	149
57.36	125	58.2	149	59.04	127	59.88	142	60.72	133	61.56	187	62.4	165	63.24	131	64.08	142	64.92	121	65.76	147
57.38	123	58.22	141	59.06	140	59.9	136	60.74	109	61.58	154	62.42	175	63.26	148	64.1	146	64.94	157	65.78	145
57.4	133	58.24	153	59.08	149	59.92	165	60.76	100	61.6	168	62.44	138	63.28	154	64.12	149	64.96	148	65.8	145
57.42	116	58.26	142	59.1	137	59.94	140	60.78	124	61.62	167	62.46	146	63.3	165	64.14	137	64.98	163	65.82	153
57.44	114	58.28	140	59.12	149	59.96	149	60.8	139	61.64	160	62.48	157	63.32	145	64.16	160	65	149	65.84	164
57.46	137	58.3	148	59.14	136	59.98	148	60.82	123	61.66	190	62.5	158	63.34	132	64.18	147	65.02	174	65.86	145
57.48	133	58.32	157	59.16	137	60	157	60.84	126	61.68	181	62.52	163	63.36	146	64.2	161	65.04	153	65.88	159
57.5	126	58.34	138	59.18	133	60.02	142	60.86	144	61.7	156	62.54	165	63.38	137	64.22	157	65.06	138	65.9	133
57.52	109	58.36	145	59.2	127	60.04	136	60.88	129	61.72	192	62.56	163	63.4	117	64.24	150	65.08	158	65.92	157
57.54	132	58.38	141	59.22	141	60.06	128	60.9	133	61.74	191	62.58	137	63.42	145	64.26	192	65.1	164	65.94	146
57.56	137	58.4	137	59.24	142	60.08	156	60.92	144	61.76	191	62.6	138	63.44	134	64.28	147	65.12	155	65.96	141
57.58	117	58.42	145	59.26	156	60.1	122	60.94	146	61.78	196	62.62	154	63.46	138	64.3	155	65.14	147	65.98	171
57.6	138	58.44	133	59.28	148	60.12	113	60.96	126	61.8	211	62.64	169	63.48	117	64.32	167	65.16	164	66	157
57.62	143	58.46	127	59.3	138	60.14	126	60.98	147	61.82	181	62.66	151	63.5	150	64.34	168	65.18	151	66.02	149
57.64	131	58.48	138	59.32	129	60.16	119	61	116	61.84	178	62.68	147	63.52	122	64.36	150	65.2	155	66.04	139
57.66	134	58.5	160	59.34	141	60.18	152	61.02	127	61.86	201	62.7	133	63.54	134	64.38	150	65.22	152	66.06	144
57.68	134	58.52	145	59.36	129	60.2	140	61.04	138	61.88	174	62.72	149	63.56	156	64.4	166	65.24	154	66.08	137
57.7	118	58.54	135	59.38	153	60.22	138	61.06	140	61.9	191	62.74	131	63.58	153	64.42	152	65.26	139	66.1	130
57.72	105	58.56	148	59.4	132	60.24	148	61.08	127	61.92	207	62.76	153	63.6	120	64.44	163	65.28	123	66.12	133
57.74	126	58.58	147	59.42	137	60.26	127	61.1	133	61.94	171	62.78	158	63.62	133	64.46	167	65.3	163	66.14	139
57.76	118	58.6	126	59.44	160	60.28	151	61.12	170	61.96	195	62.8	146	63.64	139	64.48	189	65.32	167	66.16	134
57.78	141	58.62	149	59.46	126	60.3	126	61.14	145	61.98	168	62.82	150	63.66	143	64.5	188	65.34	147	66.18	148

Angle	R.Int	Angle	R.Int	Angle	R.Int	Angle	R.Int	Angle	R.Int	Angle	R.Int	Angle	R.Int	Angle	R.Int	Angle	R.Int	Angle	R.Int
66.2	133	67.04	138	67.88	148	68.72	152	69.56	145	70.4	115	71.24	113	72.08	148	72.92	119	73.76	152	74.6	156
66.22	156	67.06	126	67.9	147	68.74	148	69.58	139	70.42	131	71.26	127	72.1	128	72.94	154	73.78	140	74.62	161
66.24	137	67.08	133	67.92	150	68.76	159	69.6	145	70.44	125	71.28	130	72.12	124	72.96	124	73.8	139	74.64	151
66.26	140	67.1	125	67.94	166	68.78	160	69.62	158	70.46	116	71.3	141	72.14	157	72.98	136	73.82	156	74.66	165
66.28	151	67.12	116	67.96	156	68.8	153	69.64	149	70.48	155	71.32	148	72.16	137	73	114	73.84	130	74.68	137
66.3	149	67.14	136	67.98	156	68.82	151	69.66	138	70.5	115	71.34	136	72.18	131	73.02	146	73.86	174	74.7	144
66.32	148	67.16	126	68	154	68.84	140	69.68	135	70.52	114	71.36	112	72.2	116	73.04	171	73.88	147	74.72	189
66.34	154	67.18	132	68.02	167	68.86	135	69.7	131	70.54	105	71.38	138	72.22	144	73.06	138	73.9	148	74.74	143
66.36	146	67.2	144	68.04	135	68.88	153	69.72	134	70.56	112	71.4	110	72.24	149	73.08	153	73.92	155	74.76	156
66.38	152	67.22	122	68.06	194	68.9	174	69.74	149	70.58	119	71.42	137	72.26	153	73.1	148	73.94	145	74.78	140
66.4	147	67.24	148	68.08	159	68.92	148	69.76	119	70.6	129	71.44	123	72.28	124	73.12	127	73.96	145	74.8	145
66.42	163	67.26	156	68.1	161	68.94	162	69.78	154	70.62	142	71.46	118	72.3	140	73.14	142	73.98	155	74.82	157
66.44	134	67.28	123	68.12	138	68.96	165	69.8	164	70.64	119	71.48	126	72.32	131	73.16	132	74	139	74.84	162
66.46	139	67.3	124	68.14	157	68.98	174	69.82	152	70.66	118	71.5	159	72.34	134	73.18	123	74.02	148	74.86	148
66.48	164	67.32	138	68.16	163	69	170	69.84	154	70.68	118	71.52	121	72.36	131	73.2	146	74.04	149	74.88	159
66.5	150	67.34	124	68.18	184	69.02	174	69.86	135	70.7	131	71.54	124	72.38	141	73.22	185	74.06	157	74.9	139
66.52	142	67.36	143	68.2	171	69.04	132	69.88	156	70.72	123	71.56	148	72.4	141	73.24	161	74.08	154	74.92	137
66.54	131	67.38	155	68.22	156	69.06	180	69.9	131	70.74	113	71.58	137	72.42	139	73.26	139	74.1	131	74.94	165
66.56	169	67.4	162	68.24	145	69.08	167	69.92	168	70.76	115	71.6	136	72.44	137	73.28	149	74.12	133	74.96	156
66.58	124	67.42	154	68.26	156	69.1	150	69.94	125	70.78	121	71.62	134	72.46	137	73.3	141	74.14	146	74.98	153
66.6	151	67.44	151	68.28	177	69.12	151	69.96	137	70.8	112	71.64	125	72.48	148	73.32	145	74.16	133	75	171
66.62	128	67.46	153	68.3	143	69.14	175	69.98	152	70.82	126	71.66	143	72.5	134	73.34	144	74.18	151	75.02	154
66.64	120	67.48	176	68.32	135	69.16	148	70	181	70.84	120	71.68	151	72.52	141	73.36	142	74.2	130	75.04	161
66.66	133	67.5	149	68.34	171	69.18	123	70.02	166	70.86	135	71.7	117	72.54	145	73.38	127	74.22	149	75.06	157
66.68	154	67.52	154	68.36	174	69.2	144	70.04	130	70.88	117	71.72	130	72.56	158	73.4	160	74.24	129	75.08	150
66.7	129	67.54	145	68.38	158	69.22	130	70.06	150	70.9	118	71.74	137	72.58	119	73.42	139	74.26	131	75.1	151
66.72	138	67.56	151	68.4	147	69.24	158	70.08	116	70.92	111	71.76	154	72.6	133	73.44	142	74.28	149	75.12	140
66.74	118	67.58	145	68.42	142	69.26	163	70.1	153	70.94	136	71.78	149	72.62	142	73.46	169	74.3	140	75.14	159
66.76	126	67.6	157	68.44	136	69.28	144	70.12	135	70.96	103	71.8	116	72.64	151	73.48	134	74.32	154	75.16	126
66.78	137	67.62	136	68.46	155	69.3	168	70.14	147	70.98	129	71.82	131	72.66	147	73.5	140	74.34	144	75.18	130
66.8	131	67.64	139	68.48	151	69.32	141	70.16	115	71	119	71.84	127	72.68	135	73.52	144	74.36	152	75.2	150
66.82	151	67.66	137	68.5	123	69.34	162	70.18	136	71.02	138	71.86	136	72.7	134	73.54	150	74.38	154	75.22	147
66.84	155	67.68	149	68.52	142	69.36	156	70.2	136	71.04	131	71.88	127	72.72	129	73.56	158	74.4	155	75.24	146
66.86	132	67.7	116	68.54	165	69.38	154	70.22	122	71.06	122	71.9	141	72.74	131	73.58	154	74.42	148	75.26	125
66.88	126	67.72	128	68.56	147	69.4	167	70.24	123	71.08	121	71.92	138	72.76	145	73.6	150	74.44	164	75.28	174
66.9	143	67.74	148	68.58	143	69.42	170	70.26	134	71.1	133	71.94	143	72.78	177	73.62	156	74.46	171	75.3	145
66.92	136	67.76	156	68.6	158	69.44	144	70.28	127	71.12	112	71.96	136	72.8	130	73.64	163	74.48	148	75.32	142
66.94	139	67.78	157	68.62	153	69.46	127	70.3	123	71.14	115	71.98	132	72.82	160	73.66	142	74.5	144	75.34	141
66.96	145	67.8	159	68.64	146	69.48	183	70.32	153	71.16	127	72	151	72.84	163	73.68	146	74.52	155	75.36	158
66.98	139	67.82	153	68.66	144	69.5	166	70.34	120	71.18	146	72.02	138	72.86	130	73.7	151	74.54	139	75.38	134
67	139	67.84	169	68.68	162	69.52	156	70.36	111	71.2	139	72.04	123	72.88	126	73.72	149	74.56	130	75.4	135
67.02	130	67.86	155	68.7	134	69.54	128	70.38	129	71.22	104	72.06	143	72.9	150	73.74	150	74.58	150	75.42	125

Angle	R.Int	Angle	R.Int	Angle	R.Int	Angle	R.Int	Angle	R.Int	Angle	R.Int
75.44	120	76.28	122	77.12	126	77.96	120	78.8	126	79.64	109
75.46	155	76.3	114	77.14	139	77.98	115	78.82	139	79.66	117
75.48	154	76.32	126	77.16	108	78	116	78.84	151	79.68	125
75.5	142	76.34	157	77.18	132	78.02	123	78.86	132	79.7	119
75.52	145	76.36	135	77.2	142	78.04	136	78.88	138	79.72	105
75.54	129	76.38	128	77.22	119	78.06	116	78.9	133	79.74	116
75.56	110	76.4	135	77.24	131	78.08	119	78.92	140	79.76	110
75.58	132	76.42	144	77.26	144	78.1	118	78.94	132	79.78	116
75.6	134	76.44	113	77.28	129	78.12	129	78.96	124	79.8	136
75.62	139	76.46	123	77.3	125	78.14	125	78.98	125	79.82	142
75.64	144	76.48	153	77.32	151	78.16	125	79	131	79.84	133
75.66	143	76.5	122	77.34	118	78.18	136	79.02	126	79.86	111
75.68	126	76.52	152	77.36	146	78.2	117	79.04	122	79.88	105
75.7	145	76.54	142	77.38	133	78.22	127	79.06	128	79.9	117
75.72	111	76.56	130	77.4	135	78.24	124	79.08	131	79.92	124
75.74	136	76.58	141	77.42	135	78.26	125	79.1	135	79.94	129
75.76	148	76.6	157	77.44	146	78.28	127	79.12	132	79.96	111
75.78	121	76.62	128	77.46	143	78.3	135	79.14	127	79.98	129
75.8	137	76.64	118	77.48	123	78.32	115	79.16	115	80	126
75.82	152	76.66	130	77.5	144	78.34	127	79.18	135		
75.84	118	76.68	142	77.52	146	78.36	114	79.2	124		
75.86	154	76.7	118	77.54	134	78.38	113	79.22	135		
75.88	137	76.72	114	77.56	125	78.4	120	79.24	139		
75.9	128	76.74	118	77.58	156	78.42	113	79.26	121		
75.92	132	76.76	151	77.6	126	78.44	118	79.28	124		
75.94	128	76.78	119	77.62	146	78.46	153	79.3	135		
75.96	123	76.8	150	77.64	130	78.48	110	79.32	117		
75.98	143	76.82	131	77.66	136	78.5	130	79.34	105		
76	133	76.84	149	77.68	132	78.52	110	79.36	134		
76.02	141	76.86	120	77.7	140	78.54	113	79.38	140		
76.04	132	76.88	150	77.72	139	78.56	129	79.4	115		
76.06	138	76.9	116	77.74	134	78.58	144	79.42	119		
76.08	135	76.92	118	77.76	132	78.6	122	79.44	124		
76.1	144	76.94	133	77.78	107	78.62	135	79.46	118		
76.12	153	76.96	130	77.8	114	78.64	120	79.48	138		
76.14	141	76.98	142	77.82	112	78.66	110	79.5	119		
76.16	141	77	124	77.84	117	78.68	142	79.52	126		
76.18	119	77.02	115	77.86	106	78.7	141	79.54	169		
76.2	115	77.04	130	77.88	116	78.72	117	79.56	110		
76.22	155	77.06	111	77.9	124	78.74	151	79.58	135		
76.24	143	77.08	124	77.92	133	78.76	132	79.6	128		
76.26	112	77.1	166	77.94	118	78.78	127	79.62	114		

Monte Giardina lava dome

Angle	R.Int	Angle	R.Int	Angle	R.Int	Angle	R.Int	Angle	R.Int	Angle	R.Int	Angle	R.Int	Angle	R.Int	Angle	R.Int	Angle	R.Int
20	197	22.05	179	24.1	146	26.15	150	28.2	138	30.25	138	32.3	118	34.35	98	36.4	93	38.45	68	40.5	59
20.05	211	22.1	196	24.15	141	26.2	160	28.25	143	30.3	135	32.35	115	34.4	90	36.45	86	38.5	65	40.55	59
20.1	190	22.15	184	24.2	153	26.25	155	28.3	149	30.35	124	32.4	105	34.45	112	36.5	88	38.55	69	40.6	76
20.15	212	22.2	194	24.25	151	26.3	139	28.35	138	30.4	178	32.45	113	34.5	108	36.55	83	38.6	90	40.65	68
20.2	184	22.25	189	24.3	143	26.35	144	28.4	114	30.45	161	32.5	112	34.55	111	36.6	74	38.65	89	40.7	67
20.25	202	22.3	193	24.35	161	26.4	152	28.45	149	30.5	160	32.55	107	34.6	109	36.65	97	38.7	93	40.75	75
20.3	172	22.35	168	24.4	156	26.45	171	28.5	127	30.55	137	32.6	108	34.65	125	36.7	74	38.75	92	40.8	82
20.35	192	22.4	188	24.45	136	26.5	158	28.55	148	30.6	150	32.65	110	34.7	150	36.75	79	38.8	77	40.85	85
20.4	186	22.45	154	24.5	134	26.55	139	28.6	134	30.65	166	32.7	98	34.75	100	36.8	95	38.85	89	40.9	59
20.45	192	22.5	143	24.55	129	26.6	170	28.65	129	30.7	153	32.75	91	34.8	107	36.85	105	38.9	91	40.95	67
20.5	203	22.55	153	24.6	155	26.65	136	28.7	133	30.75	130	32.8	123	34.85	109	36.9	69	38.95	81	41	65
20.55	192	22.6	153	24.65	132	26.7	166	28.75	132	30.8	169	32.85	94	34.9	110	36.95	88	39	54	41.05	86
20.6	200	22.65	178	24.7	145	26.75	159	28.8	143	30.85	143	32.9	111	34.95	120	37	95	39.05	81	41.1	58
20.65	203	22.7	159	24.75	126	26.8	201	28.85	135	30.9	155	32.95	112	35	113	37.05	117	39.1	82	41.15	80
20.7	194	22.75	162	24.8	157	26.85	218	28.9	126	30.95	165	33	86	35.05	109	37.1	91	39.15	67	41.2	76
20.75	230	22.8	183	24.85	143	26.9	201	28.95	133	31	134	33.05	86	35.1	128	37.15	85	39.2	80	41.25	70
20.8	192	22.85	177	24.9	138	26.95	195	29	136	31.05	128	33.1	103	35.15	108	37.2	84	39.25	60	41.3	63
20.85	205	22.9	169	24.95	150	27	224	29.05	118	31.1	147	33.15	99	35.2	117	37.25	83	39.3	62	41.35	103
20.9	217	22.95	167	25	163	27.05	210	29.1	122	31.15	144	33.2	101	35.25	119	37.3	68	39.35	64	41.4	97
20.95	190	23	172	25.05	122	27.1	253	29.15	127	31.2	153	33.25	112	35.3	127	37.35	93	39.4	76	41.45	90
21	208	23.05	173	25.1	145	27.15	286	29.2	140	31.25	145	33.3	105	35.35	127	37.4	73	39.45	71	41.5	78
21.05	240	23.1	200	25.15	128	27.2	248	29.25	145	31.3	138	33.35	102	35.4	125	37.45	93	39.5	66	41.55	71
21.1	224	23.15	157	25.2	155	27.25	269	29.3	123	31.35	113	33.4	89	35.45	124	37.5	92	39.55	64	41.6	86
21.15	213	23.2	192	25.25	140	27.3	251	29.35	116	31.4	133	33.45	96	35.5	129	37.55	73	39.6	57	41.65	80
21.2	220	23.25	200	25.3	139	27.35	269	29.4	119	31.45	110	33.5	101	35.55	126	37.6	69	39.65	63	41.7	96
21.25	232	23.3	189	25.35	140	27.4	299	29.45	158	31.5	125	33.55	104	35.6	137	37.65	78	39.7	69	41.75	91
21.3	325	23.35	215	25.4	156	27.45	270	29.5	147	31.55	153	33.6	95	35.65	140	37.7	82	39.75	92	41.8	65
21.35	311	23.4	196	25.45	155	27.5	277	29.55	178	31.6	122	33.65	93	35.7	142	37.75	99	39.8	69	41.85	67
21.4	353	23.45	192	25.5	158	27.55	215	29.6	149	31.65	128	33.7	107	35.75	173	37.8	80	39.85	66	41.9	82
21.45	393	23.5	192	25.55	161	27.6	239	29.65	177	31.7	120	33.75	110	35.8	144	37.85	70	39.9	57	41.95	49
21.5	418	23.55	195	25.6	169	27.65	207	29.7	166	31.75	102	33.8	92	35.85	132	37.9	67	39.95	78	42	67
21.55	429	23.6	147	25.65	171	27.7	204	29.75	168	31.8	117	33.85	108	35.9	114	37.95	86	40	60	42.05	64
21.6	450	23.65	148	25.7	161	27.75	206	29.8	150	31.85	97	33.9	98	35.95	115	38	59	40.05	79	42.1	82
21.65	424	23.7	148	25.75	136	27.8	164	29.85	145	31.9	106	33.95	102	36	91	38.05	76	40.1	71	42.15	74
21.7	393	23.75	149	25.8	157	27.85	202	29.9	144	31.95	115	34	96	36.05	121	38.1	84	40.15	70	42.2	59
21.75	355	23.8	149	25.85	147	27.9	165	29.95	159	32	103	34.05	95	36.1	112	38.15	70	40.2	81	42.25	91
21.8	270	23.85	152	25.9	133	27.95	168	30	150	32.05	112	34.1	103	36.15	91	38.2	67	40.25	70	42.3	84
21.85	256	23.9	159	25.95	132	28	152	30.05	121	32.1	139	34.15	99	36.2	80	38.25	75	40.3	67	42.35	89
21.9	210	23.95	133	26	143	28.05	148	30.1	156	32.15	129	34.2	99	36.25	104	38.3	84	40.35	53	42.4	73
21.95	215	24	167	26.05	129	28.1	136	30.15	157	32.2	132	34.25	106	36.3	87	38.35	92	40.4	55	42.45	82
22	163	24.05	134	26.1	128	28.15	150	30.2	137	32.25	118	34.3	95	36.35	104	38.4	92	40.45	74	42.5	82

Angle	R.Int	Angle	R.Int	Angle	R.Int	Angle	R.Int	Angle	R.Int	Angle	R.Int	Angle	R.Int	Angle	R.Int	Angle	R.Int	Angle	R.Int	Angle	R.Int
42.55	63	44.6	56	46.65	72	48.7	59	50.75	86	52.8	57	54.85	42	56.9	58	58.95	43	61	47	63.05	65
42.6	75	44.65	80	46.7	48	48.75	55	50.8	66	52.85	66	54.9	57	56.95	56	59	50	61.05	47	63.1	55
42.65	53	44.7	45	46.75	73	48.8	79	50.85	86	52.9	57	54.95	60	57	57	59.05	59	61.1	68	63.15	56
42.7	62	44.75	55	46.8	70	48.85	60	50.9	78	52.95	59	55	54	57.05	60	59.1	45	61.15	46	63.2	60
42.75	73	44.8	60	46.85	70	48.9	57	50.95	78	53	70	55.05	57	57.1	64	59.15	63	61.2	53	63.25	51
42.8	62	44.85	63	46.9	74	48.95	58	51	74	53.05	56	55.1	58	57.15	52	59.2	52	61.25	67	63.3	58
42.85	75	44.9	51	46.95	66	49	49	51.05	70	53.1	47	55.15	56	57.2	50	59.25	54	61.3	67	63.35	37
42.9	67	44.95	69	47	62	49.05	56	51.1	72	53.15	69	55.2	54	57.25	62	59.3	52	61.35	76	63.4	48
42.95	69	45	51	47.05	68	49.1	66	51.15	55	53.2	59	55.25	51	57.3	63	59.35	50	61.4	64	63.45	48
43	77	45.05	48	47.1	66	49.15	58	51.2	59	53.25	53	55.3	45	57.35	61	59.4	57	61.45	75	63.5	53
43.05	74	45.1	49	47.15	59	49.2	67	51.25	75	53.3	58	55.35	52	57.4	42	59.45	58	61.5	62	63.55	67
43.1	58	45.15	67	47.2	64	49.25	52	51.3	71	53.35	59	55.4	45	57.45	57	59.5	74	61.55	73	63.6	65
43.15	65	45.2	69	47.25	77	49.3	74	51.35	49	53.4	53	55.45	57	57.5	60	59.55	60	61.6	55	63.65	60
43.2	52	45.25	58	47.3	69	49.35	70	51.4	58	53.45	71	55.5	53	57.55	52	59.6	64	61.65	64	63.7	50
43.25	58	45.3	62	47.35	69	49.4	62	51.45	66	53.5	57	55.55	58	57.6	63	59.65	67	61.7	72	63.75	35
43.3	70	45.35	66	47.4	64	49.45	65	51.5	51	53.55	53	55.6	47	57.65	47	59.7	50	61.75	82	63.8	69
43.35	65	45.4	55	47.45	71	49.5	72	51.55	67	53.6	53	55.65	48	57.7	58	59.75	73	61.8	75	63.85	58
43.4	69	45.45	66	47.5	56	49.55	61	51.6	64	53.65	59	55.7	54	57.75	45	59.8	65	61.85	77	63.9	56
43.45	50	45.5	58	47.55	77	49.6	68	51.65	77	53.7	62	55.75	45	57.8	55	59.85	70	61.9	77	63.95	51
43.5	63	45.55	63	47.6	63	49.65	66	51.7	48	53.75	67	55.8	54	57.85	41	59.9	63	61.95	82	64	51
43.55	60	45.6	47	47.65	54	49.7	56	51.75	71	53.8	70	55.85	76	57.9	50	59.95	74	62	58	64.05	55
43.6	63	45.65	54	47.7	64	49.75	61	51.8	62	53.85	57	55.9	68	57.95	71	60	60	62.05	73	64.1	67
43.65	62	45.7	59	47.75	86	49.8	77	51.85	61	53.9	50	55.95	46	58	50	60.05	63	62.1	64	64.15	47
43.7	55	45.75	51	47.8	57	49.85	58	51.9	41	53.95	60	56	47	58.05	62	60.1	49	62.15	60	64.2	47
43.75	74	45.8	71	47.85	68	49.9	70	51.95	56	54	53	56.05	51	58.1	63	60.15	70	62.2	54	64.25	61
43.8	72	45.85	52	47.9	69	49.95	47	52	66	54.05	59	56.1	55	58.15	59	60.2	49	62.25	62	64.3	53
43.85	63	45.9	69	47.95	73	50	69	52.05	52	54.1	56	56.15	78	58.2	50	60.25	59	62.3	71	64.35	79
43.9	66	45.95	59	48	77	50.05	54	52.1	61	54.15	51	56.2	74	58.25	61	60.3	56	62.35	59	64.4	63
43.95	68	46	72	48.05	61	50.1	59	52.15	55	54.2	50	56.25	62	58.3	73	60.35	61	62.4	51	64.45	69
44	64	46.05	73	48.1	83	50.15	65	52.2	50	54.25	51	56.3	77	58.35	62	60.4	71	62.45	58	64.5	63
44.05	93	46.1	80	48.15	69	50.2	67	52.25	66	54.3	65	56.35	75	58.4	65	60.45	57	62.5	62	64.55	74
44.1	73	46.15	69	48.2	89	50.25	61	52.3	54	54.35	53	56.4	79	58.45	61	60.5	54	62.55	59	64.6	68
44.15	98	46.2	57	48.25	53	50.3	65	52.35	59	54.4	63	56.45	66	58.5	56	60.55	47	62.6	61	64.65	77
44.2	72	46.25	64	48.3	64	50.35	42	52.4	62	54.45	53	56.5	87	58.55	63	60.6	54	62.65	48	64.7	71
44.25	63	46.3	55	48.35	80	50.4	67	52.45	56	54.5	51	56.55	78	58.6	50	60.65	53	62.7	49	64.75	80
44.3	91	46.35	80	48.4	86	50.45	85	52.5	67	54.55	46	56.6	73	58.65	48	60.7	40	62.75	43	64.8	75
44.35	80	46.4	82	48.45	79	50.5	67	52.55	60	54.6	52	56.65	64	58.7	70	60.75	45	62.8	59	64.85	77
44.4	82	46.45	66	48.5	66	50.55	82	52.6	51	54.65	52	56.7	81	58.75	54	60.8	55	62.85	68	64.9	64
44.45	71	46.5	80	48.55	70	50.6	96	52.65	47	54.7	61	56.75	75	58.8	51	60.85	50	62.9	58	64.95	79
44.5	68	46.55	84	48.6	67	50.65	82	52.7	52	54.75	45	56.8	75	58.85	62	60.9	59	62.95	44	65	67
44.55	66	46.6	74	48.65	52	50.7	99	52.75	60	54.8	44	56.85	58	58.9	66	60.95	51	63	64	65.05	62

Angle	R.Int	Angle	R.Int	Angle	R.Int	Angle	R.Int	Angle	R.Int	Angle	R.Int	Angle	R.Int
65.1	58	67.3	79	69.5	50	71.7	49	73.9	64	76.1	58	78.3	53
65.15	55	67.35	51	69.55	62	71.75	58	73.95	55	76.15	58	78.35	46
65.2	67	67.4	56	69.6	61	71.8	61	74	53	76.2	46	78.4	42
65.25	62	67.45	65	69.65	56	71.85	51	74.05	73	76.25	61	78.45	52
65.3	67	67.5	61	69.7	52	71.9	66	74.1	67	76.3	48	78.5	41
65.35	60	67.55	78	69.75	52	71.95	76	74.15	66	76.35	54	78.55	63
65.4	55	67.6	52	69.8	55	72	56	74.2	56	76.4	61	78.6	61
65.45	67	67.65	61	69.85	75	72.05	56	74.25	68	76.45	50	78.65	44
65.5	54	67.7	58	69.9	55	72.1	65	74.3	57	76.5	43	78.7	43
65.55	52	67.75	67	69.95	60	72.15	53	74.35	51	76.55	60	78.75	51
65.6	46	67.8	73	70	54	72.2	77	74.4	55	76.6	59	78.8	55
65.65	46	67.85	69	70.05	61	72.25	53	74.45	57	76.65	34	78.85	58
65.7	66	67.9	65	70.1	65	72.3	71	74.5	58	76.7	59	78.9	49
65.75	49	67.95	58	70.15	50	72.35	53	74.55	61	76.75	48	78.95	59
65.8	61	68	63	70.2	60	72.4	59	74.6	44	76.8	64	79	58
65.85	65	68.05	71	70.25	55	72.45	58	74.65	57	76.85	58	79.05	52
65.9	73	68.1	56	70.3	52	72.5	61	74.7	51	76.9	47	79.1	55
65.95	61	68.15	63	70.35	62	72.55	55	74.75	56	76.95	55	79.15	62
66	54	68.2	60	70.4	54	72.6	55	74.8	64	77	49	79.2	59
66.05	55	68.25	56	70.45	48	72.65	65	74.85	59	77.05	57	79.25	46
66.1	58	68.3	60	70.5	50	72.7	54	74.9	57	77.1	50	79.3	57
66.15	61	68.35	64	70.55	48	72.75	47	74.95	62	77.15	50	79.35	65
66.2	62	68.4	65	70.6	65	72.8	50	75	46	77.2	64	79.4	64
66.25	54	68.45	48	70.65	64	72.85	58	75.05	61	77.25	40	79.45	55
66.3	64	68.5	61	70.7	56	72.9	48	75.1	61	77.3	53	79.5	52
66.35	59	68.55	53	70.75	45	72.95	62	75.15	53	77.35	55	79.55	44
66.4	50	68.6	51	70.8	42	73	59	75.2	57	77.4	49	79.6	35
66.45	52	68.65	55	70.85	54	73.05	58	75.25	67	77.45	49	79.65	58
66.5	51	68.7	50	70.9	37	73.1	72	75.3	69	77.5	47	79.7	52
66.55	51	68.75	60	70.95	66	73.15	76	75.35	58	77.55	77	79.75	39
66.6	62	68.8	66	71	49	73.2	51	75.4	38	77.6	48	79.8	48
66.65	47	68.85	72	71.05	58	73.25	46	75.45	55	77.65	51	79.85	55
66.7	74	68.9	48	71.1	64	73.3	64	75.5	57	77.7	66	79.9	43
66.75	50	68.95	66	71.15	56	73.35	51	75.55	64	77.75	49	79.95	59
66.8	56	69	58	71.2	49	73.4	56	75.6	65	77.8	45	80	63
66.85	61	69.05	65	71.25	48	73.45	52	75.65	53	77.85	44		
66.9	61	69.1	55	71.3	45	73.5	73	75.7	50	77.9	60		
66.95	48	69.15	59	71.35	58	73.55	63	75.75	64	77.95	55		
67	57	69.2	58	71.4	55	73.6	69	75.8	54	78	54		
67.05	61	69.25	62	71.45	45	73.65	68	75.85	73	78.05	54		
67.1	58	69.3	71	71.5	63	73.7	49	75.9	56	78.1	59		
67.15	60	69.35	67	71.55	54	73.75	47	75.95	42	78.15	46		
67.2	46	69.4	55	71.6	54	73.8	59	76	52	78.2	46		
67.25	68	69.45	50	71.65	46	73.85	83	76.05	63	78.25	35		

Falcone (dacite) lava dome

Angle	R.Int	Angle	R.Int	Angle	R.Int	Angle	R.Int	Angle	R.Int	Angle	R.Int	Angle	R.Int	Angle	R.Int	Angle	R.Int	Angle	R.Int
20	206	22.05	194	24.1	157	26.15	165	28.2	149	30.25	145	32.3	133	34.35	109	36.4	104	38.45	73	40.5	74
20.05	219	22.1	207	24.15	156	26.2	171	28.25	158	30.3	146	32.35	122	34.4	105	36.45	99	38.5	74	40.55	66
20.1	202	22.15	199	24.2	160	26.25	170	28.3	156	30.35	139	32.4	116	34.45	119	36.5	103	38.55	77	40.6	87
20.15	223	22.2	201	24.25	162	26.3	146	28.35	149	30.4	185	32.45	128	34.5	119	36.55	90	38.6	102	40.65	77
20.2	197	22.25	198	24.3	158	26.35	155	28.4	129	30.45	172	32.5	119	34.55	126	36.6	85	38.65	100	40.7	72
20.25	217	22.3	201	24.35	172	26.4	167	28.45	160	30.5	175	32.55	118	34.6	116	36.65	112	38.7	106	40.75	84
20.3	179	22.35	180	24.4	171	26.45	178	28.5	142	30.55	144	32.6	123	34.65	136	36.7	81	38.75	107	40.8	90
20.35	203	22.4	199	24.45	143	26.5	169	28.55	155	30.6	161	32.65	117	34.7	165	36.75	90	38.8	84	40.85	97
20.4	195	22.45	167	24.5	143	26.55	154	28.6	145	30.65	181	32.7	109	34.75	107	36.8	110	38.85	100	40.9	70
20.45	197	22.5	158	24.55	137	26.6	181	28.65	144	30.7	164	32.75	106	34.8	118	36.85	112	38.9	106	40.95	80
20.5	212	22.55	160	24.6	167	26.65	151	28.7	140	30.75	145	32.8	130	34.85	124	36.9	80	38.95	88	41	80
20.55	200	22.6	164	24.65	143	26.7	173	28.75	143	30.8	176	32.85	105	34.9	117	36.95	103	39	65	41.05	93
20.6	212	22.65	187	24.7	158	26.75	168	28.8	158	30.85	154	32.9	126	34.95	131	37	102	39.05	96	41.1	69
20.65	214	22.7	164	24.75	141	26.8	209	28.85	146	30.9	170	32.95	123	35	128	37.05	128	39.1	89	41.15	95
20.7	207	22.75	171	24.8	164	26.85	230	28.9	141	30.95	172	33	101	35.05	116	37.1	106	39.15	78	41.2	83
20.75	245	22.8	191	24.85	154	26.9	212	28.95	140	31	145	33.05	93	35.1	139	37.15	92	39.2	95	41.25	81
20.8	199	22.85	189	24.9	147	26.95	208	29	145	31.05	143	33.1	114	35.15	123	37.2	95	39.25	67	41.3	78
20.85	216	22.9	180	24.95	155	27	239	29.05	126	31.1	158	33.15	114	35.2	128	37.25	98	39.3	73	41.35	110
20.9	232	22.95	180	25	172	27.05	217	29.1	134	31.15	159	33.2	108	35.25	134	37.3	75	39.35	79	41.4	108
20.95	197	23	187	25.05	130	27.1	264	29.15	138	31.2	160	33.25	123	35.3	134	37.35	104	39.4	83	41.45	105
21	219	23.05	180	25.1	157	27.15	295	29.2	153	31.25	154	33.3	120	35.35	138	37.4	88	39.45	82	41.5	85
21.05	255	23.1	211	25.15	139	27.2	253	29.25	160	31.3	146	33.35	113	35.4	140	37.45	104	39.5	81	41.55	82
21.1	231	23.15	172	25.2	168	27.25	278	29.3	130	31.35	125	33.4	104	35.45	131	37.5	107	39.55	71	41.6	101
21.15	224	23.2	199	25.25	155	27.3	259	29.35	127	31.4	144	33.45	103	35.5	140	37.55	80	39.6	68	41.65	87
21.2	235	23.25	211	25.3	146	27.35	281	29.4	128	31.45	123	33.5	110	35.55	141	37.6	80	39.65	78	41.7	107
21.25	239	23.3	204	25.35	151	27.4	310	29.45	163	31.5	140	33.55	112	35.6	148	37.65	93	39.7	80	41.75	106
21.3	336	23.35	222	25.4	171	27.45	283	29.5	156	31.55	160	33.6	107	35.65	155	37.7	89	39.75	107	41.8	72
21.35	326	23.4	207	25.45	162	27.5	292	29.55	186	31.6	133	33.65	104	35.7	149	37.75	110	39.8	76	41.85	78
21.4	360	23.45	207	25.5	169	27.55	222	29.6	161	31.65	137	33.7	120	35.75	182	37.8	95	39.85	77	41.9	97
21.45	404	23.5	199	25.55	176	27.6	250	29.65	188	31.7	125	33.75	125	35.8	152	37.85	81	39.9	72	41.95	60
21.5	433	23.55	206	25.6	176	27.65	222	29.7	179	31.75	111	33.8	99	35.85	144	37.9	82	39.95	85	42	82
21.55	436	23.6	162	25.65	182	27.7	211	29.75	183	31.8	125	33.85	119	35.9	125	37.95	93	40	71	42.05	71
21.6	461	23.65	155	25.7	176	27.75	217	29.8	157	31.85	109	33.9	107	35.95	128	38	68	40.05	94	42.1	93
21.65	439	23.7	159	25.75	143	27.8	179	29.85	156	31.9	117	33.95	107	36	106	38.05	84	40.1	82	42.15	89
21.7	404	23.75	164	25.8	168	27.85	209	29.9	159	31.95	128	34	105	36.05	128	38.1	96	40.15	85	42.2	66
21.75	370	23.8	156	25.85	162	27.9	176	29.95	166	32	118	34.05	103	36.1	123	38.15	81	40.2	88	42.25	102
21.8	277	23.85	163	25.9	140	27.95	183	30	161	32.05	119	34.1	115	36.15	100	38.2	80	40.25	79	42.3	99
21.85	267	23.9	174	25.95	143	28	159	30.05	136	32.1	150	34.15	110	36.2	85	38.25	90	40.3	75	42.35	100
21.9	225	23.95	144	26	158	28.05	159	30.1	163	32.15	144	34.2	112	36.25	113	38.3	91	40.35	65	42.4	88
21.95	222	24	182	26.05	136	28.1	151	30.15	168	32.2	139	34.25	121	36.3	95	38.35	103	40.4	66	42.45	89
22	174	24.05	141	26.1	139	28.15	157	30.2	152	32.25	129	34.3	102	36.35	116	38.4	101	40.45	87	42.5	91

Angle	R.Int	Angle	R.Int	Angle	R.Int	Angle	R.Int	Angle	R.Int	Angle	R.Int	Angle	R.Int	Angle	R.Int	Angle	R.Int	Angle	R.Int
42.55	71	44.6	67	46.65	87	48.7	70	50.75	101	52.8	68	54.85	49	56.9	73	58.95	56	61	56	63.05	72
42.6	87	44.65	95	46.7	55	48.75	70	50.8	73	52.85	81	54.9	68	56.95	63	59	65	61.05	55	63.1	66
42.65	64	44.7	52	46.75	84	48.8	86	50.85	97	52.9	64	54.95	75	57	68	59.05	66	61.1	80	63.15	65
42.7	75	44.75	64	46.8	85	48.85	71	50.9	93	52.95	70	55	61	57.05	75	59.1	56	61.15	57	63.2	65
42.75	88	44.8	68	46.85	81	48.9	72	50.95	89	53	85	55.05	68	57.1	71	59.15	78	61.2	66	63.25	60
42.8	69	44.85	75	46.9	89	48.95	65	51	89	53.05	63	55.1	73	57.15	63	59.2	59	61.25	82	63.3	66
42.85	86	44.9	62	46.95	73	49	60	51.05	77	53.1	58	55.15	63	57.2	65	59.25	65	61.3	74	63.35	49
42.9	76	44.95	82	47	71	49.05	71	51.1	83	53.15	84	55.2	65	57.25	69	59.3	67	61.35	87	63.4	59
42.95	74	45	66	47.05	76	49.1	77	51.15	70	53.2	70	55.25	66	57.3	74	59.35	57	61.4	79	63.45	61
43	86	45.05	55	47.1	78	49.15	73	51.2	66	53.25	68	55.3	52	57.35	76	59.4	68	61.45	82	63.5	68
43.05	82	45.1	60	47.15	70	49.2	74	51.25	86	53.3	65	55.35	63	57.4	49	59.45	73	61.5	73	63.55	74
43.1	70	45.15	76	47.2	77	49.25	61	51.3	86	53.35	70	55.4	60	57.45	68	59.5	81	61.55	88	63.6	76
43.15	76	45.2	74	47.25	92	49.3	82	51.35	60	53.4	68	55.45	68	57.5	75	59.55	71	61.6	62	63.65	75
43.2	65	45.25	67	47.3	76	49.35	82	51.4	73	53.45	78	55.5	68	57.55	59	59.6	79	61.65	75	63.7	57
43.25	73	45.3	70	47.35	80	49.4	73	51.45	73	53.5	68	55.55	65	57.6	74	59.65	74	61.7	87	63.75	46
43.3	77	45.35	78	47.4	73	49.45	78	51.5	60	53.55	68	55.6	58	57.65	62	59.7	61	61.75	89	63.8	84
43.35	76	45.4	66	47.45	76	49.5	87	51.55	75	53.6	64	55.65	63	57.7	69	59.75	88	61.8	86	63.85	65
43.4	84	45.45	79	47.5	65	49.55	68	51.6	76	53.65	74	55.7	61	57.75	60	59.8	72	61.85	92	63.9	67
43.45	57	45.5	73	47.55	85	49.6	79	51.65	88	53.7	69	55.75	56	57.8	62	59.85	81	61.9	84	63.95	66
43.5	74	45.55	70	47.6	75	49.65	75	51.7	61	53.75	76	55.8	69	57.85	52	59.9	78	61.95	93	64	58
43.55	75	45.6	58	47.65	65	49.7	61	51.75	86	53.8	78	55.85	87	57.9	65	59.95	85	62	73	64.05	66
43.6	70	45.65	69	47.7	77	49.75	70	51.8	69	53.85	69	55.9	83	57.95	78	60	75	62.05	80	64.1	82
43.65	73	45.7	66	47.75	101	49.8	85	51.85	72	53.9	61	55.95	53	58	61	60.05	70	62.1	75	64.15	54
43.7	70	45.75	62	47.8	64	49.85	70	51.9	50	53.95	73	56	56	58.05	77	60.1	60	62.15	75	64.2	58
43.75	81	45.8	86	47.85	79	49.9	81	51.95	61	54	68	56.05	59	58.1	74	60.15	85	62.2	65	64.25	76
43.8	83	45.85	59	47.9	84	49.95	60	52	75	54.05	66	56.1	67	58.15	74	60.2	56	62.25	77	64.3	60
43.85	78	45.9	80	47.95	80	50	84	52.05	60	54.1	67	56.15	89	58.2	57	60.25	70	62.3	78	64.35	90
43.9	73	45.95	74	48	88	50.05	61	52.1	73	54.15	60	56.2	87	58.25	70	60.3	71	62.35	70	64.4	78
43.95	79	46	79	48.05	76	50.1	70	52.15	66	54.2	55	56.25	77	58.3	81	60.35	72	62.4	66	64.45	80
44	79	46.05	84	48.1	90	50.15	80	52.2	63	54.25	60	56.3	84	58.35	74	60.4	86	62.45	65	64.5	78
44.05	100	46.1	95	48.15	80	50.2	74	52.25	81	54.3	73	56.35	86	58.4	76	60.45	64	62.5	73	64.55	81
44.1	84	46.15	76	48.2	104	50.25	72	52.3	61	54.35	65	56.4	88	58.45	74	60.5	63	62.55	74	64.6	79
44.15	113	46.2	68	48.25	60	50.3	80	52.35	70	54.4	74	56.45	71	58.5	71	60.55	55	62.6	72	64.65	92
44.2	83	46.25	79	48.3	75	50.35	49	52.4	77	54.45	66	56.5	96	58.55	70	60.6	66	62.65	63	64.7	78
44.25	78	46.3	62	48.35	95	50.4	78	52.45	63	54.5	66	56.55	86	58.6	61	60.65	64	62.7	56	64.75	91
44.3	98	46.35	91	48.4	93	50.45	100	52.5	78	54.55	53	56.6	85	58.65	57	60.7	53	62.75	52	64.8	90
44.35	91	46.4	97	48.45	90	50.5	74	52.55	75	54.6	63	56.65	75	58.7	75	60.75	60	62.8	67	64.85	88
44.4	97	46.45	77	48.5	81	50.55	93	52.6	58	54.65	67	56.7	94	58.75	63	60.8	62	62.85	80	64.9	79
44.45	78	46.5	95	48.55	77	50.6	111	52.65	58	54.7	68	56.75	90	58.8	59	60.85	61	62.9	69	64.95	86
44.5	79	46.55	91	48.6	78	50.65	89	52.7	67	54.75	56	56.8	82	58.85	74	60.9	68	62.95	57	65	76
44.55	81	46.6	85	48.65	67	50.7	110	52.75	67	54.8	59	56.85	69	58.9	77	60.95	56	63	79	65.05	70

Angle	R.Int	Angle	R.Int	Angle	R.Int	Angle	R.Int	Angle	R.Int	Angle	R.Int	Angle	R.Int
65.1	70	67.3	87	69.5	59	71.7	56	73.9	79	76.1	67	78.3	62
65.15	66	67.35	63	69.55	70	71.75	67	73.95	62	76.15	66	78.35	51
65.2	80	67.4	67	69.6	73	71.8	69	74	62	76.2	58	78.4	51
65.25	77	67.45	78	69.65	67	71.85	63	74.05	81	76.25	76	78.45	67
65.3	74	67.5	76	69.7	65	71.9	77	74.1	79	76.3	55	78.5	48
65.35	71	67.55	93	69.75	67	71.95	89	74.15	77	76.35	65	78.55	74
65.4	64	67.6	63	69.8	62	72	71	74.2	69	76.4	70	78.6	70
65.45	72	67.65	76	69.85	86	72.05	63	74.25	83	76.45	63	78.65	49
65.5	63	67.7	65	69.9	64	72.1	76	74.3	64	76.5	58	78.7	52
65.55	60	67.75	78	69.95	65	72.15	62	74.35	62	76.55	67	78.75	66
65.6	58	67.8	88	70	63	72.2	82	74.4	64	76.6	70	78.8	62
65.65	57	67.85	76	70.05	69	72.25	62	74.45	62	76.65	43	78.85	69
65.7	79	67.9	76	70.1	77	72.3	79	74.5	67	76.7	64	78.9	58
65.75	64	67.95	73	70.15	61	72.35	65	74.55	69	76.75	57	78.95	64
65.8	68	68	74	70.2	73	72.4	70	74.6	56	76.8	72	79	67
65.85	76	68.05	86	70.25	62	72.45	71	74.65	72	76.85	70	79.05	60
65.9	88	68.1	63	70.3	63	72.5	76	74.7	58	76.9	59	79.1	67
65.95	68	68.15	74	70.35	77	72.55	62	74.75	67	76.95	67	79.15	73
66	65	68.2	75	70.4	65	72.6	66	74.8	73	77	61	79.2	72
66.05	70	68.25	63	70.45	63	72.65	80	74.85	64	77.05	69	79.25	61
66.1	65	68.3	71	70.5	57	72.7	61	74.9	66	77.1	62	79.3	64
66.15	72	68.35	79	70.55	59	72.75	58	74.95	70	77.15	62	79.35	76
66.2	77	68.4	76	70.6	80	72.8	65	75	58	77.2	76	79.4	79
66.25	61	68.45	63	70.65	71	72.85	65	75.05	76	77.25	52	79.45	62
66.3	75	68.5	68	70.7	67	72.9	59	75.1	68	77.3	65	79.5	63
66.35	74	68.55	64	70.75	60	72.95	77	75.15	64	77.35	67	79.55	59
66.4	57	68.6	66	70.8	53	73	66	75.2	66	77.4	60	79.6	42
66.45	63	68.65	62	70.85	69	73.05	69	75.25	72	77.45	64	79.65	69
66.5	66	68.7	61	70.9	44	73.1	83	75.3	78	77.5	54	79.7	67
66.55	58	68.75	75	70.95	77	73.15	91	75.35	66	77.55	88	79.75	46
66.6	73	68.8	73	71	64	73.2	58	75.4	50	77.6	63	79.8	59
66.65	62	68.85	83	71.05	65	73.25	57	75.45	70	77.65	58	79.85	70
66.7	85	68.9	63	71.1	75	73.3	75	75.5	64	77.7	77	79.9	50
66.75	65	68.95	77	71.15	71	73.35	66	75.55	75	77.75	54	79.95	70
66.8	63	69	73	71.2	60	73.4	63	75.6	74	77.8	54	80	78
66.85	72	69.05	72	71.25	63	73.45	63	75.65	58	77.85	59		
66.9	76	69.1	66	71.3	52	73.5	88	75.7	59	77.9	67		
66.95	55	69.15	74	71.35	69	73.55	70	75.75	72	77.95	66		
67	68	69.2	65	71.4	70	73.6	80	75.8	66	78	63		
67.05	76	69.25	73	71.45	52	73.65	83	75.85	88	78.05	59		
67.1	69	69.3	86	71.5	74	73.7	56	75.9	63	78.1	68		
67.15	75	69.35	78	71.55	69	73.75	58	75.95	53	78.15	61		
67.2	53	69.4	70	71.6	65	73.8	74	76	61	78.2	53		
67.25	77	69.45	57	71.65	61	73.85	94	76.05	68	78.25	46		

Falcone (rhyolite) lava dome

Angle	R.Int	Angle	R.Int	Angle	R.Int	Angle	R.Int	Angle	R.Int	Angle	R.Int	Angle	R.Int	Angle	R.Int	Angle	R.Int	Angle	R.Int	Angle	R.Int
20	445	20.82	553	21.64	1017	22.46	439	23.28	507	24.1	351	24.92	299	25.74	326	26.56	346	27.38	1006	28.2	316
20.02	497	20.84	539	21.66	953	22.48	391	23.3	544	24.12	360	24.94	314	25.76	304	26.58	370	27.4	1086	28.22	304
20.04	462	20.86	499	21.68	842	22.5	359	23.32	505	24.14	321	24.96	314	25.78	333	26.6	410	27.42	1098	28.24	315
20.06	460	20.88	558	21.7	762	22.52	398	23.34	529	24.16	301	24.98	309	25.8	321	26.62	432	27.44	1012	28.26	312
20.08	455	20.9	579	21.72	711	22.54	401	23.36	461	24.18	311	25	265	25.82	313	26.64	377	27.46	975	28.28	295
20.1	463	20.92	551	21.74	652	22.56	423	23.38	562	24.2	350	25.02	323	25.84	309	26.66	429	27.48	903	28.3	314
20.12	518	20.94	568	21.76	635	22.58	404	23.4	479	24.22	334	25.04	315	25.86	330	26.68	417	27.5	874	28.32	292
20.14	521	20.96	533	21.78	595	22.6	424	23.42	499	24.24	310	25.06	323	25.88	338	26.7	392	27.52	884	28.34	282
20.16	508	20.98	559	21.8	576	22.62	452	23.44	526	24.26	385	25.08	302	25.9	306	26.72	417	27.54	873	28.36	309
20.18	486	21	596	21.82	573	22.64	376	23.46	495	24.28	286	25.1	305	25.92	299	26.74	401	27.56	896	28.38	308
20.2	462	21.02	596	21.84	519	22.66	426	23.48	493	24.3	350	25.12	305	25.94	323	26.76	388	27.58	748	28.4	305
20.22	487	21.04	586	21.86	535	22.68	367	23.5	517	24.32	324	25.14	354	25.96	314	26.78	382	27.6	791	28.42	290
20.24	522	21.06	659	21.88	499	22.7	419	23.52	500	24.34	343	25.16	275	25.98	300	26.8	416	27.62	734	28.44	276
20.26	484	21.08	631	21.9	522	22.72	385	23.54	474	24.36	335	25.18	328	26	315	26.82	413	27.64	690	28.46	303
20.28	464	21.1	679	21.92	488	22.74	360	23.56	501	24.38	342	25.2	319	26.02	336	26.84	418	27.66	636	28.48	287
20.3	497	21.12	703	21.94	400	22.76	406	23.58	504	24.4	297	25.22	345	26.04	320	26.86	456	27.68	628	28.5	280
20.32	478	21.14	676	21.96	482	22.78	405	23.6	505	24.42	300	25.24	323	26.06	306	26.88	438	27.7	581	28.52	301
20.34	480	21.16	699	21.98	434	22.8	374	23.62	482	24.44	320	25.26	311	26.08	310	26.9	408	27.72	546	28.54	290
20.36	488	21.18	784	22	433	22.82	383	23.64	446	24.46	330	25.28	319	26.1	301	26.92	432	27.74	546	28.56	299
20.38	465	21.2	826	22.02	431	22.84	399	23.66	473	24.48	310	25.3	355	26.12	297	26.94	410	27.76	508	28.58	294
20.4	491	21.22	901	22.04	432	22.86	374	23.68	445	24.5	345	25.32	360	26.14	310	26.96	478	27.78	517	28.6	284
20.42	488	21.24	878	22.06	425	22.88	391	23.7	412	24.52	286	25.34	371	26.16	282	26.98	428	27.8	423	28.62	311
20.44	492	21.26	1039	22.08	425	22.9	401	23.72	430	24.54	309	25.36	363	26.18	307	27	500	27.82	444	28.64	276
20.46	515	21.28	1118	22.1	398	22.92	359	23.74	362	24.56	313	25.38	339	26.2	294	27.02	552	27.84	424	28.66	284
20.48	474	21.3	1193	22.12	458	22.94	416	23.76	376	24.58	300	25.4	334	26.22	290	27.04	593	27.86	435	28.68	276
20.5	506	21.32	1267	22.14	417	22.96	387	23.78	364	24.6	343	25.42	350	26.24	301	27.06	556	27.88	423	28.7	280
20.52	471	21.34	1410	22.16	446	22.98	417	23.8	389	24.62	317	25.44	379	26.26	332	27.08	564	27.9	400	28.72	292
20.54	493	21.36	1435	22.18	367	23	399	23.82	386	24.64	325	25.46	360	26.28	338	27.1	626	27.92	439	28.74	276
20.56	447	21.38	1481	22.2	421	23.02	394	23.84	345	24.66	329	25.48	371	26.3	296	27.12	638	27.94	393	28.76	264
20.58	487	21.4	1444	22.22	385	23.04	383	23.86	332	24.68	291	25.5	387	26.32	333	27.14	716	27.96	383	28.78	288
20.6	475	21.42	1455	22.24	404	23.06	439	23.88	372	24.7	285	25.52	348	26.34	304	27.16	743	27.98	402	28.8	287
20.62	498	21.44	1373	22.26	402	23.08	415	23.9	340	24.72	282	25.54	365	26.36	311	27.18	746	28	394	28.82	274
20.64	523	21.46	1323	22.28	429	23.1	425	23.92	314	24.74	298	25.56	352	26.38	311	27.2	856	28.02	365	28.84	281
20.66	478	21.48	1386	22.3	419	23.12	476	23.94	347	24.76	290	25.58	354	26.4	318	27.22	911	28.04	398	28.86	291
20.68	484	21.5	1300	22.32	413	23.14	443	23.96	339	24.78	259	25.6	328	26.42	299	27.24	962	28.06	362	28.88	293
20.7	470	21.52	1256	22.34	396	23.16	490	23.98	335	24.8	302	25.62	293	26.44	313	27.26	1030	28.08	381	28.9	290
20.72	515	21.54	1279	22.36	398	23.18	475	24	338	24.82	329	25.64	294	26.46	327	27.28	1025	28.1	378	28.92	283
20.74	520	21.56	1215	22.38	416	23.2	513	24.02	326	24.84	337	25.66	330	26.48	314	27.3	1035	28.12	347	28.94	278
20.76	511	21.58	1213	22.4	415	23.22	553	24.04	344	24.86	309	25.68	330	26.5	347	27.32	1137	28.14	331	28.96	281
20.78	503	21.6	1088	22.42	413	23.24	545	24.06	353	24.88	332	25.7	312	26.52	345	27.34	1193	28.16	308	28.98	309
20.8	524	21.62	1094	22.44	405	23.26	571	24.08	332	24.9	284	25.72	325	26.54	377	27.36	1231	28.18	334	29	282

Angle	R.Int	Angle	R.Int	Angle	R.Int	Angle	R.Int	Angle	R.Int	Angle	R.Int	Angle	R.Int	Angle	R.Int	Angle	R.Int	Angle	R.Int
29.02	293	29.84	316	30.66	374	31.48	266	32.3	241	33.12	201	33.94	219	34.76	269	35.58	412	36.4	190	37.22	217
29.04	288	29.86	302	30.68	345	31.5	276	32.32	247	33.14	242	33.96	208	34.78	275	35.6	382	36.42	226	37.24	240
29.06	289	29.88	309	30.7	333	31.52	263	32.34	240	33.16	205	33.98	212	34.8	249	35.62	391	36.44	215	37.26	211
29.08	341	29.9	353	30.72	338	31.54	261	32.36	227	33.18	221	34	221	34.82	265	35.64	360	36.46	215	37.28	193
29.1	347	29.92	330	30.74	336	31.56	280	32.38	225	33.2	202	34.02	223	34.84	240	35.66	370	36.48	207	37.3	190
29.12	285	29.94	316	30.76	326	31.58	268	32.4	233	33.22	206	34.04	233	34.86	254	35.68	351	36.5	181	37.32	189
29.14	298	29.96	334	30.78	343	31.6	258	32.42	228	33.24	232	34.06	224	34.88	248	35.7	349	36.52	238	37.34	209
29.16	275	29.98	351	30.8	333	31.62	242	32.44	211	33.26	230	34.08	225	34.9	254	35.72	373	36.54	188	37.36	199
29.18	303	30	332	30.82	326	31.64	254	32.46	218	33.28	187	34.1	189	34.92	269	35.74	316	36.56	178	37.38	223
29.2	318	30.02	325	30.84	303	31.66	245	32.48	221	33.3	222	34.12	180	34.94	248	35.76	290	36.58	208	37.4	200
29.22	294	30.04	325	30.86	323	31.68	278	32.5	205	33.32	190	34.14	229	34.96	302	35.78	347	36.6	200	37.42	209
29.24	303	30.06	334	30.88	326	31.7	273	32.52	239	33.34	209	34.16	217	34.98	289	35.8	308	36.62	202	37.44	170
29.26	316	30.08	362	30.9	324	31.72	251	32.54	237	33.36	206	34.18	209	35	327	35.82	303	36.64	210	37.46	195
29.28	290	30.1	324	30.92	323	31.74	264	32.56	232	33.38	219	34.2	218	35.02	284	35.84	289	36.66	199	37.48	169
29.3	291	30.12	381	30.94	385	31.76	243	32.58	244	33.4	213	34.22	240	35.04	332	35.86	223	36.68	208	37.5	184
29.32	355	30.14	383	30.96	338	31.78	230	32.6	207	33.42	218	34.24	247	35.06	353	35.88	276	36.7	194	37.52	193
29.34	322	30.16	349	30.98	333	31.8	219	32.62	252	33.44	193	34.26	225	35.08	332	35.9	273	36.72	233	37.54	180
29.36	325	30.18	342	31	330	31.82	248	32.64	221	33.46	195	34.28	219	35.1	335	35.92	256	36.74	199	37.56	187
29.38	356	30.2	335	31.02	307	31.84	265	32.66	219	33.48	220	34.3	204	35.12	353	35.94	237	36.76	185	37.58	185
29.4	356	30.22	359	31.04	267	31.86	272	32.68	198	33.5	189	34.32	266	35.14	334	35.96	236	36.78	229	37.6	188
29.42	335	30.24	352	31.06	310	31.88	249	32.7	230	33.52	185	34.34	214	35.16	340	35.98	229	36.8	237	37.62	196
29.44	349	30.26	399	31.08	354	31.9	259	32.72	253	33.54	214	34.36	253	35.18	348	36	243	36.82	213	37.64	178
29.46	335	30.28	359	31.1	305	31.92	239	32.74	236	33.56	201	34.38	201	35.2	353	36.02	206	36.84	200	37.66	190
29.48	333	30.3	374	31.12	335	31.94	289	32.76	255	33.58	180	34.4	251	35.22	343	36.04	211	36.86	197	37.68	146
29.5	360	30.32	352	31.14	274	31.96	270	32.78	216	33.6	226	34.42	232	35.24	362	36.06	202	36.88	204	37.7	156
29.52	383	30.34	389	31.16	299	31.98	233	32.8	208	33.62	202	34.44	230	35.26	375	36.08	220	36.9	207	37.72	195
29.54	388	30.36	398	31.18	280	32	234	32.82	247	33.64	199	34.46	290	35.28	351	36.1	209	36.92	227	37.74	172
29.56	368	30.38	354	31.2	284	32.02	260	32.84	232	33.66	185	34.48	259	35.3	376	36.12	224	36.94	207	37.76	191
29.58	335	30.4	391	31.22	253	32.04	252	32.86	220	33.68	209	34.5	234	35.32	376	36.14	205	36.96	243	37.78	175
29.6	336	30.42	367	31.24	288	32.06	261	32.88	238	33.7	185	34.52	241	35.34	361	36.16	208	36.98	224	37.8	176
29.62	352	30.44	374	31.26	244	32.08	298	32.9	246	33.72	205	34.54	264	35.36	403	36.18	202	37	237	37.82	168
29.64	339	30.46	362	31.28	264	32.1	261	32.92	219	33.74	202	34.56	263	35.38	405	36.2	201	37.02	209	37.84	160
29.66	335	30.48	368	31.3	273	32.12	269	32.94	241	33.76	211	34.58	262	35.4	423	36.22	201	37.04	200	37.86	148
29.68	308	30.5	394	31.32	288	32.14	228	32.96	208	33.78	195	34.6	262	35.42	422	36.24	229	37.06	215	37.88	178
29.7	335	30.52	382	31.34	269	32.16	262	32.98	210	33.8	216	34.62	234	35.44	392	36.26	226	37.08	212	37.9	179
29.72	334	30.54	347	31.36	310	32.18	261	33	219	33.82	206	34.64	249	35.46	397	36.28	204	37.1	201	37.92	160
29.74	315	30.56	313	31.38	255	32.2	241	33.02	224	33.84	211	34.66	244	35.48	405	36.3	197	37.12	224	37.94	160
29.76	326	30.58	370	31.4	277	32.22	230	33.04	234	33.86	194	34.68	254	35.5	459	36.32	198	37.14	181	37.96	154
29.78	323	30.6	345	31.42	274	32.24	263	33.06	217	33.88	199	34.7	250	35.52	357	36.34	201	37.16	200	37.98	204
29.8	330	30.62	332	31.44	267	32.26	221	33.08	231	33.9	215	34.72	270	35.54	411	36.36	219	37.18	204	38	157
29.82	310	30.64	336	31.46	274	32.28	228	33.1	229	33.92	188	34.74	253	35.56	385	36.38	197	37.2	201	38.02	173

Angle	R.Int	Angle	R.Int	Angle	R.Int	Angle	R.Int	Angle	R.Int	Angle	R.Int	Angle	R.Int	Angle	R.Int	Angle	R.Int	Angle	R.Int
38.04	176	38.92	167	39.8	134	40.68	169	41.56	224	42.44	209	43.32	153	44.2	169	45.08	153	45.96	152	46.84	186
38.06	161	38.94	181	39.82	155	40.7	179	41.58	232	42.46	221	43.34	139	44.22	166	45.1	157	45.98	171	46.86	134
38.08	159	38.96	187	39.84	143	40.72	139	41.6	245	42.48	166	43.36	129	44.24	147	45.12	168	46	147	46.88	176
38.1	149	38.98	171	39.86	148	40.74	158	41.62	209	42.5	172	43.38	138	44.26	169	45.14	176	46.02	166	46.9	190
38.12	160	39	178	39.88	154	40.76	156	41.64	217	42.52	192	43.4	162	44.28	145	45.16	157	46.04	144	46.92	187
38.14	184	39.02	177	39.9	153	40.78	156	41.66	231	42.54	169	43.42	163	44.3	156	45.18	153	46.06	152	46.94	186
38.16	163	39.04	155	39.92	143	40.8	168	41.68	210	42.56	200	43.44	139	44.32	155	45.2	156	46.08	154	46.96	154
38.18	144	39.06	191	39.94	167	40.82	140	41.7	223	42.58	183	43.46	165	44.34	181	45.22	119	46.1	161	46.98	161
38.2	173	39.08	148	39.96	155	40.84	164	41.72	217	42.6	169	43.48	162	44.36	156	45.24	152	46.12	160	47	156
38.22	153	39.1	176	39.98	167	40.86	154	41.74	193	42.62	196	43.5	183	44.38	196	45.26	165	46.14	151	47.02	186
38.24	150	39.12	171	40	151	40.88	160	41.76	189	42.64	147	43.52	156	44.4	169	45.28	132	46.16	164	47.04	161
38.26	157	39.14	173	40.02	163	40.9	170	41.78	196	42.66	201	43.54	149	44.42	172	45.3	144	46.18	160	47.06	181
38.28	184	39.16	174	40.04	164	40.92	160	41.8	205	42.68	171	43.56	144	44.44	160	45.32	163	46.2	186	47.08	159
38.3	161	39.18	155	40.06	149	40.94	153	41.82	207	42.7	172	43.58	171	44.46	145	45.34	151	46.22	167	47.1	144
38.32	166	39.2	165	40.08	150	40.96	159	41.84	187	42.72	188	43.6	161	44.48	154	45.36	128	46.24	152	47.12	155
38.34	185	39.22	162	40.1	170	40.98	170	41.86	169	42.74	170	43.62	158	44.5	164	45.38	155	46.26	195	47.14	145
38.36	157	39.24	126	40.12	159	41	164	41.88	205	42.76	153	43.64	160	44.52	168	45.4	162	46.28	183	47.16	163
38.38	173	39.26	157	40.14	171	41.02	148	41.9	204	42.78	170	43.66	159	44.54	158	45.42	148	46.3	197	47.18	142
38.4	168	39.28	165	40.16	180	41.04	172	41.92	191	42.8	149	43.68	166	44.56	156	45.44	142	46.32	163	47.2	152
38.42	137	39.3	129	40.18	157	41.06	165	41.94	176	42.82	153	43.7	164	44.58	150	45.46	170	46.34	176	47.22	174
38.44	169	39.32	157	40.2	153	41.08	174	41.96	150	42.84	176	43.72	169	44.6	159	45.48	159	46.36	177	47.24	150
38.46	177	39.34	177	40.22	168	41.1	146	41.98	190	42.86	157	43.74	166	44.62	163	45.5	154	46.38	162	47.26	170
38.48	169	39.36	159	40.24	149	41.12	143	42	195	42.88	124	43.76	143	44.64	170	45.52	134	46.4	179	47.28	143
38.5	178	39.38	144	40.26	147	41.14	186	42.02	183	42.9	178	43.78	188	44.66	161	45.54	157	46.42	164	47.3	151
38.52	185	39.4	137	40.28	144	41.16	153	42.04	196	42.92	177	43.8	172	44.68	142	45.56	137	46.44	176	47.32	165
38.54	179	39.42	173	40.3	146	41.18	206	42.06	198	42.94	173	43.82	174	44.7	155	45.58	189	46.46	187	47.34	124
38.56	201	39.44	159	40.32	173	41.2	167	42.08	189	42.96	177	43.84	173	44.72	152	45.6	138	46.48	190	47.36	163
38.58	158	39.46	171	40.34	159	41.22	231	42.1	201	42.98	159	43.86	149	44.74	159	45.62	152	46.5	193	47.38	166
38.6	203	39.48	162	40.36	162	41.24	190	42.12	197	43	162	43.88	167	44.76	135	45.64	119	46.52	197	47.4	139
38.62	175	39.5	143	40.38	137	41.26	223	42.14	206	43.02	151	43.9	186	44.78	153	45.66	159	46.54	199	47.42	167
38.64	183	39.52	154	40.4	139	41.28	205	42.16	208	43.04	151	43.92	155	44.8	176	45.68	166	46.56	157	47.44	150
38.66	162	39.54	173	40.42	175	41.3	191	42.18	194	43.06	164	43.94	183	44.82	179	45.7	143	46.58	191	47.46	153
38.68	173	39.56	170	40.44	160	41.32	201	42.2	202	43.08	144	43.96	194	44.84	156	45.72	158	46.6	179	47.48	138
38.7	177	39.58	137	40.46	167	41.34	209	42.22	212	43.1	160	43.98	169	44.86	132	45.74	133	46.62	202	47.5	140
38.72	194	39.6	188	40.48	131	41.36	203	42.24	190	43.12	143	44	198	44.88	149	45.76	148	46.64	176	47.52	148
38.74	165	39.62	158	40.5	147	41.38	195	42.26	200	43.14	167	44.02	166	44.9	159	45.78	154	46.66	167	47.54	148
38.76	190	39.64	173	40.52	148	41.4	212	42.28	178	43.16	162	44.04	197	44.92	153	45.8	124	46.68	171	47.56	159
38.78	182	39.66	134	40.54	137	41.42	203	42.3	188	43.18	146	44.06	183	44.94	147	45.82	129	46.7	195	47.58	149
38.8	177	39.68	162	40.56	148	41.44	209	42.32	193	43.2	168	44.08	167	44.96	159	45.84	142	46.72	174	47.6	155
38.82	162	39.7	163	40.58	153	41.46	198	42.34	221	43.22	169	44.1	178	44.98	160	45.86	156	46.74	171	47.62	143
38.84	213	39.72	155	40.6	185	41.48	198	42.36	193	43.24	158	44.12	192	45	179	45.88	157	46.76	179	47.64	164
38.86	200	39.74	186	40.62	159	41.5	212	42.38	201	43.26	153	44.14	217	45.02	157	45.9	162	46.78	174	47.66	140
38.88	170	39.76	143	40.64	164	41.52	251	42.4	159	43.28	165	44.16	191	45.04	183	45.92	148	46.8	169	47.68	158
38.9	201	39.78	168	40.66	187	41.54	232	42.42	199	43.3	177	44.18	171	45.06	153	45.94	144	46.82	162	47.7	170

Angle	R.Int	Angle	R.Int	Angle	R.Int	Angle	R.Int	Angle	R.Int	Angle	R.Int	Angle	R.Int	Angle	R.Int	Angle	R.Int	Angle	R.Int	Angle	R.Int
47.72	138	48.56	155	49.4	198	50.24	173	51.08	201	51.92	157	52.76	151	53.6	131	54.44	111	55.28	140	56.12	169
47.74	166	48.58	168	49.42	207	50.26	201	51.1	212	51.94	134	52.78	172	53.62	134	54.46	162	55.3	129	56.14	188
47.76	166	48.6	147	49.44	206	50.28	168	51.12	195	51.96	144	52.8	133	53.64	138	54.48	143	55.32	140	56.16	180
47.78	157	48.62	168	49.46	185	50.3	176	51.14	164	51.98	148	52.82	162	53.66	156	54.5	140	55.34	156	56.18	199
47.8	166	48.64	160	49.48	182	50.32	181	51.16	179	52	142	52.84	149	53.68	142	54.52	141	55.36	139	56.2	201
47.82	175	48.66	142	49.5	173	50.34	150	51.18	174	52.02	138	52.86	181	53.7	149	54.54	142	55.38	121	56.22	167
47.84	163	48.68	211	49.52	171	50.36	153	51.2	169	52.04	135	52.88	156	53.72	130	54.56	138	55.4	133	56.24	164
47.86	177	48.7	150	49.54	175	50.38	194	51.22	189	52.06	132	52.9	149	53.74	157	54.58	144	55.42	131	56.26	163
47.88	154	48.72	163	49.56	193	50.4	183	51.24	178	52.08	165	52.92	150	53.76	143	54.6	134	55.44	141	56.28	187
47.9	167	48.74	184	49.58	184	50.42	175	51.26	166	52.1	147	52.94	159	53.78	141	54.62	140	55.46	148	56.3	204
47.92	143	48.76	175	49.6	174	50.44	185	51.28	158	52.12	152	52.96	187	53.8	146	54.64	131	55.48	127	56.32	181
47.94	185	48.78	176	49.62	166	50.46	162	51.3	153	52.14	149	52.98	167	53.82	169	54.66	142	55.5	142	56.34	180
47.96	191	48.8	161	49.64	166	50.48	179	51.32	170	52.16	137	53	163	53.84	144	54.68	151	55.52	149	56.36	159
47.98	179	48.82	156	49.66	164	50.5	201	51.34	147	52.18	166	53.02	139	53.86	130	54.7	132	55.54	144	56.38	171
48	175	48.84	182	49.68	179	50.52	186	51.36	159	52.2	148	53.04	161	53.88	124	54.72	137	55.56	137	56.4	208
48.02	149	48.86	187	49.7	167	50.54	184	51.38	155	52.22	146	53.06	160	53.9	154	54.74	120	55.58	148	56.42	185
48.04	164	48.88	171	49.72	173	50.56	197	51.4	145	52.24	147	53.08	148	53.92	133	54.76	135	55.6	136	56.44	197
48.06	178	48.9	175	49.74	171	50.58	174	51.42	154	52.26	145	53.1	174	53.94	148	54.78	138	55.62	142	56.46	174
48.08	156	48.92	179	49.76	146	50.6	173	51.44	171	52.28	130	53.12	152	53.96	140	54.8	122	55.64	145	56.48	181
48.1	187	48.94	185	49.78	174	50.62	193	51.46	158	52.3	132	53.14	156	53.98	158	54.82	138	55.66	150	56.5	174
48.12	151	48.96	176	49.8	185	50.64	206	51.48	129	52.32	171	53.16	148	54	124	54.84	150	55.68	135	56.52	192
48.14	202	48.98	166	49.82	161	50.66	203	51.5	141	52.34	128	53.18	155	54.02	124	54.86	144	55.7	131	56.54	184
48.16	170	49	162	49.84	165	50.68	211	51.52	172	52.36	141	53.2	146	54.04	144	54.88	128	55.72	159	56.56	160
48.18	167	49.02	170	49.86	160	50.7	202	51.54	159	52.38	148	53.22	153	54.06	131	54.9	149	55.74	143	56.58	183
48.2	180	49.04	168	49.88	146	50.72	209	51.56	165	52.4	140	53.24	153	54.08	132	54.92	135	55.76	145	56.6	178
48.22	199	49.06	167	49.9	183	50.74	192	51.58	144	52.42	132	53.26	166	54.1	140	54.94	114	55.78	159	56.62	182
48.24	152	49.08	161	49.92	187	50.76	196	51.6	141	52.44	135	53.28	156	54.12	119	54.96	120	55.8	159	56.64	161
48.26	172	49.1	187	49.94	142	50.78	194	51.62	122	52.46	143	53.3	150	54.14	125	54.98	124	55.82	139	56.66	156
48.28	146	49.12	203	49.96	147	50.8	220	51.64	163	52.48	170	53.32	167	54.16	126	55	139	55.84	159	56.68	193
48.3	172	49.14	186	49.98	170	50.82	252	51.66	162	52.5	161	53.34	153	54.18	150	55.02	138	55.86	164	56.7	176
48.32	171	49.16	166	50	139	50.84	219	51.68	145	52.52	135	53.36	159	54.2	108	55.04	138	55.88	165	56.72	169
48.34	171	49.18	178	50.02	159	50.86	223	51.7	139	52.54	153	53.38	166	54.22	142	55.06	136	55.9	180	56.74	176
48.36	145	49.2	168	50.04	168	50.88	224	51.72	136	52.56	146	53.4	174	54.24	119	55.08	138	55.92	182	56.76	206
48.38	163	49.22	182	50.06	159	50.9	227	51.74	134	52.58	133	53.42	167	54.26	119	55.1	131	55.94	169	56.78	161
48.4	184	49.24	203	50.08	153	50.92	253	51.76	157	52.6	152	53.44	168	54.28	152	55.12	147	55.96	157	56.8	133
48.42	186	49.26	192	50.1	192	50.94	218	51.78	138	52.62	158	53.46	164	54.3	146	55.14	125	55.98	156	56.82	190
48.44	143	49.28	170	50.12	149	50.96	215	51.8	147	52.64	136	53.48	151	54.32	132	55.16	135	56	194	56.84	143
48.46	140	49.3	195	50.14	192	50.98	212	51.82	133	52.66	159	53.5	164	54.34	142	55.18	132	56.02	169	56.86	178
48.48	165	49.32	151	50.16	182	51	214	51.84	168	52.68	152	53.52	154	54.36	132	55.2	121	56.04	157	56.88	150
48.5	177	49.34	176	50.18	165	51.02	188	51.86	149	52.7	138	53.54	143	54.38	120	55.22	134	56.06	181	56.9	168
48.52	162	49.36	183	50.2	171	51.04	214	51.88	153	52.72	129	53.56	134	54.4	125	55.24	142	56.08	175	56.92	179
48.54	179	49.38	193	50.22	181	51.06	192	51.9	157	52.74	141	53.58	144	54.42	129	55.26	135	56.1	182	56.94	151

Angle	R.Int	Angle	R.Int	Angle	R.Int	Angle	R.Int	Angle	R.Int	Angle	R.Int	Angle	R.Int	Angle	R.Int	Angle	R.Int	Angle	R.Int	Angle	R.Int
56.96	151	57.8	146	58.64	118	59.48	124	60.32	140	61.16	134	62	174	62.84	146	63.68	151	64.52	173	65.36	129
56.98	186	57.82	137	58.66	138	59.5	138	60.34	128	61.18	163	62.02	164	62.86	180	63.7	156	64.54	169	65.38	155
57	159	57.84	129	58.68	157	59.52	146	60.36	139	61.2	121	62.04	190	62.88	141	63.72	165	64.56	170	65.4	138
57.02	155	57.86	145	58.7	139	59.54	136	60.38	117	61.22	149	62.06	192	62.9	149	63.74	161	64.58	176	65.42	140
57.04	128	57.88	130	58.72	136	59.56	157	60.4	152	61.24	144	62.08	202	62.92	154	63.76	154	64.6	163	65.44	135
57.06	166	57.9	126	58.74	141	59.58	149	60.42	140	61.26	133	62.1	160	62.94	147	63.78	156	64.62	170	65.46	130
57.08	139	57.92	158	58.76	164	59.6	147	60.44	129	61.28	148	62.12	175	62.96	157	63.8	127	64.64	162	65.48	120
57.1	169	57.94	132	58.78	159	59.62	132	60.46	139	61.3	136	62.14	171	62.98	172	63.82	166	64.66	175	65.5	130
57.12	141	57.96	167	58.8	156	59.64	144	60.48	131	61.32	142	62.16	189	63	145	63.84	167	64.68	175	65.52	147
57.14	142	57.98	112	58.82	141	59.66	117	60.5	137	61.34	162	62.18	183	63.02	147	63.86	155	64.7	160	65.54	137
57.16	151	58	137	58.84	124	59.68	161	60.52	167	61.36	136	62.2	189	63.04	149	63.88	166	64.72	168	65.56	152
57.18	140	58.02	144	58.86	133	59.7	160	60.54	136	61.38	154	62.22	161	63.06	160	63.9	146	64.74	166	65.58	149
57.2	153	58.04	137	58.88	143	59.72	134	60.56	143	61.4	153	62.24	162	63.08	140	63.92	143	64.76	180	65.6	147
57.22	128	58.06	157	58.9	129	59.74	159	60.58	137	61.42	151	62.26	171	63.1	137	63.94	140	64.78	186	65.62	139
57.24	140	58.08	150	58.92	151	59.76	129	60.6	133	61.44	143	62.28	179	63.12	147	63.96	154	64.8	162	65.64	137
57.26	134	58.1	146	58.94	151	59.78	141	60.62	108	61.46	161	62.3	190	63.14	149	63.98	146	64.82	148	65.66	150
57.28	133	58.12	160	58.96	136	59.8	143	60.64	111	61.48	177	62.32	175	63.16	153	64	145	64.84	159	65.68	161
57.3	126	58.14	127	58.98	138	59.82	132	60.66	137	61.5	148	62.34	196	63.18	129	64.02	157	64.86	188	65.7	150
57.32	165	58.16	143	59	152	59.84	142	60.68	145	61.52	165	62.36	177	63.2	133	64.04	173	64.88	138	65.72	142
57.34	119	58.18	121	59.02	130	59.86	162	60.7	131	61.54	148	62.38	148	63.22	143	64.06	157	64.9	175	65.74	166
57.36	119	58.2	140	59.04	134	59.88	120	60.72	131	61.56	168	62.4	180	63.24	158	64.08	135	64.92	141	65.76	169
57.38	134	58.22	156	59.06	128	59.9	136	60.74	138	61.58	160	62.42	152	63.26	175	64.1	156	64.94	164	65.78	152
57.4	143	58.24	149	59.08	139	59.92	156	60.76	120	61.6	160	62.44	180	63.28	160	64.12	173	64.96	153	65.8	163
57.42	144	58.26	137	59.1	126	59.94	165	60.78	148	61.62	189	62.46	162	63.3	164	64.14	169	64.98	161	65.82	151
57.44	115	58.28	116	59.12	127	59.96	142	60.8	135	61.64	158	62.48	162	63.32	174	64.16	163	65	150	65.84	151
57.46	152	58.3	125	59.14	133	59.98	145	60.82	151	61.66	180	62.5	162	63.34	160	64.18	155	65.02	165	65.86	154
57.48	130	58.32	150	59.16	129	60	137	60.84	151	61.68	188	62.52	174	63.36	177	64.2	165	65.04	153	65.88	115
57.5	138	58.34	124	59.18	134	60.02	165	60.86	141	61.7	204	62.54	171	63.38	139	64.22	167	65.06	155	65.9	135
57.52	143	58.36	136	59.2	132	60.04	128	60.88	134	61.72	190	62.56	174	63.4	141	64.24	198	65.08	162	65.92	146
57.54	119	58.38	132	59.22	144	60.06	126	60.9	132	61.74	162	62.58	178	63.42	159	64.26	161	65.1	132	65.94	149
57.56	135	58.4	151	59.24	159	60.08	108	60.92	128	61.76	171	62.6	170	63.44	102	64.28	144	65.12	149	65.96	178
57.58	118	58.42	149	59.26	155	60.1	144	60.94	145	61.78	176	62.62	167	63.46	139	64.3	190	65.14	170	65.98	141
57.6	131	58.44	136	59.28	153	60.12	131	60.96	134	61.8	170	62.64	180	63.48	170	64.32	167	65.16	134	66	138
57.62	109	58.46	146	59.3	131	60.14	115	60.98	135	61.82	163	62.66	160	63.5	145	64.34	168	65.18	183	66.02	145
57.64	110	58.48	121	59.32	150	60.16	155	61	155	61.84	203	62.68	155	63.52	152	64.36	148	65.2	167	66.04	163
57.66	130	58.5	134	59.34	141	60.18	138	61.02	143	61.86	173	62.7	150	63.54	151	64.38	159	65.22	141	66.06	144
57.68	128	58.52	138	59.36	137	60.2	147	61.04	148	61.88	159	62.72	146	63.56	162	64.4	157	65.24	146	66.08	133
57.7	135	58.54	138	59.38	153	60.22	186	61.06	142	61.9	156	62.74	145	63.58	151	64.42	149	65.26	132	66.1	159
57.72	142	58.56	144	59.4	134	60.24	119	61.08	131	61.92	178	62.76	177	63.6	159	64.44	190	65.28	154	66.12	152
57.74	123	58.58	158	59.42	138	60.26	132	61.1	166	61.94	174	62.78	151	63.62	147	64.46	147	65.3	158	66.14	138
57.76	124	58.6	134	59.44	133	60.28	138	61.12	123	61.96	184	62.8	149	63.64	140	64.48	168	65.32	155	66.16	152
57.78	147	58.62	142	59.46	129	60.3	131	61.14	126	61.98	175	62.82	172	63.66	152	64.5	171	65.34	155	66.18	144

Angle	R.Int	Angle	R.Int	Angle	R.Int	Angle	R.Int	Angle	R.Int	Angle	R.Int	Angle	R.Int	Angle	R.Int	Angle	R.Int	Angle	R.Int	Angle	R.Int
66.2	150	67.04	149	67.88	157	68.72	139	69.56	161	70.4	125	71.24	129	72.08	128	72.92	138	73.76	151	74.6	151
66.22	151	67.06	139	67.9	136	68.74	173	69.58	153	70.42	133	71.26	154	72.1	134	72.94	158	73.78	142	74.62	132
66.24	133	67.08	143	67.92	171	68.76	158	69.6	137	70.44	146	71.28	124	72.12	138	72.96	144	73.8	148	74.64	154
66.26	139	67.1	148	67.94	168	68.78	137	69.62	149	70.46	127	71.3	113	72.14	141	72.98	139	73.82	166	74.66	138
66.28	137	67.12	117	67.96	168	68.8	160	69.64	139	70.48	109	71.32	142	72.16	134	73	154	73.84	143	74.68	154
66.3	171	67.14	132	67.98	167	68.82	161	69.66	143	70.5	118	71.34	121	72.18	140	73.02	150	73.86	125	74.7	142
66.32	114	67.16	140	68	136	68.84	168	69.68	155	70.52	132	71.36	145	72.2	147	73.04	156	73.88	159	74.72	169
66.34	144	67.18	118	68.02	160	68.86	159	69.7	159	70.54	126	71.38	113	72.22	126	73.06	139	73.9	172	74.74	163
66.36	156	67.2	153	68.04	150	68.88	150	69.72	143	70.56	140	71.4	119	72.24	126	73.08	148	73.92	167	74.76	150
66.38	145	67.22	173	68.06	142	68.9	161	69.74	158	70.58	128	71.42	137	72.26	135	73.1	149	73.94	160	74.78	141
66.4	143	67.24	148	68.08	146	68.92	140	69.76	133	70.6	134	71.44	107	72.28	126	73.12	136	73.96	165	74.8	123
66.42	146	67.26	140	68.1	179	68.94	166	69.78	118	70.62	124	71.46	111	72.3	113	73.14	160	73.98	144	74.82	143
66.44	156	67.28	151	68.12	146	68.96	141	69.8	132	70.64	117	71.48	132	72.32	138	73.16	145	74	140	74.84	159
66.46	131	67.3	149	68.14	145	68.98	176	69.82	142	70.66	99	71.5	134	72.34	136	73.18	122	74.02	147	74.86	150
66.48	136	67.32	146	68.16	153	69	156	69.84	123	70.68	104	71.52	119	72.36	141	73.2	144	74.04	157	74.88	163
66.5	134	67.34	164	68.18	165	69.02	171	69.86	138	70.7	138	71.54	122	72.38	124	73.22	136	74.06	122	74.9	156
66.52	135	67.36	170	68.2	178	69.04	198	69.88	129	70.72	120	71.56	142	72.4	137	73.24	120	74.08	134	74.92	141
66.54	134	67.38	158	68.22	165	69.06	161	69.9	147	70.74	127	71.58	117	72.42	131	73.26	167	74.1	160	74.94	146
66.56	148	67.4	152	68.24	144	69.08	164	69.92	127	70.76	129	71.6	131	72.44	105	73.28	125	74.12	123	74.96	161
66.58	135	67.42	160	68.26	164	69.1	167	69.94	123	70.78	112	71.62	129	72.46	123	73.3	156	74.14	154	74.98	156
66.6	126	67.44	160	68.28	159	69.12	150	69.96	144	70.8	130	71.64	135	72.48	127	73.32	133	74.16	134	75	156
66.62	158	67.46	158	68.3	182	69.14	155	69.98	156	70.82	116	71.66	122	72.5	137	73.34	131	74.18	148	75.02	150
66.64	145	67.48	131	68.32	163	69.16	154	70	139	70.84	139	71.68	151	72.52	127	73.36	161	74.2	159	75.04	137
66.66	156	67.5	148	68.34	147	69.18	157	70.02	124	70.86	126	71.7	134	72.54	133	73.38	144	74.22	146	75.06	144
66.68	140	67.52	144	68.36	135	69.2	161	70.04	159	70.88	120	71.72	146	72.56	135	73.4	156	74.24	142	75.08	145
66.7	138	67.54	143	68.38	162	69.22	177	70.06	133	70.9	122	71.74	150	72.58	145	73.42	131	74.26	150	75.1	158
66.72	140	67.56	141	68.4	134	69.24	172	70.08	143	70.92	136	71.76	126	72.6	125	73.44	149	74.28	119	75.12	170
66.74	144	67.58	160	68.42	174	69.26	167	70.1	138	70.94	137	71.78	124	72.62	133	73.46	145	74.3	157	75.14	120
66.76	138	67.6	156	68.44	148	69.28	140	70.12	141	70.96	126	71.8	133	72.64	132	73.48	139	74.32	116	75.16	140
66.78	137	67.62	146	68.46	146	69.3	161	70.14	115	70.98	128	71.82	135	72.66	133	73.5	140	74.34	140	75.18	159
66.8	152	67.64	138	68.48	148	69.32	177	70.16	133	71	126	71.84	122	72.68	125	73.52	142	74.36	133	75.2	157
66.82	143	67.66	179	68.5	152	69.34	162	70.18	131	71.02	139	71.86	136	72.7	134	73.54	130	74.38	129	75.22	146
66.84	134	67.68	183	68.52	173	69.36	155	70.2	135	71.04	126	71.88	116	72.72	137	73.56	162	74.4	148	75.24	152
66.86	130	67.7	146	68.54	161	69.38	148	70.22	126	71.06	117	71.9	143	72.74	130	73.58	179	74.42	146	75.26	142
66.88	173	67.72	156	68.56	175	69.4	182	70.24	102	71.08	135	71.92	153	72.76	142	73.6	144	74.44	141	75.28	147
66.9	152	67.74	149	68.58	148	69.42	155	70.26	123	71.1	139	71.94	143	72.78	145	73.62	155	74.46	141	75.3	152
66.92	143	67.76	160	68.6	140	69.44	141	70.28	111	71.12	118	71.96	131	72.8	143	73.64	140	74.48	130	75.32	131
66.94	144	67.78	159	68.62	170	69.46	157	70.3	132	71.14	112	71.98	142	72.82	129	73.66	135	74.5	131	75.34	146
66.96	130	67.8	161	68.64	147	69.48	149	70.32	139	71.16	123	72	137	72.84	128	73.68	147	74.52	144	75.36	130
66.98	122	67.82	158	68.66	149	69.5	155	70.34	139	71.18	121	72.02	143	72.86	132	73.7	138	74.54	143	75.38	158
67	136	67.84	154	68.68	138	69.52	133	70.36	117	71.2	114	72.04	113	72.88	126	73.72	127	74.56	163	75.4	138
67.02	141	67.86	132	68.7	137	69.54	144	70.38	139	71.22	123	72.06	125	72.9	137	73.74	157	74.58	157	75.42	142

Angle	R.Int	Angle	R.Int	Angle	R.Int	Angle	R.Int	Angle	R.Int	Angle	R.Int
75.44	137	76.28	132	77.12	155	77.96	136	78.8	124	79.64	128
75.46	148	76.3	124	77.14	120	77.98	157	78.82	152	79.66	122
75.48	147	76.32	132	77.16	128	78	163	78.84	118	79.68	118
75.5	147	76.34	138	77.18	141	78.02	139	78.86	121	79.7	154
75.52	177	76.36	119	77.2	139	78.04	117	78.88	116	79.72	128
75.54	153	76.38	135	77.22	151	78.06	122	78.9	141	79.74	128
75.56	153	76.4	136	77.24	119	78.08	139	78.92	121	79.76	137
75.58	140	76.42	120	77.26	103	78.1	156	78.94	126	79.78	123
75.6	128	76.44	129	77.28	131	78.12	119	78.96	138	79.8	130
75.62	147	76.46	128	77.3	140	78.14	103	78.98	105	79.82	162
75.64	161	76.48	125	77.32	105	78.16	116	79	132	79.84	143
75.66	149	76.5	156	77.34	118	78.18	138	79.02	139	79.86	121
75.68	159	76.52	145	77.36	137	78.2	124	79.04	134	79.88	144
75.7	156	76.54	130	77.38	138	78.22	132	79.06	144	79.9	135
75.72	144	76.56	138	77.4	141	78.24	158	79.08	128	79.92	131
75.74	157	76.58	138	77.42	131	78.26	135	79.1	127	79.94	131
75.76	153	76.6	122	77.44	129	78.28	121	79.12	129	79.96	129
75.78	160	76.62	127	77.46	133	78.3	126	79.14	128	79.98	134
75.8	142	76.64	126	77.48	126	78.32	121	79.16	103	80	124
75.82	130	76.66	139	77.5	117	78.34	137	79.18	125		
75.84	135	76.68	143	77.52	112	78.36	117	79.2	104		
75.86	151	76.7	125	77.54	140	78.38	116	79.22	128		
75.88	144	76.72	121	77.56	127	78.4	134	79.24	124		
75.9	153	76.74	125	77.58	139	78.42	144	79.26	127		
75.92	135	76.76	114	77.6	120	78.44	143	79.28	137		
75.94	129	76.78	119	77.62	124	78.46	134	79.3	138		
75.96	134	76.8	114	77.64	141	78.48	125	79.32	131		
75.98	166	76.82	122	77.66	127	78.5	128	79.34	136		
76	154	76.84	132	77.68	115	78.52	138	79.36	124		
76.02	125	76.86	113	77.7	140	78.54	140	79.38	129		
76.04	140	76.88	134	77.72	133	78.56	134	79.4	157		
76.06	119	76.9	117	77.74	126	78.58	121	79.42	103		
76.08	145	76.92	133	77.76	129	78.6	137	79.44	124		
76.1	130	76.94	152	77.78	153	78.62	131	79.46	120		
76.12	132	76.96	131	77.8	138	78.64	118	79.48	114		
76.14	144	76.98	143	77.82	143	78.66	144	79.5	126		
76.16	159	77	140	77.84	129	78.68	139	79.52	148		
76.18	121	77.02	141	77.86	128	78.7	126	79.54	110		
76.2	132	77.04	110	77.88	115	78.72	117	79.56	153		
76.22	131	77.06	134	77.9	116	78.74	138	79.58	115		
76.24	143	77.08	144	77.92	146	78.76	150	79.6	139		
76.26	155	77.1	139	77.94	145	78.78	125	79.62	144		

Punta di Levante lava dome

Angle	R.Int	Angle	R.Int	Angle	R.Int	Angle	R.Int	Angle	R.Int	Angle	R.Int	Angle	R.Int	Angle	R.Int	Angle	R.Int	Angle	R.Int
20	232	22.05	208	24.1	177	26.15	177	28.2	175	30.25	164	32.3	125	34.35	120	36.4	106	38.45	106	40.5	91
20.05	215	22.1	208	24.15	187	26.2	174	28.25	166	30.3	168	32.35	134	34.4	118	36.45	102	38.5	97	40.55	71
20.1	240	22.15	210	24.2	185	26.25	148	28.3	149	30.35	170	32.4	146	34.45	130	36.5	100	38.55	98	40.6	68
20.15	231	22.2	195	24.25	170	26.3	167	28.35	159	30.4	167	32.45	140	34.5	144	36.55	94	38.6	96	40.65	96
20.2	228	22.25	203	24.3	185	26.35	186	28.4	157	30.45	150	32.5	127	34.55	132	36.6	98	38.65	92	40.7	108
20.25	210	22.3	168	24.35	158	26.4	170	28.45	188	30.5	156	32.55	138	34.6	129	36.65	106	38.7	101	40.75	92
20.3	230	22.35	201	24.4	155	26.45	165	28.5	165	30.55	199	32.6	136	34.65	120	36.7	117	38.75	98	40.8	108
20.35	188	22.4	199	24.45	198	26.5	159	28.55	159	30.6	167	32.65	167	34.7	124	36.75	89	38.8	95	40.85	98
20.4	238	22.45	203	24.5	162	26.55	186	28.6	156	30.65	153	32.7	133	34.75	148	36.8	87	38.85	119	40.9	104
20.45	212	22.5	206	24.55	175	26.6	184	28.65	162	30.7	163	32.75	126	34.8	134	36.85	107	38.9	108	40.95	88
20.5	237	22.55	202	24.6	180	26.65	193	28.7	187	30.75	159	32.8	123	34.85	149	36.9	114	38.95	108	41	86
20.55	219	22.6	199	24.65	187	26.7	169	28.75	168	30.8	157	32.85	143	34.9	112	36.95	100	39	109	41.05	97
20.6	217	22.65	178	24.7	193	26.75	202	28.8	154	30.85	185	32.9	136	34.95	144	37	97	39.05	97	41.1	101
20.65	212	22.7	239	24.75	171	26.8	199	28.85	142	30.9	157	32.95	133	35	142	37.05	100	39.1	96	41.15	105
20.7	224	22.75	187	24.8	169	26.85	187	28.9	169	30.95	169	33	138	35.05	132	37.1	89	39.15	98	41.2	102
20.75	230	22.8	207	24.85	182	26.9	205	28.95	159	31	166	33.05	153	35.1	117	37.15	98	39.2	96	41.25	107
20.8	227	22.85	205	24.9	160	26.95	182	29	157	31.05	127	33.1	151	35.15	121	37.2	125	39.25	97	41.3	82
20.85	205	22.9	212	24.95	172	27	203	29.05	156	31.1	166	33.15	121	35.2	118	37.25	103	39.3	93	41.35	94
20.9	244	22.95	181	25	169	27.05	231	29.1	163	31.15	135	33.2	119	35.25	146	37.3	107	39.35	98	41.4	106
20.95	247	23	179	25.05	185	27.1	239	29.15	150	31.2	185	33.25	142	35.3	155	37.35	125	39.4	95	41.45	98
21	233	23.05	216	25.1	156	27.15	230	29.2	147	31.25	154	33.3	126	35.35	115	37.4	123	39.45	89	41.5	114
21.05	251	23.1	209	25.15	142	27.2	228	29.25	152	31.3	164	33.35	127	35.4	132	37.45	120	39.5	101	41.55	96
21.1	233	23.15	215	25.2	171	27.25	270	29.3	164	31.35	144	33.4	124	35.45	125	37.5	87	39.55	85	41.6	94
21.15	248	23.2	212	25.25	172	27.3	269	29.35	157	31.4	142	33.45	127	35.5	120	37.55	109	39.6	77	41.65	106
21.2	246	23.25	201	25.3	162	27.35	303	29.4	148	31.45	159	33.5	125	35.55	128	37.6	106	39.65	90	41.7	110
21.25	240	23.3	248	25.35	183	27.4	300	29.45	168	31.5	149	33.55	126	35.6	126	37.65	73	39.7	112	41.75	87
21.3	263	23.35	210	25.4	181	27.45	313	29.5	175	31.55	154	33.6	114	35.65	132	37.7	106	39.75	104	41.8	84
21.35	228	23.4	217	25.45	195	27.5	296	29.55	182	31.6	151	33.65	121	35.7	127	37.75	112	39.8	102	41.85	84
21.4	225	23.45	237	25.5	185	27.55	301	29.6	180	31.65	135	33.7	125	35.75	119	37.8	96	39.85	95	41.9	92
21.45	235	23.5	234	25.55	190	27.6	313	29.65	199	31.7	147	33.75	133	35.8	116	37.85	121	39.9	82	41.95	104
21.5	260	23.55	203	25.6	187	27.65	294	29.7	189	31.75	142	33.8	131	35.85	120	37.9	113	39.95	97	42	86
21.55	275	23.6	201	25.65	185	27.7	302	29.75	168	31.8	149	33.85	125	35.9	128	37.95	107	40	94	42.05	96
21.6	273	23.65	192	25.7	210	27.75	237	29.8	165	31.85	145	33.9	116	35.95	111	38	105	40.05	66	42.1	87
21.65	277	23.7	181	25.75	172	27.8	235	29.85	172	31.9	147	33.95	123	36	95	38.05	115	40.1	92	42.15	107
21.7	287	23.75	224	25.8	187	27.85	218	29.9	169	31.95	147	34	120	36.05	110	38.1	115	40.15	85	42.2	105
21.75	304	23.8	221	25.85	150	27.9	214	29.95	162	32	145	34.05	115	36.1	111	38.15	95	40.2	65	42.25	102
21.8	302	23.85	171	25.9	152	27.95	177	30	175	32.05	162	34.1	116	36.15	108	38.2	92	40.25	102	42.3	84
21.85	257	23.9	190	25.95	156	28	174	30.05	181	32.1	145	34.15	113	36.2	106	38.25	87	40.3	85	42.35	102
21.9	247	23.95	204	26	154	28.05	169	30.1	172	32.15	139	34.2	117	36.25	117	38.3	89	40.35	88	42.4	99
21.95	206	24	179	26.05	160	28.1	188	30.15	157	32.2	136	34.25	135	36.3	107	38.35	102	40.4	86	42.45	92
22	203	24.05	193	26.1	185	28.15	175	30.2	155	32.25	130	34.3	149	36.35	109	38.4	97	40.45	104	42.5	97

Angle	R.Int	Angle	R.Int	Angle	R.Int	Angle	R.Int	Angle	R.Int	Angle	R.Int	Angle	R.Int	Angle	R.Int	Angle	R.Int	Angle	R.Int
42.55	97	44.6	84	46.65	86	48.7	85	50.75	104	52.8	76	54.85	82	56.9	69	58.95	78	61	54	63.05	75
42.6	89	44.65	95	46.7	82	48.75	100	50.8	101	52.85	79	54.9	83	56.95	63	59	76	61.05	72	63.1	70
42.65	100	44.7	87	46.75	95	48.8	98	50.85	92	52.9	72	54.95	75	57	75	59.05	80	61.1	79	63.15	69
42.7	99	44.75	75	46.8	91	48.85	93	50.9	101	52.95	71	55	72	57.05	83	59.1	83	61.15	71	63.2	67
42.75	95	44.8	72	46.85	90	48.9	86	50.95	105	53	69	55.05	74	57.1	74	59.15	67	61.2	93	63.25	85
42.8	93	44.85	81	46.9	89	48.95	73	51	104	53.05	73	55.1	73	57.15	86	59.2	64	61.25	84	63.3	87
42.85	84	44.9	74	46.95	84	49	70	51.05	97	53.1	93	55.15	66	57.2	84	59.25	66	61.3	87	63.35	91
42.9	91	44.95	86	47	82	49.05	64	51.1	100	53.15	94	55.2	65	57.25	88	59.3	88	61.35	88	63.4	88
42.95	93	45	97	47.05	90	49.1	92	51.15	79	53.2	91	55.25	87	57.3	70	59.35	67	61.4	86	63.45	73
43	90	45.05	81	47.1	85	49.15	81	51.2	77	53.25	75	55.3	65	57.35	76	59.4	78	61.45	79	63.5	75
43.05	96	45.1	89	47.15	87	49.2	84	51.25	81	53.3	82	55.35	75	57.4	73	59.45	91	61.5	78	63.55	83
43.1	78	45.15	77	47.2	84	49.25	97	51.3	75	53.35	92	55.4	73	57.45	65	59.5	75	61.55	86	63.6	69
43.15	82	45.2	75	47.25	85	49.3	93	51.35	74	53.4	74	55.45	64	57.5	77	59.55	74	61.6	83	63.65	80
43.2	83	45.25	102	47.3	81	49.35	106	51.4	71	53.45	84	55.5	74	57.55	80	59.6	72	61.65	82	63.7	75
43.25	82	45.3	80	47.35	80	49.4	104	51.45	60	53.5	73	55.55	69	57.6	74	59.65	78	61.7	73	63.75	65
43.3	79	45.35	91	47.4	80	49.45	85	51.5	82	53.55	66	55.6	66	57.65	78	59.7	67	61.75	80	63.8	63
43.35	90	45.4	88	47.45	94	49.5	80	51.55	76	53.6	64	55.65	59	57.7	63	59.75	69	61.8	91	63.85	88
43.4	88	45.45	73	47.5	65	49.55	78	51.6	70	53.65	87	55.7	72	57.75	69	59.8	66	61.85	96	63.9	64
43.45	84	45.5	82	47.55	74	49.6	75	51.65	74	53.7	85	55.75	80	57.8	67	59.85	60	61.9	97	63.95	80
43.5	78	45.55	74	47.6	72	49.65	74	51.7	90	53.75	80	55.8	78	57.85	91	59.9	62	61.95	79	64	77
43.55	83	45.6	89	47.65	89	49.7	81	51.75	77	53.8	77	55.85	72	57.9	66	59.95	77	62	77	64.05	67
43.6	80	45.65	75	47.7	67	49.75	73	51.8	75	53.85	60	55.9	76	57.95	76	60	73	62.05	77	64.1	87
43.65	74	45.7	76	47.75	85	49.8	80	51.85	93	53.9	80	55.95	74	58	73	60.05	76	62.1	93	64.15	76
43.7	101	45.75	101	47.8	82	49.85	84	51.9	81	53.95	66	56	72	58.05	65	60.1	62	62.15	79	64.2	75
43.75	83	45.8	99	47.85	58	49.9	91	51.95	72	54	69	56.05	76	58.1	76	60.15	96	62.2	76	64.25	74
43.8	105	45.85	84	47.9	71	49.95	82	52	69	54.05	95	56.1	80	58.15	82	60.2	94	62.25	78	64.3	70
43.85	76	45.9	89	47.95	71	50	80	52.05	65	54.1	84	56.15	87	58.2	76	60.25	75	62.3	78	64.35	73
43.9	78	45.95	94	48	75	50.05	89	52.1	73	54.15	82	56.2	84	58.25	85	60.3	74	62.35	88	64.4	71
43.95	92	46	91	48.05	98	50.1	74	52.15	66	54.2	80	56.25	75	58.3	61	60.35	69	62.4	72	64.45	94
44	90	46.05	84	48.1	88	50.15	101	52.2	78	54.25	90	56.3	72	58.35	84	60.4	66	62.45	82	64.5	61
44.05	90	46.1	93	48.15	85	50.2	98	52.25	72	54.3	77	56.35	83	58.4	82	60.45	63	62.5	82	64.55	71
44.1	98	46.15	88	48.2	83	50.25	86	52.3	91	54.35	67	56.4	84	58.45	73	60.5	77	62.55	75	64.6	68
44.15	77	46.2	59	48.25	91	50.3	87	52.35	73	54.4	64	56.45	84	58.5	60	60.55	71	62.6	73	64.65	85
44.2	74	46.25	98	48.3	85	50.35	79	52.4	71	54.45	72	56.5	69	58.55	74	60.6	72	62.65	87	64.7	79
44.25	100	46.3	101	48.35	95	50.4	93	52.45	71	54.5	72	56.55	70	58.6	71	60.65	73	62.7	88	64.75	68
44.3	91	46.35	79	48.4	92	50.45	82	52.5	96	54.55	74	56.6	68	58.65	66	60.7	83	62.75	80	64.8	89
44.35	93	46.4	77	48.45	80	50.5	96	52.55	78	54.6	78	56.65	97	58.7	77	60.75	70	62.8	77	64.85	78
44.4	95	46.45	96	48.5	77	50.55	94	52.6	75	54.65	79	56.7	86	58.75	75	60.8	68	62.85	73	64.9	82
44.45	98	46.5	89	48.55	92	50.6	92	52.65	67	54.7	78	56.75	83	58.8	58	60.85	79	62.9	60	64.95	75
44.5	99	46.55	79	48.6	78	50.65	108	52.7	71	54.75	70	56.8	80	58.85	102	60.9	70	62.95	71	65	73
44.55	86	46.6	76	48.65	81	50.7	104	52.75	86	54.8	68	56.85	82	58.9	76	60.95	57	63	63	65.05	71

Angle	R.Int	Angle	R.Int	Angle	R.Int	Angle	R.Int	Angle	R.Int	Angle	R.Int	Angle	R.Int
65.1	87	67.3	80	69.5	70	71.7	68	73.9	71	76.1	71	78.3	75
65.15	80	67.35	84	69.55	75	71.75	73	73.95	88	76.15	87	78.35	70
65.2	77	67.4	82	69.6	83	71.8	67	74	86	76.2	69	78.4	71
65.25	83	67.45	77	69.65	80	71.85	91	74.05	93	76.25	81	78.45	59
65.3	75	67.5	77	69.7	58	71.9	74	74.1	68	76.3	79	78.5	69
65.35	71	67.55	72	69.75	65	71.95	72	74.15	65	76.35	77	78.55	68
65.4	79	67.6	69	69.8	63	72	70	74.2	62	76.4	71	78.6	75
65.45	72	67.65	93	69.85	78	72.05	83	74.25	82	76.45	72	78.65	73
65.5	74	67.7	63	69.9	59	72.1	71	74.3	59	76.5	81	78.7	88
65.55	84	67.75	88	69.95	72	72.15	73	74.35	76	76.55	62	78.75	67
65.6	82	67.8	71	70	70	72.2	76	74.4	73	76.6	62	78.8	65
65.65	72	67.85	56	70.05	76	72.25	84	74.45	70	76.65	62	78.85	78
65.7	87	67.9	75	70.1	76	72.3	79	74.5	94	76.7	77	78.9	70
65.75	77	67.95	85	70.15	72	72.35	104	74.55	85	76.75	77	78.95	68
65.8	74	68	83	70.2	69	72.4	81	74.6	65	76.8	67	79	67
65.85	60	68.05	86	70.25	67	72.45	88	74.65	77	76.85	70	79.05	71
65.9	94	68.1	81	70.3	66	72.5	84	74.7	75	76.9	77	79.1	69
65.95	63	68.15	75	70.35	69	72.55	70	74.75	78	76.95	57	79.15	75
66	80	68.2	72	70.4	66	72.6	72	74.8	77	77	65	79.2	79
66.05	81	68.25	63	70.45	67	72.65	77	74.85	84	77.05	67	79.25	77
66.1	91	68.3	72	70.5	62	72.7	62	74.9	88	77.1	64	79.3	78
66.15	70	68.35	62	70.55	68	72.75	92	74.95	98	77.15	77	79.35	77
66.2	68	68.4	75	70.6	94	72.8	67	75	77	77.2	70	79.4	75
66.25	79	68.45	66	70.65	63	72.85	82	75.05	73	77.25	81	79.45	75
66.3	85	68.5	87	70.7	61	72.9	86	75.1	83	77.3	74	79.5	79
66.35	73	68.55	69	70.75	96	72.95	81	75.15	87	77.35	79	79.55	83
66.4	70	68.6	67	70.8	65	73	71	75.2	63	77.4	74	79.6	80
66.45	69	68.65	87	70.85	55	73.05	68	75.25	77	77.45	71	79.65	63
66.5	60	68.7	73	70.9	65	73.1	59	75.3	76	77.5	64	79.7	69
66.55	74	68.75	65	70.95	67	73.15	74	75.35	78	77.55	59	79.75	68
66.6	72	68.8	62	71	66	73.2	82	75.4	76	77.6	65	79.8	49
66.65	71	68.85	73	71.05	76	73.25	69	75.45	62	77.65	53	79.85	58
66.7	72	68.9	69	71.1	66	73.3	84	75.5	73	77.7	76	79.9	76
66.75	81	68.95	64	71.15	78	73.35	78	75.55	74	77.75	77	79.95	66
66.8	79	69	74	71.2	76	73.4	76	75.6	71	77.8	70	80	52
66.85	73	69.05	78	71.25	81	73.45	81	75.65	73	77.85	68		
66.9	72	69.1	80	71.3	79	73.5	74	75.7	63	77.9	60		
66.95	77	69.15	73	71.35	77	73.55	69	75.75	91	77.95	60		
67	74	69.2	81	71.4	80	73.6	66	75.8	87	78	80		
67.05	58	69.25	83	71.45	76	73.65	87	75.85	75	78.05	79		
67.1	64	69.3	81	71.5	73	73.7	79	75.9	93	78.1	71		
67.15	77	69.35	95	71.55	66	73.75	57	75.95	66	78.15	72		
67.2	82	69.4	82	71.6	70	73.8	72	76	60	78.2	60		
67.25	102	69.45	73	71.65	50	73.85	89	76.05	73	78.25	76		

Appendix IX – Examples of published x-ray diffraction responses

Orthoclase (American Mineralogist Crystal Structure Database Record)

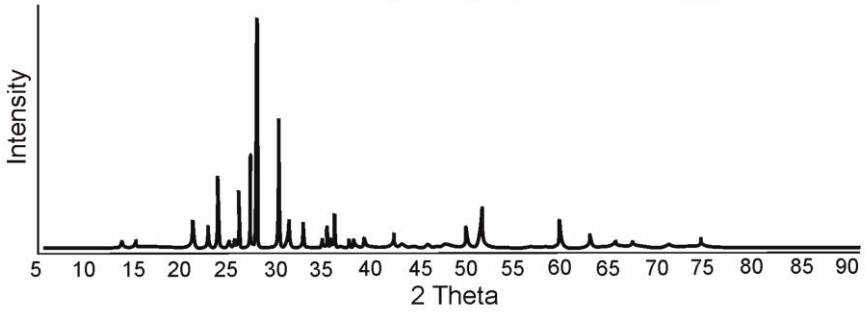

Cristobalite (American Mineralogist Crystal Structure Database Record)

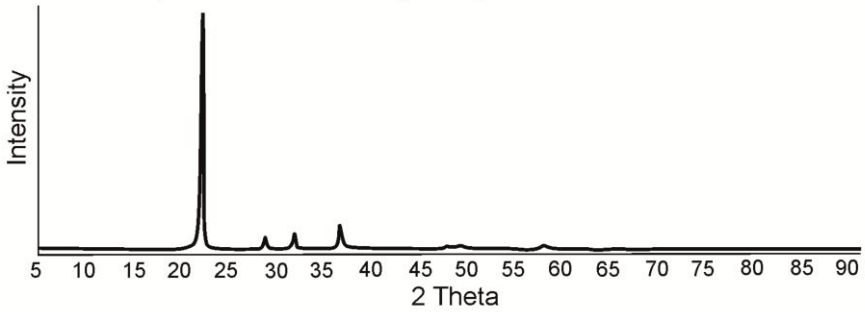

Diopside (American Mineralogist Crystal Structure Database Record)

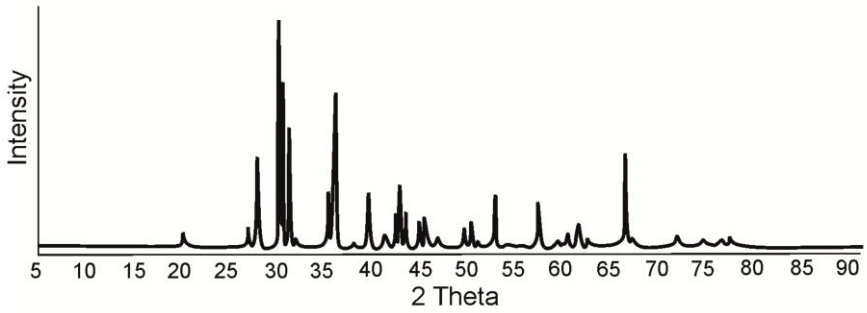

Quartz (American Mineralogist Crystal Structure Database Record)

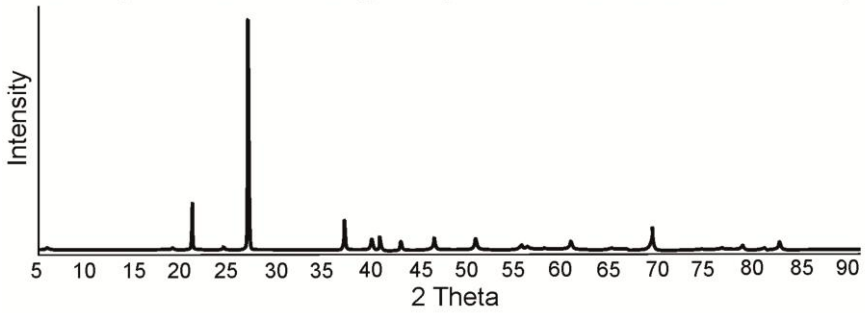

Magnetite (American Mineralogist Crystal Structure Database Record)